

# **Tailoring Siloxane Functionality for Lithography-based 3D Printing**

Justin M. Serrine

Dissertation submitted to the faculty of the Virginia Polytechnic Institute and State  
University in partial fulfillment of the requirements for the degree of

Doctor of Philosophy  
In  
Macromolecular Science and Engineering

Timothy E. Long, Chair  
Shengfeng Cheng  
Richey M. Davis  
Robert B. Moore  
Christopher B. Williams

June 19<sup>th</sup>, 2018  
Blacksburg, VA

Keywords: polysiloxanes, polyamides, hydrogen bonding, additive manufacturing, vat  
photopolymerization

Copyright 2018 Justin M. Serrine

# **Tailoring Siloxane Functionality for Lithography-based 3D Printing**

Justin M. Serrine

## **ABSTRACT**

Polymer synthesis and functionalization enabled the tailoring of polymer functionality for additive manufacturing (AM), elastomer, and biological applications. Inspiration from academic and patent literature prompted an emphasis on polymer functionality and its implications on diverse applications. Critical analysis of existing elastomers for AM aided the synthesis and characterization of novel photopolymer systems for lithography-based 3D printing. Emphasis on structure-processing-property relationships facilitated the attainment of success in proposed applications and prompted further fundamental understanding for systems that leveraged poly(dimethyl siloxane)s (PDMS), aliphatic polyesters, polyamides, and polyethers for emerging applications.

The thiol-ene reaction possesses many desirable traits for vat photopolymerization (VP) AM, namely that it proceeds rapidly to high yield, does not undergo significant side reactions, remains tolerant of the presence of water or oxygen, and remains regiospecific. Leveraging these traits, a novel PDMS-based photopolymer system was synthesized and designed that underwent simultaneous chain extension and crosslinking, affording relatively low viscosity prior to photocuring but the modulus and tensile strain at break properties of higher molecular weight precursors upon photocuring. A monomeric competition study confirmed chemical preference for the chain-extension reaction in the absence of diffusion. Photocalorimetry, photorheology, and soxhlet extraction measured photocuring kinetics and demonstrated high gel fractions upon photocuring. A further

improvement on the low-temperature elastomeric behavior occurred *via* introduction of a small amount of diphenylsiloxane or diethylsiloxane repeating units, which successfully suppressed crystallization and extended the rubbery plateau close to the glass transition temperature ( $T_g$ ) for these elastomers. Finally, a melt polymerization of PDMS diamines in the presence of a disiloxane diamine chain extender and urea afforded isocyanate-free polyureas in the absence of solvent and catalyst. Dynamic mechanical analysis (DMA) measured multiple, distinct  $\alpha$ -relaxations that suggested microphase separation. This work leverages the unique properties of PDMS and provides multiple chemistries that achieve elastomeric properties for a variety of applications.

Similar work of new polymers for VP AM was performed that leveraged the low  $T_g$  poly(propylene glycol) (PPG) and poly(tri(ethylene glycol) adipate) (PTEGA) for use in tissue scaffolding, footwear, and improved glove grip performance applications. The double endcapping of a PPG diamine with a diisocyanate and then hydroxyethyl acrylate provided a urethane/urea-containing, photocurable oligomer. Supercritical fluid chromatography with evaporative light scattering detection elucidated oligomer molecular weight distributions with repeat unit resolution, while the combination of these PPG-containing oligomers with various reactive diluents prior to photocuring yielded highly tunable and efficiently crosslinked networks with wide-ranging thermomechanical properties. Functionalization of the PTEGA diol with isocyanatoethyl methacrylate yielded a photocurable polyester for tissue scaffolding applications without the production of acidic byproducts that might induce polymer backbone scission. Initial VP AM, cell viability experiments, and modulus measurements indicate promise for use of these PTEGA oligomers for the 3D production of vascularized tissue scaffolds.

Similar review of powder bed fusion (PBF) patent literature revealed a polyamide 12 (PA12) composition that remained melt stable during PBF processing, unlike alternative commercial products. Further investigation revealed a fundamental difference in polymer backbone and endgroup chemical structure between these products, yielding profound differences for powder recyclability after printing. An anionic dispersion polymerization of laurolactam in the presence of a steric stabilizer and initiator yielded PA12 microparticles with high sphericity directly from the polymerization without significant post-processing requirements. Steric stabilizer concentration and stirring rate remained the most important variables for the control of PA12 powder particle size and melt viscosity. Finally, preliminary fusion of single-layered PA12 structures demonstrated promise and provided insight into powder particle size and melt viscosity requirements.

# Tailoring Siloxane Functionality for Lithography-based 3D Printing

Justin M. Serrine

## GENERAL AUDIENCE ABSTRACT

Additive manufacturing (AM) enables the creation of unique geometries not accessible with alternative manufacturing techniques such as injection molding, while also reducing the waste associated with subtractive manufacturing (e.g. machining). However, AM currently suffers from a lack of commercially-available polymers that provide elastomeric properties after processing. Poly(dimethyl siloxane)s (PDMS) possess distinctive properties due to their organosilicon polymer backbone that include chemical inertness, non-flammability, high gas permeability, and low surface energy. For these reasons, siloxanes enjoy wide-ranging applications from personal care products, contact lenses, elastomeric sealants, and medical devices. This dissertation focuses on the synthesis and functionalization of novel PDMS-, polyether-, polyester-, and polyamide-containing photopolymers or powders for improved performance in diverse applications that employ processing *via* vat photopolymerization (VP) or powder bed fusion (PBF) AM.

Examples from this work include a novel photopolymer composition that undergoes simultaneous chain extension and crosslinking, affording low molecular weight and low viscosity precursors prior to VP-AM but the properties of higher molecular weight precursors, once photocured. Related work involved the characterization and VP-AM of siloxane terpolymers that suppress crystallization normally observed in PDMS, resulting in 3D printed objects that retain their elastomeric properties close to the glass transition temperature ( $T_g$ ). Separate work leveraged the unique PDMS backbone for the melt

polymerization of PDMS diamines in the presence of a chain extender and urea, yielding isocyanate-free PDMS polyureas in the absence of solvent or catalyst. This reaction creates ammonia as the only by-product and avoids the use of isocyanates, as well as their highly toxic precursors, phosgene.

Finally, another research direction facilitates the understanding of observed differences in melt stability between commercially-available grades of polyamide 12 (PA12) powders for powder bed fusion. An anionic dispersion polymerization based in the patent literature facilitated further understanding of the polymerization process and produced melt-stable PA12 microparticles directly from the polymerization process, without requiring additional post-processing grinding or precipitation steps for powder production.

## Acknowledgements

First and foremost, I would like to acknowledge my advisor, Prof. Tim Long, who is a phenomenal advisor and passionate scientist. I am truly grateful for his patience and willingness to accept a materials science & engineering student with no prior organic chemistry experience, into his research group. By knocking his job out of the park, Prof. Long makes ours a little easier. This includes the task of traveling salesman (he could sell ice to eskimos), promoting our research and securing research funding. This provides a massive breadth of instrumentation and consumables to go with it that rivals corporate research labs, which in turn enables great publications. Prof. Long also holds us to an incredibly high standard, which prepares us well for the many opportunities that he provides that include plentiful conference travel (both domestic and international), exciting industrially- and publically-funded projects centered around the Edisonian philosophy of “use-inspired basic research,” internship opportunities, and connections for eventual employment. I will never forget your passion for polymer science and education. I would also like to thank my committee members – Prof. Chris Williams, Prof. Robert Moore, Prof. Richey Davis, and Prof. Shengfeng Cheng – for their time, as well as their thought-provoking suggestions and questions. Thanks also to my class instructors, especially Prof. Padma Rajagopalan, who taught me to read the literature as critically as I perform experiments in the lab.

I must also acknowledge the Long research group, who are a wonderful group of people that provide great scientific advice, mentorship, and friendship. Without all of you, I wouldn't have made nearly as much progress in graduate school. This includes Dr. David Inglefield, Dr. Ashley Nelson, Dr. Chainika Jangu, John Herlihy, Dr. Alie Schultz, Dr.

Evan Margareta, Dr. Keren Zhang, Dr. Joseph Dennis, Dr. Allison Pekkanen, Dr. Mingtao Chen, Ryan Mondschein, Katie Heifferon, Kevin Drummey, Xi Chen, Philip Scott, Tyler White, Emily Wilts, Clay Arrington, Josh Wolfgang, Mark Cashman, Chris Kasprzak, and Ke Cao. I was also extremely fortunate to work with excellent postdocs along the way who challenged me to become a better scientist, including Dr. Nicholas Moon, Dr. Asem Abdulahad, Dr. Jana Herzberger, Dr. Maruti Hegde, Dr. Chixia Tian, Dr. Akanksha Kanitkar, Dr. Donald Aduba, and Dr. Zhiyang Zhang. Kudos to Dr. Bruce Orlor as well for always being willing to answer questions and provide scientific advice, and to Dr. Charles Carfagna, for scientific advice and always keeping the mood light. You are all a wonderful group of people and I will miss you dearly. I would also like to acknowledge the many collaborators I've had along the way – Dr. Mehdi Ashraf-Khorassani, Dr. Petar Dvornic, Alisa Zlatanic, Tyler Grissom, Viswanath Meenakshisundaram, Cam Chatham, Priya Venkatraman, Logan Sturm, Maleshia Jones, and Steve McCartney.

I was also extremely fortunate to work with many talented undergraduate students – Tony Rizk, Hani Mustafa, Tobin Weiseman, and Shantel Schexnayder. I can't wait to hear about all the wonderful things you will be doing! Thanks must also go to the NMR staff at Virginia Tech – Geno Iannaccone, Ken Knott, and Dr. N. Murthy Shanaiah – who were always willing to provide advice and kept the NMRs up and running so well it was hard not to take for granted. I'd also like to thank the administrative staff I've worked with – first and foremost Dr. Kristie Dorfler, as well as Vicki Kaylor, Keith Nunn, Kim Felix, Tammy Jo Hiner, Dr. Tiffany Carpenetti, Laurie Good. Thanks especially to Keith Nunn and Rhoda Ellers for always keeping the building in working order and for their kindness, as well as Brent Bowden for always being the calm in the storm, as well as a great friend,



even looking out for me far beyond when he started his new job. Thanks also to the rest of the MII and ICTAS staff who were always super helpful and a pleasure to work with.

I am also thankful for the many colleagues I was fortunate enough to work with at DuPont, prior to attending graduate school. These folks got me excited about polymer chemistry, and for that I am forever grateful. I'd like to give special thanks to Dr. Ben Messmore for his sense of humor, calm demeanor, and help with navigating the corporate culture; Dr. Andrew Duncan for his patience and constant willingness to teach me polymer chemistry; and Dr. Donna Visioli for her mentorship and assistance with networking throughout the company. I'd also like to thank Dr. Hom Sharma, Dr. Libby Glascoe, and Dr. April Sawvel at Lawrence Livermore National Lab (LLNL) for providing a wonderful learning experience during my internship, as well as the many other researchers I worked with while there.

Lastly and most importantly, I wouldn't be where I am right now without the love and support from my friends and family. I owe everything to my parents, who molded me into the person that I am today, who instilled in me the benefits of hard work and perseverance, and who did (and still do) everything possible to provide me with what I needed to succeed. I must also thank my sisters, Allie and Liz, for their sense of humor, no-BS outlook on life, and for always being there for me. I couldn't be more proud of your success in your respective fields and am so impressed by the people you have become today. I must also acknowledge Karley Wesner, who is the strongest person I know. Finally, I am forever grateful for my girlfriend, Sara Bailey, for her unconditional love, empathy, and support. She is the rock that kept me sane throughout my later years of

graduate school, and I have learned so much from you. I could not have done this without you. I can't wait to continue our journey through life, together. I love you all dearly.

Finally, if I have forgotten you or did not mention you by name, I am sorry! If you helped me, you know who you are, and I am forever in your debt. Like Prof. Long has always said, if you're working by yourself than you're likely not solving a problem of great significance.

### **Attributions**

**Prof. Timothy E. Long** is a professor in the Department of Chemistry and the director of the Macromolecules Innovation Institute (MII). He is the author's research advisor and mentor.

**Prof. Christopher B. Williams** is an associate professor in the Department of Mechanical Engineering and the associate director of MII. He was a collaborator on Chapters 2, 3, 5, 8, 9, and 10.

**Dr. Jana Herzberger** was a postdoctoral scholar in Prof. Long's research group and a collaborator on Chapter 2.

**Dr. Nicholas Moon** was a postdoctoral scholar in Prof. Long's research group and a collaborator on Chapters 3, 4, and 7.

**Dr. Petar Dvornic** is professor of Chemistry and the Chair of the Chemistry department at Pittsburg State University (KS, USA). He was a collaborator on Chapter 5.

**Dr. Joseph M. Dennis** was a graduate student in Prof. Long's research group and a collaborator on Chapter 6.

**Dr. Mehdi Ashraf-Khorassani** is a Research Scientist in the Department of Chemistry at Virginia Tech and a collaborator on Chapter 7.

**Dr. Allison M. Pekkanen** was a graduate student in Prof. Long's research group and a collaborator on Chapter 9.

**Dr. Ashley M. Dustin (Nelson)** was a graduate student in Prof. Long's research group and a collaborator on Chapter 9.

**Viswanath Meenakshisundaram** is a graduate student in Prof. Williams' research group and a collaborator on Chapters 3 and 9.

**Philip J. Scott** is a graduate student in Prof. Long's research group and a collaborator on Chapter 3 and Chapter 4.

**Ryan J. Mondschein** is a graduate student in Prof. Long's research group and a collaborator on Chapters 3, 7, and 9.

**Tobin F. Weiseman** was an undergraduate researcher in Prof. Long's research group and a collaborator on Chapter 3.

**Alisa Zlatanic** is a Scientist at the Kansas Polymer Research Center at Pittsburg State University (KS, USA) and was a collaborator on Chapter 5.

**Shantel A. Schexnayder** was an undergraduate researcher in Prof. Long's research group and a collaborator on Chapter 6.

**Logan D. Sturm** is a graduate student in Prof. Williams' research group and a collaborator on Chapter 8.

**Nicholas A. Chartrain** is a graduate student in Prof. Williams' research group and a collaborator on Chapter 9.

**Camden A. Chatham** is a graduate student in Prof. Williams' research group and a collaborator on Chapter 10.

## Table of Contents

Chapter 1: Introduction.....	1
1.1 Dissertation Overview.....	1
1.2 References .....	3
Chapter 2: New Chemistry for 3D Printing of Elastomers: Synthesis, Characterization, and 3D Printing.....	4
2.1 Introduction .....	4
2.2 Elastomer Properties .....	5
2.3 Overview of 3D Printing techniques.....	7
2.3.1 General Overview .....	7
2.3.2 Vat Photopolymerization .....	7
2.3.3 Fused filament fabrication .....	11
2.3.4 Direct ink writing (DIW) .....	12
2.3.5 Inkjet printing / Material jetting.....	14
2.3.6 Polymer Powder bed fusion.....	15
2.4 Challenges of 3D Printing Elastomers .....	16
2.5 Silicone elastomers – synthesis and properties .....	19
2.5.1 Properties of silicone elastomers .....	19
2.5.2 Synthesis of silicone elastomers .....	20
2.5.3 Traditional processing of silicone elastomers.....	22
2.6 Additive Manufacturing of Elastomeric Architectures using Silicone Precursors	
23	
2.6.1 Motivation.....	23
2.6.2 Direct ink writing.....	23
2.6.3 Two-photon absorption microstereolithography.....	35
2.6.4 Vat photopolymerization/SLA.....	36
2.6.5 Inkjet printing of silicones .....	45
2.7 Polyurethanes .....	46
2.7.1 Chemistry of polyurethanes .....	46
2.7.2 Traditional polyurethane printing in solution (material extrusion, inkjet printing) 49	
2.7.3 Waterborne polyurethane dispersions.....	58
2.8 Photopolymers for vat photopolymerization or inkjet printing.....	68
2.9 Additive manufacturing using polymer emulsions .....	78
2.10 Liquid crystalline elastomers (LCE) .....	80
2.11 Polyesters and Polycarbonates .....	84
2.12 Acknowledgements .....	88

2.13	References .....	88
Chapter 3: Functional Siloxanes with Photo-Activated, Simultaneous Chain Extension and Crosslinking for Lithography-Based 3D Printing .....		
3.1	Abstract .....	100
3.2	Introduction .....	100
3.3	Materials & Methods.....	105
3.3.1	Materials .....	105
3.3.2	Synthesis of acrylamide-terminated poly(dimethyl siloxane) (PDMS-AA) 106	
3.3.3	Synthesis of thiol-terminated poly(dimethyl siloxane) (PDMS-SH).....	107
3.3.4	Preparation of samples for photorheology .....	107
3.3.5	Preparation of samples for Vat Photopolymerization (VPP) Additive Manufacturing (AM) .....	108
3.3.6	Analytical methods .....	108
3.3.7	Vat Photopolymerization .....	109
3.4	Results and Discussion.....	109
3.5	Conclusions .....	124
3.6	Acknowledgements .....	125
3.7	References .....	125
3.8	Supporting Information .....	128
3.8.1	Vat Photopolymerization – Apparatus.....	128
3.8.2	Vat Photopolymerization – Cure Depth and Print Parameters .....	128
3.8.3	Vat Photopolymerization – Specimen Printing.....	129
Chapter 4: Functional Siloxanes with Photo-Activated, Simultaneous Chain Extension and Crosslinking: Chain Extension Dynamics .....		
4.1	Abstract .....	132
4.2	Introduction .....	133
4.3	Materials and Methods.....	135
4.3.1	Materials .....	135
4.3.2	Competition study.....	135
4.3.3	Preparation of thiol-ene product model compound .....	136
4.3.4	Synthesis of acrylamide-terminated poly(dimethyl siloxane) (PDMS-AA) 137	
4.3.5	Synthesis of thiol-terminated poly(dimethyl siloxane) (PDMS-SH).....	137
4.3.6	Pre-extended oligomer preparation.....	138
4.3.7	Preparation of samples for photocalorimetry and photorheology.....	138
4.3.8	Analytical Methods.....	138
4.4	Results and Discussion.....	139
4.5	Conclusions .....	154

4.6	Acknowledgements .....	155
4.7	References .....	155
4.8	Supporting Information .....	157
Chapter 5: 3D-Printing Amorphous Polysiloxane Terpolymers <i>via</i> Vat Photopolymerization .....		
		160
5.1	Abstract .....	160
5.2	Introduction .....	160
5.3	Materials and Methods .....	164
5.3.1	Materials .....	164
5.3.2	Synthesis and characterization of PDMS7.0k-DiPhS and PDMS7.5k-DiEtS 164	
5.3.3	Determination of polymer vinyl and thiol content.....	165
5.3.4	Sample preparation for photocuring and 3D printing .....	165
5.3.5	Sample preparation for vat photopolymerization (VP).....	166
5.3.6	Analytical Methods .....	167
5.3.7	Vat Photopolymerization (VP) .....	168
5.4	Results and Discussion.....	168
5.5	Conclusions .....	180
5.6	Acknowledgements .....	181
5.7	References .....	181
Chapter 6: Urea as a monomer for isocyanate-free synthesis of segmented poly(dimethyl siloxane) polyureas.....		
		184
6.1	Abstract .....	184
6.2	Introduction .....	184
6.3	Materials & Methods.....	188
6.3.1	Materials .....	188
6.3.2	Synthesis of non-segmented PDMS polyureas [poly(PDMS- <i>co</i> -urea)] ...	189
6.3.3	Synthesis of segmented PDMS polyureas [poly(PDMSU)- <i>co</i> - poly(BATSU)] .....	190
6.3.4	Synthesis of hard segment homopolymer [poly(BATS- <i>co</i> -urea)] .....	191
6.3.5	Synthesis of isocyanate-based PDMS polyureas [poly(PDMS- <i>co</i> -HMDU)] 192	
6.3.6	Calculation of hard segment content.....	192
6.3.7	Nuclear magnetic resonance (NMR) spectroscopy.....	193
6.3.8	Analytical methods .....	193
6.4	Results and Discussion.....	195
6.5	Conclusions .....	208
6.6	Acknowledgements .....	209

6.7	References .....	209
6.8	Supporting Information .....	212
Chapter 7: Supercritical Fluid Chromatography with Evaporative Light Scattering Detection (SFC-ELSD) for Determination of Oligomer Molecular Weight Distributions 217		
7.1	Abstract .....	217
7.2	Introduction .....	218
7.3	Materials and Methods .....	222
7.3.1	Materials and Reagents .....	222
7.3.2	Synthesis of ADPDA .....	223
7.3.3	Synthesis of DPD .....	224
7.3.4	Photocuring and Characterization of ADPDA .....	224
7.3.5	Instrumentation and Chromatographic Conditions .....	225
7.3.6	SFC-ELSD Data Analysis .....	225
7.4	Results and Discussion .....	226
7.5	Conclusions .....	235
7.6	Acknowledgements .....	235
7.7	References .....	235
7.8	Supporting Information .....	237
Chapter 8: Photoreactive, polyether-containing photopolymers with reactive diluents for improved performance in vat photopolymerization additive manufacturing..... 241		
8.1	Abstract .....	241
8.2	Introduction .....	241
8.3	Materials & Methods.....	244
8.3.1	Materials .....	244
8.3.2	Synthesis of PPG2k-UUA.....	245
8.3.3	Sample preparation for photocuring .....	246
8.3.4	Sample preparation for vat photopolymerization (VPP) .....	246
8.3.5	Analytical Methods .....	247
8.3.6	Vat Photopolymerization (VPP) .....	248
8.4	Results & Discussion .....	248
8.5	Conclusions .....	259
8.6	Acknowledgements .....	259
8.7	References .....	259
Chapter 9: 3D-Printable Biodegradable Polyester Tissue Scaffolds for Cell Adhesion 263		

9.1	Abstract .....	263
9.2	Manuscript.....	263
9.3	Experimental .....	271
9.3.1	Synthesis of poly(tri(ethylene glycol) adipate)) (PTEGA).....	271
9.3.2	Photocuring and gel preparation for cytotoxicity assay.....	272
9.3.3	Cell culture and viability assay.....	272
9.3.4	Hydrolysis study .....	273
9.3.5	Analytical Methods.....	273
9.3.6	Microstereolithography and Characterization.....	274
9.4	Acknowledgements .....	274
9.5	References .....	274
9.6	Supplementary Material .....	277
Chapter 10: Melt Stable Polyamides for Polymer Powder Bed Fusion Applications		
	282	
10.1	Abstract .....	282
10.2	Introduction .....	282
10.3	Materials & Methods.....	285
10.3.1	Materials .....	285
10.3.2	Trifluoroacetylation of PA12 samples (TFA-PA12) .....	286
10.3.3	Rheology with dodecanediamine.....	287
10.3.4	Synthesis of PA12 microparticles.....	287
10.3.5	Analytical Methods.....	289
10.3.6	Powder Bed Fusion.....	290
10.4	Results & Discussion .....	291
10.5	Conclusions .....	307
10.6	Acknowledgements .....	307
10.7	References .....	307
10.8	Supporting Information .....	312
Chapter 11: Overall Conclusions .....		313
Chapter 12: Future Work .....		316
12.1	Thiol-ene photopolymers for simultaneous or sequential chain extension and crosslinking in air .....	316
12.2	PA12-HPBD-PA12 triblock copolymers via anionic dispersion polymerization	
	318	



12.3	Investigation into the role of silica in the anionic dispersion polymerization of lauro lactam .....	320
12.4	Isocyanate-free, segmented PDMS polyureas.....	320
12.5	Organocatalyzed- or organometallic-catalyzed, isocyanate-free, segmented PDMS polyureas .....	323
12.6	Catalyzed synthesis of isocyanate-free polyureas with dimethylcarbonate or biscarbamates .....	324
12.7	Synthesis of phosphonium-containing polyureas.....	325
12.8	References .....	326

## List of Figures

Figure 2.1. Typical stress-strain behavior for a (A) brittle polymer, (B) thermoplastic, and (C) thermoplastic elastomer. Adapted with permission. <sup>8</sup> .....	7
Figure 2.2. Schematic of three common types of vat photopolymerization. (a) Stereolithography. (b) Digital light processing vat photopolymerization. (c) Two-photon polymerization. Reproduced from Gibson, Rosen, and Stucker. <sup>11</sup> .....	9
Figure 2.3. Schematic of continuous liquid interface printing (CLIP). Adapted from Tumbleston and DeSimone, et al. <sup>13</sup> .....	10
Figure 2.4. Fused filament fabrication (FFF) process depicting a movable build platform (a), a movable build head (b) with attached filament spool (e), and polymer deposition occurring from the main filament head (c) and the support material head (d). Reproduced from <sup>10</sup> .....	12
Figure 2.5. Polymer powder bed fusion (PBF) process. Reproduced from Gibson, Rosen, and Stucker. <sup>27</sup> .....	16
Figure 2.6. A) Shear-rate dependent, apparent viscosity of Dow Corning SE1700 (uncured). B) Oscillatory stress sweep of DC SE1700 (uncured) showing storage and loss moduli. Reproduced from Wilson and co-workers. <sup>61</sup> .....	25
Figure 2.7. Image of DIW process using a blend of DC SE1700 (85 wt%) and Sylgard 184 (15 wt%). Reproduced with permission from Bertoldi et al. <sup>63</sup> .....	30
Figure 2.8. Embedded 3D printing utilized to incorporate conductive inks into the silicone elastomer to manufacture elastic electronics. Reproduced from Lewis et al. <sup>80</sup> ...	30
Figure 2.9. A: Apparent viscosity versus shear rate for the ink, reservoir material and filler fluid, utilized for embedded 3D printing. B: Shear elastic modulus versus shear stress for the same materials. Adapted from Lewis et al. <sup>80</sup> .....	31
Figure 2.10. Principle of extruding two-part PDMS (Sylgard 184) into Carbopol® medium. Adapted from Feinberg et al. <sup>83</sup> .....	32
Figure 2.11. Self-assembly of SEBS triblock and SEP diblock copolymers in mineral oil to yield jammed micro-organogels. Adapted from Angelini et al. <sup>84</sup> .....	34
Figure 2.12. Variety of geometries consisting of crosslinked PDMS and printed using two-photon absorption microstereolithography. Adapted with permission from Ober et al. <sup>89</sup> .....	36
Figure 2.13. Modulus (Pa) versus UV-illumination time (s) for poly((mercaptopropyl)methyl-siloxane- <i>co</i> -dimethylsiloxanes) with 2.5 mol% and 5 mol% pendent thiols and $\alpha,\omega$ -divinyl PDMS with molecular weights ( $M_w$ ) of 186 $\text{g}\cdot\text{mol}^{-1}$ and 6000 $\text{g}\cdot\text{mol}^{-1}$ , respectively. ....	40
Figure 2.14. Additive manufactured monolithic device utilizing thiol- and vinyl-functionalized PDMS and UV-initiated thiol-ene click chemistry. Pressurization or evacuation enabled contraction or elongation of the actuator. Adapted from Shepherd et al. <sup>92</sup> .....	41

Figure 2.15. Transparent hollow cube, 3D-printed using a PDMS-based photoresin. Reproduced from Bhattacharjee et al. <sup>93</sup> .....	43
Figure 2.16. Ink-jet printed ziggurat structure (4 mm x 4 mm) consisting of crosslinked PDMS. Adapted from Wildman et al. <sup>99</sup> .....	45
Figure 2.17. Schematic representation of a segmented polyurethane or polyurea. ....	47
Figure 2.18. (A,B) CAD models of freeze-dried polyurethane 3D vasculature models, (C) 3D printed polyurethane construct, (D) cross-section of construct shown in (C), (E) SEM micrograph of outer scaffold wall in (C). Reproduced from Xu and Zhang, et al. <sup>117</sup> .....	51
Figure 2.19. (A-D). Various images of a hierarchical construct made created by the DIW co-extrusion process. (E-F) two complex constructs undergoing in-vitro pulsatile culture. Reproduced from Huang and Wang, et al. <sup>119</sup> .....	52
Figure 2.20. Poly(ester urethane) (PEU) scaffolds produced via DIW. Reproduced from Kiziltay and Hasirci, et al. <sup>122</sup> .....	53
Figure 2.21. (A) 3D printed laboratory logo created by fused filament fabrication with thiourethane filaments. (B) scanning electron microscopy of printed objects. Reproduced from Ellson and Voit, et al. <sup>103</sup> .....	55
Figure 2.22. Inkjet printing of acetic acid/water solution on a sulfonate-containing PU substrate, producing patterns via protonation of polyurethane ionomers. (A) separate letters printed on glass slide. (B) O-rings printed on glass slide. (C) Schematic of acetic acid/water printing and subsequent protonation of polyurethane ionomers, producing water insoluble structures. Reproduced from Zhang and Boland, et al. <sup>128</sup> .....	57
Figure 2.23: Synthesis of water-dispersible polyurethane nanoparticles via the prepolymer emulsification method. ....	59
Figure 2.24: Self-assembly of water dispersible polyurethane (WDPU) nanoparticles (NP)s (a) Processing based on the self-assembly of NPs. (b) The possible mechanisms for self-assembly of NPs. Reproduced from Hsu and Lin, et al. <sup>138</sup> .....	61
Figure 2.25. Waterborne polyurethane dispersions with PCL diol and PLLA-PEO-PLLA triblock copolymers as soft segments .....	62
Figure 2.26. 3DP DIW process. Reproduced with permission. <sup>142</sup> .....	64
Figure 2.27. Typical DIW 3D printing procedures. (A) fiber stacking by manual injection, (B) manually-produced construct, (C) 3D printing with custom-designed DIW apparatus, and (D) two layers of 3D-printed fibers, constructed for the purposes of cell visualization via optical microscopy. Figure reproduced with permission. <sup>140</sup> .....	64
Figure 2.28. Schematic of PUD-Veroclear® composite scaffold. Reproduced with permission. <sup>144</sup> .....	65
Figure 2.29. White-light interferometry image and height profile (inset) of inkjet-printed single dots. Reproduced with permission. <sup>146</sup> .....	67
Figure 2.30. Cartoon representation of network structure before and after the addition of monoacrylate and dithiol chain transfer agent to a formulation that initially contains 100% of a diacrylate-functional oligomer. Figure adapted with permission. <sup>39</sup> .....	69

Figure 2.31. Photopolymer composition for the production of a blood vessel substitute via microstereolithography. ....	70
Figure 2.32. Various views of a 3D printed, highly deformable isotropic truss. ....	74
Figure 2.33. PDMS-slab with asymmetrically placed LCE (yellow material) enables temperature-induced buckling and demonstrates potential as adaptive optical element. Adapted from Sánchez-Somolinos et al. <sup>170</sup> .....	83
Figure 2.34. Additively manufactured LCE film (1 mm in thickness) performing temperature-responsive “weight lifting”. Scale bar = 5 mm. Reprinted with permission. <sup>171</sup> .....	84
Figure 2.35. (A) Illustration depicting dynamic vulcanization of an elastomer (PLBSI) and thermoplastic (PLA), resulting in a thermoplastic vulcanizates (TPVs). (B) 3D-printed PLBSI/PLA TPV. ....	85
Figure 3.1. (A) Photorheology for neat PDMS-3.2k-AA, depicting storage ( $G'$ ) and loss ( $G''$ ) modulus increase as a function of UV exposure time (on at 30 s). Panels (B), (C), and (D) depict $G'$ plateau modulus ( $G_{NO}$ ), $G'/G''$ crossover time, and gel fraction as a function of PDMS-AA oligomer $M_n$ , respectively. Error bars represent representative sample standard deviation. ....	113
Figure 3.2. $G_{NO}$ values (MPa) from photorheology and gel fraction from soxhlet extraction for photocured mixtures, depicted as a function of mol. eq. dithiol for (A) PDMS1.2k-SH and PDMS1.8k-AA, (B) PDMS1.2k-SH and PDMS5.5k-AA, (C) PDMS5.1k-SH and PDMS1.8k-AA, and (D) PDMS5.1k-SH and PDMS5.5k-AA. The brown dash-dot lines and the purple dashed lines represent the $G_{NO}$ values for PDSM11.7k-AA and PDMS30.6k-AA, respectively. ....	115
Figure 3.3. Complex viscosity ( $\eta^*$ ) via photorheology of a 1:1 mol:mol mixture of PDMS5.1k-SH and PDMS5.9k-V vs. UV irradiation time. Red = UV light on (10 min intervals) and black = UV light off (5 min intervals). Viscosity of non-irradiated PDMS5.9k-V (green long dash), PDMS5.1k-SH (purple short dash), and PDMS11.7k-AA (orange dash-dot) are provided for reference. Inset log-log plot highlights the 0.1 – 1 Pa·s viscosity range and 0.1 – 20 min time range. ....	117
Figure 3.4: (A) Schematic of the top-down scanning mask projection VPP apparatus used for AM of siloxane oligomers. (B) VPP AM apparatus showing glass dish photopolymer container, nitrogen sparge line, recoating blade, and scanning optics system. (C) 3D-printed tensile bar. (D) 3D printed squares for soxhlet extraction. ....	120
Figure 3.5: Tensile data for photocured mixtures of PDMS1.2k-SH and PDMS5.5k-AA. Photocured PDMS11.7k-AA (black dashed) is provided as a reference. The 3D printed (3DP) tensile specimens are shown in light green. ....	122
Figure 3.6. $^1\text{H}$ NMR spectroscopy determines percent acrylamide termination for PDMS oligomers as a function of PDMS molecular weight. ....	130
Figure 3.7. $^1\text{H}$ NMR spectroscopy determines percent thiol termination for PDMS oligomers as a function of PDMS molecular weight. ....	131

Figure 3.8. Working curve for the photoactive resin. The plot helps estimate the UV dose required to print layers of required thickness. ....	131
Figure 4.1. Proton nuclear magnetic resonance ( $^1\text{H}$ NMR) spectrum of the thiol-ene product in $\text{CDCl}_3$ .....	142
Figure 4.2. $^1\text{H}$ NMR spectra of NIPAM, M3MP, and poly(NIPAM), as well as competition study mixture post-irradiation and pre-irradiation, relative to an internal standard (1 mol. eq. mesitylene). ....	143
Figure 4.3. $^1\text{H}$ NMR spectroscopy depicts relative amounts of M3MP, NIPAM, thiol-ene product, and poly(NIPAM) relative to an internal standard (1 mol. eq. mesitylene) after irradiation with UV light to complete NIPAM consumption. ....	144
Figure 4.4. (A) Photorheology of neat PDMS-3.2k-AA, portraying storage ( $G'$ ) and loss ( $G''$ ) modulus versus UV exposure time (start at 30 s). (B-F) $G'$ plateau modulus ( $G_{\text{NO}}$ ) values (MPa) from photorheology and gel fraction (%) of photocured samples. (B) $G_{\text{NO}}$ versus PDMS-AA oligomer $M_n$ . (C-F) $G_{\text{NO}}$ and gel fraction values versus mol. eq. dithiol for (C) PDMS1.2k-SH and PDMS1.8k-AA, (D) PDMS1.2k-SH and PDMS5.5k-AA, (E) PDMS5.1k-SH and PDMS1.8k-AA, and (F) PDMS5.1k-SH and PDMS5.5k-AA. Green dash-dot lines and the red dashed lines depict the $G_{\text{NO}}$ values for PDMS11.7k-AA and PDMS30.6k-AA, respectively. ....	147
Figure 4.5. Photocalorimetry heat flow vs. time (A)-(D) and overall heat of reaction (E)-(H). All data is provided for (A),(E) PDMS1.2k-SH and PDMS1.8k-AA; (B),(F) PDMS1.2k-SH and PDMS5.5k-AA; (C),(G) PDMS5.1k-SH and PDMS1.8k-AA; and (D),(H) PDMS5.1k-SH and PDMS5.5k-AA. ....	150
Figure 4.6. (A) $G'$ plateau modulus from photorheology, (B) $M_c$ from photorheology using eqn. (1) and $M_n$ from $^1\text{H}$ NMR spectroscopy and Carothers equation predictions prior to photocuring, (C) $G'/G''$ crossover from photorheology, and gel fraction via soxhlet extraction of photorheology samples. ....	153
Figure 4.7. $^{13}\text{C}$ spectrum of thiol-ene product in $\text{CDCl}_3$ .....	157
Figure 4.8. COSY of the thiol-ene product in $\text{CDCl}_3$ .....	158
Figure 4.9. HSQC of thiol-ene product in $\text{CDCl}_3$ .....	159
Figure 4.10. HMBC of thiol-ene product in $\text{CDCl}_3$ .....	159
Figure 5.1. (A) Heat flow vs. time from photocalorimetry at 25 °C, with UV light on at 0 min, as a function of photoinitiator (DMPA) concentration. (B) Time at peak heat flow from (A) vs. photoinitiator concentration. (C) $G'$ vs. time from photorheology, with UV light on at 0 min. (D) $G'/G''$ crossover time from photorheology as a function of photoinitiator concentration. Error bars represent standard deviation. ....	172
Figure 5.2. Photocuring assembly and procedure that provided uniform films of consistent thickness.....	173
Figure 5.3. TGA of photocured DiPhS + SH and DiEtS + SH films overlaid with neat DiPhS- and DiEtS-containing terpolymers and SH crosslinker in nitrogen (A) and air (B). ....	174

Figure 5.4. DSC 1 <sup>st</sup> heating traces (10 °C min <sup>-1</sup> ) for photocured films of (A) DiPhS + SH or (B) DiEtS + SH networks, overlaid with corresponding traces for neat oligomeric precursors.....	176
Figure 5.5. Dynamic mechanical analyses (DMA) (3 °C min <sup>-1</sup> , 1 Hz) of photocured DiPhS + SH and DiEtS + SH films.....	178
Figure 5.6. (A) Schematic of the top-down scanning mask-projection vat photopolymerization (VP) apparatus employed for additive manufacturing (AM) of siloxane terpolymers. (B) VP-AM apparatus used in this work. (C) and (D) 3D-printed rook structures from DiPhS + SH photopolymer composition.....	179
Figure 6.1. Weight loss vs. temperature data at 10 °C min <sup>-1</sup> from TGA for (A) non-segmented poly(PDMS- <i>co</i> -urea)s and PDMS-NH <sub>2</sub> precursors, (B) segmented poly(PDMS1.7kU)- <i>co</i> -poly(BATSU) polyureas, non-segmented poly(BATS- <i>co</i> -urea) and poly(PDMS1.7k- <i>co</i> -urea), and the PDMS1.7k-NH <sub>2</sub> precursor, and (C) poly(PDMS- <i>co</i> -HMDU) polyureas synthesized with HMDI diisocyanate.....	199
Figure 6.2. DSC 1 <sup>st</sup> heating traces (10 °C min <sup>-1</sup> ) for annealed (100 °C, 18 h, vac), (A) non-segmented poly(PDMS- <i>co</i> -urea)s and PDMS-NH <sub>2</sub> precursors, (B) segmented poly(PDMS1.7kU) <sub>x</sub> - <i>co</i> -poly(BATSU) <sub>y</sub> polyureas, non-segmented poly(PDMS1.7k- <i>co</i> -urea) and poly(BATS- <i>co</i> -urea), and the PDMS1.7k-NH <sub>2</sub> precursor, and (C) poly(PDMS- <i>co</i> -HMDU) polyureas synthesized with HMDI diisocyanate.....	200
Figure 6.3. Dynamic mechanical analysis heating traces (3 °C min <sup>-1</sup> , 1 Hz) for annealed (100 °C, 18 h, in vacuo) films of segmented poly(PDMS1.7kU) <sub>x</sub> - <i>co</i> -poly(BATSU) <sub>y</sub> polyureas and non-segmented poly(PDMS1.7k- <i>co</i> -urea) and poly(BATS- <i>co</i> -urea).....	203
Figure 6.4. Dynamic mechanical analysis heating traces (3 °C min <sup>-1</sup> , 1 Hz) for annealed (100 °C, 18 h, vac) films of poly(PDMS- <i>co</i> -HMDU) polyureas synthesized with HMDI diisocyanate.....	204
Figure 6.5. (A) Tensile stress vs. strain data for annealed (100 °C, 18 h, vac) films of segmented poly(PDMS1.7kU) <sub>x</sub> - <i>co</i> -poly(BATSU) <sub>y</sub> polyureas and non-segmented poly(PDMS1.7k- <i>co</i> -urea). (B) Five-cycle hysteresis profiles for poly(PDMS1.7k) <sub>80</sub> - <i>co</i> -poly(BATS) <sub>20</sub> (4.0 wt % HS) at 100 % strain.....	206
Figure 6.6. Summary of percent hysteresis values at 100 % strain for annealed (100 °C, 18 h, vac) films of segmented poly(PDMS1.7k) <sub>80</sub> - <i>co</i> -poly(BATS) <sub>20</sub> (4.0 wt % HS) polyureas and non-segmented poly(PDMS <sub>1.7k</sub> - <i>co</i> -urea). .....	207
Figure 6.7. <sup>1</sup> H NMR spectra overlay of PDMS-NH <sub>2</sub> oligomeric starting materials in C <sub>6</sub> D <sub>6</sub> at 23 °C. ....	212
Figure 6.8. Example <sup>1</sup> H NMR spectra overlay of non-segmented, isocyanate-free poly(PDMS- <i>co</i> -urea)s [poly(PDMS3.2k- <i>co</i> -urea) shown] and starting materials in CDCl <sub>3</sub> at 23 °C. ....	212
Figure 6.9. Example number-average molecular weight (M <sub>n</sub> ) determination based on integrations from <sup>1</sup> H NMR spectra in CDCl <sub>3</sub> at 23 °C. ....	213

Figure 6.10. <sup>1</sup> H NMR spectra overlay of all isocyanate-free, segmented poly(PDMS1.7kU)- <i>co</i> -poly(BATSU), non-segmented poly(PDMS1.7k- <i>co</i> -urea) and non-segmented poly(BATS- <i>co</i> -urea) in CF <sub>3</sub> COOD at 23 °C. ....	213
Figure 6.11. Hard segment content determination, calculations, and assumptions for isocyanate-free, segmented poly(PDMS1.7kU)- <i>co</i> -poly(BATSU), non-segmented poly(PDMS1.7k- <i>co</i> -urea) and non-segmented poly(BATS- <i>co</i> -urea). ....	214
Figure 6.12. DSC 1 <sup>st</sup> heating traces (10 °C min <sup>-1</sup> ) for PDMS-NH <sub>2</sub> precursors from a liquid nitrogen cooling system (LNCS) DSC and a refrigerated cooling system (RCS) DSC. ....	215
Figure 6.13. Five-cycle, 100% hysteresis profiles for (A) poly(PDMS1.7kU)- <i>co</i> -urea), (B) poly(PDMS1.7kU) <sub>94</sub> - <i>co</i> -poly(BATSU) <sub>6</sub> , (C) poly(PDMS1.7kU) <sub>86</sub> - <i>co</i> -poly(BATSU) <sub>14</sub> , and (D) poly(PDMS1.7kU) <sub>80</sub> - <i>co</i> -poly(BATSU) <sub>20</sub> . ....	216
Figure 7.1. Supercritical fluid – evaporative light scattering detection (SFC-ELSD) chromatograms displaying separation of the PPG2K-UUA molecular weight distribution (red dotted trace). A decarboxylated HMDI-PPG-HMDI (DPD, black solid trace) is provided for comparative purposes. ....	230
Figure 7.2. Plot of percent of total peak area as a function of reaction stoichiometry, demonstrating increasing amounts of m = 1 for increasing HMDI:PPG stoichiometry. ....	232
Figure 7.3. Dynamic mechanical analysis (DMA) temperature ramp of photocured PPG2K-UUA oligomers as a function of HMDI/HEA stoichiometry. ....	233
Figure 7.4. <sup>1</sup> H NMR of dialyzed ADPDA (1.0 : 3.0 : 5.0) overlaid with isolated, decarboxylated intermediate DPD and starting materials HEA, HMDI, and PPG. ....	238
Figure 7.5. SFC-ELSD chromatogram of decarboxylated HMDI (D-HMDI). In each group of numbers above a given peak, the top number is elution time (min) and the bottom number is peak area. ....	239
Figure 7.6. SFC-ELSD chromatogram of neat 2-hydroxyethyl acrylate (HEA). In each group of numbers above a given peak, the top number is elution time (min) and the bottom number is peak area. ....	239
Figure 7.7. SFC-ELSD chromatograms used for the generation of data in Figure 7.1, displaying an elimination of the ADA, D-HMDI, and HEA peaks after post-synthesis dialysis in MWCO 1,000 g/mol dialysis bags. ....	240
Figure 8.1. (A) Viscosity as a function of constant shear rate and (B) viscosity as a function of temperature at a constant 1.0 s <sup>-1</sup> for PPG2k-UUA and the neat PPG-(NH <sub>2</sub> ) <sub>2</sub> oligomer. ....	250
Figure 8.2. Dynamic mechanical analysis heating traces (5 °C min <sup>-1</sup> , 1 Hz) for photocured PPG2k-UUA films as a function of temperature and 2,2-dimethoxy-2-phenylacetophenone (DMPA) concentration. ....	251
Figure 8.3. Dynamic mechanical analysis heating traces (5 °C min <sup>-1</sup> , 1 Hz), before and after extraction in tetrahydrofuran (THF), as a function of temperature. ....	253

Figure 8.4. (A) Viscosity as a function of constant shear rate and (B) viscosity as a function of temperature at a constant $1.0 \text{ s}^{-1}$ for PPG2k-UUA, the neat PPG-(NH <sub>2</sub> ) <sub>2</sub> oligomer, and mixtures of PPG2k-UUA and EHA, DEGEAA, or nBA at various loading. ....	254
Figure 8.5. Dynamic mechanical analysis heating traces ( $5 \text{ }^\circ\text{C min}^{-1}$ , 1 Hz) for (A) photocured combinations of PPG2k-UUA and nBA as a function of nBA content and temperature and (B) 10 wt % nBA and 30 wt % nBA samples .....	256
Figure 8.6. Dynamic mechanical analysis heating traces ( $5 \text{ }^\circ\text{C min}^{-1}$ , 1 Hz) for photocured combinations of PPG2k-UUA and nBA, EHA, or DEGEAA as a function of temperature and monomer concentration.....	256
Figure 8.7. Photographs of (A) 3D-printed pillar structure, (C) 3D-printed hex pattern, and (E) 3D-printed scaffold structure from PPG2k-UUA alone in the absence of monomer / reactive diluent. (B,D,F) Scanning electron microscope (SEM) images of A, C, and E, respectively. ....	258
Figure 9.1. (a) Photocuring of poly(tri(ethylene glycol) adipate) (PTEGA) dimethacrylate. (b) MDA-MB-231 cell viability assay indicating significantly improved cell attachment and viability as compared to non-tissue culture treated polystyrene ( $p < 0.05$ ). Asterisks signify statistical significance between the two populations at the specified $p$ value. ....	268
Figure 9.2. (a) SEM micrograph of neat, dried polyester film. (b) SEM micrograph of treated polyester films, indicating hydrolysis-induced surface roughness. (c) Image and SEM micrographs of 3D-printed polyester cylinder.....	270
Figure 9.3. <sup>1</sup> H NMR structure confirmation for (a) poly(tri(ethylene glycol) adipate)) (PTEGA) dimethacrylate and (b) PTEGA diol, overlaid with (c) decarboxylated functionalization reactant 2-aminoethyl methacrylate.....	277
Figure 9.4. <sup>13</sup> C NMR structure confirmation for (a) poly(tri(ethylene glycol) adipate)) (PTEGA) dimethacrylate and (b) PTEGA diol, overlaid with (c) decarboxylated functionalization reactant 2-aminoethyl methacrylate.....	278
Figure 9.5. <sup>1</sup> H NMR spectra and peak integrations used for molecular weight determination ( $M_n$ ) of (a) poly(tri(ethylene glycol) adipate)) (PTEGA) diol and (b) PTEGA dimethacrylate. (c) Differential Scanning Calorimetry (DSC) trace showing the PTEGA dimethacrylate glass transition temperature.....	279
Figure 9.6. Tukey's Honest Significant Difference (HSD) test for statistical significance. As shown, the three populations are not connected by the same letter and are therefore significantly different at $p < 0.050$ .....	281
Figure 10.1. (A/E) Scanning electron microscope (SEM) micrographs, (B/F) particle size analysis, (C/G) differential scanning calorimetry heat/cool cycles with different maximum heating temperatures, and (D/H) melt rheology stability studies at various temperatures for (A-D) 3DS Duraform® PA and (E-H) Arkema Orgasol® IS commercial products.....	292



Figure 10.2. Proton nuclear magnetic resonance ( <sup>1</sup> H NMR) spectra of trifluoroacetylated Sigma Aldrich PA12 pellet, Arkema Orgasol® IS powder, and 3DS Duraform® PA powder in CDCl <sub>3</sub> .....	294
Figure 10.3. Melt rheology stability study of homogenized PA12 and dodecanediamine powders at 210 °C, 1.25 % strain, and 1 Hz. ....	296
Figure 10.4. Images of products (A) PA12 microparticles v3 (sample #5) and (B) no EBS (#11). SEM images of (C) no EBS (#11), (D) 0.5x EBS (12), (E) PA12 microparticles v3 (#5, e.g. 1x EBS), (F) 2x EBS (13), (G) Arkema Orgasol® IS (#2), and (H) 300 rpm stir (#14).....	301
Figure 10.5. Melt stability study of Arkema Orgasol® IS and polymerization products synthesized with varying amounts of ethylene bis(stearamide) (EBS). Data gathered at 210 °C, 1.25 % strain, and 1 Hz.....	303
Figure 10.6. (A) schematic of powder bed fusion process. (B) photo of the DTM Sinterstation 2500 Plus with central build volume and left/right feed pistons. (C) fusion in progress. (D/G/J) Images of single-layer fused structures and (E/H/K) low- and (F/I/L) high-magnification SEM of (D-F) Arkema Orgasol® IS (#2), (G-I) PA12 microparticles v3 (#5), and (J-L) 0.5x EBS (#12). ....	306
Figure 10.7. (A) Picture of anionic dispersion polymerization reactor. (B) Picture showing full lauro lactam and EBS dissolution at 120 °C. (C) Reaction at 120 °C after NaH addition, displaying a slightly more yellow color. (D) Partway and (E) all the way through activator addition, at various stages of the dispersion polymerization.....	312

## List of Tables

<b>Table 2.1.</b> Photopolymer compositions employed by Liska and Stampfl, et al. ....	73
Table 3.1. Non-irradiated PDMS-AA oligomer $M_n$ (g/mol) as determined from $^1\text{H}$ NMR spectroscopy and calculated $M_c$ values, based on <b>GN0</b> , as determined by Equation 1..	114
<b>Table 3.2.</b> Zero-shear viscosity ( $\eta_0$ ) of various functional siloxanes and the mixture of PDMS-SH and PDMS-AA used for AM (0.75:1.0 mol:mol PDMS1.2k-SH : PDMS5.3k-AA). ....	118
Table 3.3. Stress at break, and strain at break for photocured or 3D printed (3DP) mixtures of PDMS1.2k-SH and PDMS5.5k-AA. Photocured PDMS11.7k-AA (black dashed) is provided as a reference. ....	122
Table 5.1. Compositions of amorphous siloxane terpolymers used .....	170
Table 5.2. Selected characterization data for siloxane terpolymers of Table 5.1. ....	170
Table 6.1. Summary of composition, $T_{d,5\%}$ , thermal transitions, and modulus values from $^1\text{H}$ NMR spectroscopy, TGA, DSC, and DMA, respectively. ....	201
Table 6.2. Summary of tensile and hysteresis properties for segmented poly(PDMS1.7kU)- <i>co</i> -poly(BATSU) polyureas and non-segmented poly(PDMS1.7k- <i>co</i> -urea). ....	208
Table 7.1. Summary of theoretical and experimental number-average molecular weight ( $M_n$ ) of samples obtained from SFC-ELSD analysis, according to sample stoichiometry .....	237
Table 7.2. Summary of theoretical number-average molecular weight ( $M_n$ ) of various expected species in SFC-ELSD analysis, according to number of repeat units. ....	237
Table 10.1. Summary of sample composition, polymerization conditions, isolated yields, particle size from laser diffraction, and complex viscosity at 210 °C from melt rheology stability studies.....	304

## List of Schemes

Scheme 2.1. Schematic of DIW apparatus. Adapted from Bhargava et al. <sup>19</sup> .....	13
Scheme 2.2. Schematic of inkjet printing technique. Adapted from Derby. <sup>21</sup> .....	15
Scheme 2.3. Crosslinking of polysiloxanes <i>via</i> hydrosilylation reaction utilizing a transition metal catalyst. Details on the curing mechanism are provided in literature. <sup>54</sup> .	20
Scheme 2.4. Crosslinking of acetoxy-functional polysiloxanes via condensation reaction. .....	21
Scheme 2.5. Crosslinking of polysiloxanes using alkoxy silane groups and subsequent release of <i>n</i> -propyl alcohol.....	21
Scheme 2.6. Free-radical curing mechanism of polysiloxanes. <sup>55</sup> .....	22
Scheme 2.7. Complex resin formulation to yield silicone elastomers with tunable stiffness. <sup>71</sup> .....	26
Scheme 2.8. UV-initiated thiol-ene reaction of tetrafunctional thiol and $\alpha,\omega$ -divinyl PDMS yielded silicone elastomer. ....	27
Scheme 2.9. Synthetic scheme to formulate PDMS suspensions. Adapted from Velev et al. <sup>85</sup> .....	35
Scheme 2.10. UV-crosslinking of methacrylate-functional PDMS oligomer yields silicone elastomer with high crosslinking density. ....	37
Scheme 2.11. Reaction of $\alpha,\omega$ -diamine PDMS with methacryloyl chloride in DCM in the presence of triethylamine yields $\alpha,\omega$ -dimethacrylamide polydimethylsiloxane. ....	38
Scheme 2.12. Schematic of simultaneous crosslinking and chain extension of low molecular weight thiol-functional PDMS and acrylamide-functionalized PDMS, which yielded crosslinked PDMS networks with high molecular weight between crosslinks. ..	39
Scheme 2.13. Single components of photoresin to enable 3D printing of transparent silicone elastomers. Adapted from Bhattacharjee et al. <sup>93</sup> .....	42
Scheme 2.14. Indirect AM of silicone elastomers utilizing a sacrificial scaffold. Adapted from Jiang and Wang. <sup>94</sup> .....	44
Scheme 2.15. Poly(ester urethane) (PEU) elastomers prepared from polycaprolactone (PCL) diol and lysine diisocyanate. ....	53
Scheme 2.16. Segmented poly(ester urethane) (PEU) elastomers prepared from polycaprolactone (PCL) diol, 1,4-butanediisocyanate, and L-Lysine ethyl ester dihydrochloride. ....	54
Scheme 2.17. Synthesis of thiourethanes from EDDT and HDI. ....	56
Scheme 2.18. Chemical structures of epoxy aliphatic acrylate and aliphatic urethane diacrylate.....	74
Scheme 2.19. Synthesis of bio-based, green, aliphatic urethane-containing photocurable oligomers.....	75
Scheme 2.20. Low viscosity, urethane-containing oligomers for vat photopolymerization. .....	77
Scheme 2.21. Synthetic strategy to prepare blocked isocyanates. ....	78

Scheme 2.22. Types of different liquid crystalline elastomers. Adapted from Zentel. <sup>163</sup>	81
Scheme 2.23. <i>Left</i> : Synthesis of LCE utilizing aza-Michael reaction and subsequent UV-crosslinking of the acrylate-end groups. <i>Right</i> : Schematic of the DIW-UV process and the LCE alignment. <sup>168</sup>	82
Scheme 2.24. Synthesis of PLBSI unsaturated copolyesters.	85
Scheme 2.25. Photocurable poly(glycerol sebacate)s.	86
Scheme 2.26. Synthesis of poly( $\epsilon$ -CL-b-TMC- $\epsilon$ -CL) triblock copolymers.	87
Scheme 2.27. Synthesis of photocurable poly(citrate diol) biodegradable elastomers.	88
Scheme 3.1. (A) Functionalization of bis(3-aminopropyl)-terminated poly(dimethyl siloxane) (PDMS) to afford telechelic acrylamide-functional PDMS oligomers. (B) Functionalization of bis(hydroxyalkyl)-terminated PDMS to afford telechelic thiol-functional PDMS oligomers.	111
Scheme 3.2. Chain extension (via thiol-ene coupling) and crosslinking (via conventional free radical homopolymerization) afforded upon irradiation of a mixture of PDMS dithiol and PDMS diacrylamide.	114
Scheme 4.1. Model competition study depicting the photo-irradiation of NIPAM and M3MP to afford a mixture of poly(NIPAM) and the thiol-ene product.	142
Scheme 4.2. (A) Functionalization of bis(3-aminopropyl)-terminated poly(dimethyl siloxane) (PDMS) to afford telechelic acrylamide-functional PDMS oligomers. (B) Functionalization of bis(hydroxyalkyl)-terminated PDMS to afford telechelic thiol-functional PDMS oligomers.	145
Scheme 4.3. Synthesis and photocuring of chain extended oligomers via base-catalyzed thiol-Michael addition.	151
Scheme 5.1. Crosslinking of amorphous 7.0k-DiPhS- or 7.5k-DiEtS-containing terpolysiloxanes with 7.0k-SH crosslinker and UV light in the presence of photoinitiator.	169
Scheme 6.1. Synthesis of isocyanate-free, segmented, poly(dimethyl siloxane)- (PDMS)-containing polyureas with bis(3-aminopropyl)tetramethyldisiloxane (BATS) as a chain extender via melt polycondensation in the absence of solvent and catalyst [poly(PDMS1.7kU) <sub>x</sub> -co-poly(BATSU) <sub>y</sub> ].	197
Scheme 6.2. Synthesis of PDMS polyureas via traditional solution step-growth polymerization in the presence of hydrogenated methylene diphenyl diisocyanate (HMDI) and dibutyltin dilaurate (DBTDL) [poly(PDMS-co-HMDU)].	197
Scheme 7.1. Synthesis and photocuring of urea- and urethane-containing, acrylate-terminated poly(propylene glycol) (PPG2K-UUA) photoactive oligomers. Photocuring in the presence of the photoinitiator 2,2-dimethoxy-2-phenylacetophenone (DMPA) yielded crosslinked films.	227
Scheme 8.1. Synthesis of poly(propylene glycol) (PPG)-containing urea/urethane acrylate oligomers (PPG2k-UUA) from 2,000 g/mol PPG diamine, hydrogenated methylene diphenyl diisocyanate (H <sub>12</sub> MDI), and hydroxyethylacrylate (HEA).	249

Scheme 8.2. Photocuring of mixtures of PPG2k-UUA and n-butyl acrylate (nBA), 2-ethylhexylacrylate (EHA), or di(ethylene glycol) ethyl ether acrylate (DEGEEA), forming a crosslinked network.....	254
Scheme 9.1: Synthesis, functionalization, and photocuring of poly(tri(ethylene glycol) adipate)) (PTEGA). Synthesis proceeded via melt polycondensation of tri(ethylene glycol) and adipic acid, forming PTEGA diol. Functionalization with 2-isocyanatoethyl methacrylate afforded PTEGA dimethacrylate. Finally, photocuring in the presence of the photoinitiator 2,2-dimethoxy-2-phenylacetophenone (DMPA) yielded crosslinked films. ....	266
Scheme 10.1. Reaction of polyamide 12 (PA12) and trifluoroacetic anhydride in chloroform at 23 °C, yielding chloroform-soluble, trifluoroacetylated PA12.....	293
Scheme 10.2. Reaction of homogenized PA12 and dodecanediamine powders on a parallel plate rheometer, in a probe of potential dimerization or chain extension.....	295
Scheme 10.3. Sodium lauro lactamate formation, activator formation with stearyl isocyanate activator precursor, and resulting anionic polymerization, yielding melt-stable, linear PA12 with endcapped terminal primary amine. ....	298
Scheme 10.4. Anionic dispersion polymerization of lauro lactam in the presence of ethylene bis(stearamide) steric stabilizer and silica, yielding melt-stable, linear PA12.	298
Scheme 12.1. Synthesis of a carbonyl-free PDMS dithiol.....	317
Scheme 12.2. Synthesis of a vinyl ether functional PDMS oligomer via hydrosilylation reaction.....	317
Scheme 12.3. Synthesis of a hydrogenated polybutadiene diphenyl ester .....	319
Scheme 12.4. Synthesis of segmented PDMS polyureas in the absence of isocyanates, solvent, or catalyst. ....	321
Scheme 12.5. Various diamine chain extenders and 1,12-diisocyanatododecane.....	323
Scheme 12.6. Synthesis of segmented PDMS polyureas from dimethyl carbonate in the absence of isocyanates, solvent, or catalyst. ....	324
Scheme 12.7. Synthesis of phosphonium-containing diol from 1,1,1-tris(hydroxymethyl)ethane. ....	325
Scheme 12.8. Synthesis of phosphonium diamine.....	325

## Chapter 1: **Introduction**

### 1.1 **Dissertation Overview**

Additive manufacturing (AM), otherwise known as 3D printing (3DP), enables mass customization through the rapid manufacturing of objects that are customized to the individual. Furthermore, AM allows for creation of geometries not attainable with traditional, subtractive manufacturing methods, and typically occurs *via* selective, layerwise polymer solidification, crosslinking, or deposition.<sup>1-3</sup> Vat photopolymerization (VP), otherwise known as stereolithography, remains a highly versatile form of AM that selectively photocures a UV-responsive photopolymer in a layerwise manner. Unfortunately, according to the 2016 Wohler's report (Appendix E: Material Properties),<sup>4</sup> only 7 % of commercially-available photopolymers for VP possessed a tensile modulus of  $\leq 20$  MPa once photocured.<sup>4</sup> A low modulus represents one attribute of rubbers or elastomers, which enjoy wide-ranging applications that include damping elements, footwear, seals, and automotive tires. Additionally, most elastomers possess high levels of recoverable tensile strain at break (e.g.  $> 100$  %).<sup>5,6</sup> Finally, polysiloxanes represents one well-studied vehicle for elastomer formation, and this dissertation provides many examples of such systems. Polysiloxanes remain distinct among other synthetic polymers due to their unique properties, which result from inorganic  $-(\text{Si}-\text{O})_n-$  main chains and diverse organic pendant functionality. Their highly desirable properties, in particular their prominent elasticity, arise from their inherent chain flexibility derived from greater bond angles and bond lengths of Si-O-Si ( $150^\circ$  and  $1.645 \text{ \AA}$ ) units compared to C-O-C units ( $113^\circ$  and  $1.412 \text{ \AA}$ ), as well as from very low intersegmental interactions.<sup>7,8</sup> This results in some of the lowest glass transition temperatures ( $T_g$ ) of any known polymer – e.g.  $-123 \text{ }^\circ\text{C}$  for poly(dimethyl siloxane)s (PDMS) and  $-145 \text{ }^\circ\text{C}$  for poly(diethyl siloxane)s (PDES).<sup>8</sup>

Chapter 2 provides a timely literature review of photopolymers for VP that produce elastomeric objects, with a focus on PDMS- and polyurethane-containing systems. Chapter 3 describes a photopolymer composition that possess a relatively low viscosity before photocuring but provides properties of higher molecular weight precursors after photocuring,<sup>9</sup> while Chapter 4 provides additional experiments to validate the hypotheses presented in Chapter 3. Chapter 5 describes the characterization and VP-AM of amorphous siloxane terpolymers that enable achievement of elastomeric properties close to the polysiloxane  $T_g$ . Finally, Chapter 6 describes the synthesis and characterization of segmented, isocyanate-free PDMS polyureas. These melt polymerizations occur in the absence of solvent and catalyst and provide optically clear, mechanically ductile polymers isolated directly from the melt.

Chapter 7 and Chapter 8 provide the synthesis and characterization of a poly(propylene glycol), urethane/urea-containing photocurable oligomer for improved thermomechanical properties after processing with VP-AM. Chapter 7 describes supercritical fluid chromatography with evaporative light scattering detection for determination of oligomer molecular weight distributions with repeating unit resolution,<sup>10</sup> while Chapter 8 photocures these oligomers in the presence of reactive diluents and demonstrates wide-ranging thermomechanical properties as a function of reactive diluent chemistry and concentration. Chapter 9 describes the synthesis and characterization of photocurable, low  $T_g$ , aliphatic polyester dimethacrylate oligomers for the VP-AM of polymeric tissue scaffolds.<sup>11</sup> Chapter 10 presents the synthesis and characterization of melt-stable polyamide 12 (PA12) microparticles for improved powder recyclability in powder bed fusion AM. These PA12 microparticles were created directly from the anionic

dispersion polymerization, which avoided expensive and time-consuming post-processing precipitation or grinding steps. Finally, Chapter 12 and Chapter 13 provide overall dissertation conclusions and suggested future work to continue the described research efforts, respectively.

## 1.2 References

- (1) Ligon, S. C.; Liska, R.; Stampfl, J.; Gurr, M.; Mülhaupt, R. Polymers for 3d Printing and Customized Additive Manufacturing. *Chemical Reviews* **2017**, *117*, 10212-10290.
- (2) Gibson, I.; Rosen, D. W.; Stucker, B. *Additive Manufacturing Technologies Rapid Prototyping to Direct Digital Manufacturing*, Springer, 2010, <http://site.ebrary.com/id/10356040>.
- (3) Huang, Y.; Leu, M. C.; Mazumder, J.; Donmez, A. Additive Manufacturing: Current State, Future Potential, Gaps and Needs, and Recommendations. *Journal of Manufacturing Science and Engineering* **2015**, *137*, 014001-014001.
- (4) Wohlers, T.; Alvarez-Primo, F.; English, J.; Mireles, J. *Wohlers Report 2016: 3d Printing and Additive Manufacturing State of the Industry: Annual Worldwide Progress Report, Appendix E: Material Properties*, Wohlers Associates, Inc., 2016, <http://www.wohlersassociates.com/materials2016.pdf>, 2018-03-13.
- (5) Wallin, T. J.; Pikul, J. H.; Bodkhe, S.; Peele, B. N.; Mac Murray, B. C.; Therriault, D.; McEnerney, B. W.; Dillon, R. P.; Giannelis, E. P.; Shepherd, R. F. Click Chemistry Stereolithography for Soft Robots That Self-Heal. *Journal of Materials Chemistry B* **2017**, *5*, 6249-6255.
- (6) Boonstra, B. B. Role of Particulate Fillers in Elastomer Reinforcement: A Review. *Polymer* **1979**, *20*, 691-704.
- (7) Noll, W. *Chemistry and Technology of Silicones*; Elsevier, 2012.
- (8) Dvornic, P. R. Thermal Properties of Polysiloxanes. In *Silicon-Containing Polymers: The Science and Technology of Their Synthesis and Applications*; Jones, R. G., Ando, W., Chojnowski, J., Eds.; Springer Netherlands: Dordrecht, 2000, p 185-212.
- (9) Serrine, J. M.; Meenakshisundaram, V.; Moon, N. G.; Scott, P. J.; Mondschein, R. J.; Weiseman, T. F.; Williams, C. B.; Long, T. E. Functional Siloxanes with Photo-Activated, Simultaneous Chain Extension and Crosslinking for Lithography-Based 3d Printing. *Polymer* **2018**.
- (10) Serrine, J. M.; Ashraf-Khorassani, M.; Moon, N. G.; Mondschein, R. J.; Long, T. E. Supercritical Fluid Chromatography with Evaporative Light Scattering Detection (Sfc-Elsd) for Determination of Oligomer Molecular Weight Distributions. *Chromatographia* **2016**, *79*, 977-984.
- (11) Serrine, J. M.; Pekkanen, A. M.; Nelson, A. M.; Chartrain, N. A.; Williams, C. B.; Long, T. E. 3d-Printable Biodegradable Polyester Tissue Scaffolds for Cell Adhesion. *Australian Journal of Chemistry* **2015**, *68*, 1409-1414.



## Chapter 2: **New Chemistry for 3D Printing of Elastomers: Synthesis, Characterization, and 3D Printing**

Jana Herzberger,<sup>1,a</sup> Justin M. Serrine,<sup>1,a</sup> Christopher B. Williams,<sup>b</sup> and Timothy E. Long <sup>a</sup>

<sup>1</sup> These authors contributed equally to the work

<sup>a</sup> *Department of Chemistry*, <sup>b</sup> *Department of Mechanical Engineering*  
*Macromolecules Innovation Institute*  
*Virginia Tech, Blacksburg, VA 24061, USA*

### **2.1 Introduction**

Thermoplastic elastomers and crosslinked rubbers remain an extremely important polymer class and enjoy a global demand expected to rise 5.2 % annually to a total of 6.7 million metric tons in 2019.<sup>1,2</sup> Their versatile properties render them ideal materials for everyday usage in products that include car tires and footwear, medical tubing in health care applications, automotive and aircraft sealants, and soft robots. The advent of additive manufacturing (AM), also known as three-dimensional (3D) printing, inspired academic and industrial researchers to combine elastomeric properties with design freedom and the potential for facile mass customization. For example, in 2015, a large footwear manufacturer reported the first 3D printed shoe sole utilizing selective laser sintering of thermoplastic polyurethanes.<sup>3</sup> Due to its reliance on polymer deposition only at the desired 3D pixels, or voxels, in a 3D design, instead of reliance on standard subtractive manufacturing methods, AM reduces material waste significantly, enables lightweight design through printing of low-density, high-strength truss geometries, and provides the ability for mass customization where each individual part remains customized to the needs of the individual.

This review highlights the recent achievements in additive manufacturing of elastomers. It aims to elucidate synthetic strategies and required material properties that

enable 3D printing of elastomers with the focus on silicone- and polyurethane-based materials. A brief introduction of relevant AM techniques and synthetic methods to prepare elastomers provide the reader with the proper background information for the detailed sections that discuss 3D printing of elastomers. Finally, a short perspective outlines potential future work and inspires the reader to solve ongoing challenges.

## **2.2 Elastomer Properties**

Elastomers are defined primarily by their thermal and mechanical properties. First, elastomers must undergo reversible mechanical deformation and frequently possess a relatively high ultimate tensile strength (e.g.  $\geq 400$ -1000 %) at relatively low stresses.<sup>2</sup> This typically requires a glass transition temperature ( $T_g$ ) and fully amorphous character sufficiently below the service temperature (typically room temperature).<sup>2,4</sup> Covalent crosslinking, or some other form of physical interaction combined with a microphase-separated morphology, are required as low  $T_g$  polymers in the absence of mechanical reinforcement yield viscous and/or adhesive-like properties.<sup>4</sup> PDMS polyureas and segmented thermoplastic polyurethanes remain prominent examples of the use of physical interactions (e.g. hydrogen bonding) in place of chemical crosslinking.<sup>2,5,6</sup>

Important characterization techniques for elastomers include tensile testing (e.g. stress-strain behavior), hardness measurements, compression testing, shear and flexural measurements, tear testing, and friction/abrasion property measurements.<sup>7</sup> Dynamic stress/strain measurements, including dynamic mechanical analysis (DMA) of solid-like samples or melt rheology of liquid-like samples, also provide important viscoelastic information. Fatigue measurements remain important for any object that may undergo repeated cycling, while creep, relaxation, and set measurements probe the elastomer behavior as a function of deformation and time. Gas permeability and electrical property

measurements also remain important for select applications. Details for these methods are provided elsewhere, while two common techniques are briefly discussed below.<sup>7</sup>

Shore durometer measurements represent one type of hardness measurement.<sup>7</sup> This device measures the resistance of a polymer to mechanical indentation of a spring-loaded steel rod and is frequently employed for hardness determination of elastomers. The spring force and type of indenter ranges with the type of polymer (soft vs. hard), with higher numbers representing harder polymers than softer materials. Extremely soft materials are measured using a Shore 00 durometer, whereas harder materials are characterized using a Shore D durometer. Values from 0 to 100 indicate maximum indentation and almost no indentation, respectively. Most elastomers typically fall on the Shore 00 and Shore A ranges. Due to the decrease in sensitivity of various hardness scales at the bounds of the measurement, e.g. close to 0 or 100 for a Shore A hardness measurement, care must be taken to select the proper hardness scale.

Tensile testing also provides a large quantity of useful information for the characterization of elastomer behavior.<sup>7,8</sup> Typically performed in uniaxial tension, an instrument pulls on a sample and measures force (with a load cell) as a function of extension. This data is later normalized according to sample cross-sectional area and original sample length to provide stress (e.g. MPa) vs. strain (e.g.  $l/l_0$ , unitless) behavior as a function of testing environment, which includes strain rate, temperature, and atmosphere.<sup>8</sup> Typical data for a thermoplastic elastomer is shown in **Figure 2.1** as curve C.<sup>8</sup> As mentioned above, elastomers typically possess large, recoverable strains with accompanying low stress levels. Primarily entropic in nature, ideal polymer chains possess stored elastic energy in the form of free energy.<sup>9</sup> As elastomers undergo elongation, the

original Gaussian distribution of polymer chain end-to-end distances becomes elongated up to the point of non-Gaussian behavior, where the finite extensibility of polymer chains induces strain hardening (e.g. an increase in stress at high strain).<sup>9</sup> Furthermore, the area under a tensile stress-strain curve is known as toughness, which represents the work done in deforming the material.<sup>4,8</sup> Thus, tensile testing provides lots of useful information with only one test.

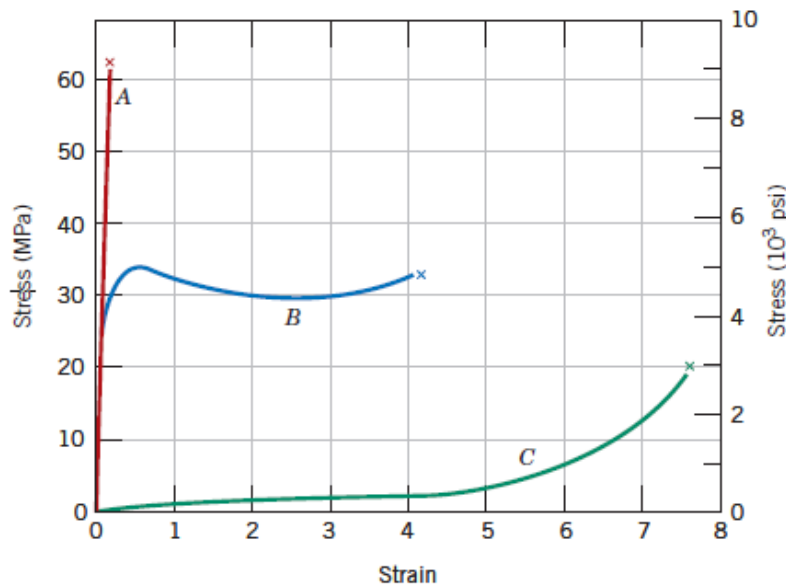


**Figure 2.1.** Typical stress-strain behavior for a (A) brittle polymer, (B) thermoplastic, and (C) thermoplastic elastomer. Adapted with permission.<sup>8</sup>

## 2.3 Overview of 3D Printing techniques

### 2.3.1 General Overview

Here, we introduce the types of additive manufacturing (AM) that are most employed in the 3D printing of elastomers. A general overview of various types of AM technologies is provided in more detail elsewhere.<sup>10</sup>

### 2.3.2 Vat Photopolymerization

Vat photopolymerization (VPP) involves directed energy deposition upon the surface of a photocurable mixture of monomers, oligomers, and/or polymers, termed a photopolymer, inside a container, or vat.<sup>10,11</sup> Multiple literature reports discuss this and

other types of additive manufacturing in great detail, elsewhere.<sup>10</sup> A recently published review also discusses photopolymers for 3D printing in general terms.<sup>12</sup> In brief, **Figure 2.2a** depicts top-down vector scan stereolithography (SL), where top-down refers to the direction of UV light impingement. Top-down SL avoids the repeated delamination step from the UV-transparent window that is common with bottom-up SL. This helps prevent damage of the soft, delicate features that are common with 3D printed elastomers. In top-down SL, the energy source, typically ultraviolet (UV) light, is reflected off a scanning galvanometer onto the photopolymer surface and initiates polymerization. After photopolymerization of the first layer in the plane of the build platform (x-y plane), the build platform lowers further into the photopolymer vat (z direction), permitting recoating of the previously printed layer with uncured photopolymer. The UV laser is then scanned across the second layer in the x-y plane. This process repeats itself until completion of the print, after which the printed object lies encased in the vat of uncured photopolymer. Isolation of printed objects simply requires removal from the build platform, removal of uncured resin and an optional post-cure in a UV chamber. Digital light processing (DLP) VPP, shown in **Figure 2.2b**, occurs in a similar manner to vector scan SL, except that the UV light is reflected onto an unmoving Digital Micromirror Device™ (DMD) that exposes entire layers with masked UV light all at once. VPP remains a popular AM method for elastomer production, typically when processed in a top-down apparatus, though challenges exist and are discussed below. In the case of two-photon polymerization (TPP), shown in **Figure 2.2c**, two independent scanning laser sources are focused on a single 3D pixel element, or voxel, within the build volume. Polymerization occurs only at the intersection of the laser sources, thus enabling a high degree of control over print

resolution. Additionally, TPP removes the need for recoating and the movement of a build platform, as the laser source intersection is controllable in the  $x$ - $y$ - $z$  build volume. However, in addition to characteristically small build volumes, TPP requires highly customized, femtosecond laser sources and printing apparatus remain relatively expensive, thus limiting applications primarily to tissue engineering.<sup>10,12</sup> Typical resolution for laser-based VPP is in the range of a few microns in the  $x$ - $y$  build plane, while DMD-based VPP possesses  $x$ - $y$  resolution in the 10-50  $\mu\text{m}$  range, due to limitations in the number of pixels/micromirrors in the DMD.<sup>10</sup> Resolution in the  $z$ -direction resolution remains controlled by the capabilities of the build platform stepper motor, as well as resin chemistry (e.g. UV absorber concentration).<sup>10</sup> Resolution in the  $x$ - $y$  plane in the case of TPP remains unrivaled, with feature sizes below 100 nm for multi-photon lithography.<sup>10</sup>

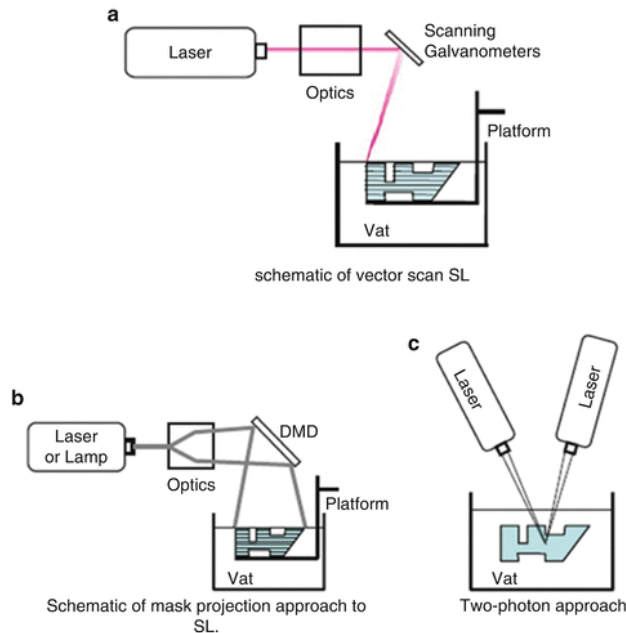


**Figure 2.2.** Schematic of three common types of vat photopolymerization. (a) Stereolithography. (b) Digital light processing vat photopolymerization. (c) Two-photon polymerization. Reproduced from Gibson, Rosen, and Stucker.<sup>11</sup>

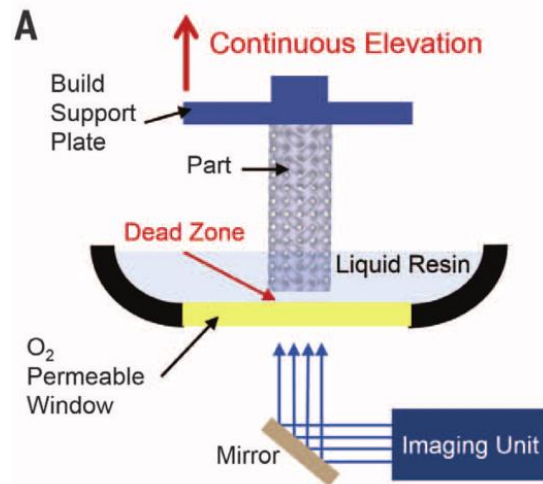


**Figure 2.3.** Schematic of continuous liquid interface printing (CLIP). Adapted from Tumbleston and DeSimone, et al.<sup>13</sup>

**Figure 2.3** depicts a relatively new type of vat photopolymerization termed continuous liquid interface printing (CLIP), a process designed and commercialized in 2015 by Joseph DeSimone and his company, Carbon™.<sup>13,14</sup> CLIP improves upon traditional bottom-up VPP through elimination of the repeated delamination steps from the bottom, UV-transparent window. An oxygen-permeable window (Teflon® AF 2400) allows diffusion of molecular O<sub>2</sub> into the bottom of the photopolymer vat, retarding free radical polymerization in the so-called “dead zone.” Fine tuning of the “dead zone” thickness occurs through control of the photoinitiator type and concentration, incident photon flux, and resin curing dosage.<sup>13</sup> Elimination of the delamination process enables continuous elevation of the build support plate, resulting in print speeds up to 100x faster than an equivalent, traditional bottom-up VPP process would provide. Though this is a bottom-up VPP approach, processing of elastomers with CLIP presents no issue as no adhesion to the bottom, O<sub>2</sub>-permeable window occurs. Carbon™ currently sells at least two elastomeric photopolymer compositions that include Silicone (CarbonResin SIL 30) and

Elastomeric Polyurethane (CarbonResin EPU 40), both of which possess a tensile strain at break > 300 %.

### **2.3.3 Fused filament fabrication**

Fused filament fabrication (FFF), otherwise known as fused deposition modeling (FDM) and a member of the material extrusion AM class, involves the directed deposition of a thermoplastic polymer filament in a layer-by-layer fashion. Shown in **Figure 2.4**, a build head forces the spooled filament through a heating element in a process similar to a hot melt adhesive (hot glue) gun. The heating element, attached to a series of motors that enable spatial control in the x-y-z build volume, rasters first in the build platform plane (x-y), depositing an entire layer of polymer. The printer then moves to the next layer (z), and the process continues. The incorporation of multiple build heads permits multi-material extrusion. This allows creation of multi-material objects or objects with complicated geometries in the case of simultaneous extrusion of the desired and sacrificial (support) materials. Build head diameter and potential die swell issues limit typical feature resolution with material deposition, but despite these issues a typical feature resolution of 100-150  $\mu\text{m}$  is achievable.<sup>10</sup> Unfortunately, elastomers typically suffer from filament buckling through the extrusion head, an extrusion failure mechanism that arises from insufficient filament elastic modulus.<sup>15</sup> The most common, commercially available polymers for FFF include poly(lactic acid), acrylonitrile butadiene styrene (ABS) random copolymer, polycarbonate (PC), and polyamides (PA), none of which are elastomers.



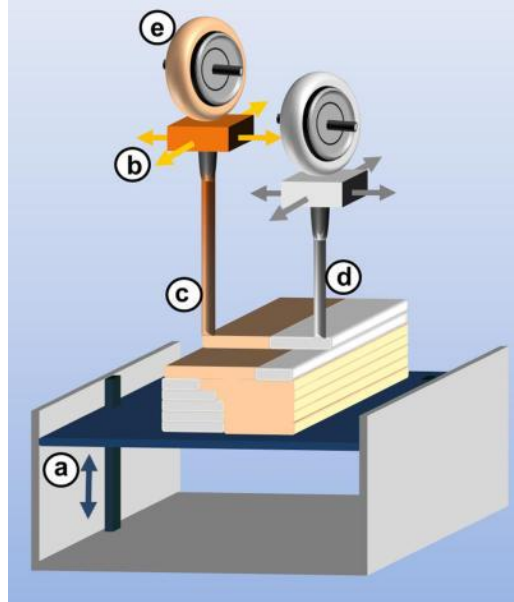


**Figure 2.4.** Fused filament fabrication (FFF) process depicting a movable build platform (a), a movable build head (b) with attached filament spool (e), and polymer deposition occurring from the main filament head (c) and the support material head (d). Reproduced from <sup>10</sup>

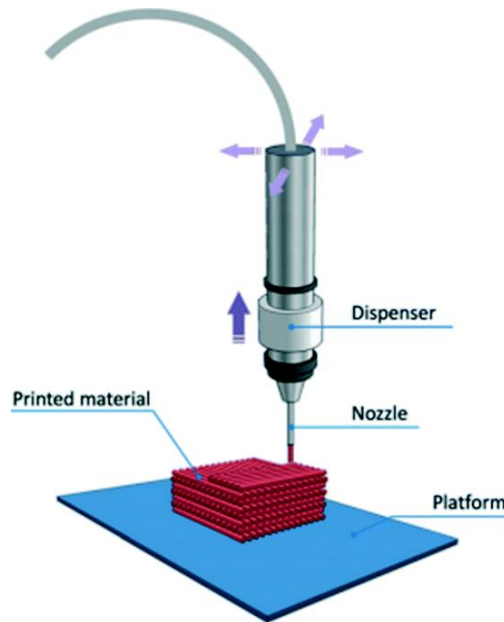
#### 2.3.4 Direct ink writing (DIW)

3D printing of elastomers via material extrusion often employs direct ink writing (DIW) methods. Direct ink writing (DIW) is a materials extrusion process, which enables printing of viscoelastic materials at ambient temperatures. It is also known by the name robocasting. Lewis et al. provided two outstanding reviews describing the concept of DIW and discussed suitable materials.<sup>16,17</sup> Here, we aim to only provide a short overview on the concept of DIW AM and we will highlight the required materials properties to enable printing briefly. **Scheme 2.1** illustrates a common DIW set-up, including a syringe with an ink-deposition nozzle and a computer-aided positioning stage. The apparatus continuously extrudes material out of the nozzle, generating 3D architectures layer-by-layer. Suitable materials for DIW should possess specific rheological properties to be processable. The material should be shear thinning to enable extrusion out of the printing nozzle. It should also possess a shear yield stress. To induce flow, a shear stress above the yield stress of the

resin is applied. Subsequently, the resin recovers its rigidity, when placed on a substrate, meaning that the shear stress is released. Polymer resins are commonly blended with fillers, e.g. silica particles or nano-clay to afford the described rheological properties. The fillers induce shear thinning flow behavior and at optimal resin/filler compositions, afford a material which possesses a shear yield stress. These rheological properties enable shape retention of the printed object, rendering self-standing structures. The Herschel-Bulkley model is frequently used to describe such yield-stress fluids (equation 1).<sup>18</sup>

$$\tau = \tau_y + K\dot{\gamma}^n \quad (\text{equation 1})$$

where  $\tau$  = shear stress,  $K$  = consistency,  $\dot{\gamma}$  = shear rate and  $n$  = flow index with  $n < 1$  for shear-thinning fluids.



**Scheme 2.1.** Schematic of DIW apparatus. Adapted from Bhargava et al.<sup>19</sup>

Alternative solidifying processes include subsequent UV-curing of the printed layer, thermal cure or extrusion into a support bath. The latter holds the printed structure in place until the deposited ink is converted into a solid. This process is often called “freeform

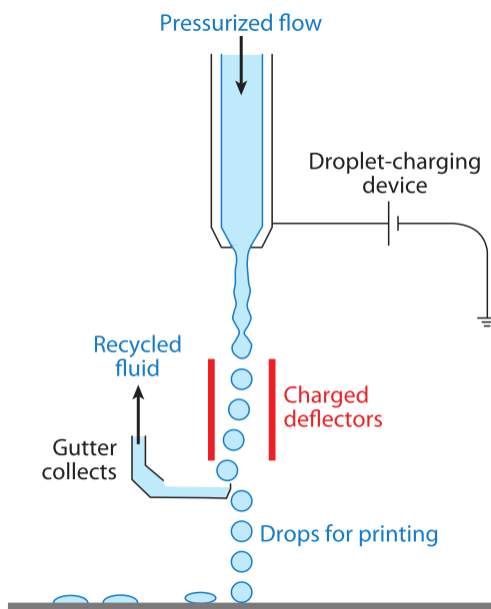
reversible embedding” (FRE). Angelini et al. recently described this concept in detail and provided an overview of the required rheological properties of the support material.<sup>20</sup> Overall, the minimum printing resolution for viscous polymer resins using DIW range from hundreds of microns to the sub-microns range and is usually dictated by the nozzle dimensions.<sup>16</sup>

### 2.3.5 Inkjet printing / Material jetting

Inkjet printing is another ink-based technique and utilizes the deposition of fluid droplets on a substrate (**Scheme 2.2**). Subsequent solvent evaporation renders the solid pattern or UV-curing transforms the liquid into a solid. Details on the required ink parameters are given in recent reviews by Derby<sup>21</sup> and Ma et al.<sup>22</sup> The solution viscosity, surface tension, density, pH and particle size of the ink determine its printability. For conventional printers, suitable inks must possess low viscosities (0.5 - 40 mPas), surface tensions in the range of 20-70 mNm<sup>-1</sup> and should enable stable droplet formation. These values are summarized in the Fromm equation with the dimensionless number  $Z$ , which equals to the inverse Ohnesorge number ( $Oh$ ) (equation 2).<sup>23</sup> Values of  $Z$  ranging from 1 to 10 indicate ideal droplet formation.<sup>18</sup>

$$Z = \frac{(d\rho\gamma)^{\frac{1}{2}}}{\eta} = Oh^{-1} \text{ (equation 2)}$$

With  $d$  = diameter of the nozzle aperture,  $\gamma$  = surface tension of the liquid,  $\rho$  = density,  $\eta$  = viscosity,  $Oh$  = Ohnesorge number.



**Scheme 2.2.** Schematic of inkjet printing technique. Adapted from Derby.<sup>21</sup>

Overall, inkjet printing is a low-cost technique, requires small amounts of material, enables fast and multi-material printing and is highly attractive to print organic thin-film transitions, sensors, microfluidic channels or organic-solar cells.<sup>24</sup> The minimum lateral printing resolutions range from 20  $\mu\text{m}$  to 70  $\mu\text{m}$  with printing heights around 100 nm to 1  $\mu\text{m}$ .<sup>16</sup> New generations of jetting printheads enable printing of highly viscous inks with viscosities of up to 100,000  $\text{mPa}\cdot\text{s}$ .<sup>25,26</sup>

### 2.3.6 Polymer Powder bed fusion

**Figure 2.5** depicts the polymer powder bed fusion (PBF) process, which is also described in great detail elsewhere.<sup>10,27</sup> Here, the entire apparatus exists inside an oven set to a temperature just below the glass transition temperature ( $T_g$ ) for amorphous polymers or the melting temperature ( $T_m$ ) for amorphous polymers. After initial polymer loading into the feed cartridges, the feed cartridge raises slightly, followed by a L-R motion of the counter-rotating, powder leveling roller, depositing an initial layer of powder onto the build platform. A  $\text{CO}_2$  laser then rasters in the x-y plane, providing the remaining thermal energy

required to raise the polymer temperature above  $T_m$ , after which the molten powder fuses together. The build platform then lowers by one-layer thickness and the process repeats itself. Traditionally, the vast majority of PBF powders remain in the nylon (polyamide, or PA) family, with PA11 and PA12 representing the two most popular compositions,<sup>10</sup> although a handful of elastomeric PBF powders exist (e.g. DuraForm Flex, Luvosint X92A-2, PrimePart ST PEBA 2301).<sup>10</sup> The latter example, PEBA 2301 contains a polyether block polyamide chemical structure that is likely synthesized via catalyzed (e.g.  $Ti(OR)_4$ ), melt esterification of diacid-terminated polyamide oligomers and hydroxyl-terminated polyether polyols, then finally processed into powder form.<sup>28</sup> Typical print resolution for the PBF process is on the order of 100  $\mu m$ , while post-processing steps help improve surface finish.<sup>10</sup>

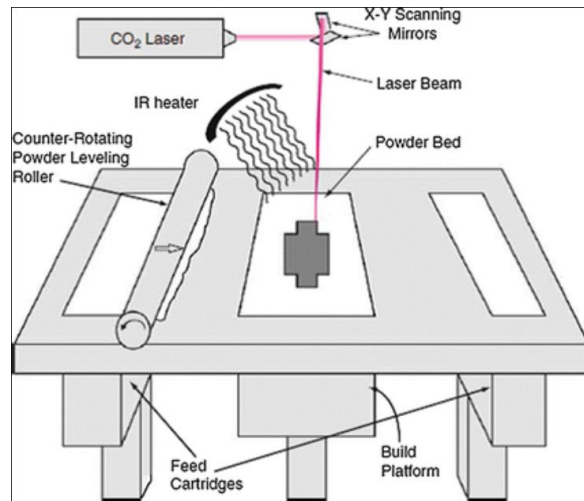


**Figure 2.5.** Polymer powder bed fusion (PBF) process. Reproduced from Gibson, Rosen, and Stucker.<sup>27</sup>

## 2.4 Challenges of 3D Printing Elastomers

Challenges related to elastomer processing with various AM technologies is highly dependent on the printing technology. Therefore, many challenges remain specific either

to the printer or the combination of the polymer and the printer. This section will highlight general challenges that relate primarily to the printing technology. One major challenge with vat photopolymerization relates to photopolymer viscosity.<sup>29</sup> Processing of photopolymers with too high viscosity often results in slower print times at best,<sup>13</sup> or warpage of the printed objects at worst.<sup>30</sup> A practical upper photopolymer viscosity limit is 5 Pa·s,<sup>31</sup> though rapid developments in printer technology often make previous restrictions obsolete. For example, recently, the use of a custom-built VPP with a recoating blade enabled selective UV-curing of a photoresin with a viscosity of 18 Pa·s. However, the use of a recoating blade is often challenging when working with elastomers because the low storage moduli of the cured networks might not withstand the shear forces during the recoating process and printed structures might deform or collapse. One common method for viscosity reduction involves the addition of reactive diluents, or monomers, to the photopolymer composition. These small molecule additives polymerize along with other reactants and become part of the crosslinked network.<sup>32</sup> Though these often impart unique functionality onto the printed object, issues of volatility and toxicity during printing must be managed.<sup>32,33</sup> Unreactive diluents, or solvents, often enable the processing of polymers that are not liquid at room temperature.<sup>34,35</sup> However, potential issues of volatility and toxicity also exist, in addition to the added complication of solvent removal, after printing, from the resulting organogel or hydrogel.<sup>35</sup> Some printers also possess the ability to heat the photopolymer vat, which can reduce photopolymer viscosity, but raises the risk of potential thermopolymerization, in the case of (meth)acrylates.<sup>36</sup>

One added complication with VPP involves the fundamentals of rubber elasticity and its implications on viscosity. For non-associating, unentangled, linear polymer chains,

which is typical for VPP due to the prevalence of low molecular weight precursors in photopolymer compositions, the affine and phantom network models apply.<sup>9</sup> Here, the relative deformation in a network strand is relative to the macroscopic, relative deformation for the entire part. Upon application of a force, e.g. stretching an elastomer, polymer chains uncoil but are limited by their finite extensibility, e.g. when reaching their maximum end-to-end distance ( $R_{\max}$ ). As  $R_{\max} = bN$ , where  $b$  is the monomer length and  $N$  the number of monomers, it is apparent that  $R_{\max}$  increases with increasing number of monomers, or molecular weight.<sup>9</sup> This corroborates the high extensibility observed in elastomers, which is primarily entropic in nature.<sup>9,37</sup> Unfortunately, melt viscosity scales with  $MW^{-1.0}$  below the entanglement molecular weight ( $M_e$ ) and with  $MW^{-3.4}$ , above  $M_e$ ,<sup>38</sup> so it would seem elasticity and precursor viscosity inherently oppose one another. In practice, this remains true, though a number of strategies exist to circumvent this issue, which include printing in the presence of chain extenders,<sup>33,39,40</sup> or a post-processing, chain extension step with blocked isocyanates.<sup>41,42</sup>

Regarding DIW, the ink must possess specific rheological properties to flow through the print nozzle and rapidly solidify after placement on the substrate, as outline in section 2.3.4.<sup>43</sup> This requires careful resin design and fillers are often indispensable. For elastomers, the curing of the precursors often requires extended time and the resulting networks possess low storage moduli. The latter might cause deformation or collapse of the printed structures under their own bodyweight. One method to overcome this challenge is the use of freeform embedded 3D printing. This AM technique utilizes a support bath, which holds the printed structure in place during the print. Details are given in section 2.6.2.

## 2.5 Silicone elastomers – synthesis and properties

### 2.5.1 Properties of silicone elastomers

Silicone elastomers are biocompatible, optically transparent, relatively chemically inert, electrically insulating, non-flammable, non-UV absorbing, exhibit low surface tensions, are water-impermeable and possess a high oxygen permeability. Furthermore, they are rather inexpensive and maintain their mechanical and electrical properties over a wide temperature range (-50 °C to +300 °C).<sup>44</sup> Applications below -50 °C are challenging due to the melt crystallization of PDMS between -75 °C and -100 °C and melting around -50 °C.<sup>45</sup> Yet, incorporating bulkier side groups, such as phenyl groups into the silicone backbone prevents cold crystallization, which allows for temperature applications below -50 °C.<sup>46</sup> These unique properties render silicone elastomers highly valuable for a variety of applications, such as medical applications for implants or prostheses, sealants in airplanes and automobiles, or as coatings for electronics. For many applications, fillers are added as reinforcing agents to increase the mechanical strength of silicone elastomers.<sup>47,48</sup> Other additives include processing aids, inert fillers, stabilizers and pigments.

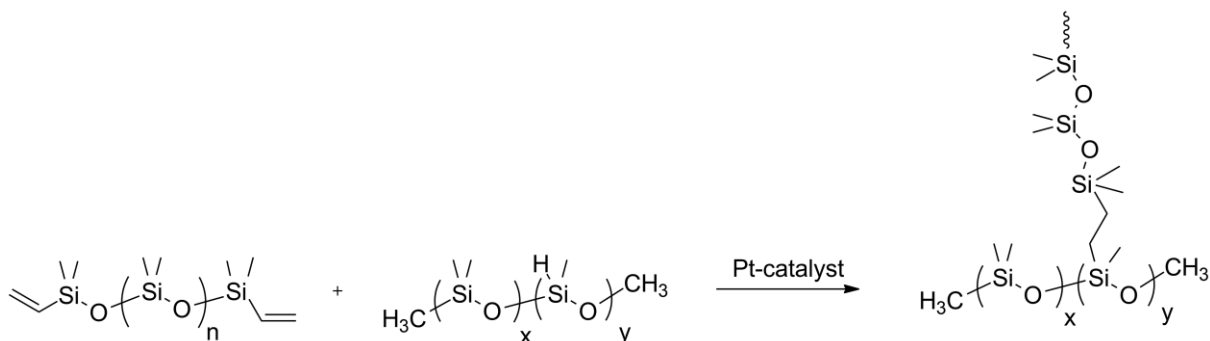
Silicone elastomers are covalently crosslinked networks of polysiloxanes. Polysiloxanes, also called siloxanes, or silicones, consist of a -Si(R)<sub>2</sub>O- repeat unit and owe most of their properties to the unique chemical nature of the Si-O bond. The large difference in electronegativity between the silicon atom ( $\Delta E_n = 1.8$ ) and the oxygen atom ( $\Delta E_n = 3.5$ ) results in a thermodynamically strong Si-O bond (452 kJ·mol<sup>-1</sup>) with 50% ionic character.<sup>46,49</sup> Furthermore, the long Si-O and Si-C bond (1.64 Å and 1.90 Å, respectively) compared to their carbon counterparts (C-O and C-C), combined with the large Si-O-Si bond angle of 143° and absence of substituents on the oxygen atom provide conformational flexibility to the polymer chains. Overall, low intermolecular forces, low surface tensions



(e.g. 20.4 mN/m for polydimethyl siloxane (PDMS)) and extremely low glass transition temperatures, (*ca.* -127 °C for PDMS) are characteristic for polysiloxanes.<sup>46,50</sup>

### 2.5.2 Synthesis of silicone elastomers

Three major crosslinking strategies yield silicone elastomers/rubber, where details on these methods are described in literature.<sup>49,51,52</sup> In brief, most thermally cured elastomers utilize the highly selective hydrosilylation reaction to form carbon-silicon bonds through an addition reaction depicted in **Scheme 2.3**. These silicones are marketed as two-part systems to avoid crosslinking during storage. For example, Sylgard 184 from Dow Corning is one of the commonly used two-part silicone resins in academic literature. Details on the composition of Sylgard 184 are provided in literature.<sup>53</sup> Part A, the so-called “base”, contains long-chain vinyl-functional silicones (e.g. -Si-CH=CH<sub>2</sub>) and a transition-metal catalyst (e.g. platinum in the form of the silicone soluble Karstedt catalyst). After mixing, the vinyl-functional silicones react with Part B, often referred to as “curing agent”, which contains hydride-functional silicones (e.g. -Si(R<sub>2</sub>)H ) and additional vinyl-functional silicones.<sup>51</sup> Crosslinking is commonly completed at elevated temperatures.

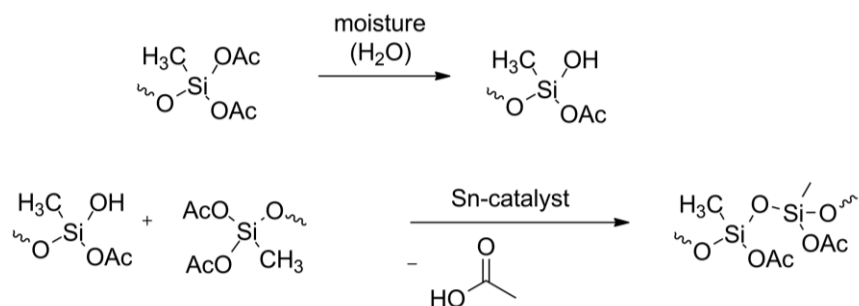


**Scheme 2.3.** Crosslinking of polysiloxanes *via* hydrosilylation reaction utilizing a transition metal catalyst. Details on the curing mechanism are provided in literature.<sup>54</sup>

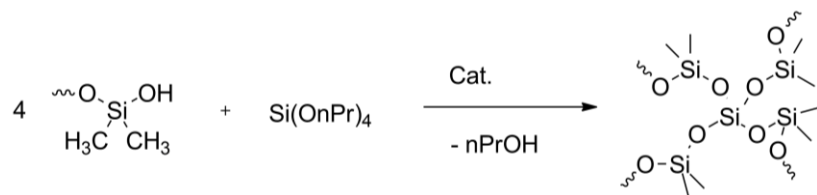
This curing reaction does not result in shrinkage or does not produce byproducts. The latter renders this process highly valuable for processing silicone elastomers for biomedical or

food-related applications. One drawback of this addition reaction is the sensitivity of the platinum catalyst to heavy metals, amines or thiols which inhibit curing due to catalyst poisoning.

Acetoxy-functional polysiloxanes crosslink through condensation reaction and belong to the family of one-part room temperature vulcanization (RTV) silicone elastomers. Upon exposure to atmospheric moisture, the acetoxy groups hydrolyze, release acetic acid, and form silanol groups which react *via* condensation reaction in the presence of a common condensation catalyst, e.g. tin catalyst (**Scheme 2.4**).

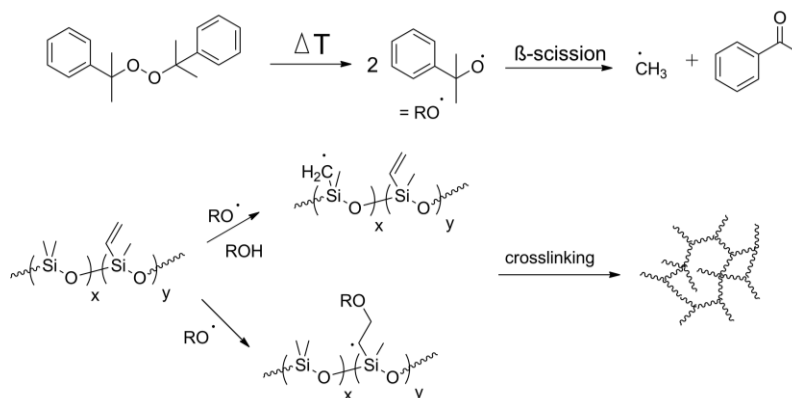


**Scheme 2.4.** Crosslinking of acetoxy-functional polysiloxanes via condensation reaction. Alternatively, other condensation-based systems utilize alkoxy silane  $\text{RSi(OR')}_3$  groups and release short alkyl chain alcohols, e.g. *n*-propyl alcohol upon contact with moisture (**Scheme 2.5**). This is of importance when the release of acetic acid may cause corrosion of the substrate. A drawback of one-part RTV systems is their slow curing processes because curing starts at the PDMS-air interface.



**Scheme 2.5.** Crosslinking of polysiloxanes using alkoxy silane groups and subsequent release of *n*-propyl alcohol.

Free radical crosslinking of silicones using peroxides to initiate crosslinking is an alternative to the described mechanisms but offers less control over cure rates and crosslinking distribution and produces residual by-products (**Scheme 2.6**). This curing technique is commonly employed for high-temperature vulcanizing (HTV) silicone rubbers.<sup>51</sup>



**Scheme 2.6.** Free-radical curing mechanism of polysiloxanes.<sup>55</sup>

### 2.5.3 Traditional processing of silicone elastomers

Traditional processing of silicone elastomers differs for HTV-silicones and liquid rubber silicones (LSR). HTV-silicones exhibit extremely high viscosities (e.g. 20-100 mooney) and are commonly distributed in block form. Additives and crosslinker (peroxides or Pt-catalyst) are blended into the silicone on a roll mill before vulcanization. Compression molding, injection molding, extrusion or calendaring are utilized to process the silicone elastomer.<sup>56</sup> In contrast, LRS consist of lower molecular weight polysiloxanes. They possess viscosities of 10-200 Pa·s, and exhibit shear thinning behavior. Commonly, LSR are distributed as two-part system (Pt-curing system only) and processed via injection molding.<sup>56</sup>

## **2.6 Additive Manufacturing of Elastomeric Architectures using Silicone Precursors**

### **2.6.1 Motivation**

AM of silicone elastomers is highly desirable for healthcare applications, e.g. fabricating microfluidic devices, implants and vascular tubes. It would also facilitate the manufacturing of soft active materials, such as actuators, robots, wearable electronics and sensing devices. For example, conventional molding processes require individual fabrication steps for each part and subsequent assembly, which are time-consuming iterative steps and hinder automation. AM of silicone elastomers in combination with other materials, e.g. conductive materials provides a highly attractive manufacturing opportunity that enables fast processing and higher throughput, which saves time and costs. In addition, AM of silicone elastomers would enable facile customization of devices for consumers, where customized prostheses and implants become accessible. The higher freedom in design compared to traditional manufacturing further enables AM of mechanical metamaterials, e.g. cellular solids, attractive for shock absorption and stress mitigation applications.<sup>57</sup>

### **2.6.2 Direct ink writing**

As outlined in section 2.3.4, the rheological properties of the polymer resins determine their printability and have a strong impact on the printing resolution because fast “solidification” of the resin after placement is required. First attempts on DIW of silicone elastomers lacked silicone precursors with optimized rheological properties. Researchers utilized a RTV silicone from 3M and silver-nanoparticle infused silicone (Silicone Solution, Twinsburg OH) to print a bionic ear<sup>58</sup> or quick-curing acetoxy silicone (Loctite 5366 bathroom sealant, LOCTITE) to design reactionware for chemical synthesis.<sup>59</sup> In both

cases, the silicone object served as bulk structure, and high printing resolutions were not required.

Corning (DC) offers one silicone resin, DC SE 1700, which fulfills all printing criteria for DIW.<sup>17</sup> DC SE 1700 is a two-part, thermally curable PDMS-based resin which contains fumed silica nanoparticles.<sup>60</sup> Due to the presence of fumed silica fillers, DC SE 1700 possesses shear-rate dependent viscosity and stress-dependent shear storage ( $G'$ ) and loss ( $G''$ ) moduli (**Figure 2.6**).<sup>61</sup> Oscillatory stress sweep measurements at room temperature (**Figure 2.6B**) demonstrated that the material exhibits solid-like behavior at lower oscillatory stress, which changes to liquid-like behavior at oscillatory stresses above the yield stress. Wilson and co-workers intensively studied the printability of DC SE 1700 and blends of DC SE 1700 with unfilled PDMS to print complex architectures.<sup>61</sup> The dilution of DC SE1700 with a blend of vinyl-terminated PDMS and trimethylsiloxane terminated PDMS-*co*-polymethylhydrosiloxane decreased the yield stress and the viscosity of the ink and allowed for tuning the resulting mechanical properties of the cured elastomers. Ideal printing compositions ranged from 100-70% DC SE 1700. Increasing the amount of unfilled PDMS-based resin further, may induce mechanical instabilities and cause collapse of the printed structure.<sup>61,62</sup> After the printing process, thermal post-curing at 150 °C transformed the resin to a crosslinked rubber. The excellent printability of these resins enabled the authors to print cellular architectures, which possessed negative shear stiffness, meaning that the load-deformation curve exhibited a negative slope.

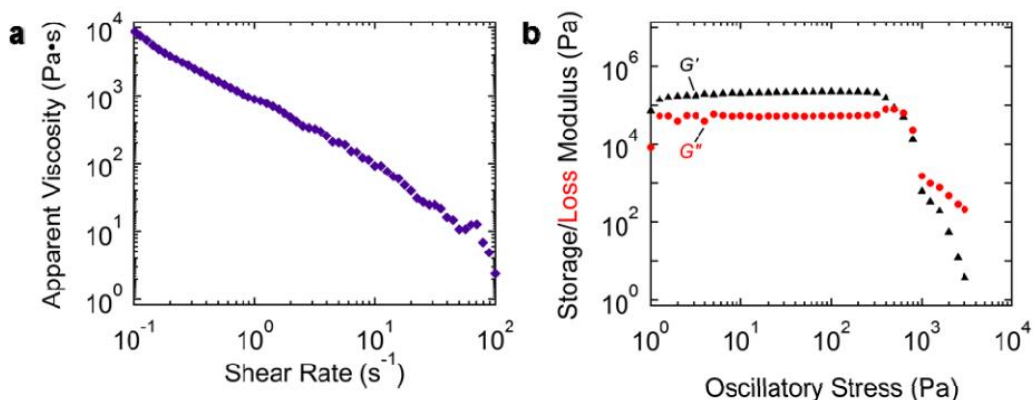
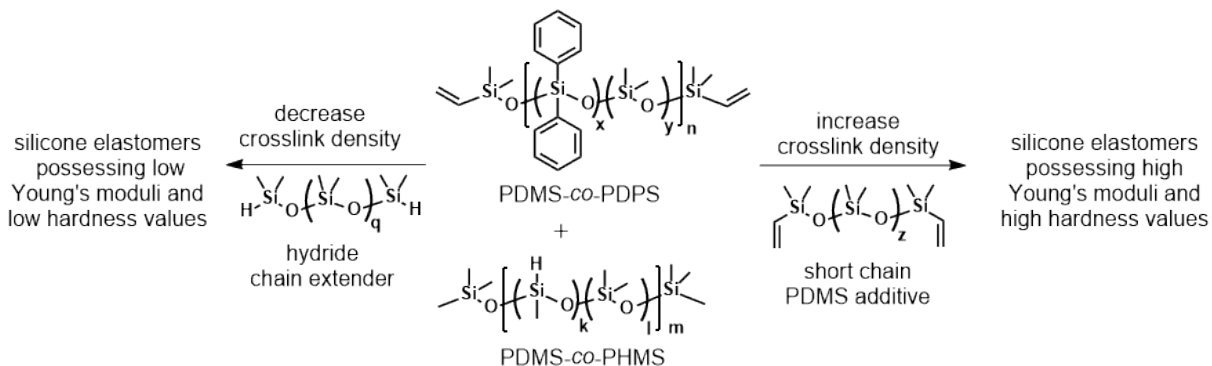


**Figure 2.6.** A) Shear-rate dependent, apparent viscosity of Dow Corning SE1700 (uncured). B) Oscillatory stress sweep of DC SE1700 (uncured) showing storage and loss moduli. Reproduced from Wilson and co-workers.<sup>61</sup>

Capitalizing on the printability of DC SE1700 and its diluted blends, various researchers designed complex architectures possessing outstanding energy trapping abilities<sup>63</sup>, programmable porosity ratios<sup>64</sup> and shape-memory behavior when combined with gas filled microspheres.<sup>65</sup> Other examples are additive manufactured foams,<sup>66</sup> vascular tissue constructs,<sup>67,68</sup> or the design of synthetic spider webs.<sup>69</sup> Ozbolat et al. observed higher strains at break of 3D printed structures using DC SE 1700/Sylgard 184 compositions compared to their mold counterparts.<sup>62</sup> The authors attributed these differences to a decrease in bubble entrapment in the printed tensile specimen. A dog-bone specimen printed along the transverse direction using a blend ratio of 9:1 DC SE1700:Sylgard 184 exhibited the highest strain at break of 400%, higher than the casted mold (max. elongation at break 200%). Intriguingly, the 3D printed structures also facilitated cell adhesion and spreading due to the presence of grooves and rougher surfaces than cast samples, making these structures attractive for bioengineering applications.

Crosslinking density, weight percent and type of filler dictate the mechanical properties of silicone elastomers. Varying the blend ratio of DC SE 1700 to unfilled two-

part silicone resin or the base to catalyst ratio impacts the mechanical properties of the resulting silicone elastomers. For example, multi-material printing of different resin compositions enabled to design architectures which possessed gradients in the elastic moduli.<sup>70</sup> Nevertheless, the limited commercial availability of silicone resins which exhibit the required rheological properties for DIW still restricts accessible materials properties. Addressing this need and expanding the tool box of silicones for DIW, Wilson and et al. formulated tailored silicone inks to render elastomers with tunable stiffness.<sup>71</sup> The fundamental concept relied on platinum-catalyzed hydrosilylation chemistry, utilizing vinyl-terminated PDMS-*co*-(diphenylsiloxane) (PDMS-*co*-PDPS) and trimethylsiloxane terminated PDMS-*co*-polymethylhydrosiloxane (PDMS-*co*-PHMS), combined with a Karstedt Pt catalyst to promote curing (**Scheme 2.7**).

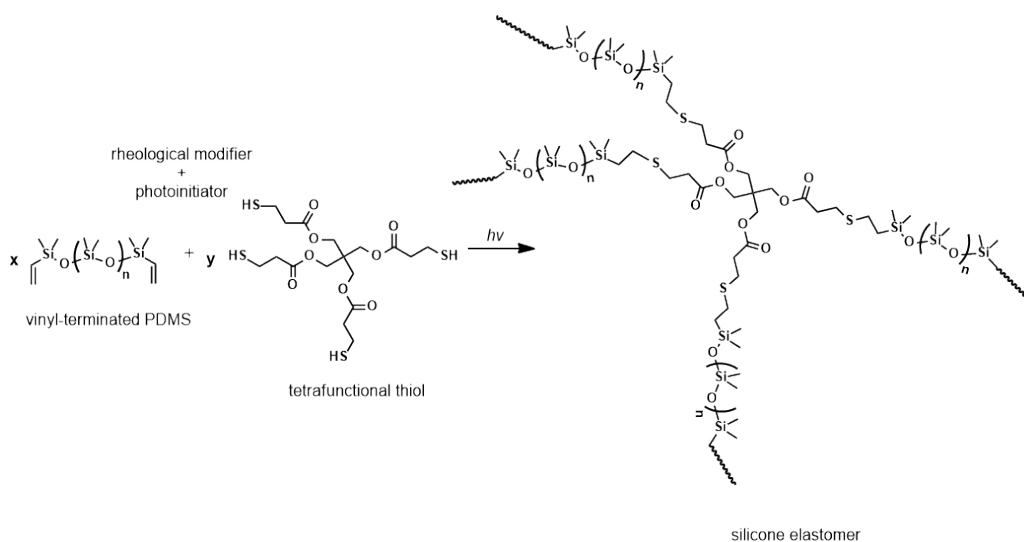


**Scheme 2.7.** Complex resin formulation to yield silicone elastomers with tunable stiffness.<sup>71</sup>

The incorporation of hexamethyldisilazane-treated silica and rheology modifying additives (silicone polyethers) rendered a pseudoplastic ink, suitable for DIW. A reaction inhibitor (1-ethynyl-1-cyclohexanol, ETCH) prolonged print time and prevented early curing events. This core ink was then combined with two different PDMS-based oligomers. Utilizing a chain extender (hydride-terminated PDMS) resulted in silicone elastomers with low stiffness. Alternatively, vinyl-terminated PDMS increased the crosslink density of the

network, rendering stiffer material. These tailor-made inks afforded elastomers with Young's moduli ranging from 0.40 MPa to 11.51 MPa and hardness values of Shore 10A to Shore 70A, respectively. Overall, the use of PDMS-co-PDPS makes this silicone elastomer attractive for low temperature applications because the bulky PDPS segments suppress undesired cold crystallization of PDMS. This approach demonstrates the opportunities for chemists and material scientists to synthesize and develop novel inks expanding the accessible materials properties of 3D-printed silicone elastomers.

Stuart et al. introduced an alternative strategy to tailor the stiffness of silicone elastomers.<sup>72</sup> The authors formulated silicone-based inks using a low molecular weight tetrafunctional thiol-crosslinker (pentaerythritol tetrakis(3-mercapto-propionate)), which they dispersed in vinyl-terminated polysiloxanes (**Scheme 2.8**). Added photoinitiator enabled UV-curability and fumed silica served as rheological modifier to yield inks, which possessed strong shear thinning behavior and a yield stress. After ink deposition, UV-light irradiation induced thiol-ene reaction and rendered crosslinked silicone networks.



**Scheme 2.8.** UV-initiated thiol-ene reaction of tetrafunctional thiol and  $\alpha,\omega$ -divinyl PDMS yielded silicone elastomer.



The choice of vinyl-terminated polysiloxanes determined the stiffness of the network. The authors formulated three different inks to tailor the flexibility of the networks. One formulation used part A of Ecoflex 00-30A and yielded a soft silicone elastomer with a Young's modulus of 0.12 MPa. A 1:1 mixture of Dragonskin 30 A and silanol-trimethylsilyl modified Q resin afforded an elastic modulus of 1 MPa. Exchanging the Dragonskin 30 A with Sylgard 184 and the addition of 15 wt% flax fibers (300-400  $\mu\text{m}$ ) yielded a stiffer network with a Young's modulus of 3.4 MPa. Elongation at break ranged from 922% for the soft network, to 267% for the intermediate, and 150% for the stiff formulation. Comparable values for printed and casted tensile specimen indicated excellent interlayer adhesion. The authors proposed that after UV-curing of one layer, unreacted thiol-groups are still available on the layer surface to participate in the crosslinking step of the next layer. Thus, forming covalent bonds between layers, responsible for good interlayer adhesion. Multimaterial DIW of the different silicone-inks enabled to locally tune the stiffness of a printed object and inspired the design of soft actuators.

Shepherd et al. formulated silicone inks for UV-DIW using two commercially-available silicones.<sup>73</sup> One component was a high molecular weight silicone (60 wt % Nuvasil® Loctite 5039) to afford the necessary flow properties (e.g. shear thinning properties). The other component was a low molecular weight, UV-sensitive silicone (40 wt % Wacker® Semicosil 912) to impart crosslinking after ink placement. This concept was then utilized to print elastic capacitive sensors harnessing the electrically insulating character of silicones.

To afford the required rheological properties for DIW, many ink formulations utilize fillers, e.g. fumed silica. Untreated fumed silica consists of amorphous SiO<sub>2</sub> particles (~10 nm) which form larger aggregates (~100 nm). Thus, it possesses an extremely high surface area and is hydrophilic due to the presence of silanol groups on the particle surface.<sup>74</sup> Hydrogen bonding facilitates the interactions between silanol groups, which enable the fumed silica to form a 3D-network in the silicone elastomer. However, they are also responsible for undesired creep hardening of silicones, where the addition of hydrophobic fumed silica prevents this problem. For example, facile silylation (e.g. with hexamethyldisilazane) of the silanol groups renders hydrophobic SiO<sub>2</sub> particles. As an alternative to silica fillers, Lipton et al. exploited paraffin wax to modify the rheological properties of silicone Ecoflex 0050 (by Smooth-On).<sup>75</sup> This strategy did not only result in printable inks, but also added a thermoresponsive character to the silicone elastomer. The paraffin wax melted upon heating, created an internal pressure and caused the structure to expand. Incorporation of conductive carbon black into the silicone-wax matrix enabled the fabrication of electrically actuated hydraulic solids.<sup>76</sup> Other conductive fillers for silicone elastomers are carbon nanotubes or silver nanoparticles, utilized to print elastic electrodes<sup>77</sup> or tactile sensors,<sup>78</sup> respectively. If no stringent printing resolution is required, rheological modifiers such as additional fillers are completely optional. Vlassak et al. utilized a commercially-available UV-curable silicone resin (Shin-Etsu Silicones, KER-4690 A/B) with an almost Newtonian flow behavior (viscosity ~4.8 Pa·s) to enable printing of elastic conductive structures.<sup>79</sup> In general, the need of fillers to achieve part fidelity using DIW diminishes the transparency of printed PDMS-based elastomers and represents one drawback of this technique. As an example, **Figure 2.7** shows an image of the DIW

process, which utilized a blend of 85 wt% DC SE1700 and 15 wt% Sylgard 184 and resulted in translucent 3D objects.

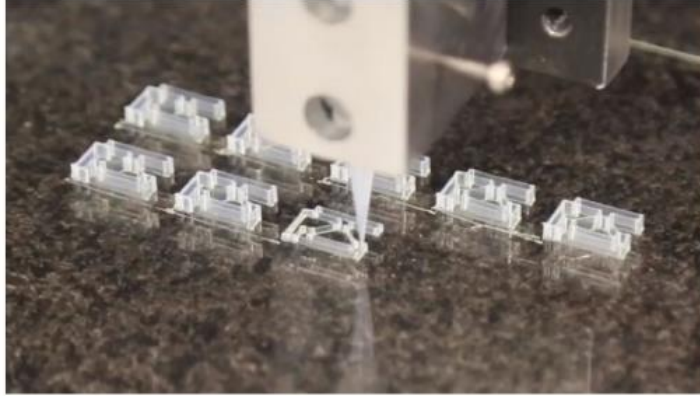


**Figure 2.7.** Image of DIW process using a blend of DC SE1700 (85 wt%) and Sylgard 184 (15 wt%). Reproduced with permission from Bertoldi et al.<sup>63</sup>

The demand for wearable electronics has motivated various researchers to investigate facile manufacturing strategies to combine soft and elastic materials with electronic devices. Lewis et al. capitalized on the flow behavior of PDMS with different molecular weights and utilized the latter for embedded 3D printing (e-3D printing).<sup>80</sup> Rheological modified silicones served as printing matrix and filler fluid, which enabled the embedding of conductive inks as illustrated in **Figure 2.8**.

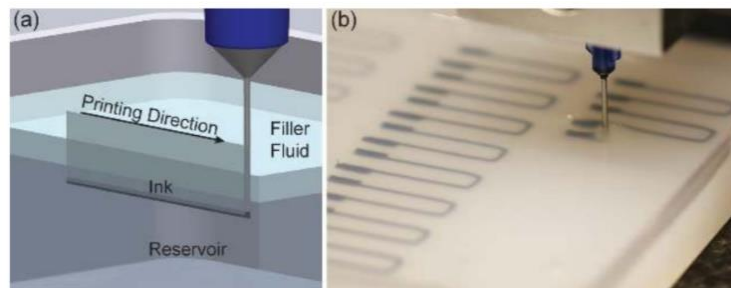


**Figure 2.8.** Embedded 3D printing utilized to incorporate conductive inks into the silicone elastomer to manufacture elastic electronics. Reproduced from Lewis et al.<sup>80</sup>

The addition of thickening and thinning agents to commercially-available Ecoflex 00-30, rendered the reservoir material possessing shear thinning properties and filler material which followed Newtonian-fluid behavior, respectively (illustrated in Error! Reference

source not found.). In particular, the reservoir material must possess a yield stress below the depositing ink and a high enough storage modulus ( $G' \sim 10^4 \text{ Pa}$ ), to enable nozzle movement but to also trap the printed pattern in place. On the other hand, low viscosities are required for the filler fluid because it must readily flow into voids, which were created by the movement of the nozzle.

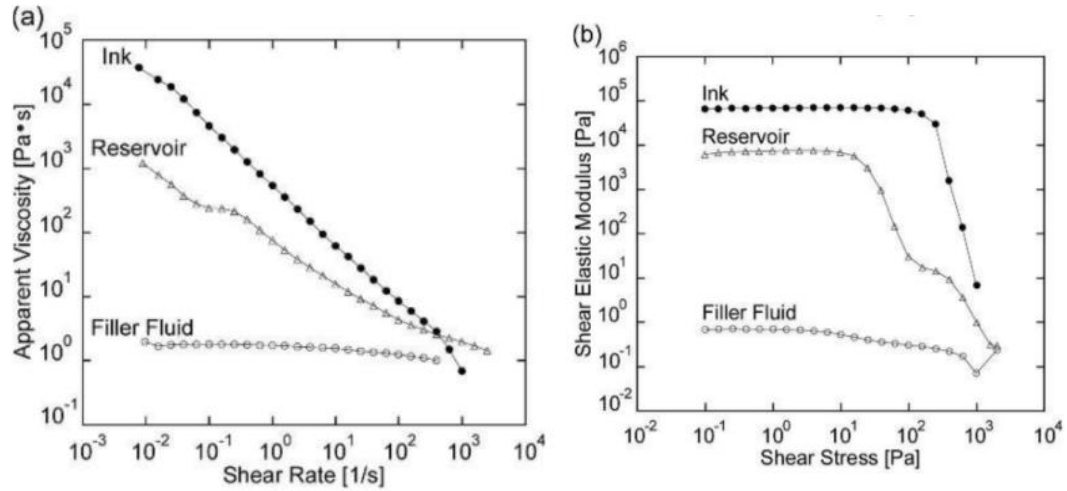


**Figure 2.9.** A: Apparent viscosity versus shear rate for the ink, reservoir material and filler fluid, utilized for embedded 3D printing. B: Shear elastic modulus versus shear stress for the same materials. Adapted from Lewis et al.<sup>80</sup>

After embedding the conductive ink, post-curing converted the matrix and the conductive ink into a highly elastomeric system, exhibiting max. elongations at break of 900% and softness between Shore Hardness of 00-30.<sup>80</sup> Intriguingly, combining this design principal with molding and soft lithography enabled the manufacturing of a soft, autonomous robot.<sup>60</sup> In addition, soft somatosensitive actuators have been fabricated recently.<sup>81</sup>

While the strategy described by Lewis et al. utilized the silicone as a bulk material, the idea of printing into a support material is highly attractive for additively manufacturing silicone elastomers in three dimensions. In particular, the matrix holds the printed objects in place, enabling printing of extremely soft materials with complex geometries. Soft silicone elastomers are highly attractive for biomedical applications, e.g. to mimic human

tissue. Exploiting the rheological properties of microgels, Angelini and co-workers demonstrated their use as support matrices for DIW. First, the authors introduced the concept of depositing aqueous solutions of UV-crosslinkable polyvinylalcohol into hydrophilic Carbopol® medium.<sup>82</sup> Carbopol® is a product line of Lubrizol, consisting of high molecular weight, crosslinked polyacrylic acid polymers. Swollen Carbopol particles fluidized upon applied stress and enabled the injection of the polymer solution. After the stress was released, the material re-solidified and trapped the PVA in place, preventing it from flowing and supporting the 3D-printed shape. The printed object remained embedded during the curing step to retain the print geometry. Utilizing this concept, the authors briefly mentioned the placement of PDMS into a silicone-based medium, consisting of a Dow Corning 9041 silicone elastomer blend, diluted with 10% silicone oil. However, the latter did not provide the necessary support to realize defined structures. Surprisingly, a nonpolar scaffold material is not directly required to support PDMS. Feinberg et al. demonstrated successful extrusion of Sylgard 184 into Carbopol® medium (**Figure 2.10**).<sup>83</sup>

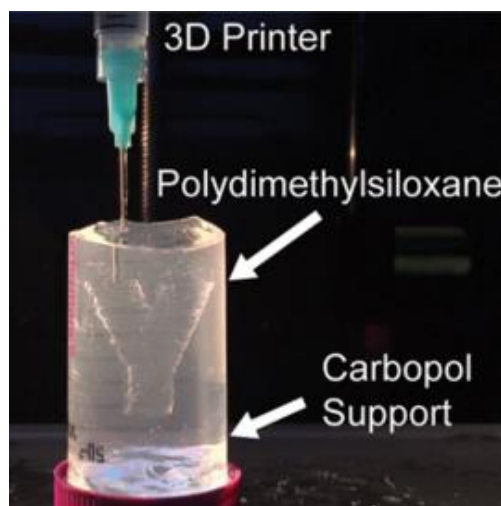


**Figure 2.10.** Principal of extruding two-part PDMS (Sylgard 184) into Carbopol® medium. Adapted from Feinberg et al.<sup>83</sup>

This approach allowed the continuous printing of complex objects (e.g. helical tubes) and their release after thermal curing, by simply removing the Carbopol using PBS-buffer solution. Unfortunately, the polarity differences of the support bath and the extruded silicone resulted in some challenges. In particular, trapped Carbopol in the silicone resin limited the printing resolution and hindered lateral layer fusion.

Currently, no commercially-available nonpolar material provides the necessary rheological properties to act as support material for PDMS-based resins. Angelini et al. outlined details on optimal rheological parameters for printing with sacrificial materials.<sup>20</sup> Facing these challenges, Angelini et al. developed nonpolar microgels exploiting the self-assembly of block copolymers in mineral oil.<sup>84</sup> In mineral oil, poly(styrene-*block*-ethylene/propylene) diblock copolymers ( $172.6\text{ k g}\cdot\text{mol}^{-1}$ ) self-assembled into micelles with glassy polystyrene cores. In contrast, triblock copolymers of poly(styrene-*block*-ethylene/butylene-*block*-styrene) ( $98.1\text{ k g}\cdot\text{mol}^{-1}$ ) formed macroscopic networks due to bridging events of ethylene/butylene blocks. Combining both at an equal 1:1 ratio and low polymer concentration (4.5 wt.%) resulted in microgels, possessing the required rheological properties for successful printing using DIW (**Figure 2.11**). This tailored microgel showed excellent support properties for various silicone inks which possessed shear viscosities ranging from 10 to 100,000 mPa·s. Overall, the authors printed complex architectures using RTV silicones (Smooth-on Mold Max 10, Sylgard 184) and UV-curable silicone (Momentive UV Electro 225). Tailoring the rheological properties of the microgel system enabled printing of feature sizes of 450  $\mu\text{m}$ , which possessed the required strength to maintain shape after support removal. They also reported the printing of feature sizes down to 250  $\mu\text{m}$ , but the parts collapsed upon removal of the support bath. 3D printed

tensile specimen revealed maximum elongations of 700%, confirming good interlayer adhesion.

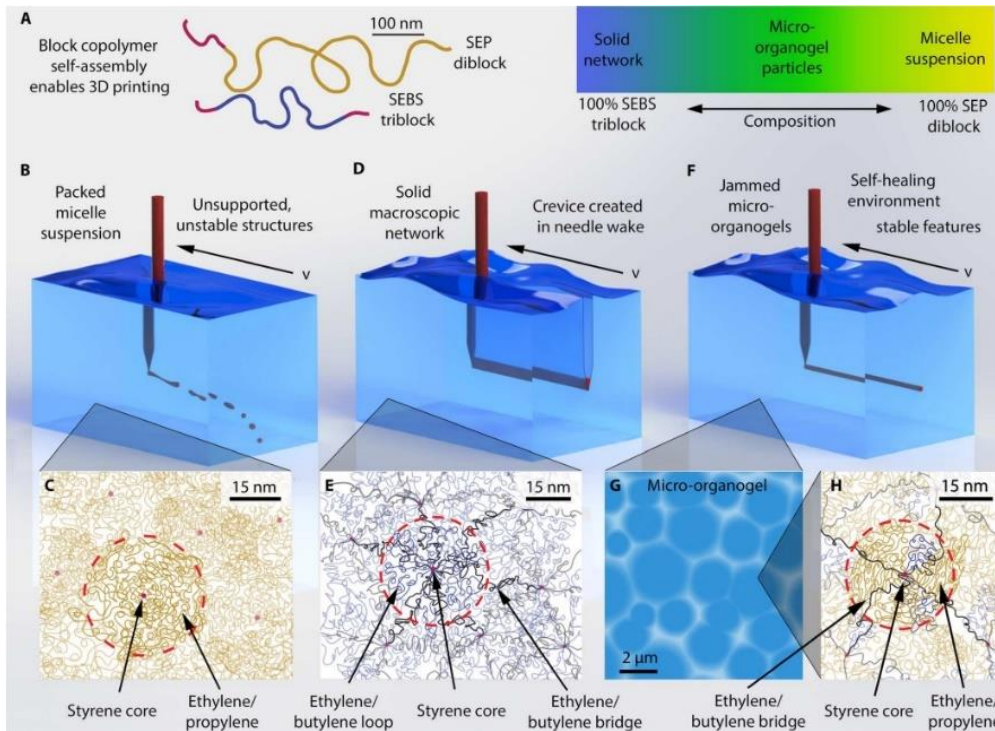
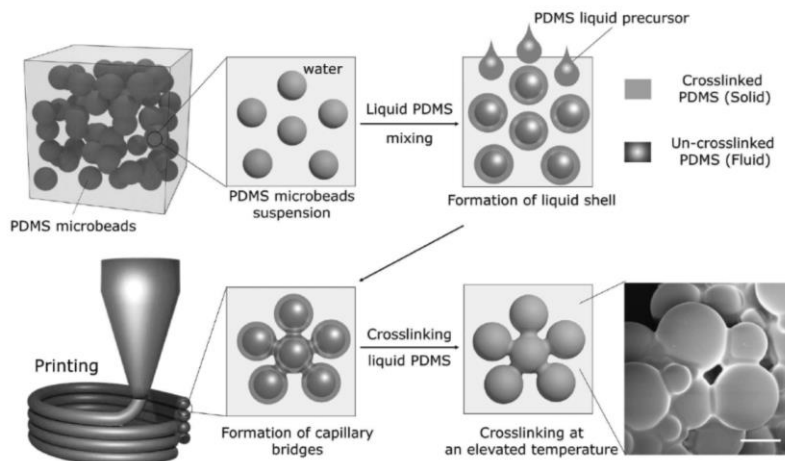


**Figure 2.11.** Self-assembly of SEBS triblock and SEP diblock copolymers in mineral oil to yield jammed micro-organogels. Adapted from Angelini et al.<sup>84</sup>

Another intriguing approach to 3D-print PDMS elastomers harnessed capillary forces.<sup>85</sup> Velev et al. described the concept of 3D printing silicones using capillary bridging forces in analogy to forming a sand castle, where water binds the sand particles. Such capillary suspension inks consisted of precured PDMS 10 μm microbeads, 2-30 vol% uncured PDMS liquid precursor and water medium (**Scheme 2.9**).



**Scheme 2.9.** Synthetic scheme to formulate PDMS suspensions. Adapted from Velev et al.  
85

Here, the uncrosslinked PDMS acted as binder and afforded a thixotropic gel-like ink. At low shear stresses, the PDMS microbead suspension exhibited gel-like behavior and showed yielding at high oscillatory shear stresses. 3D printing and drying yielded porous microfilaments. The porosity of these samples dictated their mechanical properties and molded dog-bones showed a maximum strain at break of 140%. Significantly, the authors demonstrated the ability to print in aqueous media (PBS-buffer), making this approach attractive for biomedical applications.

### 2.6.3 Two-photon absorption microstereolithography

Direct laser writing based on two-photon absorption photopolymerization is an extremely precise technique and enables printing of features down to the size of 100 nm,<sup>86</sup> which renders it attractive to manufacture optical waveguides or microfluidic devices for biological applications. In 2004, Ober et al. reported the first use of two-photon absorption microstereolithography to process PDMS-based elastomers. The authors exploited two different crosslinking systems. One utilized ( $\eta^5$ -cyclopentadienyl-methyl) trimethylplatinum as initiator, which decomposed into the active platinum hydrosilylation



catalyst upon UV illumination. The actual crosslinking took place *via* thermal hydrosilylation, which impacted the overall print resolution and decreased part fidelity due to undesired curing events. As an alternative, the authors utilized a radical photoinitiator, e.g. isopropyl-thioxanthone to improve photoimaging and enabled feature sizes of 0.3-0.6  $\mu\text{m}$  (**Figure 2.12**). Details on the utilized PDMS precursor were not provided. This work inspired others to manufacture movable microstructures,<sup>87</sup> and to improve print throughput.<sup>88</sup>

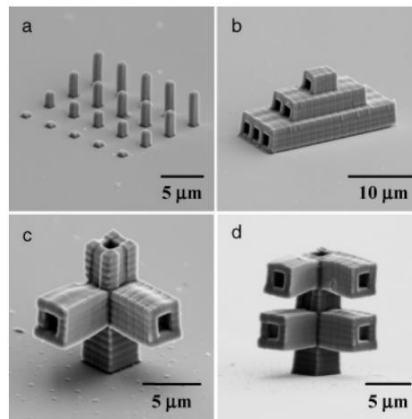


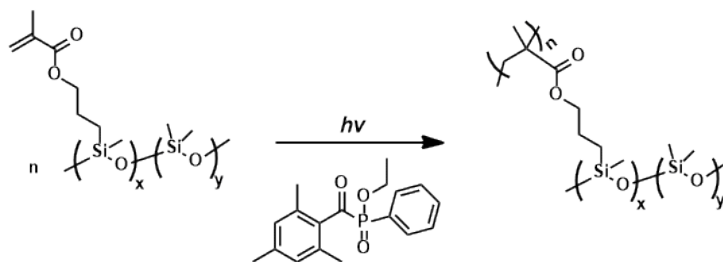
**Figure 2.12.** Variety of geometries consisting of crosslinked PDMS and printed using two-photon absorption microstereolithography. Adapted with permission from Ober et al.<sup>89</sup>

#### 2.6.4 Vat photopolymerization/SLA

Literature on the development of PDMS-based photoresins for vat photopolymerization is rather limited. As discussed in section 2.3.2, ideal photoresins must possess low viscosities ( $\eta < 5 \text{ Pa}\cdot\text{s}$ ), exhibit stability under ambient temperatures, undergo fast and controlled gelation upon UV-exposure, and yield networks with high enough storage moduli to withstand the printing procedure. Most commercial photoresins are (meth)acrylate-based systems which meet the printing requirements but result in highly crosslinked networks with rather high stiffness. Designing photoresins which enable printing and high feature resolution but yield structures with elastomeric properties remains challenging. In

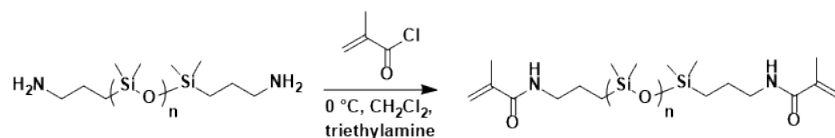
particular, printing elastomers with low moduli often demands support scaffolds to avoid collapsing of the printed object. Furthermore, the high oxygen permeability of silicones affects UV-curing of acrylates and methacrylates due to oxygen inhibition events and demands printing under inert gas. Dark-polymerization due to the low glass transition temperature of PDMS is another challenge known from 2D lithography.<sup>90</sup>

Various silicones bearing UV-reactive functional groups, e.g. methacrylate groups are commercially available. Because vat photopolymerization requires low viscosities, only silicone oligomers possess suitable properties for printing. Wessling et al. demonstrated successful vat photopolymerization of oligomeric poly(methacryloxypropyl)methylsiloxane-*co*-PDMS with 7-9 mol% methacrylate groups and a viscosity of 2-3 Pa·s (**Scheme 2.10**). The oligomeric structure resulted in a silicone elastomer with a Young's modulus of 11.45 MPa.<sup>90</sup> Maximum elongation at break was not reported.



**Scheme 2.10.** UV-crosslinking of methacrylate-functional PDMS oligomer yields silicone elastomer with high crosslinking density.

Boydston et al. reinvestigated the challenge of formulating elastomeric photoresins for digital light processing (DLP) AM.<sup>91</sup> First, they reacted an oligomeric amine-terminated PDMS with acryloyl methacrylate, affording a  $\alpha,\omega$ -dimethacrylamide polydimethylsiloxane (PDMSDMAA) ( $M_n=4.5\text{k g}\cdot\text{mol}^{-1}$ ) (**Scheme 2.11**). The latter possessed a viscosity of 0.29 Pa·s when diluted with toluene (5 wt%).

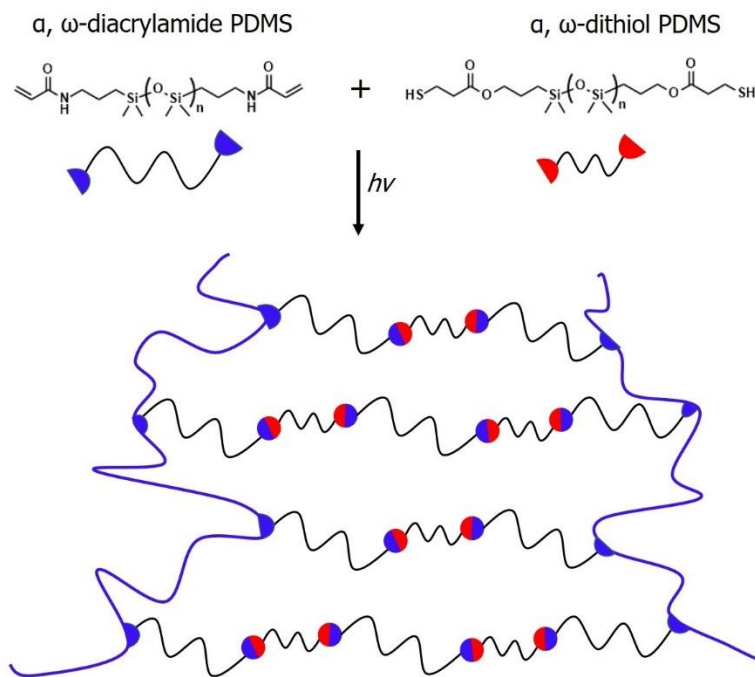


**Scheme 2.11.** Reaction of  $\alpha,\omega$ -diamine PDMS with methacryloyl chloride in DCM in the presence of triethylamine yields  $\alpha,\omega$ -dimethacrylamide polydimethylsiloxane.

As expected, UV-crosslinking of PDMSDMAA rendered a highly crosslinked network, which was reflected in a low tensile strain at break of 50%. To achieve elastomers with higher elongations, the authors explored the influence of hydrogen bonding on materials properties and utilized hydroxyethyl acrylate (HEA) for 3D-printing. Intriguingly, small traces of diacrylate impurities in HEA allowed for crosslinking and the formation of networks, which exhibited maximum strains at break of 348%. The combination of HEA (56 wt.%) with small amounts of PDMSDMAA (9 wt.%) and addition of mono-acrylate (*n*-butyl acrylate, 27 wt.%) with a surfactant to enable miscibility, afforded similar elongation at break (338%). Overall, the most successful composition was a mixture of HEA with 2-(2-ethoxyethoxy)ethyl acrylate, which possessed a maximum failure strain of 472%. While some of these photoresins exhibited highly promising elastomeric properties, the silicone resin yielded a rather stiff material because of the high crosslinking density.

Long *et al.* reported an innovative solution to print low viscosity PDMS-based photopolymers while rendering networks with high molecular weight between crosslinks. The authors conducted UV-curing experiments using mixtures of  $\alpha,\omega$ -dithiol PDMS and  $\alpha,\omega$ -diacrylamide PDMS with molecular weights ranging from 1.2-5.5k g·mol<sup>-1</sup>. Upon irradiation, two reactions occurred concurrently, thiol-ene reaction led to a chain-extension while free-radical polymerization of the acrylamides formed a polymer network (**Scheme 2.12**). The authors explored various molecular weight compositions and different thiol to acrylamide ratios. Overall, a mixture of 0.75 mol  $\alpha,\omega$ -thiol PDMS (1.2k g·mol<sup>-1</sup>) and 1 mol

$\alpha,\omega$ -acrylamide PDMS ( $5.5\text{k g}\cdot\text{mol}^{-1}$ ) yielded networks with molecular weights between crosslinks of  $M_c=12,600\text{ g}\cdot\text{mol}^{-1}$  and a gel-state modulus similar to PDMS in the molecular weight range of 11 to  $30\text{k g}\cdot\text{mol}^{-1}$ . The utilized composition exhibited a slightly lower viscosity ( $0.32\text{ Pa}\cdot\text{s}$ ) than neat  $\alpha,\omega$ -acrylamide PDMS  $5.5\text{k g}\cdot\text{mol}^{-1}$  ( $0.5\text{ Pa}\cdot\text{s}$ ), which enabled fast material refreshing after each printed layer. Tensile test specimen of the neat  $\alpha,\omega$ -acrylamide PDMS ( $M_n = 5.5\text{k g}\cdot\text{mol}^{-1}$ ) showed a maximum strain at break of 58% and a Young's modulus of 1.73 MPa, similar to the value reported by Boydston *et al.* In contrast, 3D-printed tensile specimen using the chain extended network exhibited a strain at break of 80% and a Young's modulus of 0.4 MPa. Significantly, the same polymer composition rendered a max. strain at break of 123% when cured in a mold due to better oxygen exclusion compared to the printing vat.



**Scheme 2.12.** Schematic of simultaneous crosslinking and chain extension of low molecular weight thiol-functional PDMS and acrylamide-functionalized PDMS, which yielded crosslinked PDMS networks with high molecular weight between crosslinks.

Shepherd *et al.* explored thiol-ene click chemistry using commercially-available materials to 3D print silicone elastomers.<sup>92</sup> Two poly((mercaptopropyl)methyl-siloxane-*co*-dimethylsiloxanes) with pendant thiol groups of 2-3 mol% and 4-6 mol% and molecular weights of  $M_w \sim 6000$ - $8000 \text{ g}\cdot\text{mol}^{-1}$  were reacted with various  $\alpha,\omega$ -divinyl PDMS ( $M_w \sim 200, 800, 6000, 17200, 42000 \text{ g}\cdot\text{mol}^{-1}$ ) using UV-initiated thiol-ene click chemistry. The authors evaluated 10 different mixtures with the thiol to vinyl ratio of 1:1, which possessed viscosities between 0.044 Pas to 1.88 Pa·s. Photorheology determined gel times below 2 s (1 wt% photoinitiator) and storage moduli on the order of  $10^3$  to  $10^5$  Pa, varying with the resin composition (**Figure 2.13**).

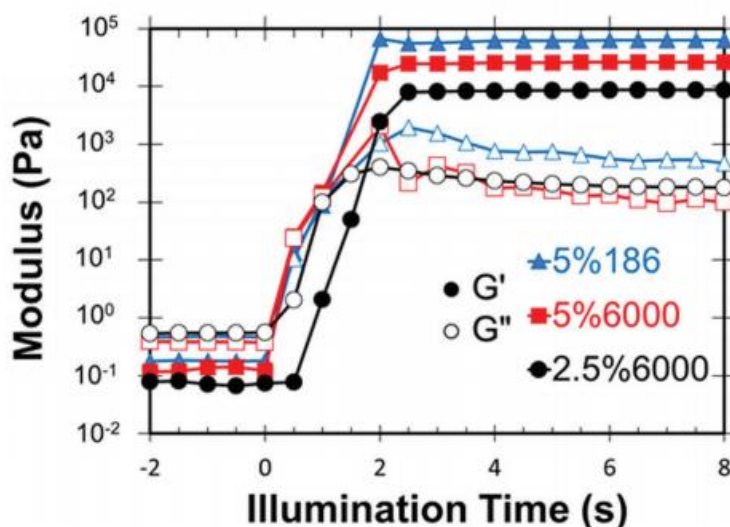


**Figure 2.13.** Modulus (Pa) versus UV-illumination time (s) for poly((mercaptopropyl)methyl-siloxane-*co*-dimethylsiloxanes) with 2.5 mol% and 5 mol% pendent thiols and  $\alpha,\omega$ -divinyl PDMS with molecular weights ( $M_w$ ) of  $186 \text{ g}\cdot\text{mol}^{-1}$  and  $6000 \text{ g}\cdot\text{mol}^{-1}$ , respectively.

In contrast to (meth)acrylate-based systems, the presence of oxygen does not inhibit thiol-ene click reactions. Photo-DSC revealed thiol conversions of 79% to 97%, calculated using an enthalpy of  $60 \text{ kJ}\cdot\text{mol}^{-1}$  for the thiol-ene reaction. Photo-cured tensile specimens revealed Young's moduli ranging from 6-287 kPa, ultimate stresses in the range of 13-129 kPa and ultimate elongations between 45% to 400%. In addition, the

photopolymerized systems showed good fatigue resistance with little hysteresis. These properties motivated the authors to 3D-print a fluidic elastomer actuator utilizing the thiol-functional PDMS (5 mol% thiols) with 6000 g·mol<sup>-1</sup> vinyl-terminated PDMS (**Figure 2.14**). Intriguingly, when the actuator is punctured, the photopolymer rapidly crosslinks when exposed to sunlight and re-seals the actuator, enabling self-healing.

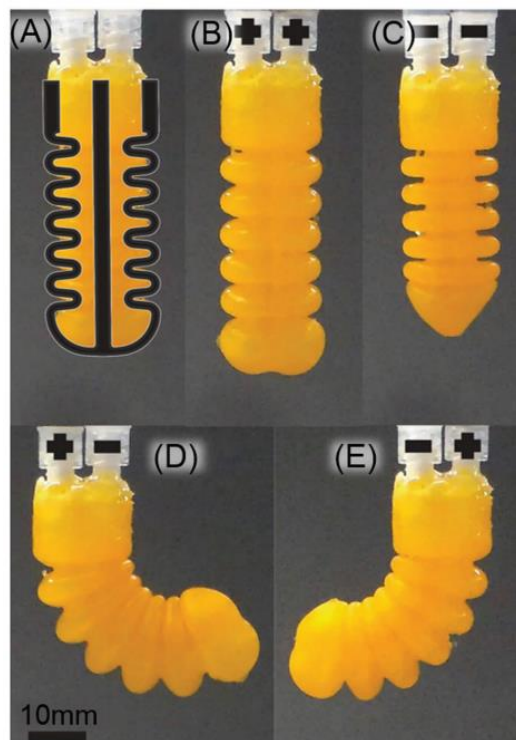
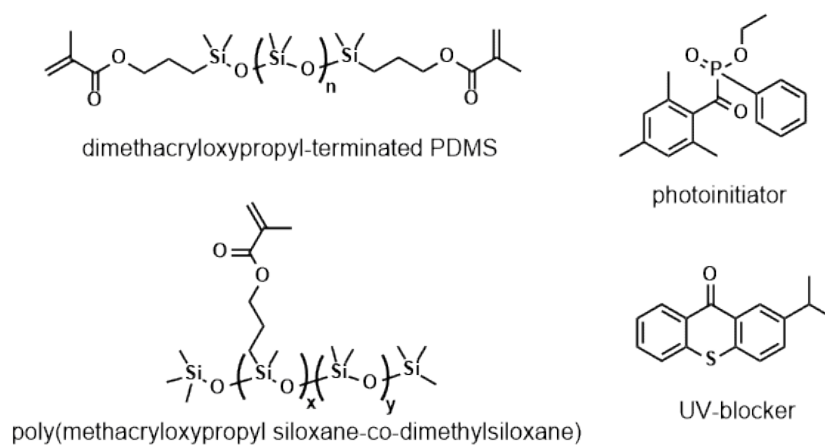


**Figure 2.14.** Additive manufactured monolithic device utilizing thiol- and vinyl-functionalized PDMS and UV-initiated thiol-ene click chemistry. Pressurization or evacuation enabled contraction or elongation of the actuator. Adapted from Shepherd et al.<sup>92</sup>

Bhattacharjee et al. addressed the need of optically transparent PDMS elastomers for the additively manufacturing of microfluidic devices.<sup>93</sup> Many attempts, such as DIW of silicones using DC SE 1700 and other blends lead to non-transparent objects due to the presence of rheological modifiers (e.g. fillers), which are required for this type of printing process (see 2.6.2). Such additional fillers are not needed for stereolithographic approaches, which enabled printing of transparent PDMS-based elastomers and rendered

this technique especially attractive to yield clear structures. The authors formulated photoresins using commercially-available polysiloxanes, e.g.  $\alpha,\omega$ -dimethacryloxypropyl PDMS (abbreviated as PDMS-E) and poly(methacryloxypropyl siloxane-*co*-dimethylsiloxane) (abbreviated as PDMS-S) with the purpose to mimic the properties of Sylgard 184 (**Scheme 2.13**). The silicone soluble (2,4,6-trimethylbenzoyl) phenyl phosphinate (TPO-L) served as photoinitiator and a utilized UV-blocker (e.g. isopropyl-thioxanthanone) ensured good Z-resolution.



**Scheme 2.13.** Single components of photoresin to enable 3D printing of transparent silicone elastomers. Adapted from Bhattacharjee et al.<sup>93</sup>

After the print, extraction with isopropanol improved the optical transparency of the material in the visible spectrum (**Figure 2.15**). Varying the ratio of PDMS-E vs PDMS-S afforded silicone elastomers with a Young's modulus of 937 kPa (PDMS-E : PDMS-S = 4) to 520 kPa (PDMS-E : PDMS-S = 19). The softest composition (PDMS-E : PDMS-S = 19) showed a maximum elongation at break of 153%. Note that the authors utilized PDMS-E and PDMS-S with different molecular weights and varying mol% of methacrylate groups. Two different PDMS-E with molecular weight of 10k and 25k  $\text{g}\cdot\text{mol}^{-1}$  were utilized and PDMS-E with 31.3k  $\text{g}\cdot\text{mol}^{-1}$  and 5 mol% methacrylate groups as well as 57.5k  $\text{g}\cdot\text{mol}^{-1}$  and

38k g·mol<sup>-1</sup> both with 16 mol% methacrylate groups. Unfortunately, no blending ratios or further details on the composition were provided.

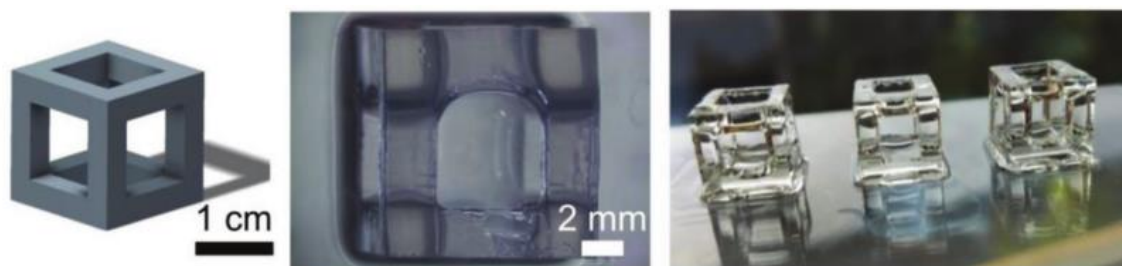
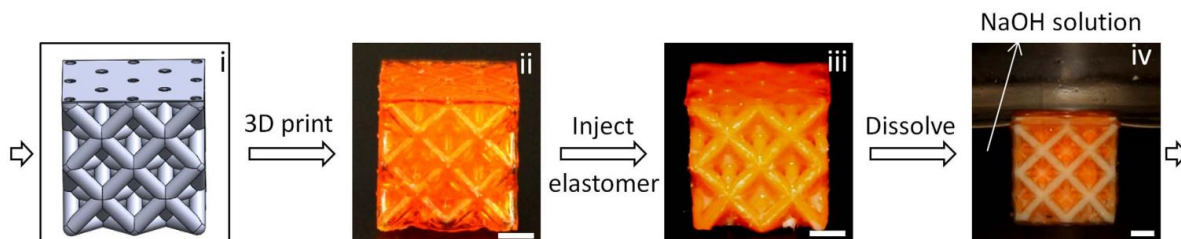


**Figure 2.15.** Transparent hollow cube, 3D-printed using a PDMS-based photoresin. Reproduced from Bhattacharjee et al.<sup>93</sup>

Bypassing the viscosity limitations of silicones for SLA, Jiang and Wang utilized an indirect AM approach. The authors printed a hollow sacrificial support scaffold first, and back-filled it with commercial silicone resin (**Scheme 2.14**).<sup>94</sup> The silicone is cured in the scaffold and treatment with alkaline solution (NaOH, 1 mol·L<sup>-1</sup>) removed the sacrificial network and released the free-standing PDMS elastomer. Liska et al. developed the compositions of the sacrificial matrix, which consisted of *N,N*-dimethylacrylamide, methacrylic acid, methacrylic anhydride, and polyvinylpyrrolidone as a water soluble filler and phenylbis(2,4,6-trimethylbenzoyl)phosphine oxide as photoinitiator.<sup>95</sup> The methacrylic anhydride acted as crosslinker and enabled degradation under alkaline conditions. Using this concept, Jiang and Wang printed tin-catalyzed condensation-based silicones, (Mold Max N14® and T10® Smooth-on) and polyurethane elastomers (PMC-724®, Smooth-on). This procedure enabled manufacturing of highly elastic, complex lattice structures with 100-1500 μm printing resolution, maximum strains at break of 414% and Young's moduli ranging between 20-400 kPa.





**Scheme 2.14.** Indirect AM of silicone elastomers utilizing a sacrificial scaffold. Adapted from Jiang and Wang.<sup>94</sup>

The authors further applied this strategy to print elastic lattice conductors by coating the PDMS elastomer with ion-doped conductive hydrogels.<sup>96</sup> Using the same sacrificial support material but Sylgard 184 (7:1 base to crosslinker) as filler, Wessling et al. printed three dimensional membranes and demonstrated the suitability of indirect AM to manufacture biomedical-relevant devices.<sup>97</sup>

In 2016, Kim et al. proposed using low one-photon polymerization (LOPP) as an alternative to conventional vat photopolymerization of UV-curable silicones.<sup>98</sup> In LOPP, a specific photoinitiator is chosen which possesses low absorption of the utilized printing wavelength. This technique enabled focal curing within the resin without polymerizing along the beam path, similar to the well-known two-photon absorption polymerization but offering much lower printing resolution. In contrast to conventional VP, printing of resins with higher viscosities was possible because the non-cured resin provided the optimal support of the cured structure and the process is stationary. The authors utilized a UV-curable silicone from Dow Corning but failed to report materials properties or resulting mechanical properties after printing. LOPP is still rather unexplored and overall improvement of the printing resolution is required to compete with conventional VP or the cost-extensive two-photon process.

### 2.6.5 Inkjet printing of silicones

In addition to SLA and DIW, researchers investigated the printability of silicones using inkjet printing, which is highly attractive for manufacturing stretchable electronics or microfluidic devices. Wildman et al. diluted a commercial two-part silicone (Polytek, PlatSil 71-SiliGlass) using octyl acetate to meet the viscosity requirement of conventional inkjet printers ( $< 30 \text{ mPa}\cdot\text{s}$ ).<sup>99</sup> In particular, PlatSil® SiliGlass is a platinum-cured two part silicone and enabled the printing of part A and B individually. Printing both parts separately prolonged ink stability, avoided clogging of the nozzle and afforded structures with feature resolutions of  $48 \mu\text{m}$  (Figure 2.16).

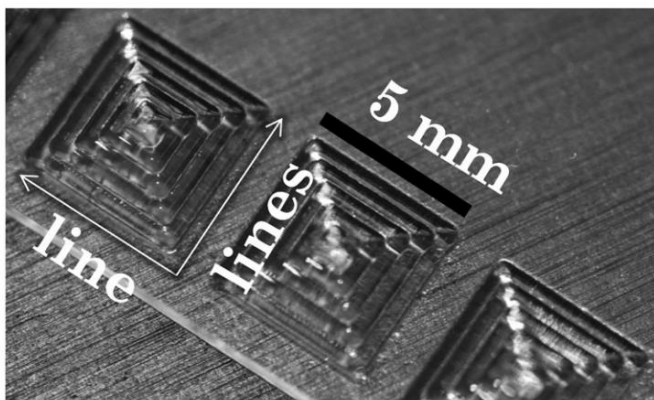


**Figure 2.16.** Ink-jet printed ziggurat structure (4 mm x 4 mm) consisting of crosslinked PDMS. Adapted from Wildman et al.<sup>99</sup>

Shortly after, Shea et al. studied seven commercially-available silicone inks for their printability in inkjet printing, aiming at fabricating dielectric elastomer actuators (DEA).<sup>100</sup> From those seven formulations, Momentive UV Silopren® Electro 225-1, a UV-curable ink which was printed in one step and NuSil CF18-2186, a thermally curable ink, which was printed in two steps provided best results. Jetting of Wacker Silpuran® 6000/05 afforded poor feature precision due to the high molecular weight of the silicone, which consequently required high ink dilution. Tensile data of printed Nusil CF18-2186 and Momentive UV Silopren® Electro 225-1 elucidated no differences between printing

directions (longitudinal or transversal) and were comparable to the blade-casted films. Reitelshöfer et al. utilized aerosol-jet-printing to fabricate stacked dielectric elastomer actuators.<sup>101</sup> A RTV 2-part PDMS served as dielectric material (Wacker Elastosil P 7670) in which both components possessed a viscosity of 1800 mPa·s. Reduced graphene oxide dispersed in a mixture of propanol and terpineol represented the conductive ink.

## **2.7 Polyurethanes**

### **2.7.1 Chemistry of polyurethanes**

Polyurethanes represent a highly versatile class of polymers and enjoy numerous applications ranging from insulation and cushioning foams to adhesives and coatings.<sup>102</sup> This versatility arises from synthetic technique for segmented polyurethanes, where variations in soft segment oligomer type and molecular weight, as well as hard segment (HS) content produce drastic morphological differences that influence polymer properties, including thermal transitions, modulus, stress at break, and strain at break.<sup>102</sup> Synthetic processes typically follow one-step (non-segmented) or two-step (segmented) solution-based processes that reacts low  $T_g$  oligomeric diamines or diols (termed soft segments, SS) with monomeric diisocyanates and monomeric diamines or diols (optional chain extenders). The incorporation of dithiols as dinucleophiles produces thiourethane linkages.<sup>103,104</sup> Urethane formation process is typically aided with inorganic (e.g. dibutyltin dilaurate) or organic (e.g. DABCO, DMF) catalysts. In the case of non-segmented polyurethanes, a monomeric or oligomeric diol/diamine is typically reacted with a diisocyanate, producing a polyurethane either in bulk (no solvent) or in solution. In the case of segmented polyurethanes, as shown in **Figure 2.17**, an oligomeric diol/diamine is reacted with an excess of diisocyanate in the first step, resulting in an isocyanate-terminated prepolymer. As a second step, a chain extender is then added, raising the overall

amine/hydroxyl:isocyanate stoichiometry and driving the reaction to high molecular weight.

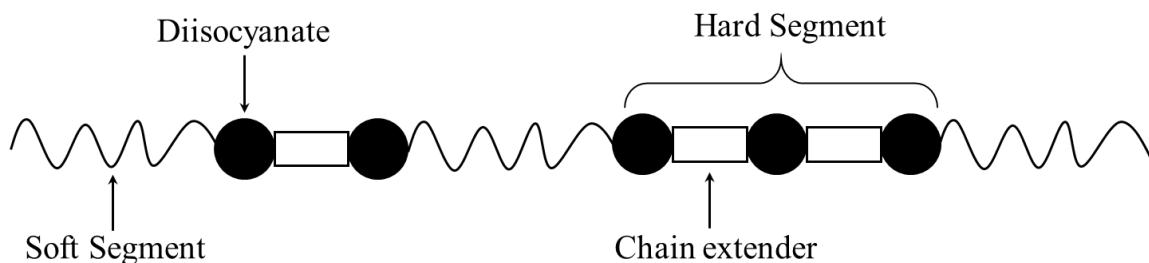


**Figure 2.17.** Schematic representation of a segmented polyurethane or polyurea.

In the case of segmented, linear polyurethanes, elasticity arises through intramolecular hydrogen bonding physical interactions and is governed by many parameters. These include hard segment content, typically measured in weight percent as a ratio of the SS/HS repeat unit weights, Hildebrand solubility parameters, strength of hydrogen bonding interactions, e.g. urea vs. urethane, and the relevant soft segment polymer structure and molecular weight.<sup>102</sup> Polymer isolation after a homogeneous solution synthetic procedure typically occurs via precipitation or solution casting and vacuum drying. In one report, an investigation of the effect of odd/even numbers of methylene units in the chain extender revealed that mechanical properties increased for polyurethanes synthesized with chain extenders that possessed an even number of methylene units, which was attributed to improved chain packing in urethane hard segments.<sup>105</sup> Furthermore, polyurethanes synthesized with > 50 wt % HS result in copolymers with HS as the continuous phase, limiting elastomeric properties.<sup>106,107</sup> To achieve elasticity, soft polyols traditionally possess molecular weight between 400-6000 g/mol and HS contents below 50 wt %.<sup>108</sup> However, recent reports demonstrate elastomeric properties (e.g. 300-600 % strain at break) with much higher SS oligomer molecular weights, employing poly(dimethyl siloxane)s (PDMS) soft segments (e.g. 32,000 g/mol)

and 2-5 wt % HS; these properties may arise from both the highly improved HS/SS phase separation for PDMS polyurethanes/polyureas and PDMS chain entanglements.<sup>109,110</sup>

There are special considerations for combinations of HS/SS in the context of specific printing technologies. For example, vat photopolymerization (VPP) requires that photopolymers remain liquid at room temperature. If printing without solvent or appreciable reactive diluent (e.g. monomer), oligomers themselves must possess sufficiently low viscosity for adequate processing. In this context, the choice of a chain extender with an odd number of methylenes could help disrupt chain packing and reduce the physical associations that occur at room temperature, to use an example from above. Another approach might involve the use of asymmetric diisocyanates, which leads to lower strength products due to the disruption in chain packing,<sup>108</sup> but offers lower viscosity oligomers at room temperature. Sinh and Jukka employed this approach with isophorone diisocyanate in the synthesis of urethane methacrylate photocurable oligomers for VPP and produced oligomers with low viscosity (2200 mPa·s) at room temperature that possessed a strain at break of 195 % once photocured.<sup>111</sup> Occasionally, what makes a polymer ‘printable’ might seem at odds with what provides improved mechanical properties, as is the case with the diisocyanate example, above. In these cases, innovative polymer chemistry often finds a solution, as is the case with a polyurethane composition for CLIP that employed blocked isocyanates during printing and relied upon a post-printing thermal cure to unblock the diisocyanate, which is described in greater detail below.<sup>41</sup>

### 2.7.2 Traditional polyurethane printing in solution (material extrusion, inkjet printing)

The primary route towards segmented polyurethane block copolymer AM lies in printing from solution, although a few examples exist for printing from the melt, with fused filament fabrication (FFF), or inkjet printing. Fortunately, many polyurethanes, poly(urethane urea)s, and polyureas remain soluble in a variety of organic solvents or binary mixtures thereof, though solubility remains highly dependent on composition. This article focuses on the attributes most important for additive manufacturing, as segmented polyurethanes are reviewed in great detail elsewhere.<sup>102,108,112,113</sup> Most polyurethanes employ soft segments comprised of polyethers [e.g poly(tetramethylene oxide) (PTMO), poly(ethylene oxide) (PEO)], polycaprolactone (PCL), PDMS, and polyolefins [e.g. polybutadiene, polyisobutylene)].<sup>102</sup> The solubility parameter difference between the aforementioned soft segments [between 15.6 - 20.2 (J/cm<sup>3</sup>)<sup>1/2</sup>] and the hard segments [urethane, 37.2 (J/cm<sup>3</sup>)<sup>1/2</sup>, and urea, 45.6 (J/cm<sup>3</sup>)<sup>1/2</sup>], hard segment content (typically measured in wt %), and number of urea/urethane functional groups in each hard segment block largely govern solubility,<sup>102</sup> with greater differences in solubility parameter, greater HS content, and longer HS blocks reducing solubility in organic solvents, in many cases. Common solvents for polyurethanes range from the moderately polar (tetrahydrofuran, chloroform, diethyl ether, isopropyl alcohol) to the more polar, aprotic solvents (e.g. *N,N*-dimethylformamide, dimethylacetamide, and *N*-methylpyrrolidone) or mixtures thereof. Moderately polar solvents remain more than adequate for dissolution of polyurethanes with low HS content, whereas highly polar solvents or binary mixtures are required for complete dissolution in cases of higher HS content.<sup>102,114</sup> Synthetic strategy for all segmented polyurethane/ureas in this section remains similar, with combinations of oligomeric and

monomeric diols/diamines/dithiols combined with diisocyanates to produce polyurethane/urea in solution.

Renji Zhang *et al.* synthesized a segmented polyurethane with two oligodiols, polycaprolactone (PCL) and poly(ethylene glycol) (PEG), hexamethylene diisocyanate (HDI), and butanediol (BDO) as a chain extender.<sup>115-117</sup> Demonstrating an innovative 3D deposition procedure, the authors prepared a polyurethane slurry in 1,4-dioxane and printed *via* direct ink write, freezing the layered structures onto a refrigerated build platform held at -28°C. Subsequent lyophilization (freeze drying) afforded the desired 3D vasculature model, shown in **Figure 2.18**. The authors advantageously built on this procedure in a later report, creating a double-walled structure consisting of a PU outer cylinder and an inner collagen surface.<sup>118</sup> Later, Xiaohong Wang, et al. synthesized the same PCL/PEG polyurethane described in their previous reports<sup>115,116</sup> and performed a co-extrusion employing the same 3D printing setup.<sup>119</sup> One syringe contained a cell-laden hydrogel precursor, while the other contained a PU-tetraglycol solution. This DIW co-extrusion process enabled the creation of layered, flexible PU-collagen conduits, and a full printed construct shown in various views in **Figure 2.19**.

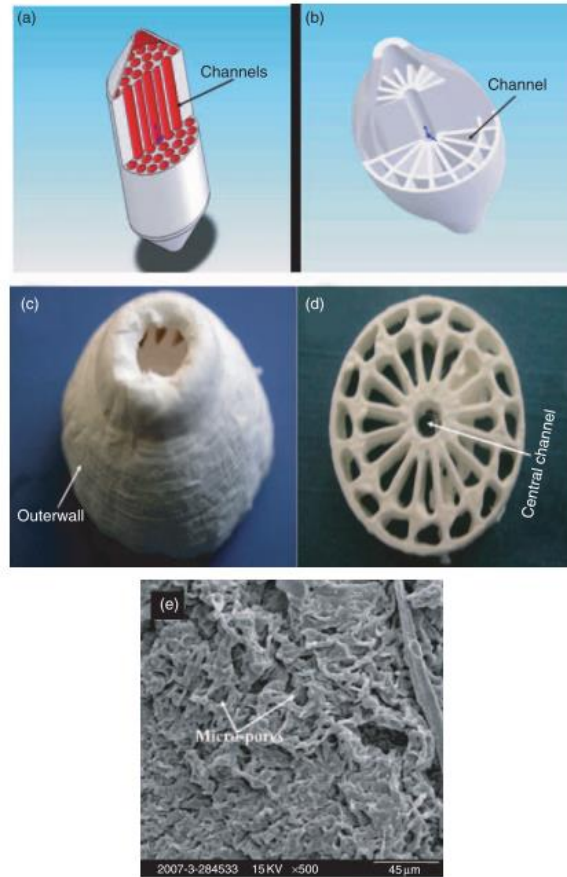


**Figure 2.18.** (A,B) CAD models of freeze-dried polyurethane 3D vasculature models, (C) 3D printed polyurethane construct, (D) cross-section of construct shown in (C), (E) SEM micrograph of outer scaffold wall in (C). Reproduced from Xu and Zhang, et al.<sup>117</sup>



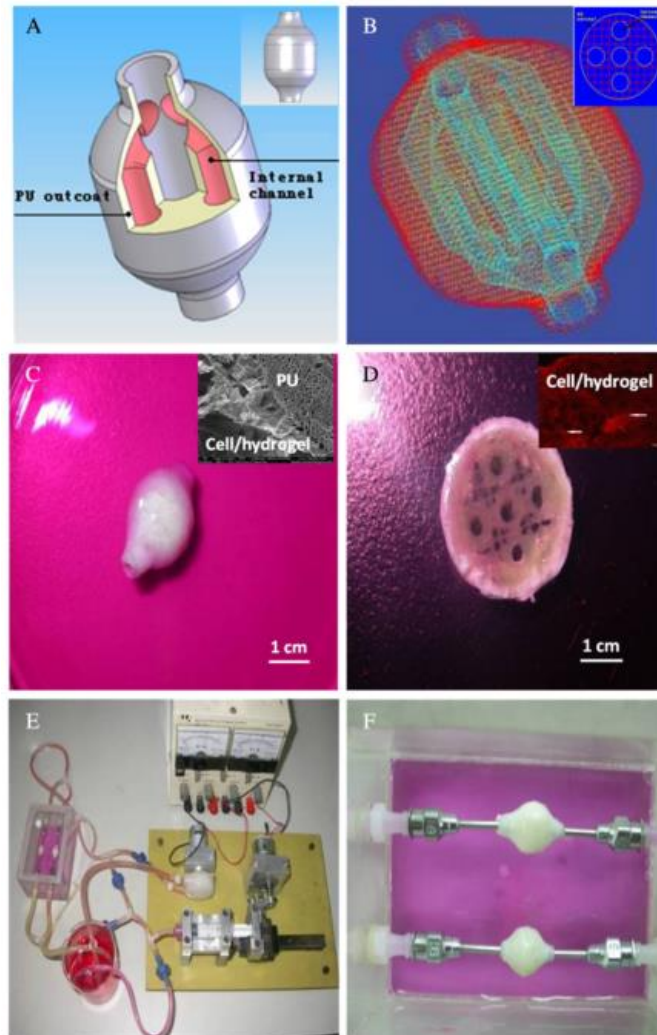
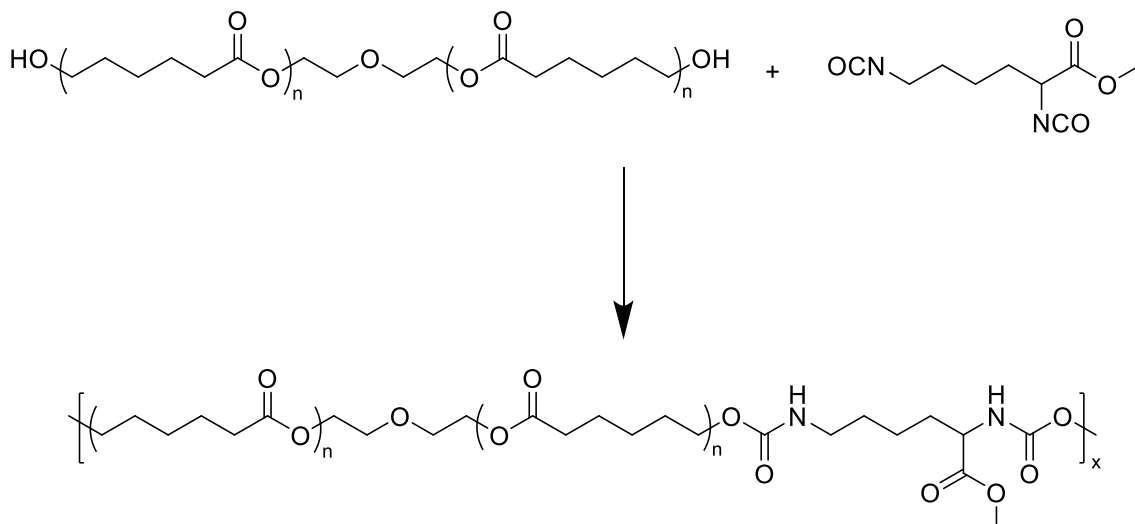


**Figure 2.19.** (A-D). Various images of a hierarchical construct made created by the DIW co-extrusion process. (E-F) two complex constructs undergoing in-vitro pulsatile culture. Reproduced from Huang and Wang, et al.<sup>119</sup>

In a similar manner but employing an amino acid-based diisocyanate, Hasirci, et al. prepared biocompatible poly(ester urethane)s (PEUs) from 1:1 molar ratio of 1,250 g/mol PCL diol and lysine diisocyanate, reacting the two in solution (shown in **Scheme 2.15**).<sup>120</sup> When employed in biodegradable polyurethanes, diisocyanatobutane (BDI) and lysine diisocyanate (LDI) degraded into non-toxic products, as compared to aromatic diisocyanates such as toluene diisocyanate (TDI) and methylene diphenyl diisocyanate (MDI).<sup>121</sup>



**Scheme 2.15.** Poly(ester urethane) (PEU) elastomers prepared from polycaprolactone (PCL) diol and lysine diisocyanate.

Solution-casted films of these biodegradable poly(ester urethane)s achieved a strain at break of ~1500 %.<sup>120,122</sup> 3D fabrication occurred via DIW and salt leaching, where the former process involved heating bulk polymer to 105 °C and extruding from a syringe. The fabricated scaffolds are shown in **Figure 2.20**.<sup>122</sup> When compared to salt-leached sponges made from the same poly(ester urethane)s, the DIW scaffolds possessed similar thermal properties to those made via salt leaching, but the DIW scaffolds possessed improved rat bone marrow stem cell viability and proliferation rates, likely due to the more interconnected pore morphology afforded by the DIW process.

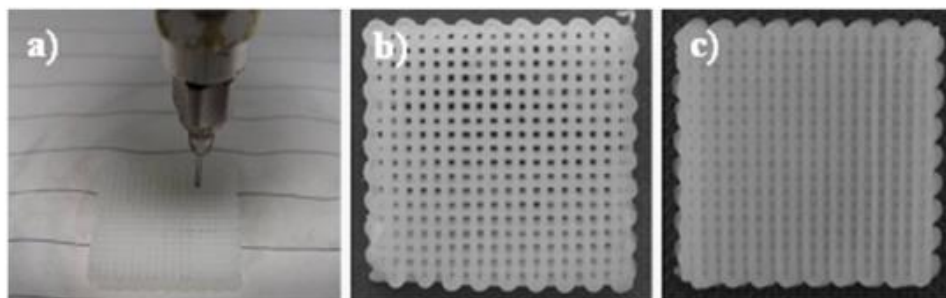
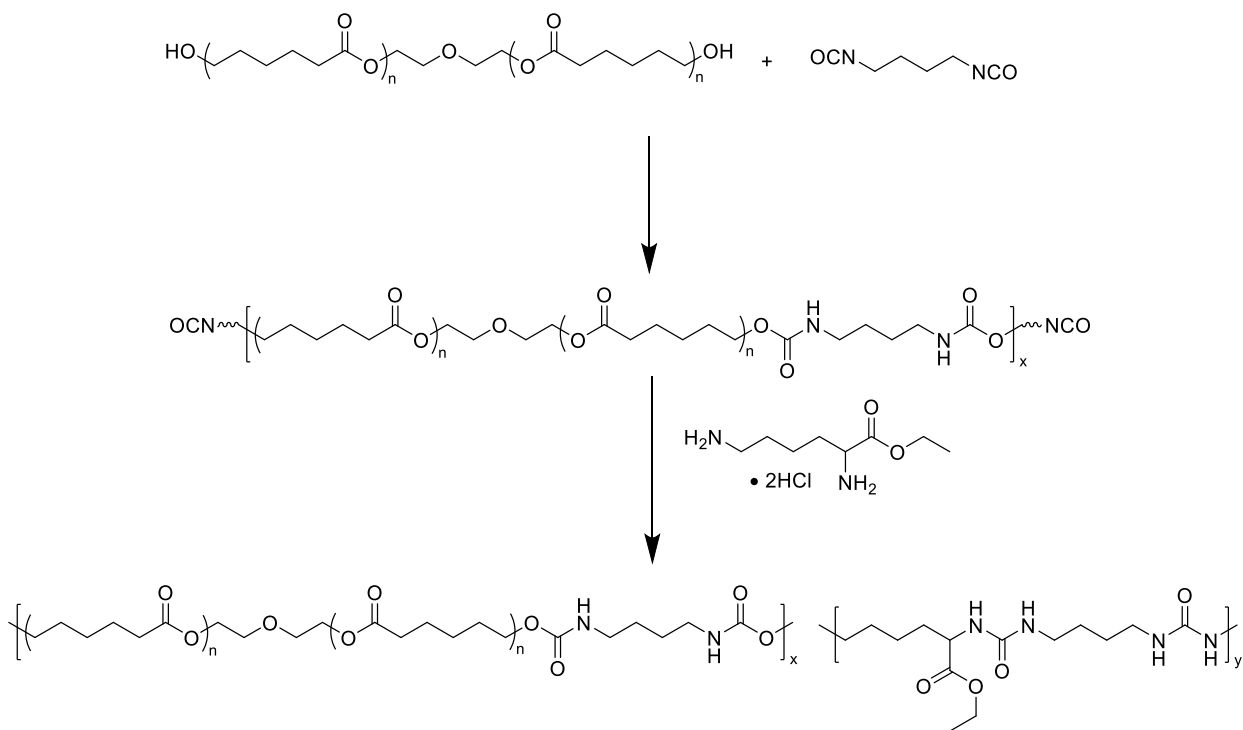


**Figure 2.20.** Poly(ester urethane) (PEU) scaffolds produced via DIW. Reproduced from Kiziltay and Hasirci, et al.<sup>122</sup>

Ciardelli, et al. prepared similar PCL-containing polyurethanes for melt extrusion DIW but instead employed 1,4-butanediisocyanate and L-lysine ethyl ester dihydrochloride as chain extender (**Scheme 2.16**).<sup>123-125</sup> Though the exact ratios of starting materials were not provided,<sup>123</sup> the authors did observe microphase-separated behavior as evidenced by DSC and obtained an elastic modulus of  $10.2 \pm 2.2$  MPa, ultimate tensile strength of  $3.3 \pm 0.2$  MPa, and a strain at break of  $693.0 \pm 15.0$  %. The scaffolds also demonstrated elastomer-like behavior as evidenced by hysteresis cycles at 10 % strain, with low permanent set (2.5 %) on the first cycle and 16 % hysteresis on the final cycle.<sup>123</sup> No 3D printing occurred during this work, but similar materials were processed with DIW in separate studies.



**Scheme 2.16.** Segmented poly(ester urethane) (PEU) elastomers prepared from polycaprolactone (PCL) diol, 1,4-butanediisocyanate, and L-Lysine ethyl ester dihydrochloride.

Hernández-Sánchez also published on the indirect printing of poly(urethane urea) (PUU), PCL-containing elastomers.<sup>126</sup> This indirect 3D printing approach involves printing

a porogen, e.g. poly(vinyl alcohol) (PVA) in this case, and casting the desired polymer around the porogen. Removal of the water-soluble PVA afforded a PUU scaffold. This indirect 3D printing approach enables the creation of geometries not achievable with a direct approach, such as 3D channels in a continuous matrix, such as those produced by Lewis and coworkers.<sup>60,80,81</sup> In a previous report, Hernández-Sánchez detailed the synthesis of PCL-containing PUUs with 14 to 40 wt % hard segment, with a wide variety of mechanical characteristics depending on the hard segment content.<sup>127</sup> Based on PCL diol as the soft segment, the polyureas contained HMDI and putrescine as a chain extender. Though the authors did not provide specific mechanical properties for all compositions, they noted that the 23 wt % and 32 wt % HS samples attained ~750 % strain at break.<sup>127</sup>

Taking a unique approach towards hydrogen bond-containing polymers and employing dithiol-containing monomers, Voit et al. leveraged a relatively underutilized family of thiourethanes for fused filament fabrication (FFF), with a 3D fabricated laboratory logo and SEM of layered structure shown in **Figure 2.21**.

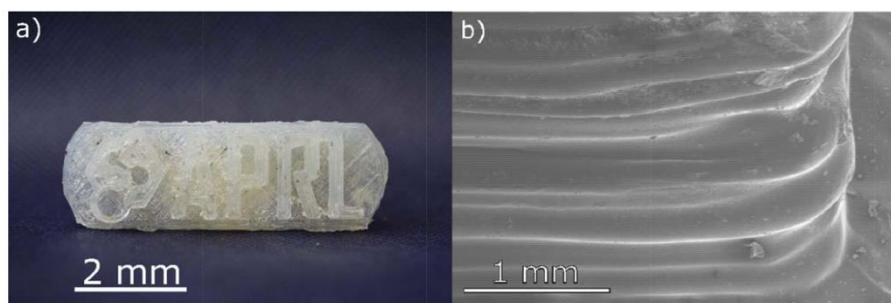
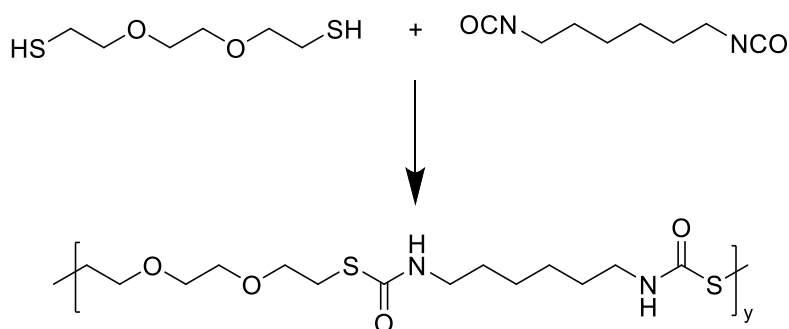


**Figure 2.21.** (A) 3D printed laboratory logo created by fused filament fabrication with thiourethane filaments. (B) scanning electron microscopy of printed objects. Reproduced from Ellson and Voit, et al.<sup>103</sup>

The step-growth polymerization of an equimolar mixture of 2,2'-(ethylenedioxy)diethanethiol (EDDT) and hexamethylene diisocyanate (HDI) in DMF afforded high molecular weight thiourethane, as show in **Scheme 2.17**.<sup>103</sup> This polymer

possessed a  $T_g$  of  $\sim 11$  °C,  $T_m$  of 111 °C, and a  $T_{d,5\%}$  of 260 °C, providing a wide temperature window with which FFF processing can occur and a low enough flow temperature for this composition to be printable in a wide variety of commercially available FFF printers.



**Scheme 2.17.** Synthesis of thiourethanes from EDDT and HDI.

A bulk film of this composition achieved an ultimate tensile strength of  $48.3 \pm 7.1$  MPa and an elongation at break of  $307.8 \pm 40.3$  %, though the printed objects suffered from a typical reduction on mechanical properties as a result of the layering process. When fabricated into bulk films and subjected to tensile testing, this elastomer outperformed T-Lyne®, a commercially-available, DuPont™ Surllyn®-based poly(ethylene-*co*-zinc methacrylate) ionomer filament manufactured by Taulman3D.

A unique approach to inkjet printing of polyurethanes was recently pursued by Thomas Boland, et al.<sup>128</sup> The authors employed a modified thermal inkjet printing approach,<sup>129</sup> which requires low viscosity for both the building material and the support material, if employed.<sup>10</sup> A biodegradable, polyurethane ionomer was synthesized from methylene diphenyl diisocyanate (MDI), 530 g/mol PCL diol, and chain extended with a sulfonic acid-containing diol or its non-charged counterpart, at 50 mol % HS.<sup>128</sup> Inkjet printing produced single-layer structures employing the deprotonated, polyurethane

ionomer dissolved in DMF/H<sub>2</sub>O at 2 % w/v, while subsequent inkjet printing of a 50 % (v/v) aqueous acetic acid solution protonated the polyurethane in selected locations, thus producing 2D patterned structures as shown in **Figure 2.22**. The 2D-fabricated structures demonstrated adequate initial cytocompatibility and show promise as tissue engineering scaffolds. Mechanical property testing for both neutral and ionic polyurethanes occurred with solution-cast films and revealed an elongation at break of 211 % for the ionomer, as compared to the neutral polyurethane at 107 % elongation.

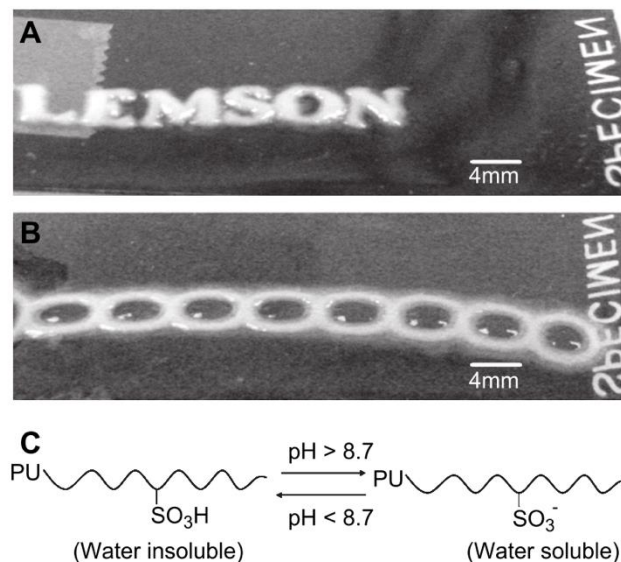


**Figure 2.22.** Inkjet printing of acetic acid/water solution on a sulfonate-containing PU substrate, producing patterns via protonation of polyurethane ionomers. (A) separate letters printed on glass slide. (B) O-rings printed on glass slide. (C) Schematic of acetic acid/water printing and subsequent protonation of polyurethane ionomers, producing water insoluble structures. Reproduced from Zhang and Boland, et al.<sup>128</sup>

Thomas Griesser, *et al.* demonstrated a unique thermal inkjet printing approach for the production of soft, elastomeric optical waveguides *via* simultaneous photopolymerization and inkjet printing of a urethane-containing, oligomeric photopolymer composition atop a PDMS substrate.<sup>130</sup> The authors inkjet printed a combination of Genomer 4267 urethane diacrylate, ethylene glycol vinyl ether (EGVE)

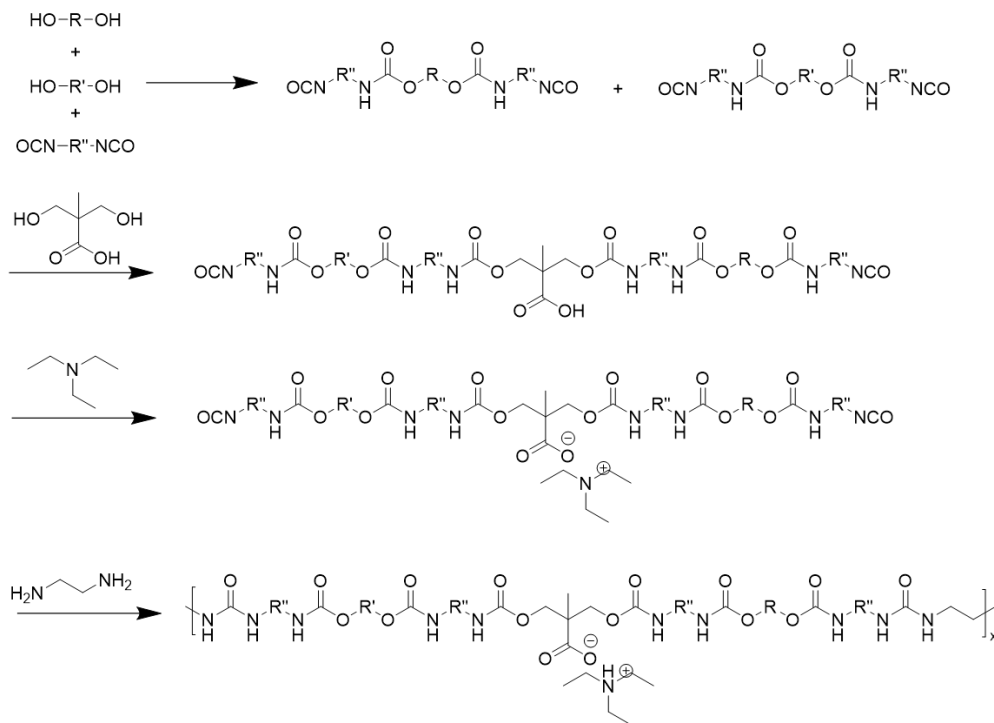
(less toxic than hydroxyethyl acrylate), 2-phenoxyethyl acrylate (PhEA) (for improved optical properties), with 1.5 wt % of a photoinitiator atop a thermally cured Sylgard 184 PDMS substrate. The authors underwent a rigorous optimization and characterization process to match the strain at break of both the PDMS substrate (143 % alone) and optical waveguides ( $\geq 120$  % when tested with the PDMS substrate), exemplified by the lack of deformation or detachment of the waveguides during the strain experiments. These optical waveguides may find application in soft robotics or biophotonics.

### **2.7.3 Waterborne polyurethane dispersions**

The synthesis of waterborne polyurethane dispersions (PUDs) mostly follows that of traditional polyurethanes, but involve additional steps for the insertion of ionic functional groups into the polyurethane backbone. This generates an ionomer and provides the ability to form colloidally stable, aqueous polyurethane dispersions if properly processed. These aqueous PUDs provide many ‘green’ alternatives to organic-solvent based polyurethane solutions, namely the avoidance of potentially toxic and volatile solvents.<sup>112,113,131</sup> The two most widely employed PUD synthetic processes are the acetone process and the prepolymer emulsification process, the details for which are provided elsewhere.<sup>131</sup> These polyurethane dispersions do not aggregate in solution and maintain colloidal stability through deprotonation of the ionic functional groups with an organic base, resulting in electrostatic repulsion between the resulting PU nanoparticles. Zeta potential (ZP), a measurement of electrokinetic potential, represents the potential difference between the dispersion medium and a stationary layer of fluid surrounding the dispersed particle. It is a strong predictor of colloidal stability.<sup>132</sup> ZP measurements occur with a dedicated ZP instrument and/or a dynamic light scattering (DLS) instrument. A ZP

> ± ~25-30 mV is widely accepted as a stable colloidal dispersion for most systems.<sup>133</sup>

Most biological applications for 3D-printed polyurethanes require high water swellability and mechanical properties specific to the type of cells or tissue being mimicked and will not be discussed here, as these polymers are reviewed elsewhere in the context of 3D printed biomaterials.<sup>31,134–137</sup>



### Waterborne, biodegradable polyurethane dispersion (PUD)

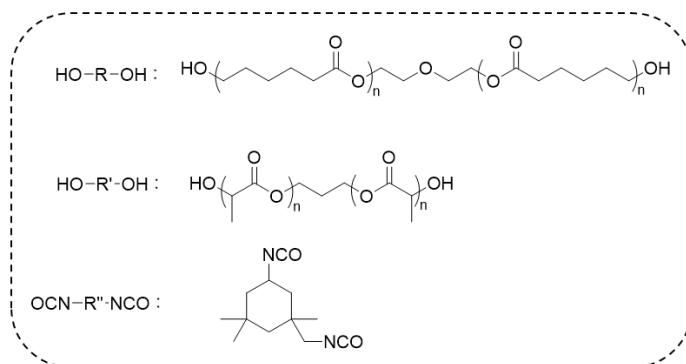


**Figure 2.23:** Synthesis of water-dispersible polyurethane nanoparticles via the prepolymer emulsification method.



**Figure 2.23** depicts the overall aqueous polyurethane dispersion synthesis process using the prepolymer emulsification method.<sup>138</sup> Shan-hui Hsu and co-workers have done much work in this area at the Institute of Polymer Science and Engineering at National Taiwan University. In this work, no printing occurred but the group later employed similar compositions for printing. Here, Hsu et al. demonstrated the versatility of PUDs and employed either a PCL diol ( $M_n$  2000 g/mol) alone or a combination of PCL diol with a second oligodiol. This second oligodiol was either an in-house synthesized poly(L-lactide) diol (PLLA diol,  $M_n$  2000 g/mol), poly(D,L-lactide) diol (PDLLA diol,  $M_n$  2000 g/mol), or a commercially available poly(ethylene butylene adipate) diol. The authors advantageously combined these oligodiols with isophorone diisocyanate (IPDI), 2,2-bis(hydroxymethyl)propionic acid (DMPA), triethylamine (TEA), and ethylene diamine as a chain extender, all of which are typical reactants for PUD synthesis, producing stable aqueous dispersions (zeta potential between -55 mV and -60 mV) of polyurethane nanoparticles with hydrodynamic diameters ranging from 30 – 50 nm. **Figure 2.24a** demonstrates possible applications of these so-called water dispersible polyurethane (WDPU) nanoparticles (NP)s, while **Figure 2.24b** provides a cartoon depiction of physical gelation for hydrogel formation, the dehydration, phase inversion, and film-forming process, or the freeze-drying process (e.g. lyophilization) that forms porous microsphere sponges. For the aforementioned composition in film form, the Young's modulus, tensile strength, and elongation at break ranged from 4.6–125 MPa, 11– 35 MPa, and 280–778%, respectively. Higher PLLA content was associated with reduced elongation at break, attributed to PLLA crystallinity, while higher content of the amorphous PDLLA diol in the PU nanoparticles resulted in increased elongation at break.

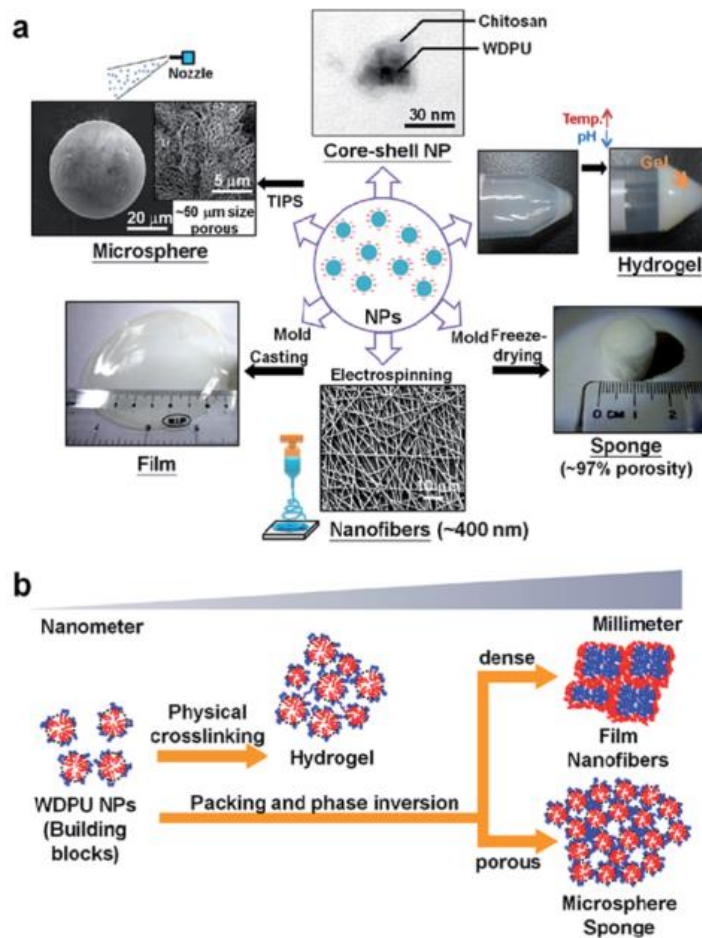


**Figure 2.24:** Self-assembly of water dispersible polyurethane (WDPU) nanoparticles (NP)s (a) Processing based on the self-assembly of NPs. (b) The possible mechanisms for self-assembly of NPs. Reproduced from Hsu and Lin, et al.<sup>138</sup>

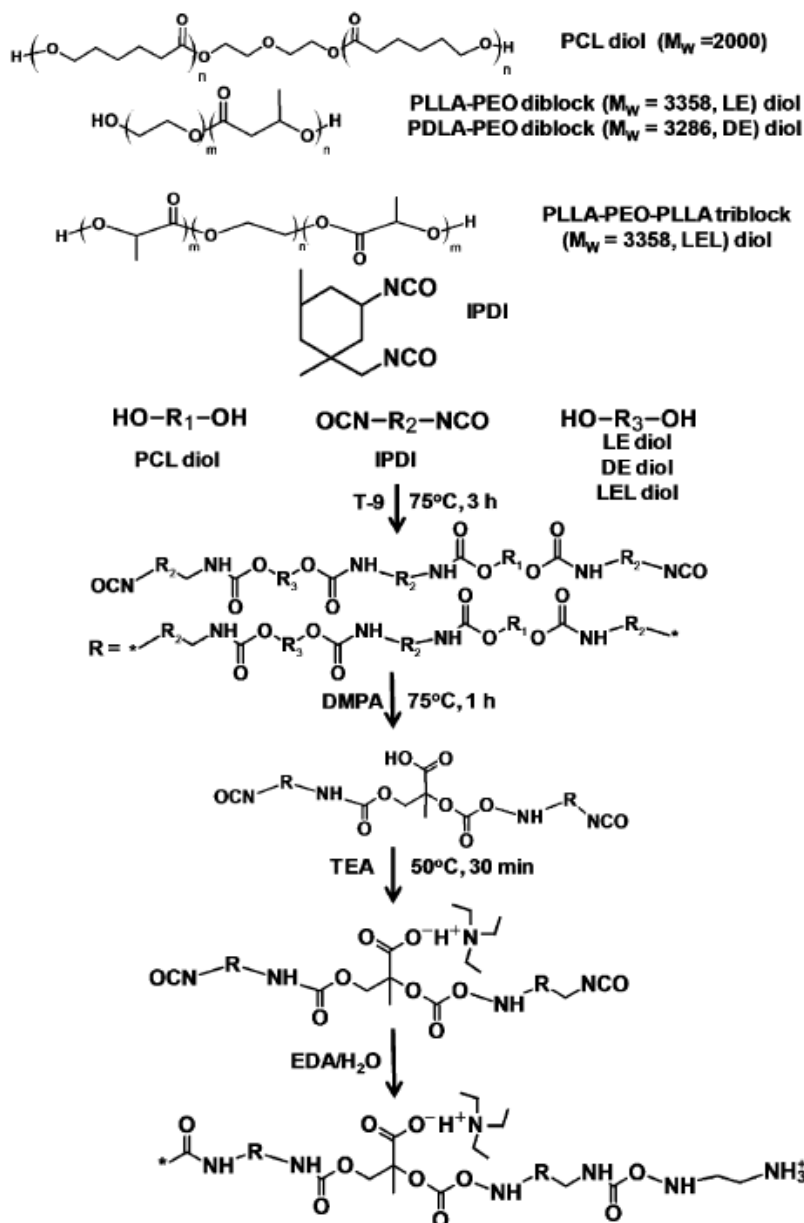


**Figure 2.25.** Waterborne polyurethane dispersions with PCL diol and PLLA-PEO-PLLA triblock copolymers as soft segments

Hsu et al. have continued the use of this family of polymers in their other work. Such polymers have been combined with neural stem cells (NSCs) to create a cell-laden ink for 3D bioprinting.<sup>139</sup> Shown in **Figure 2.25**, Hsu et al. synthesized waterborne PUDs with a similar procedure described above except now included in-house synthesized amphiphilic block copolymers, including a PLLA-PEO diblock copolymer, a PDLA-PEO diblock copolymer, or a PLLA-PEO-PLLA triblock copolymer.<sup>140</sup> This process provided

thermoreponsive, amphiphilic polyurethanes, while 3D fabrication of the cell-laden PUDs occurred via 3D printing at 25 °C followed by gelation at 37 °C.<sup>140</sup> When processed into film form, two noteworthy PUDs, PCL100 and PCL90LE10, possessed Young's moduli of 30.9 and  $18.6 \pm 2.8$  MPa respectively, while extending to  $535.5 \pm 19$  and  $650.6 \pm 10$  strain %, respectively. The non-reversible thermal gelation mechanism for this family of polymers is based primarily on self-assembly via hydrogen bonding, the dynamics of which increase with temperature.<sup>141</sup> Key characterization techniques here include size measurements (DLS, SAXS, and TEM), ZP measurements, and swelling ratios.<sup>141</sup> Typical scaffold depiction for direct-ink write (DIW) 3D printing is shown as a schematic in **Figure 2.26** and the actual process depicted in **Figure 2.27**.<sup>140,142</sup> This class of polyester or polyether-containing PUDs is diverse and enables the direct incorporation bioactive ingredients (e.g. growth factors, hyaluron)<sup>143</sup> or living cells<sup>139</sup> into a DIW 'ink'.

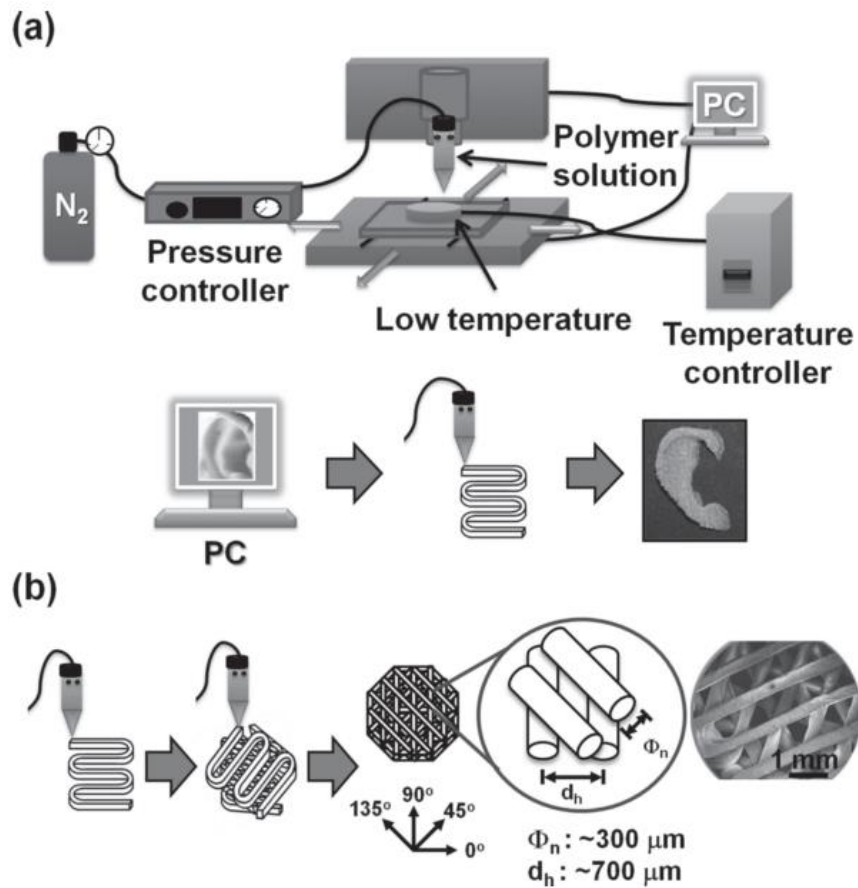


**Figure 2.26.** 3DP DIW process. Reproduced with permission.<sup>142</sup>

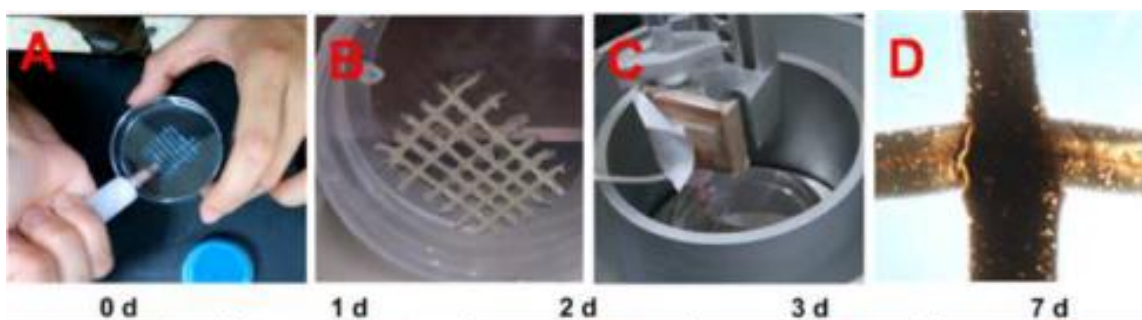


**Figure 2.27.** Typical DIW 3D printing procedures. (A) fiber stacking by manual injection, (B) manually-produced construct, (C) 3D printing with custom-designed DIW apparatus, and (D) two layers of 3D-printed fibers, constructed for the purposes of cell visualization via optical microscopy. Figure reproduced with permission.<sup>140</sup>

Li Feng, *et al.* synthesized a series of aqueous PUDs with a 2k g/mol PCL soft segment, IPDI, DMPA, and L-lysine chain extender.<sup>144</sup> Initially developed by a different research group at the same university, Qiang Fu *et al.* synthesized a series of PUDs with

16.7 – 45.0 mol % PEG soft segment that obtained tensile strengths from 16.1 – 21.8 MPa, elastic moduli from 2.6 – 4.8 MPa, and elongation at break from 1120 – 1479 % in dry, solvent-cast film form.<sup>145</sup> Li Feng, *et al.* repeated this synthesis without PEG oligodiols, employing PCL only, with a composition that contained molar feed ratios of 3 : 1 : 0.75 : 0.75 IPDI/PCL/DMPA/L-lysine.<sup>144</sup>

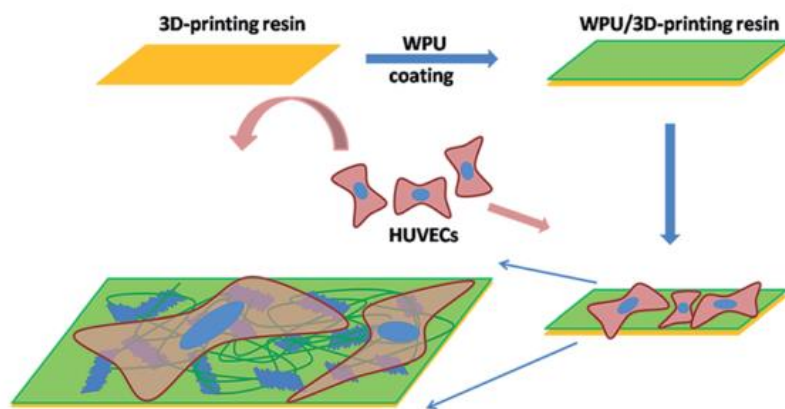


**Figure 2.28.** Schematic of PUD-Veroclear® composite scaffold. Reproduced with permission.<sup>144</sup>

After inkjet printing a commercially-available, photocurable resin (Objet Veroclear®), Feng et al. manually solution-casted this PUD dispersion onto the surface of the 3D-printed, photocured resin, a schematic of which is shown in **Figure 2.28**.<sup>144</sup> After drying the composite structures to remove water, a variety of surface and mechanical property characterization measurements were performed. The waterborne PUD film alone achieved an ultimate tensile strength and strain at break of 45.6 MPa and 716.2 %, respectively. However, the PUD-coated Veroclear® achieved only a strain at break of 14.8 %, likely limited by the commercially available photopolymer (strain at break of 13.7 % alone) and the potentially weak interface between the Veroclear® and the solution-cast PUD. Though the Veroclear® bulk scaffold limited the bulk elastomeric properties of the coating, the

local environment exposed to cells is likely still soft and suitable for cell growth, which is what the authors observed.

In another notable example of inkjet printing of PUDs, this time with a commercially-available aqueous PUD and inkjet printer, authors printed BASF LR-9005, an aromatic urethane acrylate dispersion (PUD) that contained 10-15 wt % trimethylolpropane ethoxylate triacrylate and supplied at overall 40 wt % solids in water, based on information available on the BASF website and safety data sheet for this material.<sup>146</sup> Though the PUD contained acrylate functional groups, piezoelectric inkjet printing did not employ this functionality during the printing process and followed with custom printing parameters, with a 5 min drying step in between layers to ensure proper stacking of successive layers on previously printed layers, as shown in *Figure 2.29*. This work demonstrated promise for 3D manufacturing, due to the high aspect ratio of the printed structures, and also demonstrated color gradients through addition of a water-soluble dye.

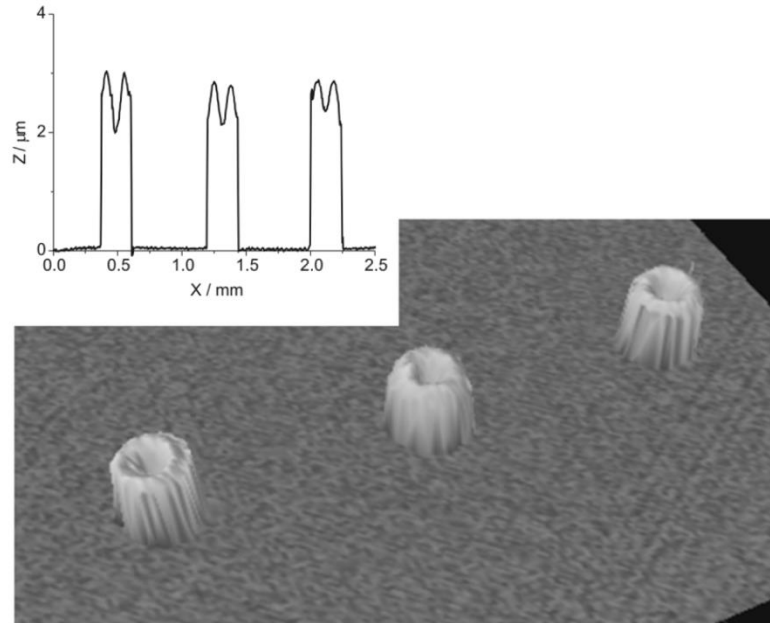


**Fig. 3** An image obtained by white-light interferometry of a sequence of single dots of 40 wt% polyurethane dispersion. The inset shows their associated profiles, which demonstrates their height and suggests the suitability of this dispersion for rapid prototyping.

**Figure 2.29.** White-light interferometry image and height profile (inset) of inkjet-printed single dots. Reproduced with permission.<sup>146</sup>



## 2.8 Photopolymers for vat photopolymerization or inkjet printing

Most photopolymer compositions for vat photopolymerization or inkjet printing remain highly formulated and contain a variety of reactants, such as photocurable oligomers, reactive diluents (e.g. monomers), solvents (e.g. unreactive diluents), photoinitiators (e.g. sensitizers), UV absorbers, chain extenders, and radical inhibitors (e.g. antioxidants).<sup>10</sup> These components are reviewed in great depth elsewhere but are briefly discussed here for context.<sup>10,134–136</sup> Each component plays a critical role. A cartoon representation of a crosslinked network containing some of these species is shown in **Figure 2.30**.<sup>39</sup> Here, the crosslinking agent, e.g. a oligomeric di(meth)acrylate, possesses two functional groups each with an effective functionality of two, as each (meth)acrylate is theoretically covalently linked to two other (meth)acrylate moieties in the absence of chain termination. Addition of a monoacrylate reactive diluent increases the distance between crosslink points, while further addition of a chain transfer agent (e.g. dithiol)<sup>33,39,148</sup> adds further distance between crosslink points. Unreactive diluents reduce viscosity and/or dissolve polymer chains, enabling processing of polymers normally highly viscous or in solid form at room temperature.<sup>34,35</sup> The remaining ingredients provide fine tuning of photochemistry, offering greater control over a variety of parameters including layer thickness, minimum feature size, and photopolymer shelf life. Photoinitiators provide the propagation center for polymerization, while radical inhibitors inhibit premature polymerization and improve resolution in the x-y build plane due to polymerization termination on the fringe regions (e.g. laser or image edges). UV absorber control vertical light penetration (z direction); small amounts of UV absorber greatly improve resolution in the z direction.<sup>10</sup> Finally, as oxygen inhibits free radical polymerization through multiple pathways, including quenching of photoinitiator excited states or termination of growing polymer chains, various small molecules are often added that act to remove oxygen inhibition.<sup>149</sup>

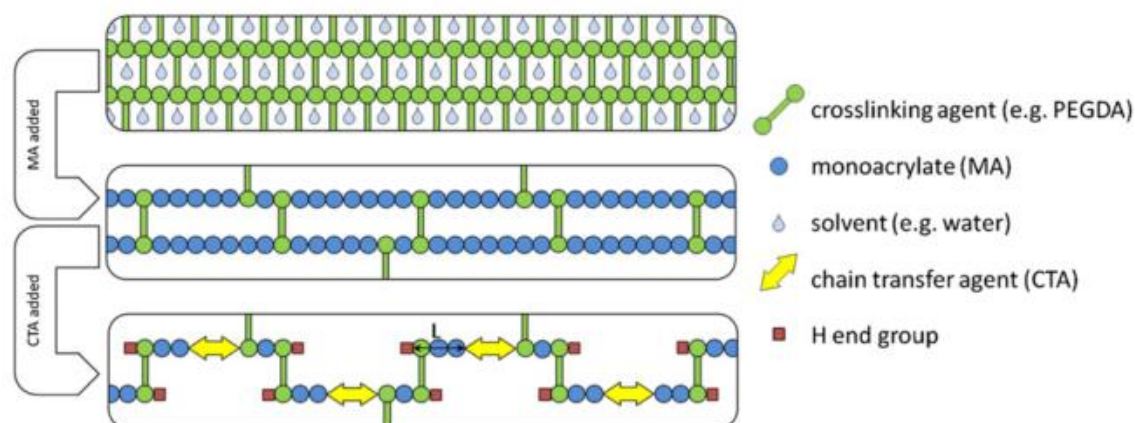


**Figure 2.30.** Cartoon representation of network structure before and after the addition of monoacrylate and dithiol chain transfer agent to a formulation that initially contains 100% of a diacrylate-functional oligomer. Figure adapted with permission.<sup>39</sup>

Much work has come from Jürgen Stampfl and Robert Liska in the Additive Manufacturing Group at TU Wien in Vienna. Much of their work involves the synthesis of photocurable monomers or oligomers and incorporation into photopolymer compositions via formulation. This group has published reviews on biomimetics,<sup>150</sup> new polymers for 3D printing,<sup>10,150–153</sup> and strategies to reduce oxygen inhibition of photopolymerization,<sup>149</sup> in addition to dozens of research papers in this field. Here, we cover their work in the area of elastomeric photopolymers. In one early effort, these authors created a series of photopolymer compositions for the purpose of creating blood vessel substitutes for cardiovascular disease treatment. Based on previously demonstrated biocompatibility of a cyanoacrylate-containing reactive diluent,<sup>30</sup> photopolymer compositions were designed to contain 45-49 wt % cyanoethylacrylate, 48.5 wt % PEG (400 g/mol), 1-5 wt % PEGDA (700 g/mol), and 1.5 wt % Irgacure 819 photoinitiator, shown in **Figure 2.31**.<sup>154</sup> The authors then compared mechanical properties of natural blood vessels (ovine arteria carotis). While the natural blood vessels possessed elastic moduli of 350-550 kPa, tensile strength of 900-1100 kPa, and strain at break between 100-150 % when tested in tension in the

circumferential direction, the photocured compositions possessed elastic moduli of 215-410 kPa, tensile strength of 121-151 kPa, and strain at break of 67-98 %.<sup>154</sup> An increase in elastic modulus and tensile strength and decrease in strain at break was associated with increasing PEGDA concentration. Though these compositions did not contain urethanes, they faithfully reproduced the tissue mechanical properties of interest, an objective of paramount importance in biomedical engineering.

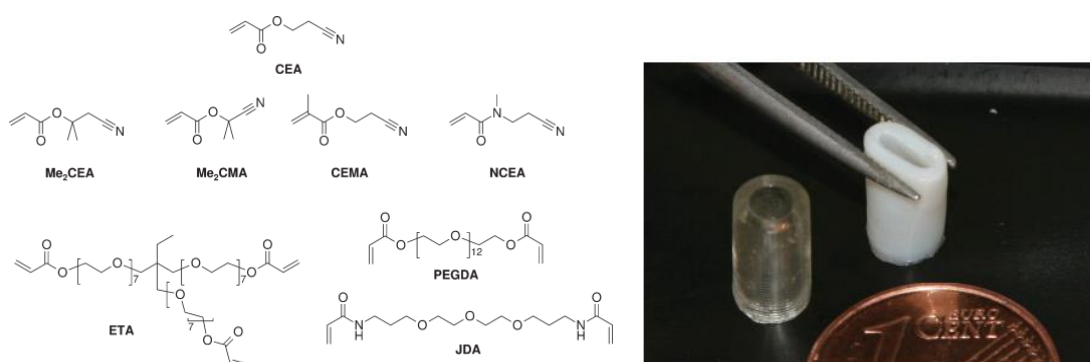


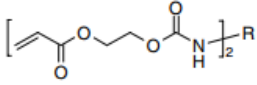
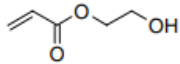
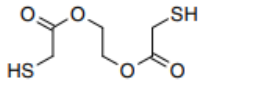
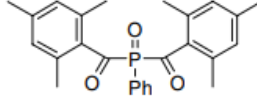
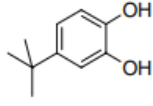
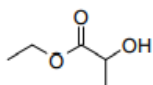
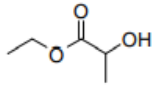
**Figure 2.31.** Photopolymer composition for the production of a blood vessel substitute via microstereolithography.

Liska and Stampfl built on this work by printing commercially available mixtures of urethane acrylates various reactive diluents in order to mimic the same blood vessel tissue previously described.<sup>40</sup> Tear resistance was also considered in this work; an optimized urethane acrylate formulation containing a dithiol chain extender matched the tear strength of blood vessel tissue. A related formulation more formally explored the role of chain extension with a dithiol, providing a highly useful cartoon representation of expected chain-extended network structure, shown in **Figure 2.30**.<sup>39,155</sup> In this representation, a crosslinked network of 100 % oligomeric diacrylate, e.g. a PEG diacrylate hydrogel, received an increase in spacing between crosslink points upon the addition of a monoacrylate (MA) reactive diluent. The space between crosslink points was further improved by the addition of a monomeric dithiol, which simultaneously increased the

distance between crosslink points by adding in between acrylate moieties, and also by decreasing the overall degree of polymerization of the polyacrylate chain through abstraction of a hydrogen from a CTA molecule. Bowman et al. corroborated this observation in a study of thiol-acrylate photopolymerizations, where stoichiometric thiol-acrylate polymerizations were observed to have an acrylate propagation constant 1.5 times greater than the rate of hydrogen abstraction from a thiol but a postulated lower average degree of polymerization.<sup>148</sup> Photopolymer compositions demonstrated high tenability, with elastic moduli ranging from ~0.6 – 4.0 MPa, tensile strength ranging from ~0.5 – 2.3 MPa, and elongation at break ranging from ~100% - 450%.<sup>39</sup> Though the mechanical property data for these photopolymer compositions are not readily obtainable due to the proprietary nature of the urethane-containing oligomers,

**Table 2.1** depicts the publically available chemical components of these photopolymer formulations. The authors most recently published on tissue scaffold fabrication employing related photoelastomer compositions and two-photon polymerization (2PP), producing relatively large scaffolds for the 2PP technique.<sup>156</sup>

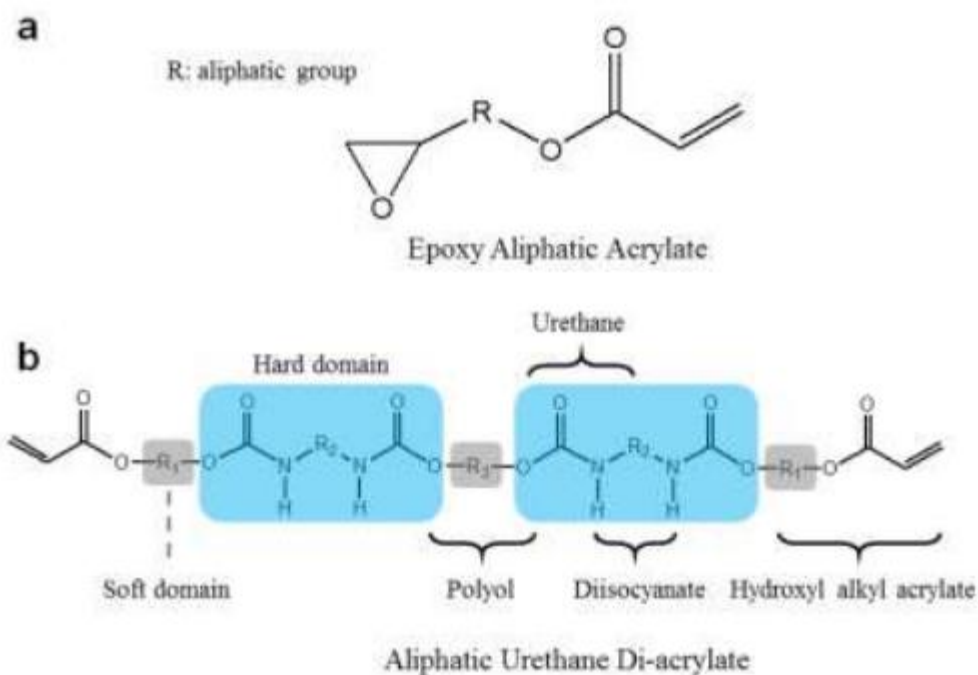
**Table 2.1.** Photopolymer compositions employed by Liska and Stampfl, et al.

Abbr.	Chemical name/brand	Structure	Function
UDA	Genomer 4215		DA
HEA	Hydroxyethylacrylate		Reactive diluent, MA
EGTG	Ethylene glycol bisthioglycolate		CTA
BPO	Phenylbis(2,4,6-trimethylbenzoyl) phosphine oxide (Irgacure <sup>®</sup> 819)		Photoinitiator
DBB	1,2-Dihydroxy-4-tert-butylbenzene		Stabilizer
ABS	CGL097	<sup>a</sup> 	Absorber
ETLA	Ethyl lactate		Solvent

<sup>a</sup>No information available.

Magdassi and coworkers have designed a series of highly elastomeric and UV curable photopolymers for vat photopolymerization that employ mixtures of an aliphatic urethane diacrylate (AUD, Ebecryl 8413, Allnex) and epoxy aliphatic acrylate (EAA, Ebecryl 113); Ebecryl itself contains 33 wt % isobornyl acrylate, with the remainder being aliphatic urethane diacrylate.<sup>147</sup> The relevant chemical structures are shown in **Scheme 2.18**, with various optical images of a 3D printed, isotropic truss shown in **Figure 2.32**. Upon varying the mixture of AUD and EAA, the authors achieved variation in Young's moduli between 0.58 – 4.21 MPa, elongation at break between ~240 % to ~1100 %, and stress at break between ~ 0.5 MPa to 7.5 MPa. This simple photopolymer system relies only on commercially available materials and vastly improves the characteristically poor strain at break of non-silicone-containing elastomers, with the highest

elongation composition containing 100 % Ebecryl 8413. The authors attribute this profound increase in strain at break to physical interactions from the aliphatic urethane diacrylate, e.g. hydrogen bonding.



**Scheme 2.18.** Chemical structures of epoxy aliphatic acrylate and aliphatic urethane diacrylate.

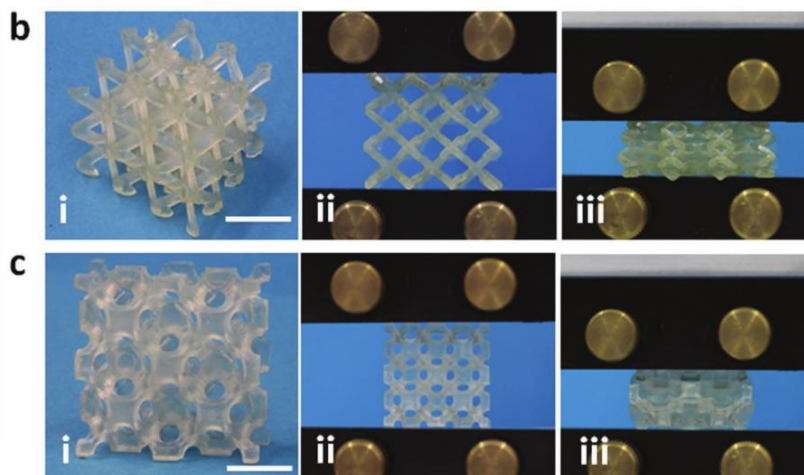
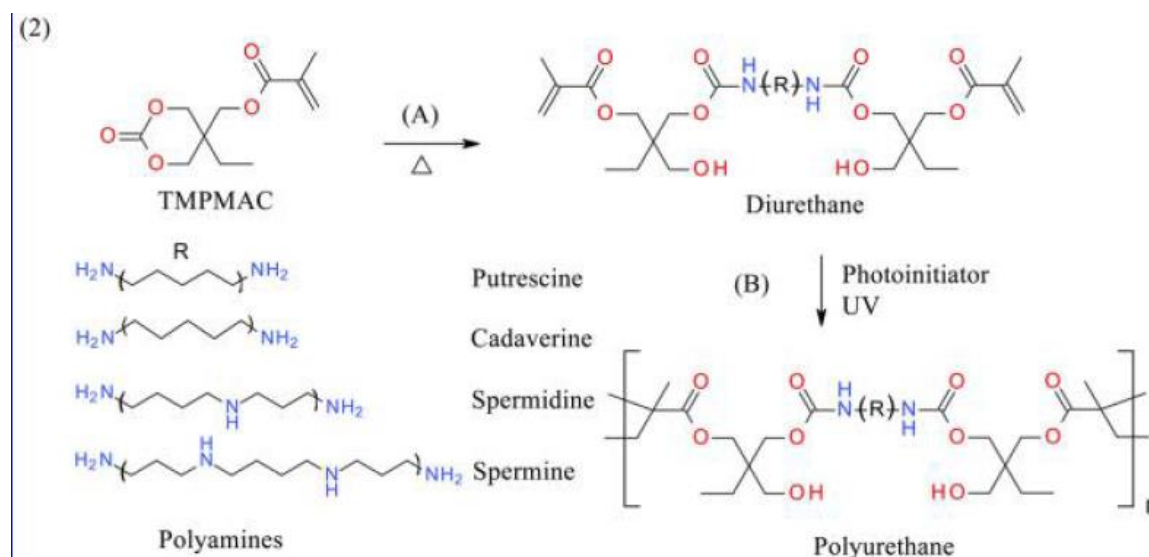


**Figure 2.32.** Various views of a 3D printed, highly deformable isotropic truss.

While many researchers optimize commercially available photocurable oligomers, some decide to synthesize oligomers in-house, due to the greater diversity enabled through synthetic chemistry. Shown in **Scheme 2.19**, Shaochen Chen, *et al.* synthesized a series of isocyanate-free, urethane-containing photocurable oligomers from a cyclic carbonate-containing methacrylate monomer and various biosourced diamines, in the absence of catalyst or solvent, in a reaction requiring only heat.<sup>157</sup> For 3D fabrication, the authors also employed a continuous liquid interface printing (CLIP) method similar to that described by Joseph Desimone, *et al.* and currently employed by *Carbon*.<sup>13,14</sup> Though the authors did not measure tensile properties of the fabricated films or structures, 3D printed squares possessed compressive storage moduli between 20 – 30 MPa determined using dynamic mechanical analysis (DMA).<sup>157</sup>

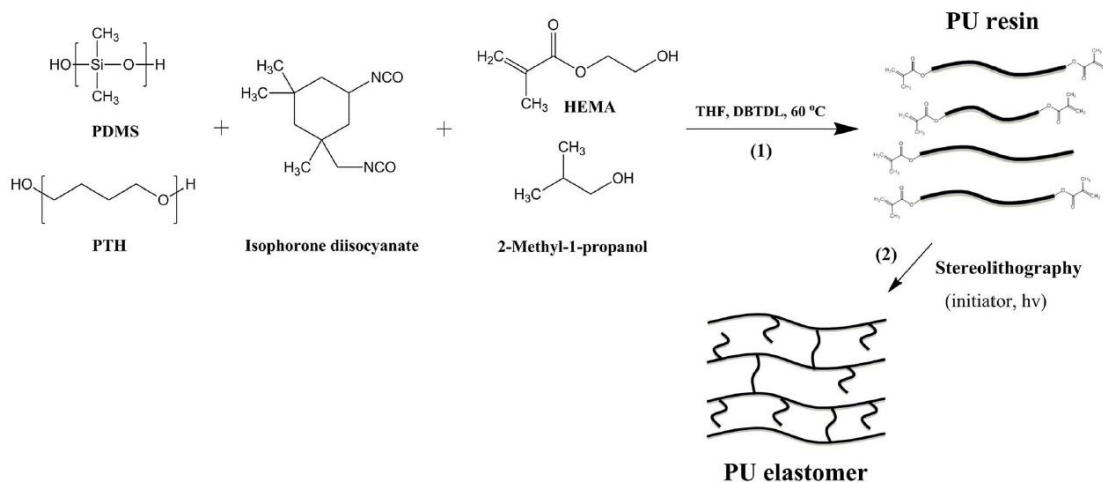


**Scheme 2.19.** Synthesis of bio-based, green, aliphatic urethane-containing photocurable oligomers.

Seppälä Jukka, *et al.* synthesized a novel, photocurable urethane acrylate oligomer and demonstrated the ability to 3D print an elastomeric object in the absence of reactive diluents.<sup>111</sup>

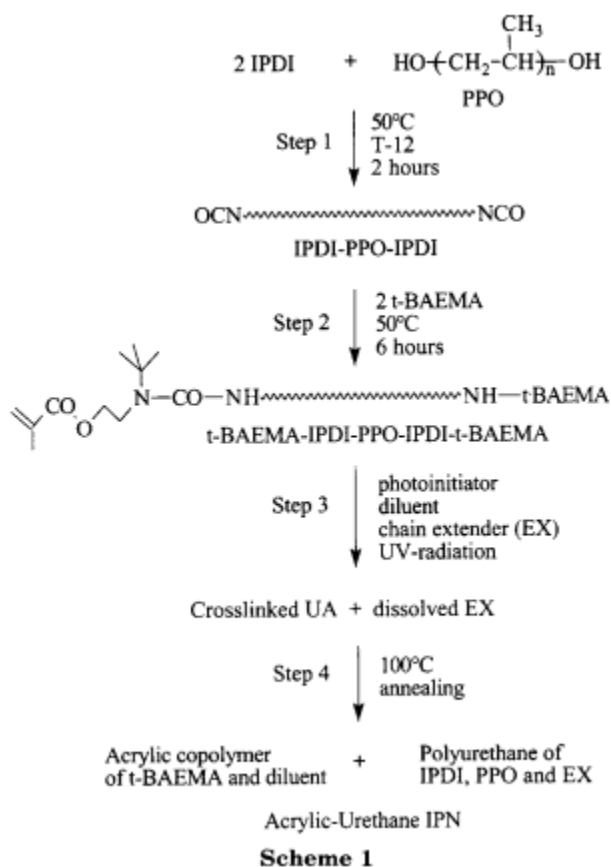


The authors overcame the typically high viscosity of urethane-containing oligomers synthesized with symmetric diisocyanates, e.g. 1,6-hexanediisocyanate (HDI) or hydrogenated methylene diphenyl diisocyanate (H<sub>12</sub>MDI) through use of the non-symmetrical isophorone diisocyanate (IPDI), which possess both a primary aliphatic and secondary cycloaliphatic isocyanate. The unequal reactivity and resulting sterically hindered hydrogen bonding results in the production of relatively low viscosity products.<sup>158</sup> In data that supports this hypothesis and in a separate study, Juin-Yih Lai *et al.* employed infrared spectroscopy to confirm the relatively low amount of hydrogen bonding present in IPDI-containing polyurethanes, vs. the more symmetrical MDI-containing polyurethanes, which they attributed to a lack of structure order and resultant increase in steric effects.<sup>159</sup> Detailed in **Scheme 2.20**, Jukka, et al. combined 550 g/mol silanol, 2k g/mol poly(tetramethylene oxide) (PTMO), IPDI, hydroxyethyl methacrylate (HEMA), and a monofunctional alcohol to control both the molecular weight, dispersity, and overall functionality of the resulting urethane acrylate oligomers. Samples possessed  $M_n = 3,600$  g/mol and  $\bar{D} = 3.27$  as measured by GPC, a single, broad  $T_g$  centered at  $-75$  °C (though the authors did not measure below  $-90$  °C), with a viscosity of 2.2 Pa·s at room temperature.<sup>111</sup> Photocured films possessed a Young's modulus, ultimate tensile strength, and elongation at break of 2.5 MPa, 3.7 MPa, and 195 %, respectively.<sup>111</sup>



**Scheme 2.20.** Low viscosity, urethane-containing oligomers for vat photopolymerization.

One unique approach toward the 3D printing of urethanes involves blocked isocyanates. Based in academic literature<sup>160</sup> and shown in **Scheme 2.21**,<sup>42</sup> synthesis of blocked isocyanate-containing photocurable oligomer initially follows the formation of an isocyanate-terminated prepolymer, in this case. Here, after endcapping of a poly(propylene oxide) oligomer with a diisocyanate, tert-butyl aminoethylmethacrylate attacks the isocyanate endgroups, producing a blocked isocyanate-containing, photocurable oligomer.<sup>42</sup> After photocuring of this oligomer in the presence of photoinitiator, diluents, and chain extenders [e.g. triethanolamine, butanediol, or 4,4'-methylenebis(cyclohexylamine)], a post-curing annealing process deblocked the urethanes in the crosslinked object, providing chain extension. This chain extension enabled strain at break values of 376 % for a photocured oligomer containing methyl methacrylate as a diluent and 4,4'-methylenebis(cyclohexylamine) as a chain extender, while the non-annealed sample only achieved 99 % strain at break. Though this work did not involve AM, it did inspire a new photopolymer chemistry at Carbon, for use in their CLIP process, as indicated by a recent patent.<sup>41</sup>



**Scheme 2.21.** Synthetic strategy to prepare blocked isocyanates.

## 2.9 Additive manufacturing using polymer emulsions

As briefly mentioned in section 2.7.3, emulsions offer great potential for AM of elastomers.

In emulsion polymerization, the water-insoluble monomers (oil-phase) are dispersed in water using surfactants. Radical polymerization yields latex particles suspended in water, which contain high molecular weight polymers. Because the polymers are formed in micelles, the viscosity of the latexes are close to the one of water ( $\eta_{H_2O} = 0.001 \text{ Pa}\cdot\text{s}$ ) and do not depend on the molecular weight of the polymers. This offers great potential to process high molecular weight polymers using AM techniques which require low viscosities, e.g. inkjet printing.

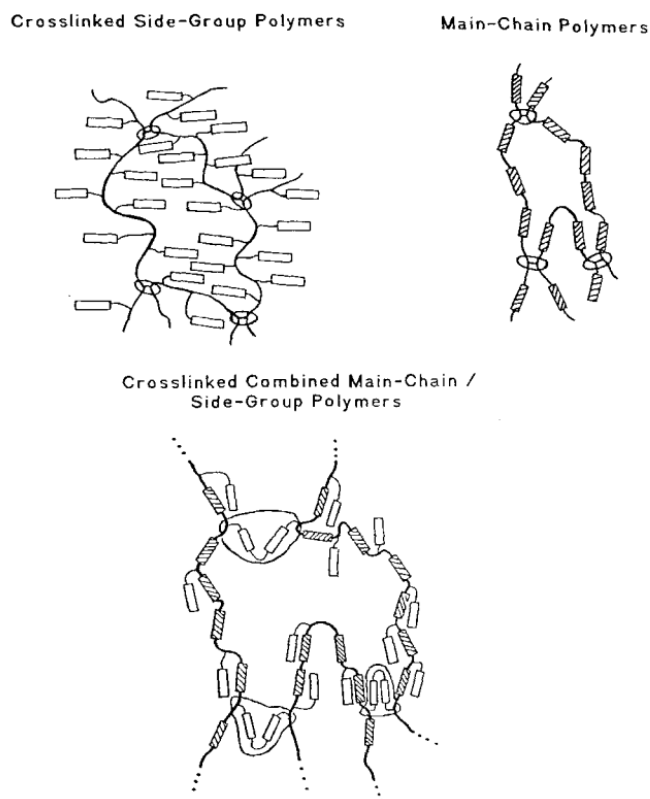
In 2016 Wells et al. investigated five different types of latex inks, all commercially available.<sup>23</sup> Materials ranged from poly(2-chloro-1,3-butadiene) (also known as neoprene), carboxylated styrene-butadiene rubber, carboxylated butadiene-acrylonitrile copolymer, natural rubber, to prevulcanized natural rubber. From this selection, only carboxylated styrene-butadiene (Litex T 71S20®) was determined suitable for inkjetting, possessing a viscosity of 12 mPa·s, particle diameters of 0.25  $\mu\text{m}$  and surface tensions of 49  $\text{mN}\cdot\text{m}^{-1}$ . However, dilution to 35 wt.% solids and addition of a non-ionic surfactant (Triton X-100) was needed to avoid agglomeration and clogging of the printer nozzle. First attempts resulted in rather low printing resolution due to the formation of small secondary satellite drops and the individual printed lines were visible after drying the ink. While this procedure demonstrated high potential of polymer emulsions for inkjet printing, optimization is required to achieve better print resolution.

Bain et al. further investigated the concept of ink-jet printing emulsions of high molecular weight polymers.<sup>161</sup> The authors studied the printability of dissolved polystyrene (PS) with molecular weights of  $M_n = 549\text{k g}\cdot\text{mol}^{-1}$  in methyl benzoate and compared it to emulsions consisting of PS with  $M_n = 419\text{k g}\cdot\text{mol}^{-1}$  and SDS (sodium dodecyl sulfate) as surfactant. These experiments revealed that emulsions with 3.8 wt % PS showed Newtonian jetting dynamics and enabled successful printing. In contrast, only 0.25 wt % of high-molecular weight PS, dissolved in methyl benzoate, were jettable. Albeit PS is not an elastomer, oil-in-water emulsions show feasibility of printing high molecular weight polymers, because the low-shear viscosity is reduced and non-Newtonian dynamics are eliminated, which is highly attractive for 3D-printing elastomers. Nevertheless, it is difficult to prepare homogenous emulsions in the laboratory and surfactants are needed to prepare oil-in-water emulsions, which might influence the overall

properties of the printed material. Recently, Doyle et al. formulated thermoresponsive nanoemulsions for selective photocuring, utilizing PDMS as oil phase and PEG-dimethacrylate and sodium dodecyl sulfate (SDS) in deionized water as continuous phase.<sup>162</sup> While the authors utilized this formulation to manufacture mesostructured hydrogels, this strategy might enable the 3D printing of elastomeric structures starting from an oil-in water emulsion.

### **2.10 Liquid crystalline elastomers (LCE)**

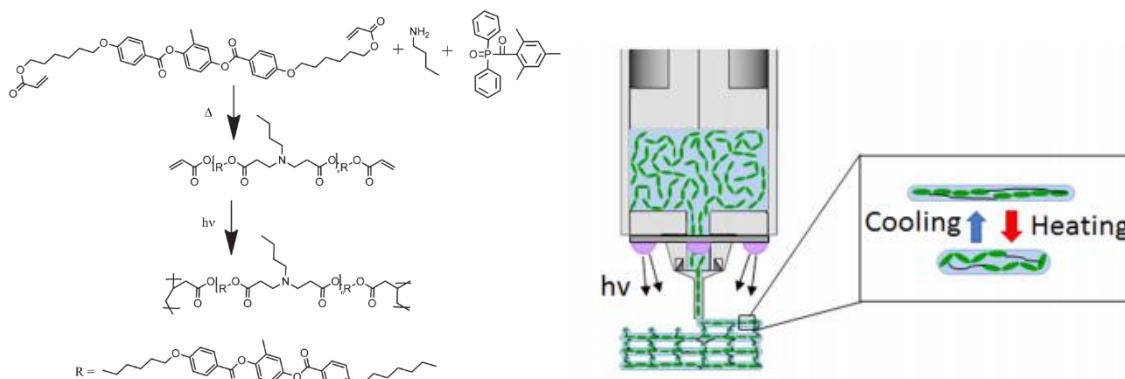
Liquid crystalline elastomers (LCEs) are slightly crosslinked, flexible polymers which bear liquid crystalline mesogenic groups in their side- or main-chains (**Scheme 2.22**). They combine the ordered and mobile character of liquid crystals with rubbery elasticity of polymers.<sup>163,164</sup> Details on the synthesis and use of LCEs for harnessing macroscale mechanical responses was recently reviewed by White and Broer.<sup>165</sup> In brief, LCE's provide the possibility of two-way actuation to a structure through the reversible transition between the LC phase and an isotropic phase.<sup>166</sup> This requires a pre-orientation step, which aligns the mesogenic units into an ordered orientation. Highly ordered systems are usually obtained *via* mechanical stretching of films, electrospinning, or the use of pre-aligned substrates. Being able to additively manufacture LCEs in three dimensions is highly attractive for creating artificial muscles, soft actuators/robots, sensing devices, smart medical devices, or dynamic functional architectures.<sup>167</sup>



**Scheme 2.22.** Types of different liquid crystalline elastomers. Adapted from Zentel.<sup>163</sup>

While Broer et al. ink-jet printed 2D layers using LCEs in 2009, only very recently, Ware et al. harnessed the anisotropic nature of DIW to fabricate aligned LCEs in 3 dimensions. The authors formulated LCE inks starting from a commercially-available liquid crystalline monomer (1,4-bis-[4-(6-acryloyloxyhexyloxy)benzoyloxy]-2-methylbenzene (RM82)) and *n*-butylamine as chain-extender.<sup>168</sup> Both were mixed in a 1.1:1 ratio, filled into the printing syringe and azo-Michael-addition at 75 °C induced chain-extension, yielding the LCE oligomers with terminal acrylate groups (**Scheme 2.23, left**). The same authors provided details on the LCE synthesis elsewhere.<sup>169</sup> The oligomers possessed shear thinning behavior at temperatures within the nematic region (85 °C) and were easily extruded. The extrusion out of a narrow nozzle (diameter = 0.31 mm) allowed for aligning the mesogens parallel to the printing path and yielded controlled

molecular orientation (**Scheme 2.23, right**). Afterwards, UV-light illumination induced crosslinking of the acrylate-end groups. The crosslinking step enabled shape retention of the extruded structures and locked the aligned polymer chains in place.



**Scheme 2.23.** *Left:* Synthesis of LCE utilizing aza-Michael reaction and subsequent UV-crosslinking of the acrylate-end groups. *Right:* Schematic of the DIW-UV process and the LCE alignment.<sup>168</sup>

Single-layered LCE films exhibited an elastic modulus of 18 MPa along the extrusion direction and a modulus of 4 MPa normal to the extrusion direction and showed maximum strains of 70-120%. The LCE oligomers exhibited a nematic to isotropic transition temperature ( $T_{NI}$ ) at 105 °C. Above the  $T_{NI}$ , the material undergoes a large, reversible contraction parallel to the direction of the mesogen alignment. Upon heating to 200 °C, the material reversibly contracted by 40% along the print direction and expanded normal to that direction. Capitalizing on the design freedom of DIW and the anisotropic deformation of aligned LCEs, the authors printed various structures, including geometries with zero, negative and positive Gaussian curvature. The combination of positive and negative Gaussian curvature in one geometry enabled the design of structures with snap-through deformation. Utilizing the same concept, Sánchez-Somolinos et al. printed a ring-shaped LCE in a PDMS slab and demonstrated their potential as a variable focusing lens.<sup>170</sup> Due to the asymmetric placement of the LCE in the PDMS, the slab maintained flat at

room temperature, but heating to 100 °C induced deformation and formed a convex front (**Figure 2.33**).

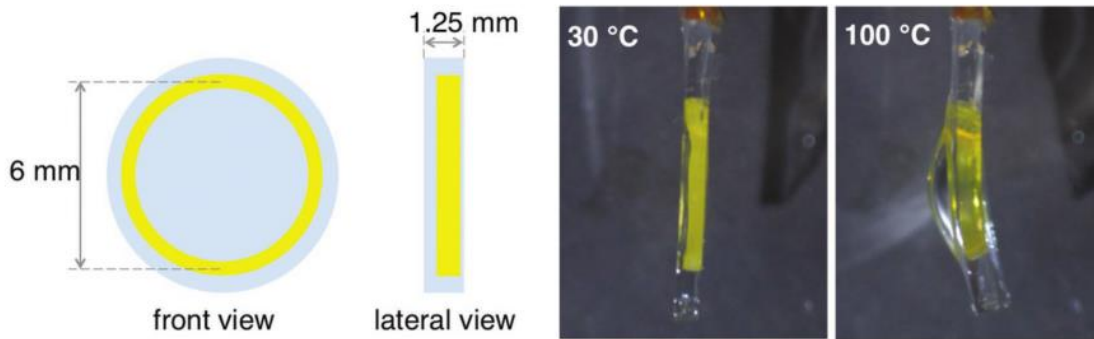


**Figure 2.33.** PDMS-slab with asymmetrically placed LCE (yellow material) enables temperature-induced buckling and demonstrates potential as adaptive optical element. Adapted from Sánchez-Somolinos et al.<sup>170</sup>

The anisotropic deformation of oriented LCEs upon heating above their nematic phase enables them to conduct specific work. Lewis et al studied the impressive weight-specific work capacity of LCEs in detail.<sup>171</sup> The authors printed LCE strips and performed weight lifting experiments. Significantly, 1 mm thick AM LCE actuators were able to lift ~1000 times of their own body weight (106 mg) as illustrated in **Figure 2.34**.



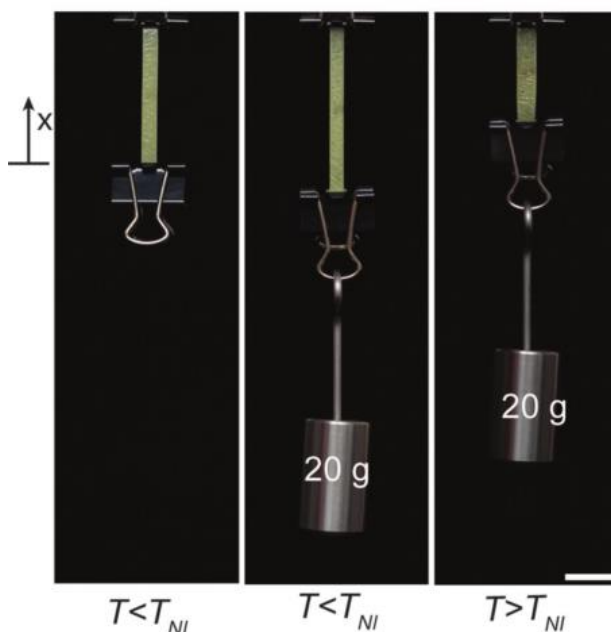


**Figure 2.34.** Additively manufactured LCE film (1 mm in thickness) performing temperature-responsive “weight lifting”. Scale bar = 5 mm. Reprinted with permission.<sup>171</sup>

## 2.11 Polyesters and Polycarbonates

A small number of 3D printable, polyester- or polycarbonate-based polymers are reported, though the volume of literature does not match that of polyurethanes or poly(dimethyl siloxane)s. In one example, Liqun Zhang, et al. synthesized and 3D printed unsaturated, low  $T_g$ , random copolyester thermoplastic vulcanizates (TPVs),<sup>172</sup> shown in **Scheme 2.24**, which are based on some of their previous work.<sup>173,174</sup> These phase-separated TPVs contain a high weight fraction of elastomer and smaller thermoplastic weight fraction and undergo phase inversion upon dynamic vulcanization, resulting in a crosslinked elastomeric phase in a thermoplastic matrix, as illustrated in **Figure 2.35a**. Depending on composition, e.g. ratio of PLBSI to PLA, the authors were able to achieve ~ 440 % strain and ~2 MPa ultimate tensile strength for PLBSI alone, while a 60/40 PLA/PLBSI TPV achieved ~320 % strain at break and ~ 20 MPa strain at break. 3D printing occurred via fused filament fabrication, the products of which are shown in **Figure 2.35b**, with the 3D printed structures (up to 75 % porous) achieving 240 – 260 % strain at break.

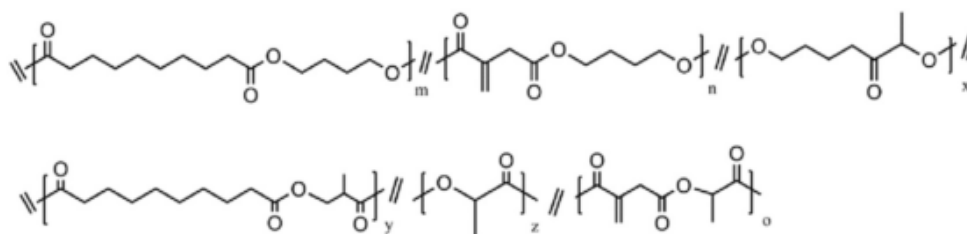


Fig. 1. Chemical structure of PLBSI.

Scheme 2.24. Synthesis of PLBSI unsaturated copolyesters.

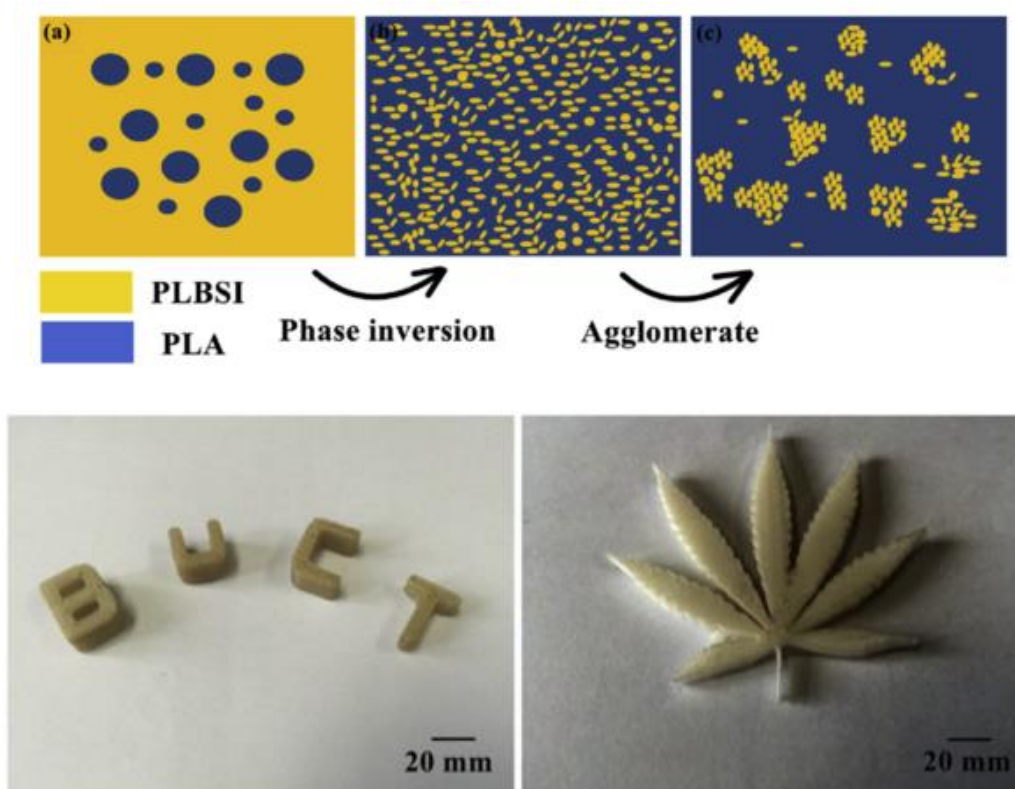
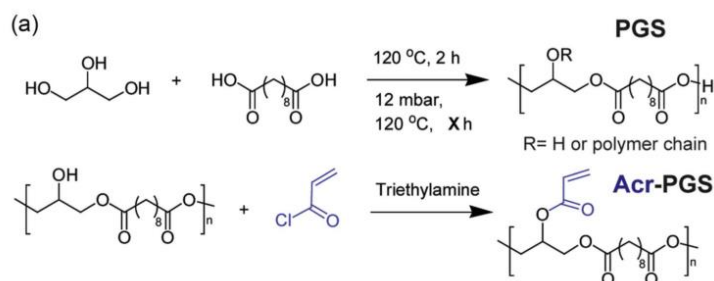


Figure 2.35. (A) Illustration depicting dynamic vulcanization of an elastomer (PLBSI) and thermoplastic (PLA), resulting in a thermoplastic vulcanizates (TPVs). (B) 3D-printed PLBSI/PLA TPV.

Jason Burdick *et al.* synthesized acrylated poly(glycerol sebacate)s macromonomers for direct ink write AM, shown in Scheme 2.25.<sup>175</sup> Macromonomers possessed a  $M_n$  of 6,000 g/mol relative to PMMA and  $\bar{D} \approx 1.7-2$ , while NMR spectroscopy measured  $\sim 15\%$  acrylate

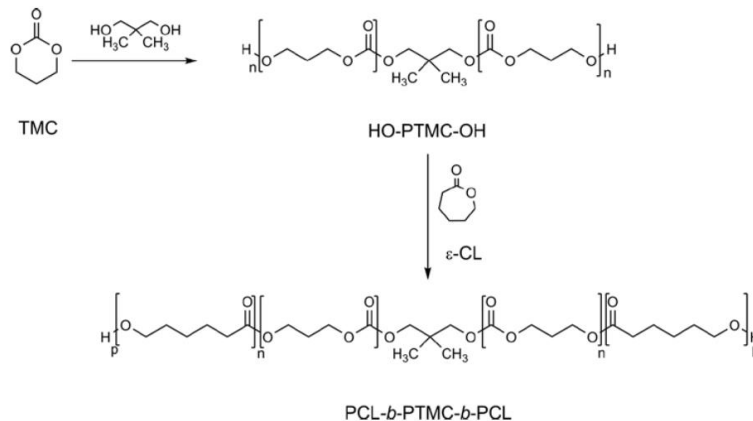
functionalization of the available hydroxyl functional groups. Photorheology indicated a  $G'/G''$  modulus crossover within seconds for all compositions, while the uncured oligomer possessed pre-cured viscosities between 3-9 Pa·s. UV irradiation occurred throughout and after the DIW process, resulting in the production of well-defined 3D scaffolds. Film-casted samples possessed a young's modulus of  $\sim 0.6$  MPa, an ultimate tensile stress of  $\sim 0.4$  MPa, and a strain at break of  $\sim 85\%$ , with DIW created samples falling slightly short of these film-casted values.



**Scheme 2.25.** Photocurable poly(glycerol sebacate)s.

Dirk Grijpma et al. synthesized biodegradable poly( $\epsilon$ -CL-*b*-TMC- $\epsilon$ -CL) triblock copolymers, shown in **Scheme 2.26** that served as melt-processable thermoplastic elastomers for tissue scaffolding applications.<sup>176</sup> Triblock copolymers were printed via material extrusion as a 20-25 wt % solution in ethylene carbonate and subsequently extracted with water and dried, generating microporous scaffold morphologies due to ethylene carbonate crystallization before solvent removal and drying. Solution-casted triblock copolymer films possessed a Young's modulus, ultimate tensile strength, and elongation at break of approximately 120 MPa, 16 MPa and 620 % respectively. Though mechanical properties were not obtained for the 3D-printed, microporous scaffolds, this effort represents a remarkable achievement in strain at break for non-

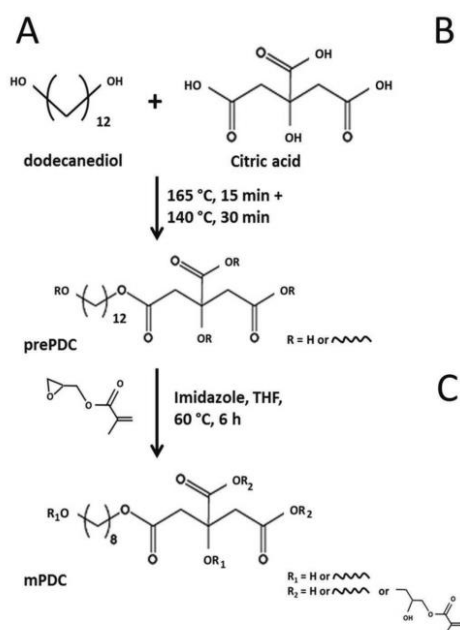
urethane-containing polymers. In this case, physical crosslinking and subsequent mechanical property improvements occur through phase separation of the PCL and PTMC blocks.



**Scheme 2.26.** Synthesis of poly( $\epsilon$ -CL-*b*-TMC- $\epsilon$ -CL) triblock copolymers.

Guillermo Ameer, et al. has reported the synthesis and characterization of poly(diols citrate) biodegradable elastomers in various earlier reports and in a recent publication discussing the 3D printing *via* an in-house designed CLIP process.<sup>177–180</sup> In an example synthesis shown in **Scheme 2.27**, the authors combined dodecanediol and citric acid in the melt, in the absence of catalyst or solvent, and freeze dried the polymers after isolation. A post-polymerization functionalization then installed methacrylate functional groups on remaining hydroxyl functional groups.<sup>179</sup> Although no tensile mechanical property data is provided, the 3D printed scaffolds qualitatively demonstrated elastic recovery after application of 25 % compressive strain.<sup>179</sup> Previous reports from Ameer *et al.* do not discuss 3D printing but provide more extensive composition and mechanical property analysis for non-photocurable analogs (e.g. just diols and citric acid alone), investigating the role of diol segment length on mechanical properties.<sup>180</sup> One notable composition, poly(1,6-hexanediol-*co*-citric acid), obtained a stress and strain at break of approximately 3 MPa and 375 %, though this composition is not 3D printable with CLIP due to the lack of photocurable functionality

in the polymer backbone. A viable alternative for printing this composition might be the melt extrusion of poly(diols citrate) pre-polymer solutions, as these pre-polymers are soluble before network formation occurs.<sup>178</sup> Furthermore, strain at break decreased for poly(diols citrate) samples after the prepolymer underwent post-polymerization network formation under vacuum, though slight increases in thermal stability and large increases in stress at break were observed, demonstrating the tenability of this poly(diols citrate) platform.<sup>178</sup>



**Scheme 2.27.** Synthesis of photocurable poly(citrate diol) biodegradable elastomers.

## 2.12 Acknowledgements

The authors would like to thank Emily M. Wilts for proof-reading the manuscript.

The authors further acknowledge Philip J. Scott for helpful discussions regarding blocked isocyanates.

## 2.13 References

- (1) Freedonia. *World Thermoplastic Elastomers*; 2015.
- (2) Odian, G. Principle of Polymerization. *Princ. Polym. Wiley sons* **2004**, 128–130.
- (3) Saunders, S. New Balance Uses Ultrasonic Equipment and Sieves to Ensure High

- Powder Throughput For 3D Printed Midsoles <https://3dprint.com/199087/new-balance-powder-case-study/> (accessed May 9, 2018).
- (4) Sperling, L. H. *Introduction to Physical Polymer Science*; 2006.
  - (5) Yilgör, E.; Yilgör, I. Silicone Containing Copolymers: Synthesis, Properties and Applications. *Progress in Polymer Science*. 2014, pp 1165–1195.
  - (6) Yilgor, I.; Yilgor, E. Structure-Morphology-Property Behavior of Segmented Thermoplastic Polyurethanes and Polyureas Prepared without Chain Extenders. *Polym. Rev.* **2007**, *47* (4), 487–510.
  - (7) Brown, R. *Physical Test Methods for Elastomers*; 2017.
  - (8) Callister, W.; Rethwisch, D. *Materials Science and Engineering: An Introduction*; 2007; Vol. 94.
  - (9) Rubinstein, M.; Colby, R. H. *Polymer Physics*. *Oxford Univ. Press New York* **2003**.
  - (10) Ligon, S. C.; Liska, R.; Stampfl, J.; Gurr, M.; Mülhaupt, R. Polymers for 3D Printing and Customized Additive Manufacturing. *Chem. Rev.* **2017**, *117* (15), 10212–10290.
  - (11) Gibson, I.; Rosen, D.; Stucker, B. *Vat Photopolymerization Processes BT - Additive Manufacturing Technologies: 3D Printing, Rapid Prototyping, and Direct Digital Manufacturing*; Gibson, I., Rosen, D., Stucker, B., Eds.; Springer New York: New York, NY, 2015; pp 63–106.
  - (12) Zhang, J.; Xiao, P. 3D Printing of Photopolymers. *Polym. Chem.* **2018**.
  - (13) Tumbleston, J. R.; Shirvanyants, D.; Ermoshkin, N.; Januszewicz, R.; Johnson, A. R.; Kelly, D.; Chen, K.; Pinschmidt, R.; Rolland, J. P.; Ermoshkin, A.; et al. Continuous Liquid Interface Production of 3D Objects. *Science* (80-. ). **2015**, *347* (6228), 1349–1352.
  - (14) Januszewicz, R.; Tumbleston, J. R.; Quintanilla, A. L.; Mecham, S. J.; DeSimone, J. M. Layerless Fabrication with Continuous Liquid Interface Production. *Proc. Natl. Acad. Sci.* **2016**, *113* (42), 11703–11708.
  - (15) Gilmer, E. L.; Miller, D.; Chatham, C. A.; Zawaski, C.; Fallon, J. J.; Pekkanen, A.; Long, T. E.; Williams, C. B.; Bortner, M. J. Model Analysis of Feedstock Behavior in Fused Filament Fabrication: Enabling Rapid Materials Screening. *Polym. (United Kingdom)* **2017**, 1–11.
  - (16) Lewis, J. A.; Gratson, G. M. Direct Writing in Three Dimensions. *Mater. Today* **2004**, *7* (7), 32–39.
  - (17) Lewis, J. A. Direct Ink Writing of 3D Functional Materials. *Adv. Funct. Mater.* **2006**, *16* (17), 2193–2204.
  - (18) Truby, R. L.; Lewis, J. A. Printing Soft Matter in Three Dimensions. *Nature* **2016**, *540* (7633), 371–378.
  - (19) Hurt, C.; Brandt, M.; Priya, S. S.; Bhatelia, T.; Patel, J.; Selvakannan, P.; Bhargava, S. Combining Additive Manufacturing and Catalysis: A Review. *Catal. Sci. Technol.* **2017**, *7*, 3421–3439.
  - (20) O’bryan, C. S.; Bhattacharjee, T.; Niemi, S. R.; Balachandar, S.; Baldwin, N.; Ellison, S. T.; Taylor, C. R.; Sawyer, W. G.; Angelini, T. E. Three-Dimensional Printing with Sacrificial Materials for Soft Matter Manufacturing. *MRS Bull.* **2017**, *42* (8), 571–577.
  - (21) Derby, B. Inkjet Printing of Functional and Structural Materials: Fluid Property

- Requirements, Feature Stability, and Resolution. *Annu. Rev. Mater. Res.* **2010**, *40* (1), 395–414.
- (22) Guo, Y.; Patanwala, H. S.; Bognet, B.; Ma, A. W. K. Inkjet and Inkjet-Based 3D Printing: Connecting Fluid Properties and Printing Performance. *Rapid Prototyp. J.* **2017**, *23* (3), 562–576.
- (23) Lukic, M.; Clarke, J.; Tuck, C.; Whittow, W.; Wells, G. Printability of Elastomer Latex for Additive Manufacturing or 3D Printing. *J. Appl. Polym. Sci.* **2016**, *133* (4), 1–7.
- (24) Singh, M.; Haverinen, H. M.; Dhagat, P.; Jabbour, G. E. Inkjet Printing-Process and Its Applications. *Adv. Mater.* **2010**, *22* (6), 673–685.
- (25) Liravi, F.; Toyserkani, E. A Hybrid Additive Manufacturing Method for the Fabrication of Silicone Bio-Structures: 3D Printing Optimization and Surface Characterization. *Mater. Des.* **2018**, *138*, 46–61.
- (26) Yang, H.; He, Y.; Tuck, C.; Wildman, R.; Hague, R. High Viscosity Jetting System for 3D Reactive Inkjet Printing. *Twenty Forth Annu. Int. Solid Free. Fabr. Symp. – An Addit. Manuf. Conf.* **2013**, 505–513.
- (27) Gibson, I.; Rosen, D.; Stucker, B. Powder Bed Fusion Processes. In *Additive Manufacturing Technologies: 3D Printing, Rapid Prototyping, and Direct Digital Manufacturing*; Springer New York: New York, NY, 2015; pp 107–145.
- (28) Buckwalter, D. J.; Dennis, J. M.; Long, T. E. Amide-Containing Segmented Copolymers. *Prog. Polym. Sci.* **2015**, *45*, 1–22.
- (29) Stansbury, J. W.; Idacavage, M. J. 3D Printing with Polymers: Challenges among Expanding Options and Opportunities. In *Dental Materials*; 2016; Vol. 32, pp 54–64.
- (30) Stampfl, J.; Baudis, S.; Heller, C.; Liska, R.; Neumeister, A.; Kling, R.; Ostendorf, A.; Spitzbart, M. Photopolymers with Tunable Mechanical Properties Processed by Laser-Based High-Resolution Stereolithography. *J. Micromechanics Microengineering* **2008**, *18* (12).
- (31) Peltola, S. M.; Melchels, F. P. W.; Grijpma, D. W.; Kellomäki, M. A Review of Rapid Prototyping Techniques for Tissue Engineering Purposes. *Ann. Med.* **2008**, *40* (4), 268–280.
- (32) Yue, J.; Zhao, P.; Gerasimov, J. Y.; Van De Lagemaat, M.; Grotenhuis, A.; Rustema-Abbing, M.; Van Der Mei, H. C.; Busscher, H. J.; Herrmann, A.; Ren, Y. 3D-Printable Antimicrobial Composite Resins. *Adv. Funct. Mater.* **2015**, *25* (43), 6756–6767.
- (33) Serrine, J. M.; Meenakshisundaram, V.; Moon, N. G.; Scott, P. J.; Mondschein, R. J.; Weiseman, T. F.; Williams, C. B.; Long, T. E. Functional Siloxanes with Photo-Activated, Simultaneous Chain Extension and Crosslinking for Lithography-Based 3D Printing. *Polym. (United Kingdom)* **2018**, 1–10.
- (34) Melchels, F. P. W.; Feijen, J.; Grijpma, D. W. A Poly(d,l-Lactide) Resin for the Preparation of Tissue Engineering Scaffolds by Stereolithography. *Biomaterials* **2009**, *30* (23–24), 3801–3809.
- (35) Hegde, M.; Meenakshisundaram, V.; Chartrain, N.; Sekhar, S.; Tafti, D.; Williams, C. B.; Long, T. E. 3D Printing All-Aromatic Polyimides Using Mask-Projection Stereolithography: Processing the Nonprocessable. *Adv. Mater.* **2017**, *29* (31), 1–7.
- (36) Schüller-Ravoo, S.; Zant, E.; Feijen, J.; Grijpma, D. W. Preparation of a Designed

- Poly(trimethylene Carbonate) Microvascular Network by Stereolithography. *Adv. Healthc. Mater.* **2014**, *3* (12), 2004–2011.
- (37) Urayama, K. An Experimentalist's View of the Physics of Rubber Elasticity. *Journal of Polymer Science, Part B: Polymer Physics*. 2006, pp 3440–3444.
- (38) Colby, R. H.; Fetters, L. J.; Graessley, W. W. Melt Viscosity-Molecular Weight Relationship for Linear Polymers. *Macromolecules* **1987**, *20* (9), 2226–2237.
- (39) Baudis, S.; Nehl, F.; Ligon, S. C.; Nigisch, A.; Bergmeister, H.; Bernhard, D.; Stampfl, J.; Liska, R. Elastomeric Degradable Biomaterials by Photopolymerization-Based CAD-CAM for Vascular Tissue Engineering. *Biomed. Mater.* **2011**, *6* (5).
- (40) Baudis, S.; Steyrer, B.; Pulka, T.; Wilhelm, H.; Weigel, G.; Bergmeister, H.; Stampfl, J.; Liska, R. Photopolymerizable Elastomers for Vascular Tissue Regeneration. *Macromol. Symp.* **2010**, *296* (1), 121–126.
- (41) Rolland, J. P.; Chen, K.; Poelma, J.; Goodrich, J.; Pinschmidt, R.; DeSimone, J. M.; Robeson, L. M. Polyurethane Resins Having Multiple Mechanisms of Hardening for Use in Producing Three-Dimensional Objects. US9453142B2, September 2016.
- (42) Velankar, S.; Pazos, J.; Cooper, S. L. High-Performance UV-Curable Urethane Acrylates via Deblocking Chemistry. *J. Appl. Polym. Sci.* **1996**, *62* (9), 1361–1376.
- (43) Yuk, H.; Zhao, X. A New 3D Printing Strategy by Harnessing Deformation, Instability, and Fracture of Viscoelastic Inks. *Adv. Mater.* **2018**, *30* (6), 1704028.
- (44) Bhattacharjee, N.; Urrios, A.; Kang, S.; Folch, A. The Upcoming 3D-Printing Revolution in Microfluidics. *Lab Chip* **2016**, *16* (10), 1720–1742.
- (45) Bosq, N.; Guigo, N.; Persello, J.; Sbirrazzuoli, N. Melt and Glass Crystallization of PDMS and PDMS Silica Nanocomposites. *Phys. Chem. Chem. Phys.* **2014**, *16* (17), 7830–7840.
- (46) Dvornic, P. R.; Mark, J. E. Silicon-Containing Polymers. *Silicon-Containing Polym.* **2000**, No. 1, 185–212.
- (47) Paul, D. R.; Mark, J. E. Fillers for Polysiloxane (“silicone”) Elastomers. *Prog. Polym. Sci.* **2010**, *35* (7), 893–901.
- (48) Kopylov, V. M.; Kostyleva, E. I.; Kostylev, I. M.; Koviazin, A. V. Silica Fillers for Silicone Rubber. *Int. Polym. Sci. Technol.* **2011**, *38* (4), 35–47.
- (49) De Buyl, F. Silicone Sealants and Structural Adhesives. *Int. J. Adhes. Adhes.* **2001**, *21* (5), 411–422.
- (50) Krumpfer, J. W. Chemistry at Silicone - Inorganic Oxide Interfaces. **2012**.
- (51) Moretto, H.-H.; Schulze, M.; Wagner, G. Silicones. *Ullmann's Encycl. Ind. Chem.* **2000**.
- (52) Shit, S. C.; Shah, P. A Review on Silicone Rubber. *Natl. Acad. Sci. Lett.* **2013**, *36* (4), 355–365.
- (53) Ortiz-Acosta, D. *Sylgard? Cure Inhibition Characterization*; 2012.
- (54) Stein, J.; Lewis, L. N.; Gao, Y.; Scott, R. A. In Situ Determination of the Active Catalyst in Hydrosilylation Reactions Using Highly Reactive Pt(0) Catalyst Precursors. *J. Am. Chem. Soc.* **1999**, *121* (15), 3693–3703.
- (55) Métivier, T.; Beyou, E.; Cassagnau, P. Dynamic Crosslinking of Silicone Elastomer: Radical Branching Controlled by Thermo-Oxidation under Shearing.



- Eur. Polym. J.* **2018**, *101* (February), 37–45.
- (56) No Title.
- (57) Weisgraber, T. H.; Metz, T.; Spadaccini, C. M.; Duoss, E. B.; Small, W.; Lenhardt, J. M.; Maxwell, R. S.; Wilson, T. S. A Mechanical Reduced Order Model for Elastomeric 3D Printed Architectures. *J. Mater. Res.* **2018**, *33* (3), 309–316.
- (58) Mannoor, M. S.; Jiang, Z.; James, T.; Kong, Y. L.; Malatesta, K. A.; Soboyejo, W. O.; Verma, N.; Gracias, D. H.; McAlpine, M. C. 3D Printed Bionic Ears. *Nano Lett.* **2013**, *13* (6), 2634–2639.
- (59) Symes, M. D.; Kitson, P. J.; Yan, J.; Richmond, C. J.; Cooper, G. J. T.; Bowman, R. W.; Vilbrandt, T.; Cronin, L. Integrated 3D-Printed Reactionware for Chemical Synthesis and Analysis. *Nat. Chem.* **2012**, *4* (5), 349–354.
- (60) Wehner, M.; Truby, R. L.; Fitzgerald, D. J.; Mosadegh, B.; Whitesides, G. M.; Lewis, J. A.; Wood, R. J. An Integrated Design and Fabrication Strategy for Entirely Soft, Autonomous Robots. *Nature* **2016**, *536* (7617), 451–455.
- (61) Duoss, E. B.; Weisgraber, T. H.; Hearon, K.; Zhu, C.; Small, W.; Metz, T. R.; Vericella, J. J.; Barth, H. D.; Kuntz, J. D.; Maxwell, R. S.; et al. Three-Dimensional Printing of Elastomeric, Cellular Architectures with Negative Stiffness. *Adv. Funct. Mater.* **2014**, *24* (31), 4905–4913.
- (62) Ozbolat, V.; Dey, M.; Ayan, B.; Povilianskas, A.; Demirel, M. C.; Ozbolat, I. T. 3D Printing of PDMS Improves Its Mechanical and Cell Adhesion Properties. *ACS Biomater. Sci. Eng.* **2018**, acsbiomaterials.7b00646.
- (63) Shan, S.; Kang, S. H.; Raney, J. R.; Wang, P.; Fang, L.; Candido, F.; Lewis, J. A.; Bertoldi, K. Multistable Architected Materials for Trapping Elastic Strain Energy. *Adv. Mater.* **2015**, *27* (29), 4296–4301.
- (64) Clausen, A.; Wang, F.; Jensen, J. S.; Sigmund, O.; Lewis, J. A. Topology Optimized Architectures with Programmable Poisson’s Ratio over Large Deformations. *Adv Mater* **2015**, *27* (37), 5523–5527.
- (65) Wu, A. S.; Small, W.; Bryson, T. M.; Cheng, E.; Metz, T. R.; Schulze, S. E.; Duoss, E. B.; Wilson, T. S. 3D Printed Silicones with Shape Memory. *Sci. Rep.* **2017**, *7* (1), 1–6.
- (66) Maiti, A.; Small, W.; Lewicki, J. P.; Weisgraber, T. H.; Duoss, E. B.; Chinn, S. C.; Pearson, M. A.; Spadaccini, C. M.; Maxwell, R. S.; Wilson, T. S. 3D Printed Cellular Solid Outperforms Traditional Stochastic Foam in Long-Term Mechanical Response. *Sci. Rep.* **2016**, *6* (April), 1–9.
- (67) Kolesky, D. B.; Homan, K. A.; Skylar-Scott, M. A.; Lewis, J. A. Three-Dimensional Bioprinting of Thick Vascularized Tissues. *Proc. Natl. Acad. Sci.* **2016**, *113* (12), 3179–3184.
- (68) Kolesky, D. B.; Truby, R. L.; Gladman, A. S.; Busbee, T. A.; Homan, K. A.; Lewis, J. A. 3D Bioprinting of Vascularized, Heterogeneous Cell-Laden Tissue Constructs. *Adv. Mater.* **2014**, *26* (19), 3124–3130.
- (69) Qin, Z.; Compton, B. G.; Lewis, J. A.; Buehler, M. J. Structural Optimization of 3D-Printed Synthetic Spider Webs for High Strength. *Nat. Commun.* **2015**, *6* (May), 1–7.
- (70) Hardin, J. O.; Ober, T. J.; Valentine, A. D.; Lewis, J. A. Microfluidic Printheads for Multimaterial 3D Printing of Viscoelastic Inks. *Adv. Mater.* **2015**, *27* (21),

- 3279–3284.
- (71) Durban, M. M.; Lenhardt, J. M.; Wu, A. S.; Small, W. th; Bryson, T. M.; Perez-Perez, L.; Nguyen, D. T.; Gammon, S.; Smay, J. E.; Duoss, E. B.; et al. Custom 3D Printable Silicones with Tunable Stiffness. *Macromol Rapid Commun* **2017**.
  - (72) Schaffner, M.; Faber, J. A.; Pianegonda, L.; Rühls, P. A.; Coulter, F.; Studart, A. R. 3D Printing of Robotic Soft Actuators with Programmable Bioinspired Architectures. *Nat. Commun.* **2018**, *9* (1).
  - (73) Robinson, S. S.; O'Brien, K. W.; Zhao, H.; Peele, B. N.; Larson, C. M.; Mac Murray, B. C.; Van Meerbeek, I. M.; Dunham, S. N.; Shepherd, R. F. Integrated Soft Sensors and Elastomeric Actuators for Tactile Machines with Kinesthetic Sense. *Extrem. Mech. Lett.* **2015**, *5*, 47–53.
  - (74) Barthel, H.; Rosch, L.; Weis, J. Fumed Silica - Production , Properties , and Applications. **1996**.
  - (75) Lipton, J. I.; Angle, S.; Lipson, H. 3D Printable Wax-Silicone Actuators. **2009**.
  - (76) Lipton, J. I.; Angle, S.; Banai, R. E.; Peretz, E.; Lipson, H. Electrically Actuated Hydraulic Solids. *Adv. Eng. Mater.* **2016**, *18* (10), 1710–1715.
  - (77) Wei, H.; Li, K.; Liu, W. G.; Meng, H.; Zhang, P. X.; Yan, C. Y. 3D Printing of Free-Standing Stretchable Electrodes with Tunable Structure and Stretchability. *Adv. Eng. Mater.* **2017**, *1700341*, 1–6.
  - (78) Guo, S.-Z.; Qiu, K.; Meng, F.; Park, S. H.; McAlpine, M. C. 3D Printed Stretchable Tactile Sensors. *Adv. Mater.* **2017**, *29* (27), 1701218--n/a.
  - (79) Tian, K.; Bae, J.; Bakarich, S. E.; Yang, C.; Gately, R. D.; Spinks, G. M.; in het Panhuis, M.; Suo, Z.; Vlassak, J. J. 3D Printing of Transparent and Conductive Heterogeneous Hydrogel–Elastomer Systems. *Adv. Mater.* **2017**, *29* (10).
  - (80) Muth, J. T.; Vogt, D. M.; Truby, R. L.; Mengüç, Y.; Kolesky, D. B.; Wood, R. J.; Lewis, J. A. Embedded 3D Printing of Strain Sensors within Highly Stretchable Elastomers. *Adv. Mater.* **2014**, *26* (36), 6307–6312.
  - (81) Truby, R. L.; Wehner, M.; Grosskopf, A. K.; Vogt, D. M.; Uzel, S. G. M.; Wood, R. J.; Lewis, J. A. Soft Somatosensitive Actuators via Embedded 3D Printing. *Submitted* **2018**, *1706383*, 1–8.
  - (82) Bhattacharjee, T.; Zehnder, S. M.; Rowe, K. G.; Jain, S.; Nixon, R. M.; Sawyer, W. G.; Angelini, T. E. Writing in the Granular Gel Medium. *Sci. Adv.* **2015**, *1* (8), e1500655–e1500655.
  - (83) Hinton, T. J.; Hudson, A.; Pusch, K.; Lee, A.; Feinberg, A. W. 3D Printing PDMS Elastomer in a Hydrophilic Support Bath via Freeform Reversible Embedding. *ACS Biomater. Sci. Eng.* **2016**, *2* (10), 1781–1786.
  - (84) O'Bryan, C. S.; Bhattacharjee, T.; Hart, S.; Kabb, C. P.; Schulze, K. D.; Chilakala, I.; Sumerlin, B. S.; Sawyer, W. G.; Angelini, T. E. Self-Assembled Micro-Organogels for 3D Printing Silicone Structures. *Sci. Adv.* **2017**, *3* (5), e1602800.
  - (85) Roh, S.; Parekh, D. P.; Bharti, B.; Stoyanov, S. D.; Velev, O. D. 3D Printing by Multiphase Silicone/Water Capillary Inks. *Adv Mater* **2017**, *29* (30).
  - (86) LaFratta, C. N.; Fourkas, J. T.; Baldacchini, T.; Farrer, R. A. Multiphoton Fabrication. *Angew. Chemie - Int. Ed.* **2007**, *46* (33), 6238–6258.
  - (87) Hasegawa, T.; Oishi, K.; Maruo, S. Three-Dimensional Microstructuring of PDMS by Two-Photon Microstereolithography. *2006 IEEE Int. Symp. Micro-Nano Mech. Hum. Sci. MHS* **2006**, 3–6.

- (88) Rekštytė, S.; Malinauskas, M.; Juodkazis, S. Three-Dimensional Laser Micro-Sculpturing of Silicone: Towards Bio-Compatible Scaffolds. *Opt. Express* **2013**, *21* (14), 17028.
- (89) Coenjarts, C. A.; Ober, C. K. Two-Photon Three-Dimensional Microfabrication of Poly(dimethylsiloxane) Elastomers. *Chem. Mater.* **2004**, *16* (26), 5556–5558.
- (90) Femmer, T.; Kuehne, A. J. C.; Wessling, M. Print Your Own Membrane: Direct Rapid Prototyping of Polydimethylsiloxane. *Lab Chip* **2014**, *14* (15), 2610.
- (91) Thrasher, C. J.; Schwartz, J. J.; Boydston, A. J. Modular Elastomer Photoresins for Digital Light Processing Additive Manufacturing. *ACS Appl. Mater. Interfaces* **2017**, *9* (45), 39708–39716.
- (92) Wallin, T. J.; Pikul, J. H.; Bodkhe, S.; Peele, B. N.; Mac Murray, B. C.; Therriault, D.; McEnerney, B. W.; Dillon, R. P.; Giannelis, E. P.; Shepherd, R. F. Click Chemistry Stereolithography for Soft Robots That Self-Heal. *J. Mater. Chem. B* **2017**, *5* (31), 6249–6255.
- (93) Bhattacharjee, N.; Parra-Cabrera, C.; Kim, Y. T.; Kuo, A. P.; Folch, A. Desktop-Stereolithography 3D-Printing of a Poly(dimethylsiloxane)-Based Material with Sylgard-184 Properties. *Adv. Mater.* **2018**, *1800001*, 1800001.
- (94) Jiang, Y.; Wang, Q. Highly-Stretchable 3D-Architected Mechanical Metamaterials. *Sci. Rep.* **2016**, *6* (May), 1–11.
- (95) Liska, R.; Schwager, F.; Maier, C.; Cano-Vives, R.; Stampfl, J. Water-Soluble Photopolymers for Rapid Prototyping of Cellular Materials. *J. Appl. Polym. Sci.* **2005**, *97* (6), 2286–2298.
- (96) Li, T.; Jiang, Y.; Yu, K.; Wang, Q. Stretchable 3D Lattice Conductors. *Soft Matter* **2017**, *13* (42), 7731–7739.
- (97) Femmer, T.; Kuehne, A. J. C.; Torres-Rendon, J.; Walther, A.; Wessling, M. Print Your Membrane: Rapid Prototyping of Complex 3D-PDMS Membranes via a Sacrificial Resist. *J. Memb. Sci.* **2015**, *478*, 12–18.
- (98) Kim, D. S. (Danny); Tai, B. L. Hydrostatic Support-Free Fabrication of Three-Dimensional Soft Structures. *J. Manuf. Process.* **2016**, *24*, 391–396.
- (99) Sturgess, C.; Tuck, C. J.; Ashcroft, I. A.; Wildman, R. D. 3D Reactive Inkjet Printing of Polydimethylsiloxane. *J. Mater. Chem. C* **2017**, *5* (37), 9733–9743.
- (100) McCoul, D.; Rosset, S.; Schlatter, S.; Shea, H. Inkjet 3D Printing of UV and Thermal Cure Silicone Elastomers for Dielectric Elastomer Actuators. *Smart Mater. Struct.* **2017**, *26* (12).
- (101) Reitelshöfer, S.; Göttler, M.; Schmidt, P.; Treffer, P.; Landgraf, M.; Franke, J. Aerosol-Jet-Printing Silicone Layers and Electrodes for Stacked Dielectric Elastomer Actuators in One Processing Device. **2016**, No. April 2016, 97981Y.
- (102) Yilgör, I.; Yilgör, E.; Wilkes, G. L. Critical Parameters in Designing Segmented Polyurethanes and Their Effect on Morphology and Properties: A Comprehensive Review. *Polym. (United Kingdom)* **2015**, *58*, A1–A36.
- (103) Ellson, G.; Carrier, X.; Walton, J.; Mahmood, S. F.; Yang, K.; Salazar, J.; Voit, W. E. Tough Thiourethane Thermoplastics for Fused Filament Fabrication. *J. Appl. Polym. Sci.* **2018**, *135* (6), 1–7.
- (104) Yanagisawa, Y.; Nan, Y.; Okuro, K.; Aida, T. Mechanically Robust, Readily Repairable Polymers via Tailored Noncovalent Cross-Linking. *Science (80-. )*. **2018**, *359* (6371), 72–76.

- (105) Prisacariu, C.; Scortanu, E. Influence of the Type of Chain Extender and Urethane Group Content on the Mechanical Properties of Polyurethane Elastomers with Flexible Hard Segments. *High Perform. Polym.* **2011**, *23* (4), 308–313.
- (106) Saiani, A.; Daunch, W. A.; Verbeke, H.; Leenslag, J.-W.; Higgins, J. S. Origin of Multiple Melting Endotherms in a High Hard Block Content Polyurethane: Effect of Annealing Temperature. *Macromolecules* **2001**, *34* (26), 9059–9068.
- (107) Saiani, A.; Novak, A.; Rodier, L.; Eeckhaut, G.; Leenslag, J. W.; Higgins, J. S. Origin of Multiple Melting Endotherms in a High Hard Block Content Polyurethane: Effect of Annealing Temperature. *Macromolecules* **2007**, *40* (20), 7252–7262.
- (108) Petrović, Z. S.; Ferguson, J. Polyurethane Elastomers. *Progress in Polymer Science*. 1991, pp 695–836.
- (109) Yilgor, I.; Eynur, T.; Bilgin, S.; Yilgor, E.; Wilkes, G. L. Influence of Soft Segment Molecular Weight on the Mechanical Hysteresis and Set Behavior of Silicone-Urea Copolymers with Low Hard Segment Contents. *Polymer (Guildf)*. **2011**, *52* (2), 266–274.
- (110) Yilgor, I.; Eynur, T.; Yilgor, E.; Wilkes, G. L. Contribution of Soft Segment Entanglement on the Tensile Properties of Silicone-Urea Copolymers with Low Hard Segment Contents. *Polymer (Guildf)*. **2009**, *50* (19), 4432–4437.
- (111) Sinh, L. H.; Harri, K.; Marjo, L.; Minna, M.; Luong, N. D.; Jurgen, W.; Torsten, W.; Matthias, S.; Jukka, S. Novel Photo-Curable Polyurethane Resin for Stereolithography. *RSC Adv.* **2016**, *6* (56), 50706–50709.
- (112) Nelson, A. M.; Long, T. E. Synthesis, Properties, and Applications of Ion-Containing Polyurethane Segmented Copolymers. *Macromol. Chem. Phys.* **2014**, *215* (22), 2161–2174.
- (113) Kim, B. K.; Lee, J. C. Waterborne Polyurethanes and Their Properties. *J. Polym. Sci. Part A Polym. Chem.* **1996**, *34* (6), 1095–1104.
- (114) Yilgor, I.; Mather, B. D.; Unal, S.; Yilgor, E.; Long, T. E. Preparation of Segmented, High Molecular Weight, Aliphatic Poly(ether-Urea) Copolymers in Isopropanol. In-Situ FTIR Studies and Polymer Synthesis. *Polymer (Guildf)*. **2004**, *45* (17), 5829–5836.
- (115) Yin, D.; Wang, X.; Yan, Y.; Zhang, R. Preliminary Studies on Peripheral Nerve Regeneration Using a New Polyurethane Conduit. *J. Bioact. Compat. Polym.* **2007**, *22* (2), 143–159.
- (116) Yan, Y.; Hong Wang, X.; Yin, D.; Zhang, R. A New Polyurethane/heparin Vascular Graft for Small-Caliber Vein Repair. *J. Bioact. Compat. Polym.* **2007**, *22* (3), 323–341.
- (117) Xu, W.; Wang, X. H.; Yan, Y. N.; Zhang, R. J. Rapid Prototyping of Polyurethane for the Creation of Vascular Systems. *J. Bioact. Compat. Polym.* **2008**, *23* (2), 103–114.
- (118) Cui, T.; Yan, Y.; Zhang, R.; Liu, L.; Xu, W.; Wang, X. Rapid Prototyping of a Double-Layer Polyurethane-Collagen Conduit for Peripheral Nerve Regeneration. *Tissue Eng Part C Methods* **2009**, *15* (1), 1–9.
- (119) Huang, Y. W.; He, K.; Wang, X. H. Rapid Prototyping of a Hybrid Hierarchical Polyurethane-Cell/hydrogel Construct for Regenerative Medicine. *Mater. Sci. Eng. C-Materials Biol. Appl.* **2013**, *33* (6), 3220–3229.

- (120) Kızıltay, A.; Fernandez, A. M.; Roman, J. S.; Hasirci, V.; Hasirci, N. Lysine Based Poly(ester-Urethane) Films for Tissue Engineering Applications. *J. Biomater. Tissue Eng.* **2012**, *2* (2), 143–153.
- (121) Gogolewski, S.; Gorna, K. Biodegradable Polyurethane Cancellous Bone Graft Substitutes in the Treatment of Iliac Crest Defects. *J. Biomed. Mater. Res. - Part A* **2007**, *80* (1), 94–101.
- (122) Kiziltay, A.; Marcos-Fernandez, A.; San Roman, J.; Sousa, R. A.; Reis, R. L.; Hasirci, V.; Hasirci, N. Poly(ester-Urethane) Scaffolds: Effect of Structure on Properties and Osteogenic Activity of Stem Cells. *J. Tissue Eng. Regen. Med.* **2015**, *9* (8), 930–942.
- (123) Chiono, V.; Mozetic, P.; Boffito, M.; Sartori, S.; Gioffredi, E.; Silvestri, A.; Rainer, A.; Giannitelli, S. M.; Trombetta, M.; Nurzynska, D.; et al. Polyurethane-Based Scaffolds for Myocardial Tissue Engineering. *Interface Focus* **2014**, *4* (1).
- (124) Sartori, S.; Boffito, M.; Serafini, P.; Caporale, A.; Silvestri, A.; Bernardi, E.; Sassi, M. P.; Boccafoschi, F.; Ciardelli, G. Synthesis and Structure-Property Relationship of Polyester-Urethanes and Their Evaluation for the Regeneration of Contractile Tissues. *React. Funct. Polym.* **2013**, *73* (10), 1366–1376.
- (125) Rechichi, A.; Ciardelli, G.; D'Acunto, M.; Vozzi, G.; Giusti, P. Degradable Block Polyurethanes from Nontoxic Building Blocks as Scaffold Materials to Support Cell Growth and Proliferation. *J. Biomed. Mater. Res. - Part A* **2008**, *84* (4), 847–855.
- (126) Hernández-Córdova, R.; Mathew, D. A.; Balint, R.; Carrillo-Escalante, H. J.; Cervantes-Uc, J. M.; Hidalgo-Bastida, L. A.; Hernández-Sánchez, F.; Hernandez-Cordova, R.; Mathew, D. A.; Balint, R.; et al. Indirect Three-Dimensional Printing: A Method for Fabricating Polyurethane-Urea Based Cardiac Scaffolds. *J. Biomed. Mater. Res. Part A* **2016**, *104* (8), 1912–1921.
- (127) May-Hernández, L.; Hernández-Sánchez, F.; Gomez-Ribelles, J. L.; Sabater-i Serra, R. Segmented Poly(urethane-Urea) Elastomers Based on Polycaprolactone: Structure and Properties. *J. Appl. Polym. Sci.* **2011**, *119* (4), 2093–2104.
- (128) Zhang, C.; Wen, X.; Vyavahare, N. R.; Boland, T. Synthesis and Characterization of Biodegradable Elastomeric Polyurethane Scaffolds Fabricated by the Inkjet Technique. *Biomaterials* **2008**, *29* (28), 3781–3791.
- (129) Boland, T.; Xu, T.; Damon, B.; Cui, X. Application of Inkjet Printing to Tissue Engineering. *Biotechnol. J.* **2006**, *1* (9), 910–917.
- (130) Samusjew, A.; Kratzer, M.; Moser, A.; Teichert, C.; Krawczyk, K. K.; Griesser, T. Inkjet Printing of Soft, Stretchable Optical Waveguides through the Photopolymerization of High-Profile Linear Patterns. *ACS Appl. Mater. Interfaces* **2017**, *9* (5), 4941–4947.
- (131) Zhou, X.; Li, Y.; Fang, C.; Li, S.; Cheng, Y.; Lei, W.; Meng, X. Recent Advances in Synthesis of Waterborne Polyurethane and Their Application in Water-Based Ink: A Review. *J. Mater. Sci. Technol.* **2015**, *31* (7), 708–722.
- (132) Hunter, R. J. *Zeta Potential in Colloid Science: Principles and Applications*; 1981; Vol. 8.
- (133) Lee, J. H.; Hwang, K. S.; Jang, S. P.; Lee, B. H.; Kim, J. H.; Choi, S. U. S.; Choi, C. J. Effective Viscosities and Thermal Conductivities of Aqueous Nanofluids Containing Low Volume Concentrations of Al<sub>2</sub>O<sub>3</sub> Nanoparticles. *Int. J. Heat*

- Mass Transf.* **2008**, *51* (11–12), 2651–2656.
- (134) Mondschein, R. J.; Kanitkar, A.; Williams, C. B.; Verbridge, S. S.; Long, T. E. Polymer Structure-Property Requirements for Stereolithographic 3D Printing of Soft Tissue Engineering Scaffolds. *Biomaterials* **2017**, *140*, 170–188.
- (135) Pekkanen, A. M.; Mondschein, R. J.; Williams, C. B.; Long, T. E. 3D Printing Polymers with Supramolecular Functionality for Biological Applications. *Biomacromolecules* **2017**, *18* (9), 2669–2687.
- (136) Chia, H. N.; Wu, B. M. Recent Advances in 3D Printing of Biomaterials. *J. Biol. Eng.* **2015**, *9* (1), 1–14.
- (137) Billiet, T.; Vandenhoute, M.; Schelfhout, J.; Van Vlierberghe, S.; Dubruel, P. A Review of Trends and Limitations in Hydrogel-Rapid Prototyping for Tissue Engineering. *Biomaterials* **2012**, *33* (26), 6020–6041.
- (138) Hsu, S.; Hung, K.-C.; Lin, Y.-Y.; Su, C.-H.; Yeh, H.-Y.; Jeng, U.-S.; Lu, C.-Y.; Dai, S. A.; Fu, W.-E.; Lin, J.-C. Water-Based Synthesis and Processing of Novel Biodegradable Elastomers for Medical Applications. *J. Mater. Chem. B* **2014**, *2* (31), 5083–5092.
- (139) Hsieh, F. Y.; Lin, H. H.; Hsu, S. hui. 3D Bioprinting of Neural Stem Cell-Laden Thermoresponsive Biodegradable Polyurethane Hydrogel and Potential in Central Nervous System Repair. *Biomaterials* **2015**, *71*, 48–57.
- (140) Tsai, Y. C.; Li, S. M.; Hu, S. G.; Chang, W. C.; Jeng, U. S.; Hsu, S. H. Synthesis of Thermoresponsive Amphiphilic Polyurethane Gel as a New Cell Printing Material near Body Temperature. *ACS Appl. Mater. Interfaces* **2015**, *7* (50), 27613–27623.
- (141) Ou, C. W.; Su, C. H.; Jeng, U. S.; Hsu, S. H. Characterization of Biodegradable Polyurethane Nanoparticles and Thermally Induced Self-Assembly in Water Dispersion. *ACS Appl. Mater. Interfaces* **2014**, *6* (8), 5685–5694.
- (142) Hung, K. C.; Tseng, C. S.; Hsu, S. H. Synthesis and 3D Printing of Biodegradable Polyurethane Elastomer by a Water-Based Process for Cartilage Tissue Engineering Applications. *Adv. Healthc. Mater.* **2014**, *3* (10), 1578–1587.
- (143) Hung, K. C.; Tseng, C. S.; Dai, L. G.; Hsu, S. H. Water-Based Polyurethane 3D Printed Scaffolds with Controlled Release Function for Customized Cartilage Tissue Engineering. *Biomaterials* **2016**, *83*, 156–168.
- (144) Lu, Z.; Jiang, X.; Zuo, X.; Feng, L. Improvement of Cytocompatibility of 3D-Printing Resins for Endothelial Cell Adhesion. *RSC Adv.* **2016**, *6* (104), 102381–102388.
- (145) Jiang, X.; Li, J.; Ding, M.; Tan, H.; Ling, Q.; Zhong, Y.; Fu, Q. Synthesis and Degradation of Nontoxic Biodegradable Waterborne Polyurethanes Elastomer with Poly( $\epsilon$ -Caprolactone) and Poly(ethylene Glycol) as Soft Segment. *Eur. Polym. J.* **2007**, *43* (5), 1838–1846.
- (146) van den Berg, A. M. J.; Smith, P. J.; Perelaer, J.; Schrof, W.; Koltzenburg, S.; Schubert, U. S. Inkjet Printing of Polyurethane Colloidal Suspensions. *Soft Matter* **2007**, *3* (2), 238–243.
- (147) Patel, D. K.; Sakhaei, A. H.; Layani, M.; Zhang, B.; Ge, Q.; Magdassi, S. Highly Stretchable and UV Curable Elastomers for Digital Light Processing Based 3D Printing. *Adv. Mater.* **2017**, *29* (15).
- (148) Cramer, N. B.; Bowman, C. N. Kinetics of Thiol-Ene and Thiol-Acrylate

- Photopolymerizations with Real-Time Fourier Transform Infrared. *J. Polym. Sci. Part A Polym. Chem.* **2001**, *39* (19), 3311–3319.
- (149) Ligon, S. C.; Husár, B.; Wutzel, H.; Holman, R.; Liska, R. Strategies to Reduce Oxygen Inhibition in Photoinduced Polymerization. *Chem. Rev.* **2014**, *114* (1), 577–589.
- (150) Stampfl, J.; Pettermann, H. E.; Liska, R. Bioinspired Cellular Structures: Additive Manufacturing and Mechanical Properties. In *Biomimetics -- Materials, Structures and Processes*; 2011; pp 105–123.
- (151) Stampfl, J.; Liska, R. New Materials for Rapid Prototyping Applications. *Macromol. Chem. Phys.* **2005**, *206* (13), 1253–1256.
- (152) Liska, R.; Schuster, M.; Inführ, R.; Turecek, C.; Fritscher, C.; Seidl, B.; Schmidt, V.; Kuna, L.; Haase, A.; Varga, F.; et al. Photopolymers for Rapid Prototyping. *J. Coatings Technol. Res.* **2007**, *4* (4), 505–510.
- (153) Stampfl, J.; Liska, R. Polymerizable Hydrogels for Rapid Prototyping: Chemistry, Photolithography, and Mechanical Properties. In *Stereolithography: Materials, Processes and Applications*; 2011; pp 161–182.
- (154) Baudis, S.; Heller, C.; Liska, R.; Stampfl, J.; Bergmeister, H.; Weigel, G. (Meth)acrylate-Based Photoelastomers as Tailored Biomaterials for Artificial Vascular Grafts. *J. Polym. Sci. Part A Polym. Chem.* **2009**, *47* (10), 2664–2676.
- (155) Baudis, S.; Pulka, T.; Steyrer, B.; Wilhelm, H.; Weigel, G.; Bergmeister, H.; Stampfl, J.; Liska, R. 3D-Printing of Urethane-Based Photoelastomers for Vascular Tissue Regeneration. *MRS Proc.* **2011**, *1239*.
- (156) Petrochenko, P. E.; Torgersen, J.; Gruber, P.; Hicks, L. A.; Zheng, J.; Kumar, G.; Narayan, R. J.; Goering, P. L.; Liska, R.; Stampfl, J.; et al. Laser 3D Printing with Sub-Microscale Resolution of Porous Elastomeric Scaffolds for Supporting Human Bone Stem Cells. *Adv. Healthc. Mater.* **2015**, *4* (5), 739–747.
- (157) Pyo, S.-H.; Wang, P.; Hwang, H. H.; Zhu, W.; Warner, J.; Chen, S. Continuous Optical 3D Printing of Green Aliphatic Polyurethanes. *ACS Appl. Mater. Interfaces* **2017**, *9* (1), 836–844.
- (158) Lomölder, R.; Plogmann, F.; Speier, P. Selectivity of Isophorone Diisocyanate in the Urethane Reaction Influence of Temperature, Catalysis, and Reaction Partners. *J. Coatings Technol.* **1997**, *69* (868), 51–57.
- (159) Huang, S. L.; Lai, J. Y. On the Gas Permeability of Hydroxyl Terminated Polybutadiene Based Polyurethane Membranes. *J. Memb. Sci.* **1995**, *105* (1–2), 137–145.
- (160) Wicks, D. A.; Wicks, Z. W. Blocked Isocyanates III: Part A. Mechanisms and Chemistry. *Prog. Org. Coatings* **1999**, *36* (3), 148–172.
- (161) Johns, A. S.; Bain, C. D. Ink-Jet Printing of High-Molecular-Weight Polymers in Oil-in-Water Emulsions. *ACS Appl. Mater. Interfaces* **2017**, *9* (27), 22918–22926.
- (162) Hsiao, L. C.; Badruddoza, A. Z. M.; Cheng, L.-C.; Doyle, P. S. 3D Printing of Self-Assembling Thermoresponsive Nanoemulsions into Hierarchical Mesostuctured Hydrogels. *Soft Matter* **2017**, *13* (5), 921–929.
- (163) Zentel, R. Liquid Crystalline Elastomers. *Adv. Mater.* **1989**, *1* (10), 321–329.
- (164) Ohm, C.; Brehmer, M.; Zentel, R. Liquid Crystalline Elastomers as Actuators and Sensors. *Adv. Mater.* **2010**, *22* (31), 3366–3387.
- (165) White, T. J.; Broer, D. J. Programmable and Adaptive Mechanics with Liquid

- Crystal Polymer Networks and Elastomers. *Nat. Mater.* **2015**, *14* (11), 1087–1098.
- (166) Yuan, C.; Roach, D. J.; Dunn, C. K.; Mu, Q.; Kuang, X.; Yakacki, C. M.; Wang, T. J.; Yu, K.; Qi, H. J. 3D Printed Reversible Shape Changing Soft Actuators Assisted by Liquid Crystal Elastomers. *Soft Matter* **2017**, *13*, 5558–5568.
- (167) White, T.; Verduzco, R. Liquid Crystal Elastomers: Emerging Trends and Applications. *Soft Matter* **2017**, *13* (24), 4320–4320.
- (168) Ambulo, C. P.; Burroughs, J. J.; Boothby, J. M.; Kim, H.; Shankar, M. R.; Ware, T. H. Four-Dimensional Printing of Liquid Crystal Elastomers. *ACS Appl. Mater. Interfaces* **2017**, *9* (42), 37332–37339.
- (169) Ware, T. H.; McConney, M. E.; Wie, J. J.; Tondiglia, V. P.; White, T. J. Voxellated Liquid Crystal Elastomers. *Science (80-. )*. **2015**, *347* (6225), 982–984.
- (170) Lopez-Valdeolivas, M.; Liu, D.; Broer, D. J.; Sanchez-Somolinos, C.; López-Valdeolivas, M.; Liu, D.; Broer, D. J.; Sánchez-Somolinos, C. 4D Printed Actuators with Soft-Robotic Functions. *Macromol. Rapid Commun.* **2017**, *1700710*, 3–9.
- (171) Kotikian, A.; Truby, R. L.; Boley, J. W.; White, T. J.; Lewis, J. A. 3D Printed Liquid Crystal Elastomer Actuators with Spatially Programmed Nematic Order. *Adv. Mater.* **2017**, *Accepted*, 1–6.
- (172) Hu, X.; Kang, H.; Li, Y.; Geng, Y.; Wang, R.; Zhang, L. Preparation, Morphology and Superior Performances of Biobased Thermoplastic Elastomer by in Situ Dynamical Vulcanization for 3D-Printed Materials. *Polym. (United Kingdom)* **2017**, *108*, 11–20.
- (173) Gao, Y.; Li, Y.; Hu, X.; Wu, W.; Wang, Z.; Wang, R.; Zhang, L. Preparation and Properties of Novel Thermoplastic Vulcanizate Based on Bio-Based Polyester/polylactic Acid, and Its Application in 3D Printing. *Polymers (Basel)*. **2017**, *9* (12).
- (174) Hu, X.; Kang, H.; Li, Y.; Li, M.; Wang, R.; Xu, R.; Qiao, H.; Zhang, L. Direct Copolycondensation of Biobased Elastomers Based on Lactic Acid with Tunable and Versatile Properties. *Polym. Chem.* **2015**, *6* (47), 8112–8123.
- (175) Yeh, Y. C.; Highley, C. B.; Ouyang, L.; Burdick, J. A. 3D Printing of Photocurable Poly(glycerol Sebacate) Elastomers. *Biofabrication* **2016**, *8* (4).
- (176) Güney, A.; Malda, J.; Dhert, W. J. A.; Grijpma, D. W. Triblock Copolymers Based on  $\epsilon$ -Caprolactone and Trimethylene Carbonate for the 3D Printing of Tissue Engineering Scaffolds. *Int. J. Artif. Organs* **2017**, *40* (4), 176–184.
- (177) Ware, H. O. T.; Farsheed, A. C.; van Lith, R.; Baker, E.; Ameer, G.; Sun, C. Process Development for High-Resolution 3D-Printing of Bioresorbable Vascular Stents. In *Proceedings of SPIE*; 2017; p 101150N.
- (178) Yang, J.; Webb, A. R.; Pickerill, S. J.; Hageman, G.; Ameer, G. A. Synthesis and Evaluation of Poly(diols Citrate) Biodegradable Elastomers. *Biomaterials* **2006**, *27* (9), 1889–1898.
- (179) van Lith, R.; Baker, E.; Ware, H.; Yang, J.; Farsheed, A. C.; Sun, C.; Ameer, G. 3D-Printing Strong High-Resolution Antioxidant Bioresorbable Vascular Stents. *Adv. Mater. Technol.* **2016**, *1* (9), 1600138.
- (180) Yang, J.; Webb, A. R.; Ameer, G. A. Novel Citric Acid-Based Biodegradable Elastomers for Tissue Engineering. *Adv. Mater.* **2004**, *16* (6), 511–516.



## Chapter 3: **Functional Siloxanes with Photo-Activated, Simultaneous Chain Extension and Crosslinking for Lithography-Based 3D Printing**

(Published in *Polymer* **2018**, online ASAP. doi: 10.1016/j.polymer.2018.02.056)

Justin M. Serrine, Viswanath Meenakshisundaram,<sup>a</sup> Nicholas G. Moon, Philip J. Scott, Ryan J. Mondschein, Tobin F. Weiseman, Christopher B. Williams,<sup>a</sup> and Timothy E. Long\*

*Department of Chemistry, <sup>a</sup> Department of Mechanical Engineering  
Macromolecules Innovation Institute  
Virginia Tech, Blacksburg, VA 24061, USA*

### **3.1 Abstract**

A novel, poly(dimethyl siloxane)-based photopolymer that exhibits simultaneous linear chain extension and crosslinking was suitable for vat photopolymerization additive manufacturing. Photopolymer compositions consisted of dithiol and diacrylate functional poly(dimethyl siloxane) oligomers, where simultaneous thiol-ene coupling and free radical polymerization provided for linear chain extension and crosslinking, respectively. Compositions possessed low viscosity before printing and the modulus and tensile strain at break of a photocured, higher molecular weight precursor after printing. Photorheology and soxhlet extraction demonstrated highly efficient photocuring, revealing a calculated molecular weight between crosslinks of 12,600 g/mol and gel fractions in excess of 90 % while employing significantly lower molecular weight precursors (i.e. < 5,300 g/mol). These photocured objects demonstrated a 2x increase in tensile strain at break as compared to a photocured 5,300 g/mol PDMS diacrylamide alone. These results are broadly applicable to the advanced manufacturing of objects requiring high elongation at break.

### **3.2 Introduction**

Additive manufacturing (AM) or 3D printing (3DP) enables the creation products featuring complex geometries that are not attainable with traditional manufacturing

methods, such as injection molding and machining.<sup>1</sup> Vat photopolymerization (VPP), also referred to as stereolithography, is widely considered the most accurate and highest-resolution AM technique.<sup>2</sup> VPP creates solid objects upon irradiation of an ultraviolet (UV) light-activated, liquid polymer, or photopolymer, with patterned light and in a layer-by-layer fashion. This layerwise, selective curing converts the photopolymer into a three-dimensional (3D), insoluble network. Photopolymers typically contain UV-reactive functional groups that either excite directly upon UV irradiation at appropriate wavelengths, or more commonly, a low concentration of photoinitiator forms a propagating intermediate upon UV irradiation. Photoinitiators for AM are selected based on the particular printing conditions, generate a variety of active centers including free radicals, cations, or bases (anions), and are generally identical to those employed in polymer synthesis.<sup>3</sup> After early AM discoveries in the 1980s, the recent expiration of several key patents<sup>4</sup> catalyzed a renaissance of fundamental and applied research, as well as the founding of several AM-based startup companies focused both on production-ready capabilities and inexpensive, consumer-grade printers. AM enjoys applications in self-healing materials,<sup>5,6</sup> biomaterials,<sup>7-19</sup> high-strength metamaterials,<sup>20,21</sup> microfluidics,<sup>22-24</sup> and AM-derived ceramics.<sup>25</sup>

VPP enjoys an extensive catalog of commercially available photopolymers.<sup>6,26,27</sup> Originally designed as UV-curable coatings, many of these photopolymers produce high modulus and often mechanically inferior objects as a result of high crosslink density due to low molecular weight (MW), often monomeric, precursors. Though appropriate for rapid prototyping, objects printed from these photopolymers suffer from brittleness, low strain at break, and sensitivity to light and humidity.<sup>25,27</sup> According to the 2016 Wohler's report

(Appendix E: Material Properties), only 7 % of commercially available photopolymers for vat photopolymerization possess a photocured tensile modulus of  $\leq 20$  MPa.<sup>27</sup> A low modulus is one characteristic of elastomers or rubbers, which enjoy a wide variety of applications including tires, athletic wear, seals, and damping elements. Most elastomers possess a low tensile modulus and high tensile strain at break (i.e.  $> 100$  %).<sup>6,28</sup> An examination of rubber elasticity theory and photopolymer viscosity requirements offers some explanation for this disproportionately small offering of commercially available photopolymers for the production of elastomeric objects.

As shown in **Equation 1**, there is an inverse relationship between molecular weight between crosslinks ( $M_c$ ), or the statistical average distance between network junctions, and plateau shear modulus as measured in the gel state ( $G_N^0$ ).<sup>29</sup> These two parameters are related by  $\rho$  (density),  $R$  (universal gas constant), and  $T$  (temperature).

$$G_N^0 = \frac{\rho RT}{M_c} \quad (1)$$

The affine network model captures this theory of rubber elasticity and states that the macroscopic network deformation is equal to the sum of the deformations of the individual network strands.<sup>29</sup> The elastic restoring force upon macroscopic deformation/elongation is entropic in nature and results in these elongated network strands regaining degrees of freedom and their Gaussian distribution of random coil conformations. In the context of vat photopolymerization, a photocured elastomeric object with high  $M_c$  typically requires a high MW photopolymer, ensuring long polymer chains that can uncoil upon loading. These higher MW precursors also provide a deleterious, concomitant increase in pre-cure viscosity, as zero-shear viscosity ( $\eta_0$ )  $\propto MW^1$  below the entanglement molecular weight ( $M_e$ ) and  $\eta_0 \propto MW^{3.4}$  above  $M_e$  for non-associating, linear polymers.<sup>30</sup> Hence, a high

viscosity photopolymer will require a comparatively long time to recoat a previously printed layer, versus a low viscosity photopolymer, upon the build stage lowering one-layer thickness at a time into the photopolymer vat. A practical upper viscosity target for photopolymer processing with VPP is 5 Pa·s.<sup>26</sup> Knowledge of MW and MW distribution is highly relevant to photopolymer processing in VPP. In previous work, a variety of techniques including supercritical fluid chromatography and size exclusion chromatography with appropriately sized columns facilitated determination of MW and MW distribution as relevant to the AM process.<sup>16,18,31,32</sup>

In top-down vat photopolymerization, processing of higher molecular weight photopolymers is facilitated in many ways. First, a ‘recoat blade’ smooths the photopolymer surface to ensure subsequent printed layers are uniformly flat.<sup>2</sup> The ‘recoat blade’ is held one-layer thickness above the previously printed layer to ensure the uncured photopolymer is uniform prior to UV irradiation. Second, reactive diluents (e.g. monomers) are admixed and reduce the viscosity of higher MW precursors.<sup>33</sup> However, these monomers are often classified as volatile and toxic, and the comonomer alters properties of the printed network. Third, unreactive diluents (e.g. solvents) reduce photopolymer viscosity but do not participate in the crosslinking reaction. Similar issues of volatility and toxicity exist, while solvent removal from the printed objects remains challenging.<sup>34</sup> Finally, heating of the vat remains the simplest method, but promotes thermal polymerization, especially for acrylate- and methacrylate-containing systems.<sup>35</sup>

The thiol-ene reaction is classified as a click reaction due to rapid rates and high yield, absence of by-products, and insensitivity to water or oxygen, and occurs under mild reaction conditions.<sup>36</sup> It also can be self-initiated with 254 nm UV irradiation,

demonstrating a particular utility for photoinitiator-free systems.<sup>36</sup> Due to step-growth polymerization kinetics, systems employing thiol-ene chemistry for crosslinking produce more homogenous networks compared to conventional free radical homopolymerization (FRP), as higher overall conversion is reached prior to vitrification.<sup>37</sup> Conversely, FRP is widely employed for network formation in vat photopolymerization, due to the fast polymerization rates and low cost of acrylates and methacrylates. However, unlike the thiol-ene reaction, FRP proceeds in a chain-growth manner, often producing highly heterogeneous networks and significant polymerization shrinkage. Bowman, *et al.* investigated the photocuring kinetics of combinations of thiols and acrylates, finding the acrylate propagation constant to be ~1.5 times the rate for hydrogen abstraction from the thiol.<sup>38</sup> This was due to an increase in chain transfer events as each individual polyacrylate chain possesses a lower degree of polymerization than would normally occur in the absence of thiols.<sup>37,38</sup>

Thiol-ene chemistry enjoys abundant use in vat photopolymerization applications.<sup>23,24,39,40</sup> Furthermore, Cramer and Bowman demonstrate that small additions of monomeric dithiols, e.g. 1,6-hexanedithiol, to low MW diacrylates, e.g. 200 g/mol poly(ethylene glycol) (PEG) diacrylate, enable networks with highly tunable glass transition temperatures and plateau moduli.<sup>38</sup> However, to the best of our knowledge, this strategy remains unprecedented for polymeric systems or vat photopolymerization. In this work, a polymeric system that employs simultaneous MW growth via the radical-mediated, step-growth thiol-ene reaction and FRP via acrylamide homopolymerization is applied to a VPP AM process. This system achieves low viscosity before printing, through use of relatively low MW precursors, and achieves relatively high  $M_c$  after photocuring. This

approach leverages the extremely low glass transition temperature ( $-123\text{ }^{\circ}\text{C}$ )<sup>41,42</sup> and nonpolar nature of poly(dimethylsiloxane)s and avoids the use of reactive diluents, heat, and solvent (beyond a low level of solvent that is required to dissolve a photoinitiator, e.g. 1 wt %, oligomer basis). Fast gelation times ( $< 5\text{ s}$ ) and high gel fractions ( $> 90\%$ ) are confirmed. Finally, mechanical properties of the photocured films and 3D-printed objects are comparable to photocured, higher MW PDMS telechelic acrylamide.

### 3.3 Materials & Methods

#### 3.3.1 Materials

2,2-Dimethoxy-2-phenylacetophenone (DMPA, 99 %), diphenyl(2,4,6-trimethylbenzoyl)phosphine oxide (TPO, 97 %), 3-mercaptopropionic acid ( $\geq 99\%$ ), acryloyl chloride, ( $\geq 97\%$ ), potassium hydroxide solution (1N in water), *p*-toluenesulfonic acid monohydrate (ACS grade,  $\geq 98.5\%$ ), and magnesium sulfate ( $\geq 98.0\%$ ) were purchased from Sigma Aldrich and used as received. Bis(3-aminopropyl)-terminated poly(dimethyl siloxane) (PDMS-NH<sub>2</sub>) was purchased from Sigma Aldrich ( $M_n \sim 2,500$  and  $\sim 27,000\text{ g/mol}$ ), Gelest (DMS-A12, DMS-A15, and DMS-A21), and donated by Wacker Chemie (Wacker Fluid NH130D). Bis(hydroxyalkyl)-terminated PDMS was purchased from Gelest (DMS-C15 and DMS-C16) and Sigma Aldrich (reported  $M_n \sim 5,600\text{ g/mol}$ ). Vinyl-terminated PDMS was purchased from Gelest (DMS-V21). All PDMS precursors were dried at  $100\text{ }^{\circ}\text{C}$  under reduced pressure for 18 h before further modification in order to remove cyclics. Chloroform-d ( $\text{CDCl}_3$ , 99.8 %) and benzene-d<sub>6</sub> ( $\text{C}_6\text{D}_6$ , 99.5 %) were purchased from Cambridge Isotope Laboratories, Inc. and used as received. Chloroform, tetrahydrofuran, dichloromethane (DCM), and toluene were purchased from Fisher Scientific (all HPLC grade) and used as received.

### 3.3.2 Synthesis of acrylamide-terminated poly(dimethyl siloxane) (PDMS-AA)

A typical synthesis proceeded according to standard Schotten-Baumann conditions.<sup>43</sup> Proton nuclear magnetic resonance (<sup>1</sup>H NMR) spectroscopy in C<sub>6</sub>D<sub>6</sub> enabled determination of actual PDMS-NH<sub>2</sub> oligomer MW after vacuum stripping of cyclics. PDMS-NH<sub>2</sub> (Gelest DMS-A21, 61.89 g, 11.33 mmol) was added to a 500-mL, 3-necked, round-bottomed flask equipped with a glass stir rod and Teflon<sup>®</sup> paddle, condenser, and addition funnel. After dissolving PDMS-NH<sub>2</sub> in DCM (200 mL), 200 mL of aqueous 1 N potassium hydroxide solution was added to the round-bottomed flask. DCM (30 mL) was added to the addition funnel, which was subsequently sealed with a rubber septum and copper wire. The reaction setup was placed in an ice water bath and purged for 30 min. Acryloyl chloride (2.29 mL, 28.32 mmol) was syringed into the addition funnel and the resulting mixture of DCM and acryloyl chloride was subsequently added dropwise over the course of 15 min with vigorous stirring. The reaction stirred for 24 h while the ice bath slowly warmed to room temperature. After stirring ceased, the reaction phase separated, and the organic phase was dried over MgSO<sub>4</sub>. DCM was removed with a rotary evaporator, and the polymer was dried at 50 °C under reduced pressure for 18 h. Isolated yield was 56.14 g (88 %). Nomenclature for these oligomers includes both MW and endgroup identification. For example, PDMS5.3k-AA represents a 5,300 g/mol PDMS diacrylamide. Products include PDMS1.8k-AA, PDMS3.2k-AA, PDMS5.3k-AA, PDMS5.5k-AA, PDMS11.7k-AA, and PDMS30.6k-AA. Polymer chemical structure and percent acrylamide termination was verified with <sup>1</sup>H NMR spectroscopy in CDCl<sub>3</sub> and is shown in **Figure 3.6**. Percent acrylamide termination ranged from 91 % to 99 %.

### 3.3.3 Synthesis of thiol-terminated poly(dimethyl siloxane) (PDMS-SH)

A typical synthesis proceeded according to standard Fisher esterification conditions.  $^1\text{H}$  NMR spectroscopy in  $\text{C}_6\text{D}_6$  enabled determination of actual PDMS-OH oligomer MWs after vacuum stripping of cyclics. Bis(hydroxyalkyl)-terminated PDMS (Gelest DMS-C15, 75.44 g, 74.92 mmol), 3-mercaptopropionic acid (24.0216, 226.32 mmol), *p*-toluenesulfonic acid (0.7175 g, 3.77), and toluene (150 mL) were added to a 500-mL, 2-necked, round-bottomed flask equipped with a Dean-Stark apparatus, magnetic stir bar, and rubber septum. The reaction was purged with nitrogen for 20 min and subsequently heated at 110 °C for 24 h. After cooling, the reaction mixture was washed with aqueous sodium bicarbonate (3 x 200 mL), aqueous brine (2 x 200 mL), and dried over sodium sulfate. Toluene was removed and the resulting viscous liquid was dried at 50 °C under reduced pressure for 18 h. Isolated yield was 79 %. Nomenclature for these oligomers includes both MW and endgroup identification. For example, PDMS5.1k-SH represents a 5,100 g/mol PDMS dithiol. Products included PDMS1.2k-SH and PDMS5.1k-SH. Polymer chemical structure and percent thiol termination was verified with  $^1\text{H}$  NMR spectroscopy in  $\text{CDCl}_3$  and is shown in **Figure 3.7**. Percent thiol termination ranged from 97 % to 100 %.

### 3.3.4 Preparation of samples for photorheology

Various molar ratios of PDMS-SH and PDMS-AA, or neat PDMS-AA at various MWs, totaling 2.00 g, were weighed into a 2-dram scintillation vial, and all samples for a single study were prepared at once. Separately, DMPA (1.00 g) and chloroform (5.00 g) were weighed into a 6-dram scintillation vial and mixed with a vortexer for 10 s; this solution was designated the photoinitiator stock solution. Finally, a 10-, 25-, or 100-microliter



syringe ensured the proper amount of photoinitiator stock solution to control DMPA loadings at 0.5 wt %. Finally, photoinitiated mixtures were mixed with a vortexer for 60 s until homogeneous and subsequently allowed to stand for 2 h to ensure the absence of bubbles.

### **3.3.5 Preparation of samples for Vat Photopolymerization (VPP) Additive Manufacturing (AM)**

Preparation of samples for VPP was identical to photorheology studies except TPO was used as a photoinitiator at 0.5 wt % due to spectral differences in the printer light source (BlueWave® 75 UV spot curing lamp [Dymax 40078])

### **3.3.6 Analytical methods**

All  $^1\text{H}$  NMR spectroscopy was performed on an Agilent U4-DD2 500 MHz NMR spectrometer with a 96 sample robot. A TA Instruments DHR-2 rheometer with concentric cylinder geometry or 40 mm parallel plate geometry was used to determine the viscosities of PDMS-AA, PDMS-SH, and various mixtures prior to photocuring. All viscosity values were obtained at 25 °C. Photorheology was conducted on a DHR-2 rheometer with Smart Swap™ UV geometry, 20 mm quartz lower parallel plate, 20 mm aluminum upper parallel plate, and an Omnicure S2000 high-pressure mercury light source with 320-500 nm filter installed. Samples were irradiated at 8.5 mW/cm<sup>2</sup> for 240 s, after confirming UV light output with a Silverline radiometer and 20 mm sensor attachment for the quartz parallel plate. Data was gathered with a 500 μm gap at 0.3 % strain, 4 Hz, in the "Fast Sampling" mode, enabling a sampling frequency of 8 s<sup>-1</sup>, with UV light turning on after 30 s of oscillatory measurement. The rheometer was set to maintain an axial force of 0 N by making slight adjustments in gap thickness. Before irradiation, samples were purged for 3

min with nitrogen using a UV guard equipped with gas inlet and outlet ports, ensuring proper removal of air/oxygen before UV irradiation. Select PDMS-AA samples were analyzed in triplicate to determine reproducibility for this technique. Shear storage plateau moduli ( $G_N^0$ ) were determined as an average of the last 30 s shear storage moduli ( $G'$ ) values.  $G'/G''$  crossover timepoints, where loss modulus is  $G''$ , were determined using the "modulus crossover" function within the TA Instruments TRIOS software. Gel fractions were determined upon soxhlet extraction in THF of photocured discs produced with the photorheology method. Soxhlet samples were dried for 18 h under reduced pressure at 50 °C, weighed, extracted for 6 h in THF under reflux, dried (18 h, 50 °C, under reduced pressure), and weighed again. Reproducibility for the soxhlet extraction was determined in triplicate for select samples. Tensile testing was performed using an Instron<sup>®</sup> 4411 Universal Testing instrument on 3D-printed ASTM D638-V dogbones. A cross-head speed of 5 mm/min at 25 °C was employed. The reported tensile strength represents the maximum tensile strength obtained. Similarly, the reported strain at break represents the maximum strain at break achieved. All values represent averages of 5 specimens.

### **3.3.7 Vat Photopolymerization**

All vat photopolymerization method information, including methods for generating the photopolymer working curve, is provided elsewhere<sup>32</sup> and in the electronic support material.

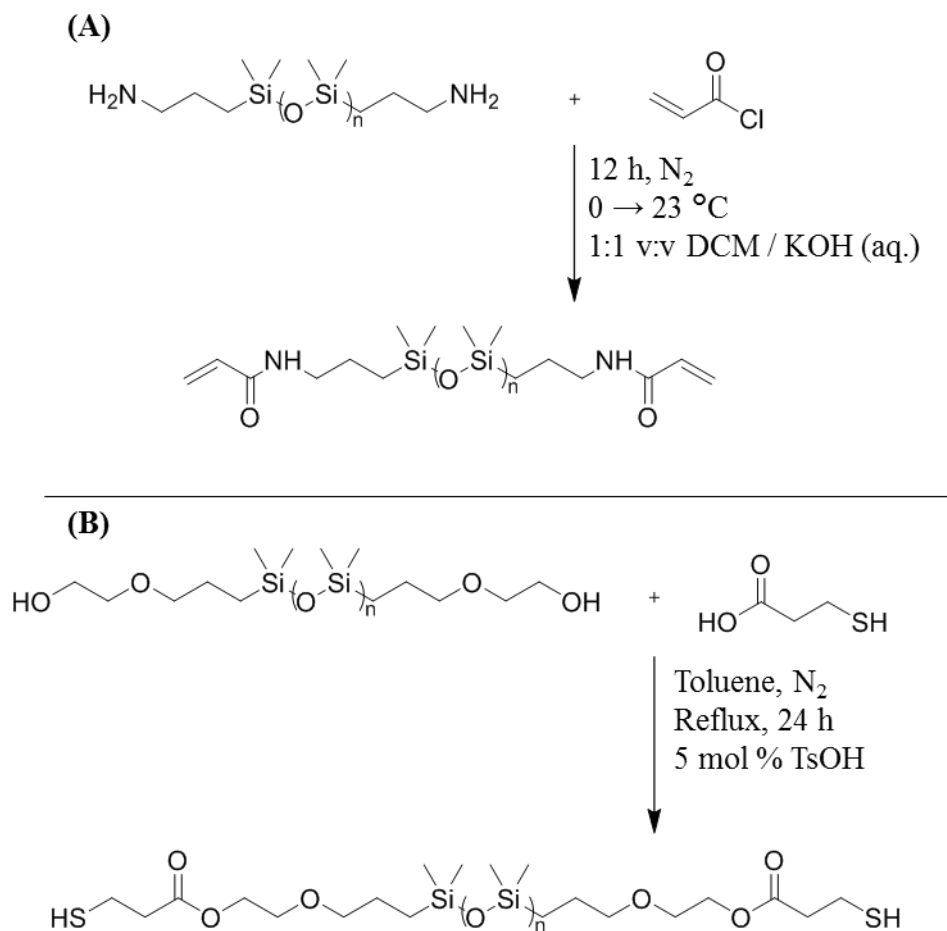
## **3.4 Results and Discussion**

This work demonstrates the synthesis, processing, and characterization of a novel, low viscosity photopolymer for vat photopolymerization that possesses the lower modulus of a photocured, higher MW precursor. This approach employs a photopolymer that contains thiol- and acrylamide-functional telechelic oligomers. When irradiated with UV

light in the presence of a photoinitiator, two radical-mediated processes occur: thiol-ene coupling, which represents a linear chain extension event, and acrylamide homopolymerization, which represents the crosslinking mechanism. In order to achieve a low modulus after crosslinking, sufficient chain extension must occur before crosslinking, i.e. thiol-ene coupling must outcompete acrylamide homopolymerization. A similar system examined by Cramer and Bowman involved small additions of monomeric dithiols, e.g. 1,6-hexanedithiol, to low MW diacrylates, e.g. 200 g/mol PEG diacrylate.<sup>38</sup> In this system, increasing dithiol content induced a lengthening of network strands (i.e. linear chain extension) as well as an increase in chain transfer, resulting in a reduced polyacrylate crosslink length compared to crosslinked PEG diacrylate alone. At very high dithiol content, close to a 1:1 molar ratio, an increased amount of dangling ends and plasticization were expected to occur.<sup>38</sup> However, remaining sufficiently below this 1:1 ratio prevents appreciable formation of these network defects. Our system builds on this previous literature and examines this approach in a macromolecular context and also directs application to VPP AM. In our system, MW influences relative reaction rates of thiol-ene coupling and acrylamide homopolymerization due to changes in endgroup diffusion rates. For example, the endgroups of a higher MW telechelic dithiol will react more slowly than a lower MW dithiol due to viscosity differences. Relative rates of thiol-ene coupling also depend on the chemical nature of both the thiol and the ene functional groups.<sup>36,44</sup>

**Scheme 3.1** illustrates the facile synthesis of acrylamide- and thiol-functional telechelic poly(dimethyl siloxane) (PDMS) oligomers. Shown in **Scheme 3.1A**, biphasic Schotten-Bauman conditions afforded acrylamide-functionalized PDMS from amine-terminated PDMS and acryloyl chloride. Originally developed for the facile modification

of amino acids, these conditions increase the heat dissipation vs. reaction in DCM alone, reduce the risk of premature crosslinking due to localized heat generation, and reduce complications in reaction workup, as both the generated HCl and acrylic acid remain in the aqueous phase.<sup>43</sup>



**Scheme 3.1.** (A) Functionalization of bis(3-aminopropyl)-terminated poly(dimethyl siloxane) (PDMS) to afford telechelic acrylamide-functional PDMS oligomers. (B) Functionalization of bis(hydroxyalkyl)-terminated PDMS to afford telechelic thiol-functional PDMS oligomers.

**Scheme 3.1B** depicts the modification of bis(hydroxyalkyl)-terminated PDMS via Fischer esterification. <sup>1</sup>H NMR spectroscopy, shown in **Figure 3.6** and **Figure 3.7**, determined > 90 % thiol or acrylamide termination for all oligomers. Percent termination dropped slightly with increasing PDMS oligomer MW for both the telechelic acrylamide-

and thiol-functional oligomers, as observed previously.<sup>45</sup> Nomenclature for these oligomers includes both MW and endgroup identification. For example, PDMS5.3k-AA represents a 5,300 g/mol PDMS diacrylamide and PDMS5.1k-SH represents a 5,100 g/mol PDMS.

Photorheology probed the photocuring kinetics of PDMS-AA in the absence of the chain-extending PDMS-SH, as a function of PDMS oligomer  $M_n$ , as measured by  $^1\text{H}$  NMR spectroscopy. **Figure 3.1A** depicts typical photocuring behavior. In these experiments, samples were first purged with nitrogen for 180 s before initial oscillation to maintain an inert photocuring environment. Afterward, storage ( $G'$ ) and loss ( $G''$ ) modulus were measured upon applied oscillatory strain, with UV light beginning after 30 s of dark oscillation. Upon UV irradiation through the bottom quartz parallel plate, a rapid  $G'/G''$  crossover occurred and  $G'$  quickly plateaued ( $G_N^0$ ). As expected and shown in **Figure 3.1B**, a systematic decrease in  $G_N^0$  is observed with increasing PDMS-AA  $M_n$ , as overall crosslink density decreases with increasing PDMS-AA  $M_n$ . Shown in **Figure 3.1C**,  $G'/G''$  crossover times, commonly referred to as an estimate of gel point for a crosslinkable polymer,<sup>46</sup> indicate rapid gelation in  $< 5$  s for even the highest MW PDMS oligomer (PDMS30.6k-AA). Finally, shown in **Figure 3.1D**, all photocured PDMS-AA oligomers exhibit gel fractions above 90 %, demonstrating efficient gelation and suitability for the additive manufacturing process.

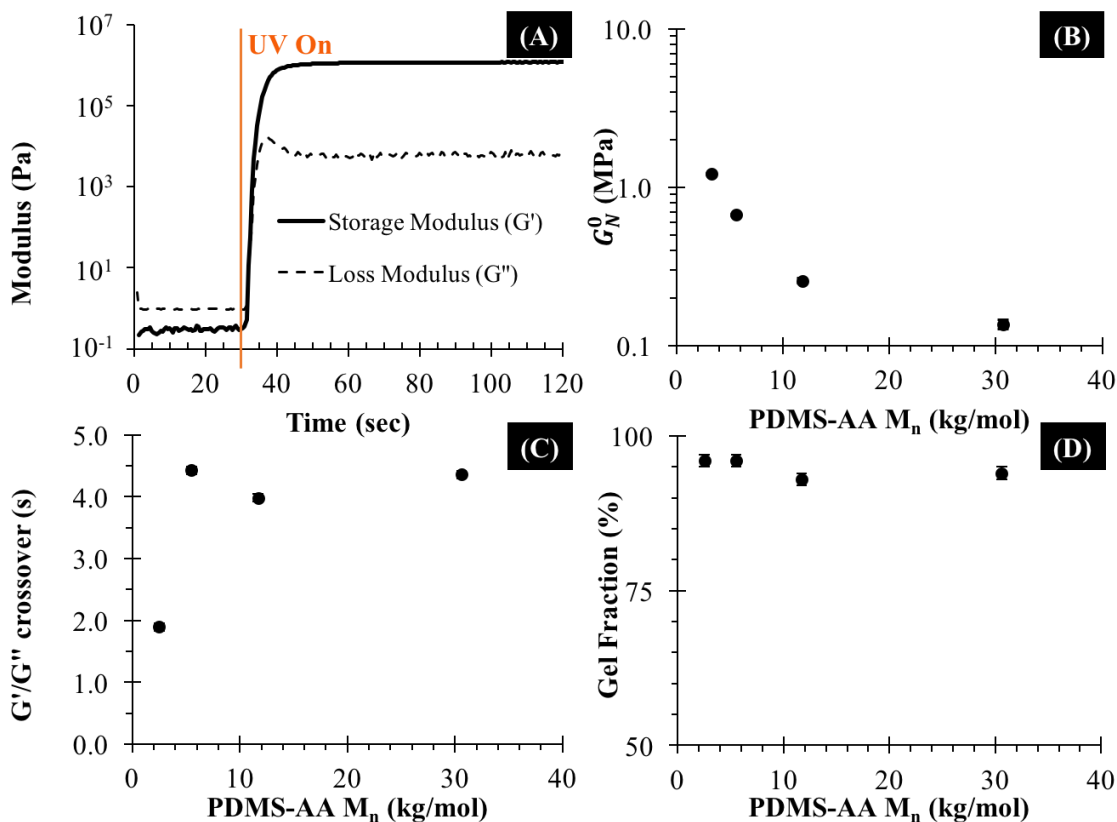


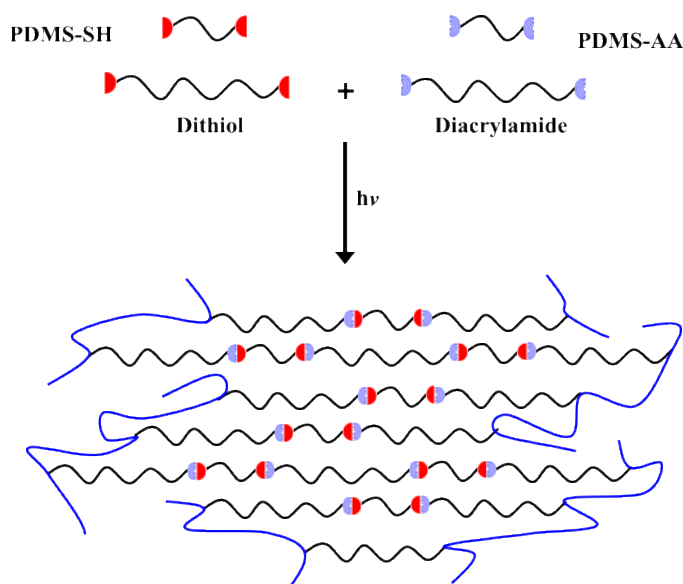
**Figure 3.1.** (A) Photoreology for neat PDMS-3.2k-AA, depicting storage ( $G'$ ) and loss ( $G''$ ) modulus increase as a function of UV exposure time (on at 30 s). Panels (B), (C), and (D) depict  $G'$  plateau modulus ( $G_N^0$ ),  $G'/G''$  crossover time, and gel fraction as a function of PDMS-AA oligomer  $M_n$ , respectively. Error bars represent representative sample standard deviation.

Rubber elasticity theory facilitated the calculation of  $M_c$  values, as shown in **Table 3.1**, by employing **Equation 1**. The contribution from the polyacrylamide chain to  $M_c$  slightly decreased the obtained  $M_c$  value as compared to the uncured oligomer  $M_n$ . The calculated  $M_c$  value for PDMS30.6k-AA deviated more strongly than the other three samples from the uncured oligomer  $M_n$  due to an entanglement contribution, as the critical entanglement molecular weight ( $M_c$ ) of PDMS was determined earlier to be 24,500 g/mol.<sup>47</sup> After probing the photocuring behavior of PDMS-AA alone, various amounts of PDMS-SH were introduced into the photopolymer system while maintaining PDMS-AA in stoichiometric excess in order to ensure crosslinking. **Scheme 3.2** depicts expected

network structure with illustrations of PDMS-AA and PDMS-SH that are employed throughout the remainder of this report.

**Table 3.1.** Non-irradiated PDMS-AA oligomer  $M_n$  (g/mol) as determined from  $^1\text{H}$  NMR spectroscopy and calculated  $M_c$  values, based on  $G_N^0$ , as determined by **Equation 1**.

PDMS-AA $M_n$ (g/mol)	Calculated $M_c$ (g/mol)
3,200	1,990
5,500	3,600
11,700	9,370
30,600	17,650



**Scheme 3.2.** Chain extension (via thiol-ene coupling) and crosslinking (via conventional free radical homopolymerization) afforded upon irradiation of a mixture of PDMS dithiol and PDMS diacrylamide.

A probe of the influence of PDMS MW on  $G_N^0$  and gel fraction enabled optimization of the chain extension process and demonstrated  $G_N^0$  tunability. As such, various combinations of dithiol and diacrylamide MWs were mixed and photocured.

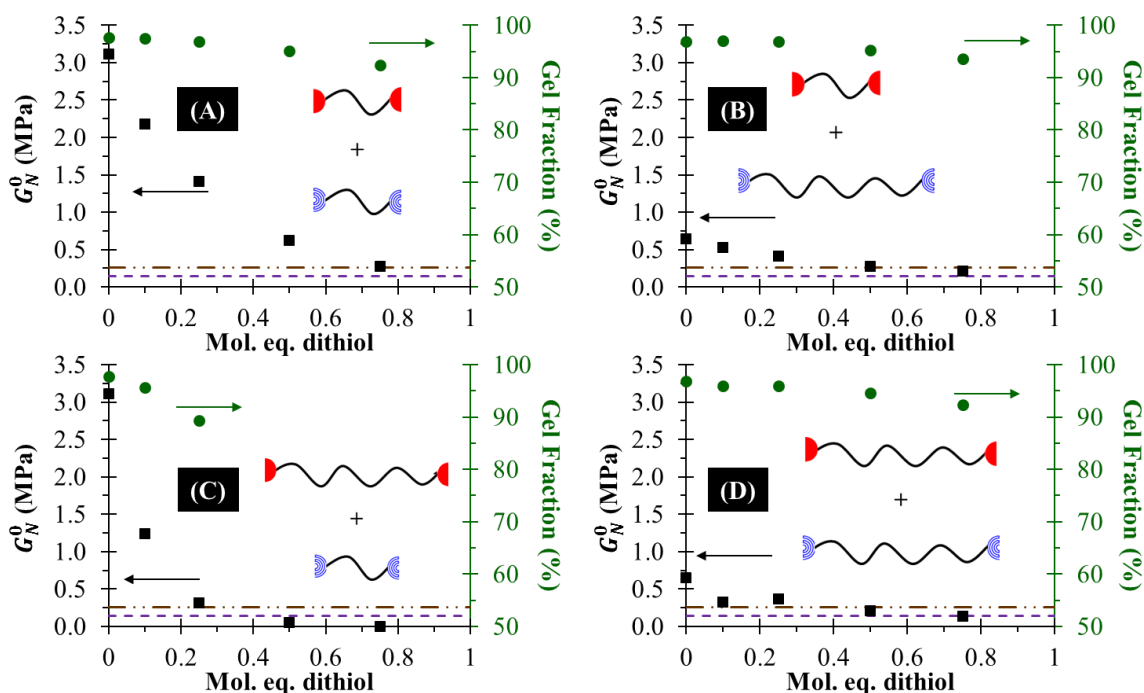


**Figure 3.2.**  $G_N^0$  values (MPa) from photorheology and gel fraction from soxhlet extraction for photocured mixtures, depicted as a function of mol. eq. dithiol for (A) PDMS1.2k-SH and PDMS1.8k-AA, (B) PDMS1.2k-SH and PDMS5.5k-AA, (C) PDMS5.1k-SH and PDMS1.8k-AA, and (D) PDMS5.1k-SH and PDMS5.5k-AA. The brown dash-dot lines and the purple dashed lines represent the  $G_N^0$  values for PDSM11.7k-AA and PDMS30.6k-AA, respectively.

As shown in **Figure 3.2** and plotted as a function of increasing mol. eq. dithiol (i.e. relative to 1 mol. eq. diacrylamide), an examination of all complementary permutation of binary mixtures of PDMS1.8k-AA, PDMS5.5k-AA, PDMS1.2k-SH, and PDMS5.1k-SH with photorheology and soxhlet extraction probed network properties and gelation efficiency.

**Figure 3.2A** displays the photocuring of PDMS1.2k-SH and PDMS1.8k-AA, affording a wide range of  $G_N^0$  values while maintaining gel fractions above 90 %. Shown for comparison are  $G_N^0$  values for PDSM11.7k-AA and PDMS30.6k-AA, depicted respectively as brown dash-dot lines and purple dashed lines. These two samples represent PDMS below and above the critical entanglement molecular weight, respectively. **Figure 3.2D** shows the complementary situation of PDMS5.1k-SH and PDMS5.5k-AA, which enabled a much narrower range of  $G_N^0$  and maintained gel fractions > 90 %.



PDMS5.1k-SH and PDMS1.8k-AA were combined and photocured with  $G_N^0$  values displayed in **Figure 3.2C**. Due to limited thiol endgroup diffusion, the diacrylamide presumably diffused faster and bridged two larger dithiol oligomers. This resulted in chain-extended oligomers that were endcapped with thiols on one or both ends, thus preventing crosslinking. As such, both the  $G_N^0$  values and gel fractions dropped precipitously with increasing dithiol content, which was immeasurable beyond 0.25 mol eq. dithiol due to the difficulty of preserving the entire sol fraction after photocuring. **Figure 3.2B** portrays the final permutation, PDMS1.2k-SH and PDMS5.5k-AA, which provided greater mobility to the chain extender and ensured acrylamide endcapping of chain-extended oligomers. This approach afforded a moderate range in  $G_N^0$  and maintained high gel fractions. In particular, the  $G_N^0$  value for the 0.75:1.0 mixture also remained in between the  $G_N^0$  values for PDMS11.7k-AA and PDMS30.6k-AA. All further experiments employed this mixture, e.g. PDMS1.2k-SH and PDMS5.5k-AA, with VPP at 0.75 mol. eq. dithiol in order to maximize the amount and preference for chain extension.

Although only a single binary composition was evaluated for printing and mechanical property characterization, this study demonstrates achievement of a full order-of-magnitude range in  $G_N^0$  (i.e. 0.25 – 3 MPa) while maintaining high gel fractions (> 90 %). While photorheology measurements do not translate precisely into VPP conditions due to differences in light sources, optics, and atmosphere (e.g. N<sub>2</sub> vs. air), these data only serve to suggest an initial photopolymer composition for VPP. In particular, a fast (< 5 s) G'/G'' crossover time suggests short layer cure times, and the magnitude of the plateau modulus indicates the self-supporting capability of a single layer to support printed layers above it

without collapsing.<sup>48</sup> Photorheology enables high-throughput screening of many compositions and facilitates selection of top candidates for VPP.

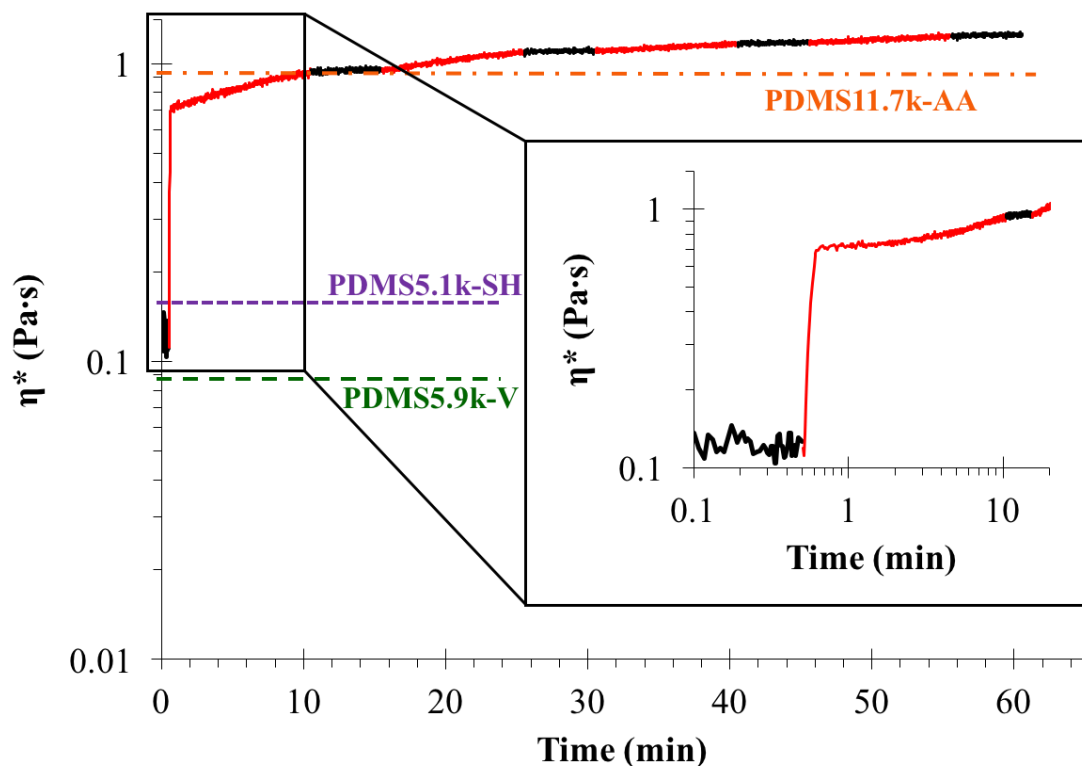


**Figure 3.3.** Complex viscosity ( $\eta^*$ ) via photorheology of a 1:1 mol:mol mixture of PDMS5.1k-SH and PDMS5.9k-V vs. UV irradiation time. Red = UV light on (10 min intervals) and black = UV light off (5 min intervals). Viscosity of non-irradiated PDMS5.9k-V (green long dash), PDMS5.1k-SH (purple short dash), and PDMS11.7k-AA (orange dash-dot) are provided for reference. Inset log-log plot highlights the 0.1 – 1 Pa·s viscosity range and 0.1 – 20 min time range.

Photocuring of a 1:1 mixture of PDMS5.1k-SH and PDMS5.9k-V (vinyl-terminated PDMS) enabled a probe of chain extension in the absence of crosslinking, as the vinyl functional groups do not self-polymerize under these conditions. This experiment examined the effect of periodic UV exposure on complex viscosity ( $\eta^*$ ). As depicted in **Figure 3.3**, after a 30 s period without UV exposure, the oligomeric mixture  $\eta^*$  increased roughly one order-of-magnitude immediately as the UV light was turned on, nearly reaching the  $\eta^*$  of PDMS11.7k-AA. After this initial increase,  $\eta^*$  increased during each

period of UV irradiation and remained unchanged during each period of UV darkness. Furthermore, the  $\eta^*$  slope decreased during each incremental 10 min window of UV exposure. As the thiol-ene reaction enables step-growth polymerization of PDMS5.1k-SH and PDMS5.9k-V under these conditions,  $\eta^*$  increases were likely limited with increasing UV exposure due to increasing linear MW and concomitantly limited endgroup diffusion. Taken in context of simultaneous thiol-ene coupling and acrylamide homopolymerization, these data indicated roughly an immediate doubling in MW as UV irradiation occurred, with acrylamide homopolymerization likely inducing vitrification, preventing further chain extension.

**Table 3.2.** Zero-shear viscosity ( $\eta_0$ ) of various functional siloxanes and the mixture of PDMS-SH and PDMS-AA used for AM (0.75:1.0 mol:mol PDMS1.2k-SH : PDMS5.3k-AA).

Sample	$\eta_0$ (Pa·s)
Water	0.001
PDMS1.2k-SH	0.030
Glycerol	0.39
PDMS5.3k-AA	0.50
PDMS11.7k-AA	0.85
PDMS30.6k-AA	2.64
0.75 : 1.0 PDMS1.2k-SH : PDMS5.3k-AA	0.32

**Table 3.2** displays zero-shear viscosity ( $\eta_0$ ) values of various acrylamide-functional siloxanes and the mixture of PDMS-SH and PDMS-AA for VPP (0.75:1.0 mol:mol PDMS1.2k-SH : PDMS5.3k-AA). Water and glycerol are presented for reference. Based upon **Figure 3.2B**, it is apparent that the 0.75:1.0 molar mixture possessed a  $G_N^0$  between PDMS11.7k-AA and PDMS30.6k-AA and a gel fraction above 90 %. These viscosity data demonstrated that the dithiol-diacrylamide mixture for AM possessed a

viscosity of 0.32 Pa·s, which is below PDMS5.3k-AA, but possessed a calculated  $M_c$  of 12,600 g/mol and a gel fraction > 90 %. Thus, the goal of low viscosity photopolymers with properties of photocured, higher MW precursors was achieved. This system is also highly tunable and demonstrated a range in  $G_N^0$  of more than a full order-of-magnitude, which were obtained by varying the dithiol/diacrylamide stoichiometry and MW.

**Figure 3.4A** depicts a schematic of the scanning-mask projection VPP apparatus. The printer consisted of a broad spectrum (300-500 nm) UV light source, a dynamic mask projection device mounted on a high-precision X-Y linear stage, imaging optics, a build platform attached to a high-resolution z-stage, and a computer to precisely control the mechatronic sub-systems.<sup>32</sup> The scanning system was custom-designed and eliminated the typical trade-off between print resolution and build area by continually scanning a UV-movie of the layer image across the photopolymer surface. **Figure 3.4B** and **Figure 3.4C** depict the printing process from various points of view with the silicone photopolymer in the glass vat. Due to high oxygen solubility in PDMS relative to other polymers,<sup>49</sup> printing in an inert environment helped to prevent oxygen diradical from terminating growing polyacrylamide chains. VPP proceeded under nitrogen sparge in an attempt to exclude oxygen from the printing process. Preliminary printed objects unfortunately contained bubbles as an artifact of the nitrogen sparge, but careful examination of tensile specimens enabled selection of dogbones with bubble- and otherwise defect-free gauge lengths. VPP AM of tensile specimens, shown in **Figure 3.4C**, demonstrated well-defined geometries and optically clear printed objects. In this work, all tensile specimens were printed in-plane with the build platform and incident UV light. Although previous work has demonstrated a statistically significant difference in elongation at break and Young's modulus for

samples printed flat and on an edge, the difference in values was small ( $\sim 5\%$ ) for their system, which employed VPP with a commercially available photopolymer.<sup>50,51</sup> Effects of print orientation on mechanical property anisotropy are generally smaller with VPP versus other techniques (e.g. fused filament fabrication or FFF), as each layer in VPP is not reacted to complete conversion, providing photocurable functionality for successive layers to react with previously printed layers.<sup>50,51</sup> This is contrasted with FFF, where polymer chain entanglements between printed layers, which must happen above the glass transition temperature ( $T_g$ ), are largely prevented due to rapid solidification of printed filaments ( $\sim 1$  s after deposition).<sup>52,53</sup>

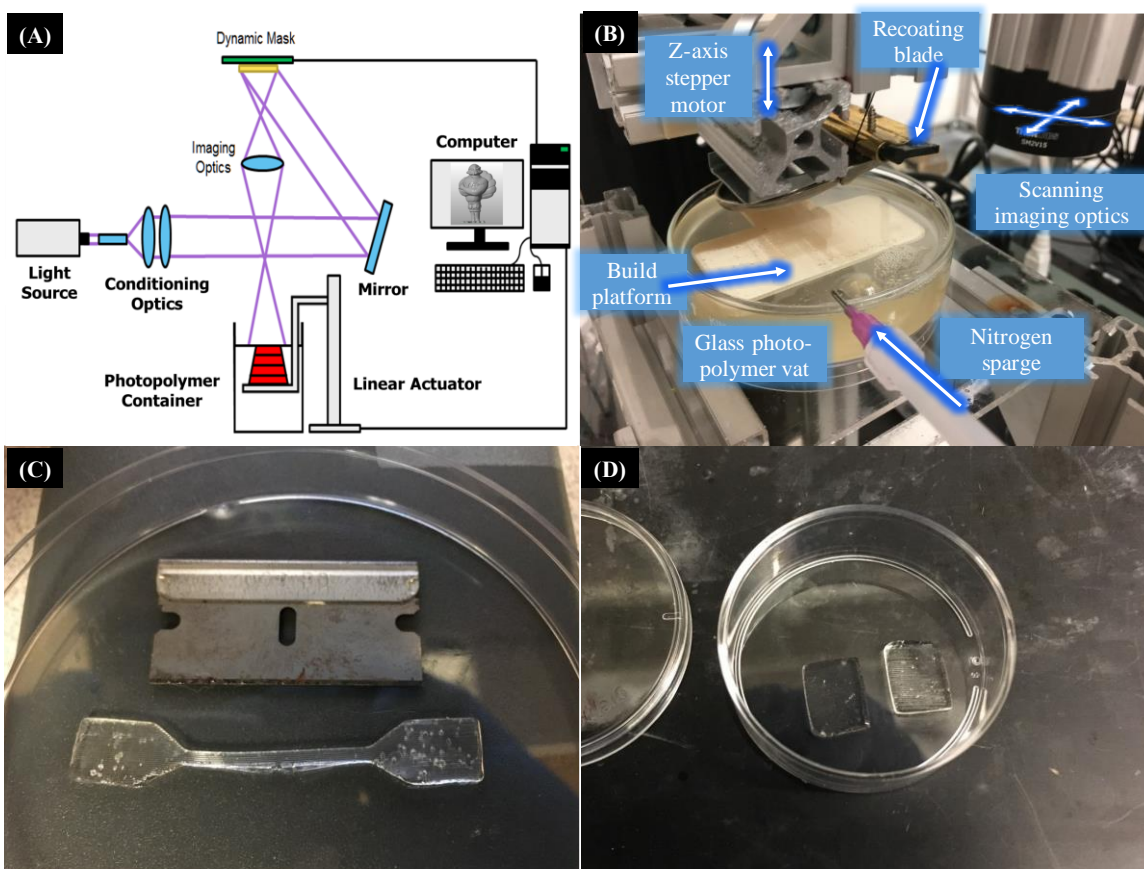


**Figure 3.4:** (A) Schematic of the top-down scanning mask projection VPP apparatus used for AM of siloxane oligomers. (B) VPP AM apparatus showing glass dish photopolymer container, nitrogen sparge line, recoating blade, and scanning optics system. (C) 3D-printed tensile bar. (D) 3D printed squares for soxhlet extraction.

**Figure 3.4D** depicts 3D printed squares employed for soxhlet analysis and the determination of gel fraction. Soxhlet extraction determined gel fraction values of 80 % for objects printed under nitrogen sparge, as opposed to values of 90 % obtained for the photorheology samples with the same stoichiometric composition, which were photocured under nitrogen purge. This difference is likely attributable to imperfect oxygen exclusion with the nitrogen sparge during the printing process. The photocuring environment in the rheometer, done under nitrogen purge, represented an ideal case for oxygen exclusion in the context of photocuring, as the UV guard surrounding the parallel plates was robust and the nitrogen flow rate was sufficiently high. As a separate experiment, a post-cure (e.g. extra UV irradiation as a second step after removal of specimens from the VPP apparatus) of the 3D printed squares and subsequent extraction elucidated gel fractions of 90 %, demonstrating that residual photocurable functionality remained in the photopolymer if not irradiated to complete conversion or if irradiated in the presence of air (e.g. oxygen). In order to probe mechanical properties of the actual network structure produced during VPP AM, tensile specimens were not post-cured before tensile testing was performed.

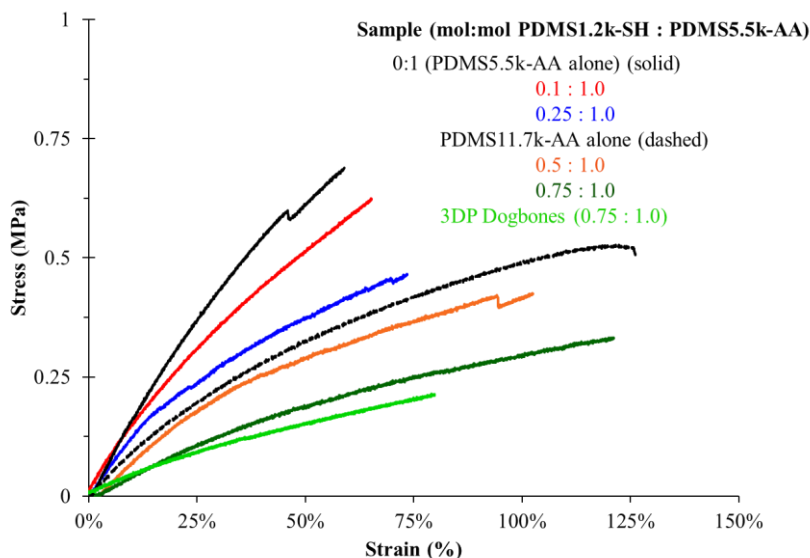


**Figure 3.5:** Tensile data for photocured mixtures of PDMS1.2k-SH and PDMS5.5k-AA. Photocured PDMS11.7k-AA (black dashed) is provided as a reference. The 3D printed (3DP) tensile specimens are shown in light green.

**Table 3.3.** Stress at break, and strain at break for photocured or 3D printed (3DP) mixtures of PDMS1.2k-SH and PDMS5.5k-AA. Photocured PDMS11.7k-AA (black dashed) is provided as a reference.

Sample (mol:mol PDMS1.2k-SH : PDMS5.5k-AA)	Stress at break (MPa)	Strain at break (%)
0:1 (PDMS5.5k-AA)	$0.65 \pm 0.15$	$58 \pm 14$
0.1 : 1.0	$0.52 \pm 0.15$	$59 \pm 22$
0.25 : 1.0	$0.43 \pm 0.09$	$63 \pm 21$
0.5 : 1.0	$0.44 \pm 0.16$	$98 \pm 48$
0.75 : 1.0	$0.32 \pm 0.08$	$123 \pm 39$
PDMS11.7k-AA	$0.43 \pm 0.05$	$138 \pm 32$
3DP Dogbones (0.75 : 1.0)	$0.22 \pm 0.02$	$80 \pm 10$

**Figure 3.5** depicts tensile stress-strain curves for various photocured samples and

**Table 3.3** displays the numerical values from these tests. In all cases except the 3D-printed tensile dogbones (light green), direct isolation of tensile specimens from the photocured discs, once removed from the rheometer, facilitated a more direct comparison between mechanical property measurements, photorheology, and VPP. As mentioned

above, preliminary printed objects unfortunately contained bubbles as an artifact of the nitrogen sparge, but careful examination of tensile specimens enabled selection of dogbones with bubble- and otherwise defect-free gauge lengths. Tensile testing measured a stress at break of  $0.65 \pm 0.15$  MPa and a strain at break of  $58 \pm 14$  for the photocured PDMS5.5k-AA sample alone, without chain extension. As the amount of PDMS1.2k-SH increased in the pre-cured formulation, stress at break systematically decreased, and strain at break systematically increased. Tensile testing of the formulation containing the highest level of dithiol incorporation (e.g. 0.75:1.0) revealed a 2x increase in strain at break vs. photocured PDMS5.5k-AA alone (e.g. 123 % vs. 58 %), indicating effective chain extension. Tensile testing also measured very similar levels of strain at break for the photocured 0.75:1.0 sample and for PDMS11.7k-AA ( $123 \pm 39$  % and  $138 \pm 32$  % respectively), corroborating the similarities in these samples observed during the previously discussed  $M_c$  calculations. However, the 3D printed dogbones only reached a strain at break of  $80 \pm 10$  %, thus indicating slightly less efficient chain extension occurring in the VPP apparatus. This may be due to imperfections in oxygen exclusion during printing, as only the glass vat is sparged with nitrogen. As a separate experiment, soxhlet extraction determined gel fraction values of 80 % for objects printed under nitrogen sparge, as opposed to values of 90 % obtained for the photorheology samples with the same stoichiometric composition, which were photocured under nitrogen purge. This difference is likely attributable to imperfect oxygen exclusion with the nitrogen sparge during printing process. Future work will include further improvements in oxygen exclusion during printing.



### 3.5 Conclusions

Synthesis, characterization, and VPP AM is reported for a low viscosity PDMS-based photopolymer that provides the properties of a photocured, higher MW precursor. This is accomplished without the use of reactive diluents (i.e. monomers), unreactive diluents (i.e. solvents), or heat. Photorheology enabled determination of curing kinetics and gel-state moduli ( $G_N^0$ ). In this system, thiols serve a dual purpose, both undergoing thiol-ene coupling with acrylamide moieties to lengthen network strands and acting as a chain transfer agent, thereby reducing the overall degree of polymerization of the polyacrylamide crosslinks.<sup>38</sup> Additionally, VPP with a combination of a relatively low MW dithiol (PDMS1.2k-SH) and a relatively high MW diacrylamide (PDMS5.5k-AA) provided further preference to thiol-ene coupling, as the thiol functionality was less diffusion-limited than the acrylamide functionality in this particular case. Rheology determined a viscosity of the 0.75:1.0 dithiol:diacrylamide below that of PDMS5.5k-AA alone and after photocuring, a calculated  $M_c$  of 12,600 g/mol, thus indicating ample chain extension. Furthermore, soxhlet extraction determined gel fractions above 90 % for these samples, indicating efficient photocuring and 3D printing. Initial VPP under inert atmosphere demonstrated well-defined geometries and tensile testing of both photocured films and 3D printed dogbones indicated a ~ 2x increase in strain at break vs. photocured PDMS5.5k-AA alone. These results exemplify photopolymer design with attention to both the printing process and the final application, and also present the first use of printing under inert atmosphere for this system. This concept is applicable to the advanced manufacturing of any object requiring high elongation at break. A continuation of this photopolymer design effort is underway and will more fundamentally examine the relative reaction rates of thiol-ene coupling and acrylamide homopolymerization under conditions relevant to VPP AM,

as well as offer an in-depth examination of chain extension in the context of vat photopolymerization. Additionally, experiments are underway towards VPP under argon purge, as argon is a heavier gas than nitrogen and may provide more robust oxygen exclusion during printing of highly gas-permeable photopolymers, e.g. PDMS. This work will be reported in future publications.

### 3.6 Acknowledgements

The authors would like to acknowledge Wacker Chemie for their gracious donation of a 12 kg/mol bis(3-aminopropyl)-terminated PDMS and Dr. Jamie Messman at the Department of Energy's Kansas City National Security Campus (managed by Honeywell) for funding. The authors would also like to thank Jonathan E. Seppala (NIST) for helpful discussions.

### 3.7 References

- (1) Huang, Y.; Leu, M. C.; Mazumder, J.; Donmez, A. *Journal of Manufacturing Science and Engineering* **2015**, *137*, 014001-014001. 10.1115/1.4028725
- (2) Gibson, I.; Rosen, D.; Stucker, B. In *Additive Manufacturing Technologies: 3D Printing, Rapid Prototyping, and Direct Digital Manufacturing*; Springer New York: New York, NY, 2015, p 63-106.
- (3) Fouassier, J. P.; Lalevée, J. *Photoinitiators for Polymer Synthesis: Scope, Reactivity, and Efficiency*; Wiley, 2012.
- (4) Bechtold, S. *IIC - International Review of Intellectual Property and Competition Law* **2016**, *47*, 517-536. 10.1007/s40319-016-0487-4
- (5) Davidson, J. R.; Appuhamillage, G. A.; Thompson, C. M.; Voit, W.; Smaldone, R. A. *ACS Applied Materials & Interfaces* **2016**, *8*, 16961-16966. 10.1021/acsami.6b05118
- (6) Wallin, T. J.; Pikul, J. H.; Bodkhe, S.; Peele, B. N.; Mac Murray, B. C.; Therriault, D.; McEnerney, B. W.; Dillon, R. P.; Giannelis, E. P.; Shepherd, R. F. *Journal of Materials Chemistry B* **2017**, *5*, 6249-6255. 10.1039/C7TB01605K
- (7) Govindarajan, S. R.; Xu, Y.; Swanson, J. P.; Jain, T.; Lu, Y.; Choi, J.-W.; Joy, A. *Macromolecules* **2016**. 10.1021/acs.macromol.5b02399
- (8) Dubbin, K.; Hori, Y.; Lewis, K. K.; Heilshorn, S. C. *Advanced Healthcare Materials* **2016**, *5*, 2488-2492. 10.1002/adhm.201600636
- (9) Jungst, T.; Smolan, W.; Schacht, K.; Scheibel, T.; Groll, J. *Chemical Reviews* **2016**, *116*, 1496-1539. 10.1021/acs.chemrev.5b00303
- (10) Kolesky, D. B.; Homan, K. A.; Skylar-Scott, M. A.; Lewis, J. A. *Proceedings of the National Academy of Sciences* **2016**, *113*, 3179-3184. 10.1073/pnas.1521342113
- (11) Panwar, A.; Tan, L. P. *Molecules* **2016**, *21*. 10.3390/molecules21060685

- (12) Hung, K.-C.; Tseng, C.-S.; Dai, L.-G.; Hsu, S.-h. *Biomaterials* **2016**, *83*, 156-168. 10.1016/j.biomaterials.2016.01.019
- (13) Sirrine, J. M.; Pekkanen, A. M.; Nelson, A. M.; Chartrain, N. A.; Williams, C. B.; Long, T. E. *Australian Journal of Chemistry* **2015**, *68*, 1409-1414. <http://dx.doi.org/10.1071/CH15327>
- (14) Shi, L.; Carstensen, H.; Hoelzl, K.; Lunzer, M.; Li, H.; Hilborn, J.; Ovsianikov, A.; Ossipov, D. A. *Chemistry of Materials* **2017**. 10.1021/acs.chemmater.7b00128
- (15) Karis, D. G.; Ono, R. J.; Zhang, M.; Vora, A.; Storti, D.; Ganter, M. A.; Nelson, A. *Polymer Chemistry* **2017**, *8*, 4199-4206. 10.1039/C7PY00831G
- (16) Zhang, M.; Vora, A.; Han, W.; Wojtecki, R. J.; Maune, H.; Le, A. B. A.; Thompson, L. E.; McClelland, G. M.; Ribet, F.; Engler, A. C.; Nelson, A. *Macromolecules* **2015**, *48*, 6482-6488. 10.1021/acs.macromol.5b01550
- (17) Peele, B. N.; Wallin, T. J.; Zhao, H.; Shepherd, R. F. *Bioinspiration & biomimetics* **2015**, *10*, 055003-055003. 10.1088/1748-3190/10/5/055003
- (18) Mondschein, R. J.; Kanitkar, A.; Williams, C. B.; Verbridge, S. S.; Long, T. E. *Biomaterials* **2017**. <https://doi.org/10.1016/j.biomaterials.2017.06.005>
- (19) Pekkanen, A. M.; Mondschein, R. J.; Williams, C. B.; Long, T. E. *Biomacromolecules* **2017**, *18*, 2669-2687. 10.1021/acs.biomac.7b00671
- (20) Zheng, X.; Lee, H.; Weisgraber, T. H.; Shusteff, M.; DeOtte, J.; Duoss, E. B.; Kuntz, J. D.; Biener, M. M.; Ge, Q.; Jackson, J. A.; Kucheyev, S. O.; Fang, N. X.; Spadaccini, C. M. *Science* **2014**, *344*, 1373-1377. 10.1126/science.1252291
- (21) Peterson, G. I.; Schwartz, J. J.; Zhang, D.; Weiss, B. M.; Ganter, M. A.; Storti, D. W.; Boydston, A. J. *ACS Applied Materials & Interfaces* **2016**, *8*, 29037-29043. 10.1021/acsami.6b09768
- (22) Kinstlinger, I. S.; Miller, J. S. *Lab on a Chip* **2016**, *16*, 2025-2043. 10.1039/C6LC00193A
- (23) Carlborg, C. F.; Haraldsson, T.; Oberg, K.; Malkoch, M.; van der Wijngaart, W. *Lab on a Chip* **2011**, *11*, 3136-3147. 10.1039/C1LC20388F
- (24) Nguyen, K. D. Q.; Megone, W. V.; Kong, D.; Gautrot, J. E. *Polymer Chemistry* **2016**, *7*, 5281-5293. 10.1039/C6PY01134A
- (25) Eckel, Z. C.; Zhou, C.; Martin, J. H.; Jacobsen, A. J.; Carter, W. B.; Schaedler, T. A. *Science* **2016**, *351*, 58-62. 10.1126/science.aad2688
- (26) Melchels, F. P. W.; Feijen, J.; Grijpma, D. W. *Biomaterials* **2010**, *31*, 6121-6130. <http://dx.doi.org/10.1016/j.biomaterials.2010.04.050>
- (27) Associates, W. *Wohlers Report*, 2016.
- (28) Boonstra, B. B. *Polymer* **1979**, *20*, 691-704. [https://doi.org/10.1016/0032-3861\(79\)90243-X](https://doi.org/10.1016/0032-3861(79)90243-X)
- (29) Rubinstein, M.; Colby, R. H. *Polymer Physics*; OUP Oxford, 2003.
- (30) Kayori, T.; Shigetomo, M.; Shinichi, K.; Kensei, E.; Hiromu, S.; Yoshiteru, H.; Hideaki, K.; Masao, B. *Metrologia* **2015**, *52*, 8
- (31) Sirrine, J. M.; Ashraf-Khorassani, M.; Moon, N. G.; Mondschein, R. J.; Long, T. E. *Chromatographia* **2016**, *79*, 977-984. 10.1007/s10337-016-3098-9
- (32) Hegde, M.; Meenakshisundaram, V.; Chartrain, N.; Sekhar, S.; Tafti, D.; Williams, C. B.; Long, T. E. *Adv Mater* **2017**, *29*. 10.1002/adma.201701240

- (33) Yue, J.; Zhao, P.; Gerasimov, J. Y.; van de Lagemaat, M.; Grotenhuis, A.; Rustema-Abbing, M.; van der Mei, H. C.; Busscher, H. J.; Herrmann, A.; Ren, Y. *Advanced Functional Materials* **2015**, *25*, 6756-6767. 10.1002/adfm.201502384
- (34) Melchels, F. P. W.; Feijen, J.; Grijpma, D. W. *Biomaterials* **2009**, *30*, 3801-3809. <http://dx.doi.org/10.1016/j.biomaterials.2009.03.055>
- (35) Schüller-Ravoo, S.; Zant, E.; Feijen, J.; Grijpma, D. W. *Advanced Healthcare Materials* **2014**, *3*, 2004-2011. 10.1002/adhm.201400363
- (36) Hoyle, C. E.; Bowman, C. N. *Angewandte Chemie International Edition* **2010**, *49*, 1540-1573. 10.1002/anie.200903924
- (37) Buback, M.; Schroeder, H.; Kattner, H. *Macromolecules* **2016**. 10.1021/acs.macromol.5b02660
- (38) Cramer, N. B.; Bowman, C. N. *Journal of Polymer Science Part A: Polymer Chemistry* **2001**, *39*, 3311-3319. 10.1002/pola.1314
- (39) Zhou, J.; Zhang, Q.; Zhang, H.; Tan, J.; Chen, S.; Liu, Q.; Ma, M.; Xin, T. *Rapid Prototyping Journal* **2016**, *22*, 465-473. doi:10.1108/RPJ-06-2013-0056
- (40) Leonards, H.; Engelhardt, S.; Hoffmann, A.; Pongratz, L.; Schriever, S.; Bläsius, J.; Wehner, M.; Gillner, A. 2015; Vol. 9353, p 93530F.
- (41) Zheng, P.; McCarthy, T. J. *Journal of the American Chemical Society* **2012**, *134*, 2024-2027. 10.1021/ja2113257
- (42) Fragiadakis, D.; Pissis, P.; Bokobza, L. *Polymer* **2005**, *46*, 6001-6008. <https://doi.org/10.1016/j.polymer.2005.05.080>
- (43) Kürti, L. s.; Czakó, B. *Strategic applications of named reactions in organic synthesis : background and detailed mechanisms*; Elsevier Academic: Burlington, MA :, 2005.
- (44) Cramer, N. B.; Reddy, S. K.; O'Brien, A. K.; Bowman, C. N. *Macromolecules* **2003**, *36*, 7964-7969. 10.1021/ma034667s
- (45) Mather, B. D.; Miller, K. M.; Long, T. E. *Macromolecular Chemistry and Physics* **2006**, *207*, 1324-1333. 10.1002/macp.200600167
- (46) Winter, H. H. *Polymer Engineering & Science* **1987**, *27*, 1698-1702. 10.1002/pen.760272209
- (47) Yilgor, I.; Eynur, T.; Bilgin, S.; Yilgor, E.; Wilkes, G. L. *Polymer* **2011**, *52*, 266-274. <http://dx.doi.org/10.1016/j.polymer.2010.11.040>
- (48) Lewicki, J. P.; Rodriguez, J. N.; Zhu, C.; Worsley, M. A.; Wu, A. S.; Kanarska, Y.; Horn, J. D.; Duoss, E. B.; Ortega, J. M.; Elmer, W.; Hensleigh, R.; Fellini, R. A.; King, M. J. *Scientific Reports* **2017**, *7*, 43401. 10.1038/srep43401
- (49) Ligon, S. C.; Husár, B.; Wutzel, H.; Holman, R.; Liska, R. *Chemical Reviews* **2014**, *114*, 557-589. 10.1021/cr3005197
- (50) Karina, P.; Karina, A.; Rolando, Q.; Ryan, B. W. *Rapid Prototyping Journal* **2012**, *18*, 374-388. 10.1108/13552541211250373
- (51) Quintana, R.; Choi, J.-W.; Puebla, K.; Wicker, R. *The International Journal of Advanced Manufacturing Technology* **2010**, *46*, 201-215. 10.1007/s00170-009-2066-z
- (52) Seppala, J. E.; Hoon Han, S.; Hillgartner, K. E.; Davis, C. S.; Migler, K. B. *Soft Matter* **2017**. 10.1039/C7SM00950J
- (53) Seppala, J. E.; Migler, K. D. *Additive Manufacturing* **2016**, *12*, 71-76. <http://dx.doi.org/10.1016/j.addma.2016.06.007>

### **3.8 Supporting Information**

#### **3.8.1 Vat Photopolymerization – Apparatus**

A custom-designed vat photopolymerization setup included a BlueWave® 75 UV spot curing lamp (Dymax 40078) with intensity adjustment, and a single pole lightguide (Dymax 5721). A UV mirror (Thor Labs PFSQ20-03-F01) was seated inside the projector to relay the light from the light guide to the dynamic mask. The projector was equipped with a Texas Instruments DLP™ 0.55 XGA DMD with a rectangular array of 1024 x 768 square micro-mirrors with a pitch and side of 10.8  $\mu\text{m}$ . Imaging lenses (Thor Labs LA4078-UV, LA4545-UV) were suitably placed in the projection path to achieve a magnification of 1:1, producing a projection area of 11.05 x 8.3 mm at the photopolymer surface. The projection system was mounted on cross-mounted high-load, high-precision linear stages (Zaber A-LST0500A-E01) for traversing the XY plane. A high-precision linear stage (Zaber A-LST0250A-E01) was used for the Z motion. The build platform was fabricated using thermoplastic filament extrusion and attached to the Z-stage. A custom 150 x 150 mm square glass vat contained the photopolymer for part manufacturing. The constructed apparatus was capable of attaining scan speeds up to 22 mm/s while utilizing a broad-spectrum UV lamp to polymerize the photopolymer with feature sizes of 150  $\mu\text{m}$  in a build area of 300 x 300 mm. The build stage was outfitted with a low-flow nozzle for nitrogen delivery.

#### **3.8.2 Vat Photopolymerization – Cure Depth and Print Parameters**

A glass petri containing 20 mL of photopolymer was placed in the printer projection area such that the photopolymer surface was level with the focus of the printer. A white image was projected onto the photopolymer surface at an intensity of 2.4  $\text{mW}/\text{cm}^2$  for 5, 6, 8, and

10 s. After sample removal, the cured specimens were rinsed with isopropyl alcohol (IPA) and dried with clean wipes. The specimen thickness was plotted vs. dosing energy to generate the working curve,<sup>2</sup> as shown in **Figure 3.8**. From the working curve, the depth of penetration and the critical energy were estimated to be 2.065 mm and critical exposure 54.05 J/m<sup>2</sup>. For a layer thickness of 150 μm, the estimated exposure time was 2.42 s, corresponding to a scan speed of 2.764 mm/s for the printer.

### **3.8.3 Vat Photopolymerization – Specimen Printing**

The STL file of the required part was sliced into 150 μm layers and pre-processed to form a moving mask with a frame rate of 256 frames/second for every layer. A photopolymer-filled glass vat was placed in the projection area with the photopolymer surface in level with the printer focus. To ensure removal of dissolved oxygen, nitrogen was bubbled through the photopolymer for 10 min. A glass slide was fixed to the build platform and lowered into photopolymer to flush the slide surface with the photopolymer surface. The flow rate of nitrogen was adjusted to continuously flood the build chamber and the photopolymer vat with fresh nitrogen. A preliminary recoating step ensured the deposition of a 150 μm photopolymer layer on the build platform. The moving mask, corresponding to the first layer, was projected on the surface of the photopolymer with a scan speed of 2.764 mm/s. The build platform was lowered into the photopolymer and an inter-layer recoating step was performed to deposit 150 μm layer of photopolymer on the cured part. The projection and recoating steps continued until all the slices of the required part were printed. Extracted parts were rinsed with IPA and dried with clean wipes.

Sample	% acrylamide termination
PDMS1.8k-AA	99
PDMS3.2k-AA	93
PDMS5.3k-AA	94
PDMS5.5k-AA	96
PDMS11.7k-AA	96
PDMS30.6k-AA	91

**PDMS5.5k-AA**

E integration set to 4.00

% acrylamide termination = (B + C)/4.00

**% acrylamide termination = 96 %**

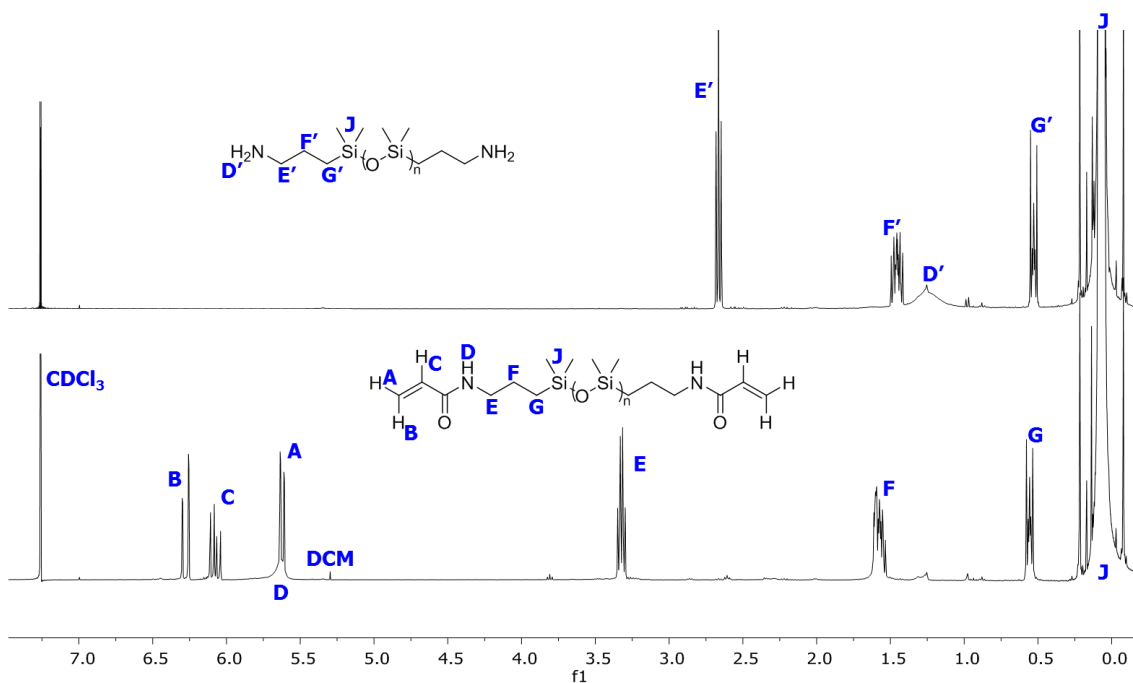


**Figure 3.6.** <sup>1</sup>H NMR spectroscopy determines percent acrylamide termination for PDMS oligomers as a function of PDMS molecular weight.

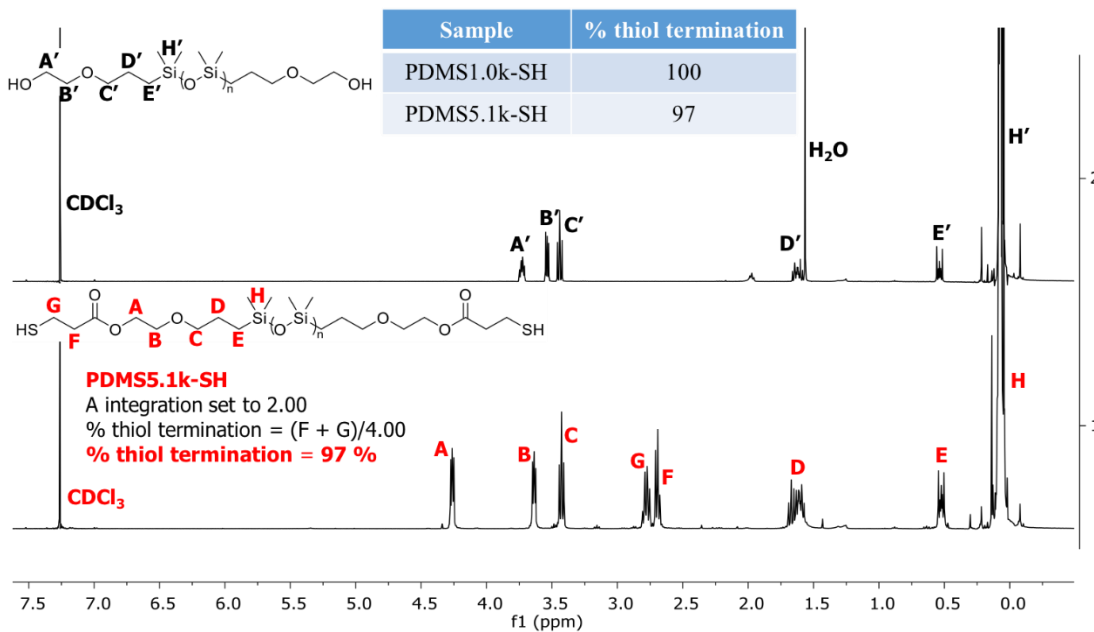


**Figure 3.7.**  $^1\text{H}$  NMR spectroscopy determines percent thiol termination for PDMS oligomers as a function of PDMS molecular weight.

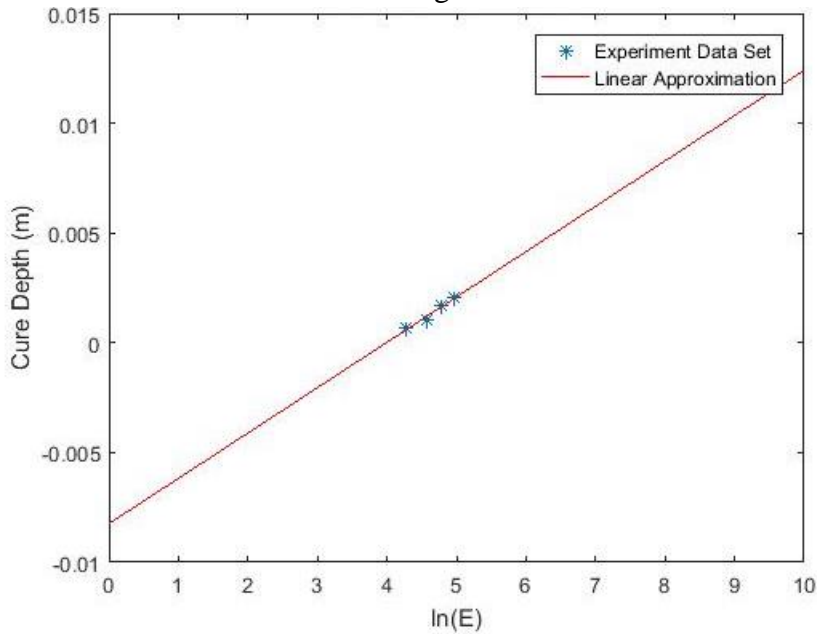


**Figure 3.8.** Working curve for the photoactive resin. The plot helps estimate the UV dose required to print layers of required thickness.



## Chapter 4: **Functional Siloxanes with Photo-Activated, Simultaneous Chain Extension and Crosslinking: Chain Extension Dynamics**

Justin M. Serrine, Nicholas G. Moon, Philip J. Scott, Timothy E. Long\*  
*Department of Chemistry, Macromolecules Innovation Institute  
Virginia Tech, Blacksburg, VA 24061, USA*

### **4.1 Abstract**

Vat photopolymerization (VPP), a type of additive manufacturing (AM), enables the creation of geometries not attainable through traditional manufacturing methods via selective, layer-by-layer photocuring of a UV-responsive polymer (e.g. photopolymer). However, viscosity remains a critical parameter for rapid processing. Previous work established the combination of dithiol- and diacrylamide-functional poly(dimethylsiloxane) oligomers as a relatively low viscosity photopolymer that retained properties of higher molecular weight precursors (e.g. strain at break and modulus). This approach avoided the use of reactive diluents, solvents, and heat for viscosity reduction, instead relying solely upon the resulting thiol-ene coupling and homopolymerization reactions for simultaneous chain extension and crosslinking, respectively. In this work, a model compound competition study determined that thiol-ene coupling outcompetes acrylamide homopolymerization 4:1 under these conditions, which corroborated literature rate constants for similar thiol/acrylate rate polymerizations. Photorheology and photocalorimetry probed the storage modulus evolution and overall polymerization exotherm as a function of UV irradiation time. Finally, a base-catalyzed, thiol-Michael reaction separated the chain extension and crosslinking into two discrete steps and indicated that only partial chain extension occurs before crosslinking, rather than the full amount predicted by the modified Carothers equation. This work validates hypotheses

based in previous work and remains applicable to any low glass transition temperature system that requires low viscosity while retaining properties of photocured, higher molecular weight precursors.

## 4.2 Introduction

Additive manufacturing (AM) or 3D printing (3DP) enables access to complex geometries not attainable with traditional manufacturing techniques. Recent developments provide layerless fabrication and fast print speeds, new printing methodologies,<sup>1-4</sup> and a plethora of new polymeric materials for emerging applications.<sup>5-12</sup> Additionally, these developments validate AM as a tool for mass customization, the notion of large production volumes with each object customized to the individual.<sup>13</sup> This enables diverse applications including biomaterials, personalized medicine, and soft robotics.<sup>14-20</sup> Vat photopolymerization (VPP) or stereolithography (SLA) remains a versatile AM technique that provides excellent surface quality and higher resolution as compared material extrusion.<sup>12</sup> VPP print speeds gain further improvement via incorporation of a digital micromirror device (DMD) that permits photocuring of entire layers at once via projection of a masked image onto the photopolymer surface.<sup>11</sup> Scanning mask projection VPP improves even further on the use of a DMD by scanning the masked image across the photopolymer surface, avoiding the typical trade-off between build area and print resolution.<sup>2,7</sup> However, despite improvements in printer technology, viscosity remains a critical issue when processing photocurable compositions with stereolithography.

The literature provides numerous approaches for processing high viscosity photopolymers, which include the use of reactive diluents (e.g. comonomers), unreactive diluents (e.g. solvents), heat, or mechanical procedures such as a recoating blade.<sup>9,18,19,21-</sup>

<sup>23</sup> Our group recently introduced a photopolymer composition that did not employ the aforementioned methods and instead underwent simultaneous, linear molecular weight growth and crosslinking, enabling low viscosity before printing (e.g.  $\sim 0.3$  Pa·s with  $< 5,300$  g/mol PDMS oligomers) and relatively high molecular weight between crosslinks ( $M_c$ ) after printing (e.g.  $12,600$  g/mol).<sup>9</sup> This simple system consisted solely of thiol- and acrylamide-terminated, telechelic poly(dimethylsiloxane) (PDMS) oligomers that underwent simultaneous, radical-mediated thiol-ene coupling and free-radical polymerization, and provided a  $\sim 2x$  increase in strain at break after photocuring, as compared to non-chain-extended photocured oligomers, while maintaining gel fractions above 90 %.

This work fundamentally examines the aforementioned chain extension and crosslinking as discrete steps. First, a model compound competition study employed <sup>1</sup>H NMR spectroscopy to probe the relative ratio of chain extension that occurs (e.g. thiol-ene product formation) vs. crosslinking (e.g. acrylamide formation), in the absence of diffusion, which corresponded well to published rate constants for thiol/acrylate polymerizations. Photorheology and photocalorimetry probed storage modulus evolution and overall heat flow for the functional oligomers as a function of UV irradiation time, providing insight into the reaction kinetics and molecular weight between crosslinks, while Soxhlet extraction of the resulting photorheology samples indicated gel fractions in excess of 90 %. Finally, the base-catalyzed thiol-Michael reaction allowed for chain extension as a discrete step in the absence of crosslinking and facilitated a probe of chain extension in the context of what the modified Carothers equation predicted for a particular stoichiometry.

## 4.3 Materials and Methods

### 4.3.1 Materials

2,2-Dimethoxy-2-phenylacetophenone (DMPA, 99 %), 3-mercaptopropionic acid ( $\geq 99$  %), acryloyl chloride, ( $\geq 97$  %), potassium hydroxide solution (1N in water), *p*-toluenesulfonic acid monohydrate (ACS grade,  $\geq 98.5$  %), magnesium sulfate ( $\geq 98.0$  %), *N*-isopropylacrylamide (97%), methyl 3-mercaptopropionate (97%), 1,8-diazabicyclo[5.4.0]undec-7-ene (DBU, 98%), mesitylene (98%), 1 N aqueous potassium hydroxide solution, and tetrahydrofuran- $d_8$  ( $\geq 99.5$  atom %) (THF- $d_8$ ) with TMS were purchased from Sigma Aldrich and used as received. Bis(3-aminopropyl)-terminated poly(dimethyl siloxane) (PDMS-NH<sub>2</sub>) was purchased from Gelest (DMS-A12, DMS-A15, and DMS-A21), Sigma Aldrich ( $M_n \sim 2,500$  and  $\sim 27,000$  g/mol), and donated by Wacker Chemie (Wacker Fluid NH130D). Bis(hydroxyalkyl)-terminated PDMS was purchased from Gelest (DMS-C15 and DMS-C16) and Sigma Aldrich (reported  $M_n \sim 5,600$  g/mol). All PDMS precursors were dried at 100 °C under vacuum for 18 h before functionalization in order to remove cyclics. Chloroform- $d$  (CDCl<sub>3</sub>, 99.8 %) and benzene- $d_6$  (C<sub>6</sub>D<sub>6</sub>, 99.5 %) were purchased from Cambridge Isotope Laboratories, Inc. and used as received. Chloroform, tetrahydrofuran, dichloromethane (DCM), and toluene (all HPLC grade) were purchased from Fisher Scientific and used as received.

### 4.3.2 Competition study

*N*-Isopropylacrylamide (NIPAM, 0.1883 g, 1.66 mmol), methyl 3-mercaptopropionate (0.2000 g, 1.66 mmol), mesitylene (0.2000 g, 1.66 mmol), and DMPA (0.5 wt %, 1.942 mg, 7.58  $\mu$ mol) were added to a 20-mL scintillation vial and dissolved in THF (2.6 g). Five

drops of the homogeneous solution were added to six separate NMR tubes, and THF-*d*<sub>8</sub> was added to each tube to a consistent 40 mm liquid level. The tubes were mixed on a vortexer for 10 s each. Only three tubes were purged with argon for 3 min, and all were immediately capped and sealed with Parafilm<sup>®</sup>. <sup>1</sup>H NMR spectra were collected for each sample. Each tube was irradiated for 30 min at 100% output (Omniscure S2000 with 320-500 nm filter), and <sup>1</sup>H NMR spectra were collected for the irradiated samples. UV irradiation on the liquid samples was not measurable in this particular configuration. However, the reaction was allowed to proceed until there was insignificant change in NMR integrations at various time points after irradiation.

### **4.3.3 Preparation of thiol-ene product model compound**

N-isopropylacrylamide (NIPAM) (1.00 g, 8.84 mmol) methyl 3-mercaptopropionate (1.52 g, 12.62 mmol), chloroform (CHCl<sub>3</sub>) (4.00 g), and 1,8-diazabicyclo[5.4.0]undec-7-ene (DBU) (0.0961 g, 0.631 mmol) were added to a one-necked, 100 mL round-bottomed flask and allowed to stir for 1 h at room temperature. After stirring, the round-bottomed flask was attached to a distillation neck with two-necked round-bottomed flask at the receiving end and the second neck attached to a Shlenck line. Then, one-necked round-bottomed flask was heated to 50 °C with an oil bath, the two-necked round-bottomed flask was cooled to -78 °C, and vacuum was applied to the apparatus to distill off excess reagents

(e.g. methyl 3-mercaptopropionate, DBU, and  $\text{CHCl}_3$ ). Nitrogen was re-introduced into the distillation apparatus, which was then allowed to cool to room temperature.

$^1\text{H}$ ,  $^{13}\text{C}$ , COSY, HSQC, and HMBC.

#### **4.3.4 Synthesis of acrylamide-terminated poly(dimethyl siloxane) (PDMS-AA)**

A typical oligomer functionalization proceeded as reported previously.<sup>9</sup> Nomenclature for these oligomers includes both MW and endgroup identification. For example, PDMS1.8k-AA represents a 1,800 g/mol PDMS diacrylamide. Products include PDMS1.8k-AA, PDMS3.2k-AA, PDMS5.3k-AA, PDMS5.5k-AA, PDMS11.7k-AA, and PDMS30.6k-AA. Polymer chemical structure and percent acrylamide termination was verified according to our previous report,<sup>9</sup> with percent acrylamide termination ranging from 91 % to 99 %.

#### **4.3.5 Synthesis of thiol-terminated poly(dimethyl siloxane) (PDMS-SH).**

A typical oligomer functionalization proceeded as reported previously.<sup>9</sup> Nomenclature for these oligomers includes both MW and endgroup identification. For example, PDMS5.1k-SH represents a 5,100 g/mol PDMS dithiol. Products included PDMS1.2k-SH and PDMS5.1k-SH. Polymer chemical structure and percent thiol termination was verified according to our previous report,<sup>9</sup> with percent thiol termination ranged from 97 % to 100 %.

#### **4.3.6 Pre-extended oligomer preparation**

Various molar ratios of PDMS1.0K-SH and PDMS5.5K-AA totaling 2.0 g and chloroform (4.0 g) were added to a 2-dram scintillation vial equipped with magnetic stir bar. One drop of DBU was added to each vial and stirred at room temperature for 24 h. Chloroform was removed and each vial was dried at 50 °C *in vacuo* for 18 h before use.

#### **4.3.7 Preparation of samples for photocalorimetry and photorheology**

Various molar ratios of PDMS-SH and PDMS-AA, or neat PDMS-AA at various molecular weights, were weighed into a 2-dram scintillation vial, and all samples for a single study were prepared at once. Separately, DMPA (1.00 g) and chloroform (5.00 g) were weighed into a 6-dram scintillation vial and mixed with a vortexer for 10 s; this was designated the photoinitiator stock solution. Finally, a 10-, 25-, or 100-microliter syringe ensured the proper amount of photoinitiator stock solution to control DMPA loadings at 0.5 wt %. Finally, photoinitiated mixtures were mixed with a vortexer for 60 s until homogeneous and subsequently allowed to stand for 2 h to ensure the absence of bubbles.

#### **4.3.8 Analytical Methods**

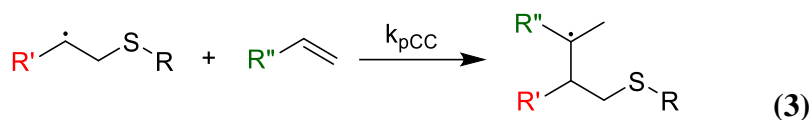
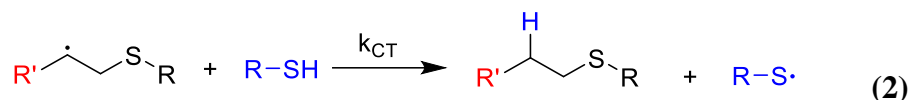
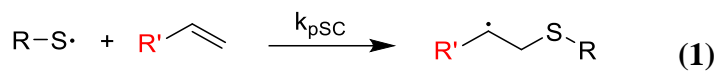
All  $^1\text{H}$ ,  $^{13}\text{C}$ , COSY, HMBC, and HSQC nuclear magnetic resonance (NMR) spectroscopy, except for the competition study, was performed on an Agilent U4-DD2 500 MHz NMR spectrometer with a 96 sample robot. The competition study was performed on a Bruker Avance II 500 MHz spectrometer equipped with a Prodigy nitrogen-cooled cryoprobe. Rheology, photorheology, and soxhlet extraction procedures were performed in accordance with our previous report.<sup>9</sup> Photocalorimetry was conducted on a TA

Instruments Q2000 differential scanning calorimeter (DSC) with the same photorheology light source (Omniscure S2000) coupled with fiber-optic waveguide. To enable comparison to the 3D printing process, samples were weighed into TA Instruments Tzero® sample pans at  $20 \pm 0.2$  mg, resulting in crosslinked films with  $\sim 180$   $\mu\text{m}$  thickness. This closely mirrored the VPP AM process, where individual layers possessed a 150  $\mu\text{m}$  thickness. Before placing the sample into the cell, UV intensity was measured with embedded sensors in the sample and reference cell posts. Once placed in the cell, samples were run in modulated DSC mode, equilibrated at 25 °C for 1 min, then irradiated at 8.0 mW/cm<sup>2</sup> for 6 min, and then held without UV irradiation for an additional 1 min to ensure proper return to baseline heat flow. Polymerization exotherms were determined upon integration of heat flow vs. time curves.

#### 4.4 Results and Discussion

The UV irradiation of a stoichiometric mixture of a dithiol and excess diacrylamide enables the formation of two primary products (assuming negligible disulfide formation).<sup>24,25</sup> First, the radical-mediated, thiol-ene reaction produces a thioether linkage via sequential chain-transfer/propagation reactions in a step-growth manner, which represents a chain extension event in this context. Second, the acrylamide moiety undergoes self-reaction, e.g. homopolymerization, which in this context represents a crosslinking event. Prevention of network plasticization occurs through proper choice of reaction stoichiometry, e.g. maintaining excess diacrylamide. Assuming negligible termination rates, **Equations 1-3** summarize reactions of generic thiols and enes and designate the appropriate rate constants.<sup>24,26,27</sup>





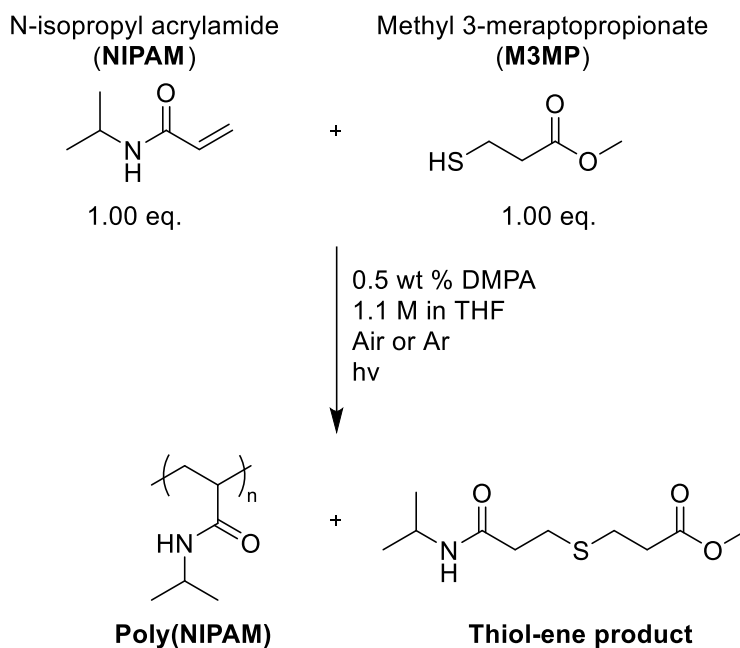
The formation of a thiyl radical occurs either via hydrogen abstraction from a thermal/photo initiator fragment or directly via irradiation with 254 nm light.<sup>24,25</sup> In the first step (**Equation 1**), a thiyl radical adds across an unsaturated C=C moiety, producing a carbon-centered radical, in a step that remains governed by the propagation rate constant for C=C addition to a thiyl radical ( $k_{pSC}$ ). This carbon-centered radical either chain-transfers back to a thiol ( $k_{CT}$ ) (**Equation 2**) or propagates across another unsaturated C=C moiety ( $k_{pCC}$ ) (**Equation 3**). Values of  $k_{pSC}/k_{CT}$  and  $k_{pCC}/k_{CT}$  for thiol-acrylate systems are reported as 13 and 1.5, respectively.<sup>24,27,28</sup> The  $k_{pCC}/k_{CT}$  ratio is commonly reported as its inverse, e.g.  $k_{CT}/k_{pCC}$  (called a  $C_s$  or  $C_x$  value). Bowman *et al.* previously reported the  $C_s$  value for a dithiol-diacrylate system as 0.67 (e.g. 1/1.5), which is close to the literature value of 0.66 for butane thiol and methyl methacrylate or 0.539 for dodecane thiol and *N*-*n*-octadecyl acrylamide.<sup>29-31</sup> Therefore, it follows that the ratio of the rate constant for thiyl radical propagation across a double bond to the homopolymerization rate constant is  $k_{pSC}/k_{pCC} \approx 9$ .<sup>26</sup> Thus, on the basis of propagation rate constants for similar thiol-acrylate systems and in the absence of diffusion, the thiol-ene reaction remains preferred to the acrylate homopolymerization by a factor of  $\sim 9$ .<sup>26,28</sup> Furthermore, polymerization in the presence of oxygen must be considered, as these telechelic dithiol/diacrylamide systems remain considered for vat photopolymerization (VPP), where printing in oxygen-free

environments presents a significant hassle as compared to printing in air. Fortunately, Bowman and coworkers previously found that the presence of even a small amount of thiol, when photocuring (meth)acrylates, is known to significantly diminish oxygen inhibition during homopolymerization, even in the case of thin films.<sup>26</sup>

Due to the lack of available data for acrylamides and carbonyl-containing thiols, where the latter exhibits more rapid rate constants for propagation and chain transfer to acrylate rate as compared to aliphatic thiols,<sup>26</sup> a monomeric competition study was performed to determine preference for the thiol-ene coupling reaction vs. homopolymerization reaction in a probe of inherent chemoselectivity, in the absence of diffusion. As shown in **Scheme 4.1**, irradiation of an equimolar mixture of N-isopropylacrylamide (NIPAM) and methyl 3-mercaptopropionate (M3MP) to complete NIPAM consumption afforded a mixture of the so-called *thiol-ene product* and poly(NIPAM). Given the equimolar starting material ratio, the ratio of products in this competition study provided the relative preference for chain extension vs. crosslinking, in the absence of diffusion. Furthermore, irradiation in both air and argon atmospheres gauged the effect of oxygen inhibition of photopolymerization.

In order to ensure proper spectroscopic identification of the various products, dedicated synthesis and subsequent analysis of the *thiol-ene product* provided the relevant <sup>1</sup>H NMR (**Figure 4.1**) and <sup>13</sup>C spectra (**Figure 4.7**), assigned with assistance from two-dimensional spectroscopy (**Figures 4.8-4.10**). As shown in the spectral overlay provided in **Figure 4.2**, the thiol-ene product remains identifiable via integration of the two methylene protons adjacent to the amide, while the thiol proton and unsaturated acrylamide protons enable identification of the NIPAM and M3MP starting materials, respectively.

Finally, due to polymer signal broadness, quantification of the poly(NIPAM) product occurred through integration of the single isopropyl methine proton for the post-irradiation spectrum, followed by subtraction of the portion of this integral caused by the *thiol-ene* product.



**Scheme 4.1.** Model competition study depicting the photo-irradiation of NIPAM and M3MP to afford a mixture of poly(NIPAM) and the thiol-ene product.

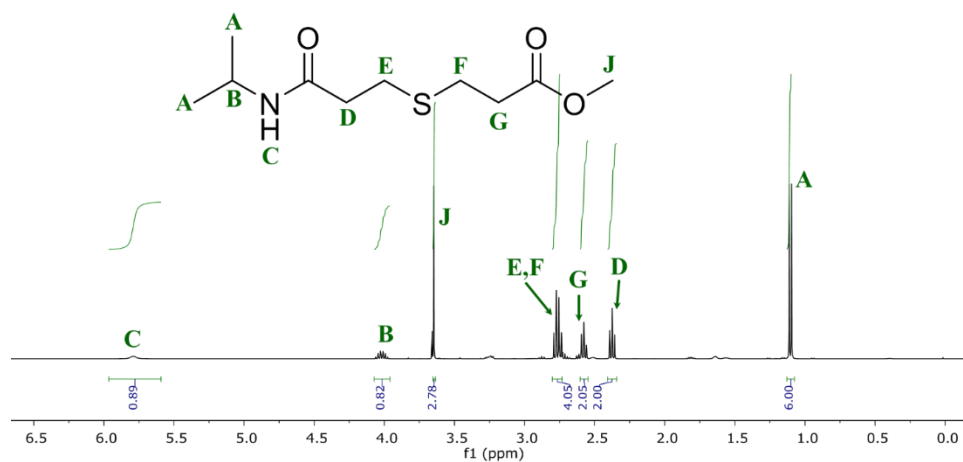


**Figure 4.1.** Proton nuclear magnetic resonance ( $^1\text{H}$  NMR) spectrum of the thiol-ene product in  $\text{CDCl}_3$ .

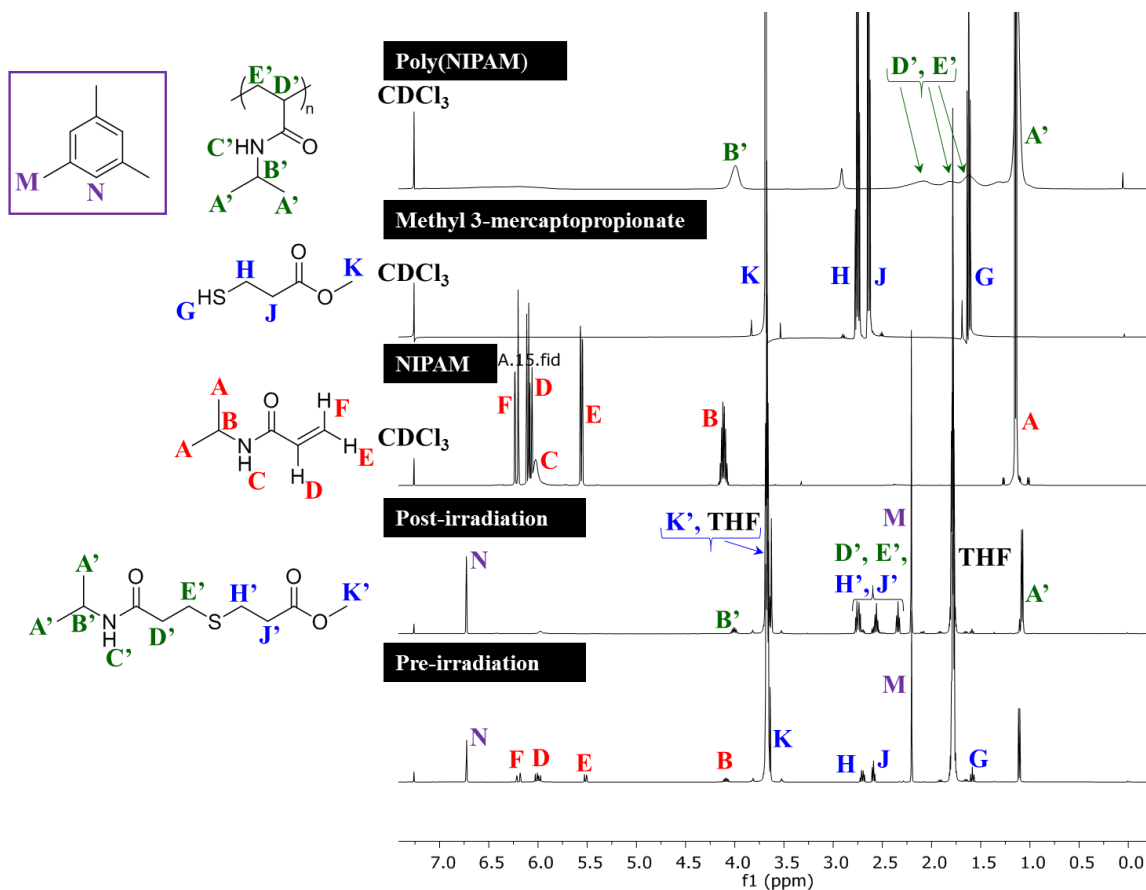


**Figure 4.2.**  $^1\text{H}$  NMR spectra of NIPAM, M3MP, and poly(NIPAM), as well as competition study mixture post-irradiation and pre-irradiation, relative to an internal standard (1 mol. eq. mesitylene).

**Figure 4.3** displays the results of this competition study in terms of mol. eq. of starting material or expected product, normalized to 1 mol. eq. of poly(NIPAM) + *thiol-ene product*. Upon complete NIPAM consumption, a small amount of M3MP thiol remains, e.g. 0.2-0.25 mol eq., similar to previous literature for stoichiometric thiol-acrylate polymerizations.<sup>24</sup> These results also indicate production of roughly 0.8 mol eq. of *thiol-ene product* in both air and argon atmospheres, thus demonstrating that roughly 4 out of 5 products are the *thiol-ene product* and 1 out of 5 products are poly(NIPAM). In other words, thiol-ene coupling out-competes acrylamide homopolymerization  $\sim 4:1$ . Therefore, upon exposure to UV light and subsequent generation of free radicals, these

particular functional groups clearly maintain a strong preference for thiol-ene coupling. In the context of dithiol- and diacrylamide-terminated PDMS oligomers for VPP, this indicates a strong preference for chain extension over crosslinking on a functional group level, e.g. in the absence of diffusion.

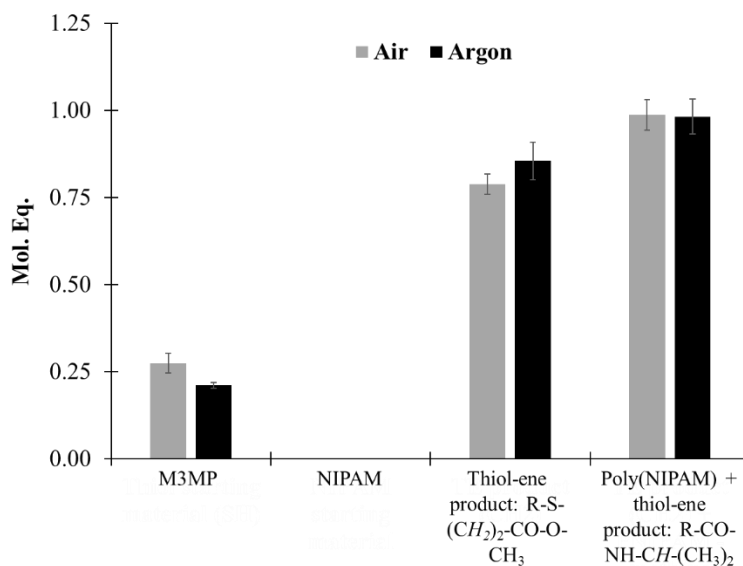
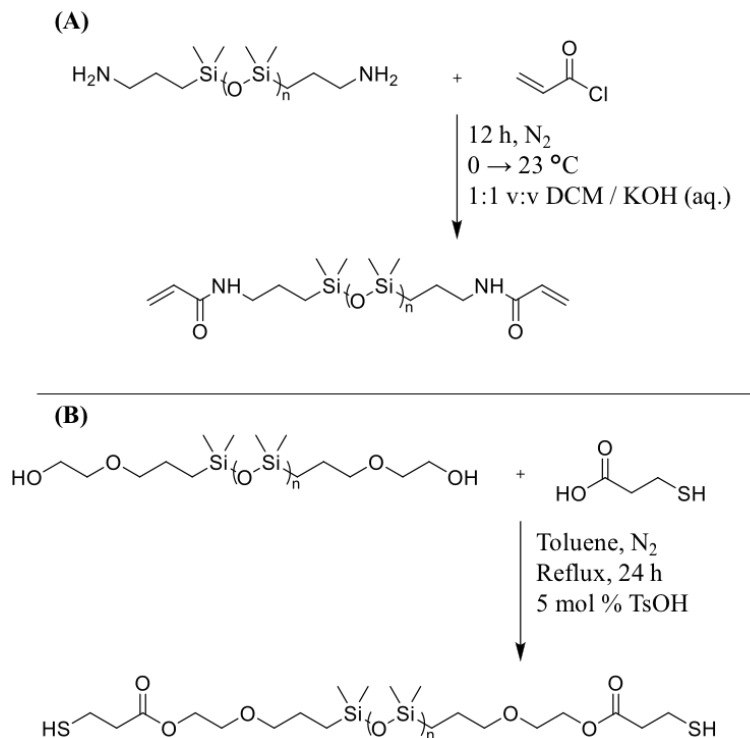


**Figure 4.3.** <sup>1</sup>H NMR spectroscopy depicts relative amounts of M3MP, NIPAM, thiol-ene product, and poly(NIPAM) relative to an internal standard (1 mol. eq. mesitylene) after irradiation with UV light to complete NIPAM consumption.



**Scheme 4.2.** (A) Functionalization of bis(3-aminopropyl)-terminated poly(dimethyl siloxane) (PDMS) to afford telechelic acrylamide-functional PDMS oligomers. (B) Functionalization of bis(hydroxyalkyl)-terminated PDMS to afford telechelic thiol-functional PDMS oligomers.

**Scheme 4.2** depicts the facile synthesis of acrylamide- and thiol-terminated PDMS oligomers from commercially-available amine- and carbinol-terminated precursors, as previously reported.<sup>9</sup> Photocuring behavior of the PDMS diacrylamides alone or dithiol/diacrylamide mixtures occurred via photorheology and photocalorimetry. Photorheology probed the storage modulus evolution as a function of UV irradiation time, with example data provided in **Figure 4.4A**. In these experiments, UV light irradiation begins at 30 s, with the storage modulus ( $G'$ ) surpassing the loss modulus ( $G''$ ) soon after UV irradiation commences. In this context, the  $G'/G''$  crossover point provides a rough indication of the gel point, given that these network polymers remain far above  $T_g$  (e.g. -123 °C for PDMS) at room temperature.<sup>32</sup> All systems examined in **Figure 4.4** attain  $G'/G''$

crossover within five seconds, indicating suitability for rapid layer cure times during the VPP AM process. Furthermore, these systems reach a storage modulus plateau ( $G_N^0$ ) at long UV irradiation times (e.g. 1-2 min).  $G_N^0$  also remains indicative of molecular weight between crosslinks ( $M_c$ ) for systems with high gel fractions and negligible network defects, e.g. dangling ends.<sup>33</sup> **Equation 4** displays the inverse relationship between  $G_N^0$  and  $M_c$ , which are related by the  $\rho$  (density),  $R$  (universal gas constant), and  $T$  (temperature).<sup>33</sup>

$$G_N^0 = \frac{\rho RT}{M_c} \quad \text{Equation 4}$$

**Figure 4.4B** depicts  $G_N^0$  and gel fraction vs. PDMS-AA oligomer  $M_n$  (via  $^1\text{H}$  NMR spectroscopy before photocuring) for PDMS-AA in the absence of the PDMS-SH chain extender, depicting a reduction in  $G_N^0$  with increasing PDMS-AA  $M_n$ , while all gel fractions remained  $\geq 90\%$ . **Figure 4.4C-F** depict photocuring of various mixtures of PDMS-SH and PDMS-AA with varying relative molecular weights, with the intent of determining the effect of diffusion limitation for one particular functional group on the resulting  $G_N^0$  or gel fraction. In other words, a terminal thiol or acrylamide functional group on a 1,000 g/mol polymer chain is less diffusion-limited than the same functional group on a 5,000 g/mol polymer chain, and is hypothesized to react more quickly in the case of the 1,000 g/mol oligomer molecular weight. Thus, the data in **Figure 4.4C-F** depicts the photocuring of all variations of binary mixtures of PDMS1.8k-AA, PDMS5.5k-AA, PDMS1.2k-SH, and PDMS5.1k-SH. **Figure 4.4C** depicts the photocuring of PDMS1.8k-AA and PDMS1.2k-SH, demonstrating more than an order-of-magnitude range in  $G_N^0$  through stoichiometry variation, while maintaining gel fractions  $\geq 90\%$ . **Figure 4.4F** depicts a similar case with for PDMS5.5k-AA and PDMS5.1k-SH, where both oligomers possess fairly equivalent

molecular weight. While gel fractions still remain  $\geq 90\%$  in this case, the range of  $G_N^0$  remains much narrower in this case, likely due to the higher precursor molecular weight.

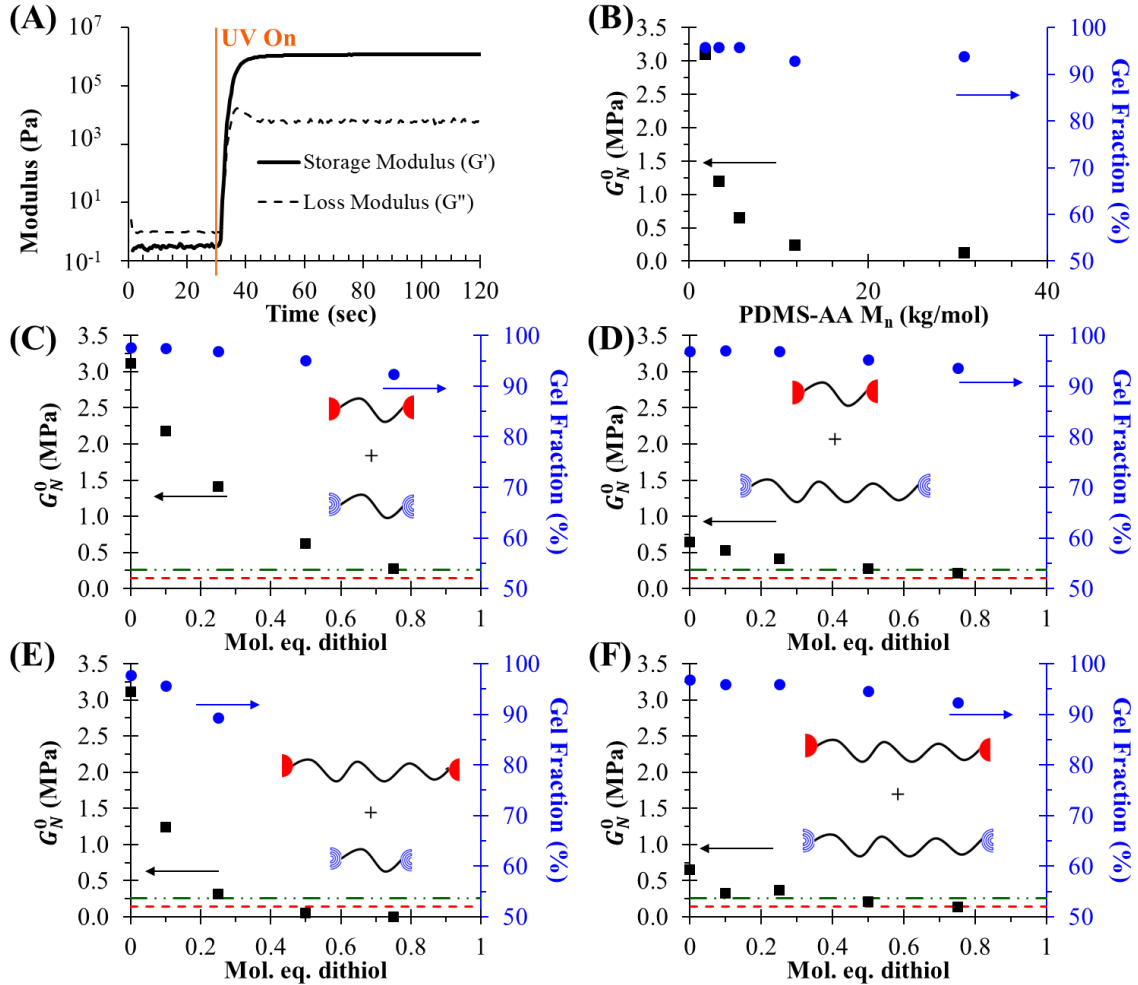


**Figure 4.4.** (A) Photorheology of neat PDMS-3.2k-AA, portraying storage ( $G'$ ) and loss ( $G''$ ) modulus versus UV exposure time (start at 30 s). (B-F)  $G'$  plateau modulus ( $G_N^0$ ) values (MPa) from photorheology and gel fraction (%) of photocured samples. (B)  $G_N^0$  versus PDMS-AA oligomer  $M_n$ . (C-F)  $G_N^0$  and gel fraction values versus mol. eq. dithiol for (C) PDMS1.2k-SH and PDMS1.8k-AA, (D) PDMS1.2k-SH and PDMS5.5k-AA, (E) PDMS5.1k-SH and PDMS1.8k-AA, and (F) PDMS5.1k-SH and PDMS5.5k-AA. Green dash-dot lines and the red dashed lines depict the  $G_N^0$  values for PDMS11.7k-AA and PDMS30.6k-AA, respectively.

**Figure 4.4E** depicts the photocuring of PDMS5.1k-SH and PDMS1.8k-AA, where the thiol functional groups remain more diffusion limited than the acrylamide functional



groups. Here, gel fractions drop precipitously with increasing dithiol content, indicating a lack of suitability for VPP AM. Finally, **Figure 4.4D** depicts the photocuring of PDMS1.2k-SH and PDMS5.5k-AA. Here, acrylamide functional groups remain relatively diffusion limited, providing preference for chain extension events. The green dash-dot lines and the red dashed lines depict the  $G_N^0$  values for PDMS11.7k-AA and PDMS30.6k-AA, respectively, which represent reference values for photocured PDMS-AA samples below and above the critical entanglement molecular weight ( $M_e$ ) for PDMS (e.g. 24,500 g/mol).<sup>34</sup> Based on these comparisons, multiple compositions achieved  $G_N^0$  values in between that measured for PDMS11.7k-AA and PDMS30.6k-AA while maintaining high gel fractions, indicating efficient chain extension and crosslinking.

**Figure 4.5A-D** depicts photocalorimetry data for the same samples analyzed above with photorheology. These data quantify heat flow as a function of UV irradiation time, with UV light on at 60 s. Integration of these exotherms, shown in **Figure 4.5E-H** provided the overall heat of reaction ( $Q$ ) as a function of dithiol content. Unfortunately, photorheology does not allow for deconvolution of acrylamide homopolymerization and thiol-ene coupling in this case, as each of these reactions possesses a different heat of reaction (e.g. ~100 kJ/mol for thiol-ene coupling<sup>35</sup> and 86 kJ/mol for acrylates<sup>36</sup>). Nonetheless, photocalorimetry enabled selection of binary systems according to trends in overall  $Q$  vs. dithiol content, as drastic decreases in  $Q$  with increasing dithiol content indicate overall decreasing amounts of chain extension + crosslinking. Photocalorimetry also enabled selection of samples according to their maximum rate of polymerization ( $R_{p,max}$ ), as the peak heat flow time in photocalorimetry corresponds to  $R_{p,max}$ . Heat flow vs. time data for all binary oligomeric mixtures demonstrated a shift in  $R_{p,max}$  towards

shorter times (e.g. closer to 60 s) even with the lowest level of thiol incorporation (e.g. 0.10 : 1.0 thiol:acrylamide). This remains in accordance with literature reports by Bowman *et al.*, where an increase in dithiol content for thiol-acrylate polymerizations increased the rate of acrylate functional group conversion.<sup>27</sup>

Photocuring of both PDMS1.2k-SH/PDMS1.8k-AA and PDMS5.1k-SH/PDMS5.5k-AA resulted in a slight decrease in overall  $Q$  with increasing dithiol content, again in accordance with the literature. Bowman and coworkers observed a decrease in thiol conversion and concomitantly smaller increase in acrylate conversion as dithiol/diacrylate stoichiometry approached unity, as the extra thiol present at 1:1 stoichiometry induced network plasticization.<sup>24</sup> Additionally, thiols act as a chain transfer agent for acrylate homopolymerization, reducing the kinetic chain length of the resulting polyacrylate chain as thiol:acrylate stoichiometry approaches 1:1.<sup>24</sup> The photocuring of PDMS5.1k-SH with PDMS1.8k-AA results in a drastic reduction in overall  $Q$  with increasing dithiol content (e.g. from ~70 to ~40 W/g), indicating much less overall chain extension and crosslinking as dithiol/diacrylamide stoichiometry approached unity. As the dithiol molecular weight remained much higher than the diacrylamide in this case, the functional group preference for thiol-ene coupling resulted in thiol-terminated, chain-extended oligomers, which did not possess the ability to crosslink, resulting in increased amounts of dangling ends. This remained consistent with the sharp reduction in gel fraction observed for this particular combination (**Figure 4.4E**). Lastly, photocuring of PDMS1.2k-SH with PDMS5.5k-AA resulted in consistent  $Q$  with increasing dithiol content, likely due to the ease with which PDMS1.2k-SH diffuses vs. PDMS5.5k-AA. Consequently, the 0.75 : 1.0 mixture of PDMS1.2k-SH : PDMS5.5k-AA was chosen for future experiments, as

well as for VPP AM in our previous work,<sup>9</sup> in order to maximize the diffusional preference for and amount of chain extension that occurred prior to crosslinking.

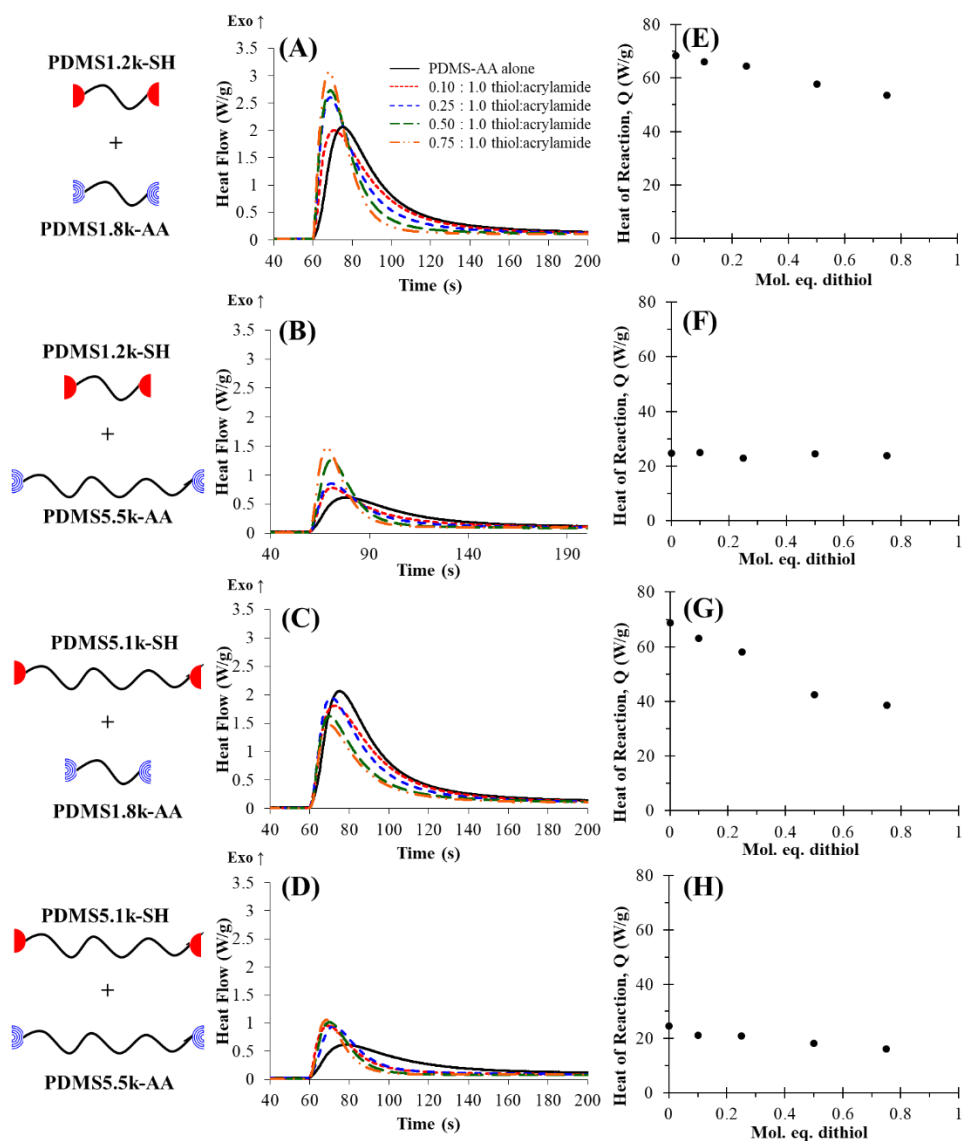
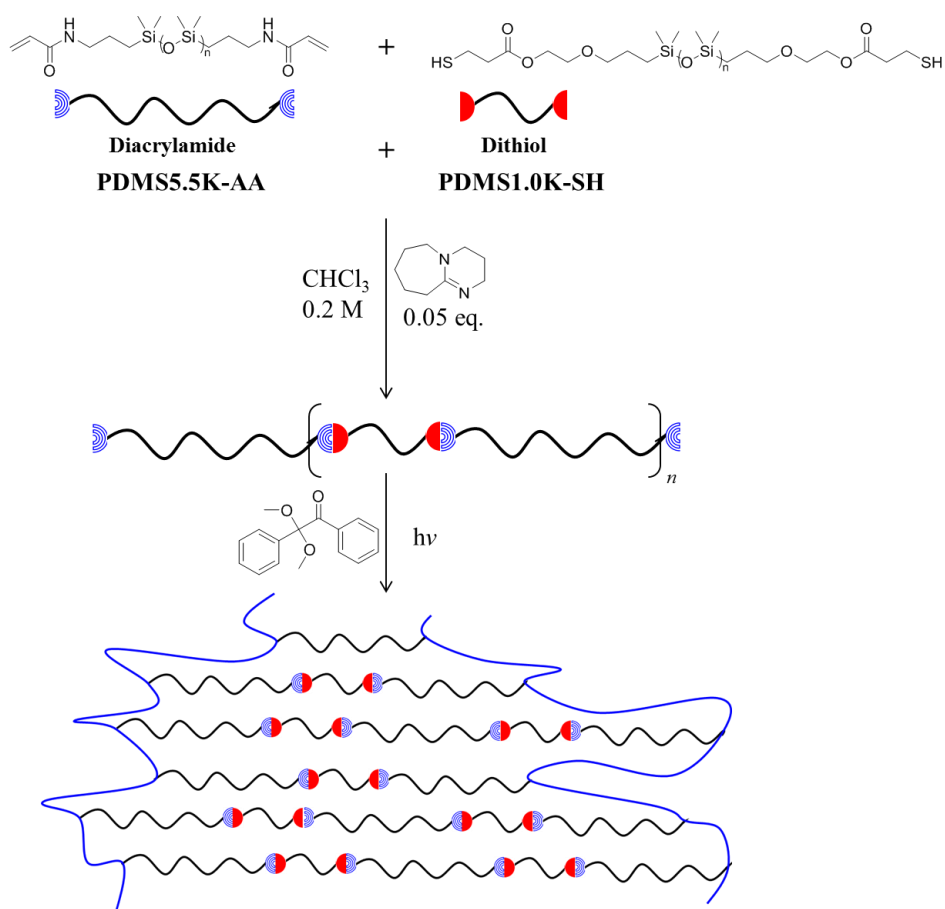


**Figure 4.5.** Photocalorimetry heat flow vs. time (A)-(D) and overall heat of reaction (E)-(H). All data is provided for (A),(E) PDMS1.2k-SH and PDMS1.8k-AA; (B),(F) PDMS1.2k-SH and PDMS5.5k-AA; (C),(G) PDMS5.1k-SH and PDMS1.8k-AA; and (D),(H) PDMS5.1k-SH and PDMS5.5k-AA.

Having selected an ideal composition for further photocuring and VPP AM, a subsequent study probed the degree of chain extension that occurred for the PDMS1.2k-SH

and PDMS5.5k-AA mixture. As shown in **Scheme 3**, a base-catalyzed, thiol-Michael reaction probed the amount of chain extension that occurred vs. thiol/acrylamide stoichiometry. This reaction yielded the same product as the radical-mediated thiol-ene reaction and did not induce acrylamide homopolymerization. Thus, the chain extension reaction reached equilibrium without being impeded by crosslinking. For stoichiometric combinations of PDMS1.2k-SH and PDMS5.5k-AA, the modified Carothers equation enabled prediction of the number of structural units (e.g. ‘monomers’), degree of polymerization, and expected  $M_n$  for a resulting polymer chain based on the given stoichiometry (**Equation 5**).<sup>37</sup>



**Scheme 4.3.** Synthesis and photocuring of chain extended oligomers via base-catalyzed thiol-Michael addition

$$X_n = \frac{1+r}{1-r} \quad (\text{Equation 5})$$

**Figure 4.6A** depicts photorheology data for the photocuring of both the simultaneous chain extension and crosslinking (open circles) and the base-catalyzed, chain-extended oligomers (closed circles). The base-catalyzed oligomers possessed a lower plateau modulus at a given stoichiometry, and  $G_N^0$  decreased with increasing mol. eq. dithiol. Provided for reference are  $G_N^0$  values for PDMS11.7K-AA and PMDS30.6K-AA, which represent crosslinked PDMS-AA below and above PDMS  $M_e$ , respectively. The highest levels of thiol incorporation, i.e. 0.75 mol. eq. dithiol, possessed a lower  $G_N^0$  than these two PDMS samples. The expected  $M_n$ , based on the modified Carothers equation, is shown as red squares in **Figure 4.6B**, and increased with increasing mol. eq. dithiol. The measured  $M_n$  of these pre-extended oligomers, as determined by  $^1\text{H}$  NMR spectroscopy, is shown as blue triangles. This also increased with increasing mol. eq. dithiol, but did not reach the level predicted by the Carothers equation, likely due to the presence of cyclics and/or imperfect oligomer difunctionality. Finally, the  $M_c$  calculated from  $G_N^0$ , using **Equation 4**, is shown as closed/open circles, respectively. **Figure 4.6C** shows  $G'/G''$  crossover time, indicating a rapid crossover for the simultaneous system (i.e.  $< 5$  s) but a slower crossover for the pre-extended oligomers, i.e.  $> 30$  s. This is likely due to the increase in viscosity of the pre-extended oligomers before photocuring (data not shown) and the decrease in acrylamide endgroup diffusion rate as a result. Finally, **Figure 4.6D** displays gel fraction as a function of increasing mol. eq. dithiol, demonstrating efficient photocuring ( $> 90\%$ ) for the simultaneous system but relative low gel fraction (as low as  $80\%$ ) for the pre-extended oligomers. These data suggest that only partial chain extension occurred in the simultaneous system. In other words, the oligomers did not extend to the

degree predicted by the modified Carothers equation, but extend only partially before diffusion limitations dominate and subsequent crosslinking occur.

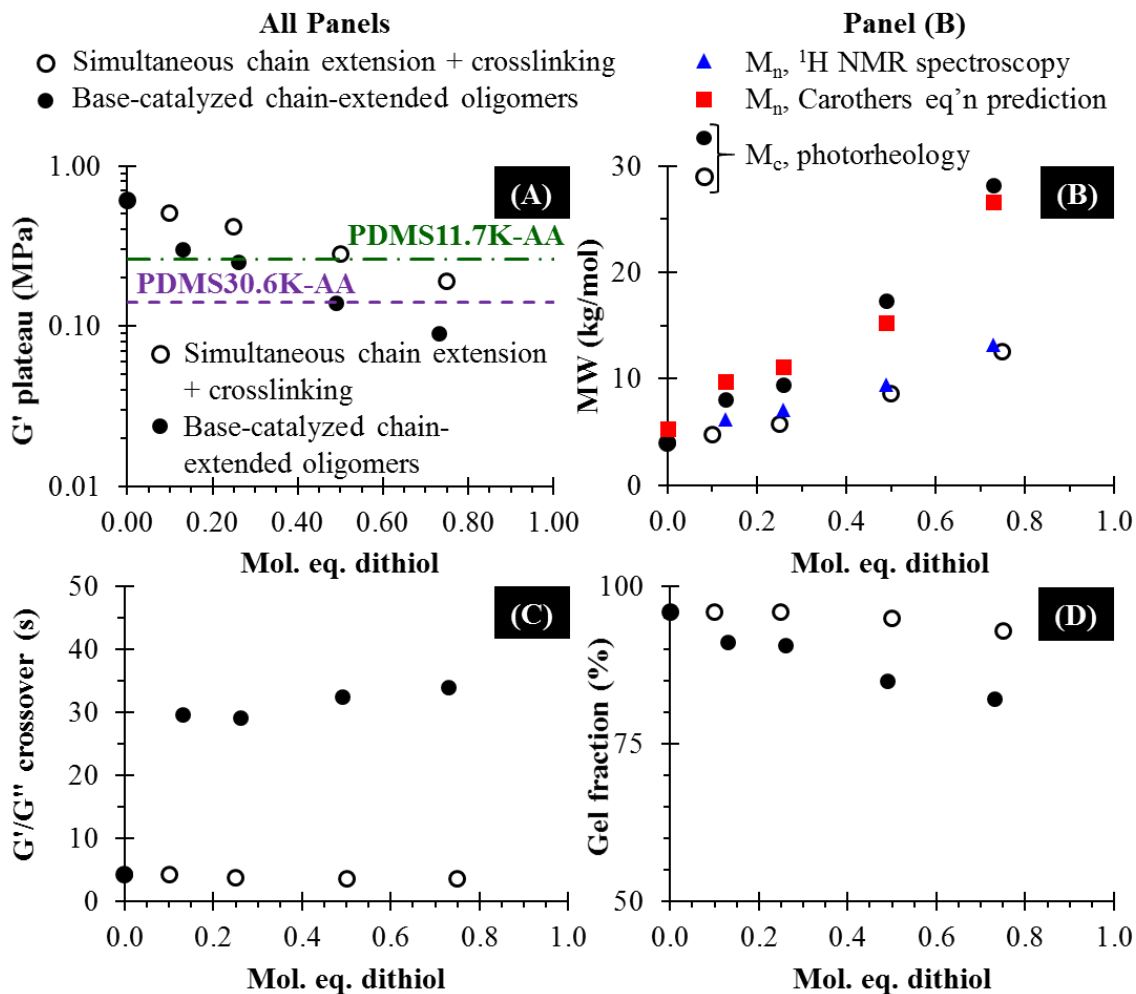


**Figure 4.6.** (A)  $G'$  plateau modulus from photorheology, (B)  $M_c$  from photorheology using eqn. (1) and  $M_n$  from  $^1\text{H}$  NMR spectroscopy and Carothers equation predictions prior to photocuring, (C)  $G'/G''$  crossover from photorheology, and gel fraction via soxhlet extraction of photorheology samples.

Interpretation of these data is also made clearer upon examination of relevant literature.<sup>24</sup> In a similar study by Bowman, *et al.* and with monomeric dithiols and diacrylates (i.e. 200 g/mol PEG diacrylate and 1,6-hexanedithiol), thiols served as both a chain extender and a chain transfer agent. In that system, an increase in dithiol content of

photocured monomeric mixtures afforded a reduction in rubbery modulus by a full order of magnitude and a reduction in network  $T_g$  from 26 °C to -43 °C. Bowman, *et al.* postulated that the chain transfer behavior of the thiol induced a lengthening of network strands and an increase in chain transfer (i.e. reduced polyacrylate kinetic chain length). Moreover, high levels of dithiol incorporation induced an increase in the number of dangling ends, resulting in overall network plasticization. The simultaneous system presented in our work is unique in that endgroup diffusion must be considered due to the oligomeric nature of the starting materials. Slight differences in functional group reactivity between these two systems also remains, e.g. acrylamides vs acrylates and aliphatic thiols vs. carbonyl-containing thiols,<sup>25,38</sup> but trends remain similar. From this examination, the final network structure for the simultaneous system presented here likely involves partial chain extension with a reduction in the polyacrylamide degree of polymerization. This remained in accordance with the conclusion of our previous work, which stated that the photocuring of PDMS1.2k-SH and PDMS5.5k-AA produced a resulting  $M_c$  of 12,600 g/mol while maintaining gel fractions in excess of 90 %.<sup>9</sup>

## 4.5 Conclusions

This report examined the synthesis and characterization of telechelic, dithiol- and diacrylamide-terminated PDMS oligomers that underwent simultaneous linear chain extension and crosslinking when diacrylamide moieties remained in excess. Presented as a continuation of our previous work,<sup>9</sup> this report examined previous hypotheses and separated chain extension and crosslinking events into discrete steps. A model compound competition study determined that thiol-ene product formation (e.g. thiol and acrylamide coupling) occurred preferentially to acrylamide homopolymerization at a 4:1 ratio. This

remained in accordance with relevant literature rate constants that dictated  $k_{pSC}/k_{pCC} \approx 9$  for similar thiol/acrylate systems. Photorheology and photocalorimetry probed storage modulus evolution and polymerization exotherm as a function of UV irradiation time, indicating maximum overall polymerization exotherm for a system containing a much lower MW dithiol than diacrylamide, e.g. PDMS1.2k-SH and PDMS5.5k-AA, which gave diffusional preference to the chain extension reaction. This system also possessed gel fractions  $\geq 90$  %, indicating efficient chain extension and crosslinking. Finally, a base-catalyzed thiol-Michael reaction enabled separation of the chain extension and crosslinking events into two discrete steps and established that chain extension did not occur to the degree predicted by the modified Carothers equation, for a given stoichiometry. Instead, partial chain extension occurred before endgroups became diffusion limited, at which point and acrylamide crosslinking dominated.

#### 4.6 Acknowledgements

The authors would like to acknowledge Wacker Chemie for their gracious donation of a 12 kg/mol bis(3-aminopropyl)-terminated PDMS (Wacker® Fluid NH 130 D).

#### 4.7 References

- (1) Peterson, G. I.; Schwartz, J. J.; Zhang, D.; Weiss, B. M.; Ganter, M. A.; Storti, D. W.; Boydston, A. J. *ACS Applied Materials & Interfaces* **2016**, *8*, 29037-29043.
- (2) Lee, M. P.; Cooper, G. J. T.; Hinkley, T.; Gibson, G. M.; Padgett, M. J.; Cronin, L. *Scientific Reports* **2015**, *5*, 9875.
- (3) Januszewicz, R.; Tumbleston, J. R.; Quintanilla, A. L.; Mecham, S. J.; DeSimone, J. M. *Proceedings of the National Academy of Sciences* **2016**.
- (4) Tumbleston, J. R.; Shirvanyants, D.; Ermoshkin, N.; Januszewicz, R.; Johnson, A. R.; Kelly, D.; Chen, K.; Pinschmidt, R.; Rolland, J. P.; Ermoshkin, A.; Samulski, E. T.; DeSimone, J. M. *Science* **2015**.
- (5) Peterson, G. I.; Larsen, M. B.; Ganter, M. A.; Storti, D. W.; Boydston, A. J. *ACS Applied Materials and Interfaces* **2015**, *7*, 577-583.
- (6) Thrasher, C. J.; Schwartz, J. J.; Boydston, A. J. *ACS Applied Materials & Interfaces* **2017**, *9*, 39708-39716.



- (7) Hegde, M.; Meenakshisundaram, V.; Chartrain, N.; Sekhar, S.; Tafti, D.; Williams, C. B.; Long, T. E. *Adv Mater* **2017**, *29*.
- (8) Sirrine, J. M.; Pekkanen, A. M.; Nelson, A. M.; Chartrain, N. A.; Williams, C. B.; Long, T. E. *Australian Journal of Chemistry* **2015**, *68*, 1409-1414.
- (9) Sirrine, J. M.; Meenakshisundaram, V.; Moon, N. G.; Scott, P. J.; Mondschein, R. J.; Weiseman, T. F.; Williams, C. B.; Long, T. E. *Polymer* **2018**.
- (10) Wu, A. S.; Small, W.; Bryson, T. M.; Cheng, E.; Metz, T. R.; Schulze, S. E.; Duoss, E. B.; Wilson, T. S. *Scientific Reports* **2017**, *7*, 1-6.
- (11) Schultz, A. R.; Lambert, P. M.; Chartrain, N. A.; Ruohoniemi, D. M.; Zhang, Z.; Jangu, C.; Zhang, M.; Williams, C. B.; Long, T. E. *ACS Macro Letters* **2014**, *3*, 1205-1209.
- (12) Ligon, S. C.; Liska, R.; Stampfl, J.; Gurr, M.; Mülhaupt, R. *Chemical Reviews* **2017**, *117*, 10212-10290.
- (13) Reeves, P.; Tuck, C.; Hague, R. In *Mass Customization: Engineering and Managing Global Operations*; Fogliatto, F. S., da Silveira, G. J. C., Eds.; Springer London: London, 2011, p 275-289.
- (14) Wallin, T. J.; Pikul, J. H.; Bodkhe, S.; Peele, B. N.; Mac Murray, B. C.; Therriault, D.; McEnerney, B. W.; Dillon, R. P.; Giannelis, E. P.; Shepherd, R. F. *Journal of Materials Chemistry B* **2017**, *5*, 6249-6255.
- (15) Wehner, M.; Truby, R. L.; Fitzgerald, D. J.; Mosadegh, B.; Whitesides, G. M.; Lewis, J. A.; Wood, R. J. *Nature* **2016**, *536*, 451-455.
- (16) Mondschein, R. J.; Kanitkar, A.; Williams, C. B.; Verbridge, S. S.; Long, T. E. *Biomaterials* **2017**.
- (17) Pekkanen, A. M.; Mondschein, R. J.; Williams, C. B.; Long, T. E. *Biomacromolecules* **2017**, *18*, 2669-2687.
- (18) Melchels, F. P. W.; Feijen, J.; Grijpma, D. W. *Biomaterials* **2010**, *31*, 6121-6130.
- (19) Melchels, F. P. W.; Feijen, J.; Grijpma, D. W. *Biomaterials* **2009**, *30*, 3801-3809.
- (20) Goyanes, A.; Buanz, A. B. M.; Basit, A. W.; Gaisford, S. *International Journal of Pharmaceutics* **2014**, *476*, 88-92.
- (21) Yue, J.; Zhao, P.; Gerasimov, J. Y.; van de Lagemaat, M.; Grotenhuis, A.; Rustema-Abbing, M.; van der Mei, H. C.; Busscher, H. J.; Herrmann, A.; Ren, Y. *Advanced Functional Materials* **2015**, *25*, 6756-6767.
- (22) Schüller-Ravoo, S.; Zant, E.; Feijen, J.; Grijpma, D. W. *Advanced Healthcare Materials* **2014**, *3*, 2004-2011.
- (23) Gibson, I.; Rosen, D.; Stucker, B. In *Additive Manufacturing Technologies: 3D Printing, Rapid Prototyping, and Direct Digital Manufacturing*; Springer New York: New York, NY, 2015, p 63-106.
- (24) Cramer, N. B.; Bowman, C. N. *Journal of Polymer Science Part A: Polymer Chemistry* **2001**, *39*, 3311-3319.
- (25) Hoyle, C. E.; Bowman, C. N. *Angewandte Chemie International Edition* **2010**, *49*, 1540-1573.
- (26) O'Brien Allison, K.; Cramer Neil, B.; Bowman Christopher, N. *Journal of Polymer Science Part A: Polymer Chemistry* **2006**, *44*, 2007-2014.
- (27) Cramer, N. B.; Reddy, S. K.; O'Brien, A. K.; Bowman, C. N. *Macromolecules* **2003**, *36*, 7964-7969.

- (28) Reddy Sirish, K.; Cramer Neil, B.; K, O. B. A.; Cross, T.; Raj, R.; Bowman Christopher, N. *Macromolecular Symposia* **2004**, *206*, 361-374.
- (29) Jordan Edmund, F.; Riser George, R.; Parker Winfred, E.; Wrigley, A. N. *Journal of Polymer Science Part A-2: Polymer Physics* **1966**, *4*, 975-996.
- (30) O'Brien, J. L.; Gornick, F. *Journal of the American Chemical Society* **1955**, *77*, 4757-4763.
- (31) Brandrup, J.; Immergut, E. H.; Grulke, E. A. *Polymer Handbook, 4th Edition*; Wiley, 1999.
- (32) Winter, H. H. *Polymer Engineering & Science* **1987**, *27*, 1698-1702.
- (33) Rubinstein, M.; Colby, R. H. *Polymer Physics*; OUP Oxford, 2003.
- (34) Yilgor, I.; Eynur, T.; Bilgin, S.; Yilgor, E.; Wilkes, G. L. *Polymer* **2011**, *52*, 266-274.
- (35) Müller, U.; Kunze, A.; Herzig, C.; Weis, J. *Journal of Macromolecular Science, Part A* **1996**, *33*, 439-457.
- (36) Bao, F.; Shi, W. *Progress in Organic Coatings* **2010**, *68*, 334-339.
- (37) Odian, G. *Principles of Polymerization*; 4th ed.; Wiley, 2004.
- (38) Northrop, B. H.; Coffey, R. N. *Journal of the American Chemical Society* **2012**, *134*, 13804-13817.

#### 4.8 Supporting Information

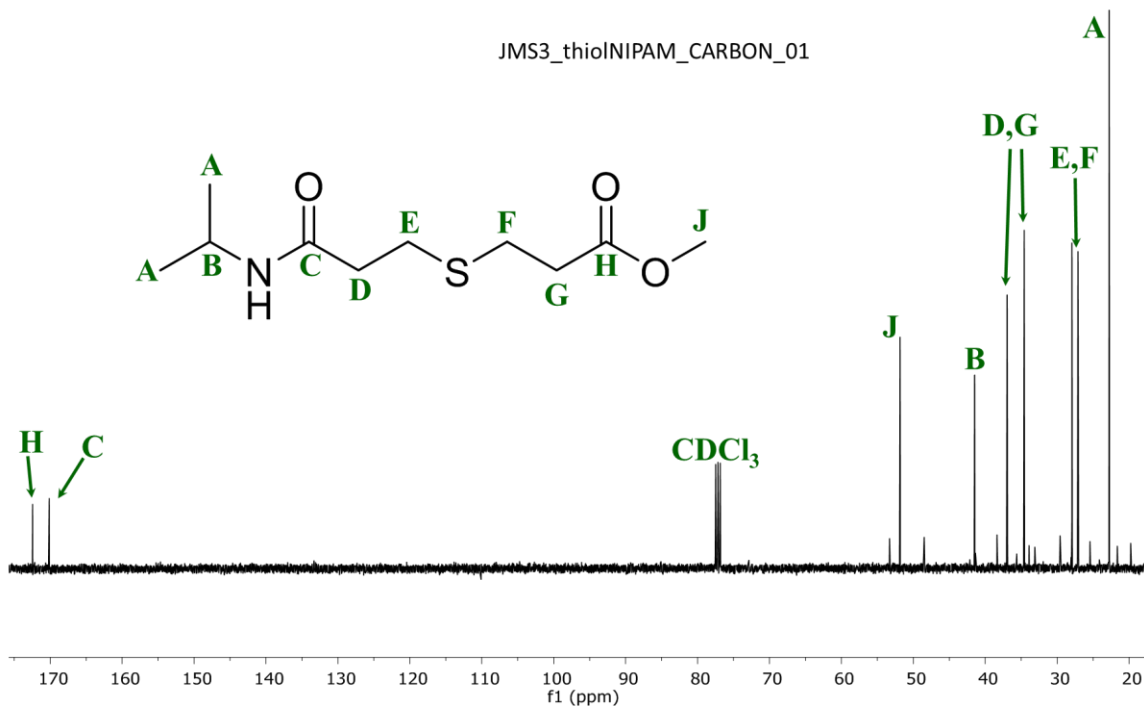
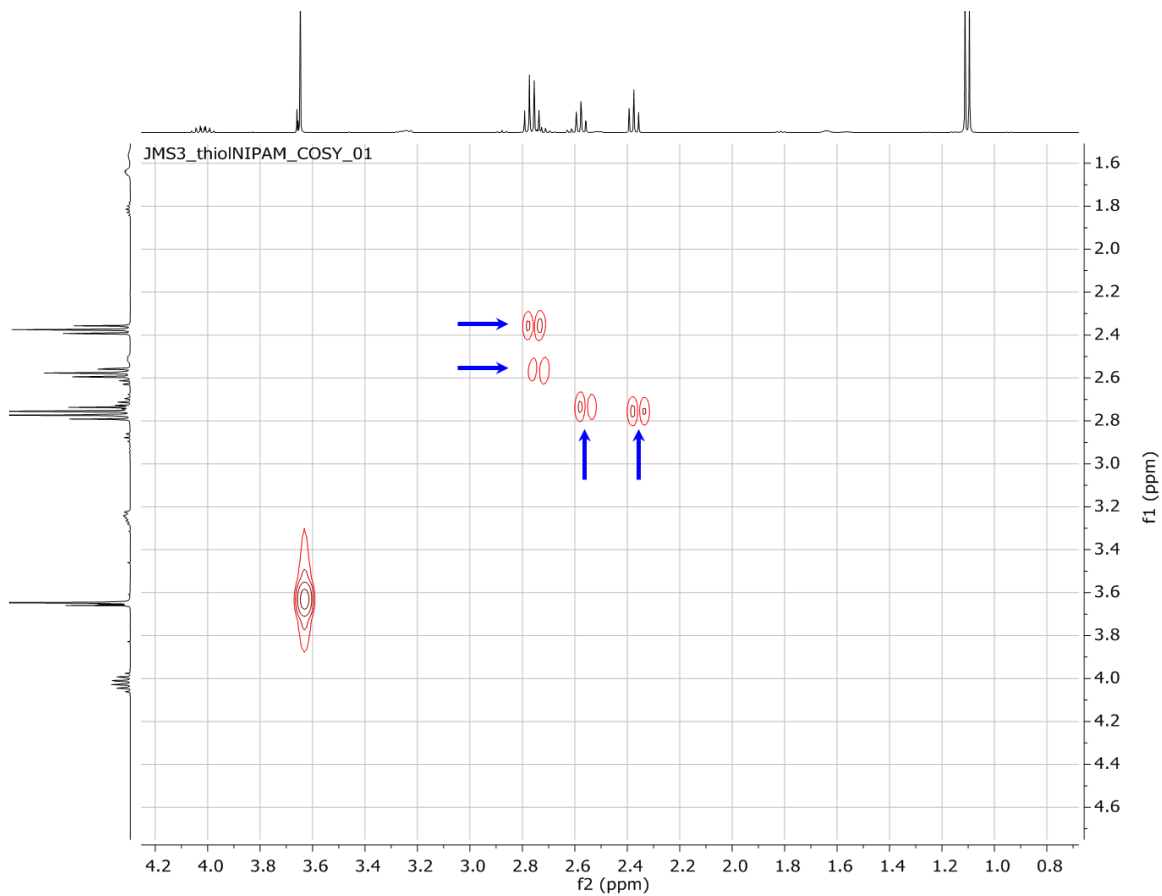
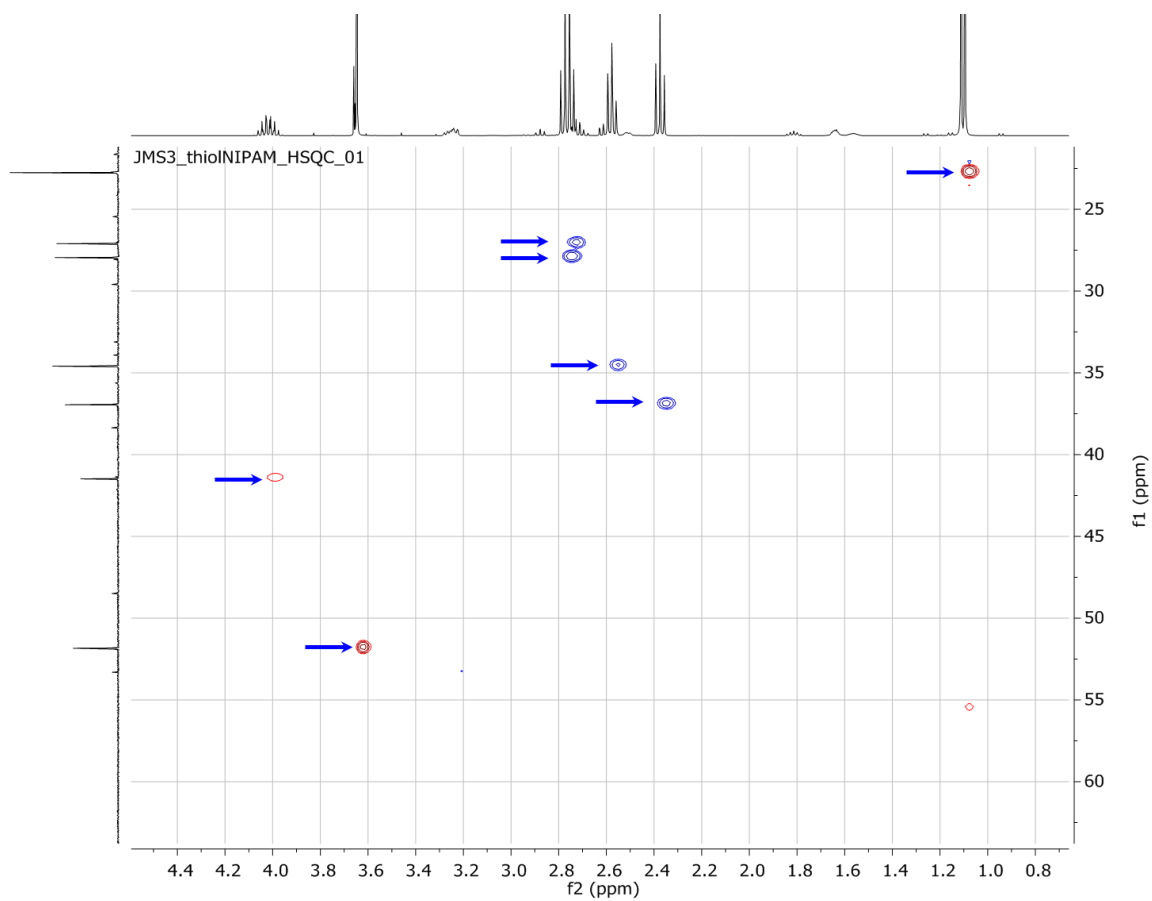


Figure 4.7.  $^{13}\text{C}$  spectrum of thiol-ene product in  $\text{CDCl}_3$



**Figure 4.8. COSY of the thiol-ene product in CDCl<sub>3</sub>**



**Figure 4.9.** HSQC of thiol-ene product in  $\text{CDCl}_3$

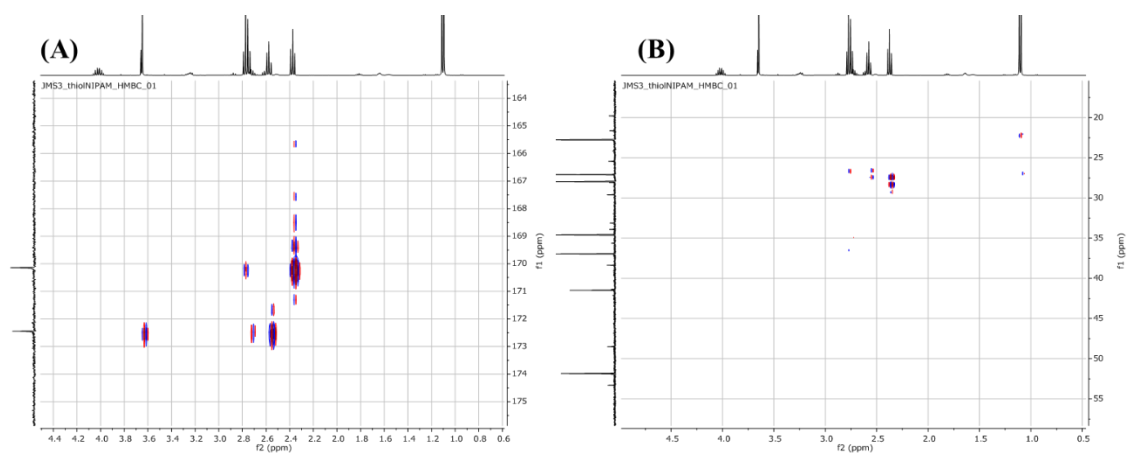


**Figure 4.10.** HMBC of thiol-ene product in  $\text{CDCl}_3$

## Chapter 5: **3D-Printing Amorphous Polysiloxane Terpolymers via Vat Photopolymerization**

Justin M. Serrine,<sup>a</sup> Alisa Zlatanic,<sup>†</sup> Viswanath Meenakshisundaram,<sup>b</sup> Christopher B. Williams,<sup>b</sup> Petar R. Dvornic,<sup>‡</sup> Timothy E. Long<sup>a,\*</sup>

<sup>a</sup> *Department of Chemistry, and* <sup>b</sup> *Department of Mechanical Engineering, Macromolecules Innovation Institute (MII), Virginia Tech, Blacksburg, VA 24061, USA*

<sup>†</sup> *Kansas Polymer Research Center and* <sup>‡</sup> *Department of Chemistry, Pittsburg State University, Pittsburg, KS 66762, USA*

### **5.1 Abstract**

Photocuring and vat photopolymerization (VP) additive manufacturing (AM) is demonstrated with two families of fully amorphous poly(dimethyl siloxane) (PDMS) terpolymers containing either diphenylsiloxy (DiPhS) or diethylsiloxy (DiEtS) repeating units. A thiol-functionalized PDMS crosslinker enabled rapid crosslinking in air using efficient thiol-ene addition. Differential scanning calorimetry and dynamic mechanical analysis confirmed the absence of crystallinity for the DiPhS-containing systems, while DMA showed a rubbery plateau extending to greater than 200 °C for the DiEtS-containing system. VP-AM of both photopolymer systems afforded well-defined 3D geometries, including high aspect ratio structures, which demonstrated feasibility of these photopolymers for the 3D-printing of unique geometric objects that require elastomeric performance to temperatures as low as -120 °C.

### **5.2 Introduction**

Polysiloxanes remain distinct among other synthetic polymers because of their unique combination of properties that result from inorganic  $-(\text{Si}-\text{O})_n-$  main chains and diverse organic pendant functionality. For example, polysiloxanes exhibit the lowest glass transition temperatures ( $T_g$ ) known to polymer science – e.g. -123 °C for poly(dimethyl siloxane)s (PDMS) and -145 °C for poly(diethyl siloxane)s (PDES).<sup>1</sup> They also exhibit

excellent chemical inertness, stability during ultraviolet (UV) radiation, low thermal conductivity, high gas permeability, high thermal and thermo-oxidative stability, low surface energies, and an unusually wide service temperature window.<sup>1-5</sup> Their extremely desirable low-temperature properties, in particular their pronounced elasticity, arise from their inherent chain flexibility derived from greater bond angles and bond lengths of Si–O–Si (150° and 1.645 Å) units compared to C–O–C units (113° and 1.412 Å), as well as from very low intersegmental interactions.<sup>1,2</sup> However, both PDMS and PDES remain susceptible to low-temperature crystallization (at ca. -40 to -50 °C and ca. -70 °C, respectively), which limits their useful service temperature range to approximately 10-20 °C above the highest transition temperature for elastomeric applications.<sup>6-11</sup> Thus, crystallization suppression represents an extremely attractive approach for improving low temperature properties of polysiloxane elastomers (e.g., for aerospace applications), which extends their use temperatures to their respective  $T_g$ s. As expected, the introduction of small amounts of randomly-placed, irregular repeating units sufficiently introduces asymmetry and effectively reduces crystallizability.<sup>6,12,13</sup> The literature provides many examples of this compositional effect.<sup>6,14-16</sup> Surprisingly, the addition of inorganic fillers (such as silica, zinc oxide, iron oxide) is known to accelerate polymer crystallization, rather than suppress, presumably due to fillers acting as nucleating agents.<sup>17</sup>

Recently, Zlatanic and Dvornic *et al.* reported the suppression of crystallization in PDMS through inclusion of only 3.6 mol % of statistically-distributed diphenylsiloxy (DiPhS) repeating units, or as low as 5 mol % of diethylsiloxy (DiEtS) units.<sup>6</sup> However, they also reported that during silanoate-initiated ring-opening polymerization (ROP), polymers containing DiPhS units underwent chain branching, producing phenyltrisiloxane

branch points in the polymer main chain with benzene serving as a leaving group. In contrast, polymers containing DiEtS repeating units did not show any branching under identical synthetic conditions, making this system more suitable for low temperature elastomer applications due to a decreased likelihood of non-load bearing, dangling chains in the networks. In addition to dimethylvinylsilyl- end groups, both of DiPhS- and DiEtS-containing terpolymers also possessed ca. 0.3 mol % of methylvinylsiloxy (MeViS) main-chain repeating units, providing a crosslinking functional greater than 2.0 for the resulting fully-amorphous polysiloxanes.<sup>6</sup> Furthermore, siloxane equilibration reactions occurred parallel to the ROP during synthesis and ensured randomization of the repeating units. The same authors also suggested a mechanism for the polymerization of DiMeS-DiPhS-containing polymers, which depicted  $(\text{DiMeS})_x$  and  $(\text{DiPhS})_y$  blocky structures initially forming upon ROP of octamethylcyclotetrasiloxane ( $\text{D}_4$ ) and octaphenylcyclotetrasiloxane ( $\text{D}_4^{\text{Ph}_2}$ ), and subsequent redistribution culminating in polymer products with single DiPhS units separated by extended PDMS segments at long reaction times (ca. 200 min).<sup>14</sup>

For the synthesis of elastomers, linear polysiloxane precursors either undergo covalent crosslinking, most commonly using free radical initiators, hydrosilylation or hydrolysis-condensation reactions,<sup>18-21</sup> or reinforcement with fillers, in order to improve mechanical properties.<sup>2,14,15</sup> Mechanical property improvements are also attainable with the synthesis of segmented, thermoplastic elastomers that undergo microphase separation, such as PDMS polyureas or PDMS-containing polyimides.<sup>3,22</sup> Thiol-ene reactions also provide an efficient method for polysiloxane crosslinking. This “click” reaction proceeds with rapid rates and high yields, insensitivity to water and oxygen (which both remain highly soluble in silicones),<sup>20,21</sup> mild conditions, and without the formation of by-

products.<sup>23</sup> Furthermore, the step-growth polymerization kinetics of thiol-ene reactions allows for higher overall conversions prior to vitrification as compared to typical addition polymerization (e.g. acrylates), which results in reduced polymerization shrinkage and improved network homogeneity.<sup>24</sup> Consequently, the thiol-ene reaction offers attractive advantages for covalently-crosslinked polysiloxane elastomers.<sup>25-31</sup>

The thiol-ene reaction has received wide attention in vat photopolymerization (VP) which is a class of layer-wise additive manufacturing (AM) that produces solid objects from liquid photopolymers upon irradiation with electromagnetic radiation (e.g., UV light).<sup>29,32-35</sup> In this application, thiol-ene addition also provides highly advantageous spatiotemporal control through formation of crosslinked networks only at the times and locations of direct UV exposure.<sup>33,36</sup> For example, a recent report from Serrine and Long *et al.* described simultaneous chain extension and crosslinking *via* thiol-ene coupling and acrylamide free radical homopolymerization, which enabled a relatively low viscosity photopolymer to provide properties of higher molecular weight precursors upon photocuring.<sup>31</sup> In another report, Wallin and Shepherd *et al.* demonstrated VP of poly(mercaptopropylmethylsiloxane-*co*-dimethylsiloxane) and  $\alpha,\omega$ -divinyl PDMS, resulting in products with strains at break over 400 % and actuatable printed objects.<sup>30</sup> However, the evaluation of sub-ambient thermal and mechanical properties of the final products were not reported earlier.<sup>32,31</sup>

To the best of our knowledge, the literature does not disclose any examples of 3D fabrication of ultra-low temperature elastomers. Here, we demonstrate rapid (within 5 s) photocuring of Zlatanic-Dvornic-type, DiPhS- or DiEtS-containing, fully amorphous siloxane oligomers with a thiol-functional PDMS at low photoinitiator content (e.g. 0.5 wt



%). Thermogravimetric analysis (TGA) probed thermal stability in nitrogen and in air, while differential scanning calorimetry (DSC) and DMA assessed low temperature transitions and thermal/thermomechanical properties. Most importantly, VP-AM enabled rapid construction of a variety of well-defined 3D geometries, while optical imaging provided visual confirmation of the resolution of printed structures for various printed objects.

### **5.3 Materials and Methods**

#### **5.3.1 Materials**

2,2-Dimethoxy-2-phenylacetophenone (DMPA, 99 %) diphenyl(2,4,6-trimethylbenzoyl)phosphine oxide (TPO, 97 %), and 2,5-Bis(5-tert-butyl-benzoxazol-2-yl)thiophene (BBOT) were purchased from Sigma Aldrich and used as received. Poly(mercaptopropylmethylsiloxane-*co*-dimethylsiloxane) random copolymer (PDMS7.4k-SH) was purchased from Gelest (SMS-042) and used as received. PDMS7.4k-SH possessed a manufacturer-reported  $M_n$  of 7,000 g/mol. It contained 5 mol % mercaptopropylmethylsiloxane repeating units, 95 mol % dimethylsiloxane repeating units, and a resulting, calculated value of 4.43 thiol functional groups per chain based on this  $M_n$  and compositional information.

#### **5.3.2 Synthesis and characterization of PDMS7.0k-DiPhS and PDMS7.5k-DiEtS**

All synthetic and characterization procedures for PDMS7.0k-DiPh and PDMS7.5k-DiEt are provided elsewhere.<sup>6,14</sup> Characterization included online determination of refractive index increment ( $dn/dc$ ), number-average molecular weight ( $M_n$ ), weight-average molecular weight ( $M_w$ ), dispersity ( $\mathcal{D}$ ), cyclic content (%), and Mark-Houwink parameters  $\alpha$  and  $K$ , *via* gel permeation chromatography (GPC). Iodine ( $I_2$ ) titration measured vinyl content as g  $I_2$  per 100 g polymer.

### 5.3.3 Determination of polymer vinyl and thiol content

Number of vinyl groups per polymer chain was calculated as depicted in **Equation 1**.

$$\# \frac{\text{vinyl}}{\text{polymer chain}} = \frac{I_{2,g,exp}}{I_{2,MW}} * \frac{M_{n,GPC}}{100} \quad (1)$$

This equation employs the iodine titration value in grams I<sub>2</sub> per 100 g polymer (I<sub>2,g,exp</sub>), the molecular weight of I<sub>2</sub> (I<sub>2,MW</sub>, 253.81 g/mol), a correction factor for the I<sub>2</sub> titration normalizing it per 1 g polymer (100), and the polymer M<sub>n</sub> as determined by light scattering detection with gel permeation chromatography (M<sub>n,GPC</sub>). This provided calculated vinyl/chain values of 2.39 for PDMS7.0k-DiPhS and 2.58 for PDMS7.5k-DiEt. The Gelest SMS-042 product possesses trimethylsilyl endgroups that show identical <sup>1</sup>H NMR spectral resonances as backbone dimethylsiloxane resonances. Therefore, the number of thiol groups per chain was calculated from manufacturer-provided theoretical molecular weight (7,000 g/mol) and theoretical mol % thiol (5 mol %). Two equations with two unknowns were formed, as shown in **Equation 2** and **Equation 3**.

$$\frac{DP_{SH}}{DP_{SH} + DP_{PDMS}} = 0.05 \quad (2)$$

$$7000 - 162.38 = DP_{SH} * 134.27 + DP_{PDMS} * 74.15 \quad (3)$$

These equations employ the degree of polymerization (DP) of the mercaptopropylmethylsiloxane monomer repeating unit (DP<sub>SH</sub>) or the dimethylsiloxane repeating unit (DP<sub>PDMS</sub>), and the molecular weights of the mercaptopropylmethylsiloxane repeating unit (134.27 g/mol), dimethylsiloxane repeating unit (74.15 g/mol), total polymer molecular weight (7,000 g/mol), and trimethylsilyl endgroups (162.38 g/mol).

### 5.3.4 Sample preparation for photocuring and 3D printing

PDMS7.4k-SH (SH) and PDMS7.0k-DiPh (DiPhS) or PDMS7.5k-DiEt (DiEtS) were added to 2-dram scintillation vials at stoichiometric functional group concentration

(e.g. 1:1 mol:mol based on functional groups per chain), totaling 2.50 g, and all samples for a single study were prepared at once. Separately, DMPA (1.00 g) and chloroform (4.00 g) were added to a 2-dram scintillation vial and homogenized with a vortexer for 20 s to form a photoinitiator stock solution. Then, a microliter syringe was used to add the proper amount of photoinitiator stock solution to the vortexed solutions such that DMPA loading occurred at 0.05, 0.1, 0.5, and 1.0 wt % for the SH/DiPhS and SH/DiEtS mixtures, totaling eight samples. Finally, photoinitiated mixtures were mixed with a vortexer for 20 s until homogeneous and subsequently allowed to stand at room temperature, covered with aluminum foil, for 2 h to ensure the absence of bubbles. Samples for TGA, DSC, and DMA were prepared by photocuring uniform films in a sandwich, structure depicted in **Figure 5.2**. Liquid photopolymer was deposited inside an aluminum shim of defined thickness, placed atop a glass plate and layer of siliconized PET (silicone-coated Mylar®). After placement of an additional layer of siliconized PET and glass atop these three bottom layers, the sandwich was photocured under a UV lamp (Hanovia med. pressure Hg lamp, PC 451050; Ace Glass photochemical safety cabinet; 120 V, 60 Hz, 450 W UV power supply) for 3 min on each side. Samples were used directly after film isolation from the photocuring sandwich.

### **5.3.5 Sample preparation for vat photopolymerization (VP)**

Preparation of samples for VP was identical to photorheology studies except that TPO was used as a photoinitiator at 0.5 wt % due to spectral differences between the printer light source (BlueWave® 75 UV spot curing lamp [Dymax 40078]) and the photorheology/photocalorimetry light source (Omniscure S2000). BBOT (0.1 wt %) was also added to the formulation to minimize cure-through during vat photopolymerization.

### 5.3.6 Analytical Methods

Proton nuclear magnetic resonance ( $^1\text{H}$  NMR) spectroscopy was performed using an Agilent U4-DD2 500 MHz NMR spectrometer and attached 96 sample robot. Photorheology was conducted on a TA Instruments DHR-2 rheometer with Smart Swap<sup>TM</sup> UV lower geometry, 20 mm quartz lower parallel plate, 20 mm aluminum upper parallel plate, and an Omnicure S2000 high-pressure mercury light source with equipped 320-500 nm filter. Samples were irradiated for 240 s at  $8.5 \text{ mW/cm}^2$ , after measuring UV light output with a Silverline radiometer. Data was gathered at a 500  $\mu\text{m}$  gap at 0.3 % strain, 1 Hz in “Fast Sampling” mode, enabling a  $2 \text{ s}^{-1}$  sampling frequency. UV irradiation commenced after 30 s of dark oscillatory measurement. The rheometer maintained an axial force of 0 N by making slight adjustments in gap thickness, removing effects of polymerization shrinkage. Shear storage plateau moduli ( $G_N^0$ ) were determined as an average of the last 30 s shear storage moduli ( $G'$ ) values.  $G'/G''$  crossover time points, where  $G''$  is loss modulus, were determined using the “modulus crossover” function in the accompanying TA Instruments TRIOS software. Soxhlet extraction by THF was used to determine gel fractions of photocured discs produced with the photorheology method. Soxhlet samples were dried for 18 h under reduced pressure at  $50 \text{ }^\circ\text{C}$ , weighed, extracted for 6 h by THF under reflux, dried for 18 h at  $50 \text{ }^\circ\text{C}$  under reduced pressure, and weighed again.

Photocalorimetry was conducted on a TA Instruments Q2000 differential scanning calorimeter (DSC) with the same light source as photorheology (Omnicure S2000) coupled with fiber-optic waveguide. To enable comparison to the 3D printing process, samples were weighed into TA Instruments Tzero<sup>®</sup> sample pans at  $20 \pm 0.2 \text{ mg}$ , resulting in

crosslinked films with ca. 180  $\mu\text{m}$  thickness. This closely mirrored the 3D printing process, where individual layers had a 150  $\mu\text{m}$  thickness. Before placing the sample into the cell, UV intensity was measured with embedded sensors in the sample and reference cell posts. Once placed in the cell, samples were analyzed in modulated DSC mode, equilibrated at 25  $^{\circ}\text{C}$  for 1 min, then irradiated at 8.0  $\text{mW}/\text{cm}^2$  for 6 min, and then held without UV irradiation for an additional 1 min to ensure proper return to baseline heat flow. Polymerization exotherms were determined upon integration of heat flow vs. time curves. Standard DSC temperature ramps were performed with a separate TA Instruments Q200 DSC equipped with liquid nitrogen cooling system (LNCS) which probed thermal transitions under constant heating/cooling rates of 10  $^{\circ}\text{C}/\text{min}$  and helium purge. Thermogravimetric analysis (TGA) was performed with a TA Instruments Q500 TGA at a heating rate of 10  $^{\circ}\text{C}/\text{min}$  under constant  $\text{N}_2$  purge. Dynamic mechanical analysis (DMA) was performed with a TA Instruments Q800 equipped with liquid nitrogen gas cooling accessory (GCA) and operated in oscillatory tension mode at 1 Hz, 0.1 % strain, and 3  $^{\circ}\text{C}/\text{min}$  heating after equilibration and 5 min isotherm at -150  $^{\circ}\text{C}$ . A Jeol NeoScope JCM-5000 scanning electron microscope (SEM) imaged 3D objects at 10 kV accelerating voltage. 3D objects were mounted directly onto the SEM sample stage and immediately imaged; no conductive sputter coating was required.

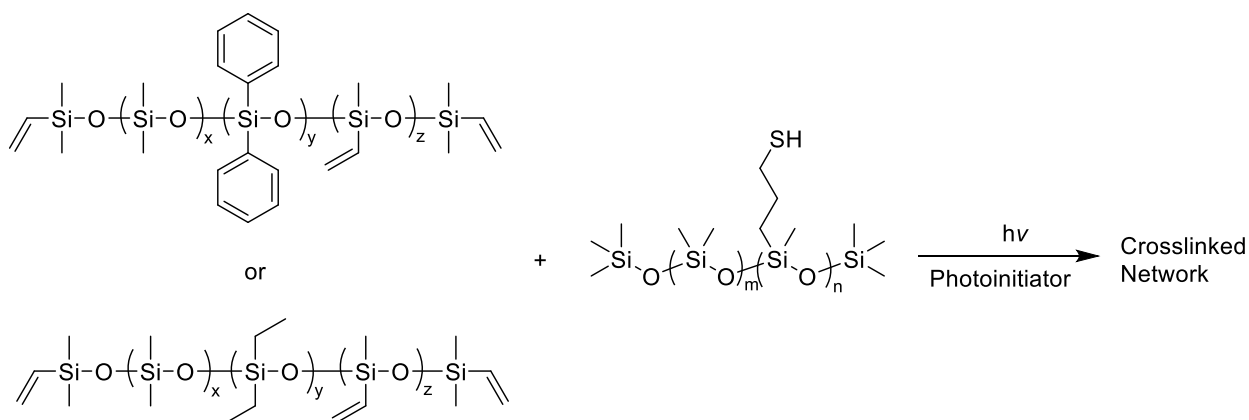
### **5.3.7 Vat Photopolymerization (VP)**

All VP information, including methods for generating the photopolymer working curve, is provided elsewhere.<sup>33,37</sup>

## **5.4 Results and Discussion**

The literature provides many examples that describe the use of thiol-ene chemistry for photocuring of polysiloxanes. Müller and Weis *et al.* described the photo-induced

radical crosslinking of an  $\alpha,\omega$ -ene-terminated polysiloxane with vinylsilyl end-groups and a thiol-containing polysiloxane, which showed nearly 100 % thiol and 98 % ene functional group consumption and a first-order, linear relationship between the reaction rate ( $R_p$ ) and the incident light intensity when stoichiometric mixtures were reacted in air.<sup>25</sup> The system did not undergo ene homopolymerization, as indicated with copolymerization parameter products ( $r_1 \cdot r_2$ ) that were lower than  $10^{-3}$ , which is a value typical for copolymerizations yielding alternating copolymer products.<sup>27,38</sup> The enthalpy of thiol-addition across the olefin used was calculated from Hess's Law and measured using DSC, providing values of 121 kJ/mol and 93 kJ/mol, respectively.<sup>27</sup> Experimentally determined reaction enthalpy values were consistently lower than calculated ones, likely due to incomplete conversion of ene groups. In another report, Cramer and Bowman described the carbon-centered radical termination process in the presence of air (e.g. oxygen), where growing polymer chains were oxidized to peroxy radicals, which subsequently underwent hydrogen transfer to regenerate thiyl radicals.<sup>39</sup> Although these conditions likely reduce photoinitiator efficiency,  $R_p$  remained largely the same in air as well as in oxygen-free environments.<sup>39</sup>



**Scheme 5.1.** Crosslinking of amorphous 7.0k-DiPhS- or 7.5k-DiEtS-containing terpolysiloxanes with 7.0k-SH crosslinker and UV light in the presence of photoinitiator.

**Scheme 5.1** represents the UV-initiated curing of DiPhS- and/or DiEtS-containing terpolysiloxanes used in this work with a thiol-containing siloxane oligomer in the presence of a DMPA photoinitiator. Terpolymer compositions and characterization information are summarized in **Table 5.1** and **Table 5.2**, respectively, and since trimethylsilyl end-groups of PDMS7.4k-SH could not be distinguished in <sup>1</sup>H NMR from dimethylsiloxy backbone resonances, the thiol content was accepted from manufacturer-provided information. The reaction was evaluated in stoichiometric mixtures of DiPhS- and DiEtS-containing terpolymers and SH crosslinker, by photocalorimetry and photorheology as a function of photoinitiator concentration.

**Table 5.1.** Compositions of amorphous siloxane terpolymers used

Sample	Composition (theoretical)			
	DiMeS	DiPhS	DiEtS	MeViS
	mol %	mol %	mol %	mol %
PDMS7.0k-DiPhS	96.1	3.6	0.0	0.3
PDMS7.5k-DiEtS	94.7	0.0	5.0	0.3

**Table 5.2.** Selected characterization data for siloxane terpolymers of **Table 5.1**.

Sample	M <sub>n</sub> , theor	GPC					MHS parameters		Iodine value		Vinyls per chain	Dynamic viscosity at 25 °C
		dn/dc (online)	M <sub>n</sub>	M <sub>w</sub>	D	Cyclic content	α	K	Theor.	Exp.	Based on I <sub>2</sub> exp and M <sub>n</sub> , GPC	
		g/mol	mL/g	g/mol	g/mol	-	%	-	mL/g	g I <sub>2</sub> /100g	g I <sub>2</sub> /100g	
PDMS7.0k- DiPh	7069	-0.071	7042	12140	1.72	1	0.676	0.0148	8.0	8.6	2.39	0.21
PDMS7.5k- DiEt	6937	-0.086	7517	11110	1.48	2	0.692	0.0131	8.6	8.7	2.58	0.16

**Figure 5.1A** depicts polymerization exotherms from the photocalorimetry of DiPhS + SH system, plotted as heat flow vs. time. Integration of these curves yielded

overall polymerization exotherm, which remained nearly constant at 12-13 W/g as a function of photoinitiator concentration for all samples tested (data not shown). **Figure 5.1B** displays time of heat flow maximum (sec), corresponding to the maximum rate of polymerization ( $R_p^{\max}$ ), as a function of photoinitiator concentration, which reached a plateau value at the highest photoinitiator concentrations (ca. 1 wt %), consistent with trends described in the literature.<sup>37</sup> **Figure 5.1C** shows shear storage modulus ( $G'$ ) as a function of irradiation time from photorheology of the DiPhS + SH system, reaching a plateau value ( $G_N^0$ ) more rapidly with increasing photoinitiator concentration. Finally, **Figure 5.1D** presents storage ( $G'$ ) and loss ( $G''$ ) modulus crossover, which was shown earlier to indicate gel point for stoichiometrically balanced systems far above  $T_g$ ,<sup>40</sup> as a function of photoinitiator concentration. It was clear that  $G'/G''$  reached a plateau value at higher DMPA concentrations, similar to the plateau in  $R_p^{\max}$ . Thus, in order to limit termination events and maximize UV penetration depth in the photopolymer, the lowest possible DMPA concentration that maximized  $R_p^{\max}$  and minimized modulus crossover  $G'/G''$  time was chosen for VP-AM (e.g. 0.5 wt %).



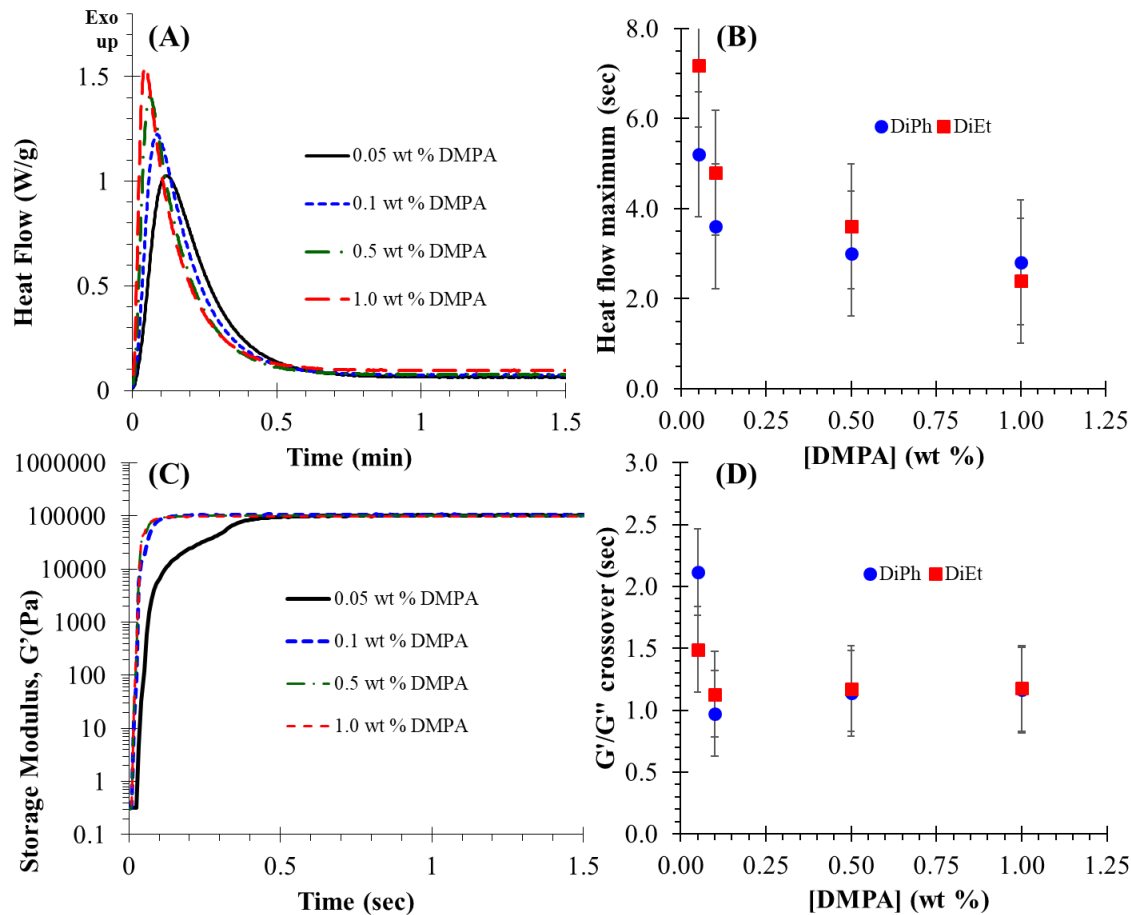


**Figure 5.1.** (A) Heat flow vs. time from photocalorimetry at 25 °C, with UV light on at 0 min, as a function of photoinitiator (DMPA) concentration. (B) Time at peak heat flow from (A) vs. photoinitiator concentration. (C)  $G'$  vs. time from photorheology, with UV light on at 0 min. (D)  $G'/G''$  crossover time from photorheology as a function of photoinitiator concentration. Error bars represent standard deviation.

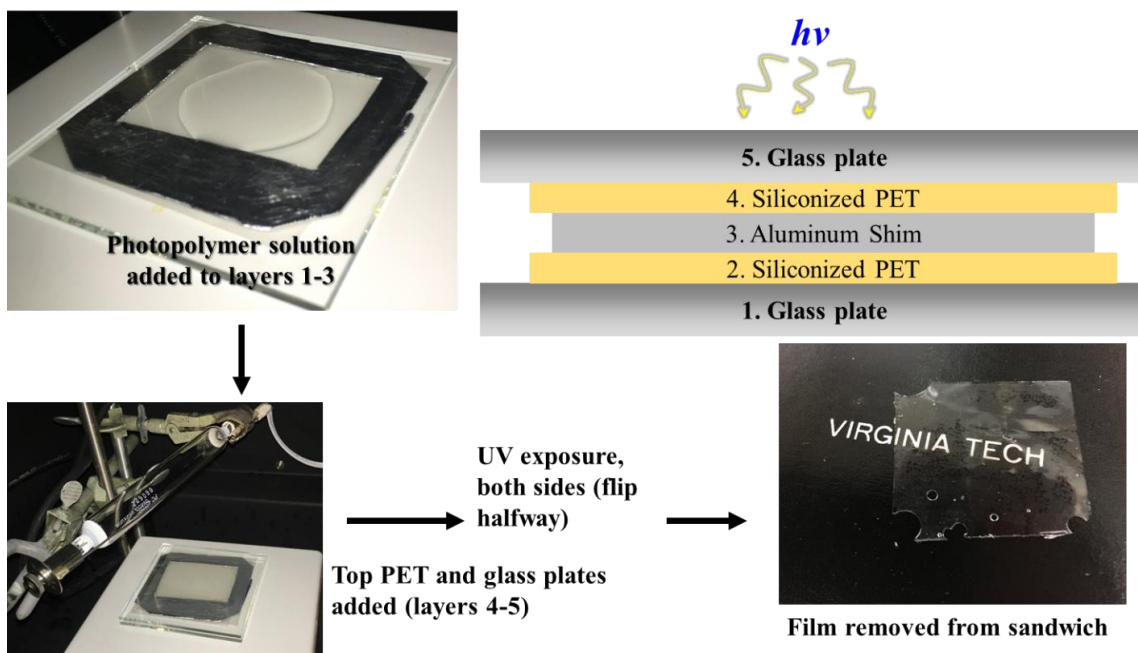


**Figure 5.2.** Photocuring assembly and procedure that provided uniform films of consistent thickness.

Thermal and thermomechanical properties of photocured siloxane networks were evaluated on films made using the sandwich geometry shown in **Figure 5.2**, which enabled production of free-standing films of uniform thickness. Soxhlet extraction of photocured films with THF indicated gel fractions ranging from 85-88 wt % for all samples, but also resulted in film cracking, which precluded their thermomechanical analysis, a sensitive measure of polymer crystallinity. As a consequence, unextracted films were used in the following analyses.

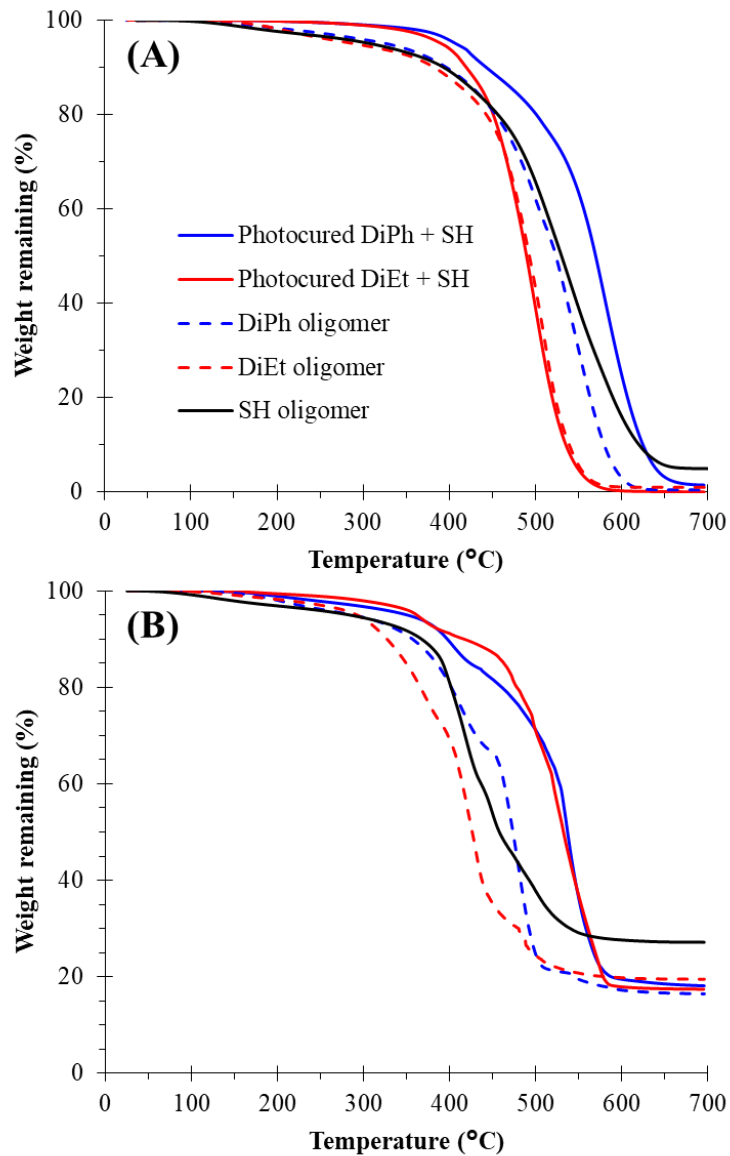


**Figure 5.3.** TGA of photocured DiPhS + SH and DiEtS + SH films overlaid with neat DiPhS- and DiEtS-containing terpolymers and SH crosslinker in nitrogen (A) and air (B).

In nitrogen, TGA traces (see **Figure 5.3A**) showed higher five-percent-weight-loss temperature ( $T_{d,5\%}$ ) for photocured DiPhS + SH sample ( $T_{d,5\%} = 408$  °C) than for the photocured DiEtS + SH ( $T_{d,5\%} = 390$  °C), with both being higher than the corresponding temperatures for neat DiPhS- and DiEtS-containing terpolymers. In air, **Figure 3B**, both photocured DiPhS + SH and DiEtS + SH samples exhibited thermal stabilities within the error of the instrument, showing  $T_{d,5\%}$  values of ca. 350 °C and 360 °C, respectively, also

significantly higher than the corresponding  $T_{d,5\%}$  values for neat oligomers. As expected, thermal stabilities of both photocured networks were higher in nitrogen than in air, and weight residues at the highest temperature tested in air, was ca. 20 wt %, consistent with the well-known thermal behavior of PDMS.<sup>1,41</sup> In nitrogen, the ultimate weight residues were negligible, also consistent with the available literature data.<sup>1,41,42</sup>

**Figure 5.4A** and **4B** display 1<sup>st</sup> heat DSC traces for photocured films of DiPhS + SH and DiEtS + SH, respectively, together with data for the corresponding neat oligomers. While all values fall within the experimental error of the DSC method, both photocured crosslinked networks displayed slightly higher  $T_g$ s than their neat oligomers, consistent with the relatively low molecular weights of the later and the more pronounced restrictions on the long-range segmental chain motions expected in covalently crosslinked networks from such precursors. The photocured DiEtS + SH films displayed slightly lower  $T_g$ s than films from the DiPhS + SH system, likely due to the lower  $T_g$  of the neat DiEtS-containing terpolymer relative to the DiPhS-containing one (e.g., -128 °C vs. -121 °C, respectively). All samples demonstrated insensitivity to photoinitiator concentration, probed at the extremes of its values with photocalorimetry and photorheology. Furthermore, samples did not display any evidence of crystallinity, or any thermal transitions between  $T_g$  and 25 °C, where endo/exotherms characteristic for polysiloxane crystallization or melting would otherwise appear.

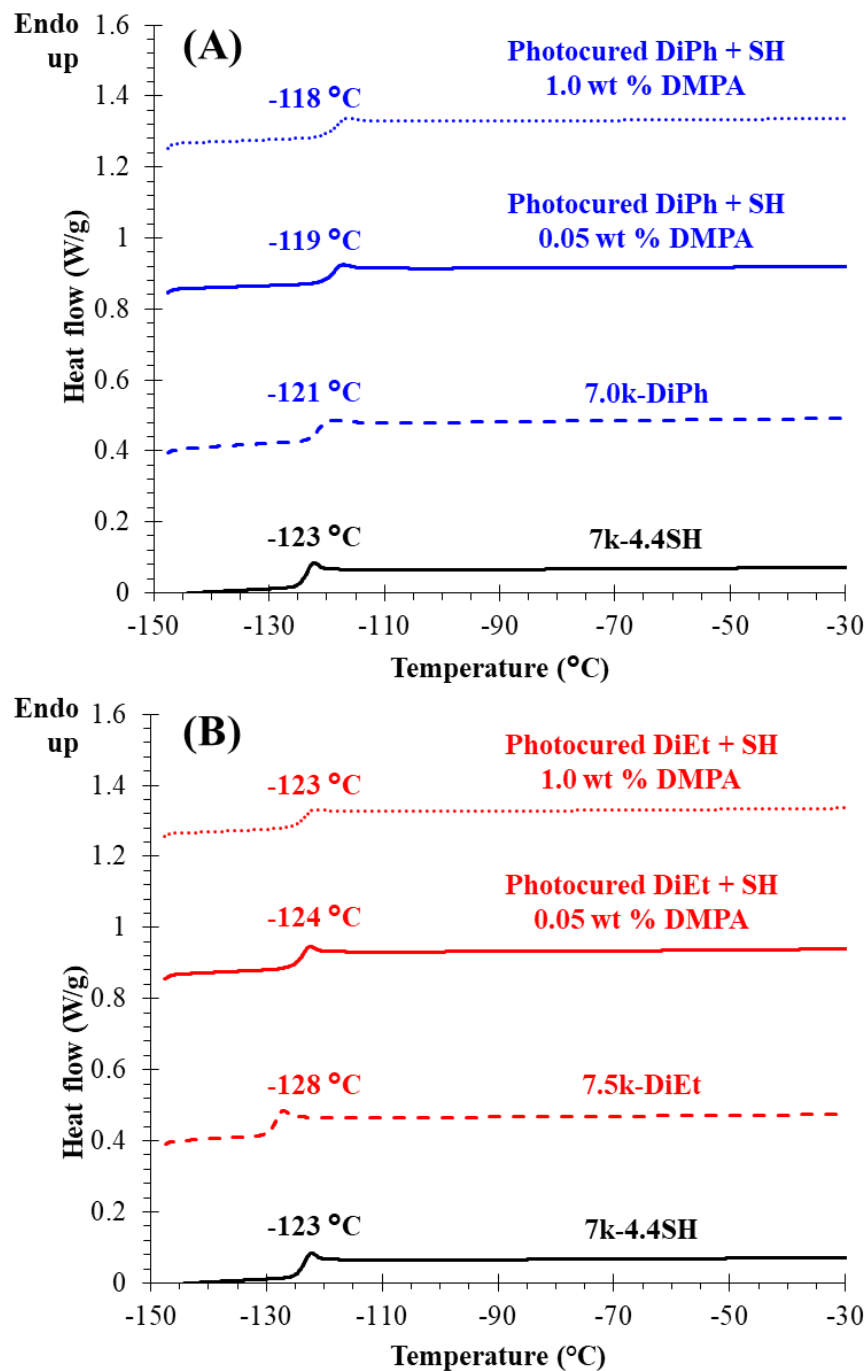


**Figure 5.4.** DSC 1<sup>st</sup> heating traces (10 °C min<sup>-1</sup>) for photocured films of (A) DiPhS + SH or (B) DiEtS + SH networks, overlaid with corresponding traces for neat oligomeric precursors.

**Figure 5.5** shows thermomechanical response at constant frequency (1 Hz) as a function of temperature for photocured DiPhS + SH and DiEtS + SH networks. Both samples underwent an orders-of-magnitude drop in storage modulus ( $E'$ ) as a function of temperature, resulting in a pronounced peak in  $\tan \delta$  that corresponded to the primary  $\alpha$ -relaxation, or  $T_g$ , in these polysiloxane networks. Photocured DiPhS + SH and DiEtS + SH systems exhibited  $\tan \delta$  peaks at  $-113\text{ }^\circ\text{C}$  and  $-118\text{ }^\circ\text{C}$ , respectively, and both were roughly  $5\text{ }^\circ\text{C}$  higher than the corresponding  $T_g$  values determined by DSC. The DiPhS + SH sample exhibited a consistent modulus from  $-90\text{ }^\circ\text{C}$  to  $80\text{ }^\circ\text{C}$ , from where it decreased until ca.  $150\text{ }^\circ\text{C}$ . In contrast to this, the photocured DiEtS + SH sample showed a small “bump” in modulus centered around  $-70\text{ }^\circ\text{C}$ , which was attributed to crystallization and melting of PDES segments expected to be present in this DiEtS-containing terpolymer. This terpolymer was synthesized from diethylsiloxane “hydrolysate”, a commercially available mixture of various DiEtS cyclic oligomers and a moderately high molecular weight PDES linear homopolymer, in a manner in which the siloxane equilibration did not fully randomize the resulting polymer structure.<sup>6</sup> This resulted in retention of somewhat longer PDES segments in this terpolymer sample, which then exhibited the observed typical PDES behavior upon thermomechanical analysis. As a consequence, it was expected that non-segmented, isolated DiEtS repeating unit containing siloxane terpolymers, which are obtained from pure cyclic hexaethylcyclotrisiloxane ( $D_3^{\text{Et}2}$ ) or octaethylcyclotetrasiloxane ( $D_4^{\text{Et}2}$ )<sup>6</sup> would be the polymers of choice when complete crystallization inhibition is desired. It is also worth noting that the DiEtS + SH photocured film demonstrated a significantly wider service temperature range, extending its unchanged modulus up to  $150\text{ }^\circ\text{C}$ .

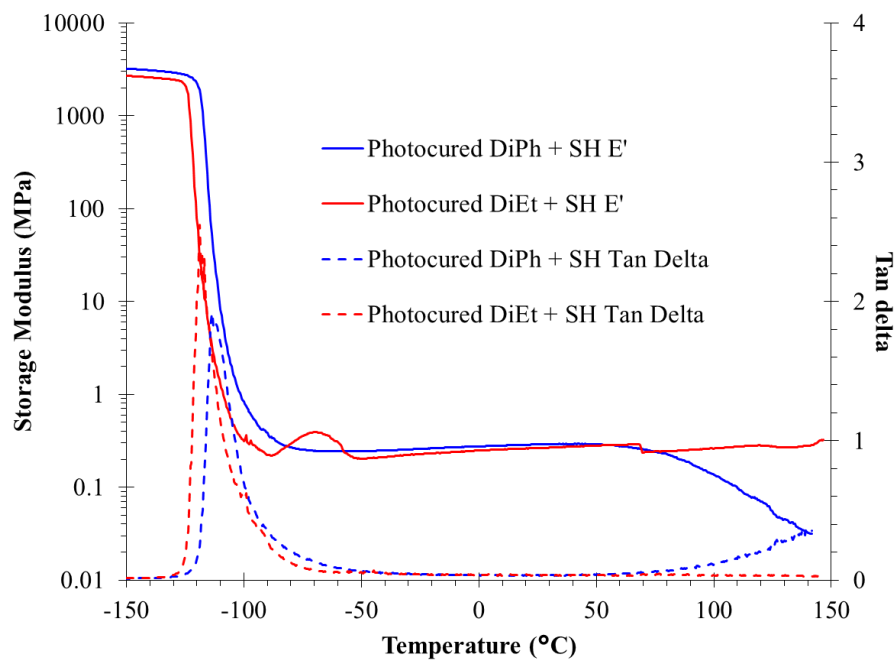


**Figure 5.5.** Dynamic mechanical analyses (DMA) ( $3\text{ }^{\circ}\text{C min}^{-1}$ , 1 Hz) of photocured DiPhS + SH and DiEtS + SH films.

**Figure 5.1A** depicts a schematic of the layer-wise VP-AM process employed for 3D printing of these siloxane-containing terpolymer systems, consisting of a UV light source, photopolymer container, build stage attached to a linear actuator, and dynamic mask, which enabled photocuring of entire layers at once. **Figure 5.1B** shows the printing apparatus with various components labeled, while **Figure 5.1C** and **Figure 5.1D** show various views of a rook structure printed from the DiPhS + SH siloxane-based photopolymer composition, displaying a well-defined structure. The rook structure demonstrates the combined ability of the printer and photopolymer to support high aspect ratio structures and limited cure-through. Printing occurred with 0.1 wt % BBOT, a UV absorber, which limited the cure-through that occurred when printing this composition without UV absorber. Aromatic rings of DiPhS repeating units may be responsible for this

phenomenon, since they will have different response to UV light than the non-UV-active ethylsilyl units of the DiEtS + SH photopolymer. We conclude that the avoidance of low-temperature crystallization and UV absorbance, i.e. a photocurable DiEtS + SH polymer system where the DiEtS terpolymer is derived from a non-hydrolyzate source reagent (such as  $D_3^{Et2}$  or  $D_4^{Et2}$  cyclic monomers described previously<sup>6</sup>) represents the most viable candidate for an ultra-low temperature elastomer from 3D printing.

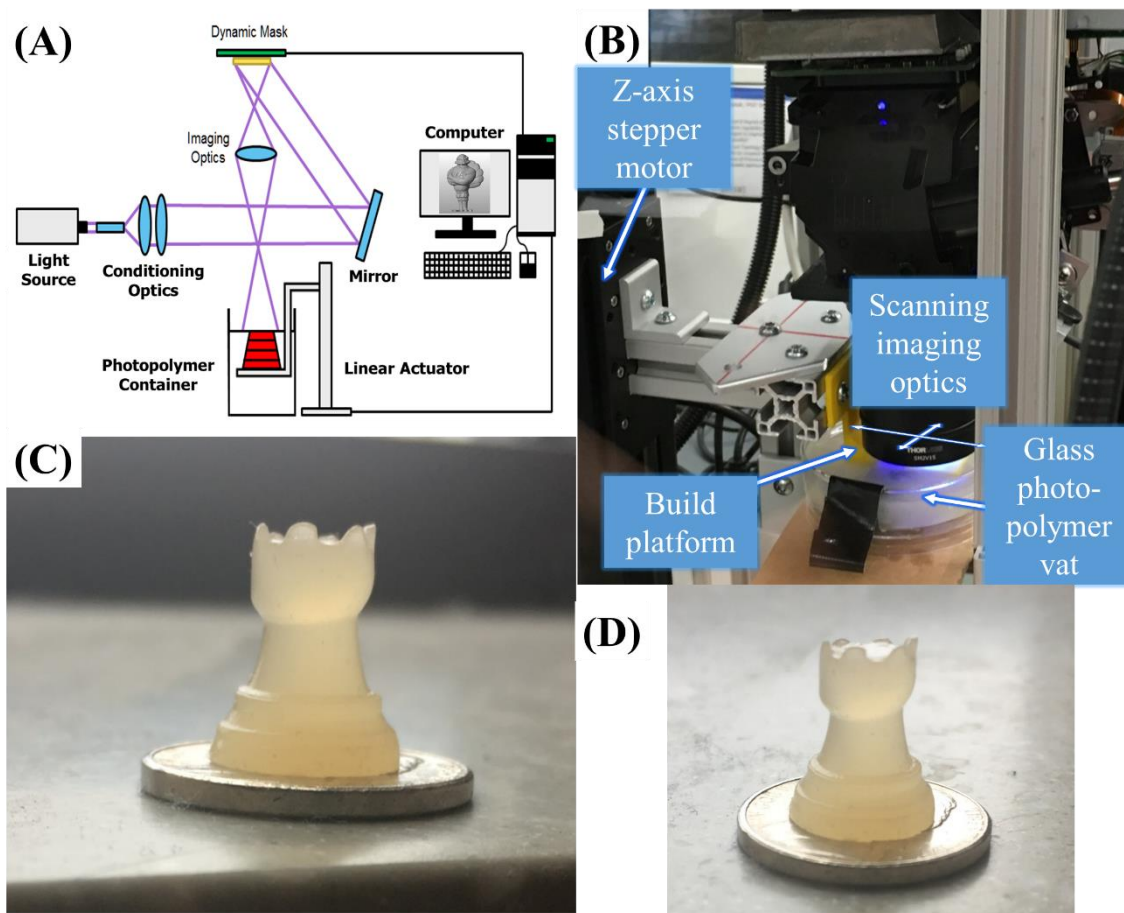


**Figure 5.6.** (A) Schematic of the top-down scanning mask-projection vat photopolymerization (VP) apparatus employed for additive manufacturing (AM) of siloxane terpolymers. (B) VP-AM apparatus used in this work. (C) and (D) 3D-printed rook structures from DiPhS + SH photopolymer composition.



## 5.5 Conclusions

Two different amorphous dimethylsiloxane terpolymers, containing diphenylsiloxy, (DiPhS) and diethylsiloxy (DiEtS) repeating units, as well as methylvinylsiloxy and chain-end vinylsilyl- functional groups, were crosslinked with a thiol-functional polydimethylsiloxane (SH). This yielded viable photopolymer systems for VP-AM *via* thiol-ene crosslinking chemistry when exposed to UV light in air. Optimal photoinitiator concentration for VP-AM was determined by photocalorimetry and photorheology, and a photocuring procedure was developed to provide homogeneous films of uniform thickness. TGA of films prepared from these polymer systems confirmed the expected high temperature stabilities in both air and nitrogen, showing  $T_{d,5\%}$  values ranging from 351 °C and 408 °C, while DSC showed complete absence of thermal transitions to 25 °C. DMA corroborated complete absence of crystallization or melting for the DiPhS + SH sample, with an orders-of-magnitude drop in  $E'$  at  $T_g$ . The photocured DiEtS + SH sample demonstrated a small “bump” in  $E'$ , centered around -70 °C and attributable to the crystallization and melting of longer than single repeating unit polydiethylsiloxane (PDES) segments, expected to be present in this sample as a side effect of the synthetic method used. Both photopolymer compositions demonstrated high versatility through initial printing of various objects and high aspect ratio structures. Future work will include the use of DiEtS-containing terpolymers prepared from alternate sources of diethylsiloxane repeating units that provide complete crystallization suppression, addition of UV blockers and radical inhibitors (e.g. antioxidants) to provide vertical ( $z$  direction) and horizontal ( $x$ - $y$  plane) resolution improvements, respectively, as well as printing in the presence of fillers, to improve the characteristically low mechanical properties of unfilled polysiloxane elastomers.

## 5.6 Acknowledgements

The authors graciously acknowledge funding from the Department of Energy's (DOE) Kansas City National Security Campus, which is operated and managed by Honeywell Federal Manufacturing & Technologies, LLC, under Contract DE-NA-0002839.

## 5.7 References

- (1) Dvornic, P. R. Thermal Properties of Polysiloxanes. In *Silicon-Containing Polymers: The Science and Technology of Their Synthesis and Applications*; Jones, R. G., Ando, W., Chojnowski, J., Eds.; Springer Netherlands: Dordrecht, 2000, p 185-212.
- (2) Noll, W. *Chemistry and Technology of Silicones*; Elsevier, 2012.
- (3) Yilgor, E.; Yilgor, I. Silicone Containing Copolymers: Synthesis, Properties and Applications. *Progress in Polymer Science* **2014**, *39*, 1165-1195.
- (4) Warrick, E. L.; Pierce, O. R.; Polmanteer, K. E.; Saam, J. C. Silicone Elastomer Developments 1967-1977. *Rubber Chemistry and Technology* **1979**, *52*, 437-525.
- (5) Weinhold, F.; West, R. The Nature of the Silicon–Oxygen Bond. *Organometallics* **2011**, *30*, 5815-5824.
- (6) Zlatanic, A.; Radojic, D.; Wan, X. M.; Messman, J. M.; Dvornic, P. R. Suppression of Crystallization in Polydimethylsiloxanes and Chain Branching in Their Phenyl-Containing Copolymers. *Macromolecules* **2017**, *50*, 3532-3543.
- (7) Helmer, J. D.; Polmanteer, K. E. Supercooling of Polydimethylsiloxane. *Journal of Applied Polymer Science* **1969**, *13*, 2113-+.
- (8) Clarkson, S. J.; Dodgson, K.; Semlyen, J. A. Studies of Cyclic and Linear Poly(Dimethylsiloxanes): 19. Glass Transition Temperatures and Crystallization Behaviour. *Polymer* **1985**, *26*, 930-934.
- (9) Molenberg, A.; Siffrin, S.; Moller, M.; Boileau, S.; Teyssie, D. Well Defined Columnar Liquid Crystalline Polydiethylsiloxane. *Macromolecular Symposia* **1996**, *102*, 199-207.
- (10) Molenberg, A.; Moller, M. Structure and Phase Transitions of Poly(Diethylsiloxane). *Macromolecules* **1997**, *30*, 8332-8337.
- (11) Miller, K. J.; Grebowicz, J.; Wesson, J. P.; Wunderlich, B. Conformations of Poly(Diethylsiloxane) and Its Mesophase Transitions. *Macromolecules* **1990**, *23*, 849-856.
- (12) Babu, G. N.; Christopher, S. S.; Newmark, R. A. Poly(Dimethylsiloxane-Co-Diphenylsiloxanes) - Synthesis, Characterization, and Sequence-Analysis. *Macromolecules* **1987**, *20*, 2654-2659.
- (13) Andrianov, K. A.; Slonimskii, G. L.; Zhdanov, A. A.; Godovskii, Y. K.; Levin, V. Y.; Moskalenko, V. A. Some Physical Properties of Polyorganosiloxanes .1. Linear Polyorganosiloxanes. *Journal of Polymer Science Part a-1-Polymer Chemistry* **1972**, *10*, 1-+.
- (14) Zlatanic, A.; Radojic, D.; Wan, X. M.; Messman, J. M.; Dvornic, P. R. Monitoring of the Course of the Silanolate-Initiated Polymerization of Cyclic

- Siloxanes. A Mechanism for the Copolymerization of Dimethyl and Diphenyl Monomers. *Macromolecules* **2018**, *51*, 895-905.
- (15) Liu, L.; Yang, S.; Zhang, Z.; Wang, Q.; Xie, Z. Synthesis and Characterization of Poly(Diethylsiloxane) and Its Copolymers with Different Diorganosiloxane Units. *Journal of Polymer Science Part A: Polymer Chemistry* **2003**, *41*, 2722-2730.
- (16) Meng, Y.; Chu, J.; Xue, J.; Liu, C.; Wang, Z.; Zhang, L. Design and Synthesis of Non-Crystallizable, Low-Tg Polysiloxane Elastomers with Functional Epoxy Groups through Anionic Copolymerization and Subsequent Epoxidation. *RSC Advances* **2014**, *4*, 31249-31260.
- (17) Bukhina, M. F.; Kurlyand, S. K. *Low-Temperature Behaviour of Elastomers*; 1st Edition ed.; CRC Press: Boca Raton, FL, 2007.
- (18) Shit, S. C.; Shah, P. A Review on Silicone Rubber. *National Academy Science Letters* **2013**, *36*, 355-365.
- (19) Zheng, P.; McCarthy, T. J. A Surprise from 1954: Siloxane Equilibration Is a Simple, Robust, and Obvious Polymer Self-Healing Mechanism. *Journal of the American Chemical Society* **2012**, *134*, 2024-2027.
- (20) Melody, D. P. Advances in Room Temperature Curing Adhesives and Sealants—a Review. *British Polymer Journal* **1989**, *21*, 175-179.
- (21) de Buyl, F. Silicone Sealants and Structural Adhesives. *International Journal of Adhesion and Adhesives* **2001**, *21*, 411-422.
- (22) Yilgor, E.; Yilgor, I. Hydrogen Bonding: A Critical Parameter in Designing Silicone Copolymers. *Polymer* **2001**, *42*, 7953-7959.
- (23) Hoyle, C. E.; Bowman, C. N. Thiol–Ene Click Chemistry. *Angewandte Chemie International Edition* **2010**, *49*, 1540-1573.
- (24) Buback, M.; Schroeder, H.; Kattner, H. Detailed Kinetic and Mechanistic Insight into Radical Polymerization by Spectroscopic Techniques. *Macromolecules* **2016**.
- (25) Campos, L. M.; Truong, T. T.; Shim, D. E.; Dimitriou, M. D.; Shir, D.; Meinel, I.; Gerbec, J. A.; Hahn, H. T.; Rogers, J. A.; Hawker, C. J. Applications of Photocurable Pmms Thiol–Ene Stamps in Soft Lithography. *Chemistry of Materials* **2009**, *21*, 5319-5326.
- (26) Carlborg, C. F.; Haraldsson, T.; Oberg, K.; Malkoch, M.; van der Wijngaart, W. Beyond Pdmms: Off-Stoichiometry Thiol-Ene (Oste) Based Soft Lithography for Rapid Prototyping of Microfluidic Devices. *Lab on a Chip* **2011**, *11*, 3136-3147.
- (27) Müller, U.; Kunze, A.; Herzig, C.; Weis, J. Photocrosslinking of Silicones. Part 13. Photoinduced Thiol-Ene Crosslinking of Modified Silicones. *Journal of Macromolecular Science, Part A* **1996**, *33*, 439-457.
- (28) Nguyen, K. D. Q.; Megone, W. V.; Kong, D.; Gautrot, J. E. Ultrafast Diffusion-Controlled Thiol-Ene Based Crosslinking of Silicone Elastomers with Tailored Mechanical Properties for Biomedical Applications. *Polymer Chemistry* **2016**, *7*, 5281-5293.
- (29) Campos, L. M.; Meinel, I.; Guino, R. G.; Schierhorn, M.; Gupta, N.; Stucky, G. D.; Hawker, C. J. Highly Versatile and Robust Materials for Soft Imprint Lithography Based on Thiol-Ene Click Chemistry. *Advanced Materials* **2008**, *20*, 3728-3733.

- (30) Kim, J.-S.; Yang, S.; Park, H.; Bae, B.-S. Photo-Curable Siloxane Hybrid Material Fabricated by a Thiol-Ene Reaction of Sol-Gel Synthesized Oligosiloxanes. *Chemical Communications* **2011**, *47*, 6051-6053.
- (31) van den Berg, O.; Nguyen, L.-T. T.; Teixeira, R. F. A.; Goethals, F.; Özdilek, C.; Berghmans, S.; Du Prez, F. E. Low Modulus Dry Silicone-Gel Materials by Photoinduced Thiol–Ene Chemistry. *Macromolecules* **2014**, *47*, 1292-1300.
- (32) Wallin, T. J.; Pikul, J. H.; Bodkhe, S.; Peele, B. N.; Mac Murray, B. C.; Therriault, D.; McEnerney, B. W.; Dillon, R. P.; Giannelis, E. P.; Shepherd, R. F. Click Chemistry Stereolithography for Soft Robots That Self-Heal. *Journal of Materials Chemistry B* **2017**, *5*, 6249-6255.
- (33) Sirrine, J. M.; Meenakshisundaram, V.; Moon, N. G.; Scott, P. J.; Mondschein, R. J.; Weiseman, T. F.; Williams, C. B.; Long, T. E. Functional Siloxanes with Photo-Activated, Simultaneous Chain Extension and Crosslinking for Lithography-Based 3d Printing. *Polymer* **2018**.
- (34) Barker, I. A.; Ablett, M. P.; Gilbert, H. T. J.; Leigh, S. J.; Covington, J. A.; Hoyland, J. A.; Richardson, S. M.; Dove, A. P. A Microstereolithography Resin Based on Thiol-Ene Chemistry: Towards Biocompatible 3d Extracellular Constructs for Tissue Engineering. *Biomaterials Science* **2014**, *2*, 472-475.
- (35) Ligon, S. C.; Liska, R.; Stampfl, J.; Gurr, M.; Mülhaupt, R. Polymers for 3d Printing and Customized Additive Manufacturing. *Chemical Reviews* **2017**, *117*, 10212-10290.
- (36) Leonards, H.; Engelhardt, S.; Hoffmann, A.; Pongratz, L.; Schriever, S.; Bläsius, J.; Wehner, M.; Gillner, A. 2015; Vol. 9353, p 93530F.
- (37) Hegde, M.; Meenakshisundaram, V.; Chartrain, N.; Sekhar, S.; Tafti, D.; Williams, C. B.; Long, T. E. 3d Printing All-Aromatic Polyimides Using Mask-Projection Stereolithography: Processing the Nonprocessable. *Adv Mater* **2017**, *29*.
- (38) Odian, G. *Principles of Polymerization*; 4th ed.; Wiley, 2004.
- (39) Cramer, N. B.; Bowman, C. N. Kinetics of Thiol–Ene and Thiol–Acrylate Photopolymerizations with Real-Time Fourier Transform Infrared. *Journal of Polymer Science Part A: Polymer Chemistry* **2001**, *39*, 3311-3319.
- (40) Winter, H. H. Can the Gel Point of a Cross-Linking Polymer Be Detected by the  $G' - G''$  Crossover? *Polymer Engineering & Science* **1987**, *27*, 1698-1702.
- (41) Camino, G.; Lomakin, S. M.; Lazzari, M. Polydimethylsiloxane Thermal Degradation Part 1. Kinetic Aspects. *Polymer* **2001**, *42*, 2395-2402.
- (42) Eckel, Z. C.; Zhou, C.; Martin, J. H.; Jacobsen, A. J.; Carter, W. B.; Schaedler, T. A. Additive Manufacturing of Polymer-Derived Ceramics. *Science* **2016**, *351*, 58-62.

## Chapter 6: Urea as a monomer for isocyanate-free synthesis of segmented poly(dimethyl siloxane) polyureas

(Submitted for publication and under review in *Polymer*, 2018)

Justin M. Serrine, Shantel A. Schexnayder, Joseph M. Dennis, Timothy E. Long\*  
*Department of Chemistry, Macromolecules Innovation Institute (MII)*  
*Virginia Tech, Blacksburg, VA 24061, USA*

### 6.1 Abstract

Poly(dimethyl siloxane)-containing (PDMS), segmented polyureas represent an important class of high-performance elastomers that leverage the low glass transition temperature ( $T_g$ ) of PDMS and superior mechanical reinforcement from bidentate hydrogen bonding. Current synthetic methods exclusively employ highly reactive/toxic isocyanate reagents and volatile organic solvents; the latter must be quantitatively removed prior to use. This report details an isocyanate-, solvent-, and catalyst-free synthetic method towards PDMS polyureas using urea and a disiloxane diamine chain extender in the melt phase. Melt polymerization afforded segmented PDMS polyureas, which formed optically clear, mechanically ductile, freestanding films. Observation of distinct thermal transitions with differential scanning calorimetry and dynamic mechanical analysis, corresponding to the respective segments, suggested microphase separation. Tensile and hysteresis measurements corroborated similarities between these PDMS polyureas and their isocyanate-containing analogues with strain at break ranging from 495 to 1180 %. This facile, isocyanate-free approach provides a commercially viable alternative to the current industrial process for high performance elastomers.

### 6.2 Introduction

Polyureas remain as a distinctive class of polymers that are utilized in wide-ranging applications from foams and coatings to self-healing materials and textiles.<sup>1-4</sup> This diversity

of application results in part from the superior bidentate hydrogen bonding for the urea carbonyl compared to monodentate hydrogen bonding for urethanes.<sup>3</sup> In contrast, highly nonpolar poly(dimethyl siloxane) (PDMS) possesses unique properties, i.e. a low glass transition temperature ( $T_g$ , -123 °C), biological inertness, high gas permeability, and high thermal/UV stability, but suffer from poor mechanical properties in their linear, homopolymer form, despite high molecular weights.<sup>5-7</sup> An expansive literature precedent exists on the structure-morphology-property relationships of PDMS polyurea copolymers.<sup>6,8,9</sup> The improvements in thermal and mechanical properties rely on microphase separation between the covalently linked, nonpolar PDMS and the highly polar urea carbonyls. Importantly, the combination of widely different solubility parameters ( $15.6 \text{ J}^{1/2}/\text{cm}^{3/2}$  for PDMS and  $45.6 \text{ J}^{1/2}/\text{cm}^{3/2}$  for urea), as well as the Flory-Huggins segment-segment interaction parameter ( $\chi$ ) and segment length ( $N$ ), primarily govern the degree of microphase separation.<sup>6,8,10-12</sup>

As a result of microphase separation, segmented PDMS polyureas possess highly desirable properties. Many of these copolymers exhibit high tensile strain at break (e.g.  $\gg 100 \%$ ) and a wide temperature range with relatively consistent modulus, which extends from the ultra-low PDMS glass transition temperature ( $T_g$ ) (e.g. -123 °C) until the flow temperature for fully amorphous PDMS-containing polyureas. (ca. 100 °C).<sup>6,8,9,13,14</sup> However, current synthetic methods exclusively employ solvent-based, step-growth polymerization with toxic isocyanates, amine-terminated PDMS oligomers, and optionally, short-chain diamines, referred to as chain extenders.<sup>6,8,9,14</sup> Solvent choice remains critical for maintaining a homogeneous reaction and avoiding viscosity increases upon polyurea formation.<sup>6,9</sup> Non-segmented PDMS polyureas follow a simple addition of co-monomers

with a noticeable change in viscosity as molecular weight increases. Segmented polyureas employ a monomeric diamine chain extender and produce polyureas with distinct properties as compared to their non-segmented analogs.<sup>8,9,13</sup> Segmented PDMS polyurea synthesis traditionally requires binary solvent mixtures; the nonpolar PDMS segments require relatively nonpolar solvents for dissolution (e.g. tetrahydrofuran (THF) or toluene) and the polar hard segments (HS) require more polar solvents (e.g. dimethylformamide (DMF), dimethylacetamide (DMAc), or *N*-methyl-2-pyrrolidone).<sup>6,9</sup> However, for segmented PDMS polyurea synthesis with high HS content, Yilgor *et al.* reported a failure of binary solvent mixtures for adequate solvation of growing polymer chains, resulting in high viscosity and low molecular weight.<sup>9</sup> Fortunately, isopropyl alcohol (IPA) alone demonstrated utility for solvating both the nonpolar PDMS and the polar HSs. A more recent report from Wilkes and Yilgor *et al.* detailed the synthesis of PDMS polyureas with low HS content in 50/50 v/v THF/IPA.<sup>8</sup> Although many reported polyurea synthetic methods require solvents to disrupt hydrogen bonding interactions and ensure endgroup accessibility during step growth polymerization, solvent elimination remains a critical goal in the twelve principles of green chemistry.<sup>15</sup>

Highly toxic isocyanates are derived from the highly toxic phosgene, which poses many environmental and health concerns.<sup>16,17</sup> Fortunately, many isocyanate-free routes towards polyurethanes and polyureas exist.<sup>3,18</sup> One of the most studied methods involves the reaction of cyclic carbonates and diamines, producing poly(hydroxy urethane)s, however the resulting pendant hydroxyl moieties influence water uptake properties of the resulting polymers.<sup>19</sup> Direct incorporation of CO<sub>2</sub> and diamines into polyureas remains promising, but unusual solvent requirements, high pressures, and potentially low isolated

yields hinder progress.<sup>1</sup> Transurethanization with a biscarbamate and diamine provides another promising route towards isocyanate-free polyureas, but requires biscarbamate synthesis as a separate step prior to polycondensation and removal of a small molecule condensate (e.g. methanol, phenol, ethylene glycol).<sup>3</sup> Although transurethanization readily occurs above 150 °C, these procedures typically require solvent and catalyst.<sup>3,20</sup> Leibler, *et al.* reported self-healing polyurea networks from multifunctional amine-derivatized fatty acids and urea, leveraging a catalyst-free melt polycondensation at 160 °C under N<sub>2</sub>.<sup>2,4</sup> Although this generated the desired, linear 1,3-dialkylurea linkage, multiple side products occurred, largely due to a stoichiometric excess of urea.<sup>2,21</sup> Further work resides in the patent literature.<sup>22-26</sup> More recently, our group leveraged this technique for the direct melt polycondensation of monomeric diamines and urea to produce linear polyurea copolymers in the absence of isocyanate reagent, catalyst, or solvent.<sup>17</sup> These polyureas remained structurally analogous to those produced with isocyanates and did not contain additional moieties, e.g. pendant hydroxyls. This reaction leverages monomeric urea as an inexpensive, non-toxic and bio-based carbonyl source. Although this family of copolyureas demonstrated wide tunability in T<sub>g</sub> and the crystalline melting point (T<sub>m</sub>), all compositions remained as semicrystalline thermoplastics.<sup>17</sup>

This work reports the synthesis and characterization of segmented, isocyanate-free, amorphous PDMS polyureas. A melt transureaization of PDMS oligomers, urea, and a disiloxane diamine chain extender occurred in the absence of solvent and catalyst, only requiring heat, while miscibility of the disiloxane chain extender in the PDMS oligomer at room temperature facilitated melt homogeneity. Ammonia, a key raw material for agricultural and industrial products, remains the only reaction byproduct.<sup>27</sup> Optimization



of polymerization conditions and reaction stoichiometry prevented urea self-reaction side products, while transureaization and a final low pressure step corrected overall reaction stoichiometry to produce high molecular weight. Upon direct isolation from the melt, thermogravimetric analysis (TGA) indicated similar thermal stability to isocyanate-based PDMS polyureas, while differential scanning calorimetry (DSC) suggested the absence of crystallinity. Dynamic mechanical analysis (DMA) provided evidence of microphase separation in the form of two prominent, sub-ambient  $\alpha$ -relaxations. Finally, tensile testing and hysteresis measurements indicated strain at break comparable to isocyanate-based, segmented PDMS polyureas (~ 400 – 500 %) and low percent hysteresis (e.g. ~20 %).

## **6.3 Materials & Methods**

### **6.3.1 Materials**

Urea (ReagentPlus®,  $\geq 99.5$  %, pellets) and dibutyltin dilaurate (DBTDL) ( $\geq 95$ %) were purchased from Sigma Aldrich. 1,3,-bis(3-aminopropyl)tetramethyldisiloxane (BATS, product code SIB1024.0,  $\geq 97$  %) was purchased from Gelest. Various aminopropyl-terminated poly(dimethyl siloxane)s (PDMS-NH<sub>2</sub>) were purchased from Gelest (DMS-A12, DMS-A15, and DMS-A21) and Sigma Aldrich ( $M_n \sim 2,500$ , #481688 and  $\sim 27,000$  g/mol, #481696), while one sample was donated by Wacker Chemie (Wacker Fluid NH130D). Desmodur® W, a high purity 4,4'-Methylenebis(cyclohexyl isocyanate) (HMDI), was graciously donated by Bayer MaterialScience (now Covestro) and used as received. Chloroform-d (CDCl<sub>3</sub>, 99.8 %), trifluoroacetic acid-d (TFA-d, 99.5%) and benzene-d<sub>6</sub> (C<sub>6</sub>D<sub>6</sub>, 99.5 %) were purchased from Cambridge Isotope Laboratories, Inc. and used as received. Chloroform, tetrahydrofuran (THF), dichloromethane (DCM), and toluene were purchased from Fisher Scientific (all HPLC grade) and used as received. All

chemicals were used as received, except for DBTDL which was used as a 1 wt % solution in THF and aminopropyl-terminated poly(dimethyl siloxane)s, which were dried at 150 °C under reduced pressure for 18 h before further modification in order to remove cyclics. Inhibitor-free THF (HPLC grade) was purchased from Spectrum and dried with an Innovative Technology PureSolv® solvent purification system before use.

### 6.3.2 Synthesis of non-segmented PDMS polyureas [poly(PDMS-*co*-urea)]

The synthesis of isocyanate-, catalyst-, and solvent-free PDMS polyureas employed a one-pot, custom melt polymerization apparatus used in our research group.<sup>17</sup> Typical synthesis of poly(PDMS1.7k-*co*-urea) proceeded as follows. Proton nuclear magnetic resonance (<sup>1</sup>H NMR) spectroscopy in C<sub>6</sub>D<sub>6</sub> enabled determination of actual PDMS-NH<sub>2</sub> oligomer M<sub>n</sub> after vacuum stripping of cyclics, by comparing the integration of backbone methyl resonances to the integration of the three methylene endgroup resonances as shown in **Figure 6.7**. PDMS-NH<sub>2</sub> (Gelest DMS-A12, 20.0000 g, 12.0555 mmol, 1.1 mol eq.) and urea (0.6582 g, 10.9595 mmol, 1.0 mol eq.) were added to a 100-mL, single-necked round-bottomed flask. The flask was equipped with a custom, t-necked glass adapter, which contained a 24/40 male joint, spherical ball joint, spherical socket joint, and nitrogen inlet (clockwise starting at bottom). The t-neck spherical ball joint was connected to a condensing tube with corresponding spherical socket joint and nitrogen outlet, while the t-neck glass adapter enabled pass-through of an overhead metal stir rod for mechanical stirring, via glass, spherical ball joint adapter attached to Tygon®, plasticized PVC tubing. Subsequent vacuum and N<sub>2</sub> purge cycles (3x) ensured proper oxygen removal and provided an inert atmosphere for polymerization. The contents were heated under constant N<sub>2</sub> flow (~ 10 mL min<sup>-1</sup>) to 160 °C and held for 3 h to ensure a homogeneous melt before further

temperature increases. Reactions were stirred vigorously (e.g. ~200 rpm) throughout the reaction to promote urea emulsification and mixing of the phase-separated urea droplets in early stages of the reaction. Evolution of ammonia gas was observed during the first 30 min, while a bubbler containing aqueous 1 M HCl enabled sequestration of the generated ammonia gas. After 3 h at 160 °C, the temperature was increased to 180 °C, 200 °C, and 220 °C each for 30 min, followed by 250 °C for 1 h, all under constant N<sub>2</sub> purge. Application of vacuum at 250 °C for an additional 1.5 h facilitated removal of excess diamine generated through transureaization. Dramatic increases in melt viscosity occurred during this final 1.5 h vacuum step, resulting in wrapping of the stir rod for poly(PDMS1.7k-*co*-urea) only. Polymers were isolated directly and used without further purification. Polymer nomenclature follows poly(PDMS $_{xx}$ k-*co*-urea) where ‘ $xx$ ’ is the PDMS oligomer molecular weight in kg/mol, as determined by <sup>1</sup>H NMR spectroscopy of the PDMS-NH<sub>2</sub> oligomeric precursors in C<sub>6</sub>D<sub>6</sub>. Products include poly(PDMS1.7k-*co*-urea), poly(PDMS3.2k-*co*-urea) and poly(PDMS5.5k-*co*-urea). Poly(PDMS1.7k-*co*-urea) remained an optically clear, elastic solid at room temperature, while poly(PDMS3.2k-*co*-urea) and poly(PDMS5.5k-*co*-urea) remained optically clear and highly viscous liquids at room temperature.

### 6.3.3 Synthesis of segmented PDMS polyureas [poly(PDMSU)-*co*-poly(BATSU)]

The synthesis of segmented PDMS polyureas employed the same reactor setup and procedure, including time/temperature schedule as for the non-segmented PDMS polyureas, except that BATS was employed as a chain extender. Before polymerization, desired reactant amounts were calculated as follows. Desired HS content was calculated based on the weight ratio of the two possible repeat unit structures. For example, if 10 wt % HS was desired with 20.0000 g PDMS-NH<sub>2</sub> (12.06 mmol), this resulted in a calculated

value of 1.2211 g urea (20.33 mmol) and 2.0566 g BATS (8.28 mmol). Then, a new BATS reactant amount was determined based on the calculated urea amount, such that the new BATS amount was 1.2 mol eq. relative to the calculated urea amount (1.0 mol eq.) For example, if 1.2211 g urea (20.33 mmol) were to be charged, a new BATS amount was 6.0631 g (24.40 mmol). This stoichiometric modification ensured no formation of undesired urea side products during polymerization. Typical synthesis of poly(PDMS1.7kU)<sub>80-co</sub>-poly(BATSU)<sub>20</sub> proceeded as follows. PDMS-NH<sub>2</sub> (Gelest DMS-A12, 20.0013 g), urea (3.2827 g), and BATS (10.5868 g) were added to a 100-mL, 1-necked round-bottomed flask. The rest of the setup and polymerization followed the synthesis of poly(PDMS1.7k-co-urea). Like poly(PDMS1.7k-co-urea), dramatic increases in melt viscosity occurred during the final 1.5 h vacuum step, resulting in wrapping of the stir rod for all samples. Polymers were isolated directly and used without further purification. All polymers remained optically clear, elastic solids at room temperature, with a slight yellow color imparted for higher HS content samples. Polymer nomenclature follows poly(PDMS1.7kU)<sub>x-co</sub>-poly(BATSU)<sub>y</sub> where 'x' and 'y' are the weight percent of the respective repeat unit structure in the final polymer, as determined by <sup>1</sup>H NMR spectroscopy in TFA-*d*.

#### **6.3.4 Synthesis of hard segment homopolymer [poly(BATS-co-urea)]**

The synthesis of the non-segmented poly(BATS-co-urea) homopolymer proceeded as follows. BATS (20.0000 g, 80.4764 mmol, 1.1 mol eq.) and urea (4.3940 g, 73.1604 mmol, 1.0 mol eq.) were added to a 100-mL, 1-necked round-bottomed flask. Polymerization employed the same reactor setup and procedure, including time/temperature schedule as for the non-segmented PDMS polyureas. Poly(BATS urea) remained a glassy, yellow, transparent solid at room temperature.

### 6.3.5 Synthesis of isocyanate-based PDMS polyureas [poly(PDMS-*co*-HMDU)]

The synthesis of the non-segmented, isocyanate-based PDMS copolyurea control samples proceeded as follows. PDMS-NH<sub>2</sub> (Gelest DMS-A21, 20.000 g, 7.3222 mmol) was added to a 500-mL, 3-necked round-bottomed flask equipped with condenser, addition funnel, and overhead mechanical stirrer with Teflon stir blade and glass rod stir shaft. The addition funnel and condenser were capped with a 24/40 septa and sealed with copper wire, and then the entire reactor was purged with dry N<sub>2</sub> for 30 minutes. Afterward, 50 ppm DBTDL (total solids basis) was added as a 1 wt % solution in THF. Dry THF was cannulated into the round-bottomed flask (~150 mL) via the addition funnel, and into the addition funnel itself (~20 mL), which achieved 20 wt % solids after all chemicals are in the flask. HMDI was then cannulated into the addition funnel (1.80mL, 1.92 g, 7.32 mmol) and allowed to mix with the dry THF. The THF/HMDI mixture was then added dropwise to the flask containing DMS-A12/THF under vigorous mechanical stirring (~100 rpm) and allowed to react at 60 °C for 24 h. After cooling to room temperature, films were solution cast directly from the diluted reaction mixture (10 wt % polymer) without further purification. Samples sat in Teflon® PTFE molds for 24 h at room temperature and then an additional 18 h at 100 °C under vacuum. Samples were stored in a vacuum desiccator before analysis. Samples nomenclature includes MW information and sample type. For example, poly(PDMS5.5k-*co*-HMDU) represents a 5,500 g/mol, isocyanate-derived PDMS polyurea. Samples include poly(PDMS3.2k-*co*-HMDU), poly(PDMS5.5-*co*-HMDU), poly(PDMS11.7-*co*-HMDU), and poly(PDMS30.6k-*co*-HMDU).

### 6.3.6 Calculation of hard segment content

Hard segment content for the segmented, isocyanate-free PDMS polyureas was calculated as the weight ratio between the BATS/urea repeat unit and the PDMS-NH<sub>2</sub>/urea

repeat unit, based on mol % of each repeat unit, measured from  $^1\text{H}$  NMR spectroscopy. Hard segment content for the non-segmented, isocyanate-free PDMS polyureas and for the isocyanate-containing, non-segmented PDMS polyureas is calculated based on a theoretical 1:1 molar ratio of diamine:urea. Hard segment content is reported as wt %.

### **6.3.7 Nuclear magnetic resonance (NMR) spectroscopy**

$^1\text{H}$  NMR spectroscopy was performed with an Agilent U4-DD2 spectrometer operating at 400 MHz and 23 °C, with PDMS-NH<sub>2</sub> precursors dissolved in deuterated benzene (C<sub>6</sub>D<sub>6</sub>) and poly(PDMS-*co*-HMDU) samples dissolved in deuterated chloroform (CDCl<sub>3</sub>). Isocyanate-free, non-segmented poly(PDMS3.2k-*co*-urea) and poly(PDMS5.4k-*co*-urea) were dissolved in CDCl<sub>3</sub>, while non-segmented poly(PDMS1.7k-*co*-urea), poly(BATS-*co*-urea) and segmented poly(PDMSU)<sub>x</sub>-*co*-poly(BATSU)<sub>y</sub> polyureas required deuterated trifluoroacetic acid (TFA-d) for dissolution, due to insolubility in common organic solvents. All samples achieved full dissolution in their respective solvents within minutes at 23 °C with moderate vortexer mixing, and  $^1\text{H}$  NMR spectra were gathered within 3-4 h of PDMS polyurea dissolution in TFA-d.

### **6.3.8 Analytical methods**

Directly after isolation, melt-polymerized, isocyanate-free polyureas were dried at 80 °C for 18 h under vacuum before film preparation. Samples were then compression molded with a Carver model 3856 hydraulic press equipped with model #3925 hydraulic unit. Samples were pressed at 205 °C with 0.020” shims between two sheets of siliconized poly(ethylene terephthalate) (PET), with three 5,000 lb presses (30 s each) and two 10,000 lb presses (30 s each), generating free-standing films with uniform thickness. After cooling to room temperature, dogbone specimens were punched out of the PET-PDMS-PET sandwich using a ASTM D638-V cutting die. Samples were subsequently frozen in liquid

N<sub>2</sub> to facilitate PET film removal, keeping the PDMS in the glassy state. Free-standing isocyanate-free polymer films were then annealed and dried on a Teflon® substrate for 18 h at 100 °C under vacuum, and stored under vacuum at room temperature before analysis. Thermogravimetric analysis (TGA) was performed with a TA Instruments Q500 TGA at a heating rate of 10 °C/min under constant N<sub>2</sub> purge. TGA calibration was performed with a magnet and ferromagnetic transition (Curie) metals, e.g. Alumel, nickel, Perkalloy, and iron, while calibration was confirmed with calcium oxalate. Differential scanning calorimetry (DSC) was performed with a TA Instruments Q200 DSC equipped with liquid nitrogen cooling system (LNCS), which probed thermal transitions under constant heating/cooling rates of 10 °C/min and helium purge. To investigate baseline noise in data from this LNCS DSC, a second DSC with refrigerated cooling system (RCS-DSC) measured thermal transitions in PDMS-NH<sub>2</sub> oligomeric precursors under constant heating/cooling rates of 10 °C/min and nitrogen purge, with a five minute isothermal step at -90 °C prior to heating scans. DSC calibration was performed with manufacturer-provided calibration sapphires, while temperature and heat flow calibration was confirmed with indium metal. Dynamic mechanical analysis (DMA) was performed with a TA Instruments Q800 equipped with liquid nitrogen gas cooling accessory (GCA) and operated in oscillatory tension mode at 1 Hz, 0.1 % strain, and 3 °C/heating after equilibration and 5 min isotherm at -150 °C. Tensile and hysteresis analysis was performed on an Instron® 5500R (model 1123) universal testing system. Tensile experiments were performed at a constant crosshead speed of 50 mm/min, with single representative stress/strain curves depicted and tensile values reported as an average of 5 samples. Grip patterns were clearly visible on analyzed sample grip sections, indicating the lack of grip slip during analysis.

Hysteresis experiments were conducted at a maximum of 100 % strain at a rate of 2 %/sec over 5 full cycles, with 30 s rest at 0% strain in between each cycle. The area under the loading and unloading curve was calculated using the trapezoid method of analysis, with area increments calculated between each data point and summed for each sample. Percent hysteresis was calculated with load (N) vs. extension (mm) curves as % hysteresis = (Area under loading curve – Area under recovery curve)/Area under loading curve \* 100.<sup>8</sup>

#### 6.4 Results and Discussion

The reaction of amines with urea is well-understood.<sup>2,4,17,21</sup> As shown in **Scheme 6.1**, the melt polymerization of oligomeric PDMS diamines, urea, and the optional 1,3-bis(3-aminopropyl)tetramethyldisiloxane (BATS) yielded non-segmented [poly(PDMS-*co*-urea)] and segmented copolymers [poly(PDMS1.7kU)<sub>x</sub>-*co*-poly(BATSU)<sub>y</sub>]. Due to the lack of solvent, these polymerizations must occur above the crystalline melting point (133-135 °C) of urea. Above 150 °C, urea decomposes into ammonia and isocyanic acid, which reacts with primary amines and forms the desired 1,3-dialkylurea linkages in the absence of isocyanate reagent.<sup>2</sup> Care must be taken to avoid side product formation, which in the context of linear polyureas includes urea biurets, 1,1-dialkylurea, or imidazolidone cycles.<sup>2,21</sup> This includes the use of primary amines only, a stoichiometric excess of diamine vs. urea, and temperatures in excess of 200 °C.<sup>2,21</sup>

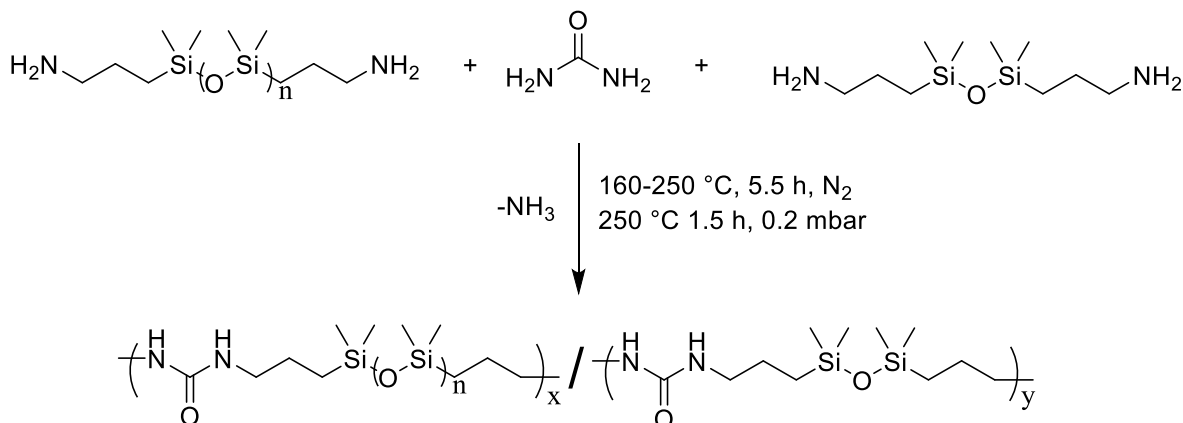
Traditional segmented polyurea synthesis with diisocyanates relies on an overall 1:1 diamine:diisocyanate stoichiometry, with the ratio of oligomeric to monomeric diamine determining HS content. However, the synthesis of segmented copolymers from a mixture of monomers and oligomers required further care.<sup>28</sup> Previous literature demonstrated that due to increased endgroup diffusion, monomers polymerize to form oligomers prior to



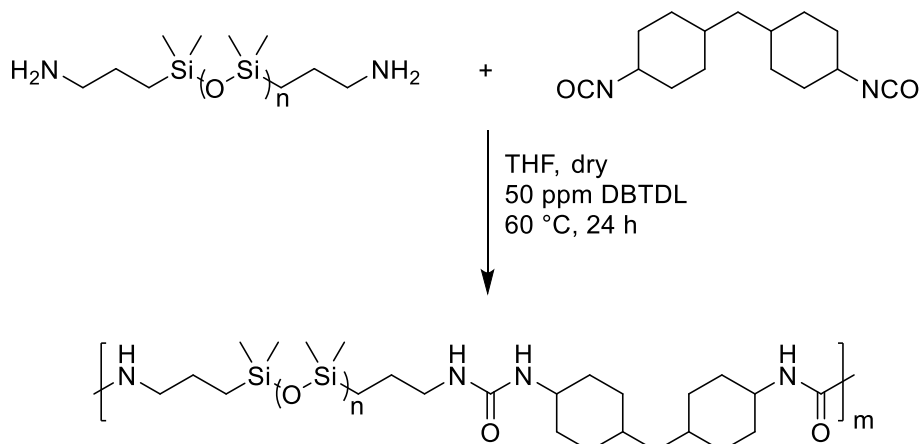
oligomer incorporation.<sup>28,29</sup> An overall 1:1 diamine:urea stoichiometry for a segmented polyurea, where the 1 eq. diamine includes both PDMS and chain extender, would result in a local stoichiometric excess of urea during polymerization of urea and chain extender, thus promoting side product formation.<sup>2,21</sup> Polymerization with a monomeric diamine excess, relative to total urea (e.g. 1.2 : 1.0 eq.), prevented side reactions and resulted in a predictable hard segment number-average molecular weight ( $M_n$ ) of 1,510 g/mol based on the Carothers equation. Based on previous literature indicating melt homogeneity issues for melt polymerizations with increasing oligomer  $M_n$ ,<sup>28,29</sup> a low PDMS oligomer  $M_n$  (e.g. 1,700 g/mol) facilitated incorporation into the melt. Maintenance of desired HS content below ~ 40 wt % ensured retention of elastomeric properties and prevented phase mixing/inversion and formation of thermoplastic polyureas.<sup>30</sup> Initial reaction at 160 °C facilitated monomer incorporation and formation of a homogeneous melt. Non-segmented samples achieved melt homogeneity at 160 °C, while segmented polyureas required additional time above 160 °C. All samples remained homogeneous at 250 °C, which reduced melt viscosity and facilitated further reaction. Polymerizations continued under reduced pressure at 250 °C until melt viscosity remained stable.

Finally, **Scheme 6.2** depicts the synthesis and characterization of traditional, solvent-based polyureas from PDMS diamines and hydrogenated methylene diphenyl diisocyanate (HMDI) [poly(PDMS-*co*-HMDU)], which provided comparable examples for these novel, isocyanate-free PDMS polyureas. Although isocyanate-free PDMS polyureas presented in **Scheme 6.1** contain different chemical structure than these model, isocyanate-containing PDMS polyureas, those presented in **Scheme 6.2** remain identical in

composition to earlier literature that employs PDMS diamines and HMDI, which facilitates comparison to the literature.<sup>6,31</sup>



**Scheme 6.1.** Synthesis of isocyanate-free, segmented, poly(dimethyl siloxane)- (PDMS)-containing polyureas with bis(3-aminopropyl)tetramethyldisiloxane (BATS) as a chain extender via melt polycondensation in the absence of solvent and catalyst [poly(PDMS1.7kU)<sub>x</sub>-co-poly(BATSU)<sub>y</sub>].



**Scheme 6.2.** Synthesis of PDMS polyureas via traditional solution step-growth polymerization in the presence of hydrogenated methylene diphenyl diisocyanate (HMDI) and dibutyltin dilaurate (DBTDL) [poly(PDMS-co-HMDU)].

<sup>1</sup>H NMR spectroscopy (**Figure 6.7**, **Figure 6.8**, **Figure 6.9**) determined M<sub>n</sub> via endgroup analysis for non-segmented PDMS polyureas, with measured values of 48,000 g/mol and 45,000 g/mol for poly(PDMS3.2k-co-urea) and poly(PDMS5.4k-co-urea),

respectively. This measurement required the assumption of 100 % bis(3-aminopropyl) termination, which remains valid due to the PDMS diamine stoichiometric excess. Unfortunately, aggregation of these polymers in solution, as measured by dynamic light scattering, precluded molecular weight determination by size exclusion chromatography (SEC). Furthermore, the lack of solubility of poly(PDMS1.7k-*co*-urea), poly(BATS-*co*-urea) and all segmented polyureas in common organic solvents precluded SEC and detailed spectroscopic studies. However, solubility in trifluoroacetic acid (TFA) enabled HS content determination via  $^1\text{H}$  NMR spectroscopy (**Figure 6.10**). TFA-d is a reactive solvent for PDMS, with products well-understood in the literature.<sup>32,33</sup> Briefly, TFA-d cleaves Si-O bonds but leaves Si-C, C-C, and C-H bonds intact. TFA-d also enjoys wide use as an NMR solvent for polyamides, polyureas, and polyurethanes.<sup>34</sup> For this reason,  $^1\text{H}$  NMR spectroscopy in TFA-d was employed only for determination of relative hard/soft segment contents for segmented copolymers, with samples discarded after analysis. **Figure 6.11** discusses calculations for HS content determination. Briefly, the ratio between integrations of the three terminal methylene units and the backbone Si-CH<sub>3</sub> protons was determined for all samples. Subsequently, an internal calibration curve determined HS content relative to poly(PDMS1.7k-*co*-urea) (0 wt % HS) and poly(BATS-*co*-urea) (100 wt % HS).

The actual wt % HS content remained far below the desired amount (e.g. 42 wt % HS charged, 4.0 wt % measured), likely due to transureaization (i.e. transesterification but for ureas) and loss of low molecular weight species throughout the polymerization and especially during the final high vacuum step, which is required for achievement of high molecular weight. A large difference molecular weight (1,700 g/mol for PDMS-NH<sub>2</sub> and 248.51 g/mol for BATS) results in drastically different boiling points for PDMS-NH<sub>2</sub> and

BATS, the latter of which is reported as 134 – 142 °C at 11.5 mm Hg.<sup>35</sup> When adjusted with a pressure-temperature nomograph, this is 268 – 278 °C while at ambient pressure and 63 – 70 °C at 0.2 mbar, the pressure achieved during our final vacuum step. Although monomer is likely fully incorporated during the slow temperature ramp from 160 – 250 °C under ambient pressure, transureaization during the final application of high vacuum at 250 °C is likely responsible for the large discrepancy in charged vs. actual HS content.

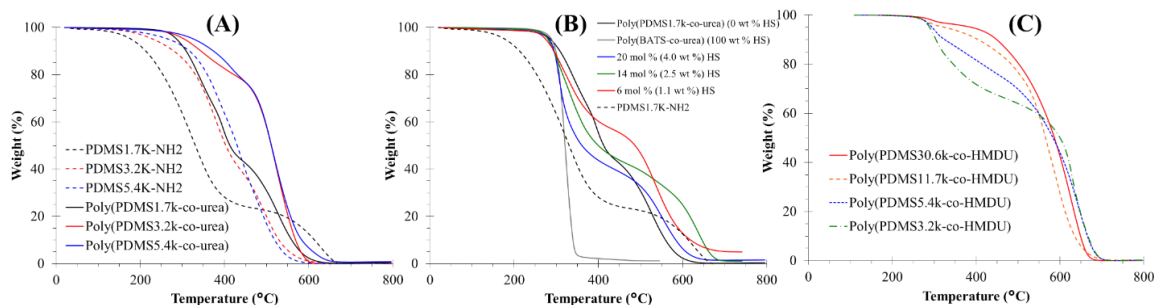


**Figure 6.1.** Weight loss vs. temperature data at 10 °C min<sup>-1</sup> from TGA for (A) non-segmented poly(PDMS-*co*-urea)s and PDMS-NH<sub>2</sub> precursors, (B) segmented poly(PDMS1.7kU)-*co*-poly(BATSU) polyureas, non-segmented poly(BATS-*co*-urea) and poly(PDMS1.7k-*co*-urea), and the PDMS1.7k-NH<sub>2</sub> precursor, and (C) poly(PDMS-*co*-HMDU) polyureas synthesized with HMDI diisocyanate.

Due to the hygroscopic nature of polyureas, all compression molding and analysis occurred after a sample drying procedure. As shown in **Figure 6.1**, TGA indicated the absence of weight loss up to 270 °C for all samples and increasing thermal stability with decreasing urea content. The first weight loss step at 270 °C occurred due to urea linkage degradation, and greater weight loss ensued at this temperature for samples containing higher hard segment content. **Figure 6.2A** depicts DSC thermograms for non-segmented poly(PDMS-*co*-urea)s and PDMS-NH<sub>2</sub> precursors, displaying clear crystallization exotherms and melting endotherms for PDMS precursors but a lack of crystallization/melting transitions for poly(PDMS-*co*-urea)s, except in the case of poly(PDMS5.4k-*co*-urea), likely due to the higher PDMS segment molecular weight. The

slight endotherm at  $\sim -30$  °C present for all samples is an instrument artifact and was not present on a 1<sup>st</sup> heating trace on a separate instrument (**Figure 6.12**).

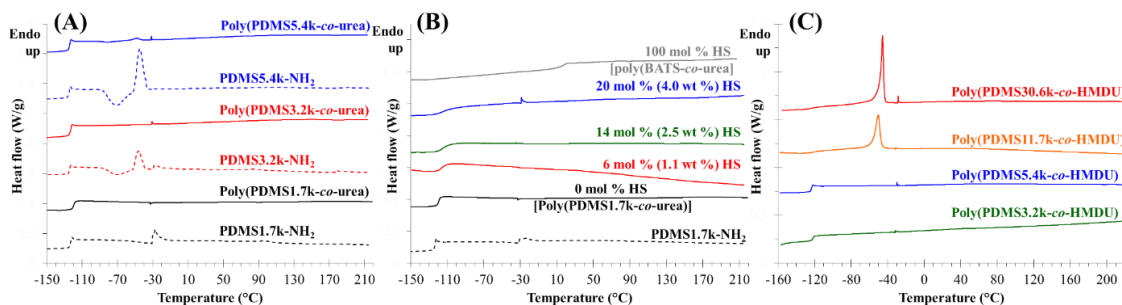


**Figure 6.2.** DSC 1<sup>st</sup> heating traces ( $10$  °C  $\text{min}^{-1}$ ) for annealed ( $100$  °C,  $18$  h, vac), (A) non-segmented poly(PDMS-*co*-urea)s and PDMS-NH<sub>2</sub> precursors, (B) segmented poly(PDMS1.7kU)<sub>x</sub>-*co*-poly(BATSU)<sub>y</sub> polyureas, non-segmented poly(PDMS1.7k-*co*-urea) and poly(BATS-*co*-urea), and the PDMS1.7k-NH<sub>2</sub> precursor, and (C) poly(PDMS-*co*-HMDU) polyureas synthesized with HMDI diisocyanate.

Although poly(PDMS3.2k-*co*-urea) and poly(PDMS5.4k-*co*-urea) were highly viscous liquids at room temperature, poly(PDMS1.7k-*co*-urea) remained an elastic solid at room temperature. Thus, all segmented compositions employed the oligomeric precursor PDMS1.7k-NH<sub>2</sub>. While  $T_g$  remained relatively unchanged from PDMS-NH<sub>2</sub> oligomeric precursors for poly(PDMS3.2k-*co*-urea) and poly(PDMS5.4k-*co*-urea), poly(PDMS1.7k-*co*-urea) demonstrated a slight increase in  $T_g$  attributed to the higher physical-crosslink density of the urea bidentate hydrogen bonding (see **Table 6.1** for numerical values). Shown in **Figure 6.2B**, segmented polyureas demonstrated similarly small  $T_g$  increases as compared to poly(PDMS1.7k-*co*-urea).

**Table 6.1. Summary of composition,  $T_{d,5\%}$ , thermal transitions, and modulus values from  $^1\text{H}$  NMR spectroscopy, TGA, DSC, and DMA, respectively.**

Sample	NCO-free	Desired hard segment content (wt %)	$^1\text{H}$ NMR spectroscopy			Actual Hard Segment content (wt %)	TGA	DSC <sup>a</sup>			DMA <sup>d</sup>			
			PDMSU	BATSU	HMDI		$T_{d,5\%}$	$T_g$ <sup>b</sup>	$T_c$ <sup>c</sup>	$T_m$ <sup>c</sup>	$T_{g1}$ <sup>e</sup>	$T_{g2}$ <sup>e</sup>	$E'_{22^\circ\text{C}}$	$T_f$ <sup>f</sup>
			(mol %)	(mol %)	(mol %)		(°C)	(°C)	(°C)	(°C)	(°C)	(°C)	MPa	(°C)
Poly(PDMS1.7k- <i>co</i> -urea)	Yes	0	100	0	-	0	287	-119	-	-	-115	-50	0.18	67
Poly(PDMS3.2k- <i>co</i> -urea)	Yes	0	100	0	-	0	305	-123	-	-	N.D.	N.D.	N.D.	N.D.
Poly(PDMS5.4k- <i>co</i> -urea)	Yes	0	100	0	-	0	328	-124	-82	-48	N.D.	N.D.	N.D.	N.D.
poly(PDMS1.7kU) <sub>94</sub> - <i>co</i> -poly(BATSU) <sub>6</sub>	Yes	21	94	6	-	1.1	275	-117	-	-	-104	-44	0.17	114
poly(PDMS1.7kU) <sub>86</sub> - <i>co</i> -poly(BATSU) <sub>14</sub>	Yes	28	86	14	-	2.5	280	-116	-	-	-102	-42	0.48	153
poly(PDMS1.7kU) <sub>80</sub> - <i>co</i> -poly(BATSU) <sub>20</sub>	Yes	42	80	20	-	4.0	283	-115	-	-	-104	-22	0.73	173
Poly(BATS- <i>co</i> -urea)	Yes	100	0	100	-	100	289	18	-	-	37	-	478	200
Poly(PDMS3.2k- <i>co</i> -HMDU)	No	11	50	-	50	11	277	-122	-	-	-111	-	8.9	129
Poly(PDMS5.4k- <i>co</i> -HMDU)	No	5.6	50	-	50	5.6	290	-124	-	-	-116	-	3.0	150
Poly(PDMS11.7k- <i>co</i> -HMDU)	No	2.4	50	-	50	2.4	325	-121	-	-51	-112	-	1.0	124
Poly(PDMS30.6k- <i>co</i> -HMDU)	No	1.1	50	-	50	1.1	389	-124	-	-46	-115	-	0.49	92
PDMS1.7k-NH <sub>2</sub>	N/A	-	-	-	-	-	179	-123	-	-	N.D.	N.D.	N.D.	N.D.
PDMS3.2k-NH <sub>2</sub>	N/A	-	-	-	-	-	231	-124	-72	-46	N.D.	N.D.	N.D.	N.D.
PDMS5.4k-NH <sub>2</sub>	N/A	-	-	-	-	-	267	-124	-70	-45	N.D.	N.D.	N.D.	N.D.

<sup>a</sup> Heating/cooling/heating thermal cycles of 10 °C min<sup>-1</sup>, values determined from first heating scans for all samples. Samples annealed at 100 °C under vacuum for 18 h and stored under vacuum at room temperature prior to analysis. <sup>b</sup>  $T_g$  values determined by inflection point. <sup>c</sup>  $T_c$  and  $T_m$  values are measured as the peak minimum or maximum, respectively. <sup>d</sup> Heating rate of 3 °C min<sup>-1</sup>, 0.1 % strain, 1 Hz. <sup>e</sup>  $T_g$  reported as tan  $\delta$  peak temperature. <sup>f</sup>  $T_f$  reported as highest temperature before flow.

The non-segmented poly(BATS-*co*-urea) did not display a PDMS  $T_g$  despite regular disiloxane backbone units and instead exhibited a single, broad  $T_g$  at 18 °C. Except for slight crystallization and melting endotherms observed on the first heat for poly(PDMS5.4k-*co*-urea), all polyureas demonstrated a lack of transition temperatures up to 220 °C, which is in agreement with prior literature.<sup>6</sup> Similarly, as shown in **Figure 6.2C**, the isocyanate-based, monodisperse hard segment-containing PDMS polyureas displayed only the PDMS  $T_g$  for poly(PDMS3.2k-*co*-HMDU) and poly(PDMS5.4k-*co*-HMDU), while the samples containing a higher PDMS segment length underwent crystallization (cooling trace not shown) and melting. **Table 6.1** summarizes composition and thermal transitions for all samples in this report.

**Figure 6.3A** illustrates the thermomechanical behavior of segmented polyureas, poly(PDMS1.7k-*co*-urea) (0 wt % HS), and poly(BATS-*co*-urea) (100 wt % HS). All samples possessed a sloped  $E'$  in the glassy regime, consistent with previous isocyanate-free, semicrystalline polyureas and with literature reports of thermomechanical behavior for similar samples.<sup>9,11,17</sup> The  $E'$  vs.  $T$  behavior for poly(BATS-*co*-urea) exacerbated this phenomenon. Although the reasoning for this remained elusive, it was presumed based on earlier literature that low-temperature plastic deformation in the glassy state<sup>36</sup> or sub- $T_g$  stress relaxation was responsible.<sup>37,38</sup> All isocyanate-free PDMS polyureas except poly(BATS-*co*-urea) exhibited two, large  $\alpha$ -relaxations (**Figure 6.3B**). The first relaxation corresponded to the PDMS  $T_g$  and agreed well with DSC measurements, with variability likely due to the different analytical methods. Though PDMS polyureas generally possess a high degree of microphase separation, due to aforementioned differences in solubility parameter for PDMS and urea, literature precedent for segmented PDMS polyureas with

relatively low oligomer  $M_n$  (e.g.  $<3,000$  g/mol) report a higher degree of phase mixing between PDMS and urea segments, placing further restrictions on long-range, cooperative, segmental chain mobility.<sup>11</sup>

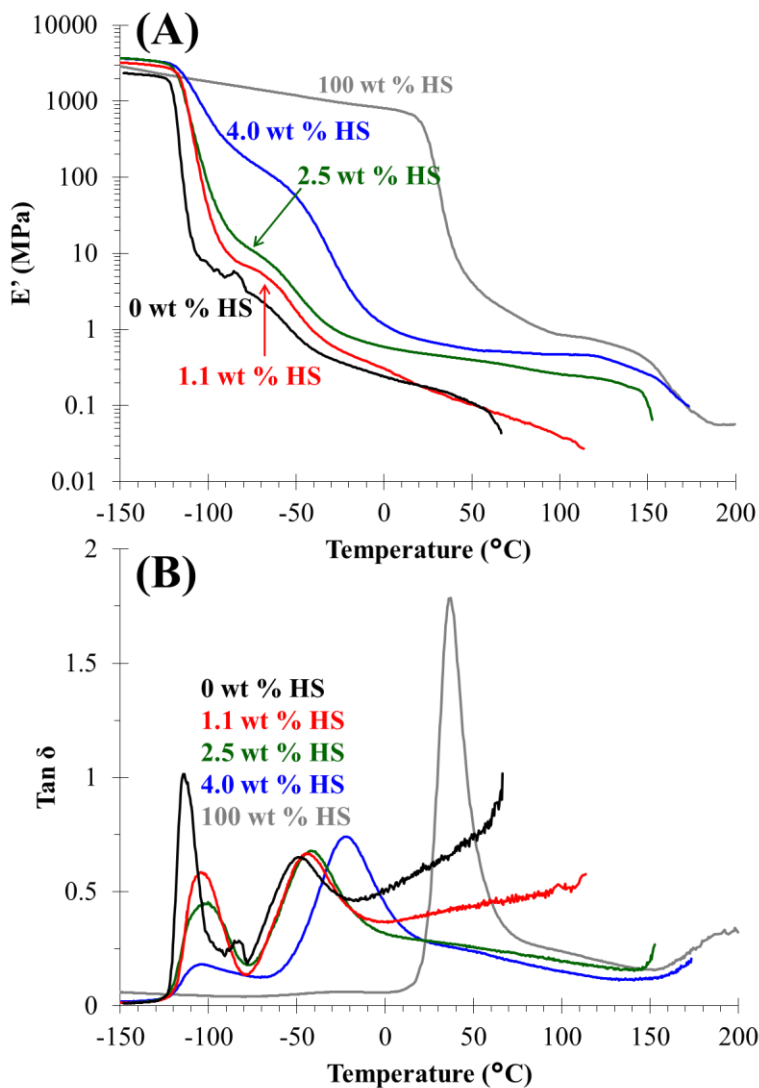


**Figure 6.3.** Dynamic mechanical analysis heating traces ( $3\text{ }^{\circ}\text{C min}^{-1}$ , 1 Hz) for annealed ( $100\text{ }^{\circ}\text{C}$ , 18 h, in vacuo) films of segmented poly(PDMS1.7kU)<sub>x</sub>-co-poly(BATSU)<sub>y</sub> polyureas and non-segmented poly(PDMS1.7k-co-urea) and poly(BATS-co-urea).

Wilkes, Yilgor, and Beyer also observed two  $\alpha$  relaxations for segmented PDMS polyureas with similar HS content.<sup>11</sup> They reported the second as PDMS segment melting for samples with 2,500 g/mol segment length, though they postulated that a segmented polyurea with



~900 g/mol PDMS segments underwent an order-disorder transition (ODT) during the DMA heating scan.<sup>11</sup> These authors also reported significantly decreased microphase separation for segmented polyureas comprised of ~900 g/mol PDMS segments as compared to polyureas containing higher molecular weight PDMS segments (e.g. 2,500 g/mol and above).<sup>11</sup> Our isocyanate-free polyureas possessed a PDMS segment length of 1,700 g/mol, which lies between these literature-based reports with 900 and 2,500 g/mol PDMS segment lengths. Although our isocyanate-free, segmented PDMS polyureas exhibited similar, double  $\alpha$ -relaxations as these literature reports, the complexity of the expected morphology requires further investigation and is outside the scope of this initial report.

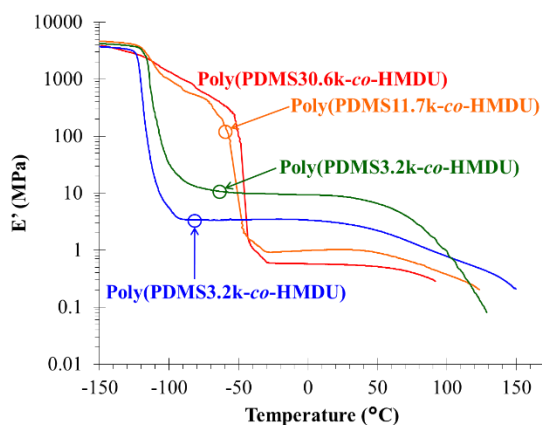


**Figure 6.4.** Dynamic mechanical analysis heating traces ( $3\text{ }^{\circ}\text{C min}^{-1}$ , 1 Hz) for annealed ( $100\text{ }^{\circ}\text{C}$ , 18 h, vac) films of poly(PDMS-*co*-HMDU) polyureas synthesized with HMDI diisocyanate.

**Figure 6.4** displays thermomechanical behavior of monodisperse hard segment-containing PDMS polyureas synthesized from diisocyanates (**Scheme 6.2**). This behavior contrasted the trends depicted in for the isocyanate-free polyureas (**Figure 6.3**), and arises from differences in polymer structure. In the case of the isocyanate-containing PDMS polyureas, PDMS oligomer and HMDU units must perfectly alternate, except in the case

of side products (e.g. decarboxylated HMDI producing multiple adjacent HMDU units). This resulted in much higher degrees of phase mixing as compared to chain-extended, segmented PDMS polyureas. As a result of this phase mixing, the poly(PDMS-*co*-HMDU) plateau moduli displayed great sensitivity to PDMS oligomer molecular weight (see **Table 6.1** for numerical values). Literature reports corroborated these observations, with an orders-of-magnitude drop in modulus at the PDMS  $T_g$  and a relatively temperature-independent rubbery plateau.<sup>6</sup> Furthermore, poly(PDMS11.7k-*co*-HMDU) and poly(PDMS31.6k-*co*-HMDU) displayed a melting point during DMA, corroborating DSC measurements and matching similar compositions in the literature.<sup>13,31</sup>

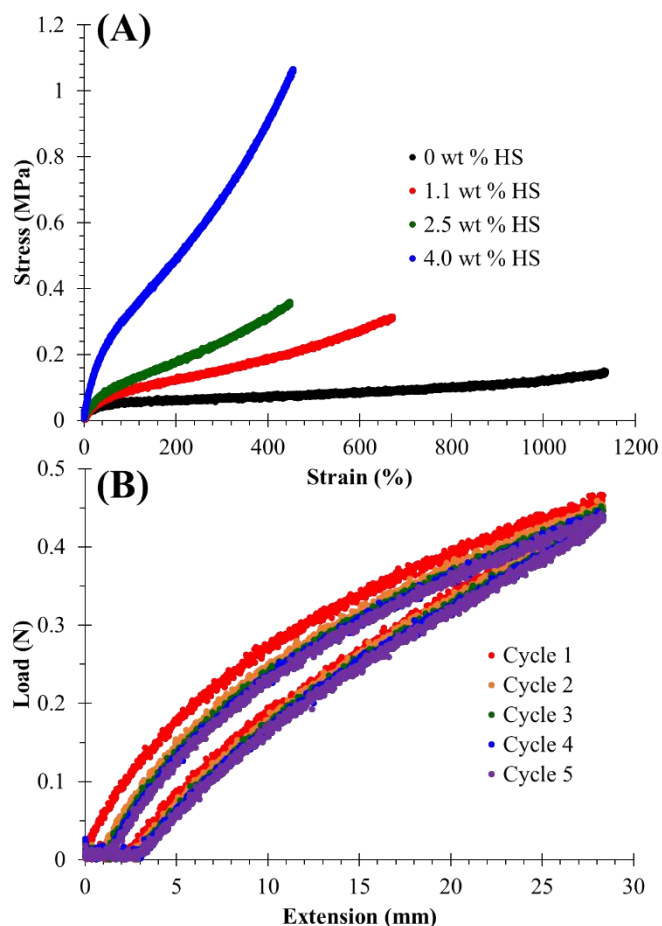


**Figure 6.5.** (A) Tensile stress vs. strain data for annealed (100 °C, 18 h, vac) films of segmented poly(PDMS1.7kU)<sub>x</sub>-co-poly(BATSU)<sub>y</sub> polyureas and non-segmented poly(PDMS1.7k-co-urea). (B) Five-cycle hysteresis profiles for poly(PDMS1.7k)<sub>80</sub>-co-poly(BATS)<sub>20</sub> (4.0 wt % HS) at 100 % strain.

**Figure 6.5A** displays tensile stress-strain behavior for the isocyanate-free poly(PDMS1.7k-co-urea) and segmented poly(PDMS1.7kU)-co-poly(BATSU)s. Here, stress at break and strain at break increased and decreased, respectively, with increasing hard segment content, again corroborating literature behavior.<sup>11</sup> Strain at break ranged from 495 % for the 4.0 wt % HS sample to 1177 % for the non-segmented poly(PDMS1.7k-co-urea), demonstrating a wide range of properties attainable by tuning HS content. **Figure 6.5B** depicts five-cycle, 100 % hysteresis curves for poly(PDMS1.7kU)<sub>80</sub>-co-

poly(BATSU)<sub>20</sub> (4.0 wt % HS), with the remaining samples shown in **Figure 6.13**. **Figure 6.6** summarizes these hysteresis measurements, displaying percent hysteresis as a function of wt % HS and cycle number, while **Table 6.2** tabulates both the tensile and percent hysteresis values. Classically, hysteresis arises from internal damping, while percent hysteresis decreases with increasing strength of hydrogen bonding interactions.<sup>8,31,39</sup> These isocyanate-free PDMS polyureas also exhibited this trend with each sample displaying small levels of permanent set, while percent hysteresis decreased with increasing HS content.

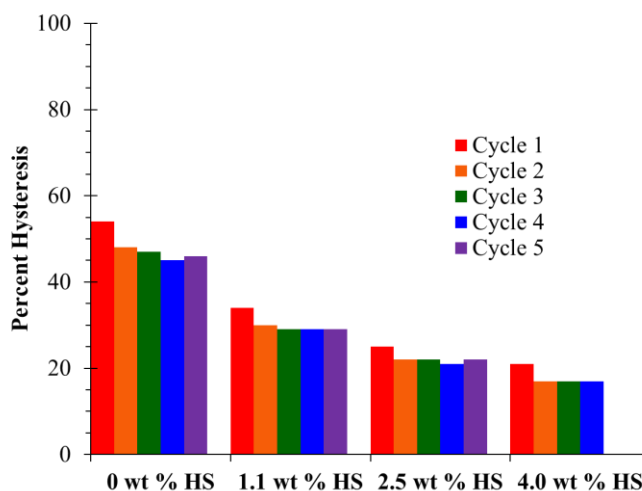


**Figure 6.6.** Summary of percent hysteresis values at 100 % strain for annealed (100 °C, 18 h, vac) films of segmented poly(PDMS<sub>1.7k</sub>)<sub>80-co</sub>-poly(BATSU)<sub>20</sub> (4.0 wt % HS) polyureas and non-segmented poly(PDMS<sub>1.7k-co</sub>-urea).

**Table 6.2.** Summary of tensile and hysteresis properties for segmented poly(PDMS1.7kU)-*co*-poly(BATSU) polyureas and non-segmented poly(PDMS1.7k-*co*-urea).

Sample	Hard segment content	Tensile modulus	Tensile stress at break	Tensile strain at break	Hysteresis at 100 % strain				
					Cycle 1	Cycle 2	Cycle 3	Cycle 4	Cycle 5
	(wt %)	(MPa)	(MPa)	(%)	(%)	(%)	(%)	(%)	(%)
Poly(PDMS1.7k- <i>co</i> -urea)	0	0.07 ± 0.024	0.12 ± 0.039	1177 ± 119	54	48	47	45	46
poly(PDMS1.7kU) <sub>94</sub> - <i>co</i> -poly(BATSU) <sub>6</sub>	1.1	0.14 ± 0.015	0.28 ± 0.034	639 ± 30	34	30	29	29	29
poly(PDMS1.7kU) <sub>86</sub> - <i>co</i> -poly(BATSU) <sub>14</sub>	2.5	0.17 ± 0.005	0.36 ± 0.039	448 ± 25	25	22	22	21	22
poly(PDMS1.7kU) <sub>80</sub> - <i>co</i> -poly(BATSU) <sub>20</sub>	4.0	0.45 ± 0.057	1.16 ± 0.463	495 ± 86	21	17	17	17	17

## 6.5 Conclusions

In conclusion, the melt polymerization of PDMS diamines, chain extender, and urea afforded a family of isocyanate-free PDMS polyureas in the absence of catalyst and solvent. As isolated, these polymers remained optically clear and formed free-standing, creaseable films. Observation of distinct thermal transitions with DSC and DMA suggested microphase separation. Tensile testing measured between 495 to 1180 % strain at break, values that remained comparable to literature reports of isocyanate-based PDMS polyureas with similar HS content, while five-cycle hysteresis measurements indicated decreasing percent hysteresis with increasing hard segment content. Future studies will include adjustment of reaction conditions and stoichiometry to achieve higher hard segment contents, up to 20-30 wt % HS. Finally, in-depth morphological investigations, including transmission electron microscopy (TEM) and small-angle x-ray scattering (SAXS) will provide further information on the degree of microphase separation as a function of HS content and chain extender structure.

## 6.6 Acknowledgements

The authors acknowledge funding from the Department of Energy's (DOE) Kansas City National Security Campus, which is operated and managed by Honeywell Federal Manufacturing & Technologies, LLC, under Contract DE-NA-0002839. The authors would like to thank Covestro for their gracious donation of Desmodur® W, a high purity 4,4'-methylenebis(cyclohexyl isocyanate), and Wacker Chemie for their gracious donation of the 11.7 kg/mol bis(3-aminopropyl)-terminated PDMS (Wacker® Fluid NH 130 D). Finally, the authors thank Jana Herzberger for helpful discussions and manuscript revisions.

## 6.7 References

- (1) Wang, P.; Ma, X.; Li, Q.; Yang, B.; Shang, J.; Deng, Y. Green Synthesis of Polyureas from CO<sub>2</sub> and Diamines with a Functional Ionic Liquid as the Catalyst. *RSC Advances* **2016**, *6*, 54013-54019.
- (2) Montarnal, D.; Cordier, P.; Soulié-Ziakovic, C.; Tournilhac, F.; Leibler, L. Synthesis of Self-Healing Supramolecular Rubbers from Fatty Acid Derivatives, Diethylene Triamine, and Urea. *Journal of Polymer Science Part A: Polymer Chemistry* **2008**, *46*, 7925-7936.
- (3) Maisonneuve, L.; Lamarzelle, O.; Rix, E.; Grau, E.; Cramail, H. Isocyanate-Free Routes to Polyurethanes and Poly(Hydroxy Urethane)s. *Chemical Reviews* **2015**, *115*, 12407-12439.
- (4) Cordier, P.; Tournilhac, F.; Soulié-Ziakovic, C.; Leibler, L. Self-Healing and Thermoreversible Rubber from Supramolecular Assembly. *Nature* **2008**, *451*, 977.
- (5) Polmanteer, K. E. Current Perspectives on Silicone Rubber Technology. *Rubber Chemistry and Technology* **1981**, *54*, 1051-1080.
- (6) Yilgor, E.; Yilgor, I. Hydrogen Bonding: A Critical Parameter in Designing Silicone Copolymers. *Polymer* **2001**, *42*, 7953-7959.
- (7) Noll, W. *Chemistry and Technology of Silicones*; Elsevier, 2012.
- (8) Yilgor, I.; Eynur, T.; Bilgin, S.; Yilgor, E.; Wilkes, G. L. Influence of Soft Segment Molecular Weight on the Mechanical Hysteresis and Set Behavior of Silicone-Urea Copolymers with Low Hard Segment Contents. *Polymer* **2011**, *52*, 266-274.
- (9) Yilgor, E.; Ekin Atilla, G.; Ekin, A.; Kurt, P.; Yilgor, I. Isopropyl Alcohol: An Unusual, Powerful, 'Green' Solvent for the Preparation of Silicone-Urea Copolymers with High Urea Contents. *Polymer* **2003**, *44*, 7787-7793.
- (10) Bates, F. S. Polymer-Polymer Phase Behavior. *Science* **1991**, *251*, 898-905.

- (11) Sheth, J. P.; Aneja, A.; Wilkes, G. L.; Yilgor, E.; Atilla, G. E.; Yilgor, I.; Beyer, F. L. Influence of System Variables on the Morphological and Dynamic Mechanical Behavior of Polydimethylsiloxane Based Segmented Polyurethane and Polyurea Copolymers: A Comparative Perspective. *Polymer* **2004**, *45*, 6919-6932.
- (12) Yilgör, I.; Riffle, J. S.; Wilkes, G. L.; McGrath, J. E. Siloxane-Urea Segmented Copolymers. *Polymer Bulletin* **1982**, *8*, 535-542.
- (13) Yilgor, I.; Eynur, T.; Yilgor, E.; Wilkes, G. L. Contribution of Soft Segment Entanglement on the Tensile Properties of Silicone–Urea Copolymers with Low Hard Segment Contents. *Polymer* **2009**, *50*, 4432-4437.
- (14) Yilgor, I.; Yilgor, E.; Wilkes, G. L. Critical Parameters in Designing Segmented Polyurethanes and Their Effect on Morphology and Properties: A Comprehensive Review. *Polymer* **2015**, *58*, A1-A36.
- (15) Anastas, P.; Eghbali, N. Green Chemistry: Principles and Practice. *Chemical Society Reviews* **2010**, *39*, 301-312.
- (16) Redlich, C. A.; Karol, M. H. Diisocyanate Asthma: Clinical Aspects and Immunopathogenesis. *International Immunopharmacology* **2002**, *2*, 213-224.
- (17) Dennis, J. M.; Steinberg, L. I.; Pekkanen, A. M.; Maiz, J.; Hegde, M.; Muller, A. J.; Long, T. E. Synthesis and Characterization of Isocyanate-Free Polyureas. *Green Chemistry* **2018**, *20*, 243-249.
- (18) Ma, S.; Liu, C.; Sablong, R. J.; Noordover, B. A. J.; Hensen, E. J. M.; van Benthem, R. A. T. M.; Koning, C. E. Catalysts for Isocyanate-Free Polyurea Synthesis: Mechanism and Application. *ACS Catalysis* **2016**, *6*, 6883-6891.
- (19) Zhang, K.; Nelson, A. M.; Talley, S. J.; Chen, M.; Margareta, E.; Hudson, A. G.; Moore, R. B.; Long, T. E. Non-Isocyanate Poly(Amide-Hydroxyurethane)S from Sustainable Resources. *Green Chemistry* **2016**, *18*, 4667-4681.
- (20) Tang, D.; Mulder, D. J.; Noordover, B. A.; Koning, C. E. Well-Defined Biobased Segmented Polyureas Synthesis Via a Tbd-Catalyzed Isocyanate-Free Route. *Macromolecular rapid communications* **2011**, *32*, 1379-1385.
- (21) Erickson, J. G. Reactions of Long-Chain Amines. Ii. Reactions with Urea. *Journal of the American Chemical Society* **1954**, *76*, 3977-3978.
- (22) Mathis, R., Polyurea Fibers Based on Poly (4, 4 {40-Methylenedicyclohexylene) Urea. US3857819A, 1974.
- (23) Isidor, K.; Bouboulis, C. J.; White, C. M., Flexible Polyureas. US3390137A, 1968.
- (24) Bouboulis, C. J.; Isidor, K., Polyureas. US3412072A, 1968.
- (25) Wolfgang, I.; Peter, B., Thermoplastic Polyureas Prepared from Araliphatic Diamines. US3388103A, 1968.
- (26) Rudolf, G.; Helmut, M., Preparation of Linear Polyurea Polymers from Urea and an Alicyclic Diamine. US3223682A, 1965.
- (27) Modak, J. M. Haber Process for Ammonia Synthesis. *Resonance* **2002**, *7*, 69-77.
- (28) Dennis, J. M.; Fahs, G. B.; Moore, R. B.; Turner, S. R.; Long, T. E. Synthesis and Characterization of Polysulfone-Containing Poly(Butylene Terephthalate) Segmented Block Copolymers. *Macromolecules* **2014**, *47*, 8171-8177.
- (29) Dennis, J. M.; Fahs, G. B.; Moon, N. G.; Mondschein, R. J.; Moore, R. B.; Wilkes, G. L.; Long, T. E. Synthesis of Polysulfone-Containing Poly(Butylene

- Terephthalate) Segmented Block Copolymers: Influence of Segment Length on Thermomechanical Performance. *Macromolecules* **2017**, *50*, 5107-5113.
- (30) Seefried, C. G.; Koleske, J. V.; Critchfield, F. E. Thermoplastic Urethane Elastomers. Ii. Effects of Variations in Hard-Segment Concentration. *Journal of Applied Polymer Science* **1975**, *19*, 2503-2513.
- (31) Buckwalter, D. J.; Zhang, M.; Inglefield Jr, D. L.; Moore, R. B.; Long, T. E. Synthesis and Characterization of Siloxane-Containing Poly(Urea oxamide) Segmented Copolymers. *Polymer* **2013**, *54*, 4849-4857.
- (32) Lee, J. N.; Park, C.; Whitesides, G. M. Solvent Compatibility of Poly(Dimethylsiloxane)-Based Microfluidic Devices. *Analytical Chemistry* **2003**, *75*, 6544-6554.
- (33) Wilczek, L.; Chojnowski, J. Acidolytic Ring Opening of Cyclic Siloxane and Acetal Monomers. Role of Hydrogen Bonding in Cationic Polymerization Initiated with Protonic Acids. *Macromolecules* **1981**, *14*, 9-17.
- (34) Kricheldorf, H. R. 15n-Nmr Spectroscopy. Xviii. Sequence Analysis of Linear Polyureas. *Journal of Macromolecular Science: Part A - Chemistry* **1980**, *14*, 959-975.
- (35) Saam, J.; Speier, J. Notes. Preparation of 3-Triethoxysilylpropylamine and 1,3-Bis(3-Aminopropyl)Tetramethyldisiloxane. *The Journal of Organic Chemistry* **1959**, *24*, 119-120.
- (36) Argon, A. S. A Theory for the Low-Temperature Plastic Deformation of Glassy Polymers. *The Philosophical Magazine: A Journal of Theoretical Experimental and Applied Physics* **1973**, *28*, 839-865.
- (37) Wietor, J.-L.; Dimopoulos, A.; Govaert, L. E.; van Benthem, R. A. T. M.; de With, G.; Sijbesma, R. P. Preemptive Healing through Supramolecular Cross-Links. *Macromolecules* **2009**, *42*, 6640-6646.
- (38) Dimopoulos, A.; Wietor, J.-L.; Wübbenhorst, M.; Napolitano, S.; van Benthem, R. A. T. M.; de With, G.; Sijbesma, R. P. Enhanced Mechanical Relaxation Below the Glass Transition Temperature in Partially Supramolecular Networks. *Macromolecules* **2010**, *43*, 8664-8669.
- (39) Riehle, N.; Thude, S.; Götz, T.; Kandelbauer, A.; Thanos, S.; Tovar, G. E. M.; Lorenz, G. Influence of Pdms Molecular Weight on Transparency and Mechanical Properties of Soft Polysiloxane-Urea-Elastomers for Intraocular Lens Application. *European Polymer Journal* **2018**.



## 6.8 Supporting Information

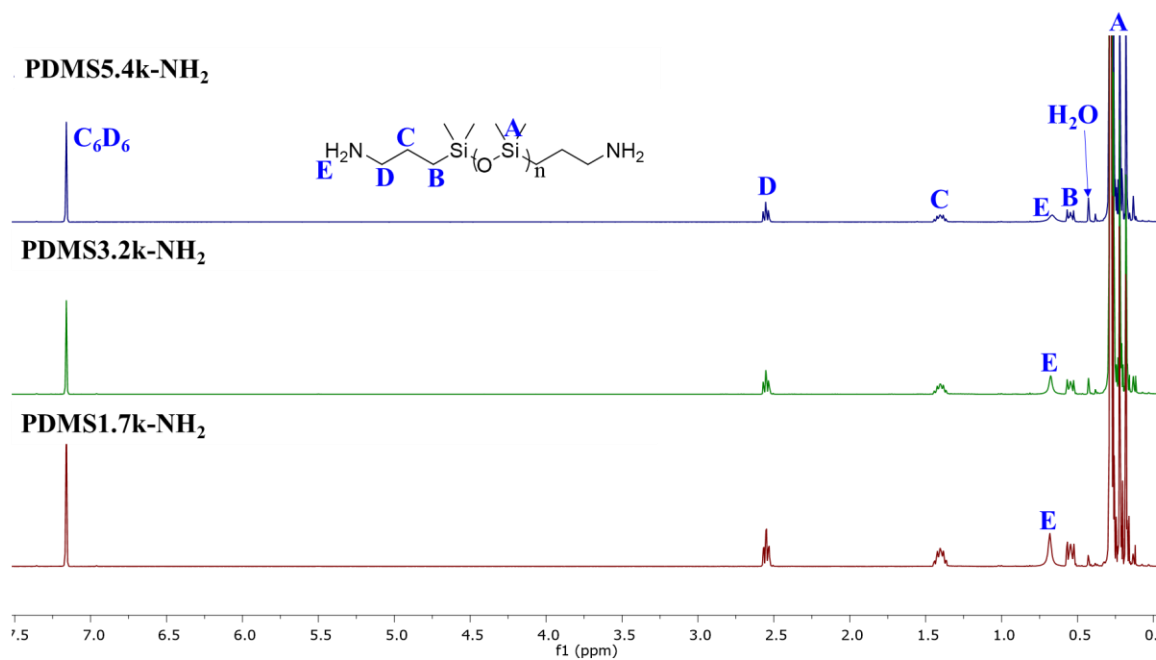


**Figure 6.7.**  $^1\text{H}$  NMR spectra overlay of PDMS-NH<sub>2</sub> oligomeric starting materials in C<sub>6</sub>D<sub>6</sub> at 23 °C.

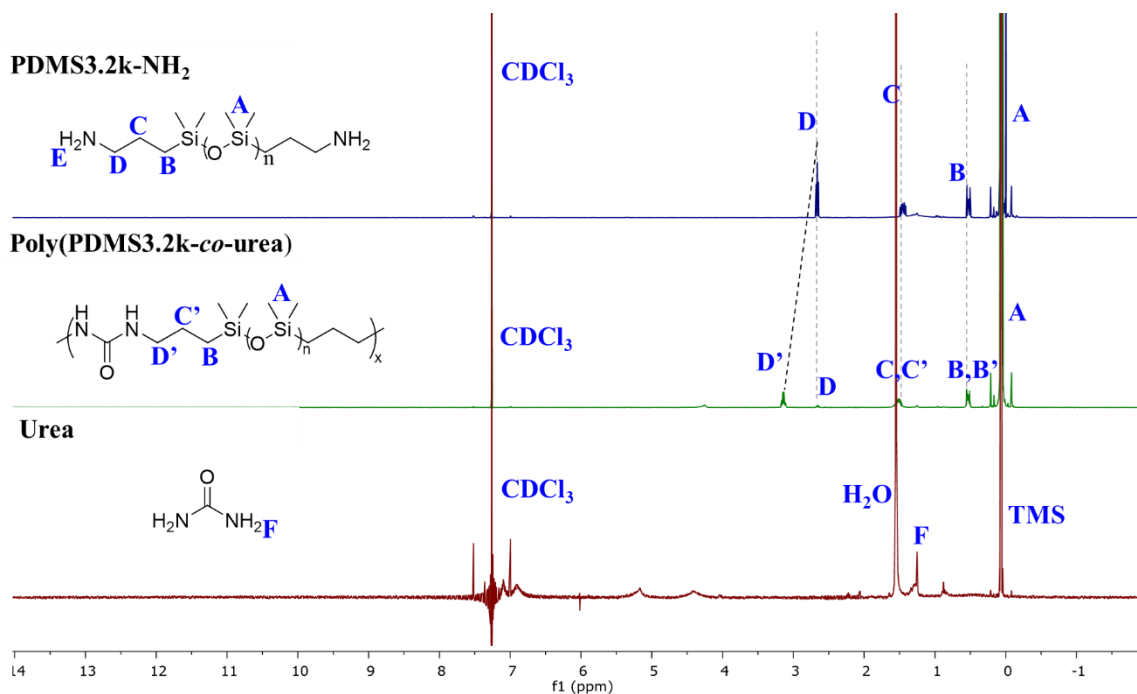
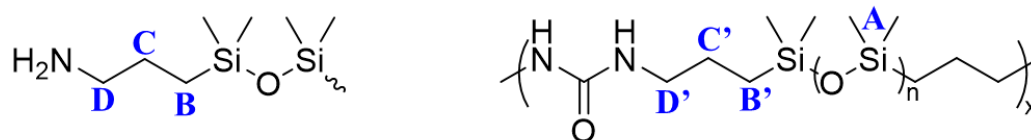


**Figure 6.8.** Example  $^1\text{H}$  NMR spectra overlay of non-segmented, isocyanate-free poly(PDMS-*co*-urea)s [poly(PDMS3.2k-*co*-urea) shown] and starting materials in CDCl<sub>3</sub> at 23 °C.



- Assume 3-aminopropyl terminated polyureas, due to stoichiometric PDMS excess
  - PDMS3.2k-NH<sub>2</sub> = 3186 g/mol, repeat unit MW (RUMW) = 3212 g/mol
  - PDMS5.4k-NH<sub>2</sub> = 5403 g/mol, RUMW = 5403 g/mol
  - Endgroups (EG) = PMDS-NH<sub>2</sub> MW
  - $\int D$  set to 4.00 for all samples
  - $\#RUS = \frac{\int B, B' - \int D}{4}$
  - $M_{n, NMR} = \#RUS * RUMW - EG$
- | Sample                 | M <sub>n</sub> , <sup>1</sup> H NMR spectroscopy |
|------------------------|--|
| Poly(PDMS3.2k-co-urea) | 47,720   |
| Poly(PDMS5.4k-co-urea) | 45,400   |

**Figure 6.9.** Example number-average molecular weight (M<sub>n</sub>) determination based on integrations from <sup>1</sup>H NMR spectra in CDCl<sub>3</sub> at 23 °C.

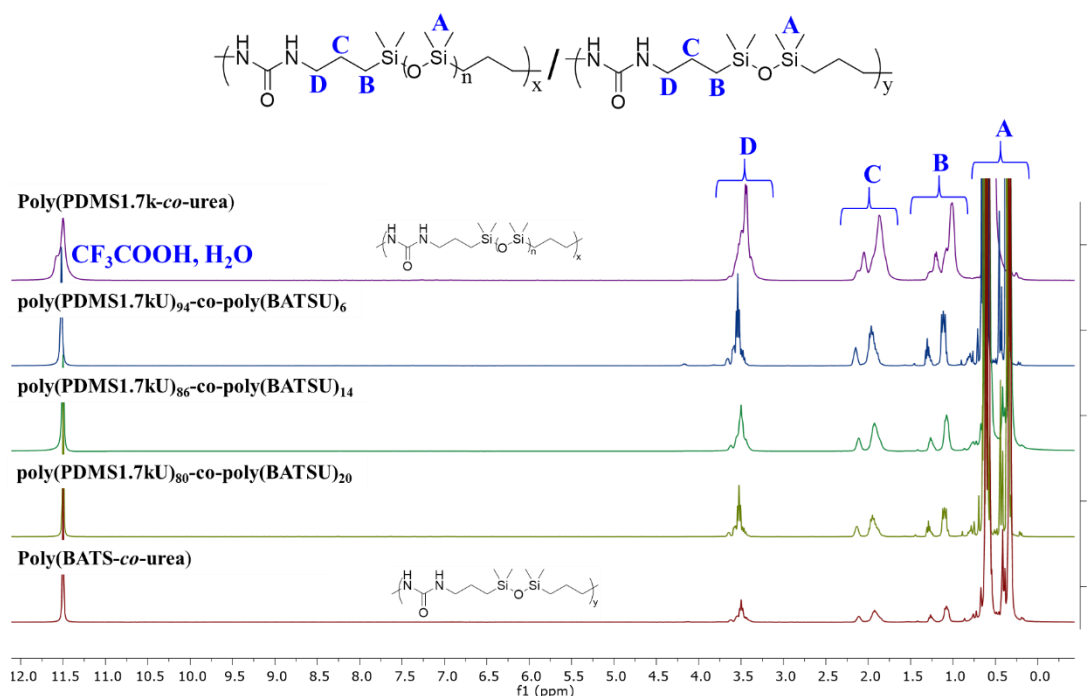
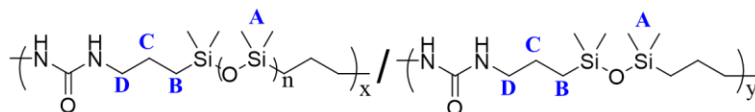


**Figure 6.10.** <sup>1</sup>H NMR spectra overlay of all isocyanate-free, segmented poly(PDMS1.7kU)-co-poly(BATSU), non-segmented poly(PDMS1.7k-co-urea) and non-segmented poly(BATS-co-urea) in CF<sub>3</sub>COOD at 23 °C.



#### Hard segment content determination

- Set D integral to 4.
- Region A is integrated and a value of  $(4 - \int B)$  is subtracted from it, to account for any B signal overlap within region A.
- Ratio of  $\frac{\int C + \int D + 4}{\int A}$  determined for each sample. 4 is added due to B signal not integrating to 4.
- Ratio of  $\frac{\int C + \int D + 4}{\int A}$  defined as 0 wt % HS for poly(PDMS1.7k-co-urea) (0.081927) and defined as 100 wt % HS for poly(BATS-co-urea) (0.99011), then ratios for all segmented copolymers normalized between 0-100 using the formula  $\frac{x - \min}{\max - \min} * 100$  where  $x$  is the integration ratio, min is 0.081927 and max is 0.99011.
  - The ratio of  $\frac{x - \min}{\max - \min} * 100$  is the mol % hard segment (HS)
- Mol % soft segment (SS) = 1 – mol % HS
- Define the following variables:
  - Let  $z$  = mol fraction hard segment (between 0-1)
  - Let  $g$  = poly(PDMS1.7k-co-urea) repeat unit molecular weight = 1685 g/mol
  - Let  $h$  = poly(BATS-co-urea) repeat unit molecular weight = 274.53 g/mol
- Hard segment is defined as poly(BATS-co-urea) repeat units only, since ureas within the poly(PDMS1.7k-co-urea) repeat unit are likely not phase separated from the PDMS-rich phase.
- $Wt \% HS = \frac{z \cdot h}{(z \cdot h) + (1 - z) \cdot g} * 100$

Moiety	MW (g/mol)
PDMS1.7k-NH <sub>2</sub>	1659
Poly(PDMS1.7k-co-urea) RUMW	1685
BATS	248.52
Poly(BATS-co-urea) RUMW	274.53

Sample	Integration					Mol % HS	Mol % SS	wt % HS
	D	C	B	A	(C+D)/ (A)			
Poly(PDMS1.7k-co-urea)	4.00	4.04	3.79	146.96	0.08	0	100	<b>0.0</b>
poly(PDMS1.7kU) <sub>94</sub> -co-poly(BATSU) <sub>6</sub>	4.00	4.01	3.57	85.54	0.14	6	94	<b>1.1</b>
poly(PDMS1.7kU) <sub>86</sub> -co-poly(BATSU) <sub>14</sub>	4.00	4.03	3.49	58.79	0.20	14	86	<b>2.5</b>
poly(PDMS1.7kU) <sub>80</sub> -co-poly(BATSU) <sub>20</sub>	4.00	4.19	3.67	45.81	0.27	20	80	<b>4.0</b>
Poly(BATS-co-urea)	4.00	4.02	3.94	12.14	0.99	100	0	<b>100.0</b>

**Figure 6.11.** Hard segment content determination, calculations, and assumptions for isocyanate-free, segmented poly(PDMS1.7kU)-co-poly(BATSU), non-segmented poly(PDMS1.7k-co-urea) and non-segmented poly(BATS-co-urea).

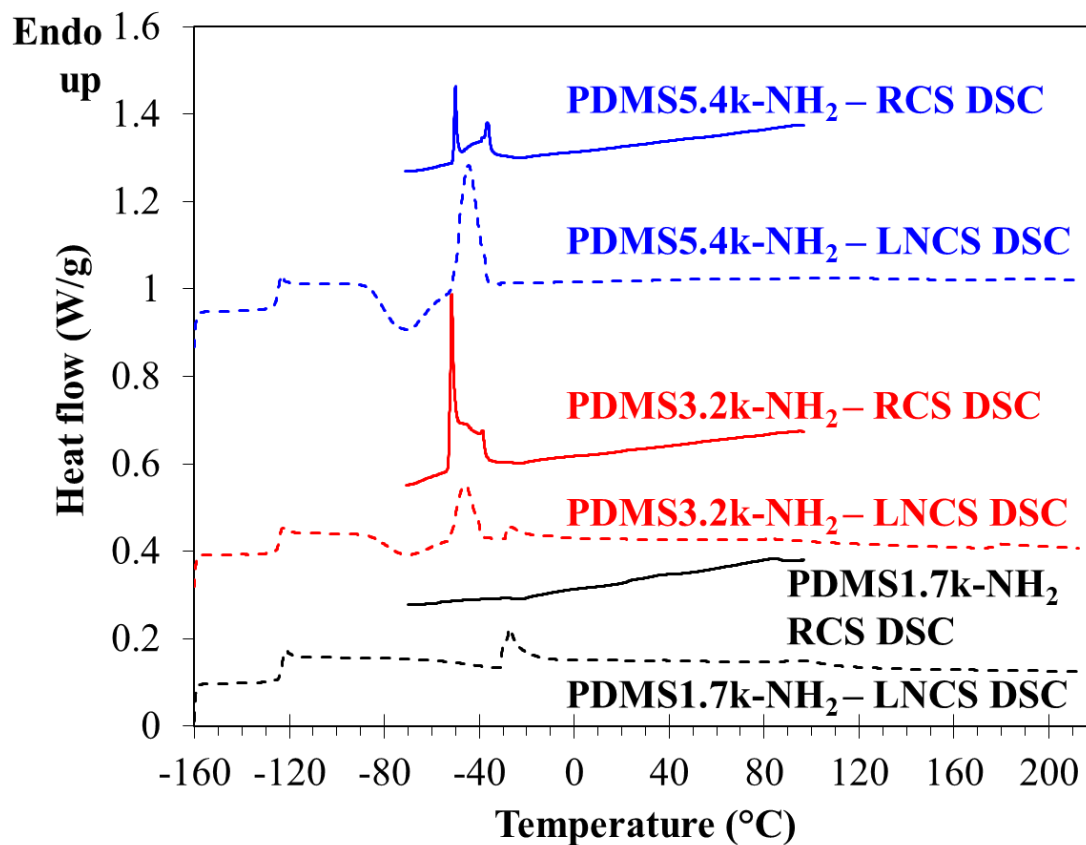


**Figure 6.12.** DSC 1<sup>st</sup> heating traces (10 °C min<sup>-1</sup>) for PDMS-NH<sub>2</sub> precursors from a liquid nitrogen cooling system (LNCS) DSC and a refrigerated cooling system (RCS) DSC.

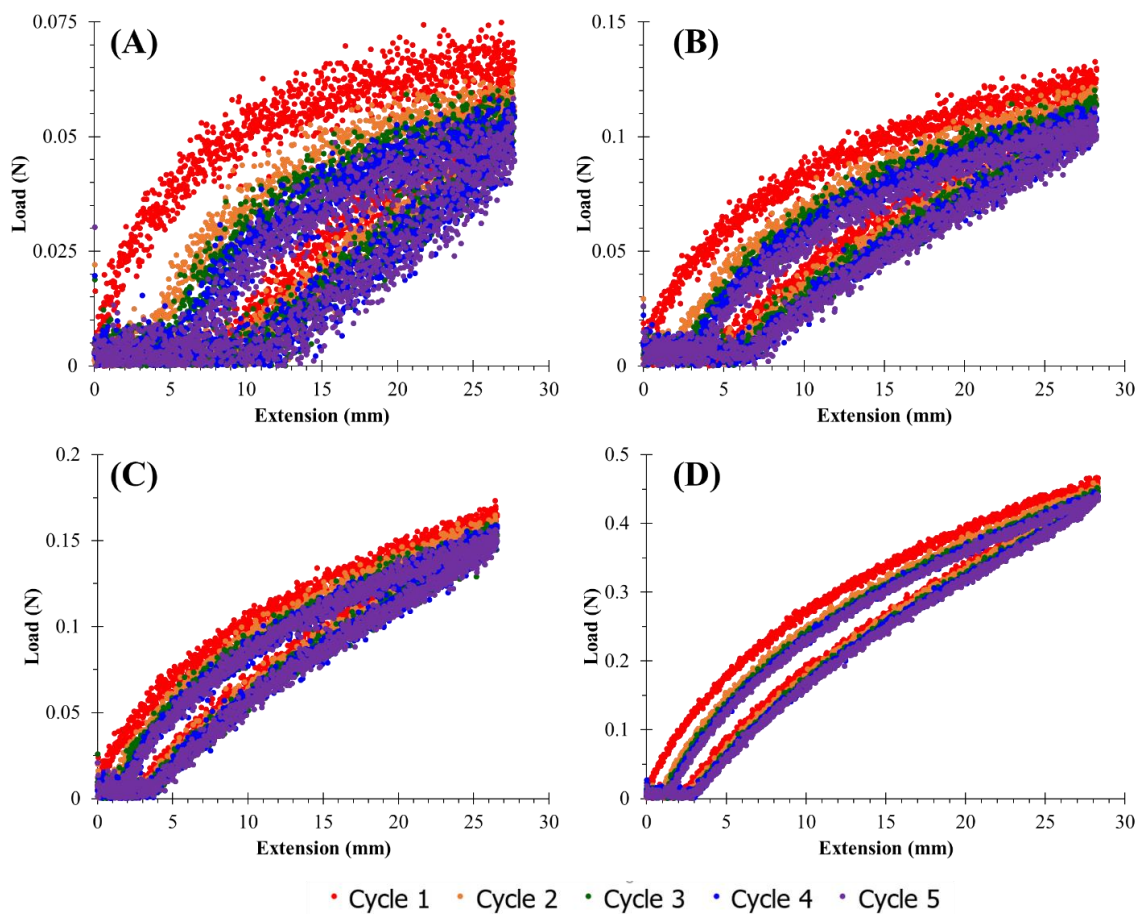


**Figure 6.13.** Five-cycle, 100% hysteresis profiles for (A) poly(PDMS1.7kU-*co*-urea), (B) poly(PDMS1.7kU)<sub>94</sub>-*co*-poly(BATSU)<sub>6</sub>, (C) poly(PDMS1.7kU)<sub>86</sub>-*co*-poly(BATSU)<sub>14</sub>, and (D) poly(PDMS1.7kU)<sub>80</sub>-*co*-poly(BATSU)<sub>20</sub>.

## Chapter 7: **Supercritical Fluid Chromatography with Evaporative Light Scattering Detection (SFC-ELSD) for Determination of Oligomer Molecular Weight Distributions**

(Published in *Chromatographia* **2016**, 79, 977-984.)

Justin M. Sirrine, Mehdi Ashraf-Khorassani, Nicholas G. Moon, Ryan J. Mondschein,  
and Timothy E. Long

*Macromolecules and Interfaces Institute, Department of Chemistry,  
Virginia Tech, Blacksburg, VA 24061*

### **7.1 Abstract**

Ultraviolet- (UV) curable polyureas and polyurethanes enjoy a wide range of applications in the coatings industry. They demand less energy for curing compared to thermal processes, offer relatively low viscosities before photocuring, and provide mechanical property improvements due to hydrogen bonding physical crosslinks. Mechanical properties of the coatings are dependent on a variety of factors including chemical composition, molecular weight, and molecular weight distribution. Formulations are designed for a wide variety of end use applications, ranging from soft, elastomeric coatings to harder, nonflexible sealants. This report demonstrates that the thermomechanical behavior of photocured coatings is a function of molecular weight distribution. Step-growth polymerization and endcapping afforded a variety of acrylate-terminated, urea-/urethane-containing photocurable oligomers from amine-terminated poly(propylene glycol) (PPG), dicyclohexylmethane-4,4'-diisocyanate (HMDI), and 2-hydroxyethyl acrylate (HEA) at various stoichiometric ratios. State-of-the-art supercritical fluid chromatography coupled with evaporative light scattering detection (SFC-ELSD) enabled the elucidation of oligomeric molecular weight distributions as a function of reaction stoichiometry. SFC-ELSD demonstrated efficient separation of oligomeric species

with single repeat unit resolution (i.e.  $n = 2$  vs.  $n = 3$ ). Dynamic mechanical analysis (DMA) probed thermomechanical response of photocured films as a function of molecular weight distribution and demonstrated that the presence of a hydrogen-bonding, small molecule photoactive reaction byproduct, i.e. HEA doubly-encapped HMDI, had a much more profound effect on thermomechanical response as compared to changes in oligomer molecular weight in the molecular weight range investigated. This combination of chromatographic technique and thermomechanical analysis afforded an in-depth investigation of the structure-property relationships of urea-/urethane-containing photocurable oligomers.

## 7.2 Introduction

Ultraviolet- (UV) curable oligomers and polymers enjoy a wide spectrum of applications including coatings,<sup>1,2</sup> pressure-sensitive adhesives (PSAs),<sup>3</sup> additive manufacturing,<sup>4</sup> and biomaterials.<sup>5</sup> Referred to herein as photocurable oligomers/polymers or photopolymers, these compositions contain UV-reactive functional groups that react with one another to form a covalently crosslinked network and serve to raise the modulus of the material upon UV irradiation. Our group has recently reported on a variety of photocurable chemistries, including star-shaped poly(D,L-lactide) networks,<sup>6</sup> cinnamate-functionalized fibers for electrospinning,<sup>7</sup> hydrogen-bonding photocurable acrylics,<sup>3</sup> and photocurable polyesters for 3D-printable tissue scaffolds.<sup>4</sup> Many applications require soft, low modulus (stiffness) compositions that maintains mechanical integrity through the entire application temperature window. These compositions often feature a soft, flexible component and hard, rigid component. At the application temperature, the flexible component is above its glass transition temperature ( $T_g$ ), which is a reversible transition in amorphous regions of polymers between a rigid, “glassy” state to a flexible, “rubbery” state

that occurs upon a temperature increase. The rigid component provides overall mechanical integrity and frequently contains permanent covalent crosslinks or temporary physical (non-covalent) crosslinks that remain intact, or rapidly reform upon breaking, at the application temperature. Examples of these two-phase materials include coatings for fiber optic waveguides, substrates for soft tissue engineering scaffolds, and anti-fouling coatings.<sup>2,4</sup> Hydrogen bonding is a temperature-dependent physical interaction that offers mechanical property improvements through dynamic physical crosslinks. Hydrogen bonding is easily achieved synthetically through the introduction of urethane or urea functional groups.<sup>3</sup>

Urethane acrylates remain one of the most ubiquitous forms of UV-curable coatings. Synthesis typically proceeds in a two-step, one-pot reaction, known as the direct addition procedure.<sup>8</sup> A diisocyanate (D) endcaps a telechelic polyol (P), and then a hydroxyl-functional acrylate (A) reacts with remaining isocyanate functional groups, forming urethanes. In this manner, the idealized, linear, photocurable urethane acrylate oligomer consists of ADPDA, or A(DP)<sub>1</sub>DA, with a DP repeat unit length of  $m = 1$ . A potential also exists for the formation of higher molecular weight analogs, i.e. ADPDPDA, or A(DP)<sub>2</sub>DA ( $m = 2$ ) and higher ( $m = 3, 4$ , etc.). For any idealized mixture of telechelic, photocurable oligomers where only endgroups are capable of crosslinking, the ratio between polymerized species ( $m = 2, 3, 4$ , etc.) and endcapped species ( $m = 1$ ) relates to the overall molecular weight distribution. For telechelic systems, upon subsequent UV curing, the molecular weight between crosslinks ( $M_c$ ) is determined by the number-average oligomer molecular weight ( $M_n$ ).  $M_c$  influences structure-property relationships, e.g., a



photocured coating with the same chemical composition but lower  $M_c$  will have a higher modulus than a sample with higher  $M_c$ .<sup>9</sup>

Many analytical techniques exist for the characterization of polymer molecular weight, molecular weight distribution, and chemical composition, including Fourier transform infrared spectroscopy (FTIR) and nuclear magnetic resonance (NMR) spectroscopy. Advanced mass spectrometry (MS) techniques, i.e. matrix-assisted laser desorption/ionization time-of-flight (MALDI-TOF) mass spectrometers and chromatographic techniques, i.e. size-exclusion chromatography (SEC) also provide absolute mass and molecular weight/molecular weight distribution information. However, due to cost and maintenance requirements, the availability of this instrumentation is limited. Additionally, SEC requires specialized columns for efficient separation of low molecular weight polymers (oligomers). Alternative techniques such as supercritical fluid chromatography (SFC) gain advantages over other techniques due to the mobile phase. Supercritical fluids typically have a density similar to liquids but a viscosity and diffusivity closer to a gas, enabling faster and more efficient separation of high molecular weight compounds.<sup>10</sup> The separation of oligomers with packed or capillary column SFC is well established.<sup>11-14</sup> Supercritical carbon dioxide ( $scCO_2$ ) is the most common mobile phase, as it is low cost, non-toxic, and solvating power can be modulated with pressure. Mobile phase polarity and solvating power are increased through the addition of polar solvents (i.e. methanol or ethanol) as mobile phase modifiers.  $scCO_2$  also offers lower viscosity and higher diffusivity, which enhances separation efficiency and reduces analysis time.

SFC and hyphenated techniques are routinely employed for polymer separation and characterization. Pinkston *et al.* used SFC-MS to characterize low molecular weight

alkoxylated polymers and determined molecular weight of polymers up to 2,200 m/z.<sup>15</sup> Hoffman *et al.* used SFC to separate oligomers of alcohol ethoxylates (AEOs) and propoxylates (APOs) in pure scCO<sub>2</sub>.<sup>11</sup> Derivatization of AEOs and APOs with UV-active chromophores and reduction in scCO<sub>2</sub> pressure/temperature facilitated detection at 215 nm with no mobile phase interference. Unfortunately, UV detection occasional poses problems; baseline drift is observed at short UV wavelengths with gradient polar organic mobile phase modifiers.<sup>16</sup> Universal detectors, i.e. MS or evaporative light scattering detection (ELSD) are frequently coupled with SFC and avoid sample derivatization requirements or baseline drift issues due to mobile phase modifier gradient. SFC is applicable to a variety of polymeric chemistries and has enabled fractionation of poly(ethylene glycol) (PEG) oligomers, various aliphatic polyester oligomers and cyclics, and polystyrene oligomers.<sup>10,17-19</sup> Two other recent SFC reports examine the effect of various experimental parameters including flow rate, injection volume, mobile phase modifier, and drift tube temperature on ELS detection of small molecules, including caffeine, hydrocortisone, and various phthalate plasticizers for biomedical applications.<sup>20,21</sup> While there are other separatory and analytical techniques that might suit this study, SFC-ELSD was chosen for ease of operation, speed of equilibration, and versatility of the scCO<sub>2</sub> mobile phase.

This study employs SFC-ELSD for the characterization of UV-curable oligomer populations according to repeat unit (i.e. by  $m = 1$ ,  $m = 2$ , etc.). Additionally, a combination of SFC and dynamic mechanical analysis (DMA) provides a concurrent evaluation of oligomer molecular weight distributions and correlation to changes in thermomechanical behavior. DMA is a powerful polymer characterization technique that probes viscoelastic

response to a sinusoidally applied load, and is often performed as a function of temperature, oscillation frequency, or oscillation amplitude. DMA is much more sensitive to glass transition temperatures and other molecular motions as compared to differential scanning calorimetry (DSC), as it observes these transitions in a mechanical manner. In this work, the combination of advanced chromatography and thermomechanical analysis allows for an in-depth probe of  $M_c$  and structure-property relationships. Previous studies have examined the synthetic approach used to produce UV-curable coatings,<sup>8</sup> probed molecular weight distributions with various chromatographic techniques,<sup>18</sup> or examined thermomechanical properties of UV-curable coatings,<sup>22</sup> but to our knowledge there is no study that combines these approaches. In this work, poly(propylene glycol) (PPG) and urea-/urethane-containing acrylate telechelic oligomers were chosen as a model system as they represent an industrially relevant chemistry for soft coatings applications. Molecular weight distributions are determined via SFC-ELSD and thermomechanical response of photocured films is probed as a function of reaction stoichiometry.

### **7.3 Materials and Methods**

#### **7.3.1 Materials and Reagents**

Poly(propylene glycol) bis(2-aminopropyl ether) (average  $M_n \sim 2,000$  g/mol) (PPG) was purchased from Sigma Alrich (St. Louis, MO, USA) and dried under reduced pressure for 12 h at 40 °C before use. Dicyclohexylmethane-4,4'-diisocyanate (HMDI) (99.5%) was kindly provided by Bayer MaterialScience (now Covestro) (Pittsburgh, PA, USA) and used as received. 2-hydroxyethyl acrylate (HEA) (96%) was purchased from Sigma Aldrich and distilled from calcium hydride before use. Dibutyltin dilaurate (DBTDL) ( $\geq 95\%$ ) was purchased from Sigma Aldrich and used as a 1 wt % solution in tetrahydrofuran (THF). 4-methoxyphenol (MEHQ) (purity,  $\geq 98.0\%$ ), 2,2-dimethoxy-2-

phenylacetophenone (DMPA) (99%), and formic acid (ACS grade) were purchased from Sigma Aldrich and used as received. Tetrahydrofuran (THF) (HPLC grade) was purchased from Spectrum (New Brunswick, NJ, USA) and dried with an Innovative Technology PureSolv (Amesbury, MA, USA) solvent purification system before use. Methanol (HPLC grade) was purchased from Thermo-Fisher (Waltham, MA, USA) and used as received. Industrial grade liquid carbon dioxide (CO<sub>2</sub>) was obtained from Praxair (Danbury, CT, USA) and used as received. Spectra/Por® 7 Dialysis Membranes with molecular weight cutoff (MWCO) 1,000 g/mol were purchased from VWR (Radnor, PA, USA) and used as received.

### 7.3.2 Synthesis of ADPDA

A three-necked, 250 mL round-bottomed flask was fitted with an addition funnel, nitrogen inlet, outlet bubbler, overhead mechanical stirrer, and condenser column, and subsequently flame-dried while under nitrogen purge. After cooling, glass joints were sealed with Teflon® tape and Parafilm®. Typical synthesis followed a two-step, one-pot synthetic route without isolation or workup between steps one and two, and was conducted under inert N<sub>2</sub> atmosphere. PPG (15.30 g, 7.44 mmol, 1.0 eq.) was added dropwise to a reaction flask containing HMDI (3.90 g, 14.88 mmol, 2.0 eq.), 50 ppm DBTDL, and dry THF (~100 mL) at 60 °C over 30 min and reacted for 4 h to form the isocyanate-terminated prepolymer. HEA (1.90 g, 16.37 mmol, 2.2 eq.) was then added at once to the prepolymer solution and reacted for a further 24 h. In order to prevent premature acrylate thermopolymerization during subsequent characterization, 1000 ppm (0.021 g, 0.170 mmol) MEHQ was added to the final reaction mixture. THF was removed with a rotary evaporator under reduced pressure and the product was subsequently dried *in vacuo* at 40 °C for 12 h. The resulting slightly yellow, viscous liquid was stored at -20 °C for

subsequent characterization. In select samples, the isolated, photocurable oligomer was dialyzed for 72 h against THF with dialysis media changed every 24 h. Finally, an additional 1000 ppm MEHQ was added. The THF was removed with a rotary evaporator under reduced pressure, and the product was subsequently dried *in vacuo* at 40 °C for 12 h. <sup>1</sup>H nuclear magnetic resonance (<sup>1</sup>H NMR) spectroscopy of the crude, uncured oligomer was performed using a Varian Unity 400 MHz spectrometer with CDCl<sub>3</sub> at 23°C and is provided in **Figure 7.4**.

### **7.3.3 Synthesis of DPD**

The synthesis was conducted similarly to the ADPDA samples, above. After the formation of the isocyanate-terminated prepolymer in the first step, methanol (MeOH) (excess) was added to the reaction in place of the HEA and mixed for 24 h at 60 °C under a N<sub>2</sub> atmosphere. THF and MeOH were removed with a rotary evaporator under reduced pressure and the product was subsequently dried *in vacuo* at 40 °C for 12 h. The resulting slightly yellow, viscous liquid was stored at -20 °C for subsequent characterization.

### **7.3.4 Photocuring and Characterization of ADPDA**

2,2-dimethoxy-2-phenylacetophenone was dissolved in THF and added to the photocurable oligomer at 2 wt % DMPA. The resulting mixture was homogenized and photocured under a UV lamp (Hanovia medium-pressure Hg lamp, PC 451050; Ace Glass photochemical safety cabinet; 120 V, 60 Hz, 450-W UV power supply) for 6 min. The resulting gel was dried at 40 °C under reduced pressure for 12 h. Dynamic mechanical analysis (DMA) was performed using a TA Instruments Q800 in film tension mode, at a frequency of 1 Hz with a constant 0.1 % applied strain, with temperature ramps performed at 3 °C/min

### 7.3.5 Instrumentation and Chromatographic Conditions

Supercritical fluid chromatography experiments were performed using a Waters Acquity UPC<sup>2</sup>™ (ultra-performance convergence chromatography) system (Milford, MA, USA) equipped with a high pressure mixing binary solvent delivery manager, a fixed-loop design autosampler, an active back pressure regulator, column compartment with active heating and column switching control, photodiode array (PDA) and evaporative light scattering (ELSD) detectors. The experiment was carried out using Acquity UPC<sup>2</sup> BEH 2-EP columns (100 mm x 2.1 mm, 1.7 μm) with a column temperature of 40°C. A binary mobile phase was employed, where mobile phase A consisted of compressed CO<sub>2</sub> and mobile phase B consisted of 0.1 % formic acid in methanol. The mobile phase flow rate was maintained at 1 mL/min for a total run time of 22 min. An A/B gradient was employed with 95/5% A/B to 60/40% A/B over 15 min, constant 60/40% A/B for 6 min, and return back to 95/5% A/B to equilibrate the column to the initial condition. The column backpressure was maintained isobarically by the Acquity CCM active backpressure regulator at 10.3 MPa (1500 psi). Sample concentration was maintained at 10 mg/mL with an injection volume of 2 μL. The Waters Acquity ELSD detector was operated with nebulizer cooling, drift tube temperature of 50 °C, gas pressure of 276 kPa (40 psi), and detector signal gain 10. An isopropyl alcohol makeup flow was introduced at 0.2 mL/min before ELSD. The solvent flow was split prior to automatic backpressure regulation (ABPR) for ELSD (split ratio 1:3).

### 7.3.6 SFC-ELSD Data Analysis

All SFC-ELSD data, normally in the form of light scattering units (l.s.u.) vs. elution time (min), was y-axis normalized between 0 and 1 for comparative purposes. The renormalization occurred according to **Equation 1**, where min (l.s.u.) and max (l.s.u.) refer to

the minimum or maximum  $y$ -axis value in the entire chromatogram and  $x$  is the value of elution time (min) at any  $y$  point in the chromatogram.

$$\text{Relative Intensity } (x) \text{ (A. U.)} = \frac{\text{l.s.u.}(x) - \min(\text{l.s.u.})}{\max(\text{l.s.u.}) - \min(\text{l.s.u.})} \quad (1)$$

The peak area % values were calculated according to **Equation 2**, where  $A_m$  is the peak area integration value for the  $m^{\text{th}}$  peak that eluted above 5 min. Peak integration values for the first four peaks that eluted above 5 min, or less if higher order peaks were not present, as well as the peak area for peaks below 4 min, are summed in the denominator.

$$\text{Peak } m \% = \frac{A_m}{A_{<4 \text{ min}} + A_1 + A_2 + \dots + A_m} \quad (2)$$

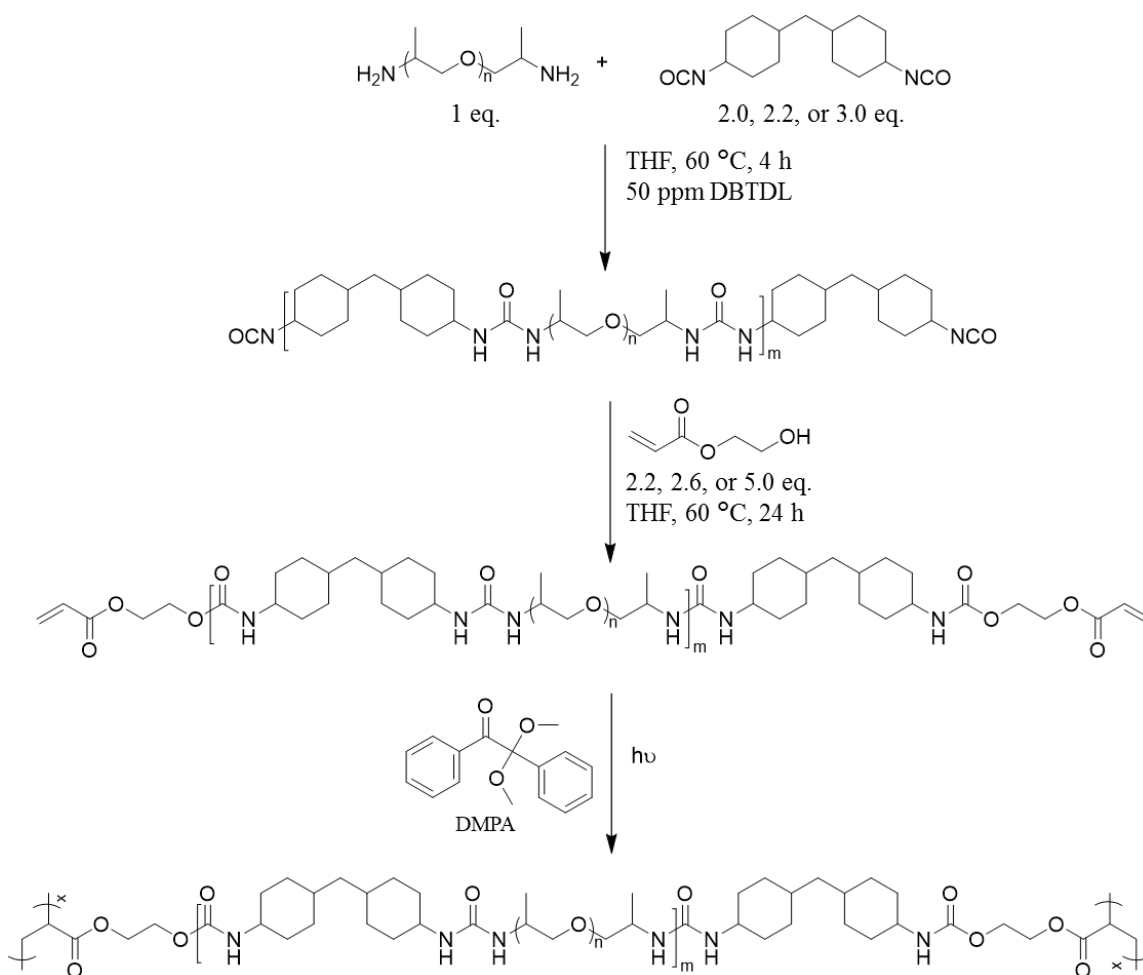
As shown in **Equation 3**, the total area of all peaks that eluted below 4 min, excluding baseline noise, was summed and divided by the peak integration values for the first four peaks that eluted above 5 min, or less if higher order peaks were not present, as well as the peak area for peaks below 4 min. This is reported as “ADA, AD\*, D\*, A (%)”

$$\text{ADA, AD}^*, \text{D}^* (\% \text{ of total } m = 1 - 4 \text{ series}) = \frac{A_{<4 \text{ min}}}{A_{<4 \text{ min}} + A_1 + A_2 + \dots + A_m} \quad (3)$$

## 7.4 Results and Discussion

Synthesis of a urea-/urethane-containing photocurable oligomer involved a two-step, single flask synthesis as shown in **Scheme 7.1**, where the second step occurred without isolation or purification of the product from the first step. Reactants and procedures were chosen to produce a standard soft coating for outdoor applications.<sup>2</sup> In this approach, an aliphatic diisocyanate (HMDI) endcaps a low glass transition temperature ( $T_g$ ) poly(propylene glycol) (PPG) oligomer to form an isocyanate-terminated prepolymer, which is subsequently functionalized with 2-hydroxyethyl acrylate (HEA). The neat, 2,000 g/mol PPG oligomer possesses a  $T_g$  of  $-65$  °C, enabling soft and flexible photocured films

or coatings for a wide application temperature window. The aliphatic diisocyanate does not yellow upon UV exposure, unlike its aromatic counterparts. The urea-/urethane-containing oligomers also gain further mechanical property improvements due to the dynamic physical crosslinks provided by hydrogen bonding between urea and urethane groups, as well as to the ether oxygen atoms in the soft segment backbone, which act as hydrogen bond acceptors.



**Scheme 7.1.** Synthesis and photocuring of urea- and urethane-containing, acrylate-terminated poly(propylene glycol) (PPG2K-UUA) photoactive oligomers. Photocuring in the presence of the photoinitiator 2,2-dimethoxy-2-phenylacetophenone (DMPA) yielded crosslinked films.



The endcapping of the 2,000 g/mol, amine-terminated poly(propylene glycol) (PPG) oligomer with excess hydrogenated methylene diphenyl diisocyanate (HMDI) afforded an isocyanate-terminated prepolymer. Various ratios of PPG : HMDI led to the production of lower molecular weight species (DPD,  $m = 1$ ) and higher molecular weight, polymerized species ( $m = 2, 3$ , etc.). In the second synthetic step, excess 2-hydroxyethyl acrylate (HEA) was added to ensure quantitative functionalization. Three final reactant stoichiometries were investigated – 1.0 : 2.0 : 2.2, 1.0 : 2.2 : 2.6, or 1.0 : 3.0 : 5.0 mol eq. of PPG : HMDI : HEA. This final oligomer is herein referred to as a 2KPPG urea/urethane acrylate (2KPPG-UUA). It is important to note that even at ratios of 1.0 : 2.0 : 2.2 or higher (i.e. 1.0 : 3.0 : 5.0), the modified Carothers equation, commonly used by polymer chemists to predict molecular weight based on stoichiometry, predicts the overall molecular weight distribution shown in **Table 7.1**.<sup>23</sup> For example, at a ratio of 1.0 : 2.0 : 2.2, the modified Carother's equation predicts a theoretical  $M_n = 3,972$  g/mol, as opposed to a predicted molecular weight of 2,813 g/mol for  $m = 1$ , or ADPDA. <sup>1</sup>H NMR spectroscopy confirmed the chemical structure and quantitative acrylate termination for a dialyzed 1.0 : 2.0 : 2.2 sample, shown and assigned in **Figure 7.4**.

It was hypothesized that higher reaction stoichiometries would produce a greater ratio of lower molecular weight species ( $m = 1$ ) to higher molecular weight species ( $m = 2, 3$ , etc.), i.e. the ratio would be higher for 1.0 : 3.0 : 5.0 vs. 1.0 : 2.0 : 2.2. To confirm this hypothesis, a variety of analytical techniques were considered for determination of overall oligomer molecular weight distribution. <sup>1</sup>H NMR spectroscopy was useful for determining quantitative acrylate functionalization, but contained too many overlapping resonances to determine oligomer molecular weight. Size exclusion chromatography provides adequate

separation of low molecular weight species, but requires specialized columns. In one recent study by Pretorius *et al.*, SFC provided much better separation of aliphatic polyester oligomers as compared to SEC, with nearly baseline separated oligomer peaks observed with SFC.<sup>19</sup> These authors confirmed that SFC separates in the direction of increasing molar mass with lower mass fractions eluting first. Stand-alone mass spectrometry was attempted with these samples (data not shown), but the lack of separatory capability resulted in an overly convoluted mass spectrum. For these reasons, these photocurable oligomer molecular weight distributions were examined using SFC-ELSD.

During SFC experiments, smaller and less polar molecules elute with shorter retention times, when the polar MeOH modifier concentration is lower. Accurate mass determination was not performed during our experiments, as our SFC-ELSD system is not coupled with a mass spectrometer. However, based on knowledge of all possible species in a given sample, process of elimination can help identify these populations. As SFC-ELSD is suitable for separation and identification of oligomeric populations below 10,000 g/mol,<sup>24</sup> one can assume a minimal presence of higher molecular weight species with ELSD. The theoretical molecular weight for the variety of expected species is calculated and tabulated in **Table 7.2**. First, there is a large molecular weight gap between A, D\*, ADA (which are 116, 210, and 495 g/mol, respectively) and the endcapped PPG oligomers (which are  $\geq 2,056$  g/mol). Second, the likelihood of a non-endcapped or singly-endcapped PPG oligomer is low due to the excess HMDI employed during synthesis. Thus, the lowest plausible molecular weight of an endcapped oligomer is 2,529 g/mol, leaving a  $\sim 2,000$  g/mol gap between these species and the A, D\*, and ADA population. Finally, in the high

molecular weight region, there is a low statistical likelihood of an  $m \geq 4$  oligomer due to the previously mentioned excess HMDI.

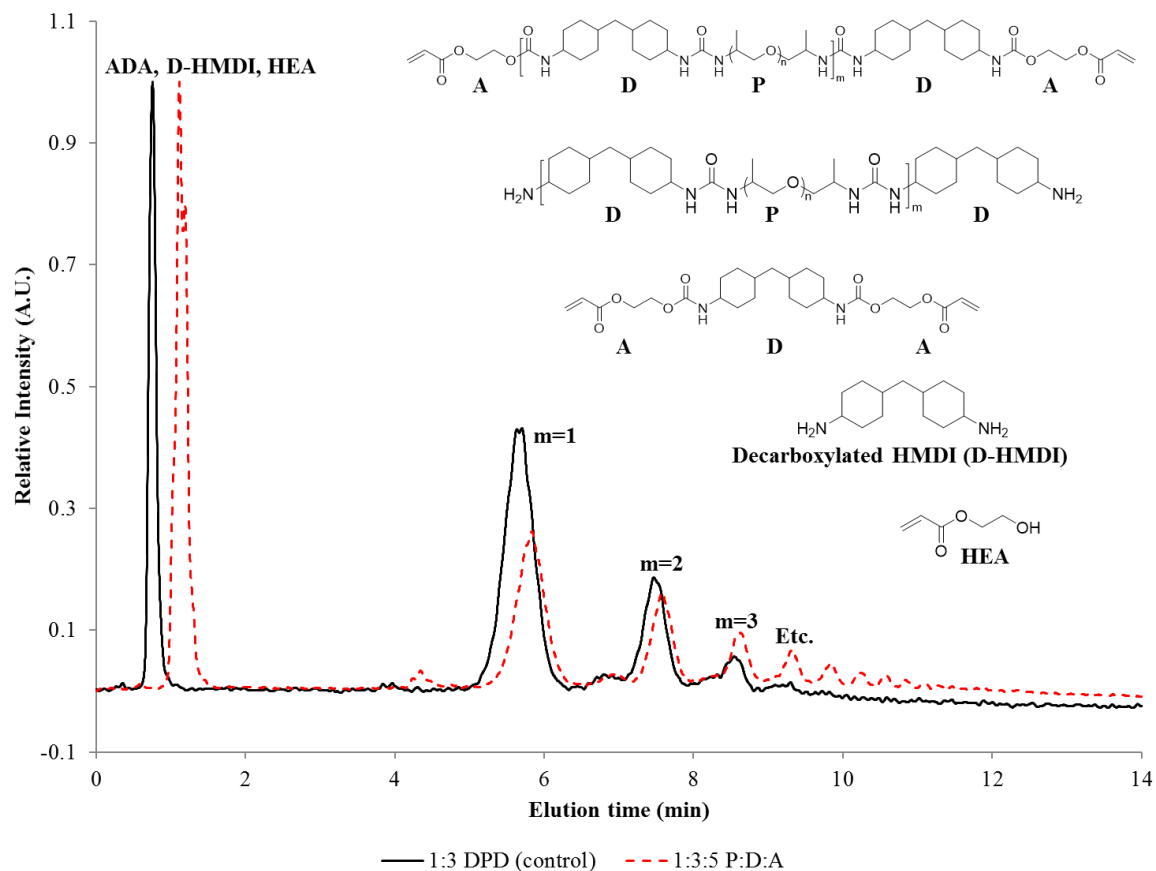


**Figure 7.1.** Supercritical fluid – evaporative light scattering detection (SFC-ELSD) chromatograms displaying separation of the PPG2K-UUA molecular weight distribution (red dotted trace). A decarboxylated HMDI-PPG-HMDI (DPD, black solid trace) is provided for comparative purposes.

**Figure 7.1** shows SFC-ELSD analysis of the 1.0 : 3.0 : 5.0 sample overlaid with a DPD sample (1.0 : 3.0 PPG:HMDI) for comparative purposes. As discussed above, the peak at ~ 1 min in both chromatograms is assigned to a combined population of ADA, decarboxylated HMDI (D\*), singly decarboxylated HEA-HMDI (\*DA) and/or HEA. These assignments were confirmed in a series of individual experiments shown in the Supporting Information. In **Figure 7.5** and **Figure 7.6** respectively, samples containing

solely D\* or HEA eluted at ~ 0.5 min. Further, **Figure 7.7** shows a 1.0 : 3.0 : 5.0 PPG2K-UUA sample purified with 1,000 g/mol MWCO dialysis that contained no populations eluting below 5 min, further confirming that only species below 1,000 g/mol elute below 5 min. The population of successively smaller peaks above 5 min is assigned based on statistics. With a 1.0 : 3.0 PPG:HMDI stoichiometry, the likelihood of a  $m = y + 1$  oligomer population is less likely than a population of  $m = y$ . Therefore, the peaks at 5.8 min, 7.6 min, 8.6 min, and 9.3 min are assigned to  $m = 1, 2, 3,$  and  $4$ , respectively. As evidenced by the similarity between the 1.0 : 3.0 : 5.0 and 1.0 : 3.0 PPG:HMDI samples shown in **Figure 7.2**, our particular SFC-ELSD system cannot differentiate between oligomers with or without acrylate termination, under these conditions. Fortunately,  $^1\text{H}$  NMR spectroscopy confirmed 95 % acrylate termination for the 1.0 : 2.0 : 2.2 sample. Finally, elution time for a given population was observed to fluctuate slightly between sample sets. Past reports have documented and attributed this phenomenon to slight changes in sample concentration between runs.<sup>25</sup>

Using the assignments discussed above, the effect of reaction stoichiometry on oligomer populations was calculated and is displayed in **Figure 7.2**. An increase in the  $m = 1$  peak area occurs as the ratio of HMDI:PPG increases. Additionally, a decrease in higher order peak area ( $m \geq 2$ ) occurs as this ratio increases. This trend is logical, as an increase in the stoichiometric offset between one bifunctional reactant to another reduces overall oligomer molecular weight, according to the modified Carothers equation. These theoretical  $M_n$  values are tabulated in **Table 7.1**. Furthermore, the peak area of the A, D\*, AD\*, and ADA populations also increases the ratio of HMDI:PPG increases. In order for perfect HMDI endcapping and HEA functionalization to occur, every 1 mol. eq. PPG

requires 2 mol. eq. HMDI and 2 mol. eq. HEA. When higher order populations are considered ( $m \geq 2$ ), a reduced amount of HMDI and HEA are required. Finally, no ADA, AD\*, D\*, and A population existed for a 1.0:3.0:5.0 sample dialyzed against THF in 1000 g/mol MWCO dialysis bags, confirming the assignment for peaks below 4 min elution time. WCO dialysis bags, confirming the assignment for peaks below 4 min elution time.

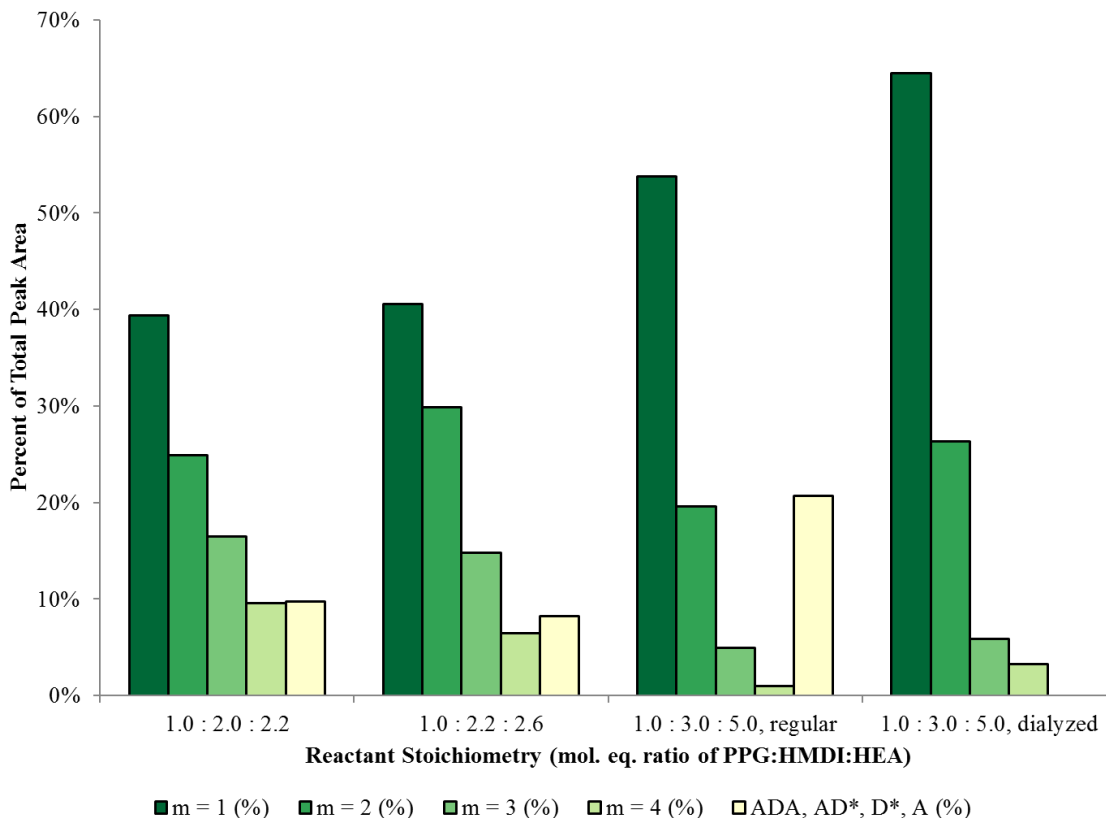


**Figure 7.2.** Plot of percent of total peak area as a function of reaction stoichiometry, demonstrating increasing amounts of  $m = 1$  for increasing HMDI:PPG stoichiometry.

In order to relate this chromatographic information to photocured 2KPPG-UUA film properties, thermomechanical analysis was performed after photocuring in the presence of the photoinitiator 2,2-dimethoxy-2-phenylacetophenone (DMPA). Photocuring of all four samples occurred directly after concentration of the reaction

mixture. For comparative purposes, a portion of the 1.0 : 3.0 : 5.0 sample was dialyzed before photocuring.

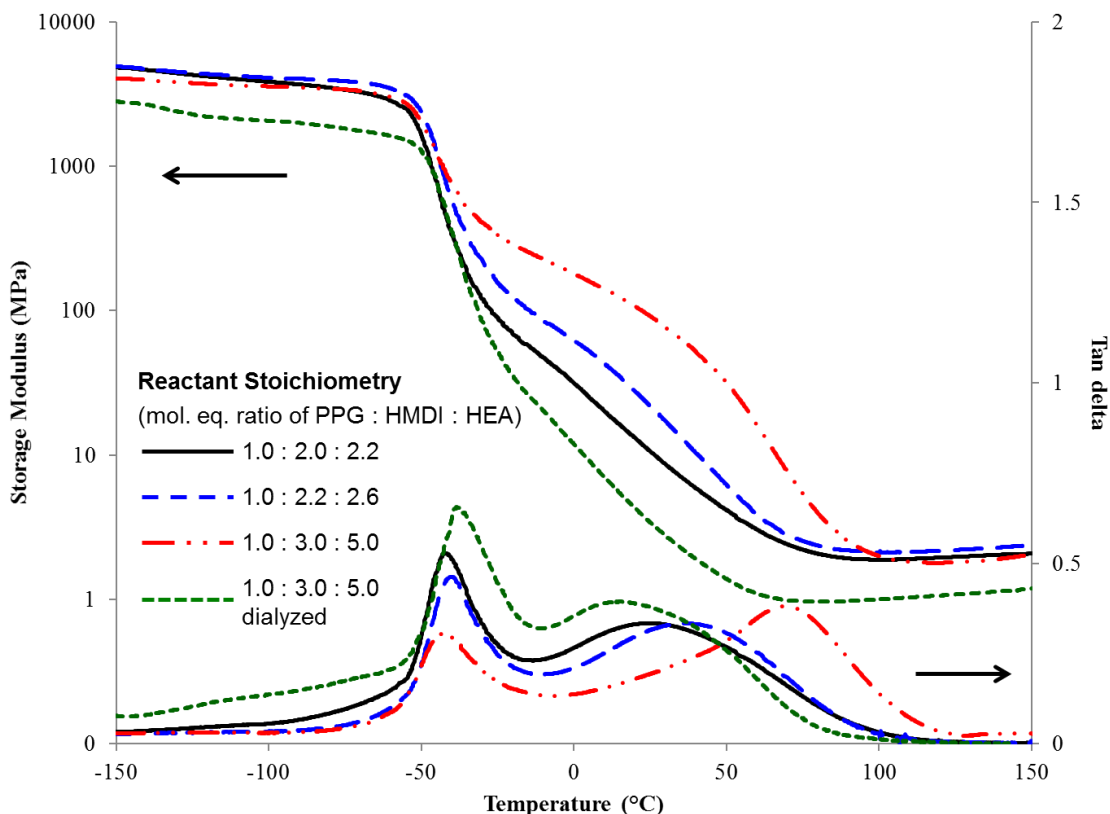


**Figure 7.3.** Dynamic mechanical analysis (DMA) temperature ramp of photocured PPG2K-UUA oligomers as a function of HMDI/HEA stoichiometry.

**Figure 7.3** displays DMA data as a function of temperature, which is a commonly used technique for measuring viscoelastic mechanical properties. Here, storage modulus and tan delta are plotted as a function of increasing temperature, where storage modulus is the purely elastic stiffness of a sample and tan delta is the ratio of loss modulus (purely viscous response) to storage modulus. A high value of tan delta at any given temperature indicates high levels of damping or energy absorption. All samples remain glassy until the transition at  $-40\text{ }^{\circ}\text{C}$ , identified by a peak in the tan delta curve, and attributed to the PPG  $T_g$ . Beyond  $T_g$ , the storage modulus does not undergo an immediate 2-3 decade drop to a flat rubbery

plateau (the temperature region between  $T_g$  and the melting or degradation temperature), as is commonly observed for well phase-separated blocky polyurethanes, but rather a sloped decay to an eventual rubbery plateau close to 100 °C. This sloped rubbery behavior is likely due to poor phase separation between the hard segments (i.e. HMDI + urea/urethane functional groups) and the PPG soft segments. This poor phase separation arises from the PPG ether linkages serving as hydrogen bond acceptors, as previously observed in the DMA of polyether-polyurethane block copolymers.<sup>26</sup>

In **Figure 7.3**, each sample undergoes a broader, second transition above  $T_g$ , with peak tan delta occurring between 15 °C (for 1.0 : 3.0 : 5.0 dialyzed) and 70 °C (for the neat 1.0 : 3.0 : 5.0). The 1.0 : 3.0 : 5.0 dialyzed sample exhibits similar tan delta shape and peak temperature to the 1.0 : 2.0 : 2.2 sample, suggesting that the difference in  $M_c$  of the 1.0 : 3.0 : 5.0 dialyzed sample and the 1.0 : 2.0 : 2.2 sample is not significant enough to produce an appreciable difference in photocured film thermomechanical properties. An increasing ratio of HMDI:PPG produces an increasing amount of ADA, which acts as a hard segment when crosslinked into the photocured network. Therefore, this second relaxation is possibly attributed to hard segment dissociation, as the peak tan delta temperature increases with increasing amount of ADA. This is consistent with a literature report on polyether-polyurethane block copolymers where an increase in the peak tan delta temperature was attributed to a greater fraction of hard segment dissolved in the soft phase.<sup>26</sup> These results shown in **Figure 7.3** suggest that the presence of a photoactive, hydrogen-bonding small molecule reaction byproduct (ADA), as well as HEA, has a much more profound effect on photocured film properties as compared to small changes in  $M_c$  induced by changes in stoichiometry between HMDI and PPG.

## 7.5 Conclusions

Endcapping of a 2,000 g/mol, amine-terminated PPG oligomer with a diisocyanate and 2-hydroxyethyl acrylate afforded a urea-/urethane-containing, acrylate-terminated photocurable oligomer for use in coatings applications. SFC-ELSD enabled the precise determination of the oligomeric molecular weight distributions as a function of reaction stoichiometry, and enabled the detection and quantification of excess reactants. The ratio of lower molecular weight species ( $m = 1$ ) to higher molecular weight species ( $m = 2, 3$ , etc.) increased as the ratio of HMDI:PPG increased, as was expected. DMA probed the thermomechanical behavior of photocured films as a function of reaction stoichiometry, determining that the observed hydrogen bond dissociation temperature increased as the amount of low molecular weight, hydrogen-bonding ADA molecules in the overall composition increased, possibly due to an increased amount of hard segment dissolved in the soft segment before photocuring. This work demonstrates the capability of combined chromatographic and thermomechanical characterization, allowing for more fundamental elucidation of structure-processing-property relationships.

## 7.6 Acknowledgements

The authors acknowledge Bayer MaterialScience (now Covestro) for providing HMDI.

The authors also acknowledge TA Instruments-Waters LLC for loaning the Aquity UPC<sup>2</sup> SFC-ELSD system.

## 7.7 References

- (1) Raynor, M. W.; Bartle, K. D. *The Journal of Supercritical Fluids* **1993**, *6*, 39-49.
- (2) Levy, N., Low Tg soft UV-curable coatings. U.S. 4324575 A, Apr 13, 1982.
- (3) Cashion, M. P.; Park, T.; Long, T. E. *The Journal of Adhesion* **2009**, *85*, 1-17.
- (4) Serrine, J. M.; Pekkanen, A. M.; Nelson, A. M.; Chartrain, N. A.; Williams, C. B.; Long, T. E. *Australian Journal of Chemistry* **2015**, *68*, 1409-1414.
- (5) Lee, J. W.; Kang, K. S.; Lee, S. H.; Kim, J.-Y.; Lee, B.-K.; Cho, D.-W. *Biomaterials* **2011**, *32*, 744-752.



- (6) Karikari, A. S.; Edwards, W. F.; Mecham, J. B.; Long, T. E. *Biomacromolecules* **2005**, *6*, 2866-2874.
- (7) Gupta, P.; Trenor, S. R.; Long, T. E.; Wilkes, G. L. *Macromolecules* **2004**, *37*, 9211-9218.
- (8) Swiderski, K. W.; Khudyakov, I. V. *Industrial & Engineering Chemistry Research* **2004**, *43*, 6281-6284.
- (9) Temenoff, J. S.; Athanasiou, K. A.; Lebaron, R. G.; Mikos, A. G. *J. Biomed. Mater. Res.* **2002**, *59*, 429-437.
- (10) Schou-Pedersen, A. M. V.; Østergaard, J.; Johansson, M.; Dubant, S.; Frederiksen, R. B.; Hansen, S. H. *Journal of Pharmaceutical and Biomedical Analysis* **2014**, *88*, 256-261.
- (11) Hoffman, B. J.; Taylor, L. T.; Rumbelow, S.; Goff, L.; Pinkston, J. D. *Journal of chromatography. A* **2004**, *1034*, 207-212.
- (12) Pinkston, J. D.; Delaney, T. E.; Bowling, D. J. *Journal of Microcolumn Separations* **1990**, *2*, 181-187.
- (13) J. Carrott, M.; Davidson, G. *Analyst* **1999**, *124*, 993-997.
- (14) Ute, K. In *Supercritical fluid chromatography with packed column. Chromatographic Science Series* 1997; Vol. 75, p 349-368.
- (15) Pinkston, J. D.; Marapane, S. B.; Jordan, G. T.; Clair, B. D. *Journal of the American Society for Mass Spectrometry* **2002**, *13*, 1195-1208.
- (16) Yip, H.; Ashraf-Khorassani, M.; Taylor, L. *Chromatographia* **2007**, *65*, 655-665.
- (17) Bartle, K. D.; Boddington, T.; Clifford, A. A.; Cotton, N. J.; Dowle, C. J. *Analytical Chemistry* **1991**, *63*, 2371-2377.
- (18) Takahashi, K. *Journal of Bioscience and Bioengineering* **2013**, *116*, 133-140.
- (19) Pretorius, N. O.; Willemse, C. M.; de Villiers, A.; Pasch, H. *Journal of chromatography. A* **2014**, *1330*, 74-81.
- (20) E. Lesellier; Valarché, A.; West, C.; Dreux, M. *Journal of Chromatography A* **2012**, *1250*, 220-226.
- (21) Lecoeur, M.; Simon, N.; Sautou, V.; Decaudin, B.; Vaccher, C.; group, A. s. *Journal of chromatography. A* **2014**, *1333*, 124-133.
- (22) Chattopadhyay, D. K.; Panda, S. S.; Raju, K. V. S. N. *Progress in Organic Coatings* **2005**, *54*, 10-19.
- (23) Odian, G. *Principles of Polymerization*; 4th ed.; Wiley, 2004.
- (24) Taylor, L. T. *The Journal of Supercritical Fluids* **2009**, *47*, 566-573.
- (25) Maftouh, M.; Granier-Loyaux, C.; Chavana, E.; Marini, J.; Pradines, A.; Heyden, Y. V.; Picard, C. *Journal of Chromatography A* **2005**, *1088*, 67-81.
- (26) Miller, J. A.; Lin, S. B.; Hwang, K. K. S.; Wu, K. S.; Gibson, P. E.; Cooper, S. L. *Macromolecules* **1985**, *18*, 32-44.

## 7.8 Supporting Information

**Table 7.1.** Summary of theoretical and experimental number-average molecular weight ( $M_n$ ) of samples obtained from SFC-ELSD analysis, according to sample stoichiometry

Sample	r	Xn	Theoretical $M_n$ , Carothers Equation	$M_n$ from SFC-ELSD <sup>a</sup>
1.0 : 2.0 : 2.2	0.5000	3.00	3,972	5,480
1.0 : 2.2 : 2.6	0.4545	2.67	3,586	4,807
1.0 : 3.0 : 5.0, regular	0.3333	2.00	2,813	3,760
1.0 : 3.0 : 5.0, dialyzed				4,127

<sup>a</sup> Assuming perfect endcapping with HEA, i.e. all  $A(DP)_mDA$

**Table 7.2.** Summary of theoretical number-average molecular weight ( $M_n$ ) of various expected species in SFC-ELSD analysis, according to number of repeat units.

Species	Theoretical $M_n$ (g/mol)	
A	116	
D*	210	
ADA	495	
P	2,056	
DPD*	2,529	
ADPD*	2,671	
Acrylate-terminated telechelic oligomer	m=1	2,813
	m=2	5,131
	m=3	7,450
	m=4	9,768
	m=5	12,086
	m=6	14,405

\*Terminal  $-NCO$  decarboxylates to  $-NH_2$

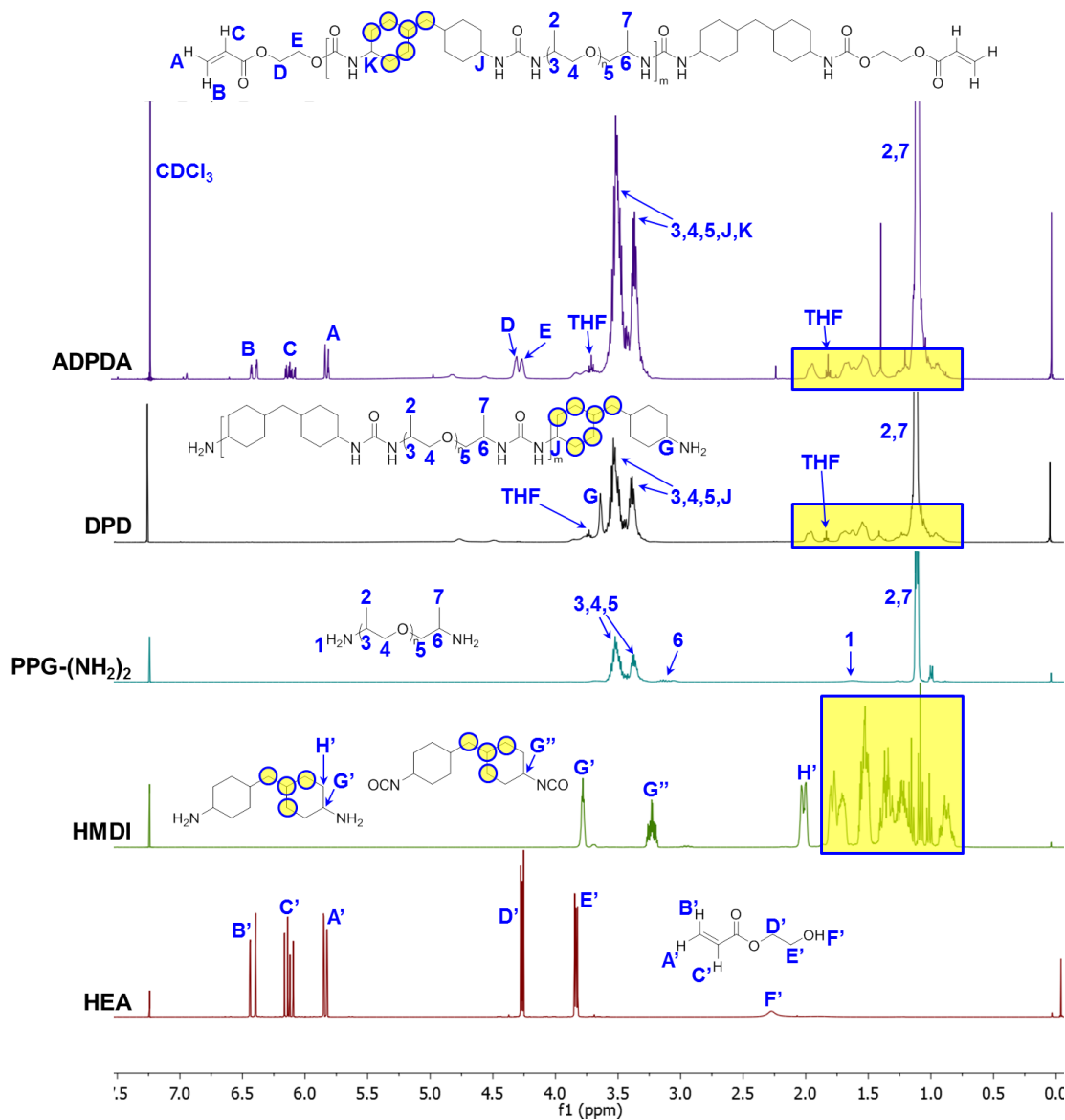


**Figure 7.4.**  $^1\text{H}$  NMR of dialyzed ADPDA (1.0 : 3.0 : 5.0) overlaid with isolated, decarboxylated intermediate DPD and starting materials HEA, HMDI, and PPG

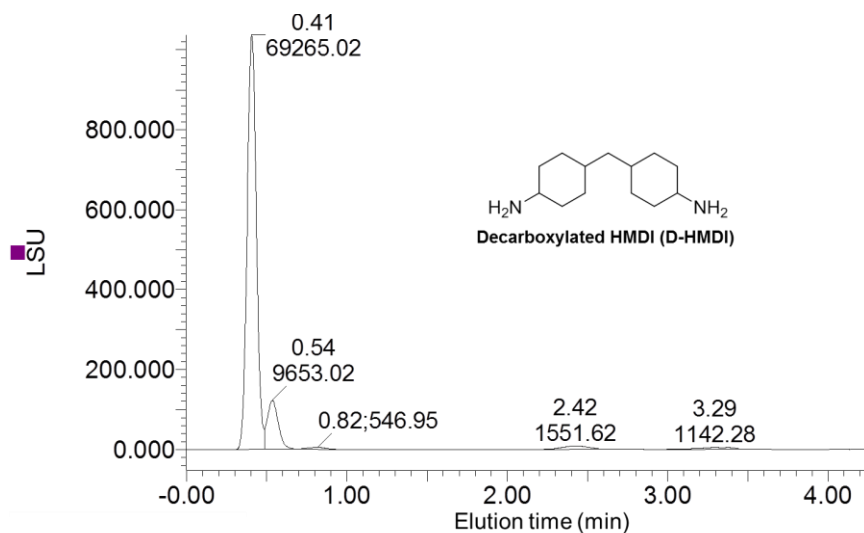


**Figure 7.5.** SFC-ELSD chromatogram of decarboxylated HMDI (D-HMDI). In each group of numbers above a given peak, the top number is elution time (min) and the bottom number is peak area.

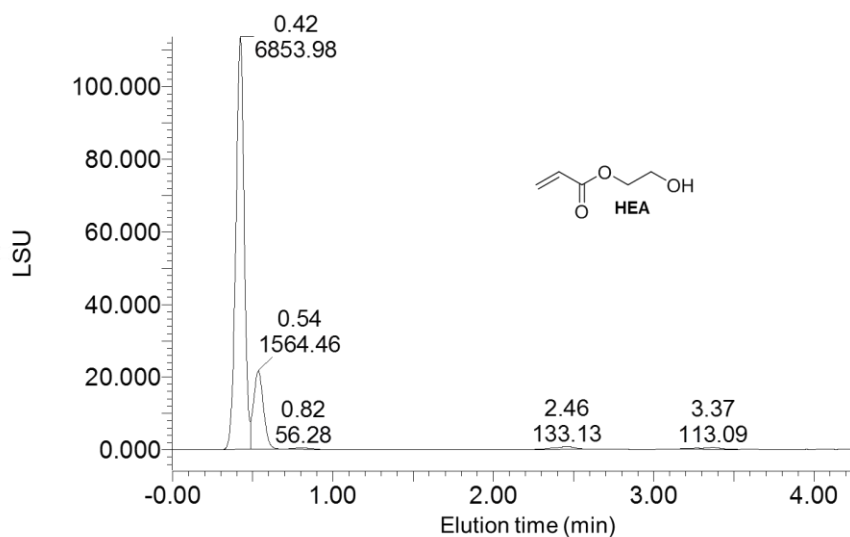


**Figure 7.6.** SFC-ELSD chromatogram of neat 2-hydroxyethyl acrylate (HEA). In each group of numbers above a given peak, the top number is elution time (min) and the bottom number is peak area.

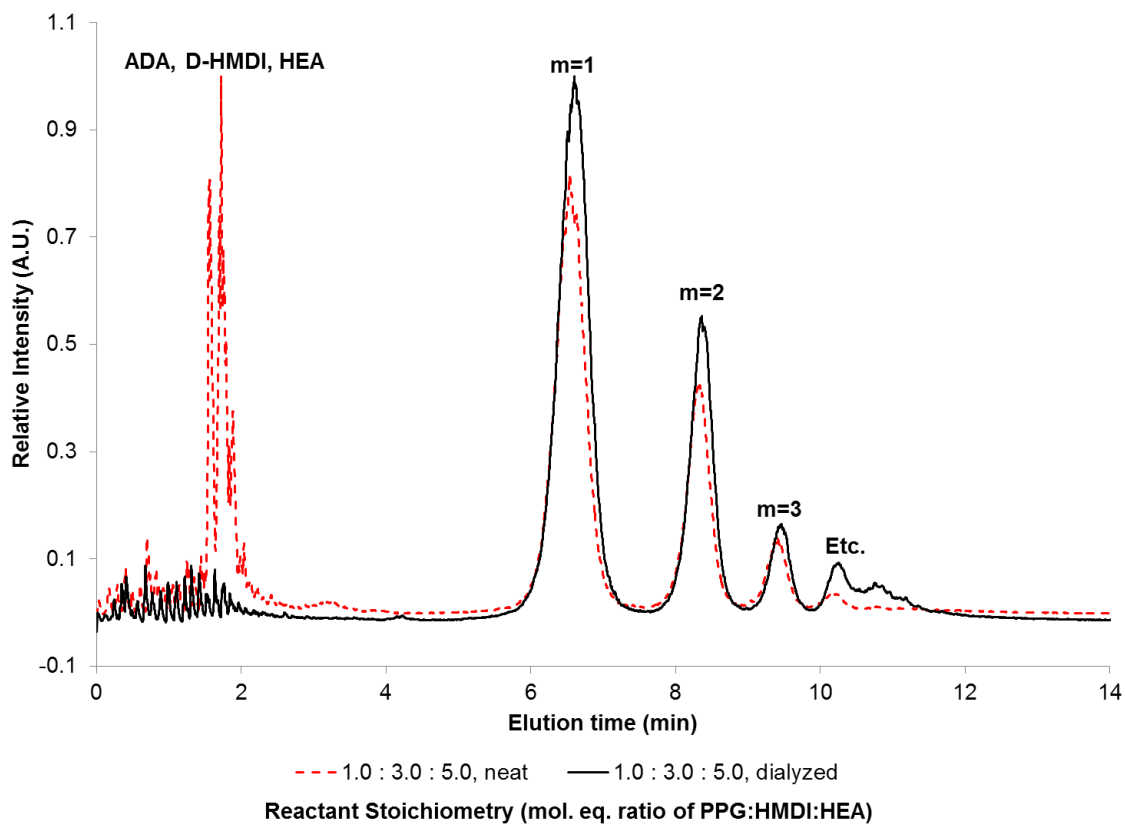


**Figure 7.7.** SFC-ELSD chromatograms used for the generation of data in **Figure 7.1**, displaying an elimination of the ADA, D-HMDI, and HEA peaks after post-synthesis dialysis in MWCO 1,000 g/mol dialysis bags.

## Chapter 8: **Photoreactive, polyether-containing photopolymers with reactive diluents for improved performance in vat photopolymerization additive manufacturing**

Justin M. Serrine,<sup>a</sup> Logan D. Sturm,<sup>b</sup> Christopher B. Williams,<sup>b</sup> Timothy E. Long<sup>a,\*</sup>

<sup>a</sup>*Department of Chemistry, and* <sup>b</sup>*Department of Mechanical Engineering, Macromolecules Innovation Institute, Virginia Tech, Blacksburg, VA 24061, USA*

### **8.1 Abstract**

Vat photopolymerization (VPP), a type of additive manufacturing (AM) that selectively cures photopolymer in a layer-by-layer fashion to afford three-dimensional objects of unlimited geometric complexity, suffers from a lack of commercially available photopolymers that produce low modulus objects upon photocuring (e.g.  $\leq 20$  MPa). Incorporation of physical interactions such as hydrogen bonding offers a unique method for improving mechanical properties with relatively low molecular weight precursors. This work reports the synthesis and characterization of a low glass transition temperature ( $T_g$ ), urethane/urea-containing, diacrylate oligomer based on poly(propylene glycol) (PPG). Thermomechanical analysis evaluated modulus vs. temperature behavior for this photocured PPG-based oligomer. Subsequent mixture with various acrylate-containing reactive diluents provided a unique method for decreasing crosslink density, resulting in a reduction in room-temperature elastic modulus. Finally, VPP AM with these PPG-based oligomers demonstrated well-defined geometries for objects that included high aspect ratio pillars, a hexagon pattern, and a 3D scaffold structure.

### **8.2 Introduction**

The recent research surge in additive manufacturing (AM), otherwise known as 3D printing, expands the prototyping and production toolbox and facilitates the creation of

geometries not attainable with alternative manufacturing methods, while reducing waste that remains common with subtractive manufacturing methods.<sup>1-5</sup> Recent forays into polymeric materials for additive manufacturing offer drastic improvements in thermal and mechanical properties over traditional polymers for AM applications (e.g. polylactides, acrylonitrile butadiene styrene thermoplastics, and polyamide 12),<sup>6-8</sup> with examples that include polymer-derived ceramics,<sup>9</sup> all-aromatic polyimides,<sup>10</sup> and ultra-light, ultra-stiff polymeric metamaterials.<sup>11</sup> Recent examples also include AM of polyurethanes and polyureas, which impart hydrogen bonding physical interactions that lend drastic mechanical property improvements to the final printed object, especially in network-forming systems that rely solely on covalent crosslinking.<sup>12-16</sup> Urethane-containing oligomers represent the simplest polyurethanes employed for AM and typically enjoy use in either vat photopolymerization (VPP) or inkjet printing techniques, both of which involve ultraviolet (UV) irradiation of photocurable compositions.<sup>6</sup> These commercially-available oligomers typically contain just a few urethane/urea functional groups per oligomer and frequently possess photocurable functionality, e.g. (meth)acrylates.<sup>6,8,17-19</sup> In contrast, segmented polyurethane/polyurea block copolymers typically possess much higher molecular weight and gain their superior mechanical properties from microphase separation between a low glass transition temperature ( $T_g$ ) block and a higher  $T_g$  (e.g. above room temperature) block. VPP of segmented polyurethanes typically occurs from waterborne polyurethane dispersions due to viscosity restrictions typically associated with VPP.<sup>20-22</sup>

Viscosity becomes an issue for VPP of polyurethanes due to hydrogen bonding physical interactions, which often lead to mechanical property improvements after

photocuring but create processing challenges during VPP due to increase in photopolymer viscosity.<sup>4,23</sup> The literature provides many examples of polyurethanes for VPP which address these challenges through innovative polymer chemistry. One recent example by Sinh and Jukka *et al.* addresses the typically high viscosity of polyurethane photopolymers through creative choice of a non-symmetric diisocyanate and mixture of poly(dimethylsiloxane) (PDMS) and poly(tetramethylene oxide) (PTMO) soft segments.<sup>23</sup> This likely induced phase mixing and sterically hindered hydrogen bonding as compared to more symmetric diisocyanates, e.g. hydrogenated methylene diphenyl diisocyanate (H<sub>12</sub>MDI).<sup>23</sup> One route recently undertaken by Rolland and DeSimone *et al.* for Carbon3D photocurable resins involves the use of blocked isocyanates, whereby a ‘green body’ is photocured during the VPP process that contains residual diamine functionality, which deblocks the blocked isocyanates and forms urethanes during a post-printing heat-treatment step.<sup>3,24-26</sup> Pyo and Chen, *et al.* discuss the synthesis and 3D printing of isocyanate-free urethane-containing oligomers synthesized from a cyclic-carbonate-containing methacrylate and various bio-based diamines.<sup>14</sup> Another unique approach involves the VPP of waterborne polyurethane dispersions, which contain ionic functionality in the backbone of a segmented polyurethane that enables formation of colloidally-stable, photocurable aqueous polyurethane nanoparticle dispersions, which enjoy widespread use in tissue engineering applications.<sup>20,21,27</sup> Lastly, Liska and Stampfl *et al.* extensively reported on the VPP of commercially-available and novel urethane-containing (meth)acrylates and reactive diluent monomers, primarily for tissue engineering applications.<sup>8,19,28</sup>



This work demonstrates the synthesis, characterization, and photocuring of a photocurable urethane/urea acrylate oligomer based on poly(propylene glycol) (PPG) diamine, H<sub>12</sub>MDI, and hydroxyethyl acrylate (PPG2k-UUA). Mixture of this highly viscous PPG2k-UUA oligomer with various reactive diluent monomers afforded a reduction in processing viscosity of multiple orders of magnitude, which provided utility for rapid processing with VPP. Dynamic mechanical analysis probed thermomechanical properties of photocrosslinked films as a function of photoinitiator concentration and reactive diluent concentration, revealing a reduction in room-temperature elastic modulus by roughly an order-of-magnitude with the highest levels of reactive diluent incorporation (e.g. 80-90 wt %). Finally, initial VPP with PPG2k-UUA revealed well-defined geometries that included scaffold structures, high aspect-ratio pillars, and raised-hexagon-patterned surfaces.

## **8.3 Materials & Methods**

### **8.3.1 Materials**

Poly(propylene glycol) bis(2-aminopropyl ether) (PPG2k-(NH<sub>2</sub>)<sub>2</sub>), dibutyltin dilaurate (95 %), 2-hydroxyethyl acrylate (HEA, 96%), n-butyl acrylate (nBA, ≥ 99 %), 2-ethylhexyl acrylate (EHA, 98 %), di(ethylene glycol) ethyl ether acrylate (DEGEEA, ≥ 90 %), Magnesium sulfate (MgSO<sub>4</sub>, anhydrous, ReagentPlus®, ≥99.5%), 4-methoxyphenol (MEHQ, purum, ≥98.0%) and 2,2-dimethoxy-2-phenylacetophenone (DMPA, 99 %) were purchased from Sigma Aldrich and used as received unless otherwise noted. A sample of hydrogenated methylene diphenyl diisocyanate (H<sub>12</sub>MDI) was graciously donated by Bayer MaterialScience (now Covestro). Tetrahydrofuran (THF) and dichloromethane (DCM) were purchased from Fisher Scientific (all HPLC grade), and THF was dried with

an Innovative Technology PureSolv (Amesbury, MA, USA) solvent purification system before use in PPG2k-UUA synthesis, or used as received for all other experiments. PPG2k-(NH<sub>2</sub>)<sub>2</sub> was dried at 60 °C for 18 h *in vacuo* before use. DBTDL was used as a 1 wt % solution in THF.

### 8.3.2 Synthesis of PPG2k-UUA

A three-necked, 1000 mL round-bottomed flask was equipped with condenser column, overhead mechanical stirring apparatus, addition funnel, nitrogen inlet (through addition funnel) and bubbler outlet (through condenser column). The mechanical stirring apparatus consisted of an overhead mechanical stirrer attached to 10 mm diameter glass stir rod, PTFE stir blade, and 24/40 glass stir rod adapter. The entire apparatus was then flame-dried under constant N<sub>2</sub> purge and allowed to cool for 20 min. Subsequently, 50 ppm DBTDL (based on total reactant weight) and H<sub>12</sub>MDI (72.91 g, 0.249 mol, 2.0 mol eq.) were added to the flask via the addition funnel, which was subsequently rinsed with dry THF (~10 mL). The flask was immersed in an oil bath heated to 60 °C, and the reaction was allowed to equilibrate for 5 min. Then, dry PPG2k-(NH<sub>2</sub>)<sub>2</sub> (249.0 g, 0.1245 mol, 1.0 mol eq.) was cannulated into the addition funnel, which was subsequently added dropwise to the flask containing H<sub>12</sub>MDI. The addition funnel was then rinsed again with dry THF after complete H<sub>12</sub>MDI addition (~10 mL). After 4 h at 60 °C, HEA (31.93 g, 0.275 mol, 2.2 mol eq.) was cannulated into the addition funnel and subsequently added to the reaction, followed by a third rinse of the addition funnel with dry THF (10 mL). Dry THF was added to the reaction to bring the total solids content to 50 wt % (e.g. total 400 mL THF). The reaction was subsequently allowed to proceed for 24 h at 60 °C. After cooling to room temperature, THF was removed with a rotary evaporator and the product was redissolved

in dichloromethane. Subsequently, 3x washes with deionized water and 1x wash with brine ensured complete removal of excess hydroxyethyl acrylate. The product was dried over  $\text{MgSO}_4$  and 1000 ppm MEHQ (based on total solids weight) was added to the reaction to prevent thermal crosslinking. Finally, DCM was removed with a rotary evaporator and the product was allowed to dry at 40 °C for 18 h *in vacuo*. Isolated yield = 70.0 % as a viscous, slightly yellow liquid. Products were stored in a -20 °C freezer and wrapped with aluminum foil to prevent premature thermal crosslinking.

### 8.3.3 Sample preparation for photocuring

In preparation for photocuring and 3D printing, desired amounts of PPG2k-UUA and if used, reactive diluent (e.g. EHA, nBA, DEGEEA) were added to a 6-dram vial, totaling 10.0 g. Separately, DMPA (0.5 wt % based on solids content, except photoinitiator study done at 0.1, 0.5, and 1.0 wt %) was weighed into a 1-dram vial and mixed with DCM at a ratio of 1.0 g / 5.0 g DMPA/DCM. After complete DMPA dissolution in DCM, this photoinitiator solution was mixed with the PPG2k-UUA / monomer mixture and vortexed until thoroughly mixed. Finally, photoinitiated mixtures were mixed with a vortexer for 20 s until homogeneous and subsequently allowed to stand at room temperature, covered with aluminum foil, for 2 h to ensure absence of bubbles.

### 8.3.4 Sample preparation for vat photopolymerization (VPP)

PPG2k-UUA (75.0 g) and a magnetic stirring bar were added to a 120-mL amber jar. Separately, DMPA (0.5 wt %) was weighed into a 6-dram vial and mixed with 5.0 mL THF. The photoinitiator solution was added to the amber jar and the jar was allowed to mix on a stir plate for 3 h until homogeneous, then allowed to stand at room temperature, in the absence of mixing, for 2 h to ensure the absence of bubbles.

### 8.3.5 Analytical Methods

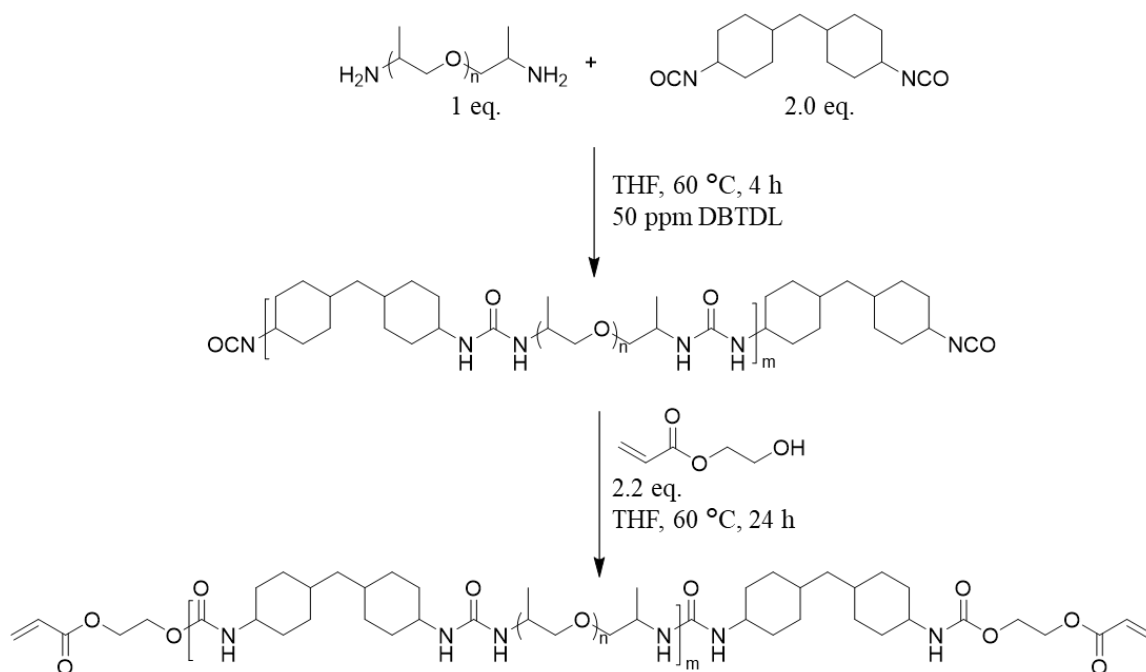
A TA Instruments Q500 thermogravimetric analyzer (TGA) enabled measurement of weight loss vs. temperature behavior for all samples. A TA Instruments Q2000 differential scanning calorimeter (DSC) equipped with refrigerated cooling system (RCS) enabled measurement of thermal transitions at a constant 10 °C/min heating/cooling rate, as a function of temperature. A TA Instruments Q800 dynamic mechanical analyzer (DMA) equipped with liquid nitrogen gas cooling accessory (GCA) measured thermomechanical properties in film tension mode as a function of temperature at a constant 0.1 % strain, 1 Hz, and 5 °C/min heating rate, after a 5 min isotherm at -150 °C. A TA Instruments DHR-2 rheometer equipped with concentric cylinder geometry operated in flow mode and measured viscosity vs. shear rate or viscosity vs. temperature behavior for all photocurable mixtures. Film production for DMA involved pouring the above-described photocurable mixtures into PTFE molds and photocuring under a UV lamp (Hanovia medium-pressure Hg lamp, PC 451050; Ace Glass photochemical safety cabinet; 120 V, 60 Hz, 450-W UV power supply) for 6 min. The resulting gel was dried at 40 °C under reduced pressure for 18 h. Soxhlet extraction occurred for 6 h at 80 °C under refluxing THF, while samples were dried *in vacuo* at 60 °C for 18 h, both before and after soxhlet extraction, to obtain accurate sample weights. A Jeol NeoScope JCM-5000 scanning electron microscope (SEM) imaged 3D objects at 10 kV accelerating voltage. 3D objects were mounted directly onto the SEM sample stage and immediately imaged; no conductive sputter coating was required.

### 8.3.6 Vat Photopolymerization (VPP)

All vat photopolymerization method information, including methods for generating the photopolymer working curve, is provided elsewhere.<sup>4,10</sup>

## 8.4 Results & Discussion

**Scheme 8.1** depicts the synthesis of 2,000 g/mol poly(propylene glycol) (PPG)-containing urea/urethane acrylate oligomers, which occurred via the traditional, isocyanate-terminated prepolymer method. Dropwise addition of the PPG diamine to the diisocyanate minimized production of higher molecular intermediates, although previous literature indicates that low degrees of polymerization (e.g.  $m = 2, 3$ ) occur even at 1.0 : 2.0 mol : mol diamine:diisocyanate.<sup>29</sup> Endcapping with a slight molar excess of hydroxyethyl acrylate (HEA) (e.g. 2.2 mol eq.) ensured quantitative functionalization of these PPG2k-UUA oligomers, while a final aqueous wash step removed excess HEA before photocuring and VPP occurred. Our previous work with these identical oligomers provides complete proton nuclear magnetic resonance (<sup>1</sup>H NMR) spectroscopy data, as well as supercritical fluid chromatography with evaporative light scattering detection (SFC-ELSD) data, which indicates that an overall PPG2k-(NH<sub>2</sub>)<sub>2</sub> : H<sub>12</sub>MDI : HEA stoichiometry of 1.0 : 2.0 : 2.2 used in this report produces an  $M_n$  of 5,480 g/mol,<sup>29</sup> roughly 2.75 times the PPG2k-(NH<sub>2</sub>)<sub>2</sub> oligomer  $M_n$  (e.g. 2,000 g/mol).



**Scheme 8.1.** Synthesis of poly(propylene glycol) (PPG)-containing urea/urethane acrylate oligomers (PPG2k-UUA) from 2,000 g/mol PPG diamine, hydrogenated methylene diphenyl diisocyanate (H<sub>12</sub>MDI), and hydroxyethylacrylate (HEA).

**Figure 8.1A** depicts the steady-shear viscosity ( $\eta$ ) for the PPG2k-UUA oligomer at both 25 °C and 40 °C, indicating roughly an order-of-magnitude decrease in viscosity for PPG2k-UUA at 40 °C vs. 25 °C (e.g. 110 Pa·s vs. 670 Pa·s). Notably, PPG2k-UUA possesses a room-temperature viscosity that remains almost four orders-of-magnitude higher than the neat PPG2k-(NH<sub>2</sub>)<sub>2</sub> precursor (e.g. 670 Pa·s vs. 0.22 Pa·s), which highlights the impact of the hydrogen bonding physical interactions, especially considering the minimal difference in  $M_n$  between PPG2k-UUA and PPG2k-(NH<sub>2</sub>)<sub>2</sub> (e.g. 5,480 g/mol vs. 2,000 g/mol). Finally, **Figure 8.1B** indicates viscosity vs. temperature at constant shear rate for the PPG2k-UUA and PPG2k-(NH<sub>2</sub>)<sub>2</sub> oligomers, indicating a roughly linear relationship between  $\log \eta$  vs.  $T$  for the investigated temperature range.

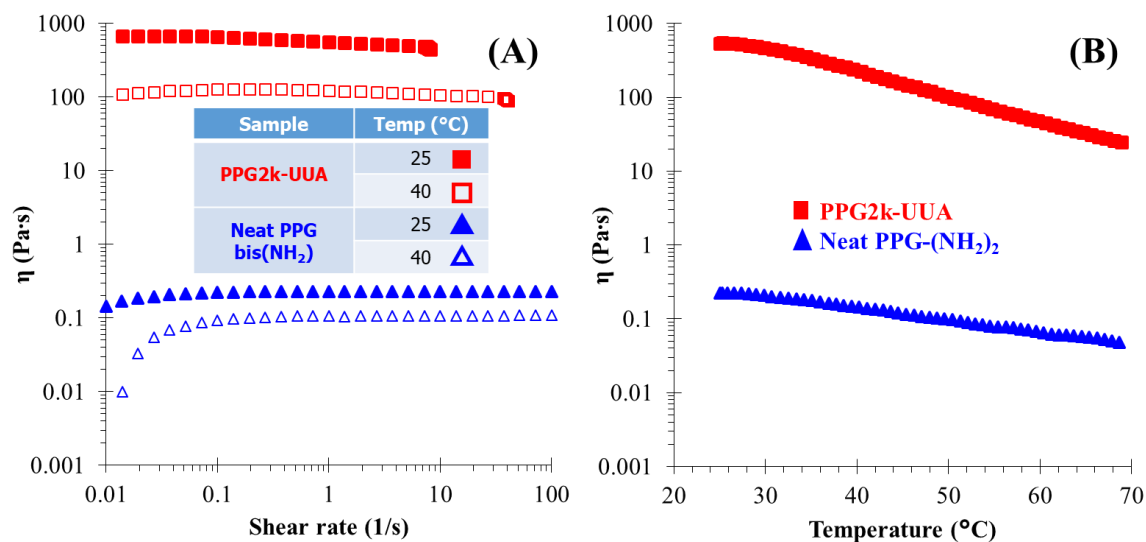


**Figure 8.1.** (A) Viscosity as a function of constant shear rate and (B) viscosity as a function of temperature at a constant  $1.0 \text{ s}^{-1}$  for PPG2k-UUA and the neat PPG-(NH<sub>2</sub>)<sub>2</sub> oligomer.

Next, photocuring in the presence of varying amounts of 2,2-dimethoxy-2-phenylacetophenone (DMPA) and subsequent dynamic mechanical analysis (DMA) enabled a probe of thermomechanical properties as a function of photoinitiator concentration. Determination of optimal photoinitiator concentration remains critical. Typically, a plateau is reached in plots of storage and loss modulus crossover time vs. photoinitiator concentration, as determined via photorheology, or plots of conversion vs. photoinitiator concentration, as determined via photocalorimetry.<sup>10,30</sup> These plots enable a selection of the minimum photoinitiator concentration required to reach the plateau, preventing issues of poor gel fraction and mechanical/physical properties.<sup>10,30</sup> This remains

advantageous as systems containing excess photoinitiator remain prone to increased termination events due to residual photoinitiator fragments.

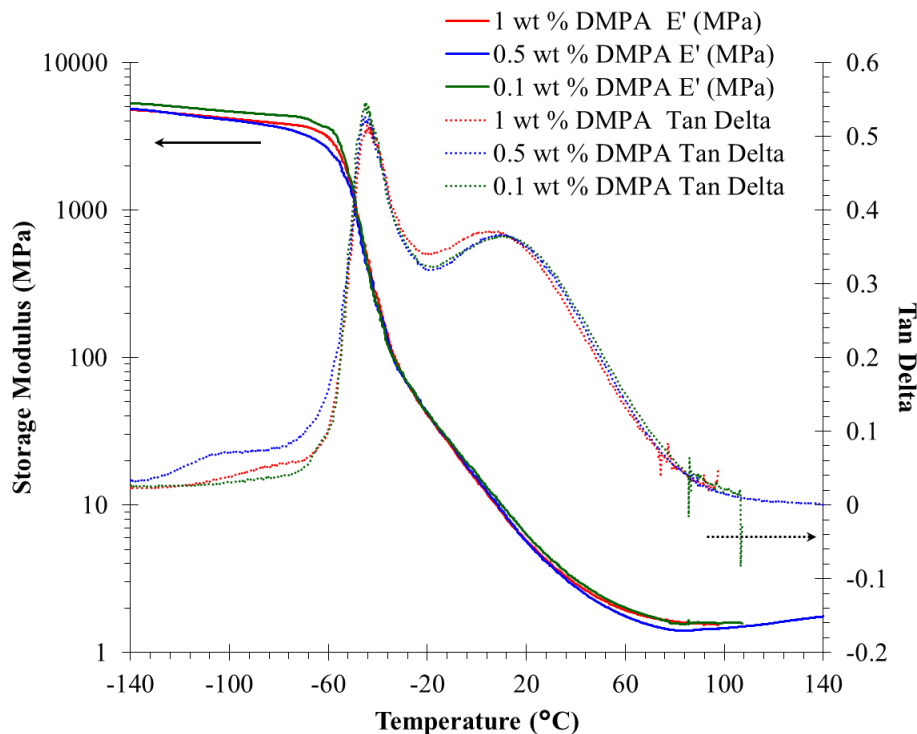


**Figure 8.2.** Dynamic mechanical analysis heating traces ( $5\text{ }^{\circ}\text{C min}^{-1}$ ,  $1\text{ Hz}$ ) for photocured PPG2k-UUA films as a function of temperature and 2,2-dimethoxy-2-phenylacetophenone (DMPA) concentration.

**Figure 8.2** depicts storage modulus vs. temperature data for photocured PPG2k-UUA at 0.1, 0.5, or 1.0 wt % DMPA, indicating virtually identical thermomechanical behavior for all probed photoinitiator concentrations. Although these data indicate that any of these photoinitiator concentrations remain suitable for subsequent photocuring, 0.5 wt % DMPA was chosen based on photoinitiator concentration studies in previous systems.

**Figure 8.3** depicts thermomechanical behavior of photocured PPG2k-UUA before and after extraction in THF. The sample before extraction possessed  $\alpha$ -relaxations at the two tan  $\delta$  peaks, which occurred at  $-50\text{ }^{\circ}\text{C}$  and  $25\text{ }^{\circ}\text{C}$ , respectively. The first  $\alpha$ -relaxation is likely caused by the PPG glass transition temperature, which ranges from  $-60$  to  $-75\text{ }^{\circ}\text{C}$  for



oligomers ranging in molecular weight from 150 – 4000 g/mol.<sup>31</sup> The higher  $T_g$  observed from the first DMA  $\alpha$ -relaxation remains slightly higher than for the free oligomer due to the restricting effect on segmental motion that covalent crosslinks and hydrogen bonding impart. The second  $\alpha$ -relaxation was not observed for related, covalently crosslinked PPG-containing networks formed by the base-catalyzed, carbon-Michael addition reaction between PPG bis(acetoacetate) (bisAcAc) and non-urethane-containing diacrylates (e.g. neopentyl glycol diacrylate), suggesting that hydrogen bonding remains responsible for this second  $\alpha$ -relaxation.<sup>32</sup> However, the  $\alpha$ -relaxation observed via DMA for networks formed from PPG bisAcAc and a urethane-containing crosslinker (e.g. HEA-H<sub>12</sub>MDI-HEA) remained as high as 12 °C.<sup>32</sup> Therefore, this second  $\alpha$ -relaxation is primarily caused by dampening from the hydrogen bond physical interactions. The extracted PPG2k-UUA sample possessed slightly higher  $\alpha$ -relaxation temperatures (e.g. -46 vs. -50 °C and 34 vs. 25 °C), likely due to the removal of the non-crosslinked, sol fraction that plasticized the networks. This photocured and extracted PPG2k-UUA sample possessed a gel fraction of 95 %. For purposes of uniformity, no DMA specimens except this one were extracted before DMA, as extraction represents an undesirable, additional post-processing step for VPP.

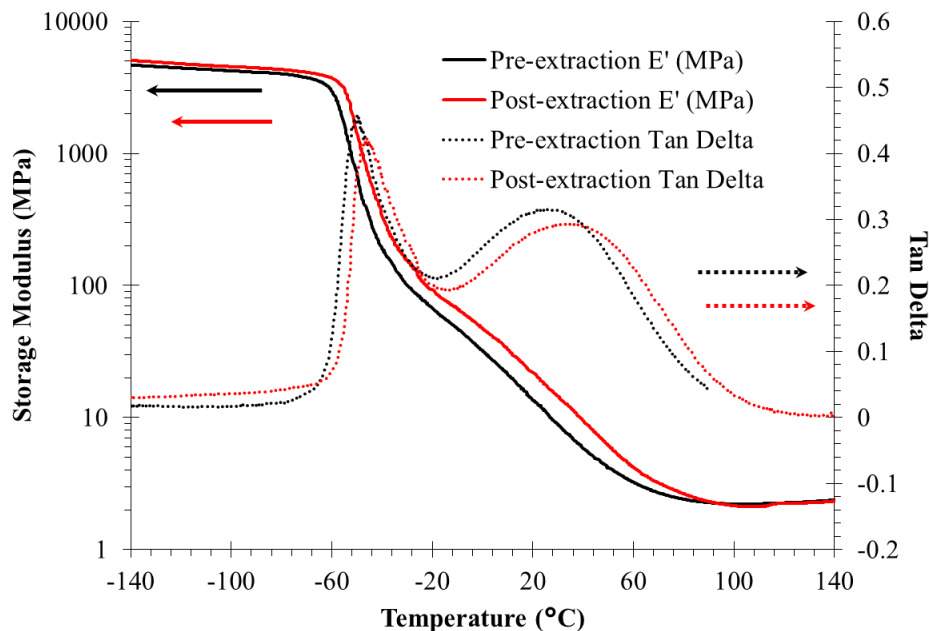
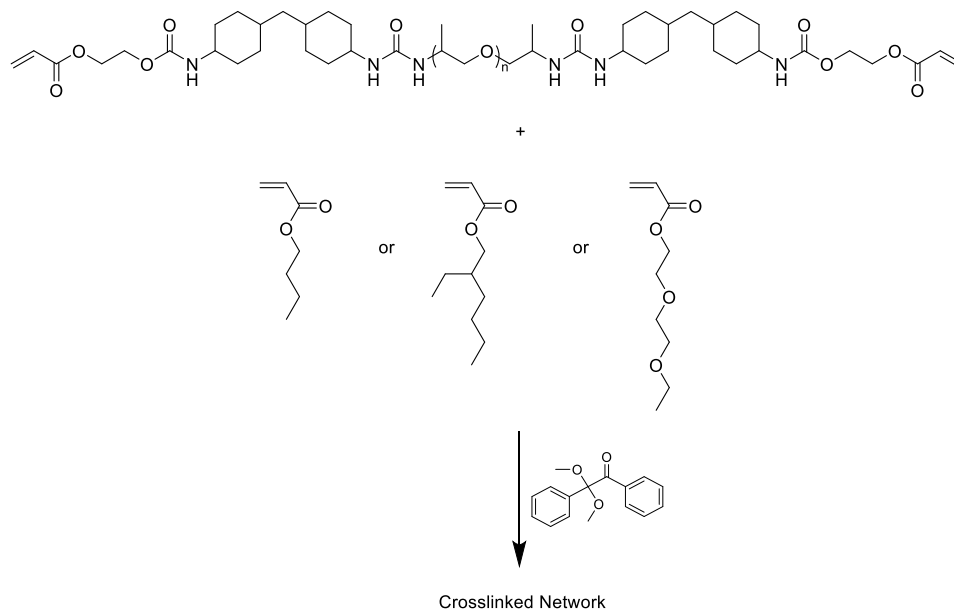


**Figure 8.3.** Dynamic mechanical analysis heating traces ( $5\text{ }^{\circ}\text{C min}^{-1}$ , 1 Hz), before and after extraction in tetrahydrofuran (THF), as a function of temperature.

**Scheme 8.1** depicts the mixing and subsequent photocuring of PPG2k-UUA with either n-butyl acrylate (nBA), 2-ethylhexylacrylate (EHA), or di(ethylene glycol) ethyl ether acrylate (DEGEEA). Photocuring the difunctional, urethane/urea-containing acrylate with these reactive diluents is known to reduce overall photopolymer viscosity and increase the molecular weight between crosslinks along the polyacrylate backbone, thus affording lower modulus objects.<sup>8,33</sup> **Figure 8.4A** depicts the viscosity of select binary mixtures of PPG2k-UUA and a single reactive diluent, overlaid with the viscosity of PPG2k-UUA and PPG2k-(NH<sub>2</sub>)<sub>2</sub> at 25 °C and 40 °C. Here, mixtures of 80 wt % EHA or DEGEEA with 20 wt % PPG2k-UUA, or a mixture of 90 wt % nBA with 10 wt % PPG2k-UUA, possessed viscosity almost one or two orders-of-magnitude below the neat PPG2k-(NH<sub>2</sub>)<sub>2</sub> oligomer, respectively, indicating promise for VPP. These binary mixtures also possessed a roughly linear relationship between  $\log \eta$  vs. T for the investigated temperature range, similar to PPG2k-UUA and the neat oligomer, alone.



**Scheme 8.2.** Photocuring of mixtures of PPG2k-UUA and n-butyl acrylate (nBA), 2-ethylhexylacrylate (EHA), or di(ethylene glycol) ethyl ether acrylate (DEGEEA), forming a crosslinked network.

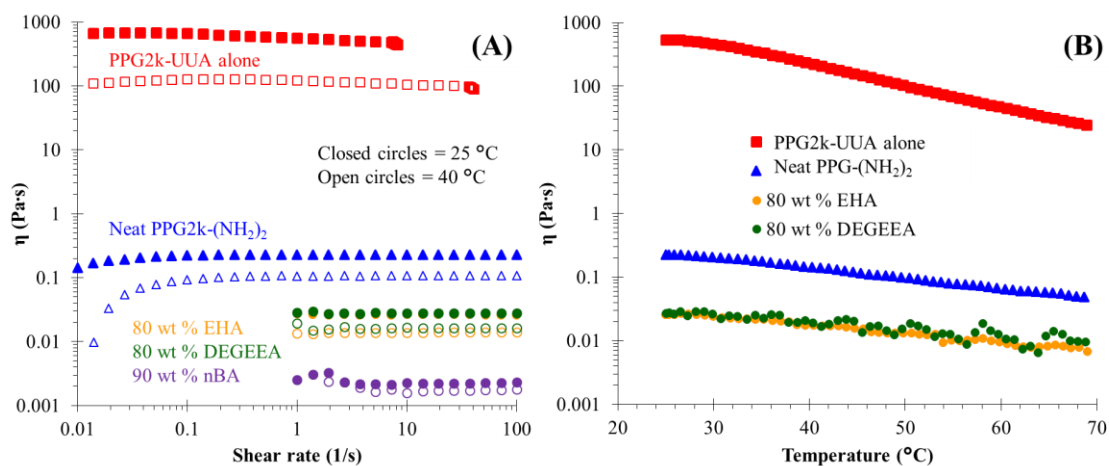


**Figure 8.4.** (A) Viscosity as a function of constant shear rate and (B) viscosity as a function of temperature at a constant 1.0 s<sup>-1</sup> for PPG2k-UUA, the neat PPG-(NH<sub>2</sub>)<sub>2</sub> oligomer, and mixtures of PPG2k-UUA and EHA, DEGEEA, or nBA at various loading.

**Figure 8.5A** depicts thermomechanical behavior for photocured, binary mixtures of PPG2k-UUA and nBA, indicating a decreasing plateau modulus with increasing nBA content, which occurs due to the increase in molecular weight between crosslinks with increasing nBA content. Furthermore, as shown **Figure 8.5B**,  $\tan \delta$  indicates double  $\alpha$ -

relaxations occurring for the 10 wt % nBA sample but not for the 30 wt % nBA sample, suggesting that a fundamental morphological change occurs between these two compositional data points. An increase in nBA content induces increases in molecular weight between crosslinks, which effectively increases the spacing between urethane functional groups. This data indicates that a predominantly phase-mixed morphology begins to dominate at 30 wt % nBA, and was observed at the same wt % loadings for similar compositional series with EHA and DEGEEA. Compositions containing majority reactive diluent by weight saw their peak  $\tan \delta$  shift towards the homopolymer  $T_g$  for the respective reactive diluent, e.g.  $-54\text{ }^\circ\text{C}$  for nBA and  $-50\text{ }^\circ\text{C}$  for EHA. Additionally, all samples for all three compositional series (e.g. nBA, EHA, and DEGEEA) possessed gel fractions above 92 wt %. Finally, **Figure 8.6** provides DMA heating traces for a variety of compositions containing either 50 or 70 wt % reactive diluent, and reveals similar thermomechanical behavior irrespective of reactive diluent composition. However, samples containing 70 wt % DEGEEA possessed a slightly lower modulus at  $22\text{ }^\circ\text{C}$  than samples containing the same content of EHA or nBA, likely due to the increased molecular weight and side chain flexibility afforded by the di(ethylene glycol) unit as compared to the shorter hydrocarbon side chains with EHA and nBA.

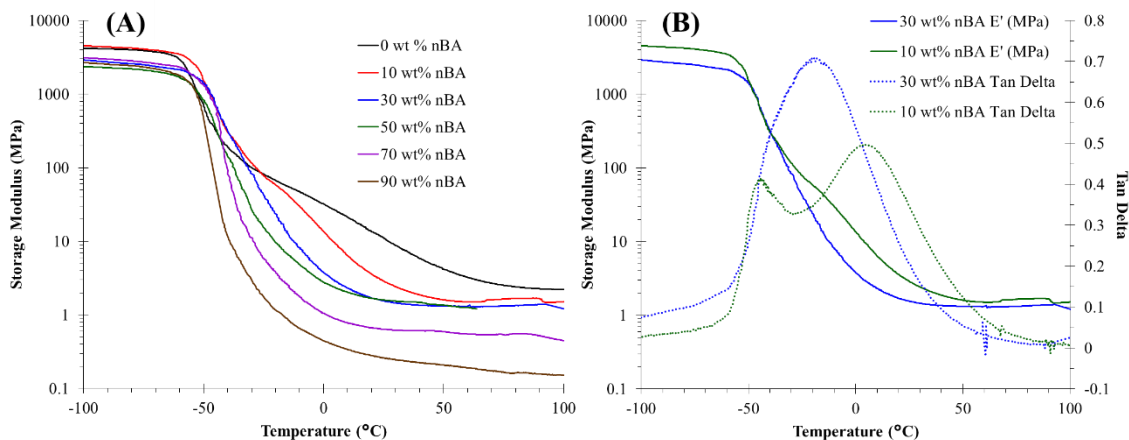


**Figure 8.5.** Dynamic mechanical analysis heating traces ( $5\text{ }^{\circ}\text{C min}^{-1}$ , 1 Hz) for (A) photocured combinations of PPG2k-UUA and nBA as a function of nBA content and temperature and (B) 10 wt % nBA and 30 wt % nBA samples

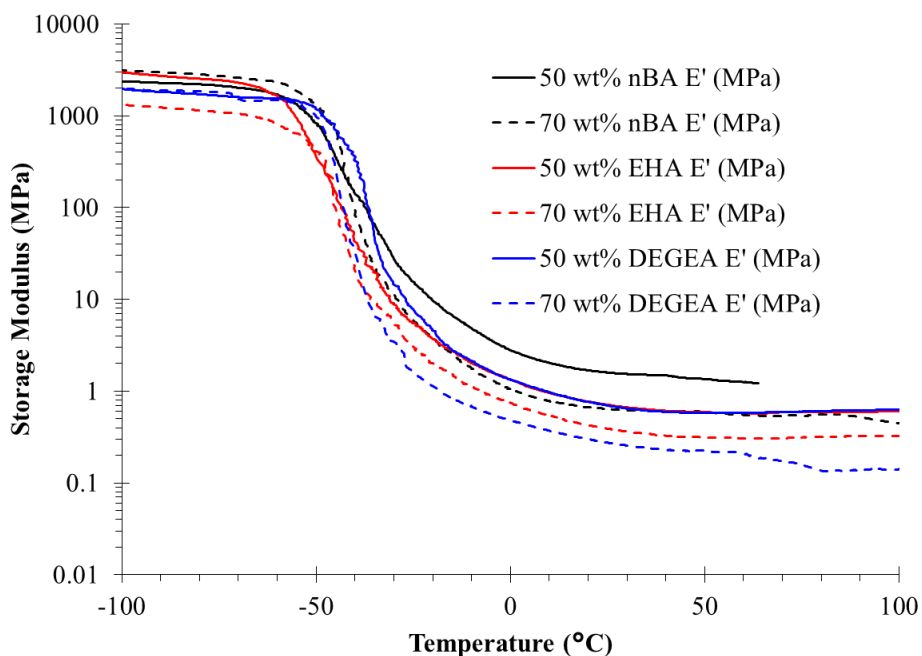


**Figure 8.6.** Dynamic mechanical analysis heating traces ( $5\text{ }^{\circ}\text{C min}^{-1}$ , 1 Hz) for photocured combinations of PPG2k-UUA and nBA, EHA, or DEGEAA as a function of temperature and monomer concentration.

Due to potential issues of monomer volatility and toxicity, VPP proceeded with compositions consisting solely of photoinitiated PPG2k-UUA and a small amount of a relatively non-toxic unreactive diluent (e.g. THF,  $\sim 20\text{ wt } \%$ ). **Figure 8.7(A,C,E)** depicts

images of various 3D printed objects including high aspect ratio pillars, a hex pattern, and a scaffold structure. **Figure 8.7(B,D,F)** portrays scanning electron microscope (SEM) images of these 3D printed objects. Due to handling difficulties, some 3D structures underwent failure in between the time that printing and imaging occurred. Despite this, the high aspect ratio pillar structure reveals ideal structural definition, with the appearance of uniform circumference across the entire height of the pillars. This type of structural feature remains accurately reproducible with VPP, as printing of this object requires exposure of repeating rectangular cross-sections, followed by repeated circular cross-sections, as the object is built from the bottom to the top in the so-called  $z$ -direction. The 3D-printed hex pattern also displays minimal non-uniformities, as each successive layer requires exposure of a circle with smaller and smaller area. Finally, the scaffold structure was built from left-to-right as displayed in **Figure 8.7E**, which represents the most challenging build orientation of these three objects. As these compositions did not contain UV absorber, this printed scaffold demonstrated prominent cure-through (e.g. photocuring of non-cured sections of previous layers).

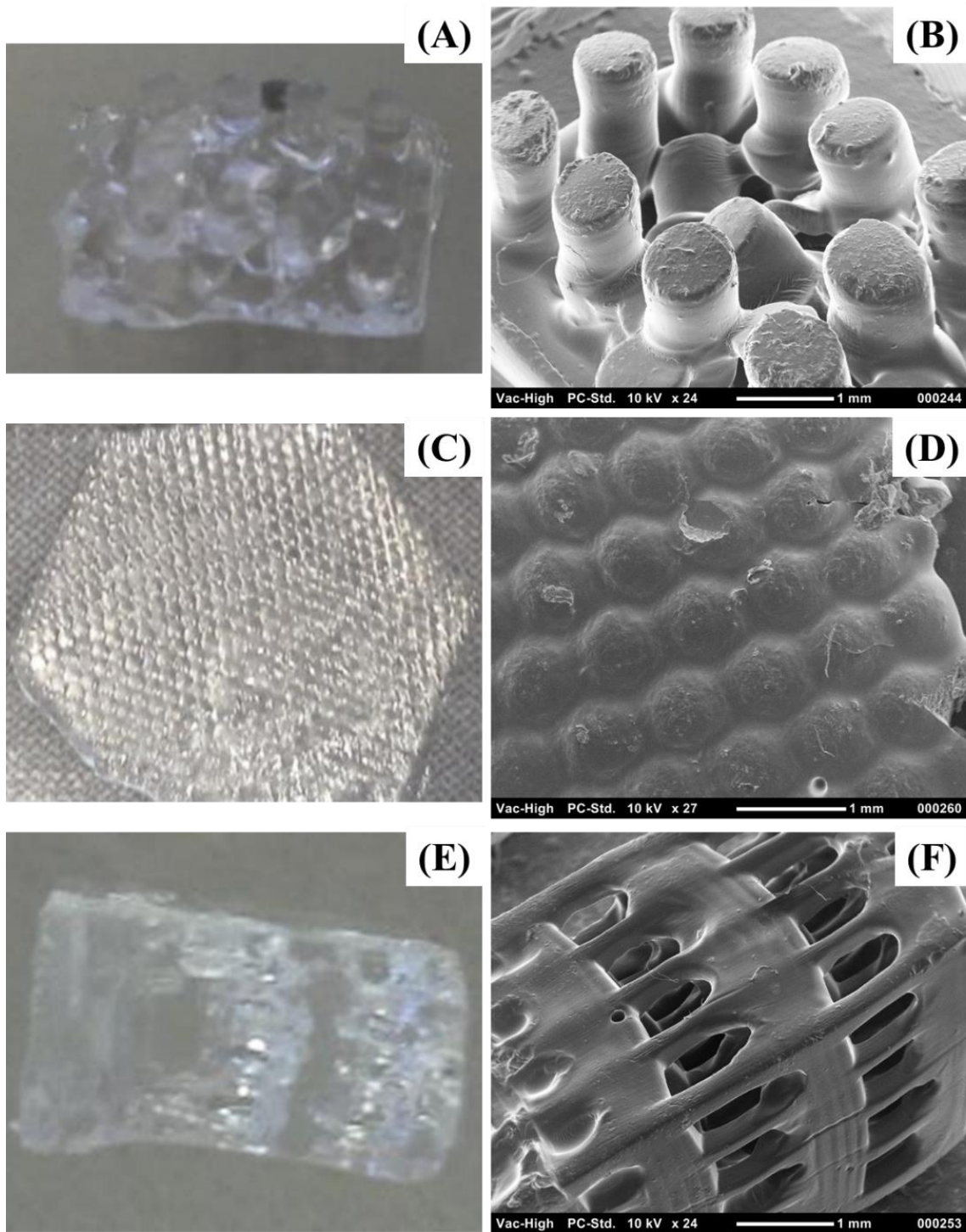


**Figure 8.7.** Photographs of (A) 3D-printed pillar structure, (C) 3D-printed hex pattern, and (E) 3D-printed scaffold structure from PPG2k-UUA alone in the absence of monomer / reactive diluent. (B,D,F) Scanning electron microscope (SEM) images of A, C, and E, respectively.

## 8.5 Conclusions

This work demonstrates the synthesis, characterization, photocuring, and VPP of a novel, urethane/urea-containing PPG acrylate that possesses multiple hydrogen bonding functional groups, affording strong physical interactions that complement covalent crosslinking. Steady-shear rheology measured the pre-cure PPG2k-UUA viscosity, revealing an orders-of-magnitude increase in  $\eta$  as compared to the neat PPG2k-(NH<sub>2</sub>)<sub>2</sub> oligomer with only a 2.75 times increase in molecular weight vs. the neat oligomer, which is attributed to the strong, intermolecular hydrogen bonding. DMA indicated two primary  $\alpha$ -relaxations for the photocured PPG2k-UUA sample alone, suggesting microphase separation between the PPG polymer backbone and the H<sub>12</sub>MDI urea/urethane moieties. Thermomechanical analysis of photocured, binary mixtures of various reactive diluents (e.g. nBA, EHA, and DEGEEA) and PPG2k-UUA demonstrated a single  $\tan \delta$  peak beyond 30 wt % incorporation, suggesting that phase mixing occurs as the distance between network junctions increases. Finally, VPP of PPG2k-UUA alone demonstrated well-defined geometries for high aspect ratio pillar and hex pattern structures, with reduced structural definition for a 3D scaffold geometry. Future work will include VPP with both antioxidants and UV blockers, which are expected to lend drastic improvements toward build resolution in the  $x$ - $y$  (build plane) and  $z$  planes.<sup>6,8</sup>

## 8.6 Acknowledgements

The authors graciously acknowledge funding from a leading footwear manufacturer in the United States, and a gracious donation of hydrogenated methylene diphenyl diisocyanate (H<sub>12</sub>MDI) from Bayer MaterialScience (now Covestro).

## 8.7 References

- (1) Reeves, P.; Tuck, C.; Hague, R. Additive Manufacturing for Mass Customization. In *Mass Customization: Engineering and Managing Global Operations*;



- Fogliatto, F. S., da Silveira, G. J. C., Eds.; Springer London: London, 2011, p 275-289.
- (2) Huang, Y.; Leu, M. C.; Mazumder, J.; Donmez, A. Additive Manufacturing: Current State, Future Potential, Gaps and Needs, and Recommendations. *Journal of Manufacturing Science and Engineering* **2015**, *137*, 014001-014001.
  - (3) Tumbleston, J. R.; Shirvanyants, D.; Ermoshkin, N.; Janusziewicz, R.; Johnson, A. R.; Kelly, D.; Chen, K.; Pinschmidt, R.; Rolland, J. P.; Ermoshkin, A.; Samulski, E. T.; DeSimone, J. M. Continuous Liquid Interface Production of 3d Objects. *Science* **2015**.
  - (4) Serrine, J. M.; Meenakshisundaram, V.; Moon, N. G.; Scott, P. J.; Mondschein, R. J.; Weiseman, T. F.; Williams, C. B.; Long, T. E. Functional Siloxanes with Photo-Activated, Simultaneous Chain Extension and Crosslinking for Lithography-Based 3d Printing. *Polymer* **2018**.
  - (5) Gibson, I.; Rosen, D.; Stucker, B. Vat Photopolymerization Processes. In *Additive Manufacturing Technologies: 3d Printing, Rapid Prototyping, and Direct Digital Manufacturing*; Springer New York: New York, NY, 2015, p 63-106.
  - (6) Ligon, S. C.; Liska, R.; Stampfl, J.; Gurr, M.; Mülhaupt, R. Polymers for 3d Printing and Customized Additive Manufacturing. *Chemical Reviews* **2017**, *117*, 10212-10290.
  - (7) Melchels, F. P. W.; Domingos, M. A. N.; Klein, T. J.; Malda, J.; Bartolo, P. J.; Huttmacher, D. W. Additive Manufacturing of Tissues and Organs. *Progress in Polymer Science* **2012**, *37*, 1079-1104.
  - (8) Liska, R.; Schuster, M.; Inführ, R.; Turecek, C.; Fritscher, C.; Seidl, B.; Schmidt, V.; Kuna, L.; Haase, A.; Varga, F. Photopolymers for Rapid Prototyping. *J Coat Technol Res* **2007**, *4*, 505-510.
  - (9) Eckel, Z. C.; Zhou, C.; Martin, J. H.; Jacobsen, A. J.; Carter, W. B.; Schaedler, T. A. Additive Manufacturing of Polymer-Derived Ceramics. *Science* **2016**, *351*, 58-62.
  - (10) Hegde, M.; Meenakshisundaram, V.; Chartrain, N.; Sekhar, S.; Tafti, D.; Williams, C. B.; Long, T. E. 3d Printing All-Aromatic Polyimides Using Mask-Projection Stereolithography: Processing the Nonprocessable. *Adv Mater* **2017**, *29*.
  - (11) Zheng, X.; Lee, H.; Weisgraber, T. H.; Shusteff, M.; DeOtte, J.; Duoss, E. B.; Kuntz, J. D.; Biener, M. M.; Ge, Q.; Jackson, J. A.; Kucheyev, S. O.; Fang, N. X.; Spadaccini, C. M. Ultralight, Ultrastiff Mechanical Metamaterials. *Science* **2014**, *344*, 1373-1377.
  - (12) Hsieh, F.-Y.; Lin, H.-H.; Hsu, S.-h. 3d Bioprinting of Neural Stem Cell-Laden Thermoresponsive Biodegradable Polyurethane Hydrogel and Potential in Central Nervous System Repair. *Biomaterials* **2015**, *71*, 48-57.
  - (13) Christ, J. F.; Aliheidari, N.; Ameli, A.; Pötschke, P. 3d Printed Highly Elastic Strain Sensors of Multiwalled Carbon Nanotube/Thermoplastic Polyurethane Nanocomposites. *Materials and Design* **2017**, *131*, 394-401.
  - (14) Pyo, S.-H.; Wang, P.; Hwang, H. H.; Zhu, W.; Warner, J.; Chen, S. Continuous Optical 3d Printing of Green Aliphatic Polyurethanes. *ACS Applied Materials & Interfaces* **2017**, *9*, 836-844.

- (15) Xu, W.; Wang, X. H.; Yan, Y. N.; Zhang, R. J. Rapid Prototyping of Polyurethane for the Creation of Vascular Systems. *Journal of Bioactive and Compatible Polymers* **2008**, *23*, 103-114.
- (16) Le Hoang, S.; Harri, K.; Marjo, L.; Minna, M.; Nguyen Dang, L.; Juergen, W.; Torsten, W.; Matthias, S.; Jukka, S. Novel Photo-Curable Polyurethane Resin for Stereolithography. *Rsc Advances* **2016**, *6*, 50706-50709.
- (17) Liska, R.; Schwager, F.; Maier, C.; Cano-Vives, R.; Stampfl, J. Water-Soluble Photopolymers for Rapid Prototyping of Cellular Materials. *Journal of Applied Polymer Science* **2005**, *97*, 2286-2298.
- (18) Baudis, S.; Heller, C.; Liska, R.; Stampfl, J.; Bergmeister, H.; Weigel, G. (Meth)Acrylate-Based Photoelastomers as Tailored Biomaterials for Artificial Vascular Grafts. *Journal of Polymer Science Part A: Polymer Chemistry* **2009**, *47*, 2664-2676.
- (19) Baudis, S.; Steyrer, B.; Pulka, T.; Wilhelm, H.; Weigel, G.; Bergmeister, H.; Stampfl, J.; Liska, R. Photopolymerizable Elastomers for Vascular Tissue Regeneration. *Macromolecular Symposia* **2010**, *296*, 121-126.
- (20) Tsai, Y. C.; Li, S. M.; Hu, S. G.; Chang, W. C.; Jeng, U. S.; Hsu, S. H. Synthesis of Thermoresponsive Amphiphilic Polyurethane Gel as a New Cell Printing Material near Body Temperature. *Acs Applied Materials & Interfaces* **2015**, *7*, 27613-27623.
- (21) Lu, Z.; Jiang, X.; Zuo, X.; Feng, L. Improvement of Cytocompatibility of 3d-Printing Resins for Endothelial Cell Adhesion. *RSC Advances* **2016**, *6*, 102381-102388.
- (22) Hung, K. C.; Tseng, C. S.; Hsu, S. H. 5 - 3d Printing of Polyurethane Biomaterials. In *Advances in Polyurethane Biomaterials*; Woodhead Publishing: 2016, p 149-170.
- (23) Sinh, L. H.; Harri, K.; Marjo, L.; Minna, M.; Luong, N. D.; Jurgen, W.; Torsten, W.; Matthias, S.; Jukka, S. Novel Photo-Curable Polyurethane Resin for Stereolithography. *Rsc Advances* **2016**, *6*, 50706-50709.
- (24) Rolland, J. P. Functional Materials for 3d Manufacturing Using Carbon's Clip Technology. *Journal of Photopolymer Science and Technology* **2016**, *29*, 451-452.
- (25) Rolland, J. P.; Chen, K.; Poelma, J.; Goodrich, J.; Pinschmidt, R.; DeSimone, J. M.; Robeson, L. M., Polyurethane Resins Having Multiple Mechanisms of Hardening for Use in Producing Three-Dimensional Objects.
- (26) Velankar, S.; Pazos, J.; Cooper, S. L. High-Performance Uv-Curable Urethane Acrylates Via Deblocking Chemistry. *Journal of Applied Polymer Science* **1996**, *62*, 1361-1376.
- (27) Hung, K.-C.; Tseng, C.-S.; Hsu, S.-h. Synthesis and 3d Printing of Biodegradable Polyurethane Elastomer by a Water-Based Process for Cartilage Tissue Engineering Applications. *Advanced Healthcare Materials* **2014**, *3*, 1578-1587.
- (28) Baudis, S.; Nehl, F.; Ligon, S. C.; Nigisch, A.; Bergmeister, H.; Bernhard, D.; Stampfl, J.; Liska, R. Elastomeric Degradable Biomaterials by Photopolymerization-Based Cad-Cam for Vascular Tissue Engineering. *Biomedical Materials* **2011**, *6*.

- (29) Sirrine, J. M.; Ashraf-Khorassani, M.; Moon, N. G.; Mondschein, R. J.; Long, T. E. Supercritical Fluid Chromatography with Evaporative Light Scattering Detection (Sfc-Elsd) for Determination of Oligomer Molecular Weight Distributions. *Chromatographia* **2016**, *79*, 977-984.
- (30) Musanje, L.; Ferracane, J. L.; Sakaguchi, R. L. Determination of the Optimal Photoinitiator Concentration in Dental Composites Based on Essential Material Properties. *Dental Materials* **2009**, *25*, 994-1000.
- (31) Kulinski, Z.; Piorkowska, E.; Gadzinowska, K.; Stasiak, M. Plasticization of Poly(L-Lactide) with Poly(Propylene Glycol). *Biomacromolecules* **2006**, *7*, 2128-2135.
- (32) Williams, S. R.; Mather, B. D.; Miller, K. M.; Long, T. E. Novel Michael Addition Networks Containing Urethane Hydrogen Bonding. *Journal of Polymer Science Part A: Polymer Chemistry* **2007**, *45*, 4118-4128.
- (33) Schuster, M.; Turecek, C.; Mateos, A.; Stampfl, J.; Liska, R.; Varga, F. Evaluation of Biocompatible Photopolymers Ii: Further Reactive Diluents. *Monatshefte für Chemie - Chemical Monthly* **2007**, *138*, 261-268.

## Chapter 9: 3D-Printable Biodegradable Polyester Tissue Scaffolds for Cell Adhesion

(Published in *Aust. J. Chem.* **2015**, 68, 1409-1414.)

Justin M. Sirrine<sup>A</sup>, Allison M. Pekkanen<sup>B</sup>, Ashley M. Nelson<sup>A</sup>, Nicholas A. Chartrain<sup>C</sup>, Christopher B. Williams<sup>D</sup>, and Timothy E. Long<sup>A,B,E</sup>

<sup>A</sup>*Department of Chemistry*, <sup>B</sup>*School of Biomedical Engineering and Sciences*,  
<sup>C</sup>*Department of Materials Science and Engineering*, <sup>D</sup>*Department of Mechanical Engineering*  
*Macromolecules and Interfaces Institute, Virginia Tech, Blacksburg, VA 24061*

### 9.1 Abstract

Additive manufacturing, or three-dimensional (3D) printing, has emerged as a viable technique for the production of vascularized tissue engineering scaffolds. In this report, a biocompatible and biodegradable poly(tri(ethylene glycol) adipate) dimethacrylate was synthesized and characterized for suitability in soft tissue scaffolding applications. The polyester dimethacrylate exhibited highly efficient photocuring, hydrolyzability, and 3D printability in a custom microstereolithography system. The photocured polyester film demonstrated significantly improved cell attachment and viability as compared to controls. These results indicate promise of novel, printable polyesters for 3D patterned, vascularized soft-tissue engineering scaffolds.

### 9.2 Manuscript

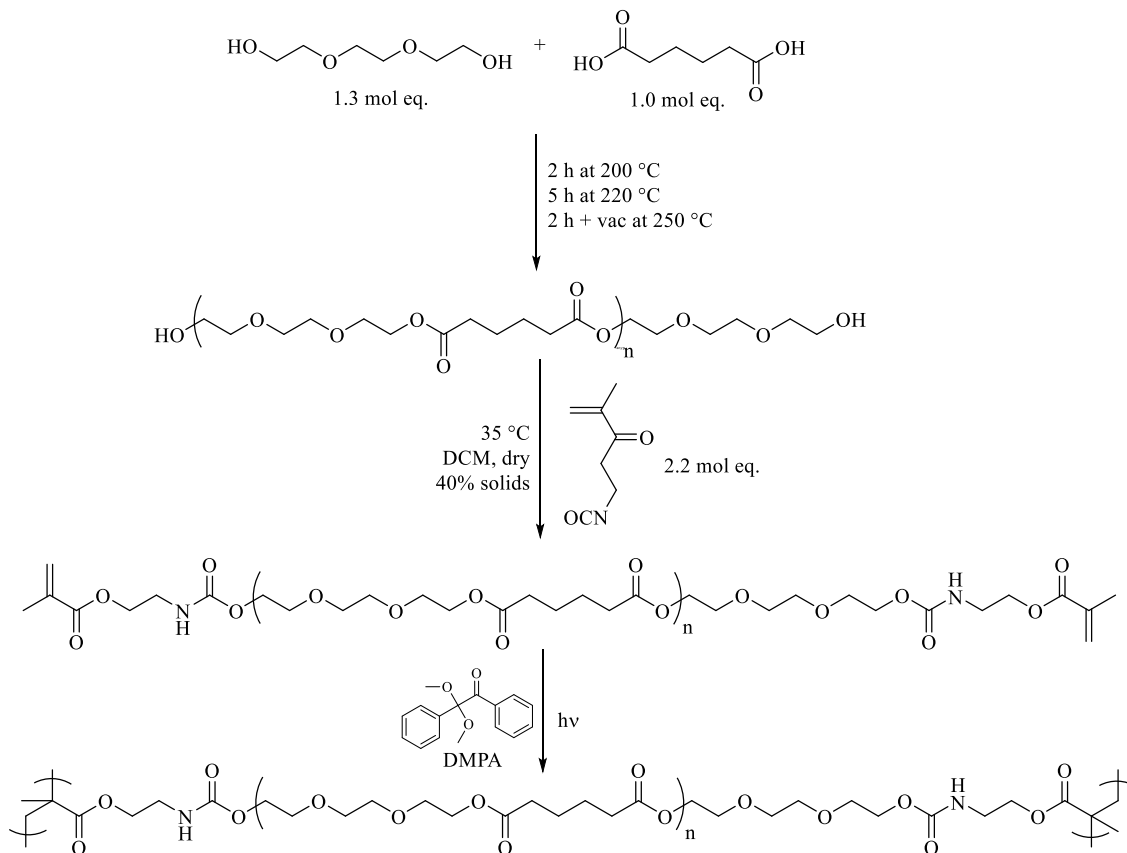
The use of aliphatic polyesters for three-dimensional (3D) printing of constructs for cell and tissue growth is widespread.<sup>1-7</sup> In the context of cell growth, polyester-based biomaterials serve to imitate the mechanical support provided by the extracellular matrix (ECM) and afford both the detailed study of cell and tissue growth in 3D,<sup>8,9</sup> as well as the investigation of the 3D cellular response to biochemical factors.<sup>8,10-13</sup> Additive manufacturing (AM), otherwise known as 3D printing, comprises many techniques and

enables the creation of geometries not attainable by traditional manufacturing methods.<sup>14-</sup>  
<sup>16</sup> Considerable precedence exists for the AM processing of synthetic, biodegradable polymers via stereolithography (SLA),<sup>17-19</sup> fused deposition modeling (FDM),<sup>20-22</sup> and selective laser sintering (SLS),<sup>23,24</sup> as well as other techniques.<sup>25</sup> Stereolithography, a form of AM that employs patterned UV light for the layer-by-layer curing of a photopolymer into a 3D structure, offers the creation of tissue scaffolds with unique porosity and connectivity, along with the ability to replicate vasculature<sup>26</sup> and tissue microstructure.<sup>19</sup> Recent developments in the print speed<sup>27</sup> and resolution<sup>28</sup> of the SLA process make this technique an ideal AM method for generating tissue scaffolds.<sup>29</sup> Biodegradable polymers typically contain ester or carbonate functional groups that hydrolyze under physiologically relevant acidic conditions.<sup>30</sup> Recent work includes the printing of homopolymers or copolymers poly( $\epsilon$ -caprolactone) (PCL),<sup>17,31,32</sup> poly(D,L-lactide) (PDLLA),<sup>3,18,33</sup> poly(propylene fumarate) (PPF),<sup>34-36</sup> and trimethylene carbonate (TMC).<sup>32,37-39</sup> In this work, a 3D printable, UV-curable poly(tri(ethylene glycol) adipate) (PTEGA) dimethacrylate polyester is synthesized and characterized for its suitability in soft tissue scaffold applications.

Melt polycondensation of tri(ethylene glycol) (TEG) and adipic acid and subsequent methacrylate functionalization afforded telechelic polyester dimethacrylates, as shown in **Scheme 9.1**. This composition holds many advantages as compared to other polyesters. First, adipic acid demonstrates low acute toxicity in rats, with LD<sub>50</sub> >5000 mg/kg.<sup>40</sup> Even-chain diacids, including adipic acid, are partially metabolized in human mitochondria<sup>41</sup> to form acetyl CoA and succinyl CoA, which represent the starting point or an intermediate in the Krebs cycle, respectively,<sup>5</sup> and unmodified adipic acid is typically

excreted in urine.<sup>40</sup> Additionally, TEG exhibits significantly reduced toxicity as compared to its lower molecular weight analogs, di(ethylene glycol) and ethylene glycol.<sup>42</sup> Presumably, no free monomer or condensation byproducts exist in final oligomer compositions or photocured films for cell studies, due to the vacuum step in polyester synthesis and photocured film sol fraction extraction, respectively. However, monomer toxicity for this system must be considered, as hydrolysis of backbone ester groups will result in this particular composition reverting back to monomer.

Functionalization of the PTEGA diols with 2-isocyanatoethyl methacrylate yielded quantitative methacrylate functionalization. The speed of the primary hydroxyl – isocyanate reaction, coupled with the lack of byproducts,<sup>43</sup> made this reaction an attractive choice for polyesters in biological applications. This reaction proceeded in the absence of dibutyltin dilaurate (DBTDL), a typical catalyst for isocyanate-alcohol coupling, in order to mitigate concerns of toxicity in the subsequent cell viability assay. Additionally, this synthetic route avoided the production of hydrochloric acid (HCl), produced with the use of acyl chlorides, which would degrade the polyester oligomer backbone. Similarly, the use of acrylic (methacrylic) anhydride as a functionalizing agent would produce acrylic (methacrylic) acid, also potentially hydrolyzing the polyester oligomer backbone. This melt polycondensation and subsequent methacrylate functionalization method provided PTEGA dimethacrylate oligomers of  $M_n = 1,600$  g/mol. Molecular weight determination and structure confirmation was performed by <sup>1</sup>H NMR end-group analysis and is presented in further detail in the Supplementary Material.



**Scheme 9.1:** Synthesis, functionalization, and photocuring of poly(tri(ethylene glycol) adipate) (PTEGA). Synthesis proceeded via melt polycondensation of tri(ethylene glycol) and adipic acid, forming PTEGA diol. Functionalization with 2-isocyanatoethyl methacrylate afforded PTEGA dimethacrylate. Finally, photocuring in the presence of the photoinitiator 2,2-dimethoxy-2-phenylacetophenone (DMPA) yielded crosslinked films.

Photocuring of the prepared PTEGA dimethacrylate in the presence of the photoinitiator 2,2-dimethoxy-2-phenylacetophenone (DMPA) afforded robust films. Soxhlet sol-gel analysis in THF revealed highly crosslinked films, with 96 wt % gel fraction. For cell studies, an alternative extraction method of ultrasonication in THF was used due to the brittle nature of the soxhlet-extracted films. **Figure 9.1a** demonstrates the photocuring process and indicates a slight curvature in the photocured films, potentially due to the difference in UV exposure ( $\text{W}/\text{cm}^2$ ) at the top versus the bottom of the film. This gradient in exposure energy likely created differences in cure time throughout the film

thickness, resulting in the creation of residual stresses<sup>44</sup> that were liberated upon release of the cured film from the Teflon<sup>®</sup> mold. Further confirming this hypothesis and discussed further below, a 3D-printed cylinder with sufficiently thin layers, ca. 25  $\mu\text{m}$ ,<sup>45</sup> did not contain any observable curvature. If desired, this residual stress-induced curvature can be controlled by reducing film thickness, or through curing thin layers of material in an iterative fashion, thus minimizing the gradient in UV exposure. These residual stresses are controllable for the self-assembly of complex 3D objects, such as cylinders or vessels, as Gracias and coworkers demonstrated.<sup>46-49</sup> Briefly, 3D structures assembled upon the release of metal- and polymer-containing 2D thin films from a substrate or sacrificial layer, in some cases achieving bidirectional curvature in a 2D film.

Following successful photocuring and extraction, an ethanol soak and a series of media soaks provided sterile and swelled gels. MDA-MB-231 human breast cancer cells were seeded onto gels and wells on both tissue- and non-tissue culture treated 24-well plates at a density of 25,000 cells/well. A CellTiter-Glo<sup>®</sup> assay performed after 24 h evaluated relative cell attachment, the results of which are presented in **Figure 9.1b**. Although underperforming the standard tissue culture treated polystyrene, the photocured film significantly improved cell attachment and viability compared to non-tissue culture treated polystyrene ( $p < 0.05$ ), which serves as the standard for comparison in this experiment. The Tukey's HSD test data is provided in the Supporting Material. Optimization of PTEGA molecular weight and photocured film sample preparation will improve the viability of these polyesters as compared to tissue culture treated polystyrene. No discernable bulk hydrolysis occurred during the course of the experiment, indicating the potential longevity of an implanted soft tissue scaffold.



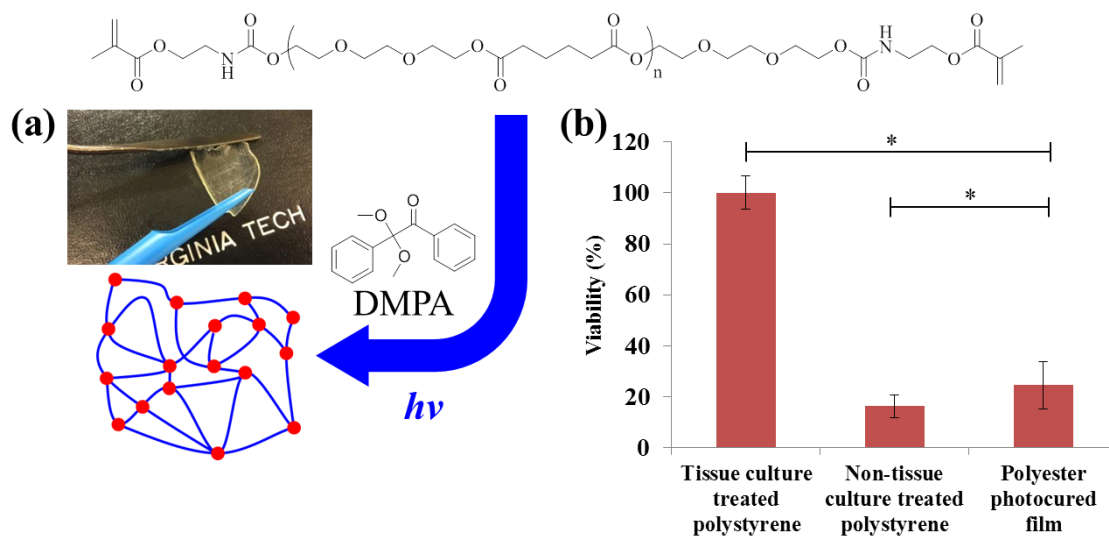


**Figure 9.1.** (a) Photocuring of poly(tri(ethylene glycol) adipate) (PTEGA) dimethacrylate. (b) MDA-MB-231 cell viability assay indicating significantly improved cell attachment and viability as compared to non-tissue culture treated polystyrene ( $p < 0.05$ ). Asterisks signify statistical significance between the two populations at the specified  $p$  value.

In an effort to further probe gel hydrolyzability and facilitate cleavage of ester bonds, exposure of the photocured gels to a concentrated HCl solution at room temperature induced polymer backbone hydrolysis and both surface and bulk degradation occurred. Scanning electron microscopy (SEM) of the treated films provided visualization of the surface degradation and cracking, shown in **Figure 9.2b**. Exposure of the films to reverse osmosis (R.O.) water over the same time periods did not produce observable surface or bulk degradation, signifying the potential durability of an implanted scaffold. This study demonstrates proof-of-concept hydrolyzability on a short time scale; further studies at physiologically relevant temperatures and salt concentrations, along with an expanded series of timepoints, will further elucidate the hydrolysis kinetics of this particular polyester composition. Finally, a custom-built microstereolithography machine demonstrated 3D printing of PTEGA dimethacrylate.<sup>45</sup> The realization of adequate vascularization persists as a prominent issue for tissue engineering scaffolds.<sup>50</sup> In this work, the 3D printing of a

cylindrical geometry demonstrated the proof-of-concept for scaffold walls with the capability to sustain vasculature. Further study of photocured films and simple printed geometries will reveal bulk mechanical properties before a more complex printing process is realized.

Shown in **Figure 9.2c**, the 3D printed cylinder displayed a uniform wall thickness and height. Surface roughness is noticeably different in the cylinder interior versus cylinder exterior. As surface roughness is known to have a strong influence on cell behavior,<sup>51</sup> an optimized printing procedure could control roughness. For example, previous work indicated that 3T3 mouse fibroblast cells can detect and respond to gradients in PLA surface roughness, indicating a preference for surfaces of higher rigidity in the absence of growth factors.<sup>52</sup> In the 3D printing of PTEGA dimethacrylate, an exploration of alternative printing orientations or CAD file optimization could optimize the surface roughness variability. As compared to the photocured film, the printed cylinder contained no visibly apparent curvature or geometric distortions, indicating high fidelity printing. As layer thickness in this microstereolithography process remains only ca. 25  $\mu\text{m}$ <sup>45</sup>, there is likely no appreciable difference in exposure energy ( $\text{W}/\text{cm}^2$ ) at the top versus bottom of the photocuring layer, and therefore no appreciable residual stresses locked into the printed object available to cause geometric distortion.

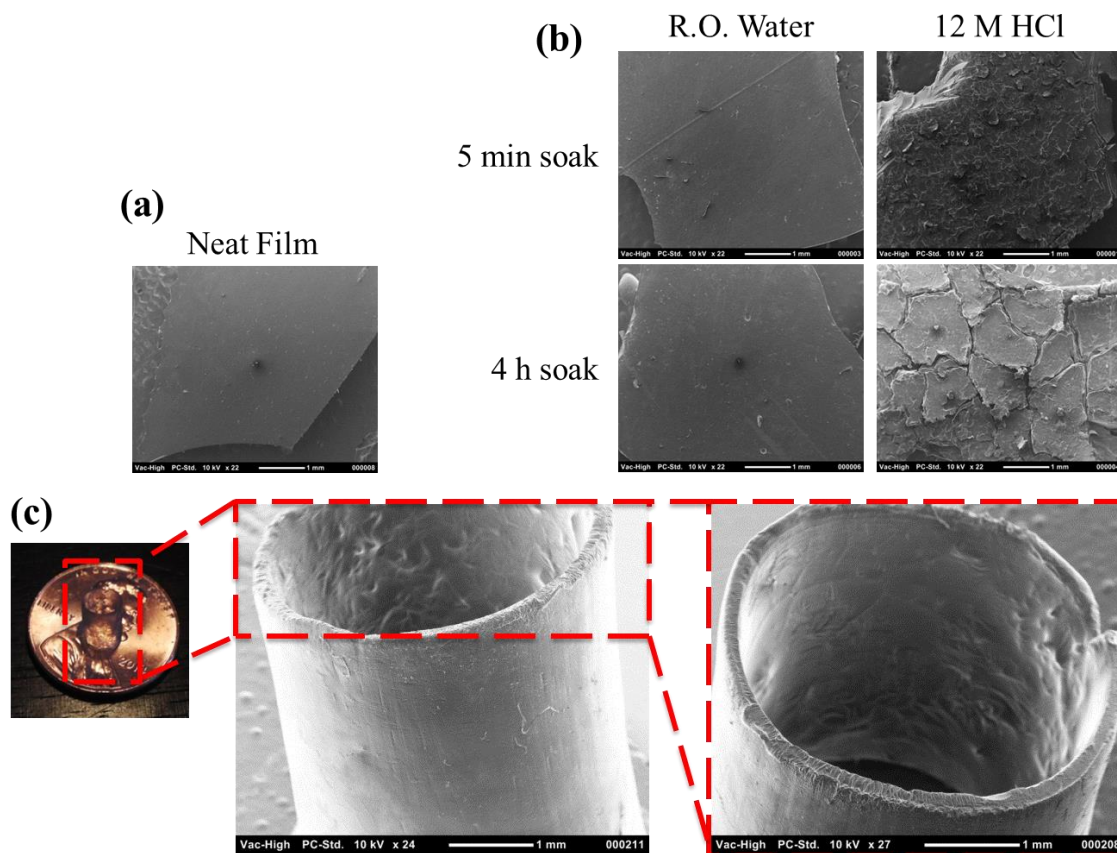


**Figure 9.2.** (a) SEM micrograph of neat, dried polyester film. (b) SEM micrograph of treated polyester films, indicating hydrolysis-induced surface roughness. (c) Image and SEM micrographs of 3D-printed polyester cylinder.

Synthesis of PTEGA dimethacrylate and characterization of the photocured films and 3D-printed geometries is reported for the first time. Photocuring, subsequent soxhlet extraction, and an optimized sample preparation extraction method revealed highly efficient photocuring, as well as robust films for cell attachment and viability assays. These polyester films demonstrated significantly improved cell attachment and viability as compared to non-tissue culture treated polystyrene, indicating strong potential as scaffolds for soft tissue applications. A preliminary hydrolysis study suggested hydrolyzability of the polyester film upon exposure to an acid solution. Finally, the suitability of this new

polyester dimethacrylate for 3D printing was demonstrated with the printing and characterization of a polyester cylinder. These results indicate the potential for 3D printed polyesters in a wide range of biological application.

### **9.3 Experimental**

#### **9.3.1 Synthesis of poly(tri(ethylene glycol) adipate) (PTEGA)**

Triethylene glycol (99 %; TEG) was purchased from Sigma-Aldrich and adipic acid ( $\geq 99.5$  %; AA) was purchased from Fluka Analytical. 2-isocyanatoethyl methacrylate was purchased from TCI America. All reagents were used as received. The modified Carothers' equation was used to offset stoichiometry and target a 1000 g/mol oligomer.<sup>53</sup> Melt polycondensation afforded the oligomer in the absence of catalyst and was prepared in the following manner. Triethylene glycol (74.96 g, 0.50 mol) and adipic acid (56.12 g, 0.38 mol) were added to a dry 250-mL round-bottomed flask. The reaction flask was equipped with a mechanical stirrer, t-neck, and distillation neck. To remove oxygen, the reaction was purged with N<sub>2</sub> and degassed three times. The reaction was lowered into a molten metal bath at 200 °C with a constant N<sub>2</sub> purge and stirring and allowed to react for 2 h. The reaction temperature was then raised to 220 °C for an additional 5 h. Finally, the temperature was raised to 250 °C and vacuum was applied with continuous stirring for 2 h. After cooling under inert atmosphere, the oligomer was removed from the round-bottomed flask and used without any purification.

The resulting polyester diol (94.71 g, 0.09471 mol) was placed in a 250-mL round bottomed flask equipped with condenser, overhead stirrer, and addition funnel. The system was purged with nitrogen for 1 h and equilibrated at 35 °C, and anhydrous dichloromethane (DCM) was introduced to achieve 40 % solids. 2-isocyanatoethyl methacrylate (33.8 g, 0.21785 mol) was added dropwise and the reaction proceeded in the absence of catalyst for

18 h. The resulting polyester dimethacrylate reaction mixture was separated 3x against water to remove excess 2-aminoethyl methacryate and DCM was removed under reduced pressure. Finally, 1000 ppm hydroquinone (radical inhibitor) was added and the final product was dried overnight at 35 °C under reduced pressure (98% isolated yield).

### **9.3.2 Photocuring and gel preparation for cytotoxicity assay**

2,2-dimethoxy-2-phenylacetophenone (DMPA) was dissolved in acetone and added to PTEGA dimethacrylate at 2 wt % DMPA. The resulting mixture was homogenized and photocured under a UV lamp (Hanovia med. pressure Hg lamp, PC 451050; Ace Glass photochemical safety cabinet; 120 V, 60 Hz, 450 W UV power supply) for 8 min. The resulting gel was dried at 40 °C under reduced pressure. For sol-gel analysis, the samples were extracted in THF under reflux for 6 h, dried, and weighed. For cytotoxicity measurements, photocured gels were extracted for 90 min via ultrasonication in THF. After drying under reduced pressure 40 °C for 6 h, the gels were swelled overnight in water, sterilized in 70/30 vol/vol EtOH/H<sub>2</sub>O for 3 h, and swelled in media with 4 media changeovers at least 1 h apart to provide sterile, ethanol-free, media-swelled gels.

### **9.3.3 Cell culture and viability assay**

MDA-MB-231 cells were cultured in Dulbecco's Modified Eagle Medium (DMEM) supplemented with Factor 12 (DMEM-F12) (Fisher Scientific), 10% fetal bovine serum and 1% penicillin/streptomycin (Sigma Aldrich). Cells were maintained at 37 °C with 5% CO<sub>2</sub> until 70-80% confluent, at which point they were lifted from the plate with 0.25% Trypsin-EDTA (Sigma Aldrich). Following centrifugation to form a pellet, MDA-MB-231 cells were counted with a hemocytometer and seeded into 24 well plates at a density of 25,000 cells/well. Gels were placed in non-tissue culture treated plates and control cells were seeded into both tissue culture and non-tissue culture treated polystyrene well plates.

After a 24 hour incubation period, a CellTiter-Glo<sup>®</sup> assay (Promega) was performed following manufacturer's specifications. Briefly, cells were allowed to equilibrate to room temperature and an equal volume of CellTiter-Glo<sup>®</sup> reagent was added to each well. Gels were transferred to a new well plate to prevent false positive readings due to cells attached to the well bottoms. Luminescence readings were performed on a GloMax Luminometer following the standard protocol. Viability was calculated as percentage of control cells on tissue culture treated polystyrene compared to media without cells. In this assay, tissue culture treated polystyrene served as the positive control and a combination of CellTiter-Glo<sup>®</sup> reagent and media without cells served as the negative control. Non-tissue culture treated polystyrene served as the standard for comparison. Statistical comparisons were made with ANOVA followed by Tukey's HSD, which was performed in JMP. Asterisks signify statistical significance at the specified level (\* =  $p < 0.05$ ).

#### **9.3.4 Hydrolysis study**

Photocured, dried PTEGA films were soaked at room temperature (22 °C) for 5 m or 4 h in either reverse osmosis (R.O.) water or 12 M hydrochloric acid (HCl, ACS reagent, 36.5-38.0% HCl basis). After soaking, films were rinsed with R.O. water, dried under reduced pressure at 40 °C overnight, and imaged.

#### **9.3.5 Analytical Methods**

<sup>1</sup>H nuclear magnetic resonance spectroscopy (<sup>1</sup>H NMR) spectroscopy was performed using a Varian Unity 400 MHz spectrometer with CDCl<sub>3</sub> at 23 °C. Differential Scanning Calorimetry (DSC) was performed with a TA Instruments Q1000 DSC under constant N<sub>2</sub> purge, with a heat/cool/heat cycle at 10 °C/min heating and quench cooling. Reported T<sub>g</sub> values are from the second heating cycle.

### 9.3.6 Microstereolithography and Characterization

A custom-built mask-projection microstereolithography (MP $\mu$ SL) setup consisted of a UV light source (Hamamatsu LightningCure LC-L1V3 UV LED), conditioning optics (Edmund Optics), a dynamic mask with connected computer, imaging optics, and a 25-mL beaker with a linear actuator-mounted stage (Zaber NA11B60).<sup>45</sup> A Jeol NeoScope JCM-5000 scanning electron microscope (SEM) imaged complex 3D objects for analyzing architectural features, printing resolution, and build reproducibility. 3D objects were mounted directly onto the SEM sample stage and immediately imaged; no conductive sputter coating was required.

## 9.4 Acknowledgements

This material is based upon work supported in part by the Howard Hughes Medical Institute through the Sciencering Program. We acknowledge the Institute for Critical Technology and Applied Science (ICTAS) and the Design, Research, and Education for Additive Manufacturing Systems (DREAMS) laboratories at Virginia Tech for instrumental support.

## 9.5 References

- (1) Arcaute, K.; Mann, B.; Wicker, R. *Acta Biomaterialia* **2010**, *6*, 1047-1054.
- (2) Melchels, F. P. W.; Feijen, J.; Grijpma, D. W. *Biomaterials* **2010**, *31*, 6121-6130.
- (3) Melchels, F. P. W.; Feijen, J.; Grijpma, D. W. *Biomaterials* **2009**, *30*, 3801-3809.
- (4) Makitie, A. A.; Korpela, J.; Elomaa, L.; Reivonen, M.; Kokkari, A.; Malin, M.; Korhonen, H.; Wang, X.; Salo, J.; Sihvo, E.; Salmi, M.; Partanen, J.; Paloheimo, K.-S.; Tuomi, J.; Narhi, T.; Seppala, J. *Acta Oto-Laryngologica* **2013**, *133*, 412-417.
- (5) Barrett, D.; Yousaf, M. *Molecules* **2009**, *14*, 4022-4050.
- (6) Puppi, D.; Mota, C.; Gazzarri, M.; Dinucci, D.; Gloria, A.; Myrzabekova, M.; Ambrosio, L.; Chiellini, F. *Biomedical Microdevices* **2012**, *14*, 1115-1127.
- (7) Freed, L. E.; Vunjak-Novakovic, G.; Biron, R. J.; Eagles, D. B.; Lesnoy, D. C.; Barlow, S. K.; Langer, R. *Nature Biotechnology* **1994**, *12*, 689-693.
- (8) Tian, B.; Liu, J.; Dvir, T.; Jin, L.; Tsui, J. H.; Qing, Q.; Suo, Z.; Langer, R.; Kohane, D. S.; Lieber, C. M. *Nature Materials* **2012**, *11*, 986-994.
- (9) Kraehenbuehl, T. P.; Langer, R.; Ferreira, L. S. *Nature Methods* **2011**, *8*, 731-736.

- (10) Dvir, T.; Timko, B. P.; Kohane, D. S.; Langer, R. *Nature Nanotechnology* **2011**, *6*, 13-22.
- (11) Kloxin, A. M.; Kasko, A. M.; Salinas, C. N.; Anseth, K. S. *Science* **2009**, *324*, 59-63.
- (12) Place, E. S.; George, J. H.; Williams, C. K.; Stevens, M. M. *Chemical Society Reviews* **2009**, *38*, 1139-1151.
- (13) Wylie, R. G.; Ahsan, S.; Aizawa, Y.; Maxwell, K. L.; Morshead, C. M.; Shoichet, M. S. *Nature Materials* **2011**, *10*, 799-806.
- (14) Vaezi, M.; Seitz, H.; Yang, S. *The International Journal of Advanced Manufacturing Technology* **2013**, *67*, 1721-1754.
- (15) Kruth, J. P.; Leu, M. C.; Nakagawa, T. *CIRP Annals - Manufacturing Technology* **1998**, *47*, 525-540.
- (16) Schultz, A. R.; Lambert, P. M.; Chartrain, N. A.; Ruohoniemi, D. M.; Zhang, Z.; Jangu, C.; Zhang, M.; Williams, C. B.; Long, T. E. *ACS Macro Letters* **2014**, *3*, 1205-1209.
- (17) Skoog, S.; Goering, P.; Narayan, R. *J Mater Sci: Mater Med* **2014**, *25*, 845-856.
- (18) Ronca, A.; Ambrosio, L.; Grijpma, D. W. *Acta Biomaterialia* **2013**, *9*, 5989-5996.
- (19) Gauvin, R.; Chen, Y.-C.; Lee, J. W.; Soman, P.; Zorlutuna, P.; Nichol, J. W.; Bae, H.; Chen, S.; Khademhosseini, A. *Biomaterials* **2012**, *33*, 3824-3834.
- (20) Hutmacher, D. W.; Schantz, T.; Zein, I.; Ng, K. W.; Teoh, S. H.; Tan, K. C. *J. Biomed. Mater. Res.* **2001**, *55*, 203-216.
- (21) Zein, I.; Hutmacher, D. W.; Tan, K. C.; Teoh, S. H. *Biomaterials* **2002**, *23*, 1169-1185.
- (22) Korpela, J.; Kokkari, A.; Korhonen, H.; Malin, M.; Närhi, T.; Seppälä, J. *Journal of Biomedical Materials Research Part B: Applied Biomaterials* **2013**, *101B*, 610-619.
- (23) Niino, T.; Hamajima, D.; Montagne, K.; Oizumi, S.; Naruke, H.; Huang, H.; Sakai, Y.; Kinoshita, H.; Fujii, T. *Biofabrication* **2011**, *3*, 034104.
- (24) Zhang, Y.; Hao, L.; Savalani, M. M.; Harris, R. A.; Di Silvio, L.; Tanner, K. E. *Journal of Biomedical Materials Research Part A* **2009**, *91A*, 1018-1027.
- (25) Hung, K.-C.; Tseng, C.-S.; Hsu, S.-h. *Advanced Healthcare Materials* **2014**, *3*, 1578-1587.
- (26) Wetzel, S. G.; Ohta, M.; Handa, A.; Auer, J.-M.; Lylyk, P.; Lovblad, K.-O.; Babic, D.; Rufenacht, D. A. *American Journal of Neuroradiology* **2005**, *26*, 1425-1427.
- (27) Tumbleston, J. R.; Shirvanyants, D.; Ermoshkin, N.; Januszewicz, R.; Johnson, A. R.; Kelly, D.; Chen, K.; Pinschmidt, R.; Rolland, J. P.; Ermoshkin, A.; Samulski, E. T.; DeSimone, J. M. *Science* **2015**.
- (28) Brandi, F.; Anjum, F.; Ceseracciu, L.; Barone, A. C.; Athanassiou, A. *Journal of Micromechanics and Microengineering* **2011**, *21*, 054007.
- (29) Savalani, M. M.; Harris, R. A. *Proceedings of the Institution of Mechanical Engineers, Part H: Journal of Engineering in Medicine* **2006**, *220*, 505-520.
- (30) Croll, T. I.; O'Connor, A. J.; Stevens, G. W.; Cooper-White, J. J. *Biomacromolecules* **2004**, *5*, 463-473.
- (31) Cai, L.; Wang, S. *Polymer* **2010**, *51*, 164-177.



- (32) Matsuda, T.; Mizutani, M. *J. Biomed. Mater. Res.* **2002**, *62*, 395-403.
- (33) Seck, T. M.; Melchels, F. P. W.; Feijen, J.; Grijpma, D. W. *Journal of Controlled Release* **2010**, *148*, 34-41.
- (34) Childers, E. P.; Wang, M. O.; Becker, M. L.; Fisher, J. P.; Dean, D. *MRS Bulletin* **2015**, *40*, 119-126.
- (35) Lee, J. W.; Kang, K. S.; Lee, S. H.; Kim, J.-Y.; Lee, B.-K.; Cho, D.-W. *Biomaterials* **2011**, *32*, 744-752.
- (36) Cai, L.; Wang, K.; Wang, S. *Biomaterials* **2010**, *31*, 4457-4466.
- (37) Sharifi, S.; Blanquer, S. B. G.; van Kooten, T. G.; Grijpma, D. W. *Acta Biomaterialia* **2012**, *8*, 4233-4243.
- (38) Schüller-Ravoo, S.; Teixeira, S. M.; Feijen, J.; Grijpma, D. W.; Poot, A. A. *Macromolecular Bioscience* **2013**, *13*, 1711-1719.
- (39) Dargaville, B. L.; Vaquette, C.; Peng, H.; Rasoul, F.; Chau, Y. Q.; Cooper-White, J. J.; Campbell, J. H.; Whittaker, A. K. *Biomacromolecules* **2011**, *12*, 3856-3869.
- (40) Kennedy, G. L. *Drug and Chemical Toxicology* **2002**, *25*, 191-202.
- (41) Mingrone, G.; Castagneto, M. *Nutrition Reviews* **2006**, *64*, 449-456.
- (42) Borron, S. W.; Baud, F. J.; Garnier, R. *Veterinary and Human Toxicology* **1997**, *39*, 26-28.
- (43) Mormann, W.; Michel, U. *Carbohydrate Polymers* **2002**, *50*, 201-208.
- (44) Luan, B.; Liu, X. Y.; Nagata, J.; Cheong, W.-J. *Surface and Coatings Technology* **2005**, *192*, 323-330.
- (45) Lambert, P. M., Virginia Tech, 2014.
- (46) Cho, J.-H.; James, T.; Gracias, D. H. *Advanced Materials* **2010**, *22*, 2320-2324.
- (47) Leong, T. G.; Randall, C. L.; Benson, B. R.; Bassik, N.; Stern, G. M.; Gracias, D. H. *Proceedings of the National Academy of Sciences* **2009**, *106*, 703-708.
- (48) Bassik, N.; Stern, G. M.; Gracias, D. H. *Applied Physics Letters* **2009**, *95*, 091901.
- (49) Bassik, N.; Stern, G. M.; Jamal, M.; Gracias, D. H. *Advanced Materials* **2008**, *20*, 4760-4764.
- (50) Novosel, E. C.; Kleinhans, C.; Kluger, P. J. *Advanced Drug Delivery Reviews* **2011**, *63*, 300-311.
- (51) Xu, C.; Yang, F.; Wang, S.; Ramakrishna, S. *Journal of Biomedical Materials Research Part A* **2004**, *71A*, 154-161.
- (52) Liao, Y.-C.; Ma, Y.-T.; Huang, C.-H.; Yu, J.; Hsiao, H.-M. *ACS Applied Materials & Interfaces* **2012**, *4*, 3335-3339.
- (53) Odian, G. *Principles of Polymerization*; 4th ed.; Wiley, 2004.

## 9.6 Supplementary Material

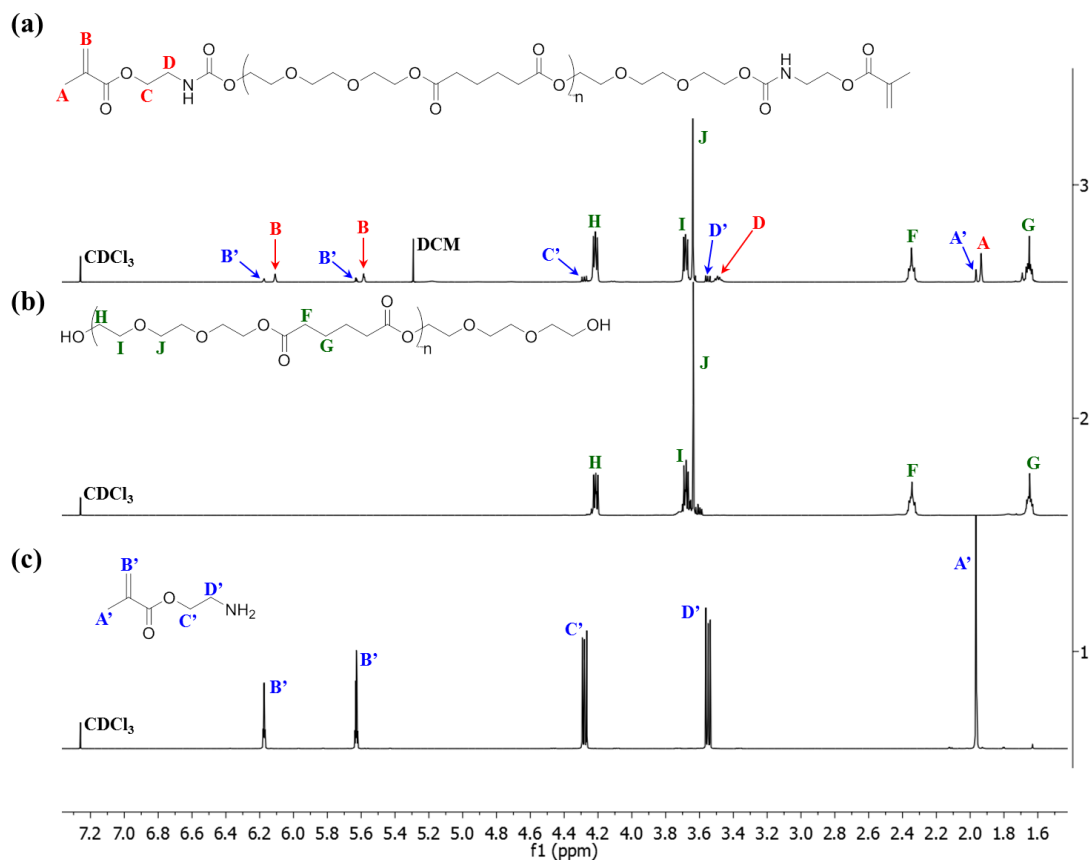


**Figure 9.3.**  $^1\text{H}$  NMR structure confirmation for (a) poly(tri(ethylene glycol) adipate) (PTEGA) dimethacrylate and (b) PTEGA diol, overlaid with (c) decarboxylated functionalization reactant 2-aminoethyl methacrylate.

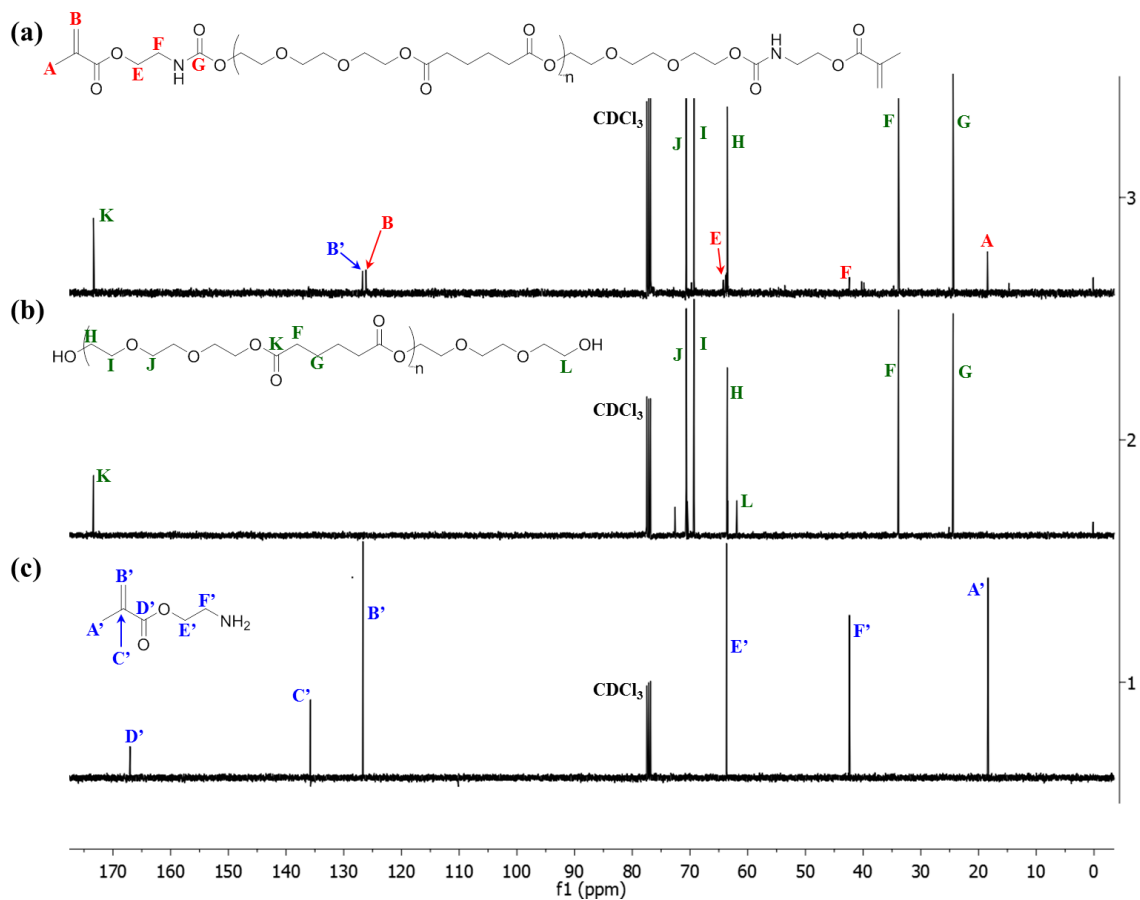
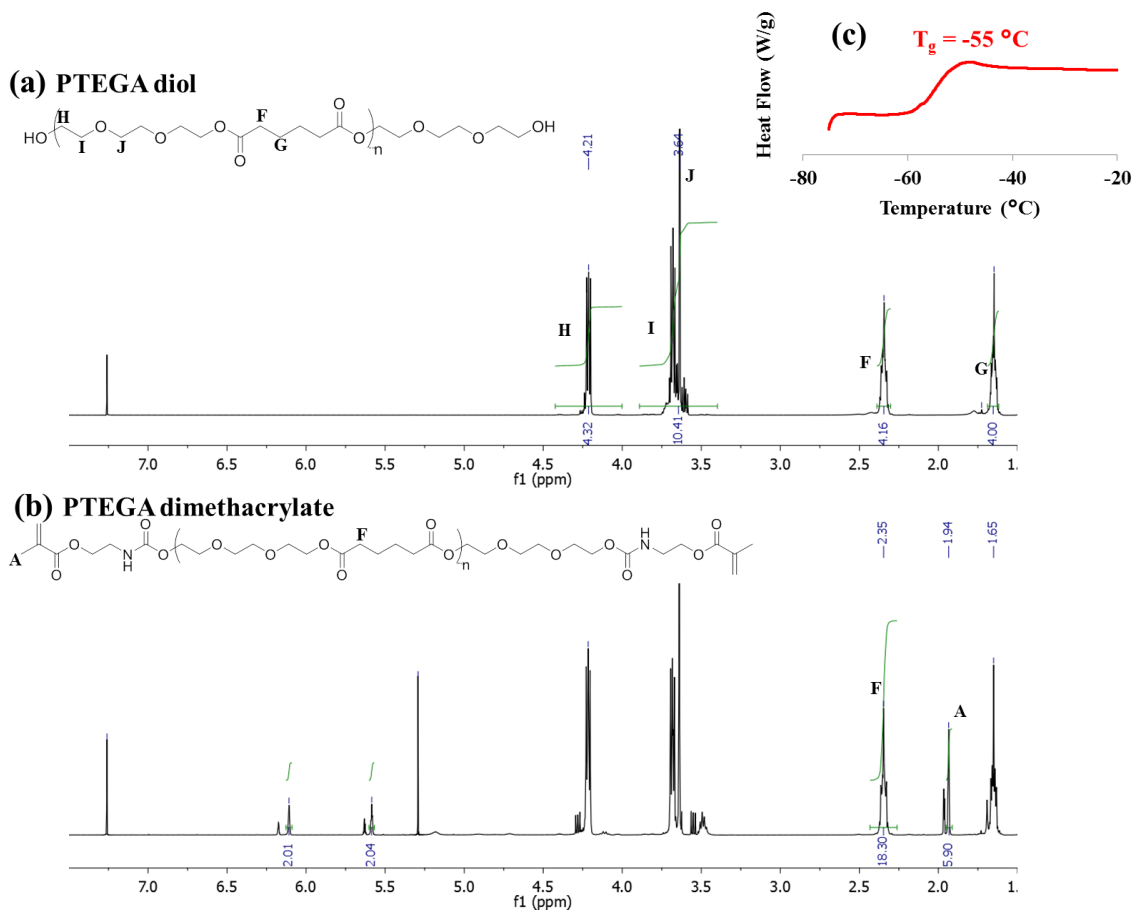


**Figure 9.4.**  $^{13}\text{C}$  NMR structure confirmation for (a) poly(tri(ethylene glycol) adipate) (PTEGA) dimethacrylate and (b) PTEGA diol, overlaid with (c) decarboxylated functionalization reactant 2-aminoethyl methacrylate.



<sup>1</sup>H NMR endgroup analysis provided the number average molecular weight ( $M_n$ ) of the poly(tri(ethylene glycol) adipate) (PTEGA) diol precursor. These calculations are as follows:

$$\frac{\int H + \int I + \int J}{\int G} = \frac{12n + 12}{4n} = \frac{4.32 + 10.41}{4.00} \Rightarrow n = 4.40$$

Repeat unit = 260.3 g/mol

Endgroups = 150.2 g/mol

**PTEGA diol  $M_n = 1,296$  g/mol**

Based on the above PTEGA diol integrations for **F** and degree of polymerization  $n$ , the PTEGA dimethacrylate **F** peak was set to  $F = 4.16 * 4.40 = 18.30$ . Then, % methacrylate termination was based on the actual **A** integration value over the theoretical 6.00 integration value. Accounting for the methacrylate endgroups afforded the PTEGA dimethacrylate  $M_n$ .

$$\% \text{ methacrylate termination} = \frac{5.90}{6.00} = 98 \%$$

$M_n$  of the PTEGA dimethacrylate can be estimated by adding the theoretical molecular weight of the 2-isocyanatoethyl methacrylate to the PTEGA diol molecular weight and accounting for the % methacrylate termination, as was calculated above.

$$\text{PTEGA dimethacrylate } M_n = 1,296 + (155.15 * 2) * 0.98$$

**PTEGA dimethacrylate  $M_n = 1,600$  g/mol**

**LSMeans Differences Tukey HSD**

$\alpha = 0.050$   $Q = 2.42949$

		LSMean[j]		
Mean[i]-Mean[j]		non-tissue culture treated polystyrene	polyester photocured film	tissue culture treated polystyrene
Std Err Dif				
Lower CL Dif				
Upper CL Dif				
non-tissue culture treated polystyrene	LSMean[i]	0	-474664	-4.8e+6
		0	143933	130192
		0	-824348	-5.1e+6
		0	-124980	-4.4e+6
polyester photocured film	LSMean[i]	474664	0	-4.3e+6
		143933	0	162378
		124980	0	-4.7e+6
		824348	0	-3.9e+6
tissue culture treated polystyrene	LSMean[i]	4754244	4279580	0
		130192	162378	0
		4437943	3885083	0
		5070545	4674076	0

Level		Least Sq Mean
tissue culture treated polystyrene	A	5680029.8
polyester photocured film	B	1400450.1
non-tissue culture treated polystyrene	C	925786.0

Levels not connected by same letter are significantly different.

**Figure 9.6.** Tukey’s Honest Significant Difference (HSD) test for statistical significance. As shown, the three populations are not connected by the same letter and are therefore significantly different at  $p < 0.050$ .

## Chapter 10: Melt Stable Polyamides for Polymer Powder Bed Fusion Applications

*Justin M. Surrine,<sup>†</sup> Camden A. Chatham,<sup>‡</sup> Christopher B. Williams,<sup>‡</sup> Timothy E. Long<sup>†\*</sup>*

<sup>†</sup>Department of Chemistry, <sup>‡</sup>Department of Mechanical Engineering  
Macromolecules Innovation Institute (MII), Virginia Tech, Blacksburg, VA 24061

### 10.1 Abstract

Polymer powder bed fusion (PBF), or selective laser sintering (SLS), remains a highly versatile additive manufacturing (AM) process that enjoys applications ranging from rapid prototyping to small-scale manufacturing. Polyamides represent the vast majority of commercially-available PBF powders due to their high chemical resistance, toughness, and discrete transition temperatures, with polyamide 12 (PA12) enjoying the greatest overall use. Nuclear magnetic resonance spectroscopy, thermal, and rheological analysis of two commercially-available PA12 powders provided evidence of endgroup chemical structure, which held broad implications for differences in observed melt stability. An anionic dispersion polymerization based in the patent literature yielded highly spherical, melt-stable, PA12 microparticles that precipitated directly from solution, eliminating the need for expensive and time-consuming post-processing steps. A probe of polymerization conditions identified steric stabilizer concentration as the key parameter affecting mean particle diameter, particle morphology, and melt viscosity. Finally, preliminary fusion of single-layered PA12 structures provided insight into important powder characteristics for successful PBF.

### 10.2 Introduction

Powder bed fusion (PBF), otherwise known as selective laser sintering (SLS) and a subset of additive manufacturing (AM), enables the production of highly intricate and

individually customizable objects without separate tooling steps, through direct laser melting, coalescence, and solidification of polymer powders in a layer-by-layer fashion.<sup>1-3</sup> PBF machines deposit uniform layers (e.g. 100-150  $\mu\text{m}$ ) of polymer powder atop a build piston *via* a counter-rotating roller, which is held at an elevated temperature just below the highest observed transition temperature under constant nitrogen ( $\text{N}_2$ ) purge. Subsequently, a scanning laser provides the final amount of thermal energy required to surpass the flow temperature – either the highest glass transition ( $T_g$ ) or crystalline melting point ( $T_m$ ).<sup>1</sup> The build piston then moves down by one layer thickness and the process repeats until completion of the build. Polyamide (nylon) 11 and 12 make up the vast majority of polymer powder for PBF processes,<sup>1-8</sup> while the remaining polymers include commercially available thermoplastic polyurethane (TPU) powders,<sup>9,10</sup> polystyrene,<sup>11-13</sup> polyetheretherketone (PEEK),<sup>14,15</sup> polycaprolactone (PCL),<sup>16,17</sup> and polycarbonate.<sup>18,19</sup> Though an expansion to include non-polyamide powders remains highly desirable, a critical need for fundamental understanding of polyamide powder behavior during the fusion process still remains. The literature provides examples of this characterization via solution viscosity,<sup>20</sup> melt rheology,<sup>20-22</sup> melt flow rate (MFR),<sup>23-25</sup> and size exclusion chromatography.<sup>21,24</sup>

Typical industrial-scale polyamide 12 synthesis involves hydrolytic polymerization of either cyclic laurolactam or the corresponding, linear  $\omega$ -amino acid at relatively high temperatures (e.g. 300  $^\circ\text{C}$ ).<sup>26</sup> Despite the inexpensive nature of this process, PA12 produced in this manner still requires an additional, expensive precipitation or milling/grinding processing step for powder formation, which typically produces non-spherical powders that remain less-than-desirable for fusion processes.<sup>1,27,28</sup> Mechanistic



insight into the hydrolytic polymerization reveals free amine endgroups, which create potential for post-condensation behavior in the melt, e.g. during printing.<sup>29</sup> Two commercially available PA12 powders, 3D Systems (3DS) Duraform® PA and EOS PA2200, are based on Evonik Vestosint® powder.<sup>30</sup> Duraform® PA achieves powder form via precipitation, yielding less-than-desirable “potato”-shaped particles.<sup>30</sup> Duraform® PA is also thought to possess free amine and carboxylic acid chain ends, which is evidenced by the post-condensation behavior typically observed for this commercially-available powder.<sup>30</sup> Advantageously, this post-condensation behavior observed with Duraform® PA actually leads to improved mechanical properties, but also drastically reduces powder recyclability.<sup>30</sup>

The PA12 PBF literature also examines Arkema Orgasol® IS, an alternative powder synthesized via anionic dispersion polymerization.<sup>1,5,30-32</sup> Unlike Duraform® PA, Orgasol® demonstrates limited post-condensation behavior, as evidenced by literature reports of melt stability and consistent crystallization temperature ( $T_c$ ) with heat/cool cycling in differential scanning calorimetry (DSC).<sup>5,30</sup> This anionic dispersion polymerization process is well-known for producing relatively unimodal polystyrene microspheres with narrow particle size distribution through use of a steric stabilizer,<sup>33-35</sup> and ring-opening polymerization of lactams for polyamide (PA) powders that serve in the sorption of reactive dyes from aqueous solutions.<sup>36-39</sup> This technique involves lactam polymerization in a medium that dissolves the lactam but not the PA, resulting in polymer precipitation throughout the polymerization.<sup>33</sup> This creates great advantage for PBF applications, as direct, spherical powder production occurs without post-processing. Unfortunately, literature reports of anionic dispersion polymerization of laurolactam

remain sparse. One report provides only a single sample of PA12 synthesized in this manner.<sup>37</sup> Other reports only discuss PA6 polymerization under different conditions, e.g. in the absence of steric stabilizer,<sup>36,38-40</sup> for nanocomposite formation,<sup>41</sup> or anionic polymerizations occurring in the melt.<sup>42,43</sup> Still other reports discuss PA12 microsphere preparation from previously synthesized PA12 and require a dedicated sample preparation step to convert bulk PA12 into the desired powder.<sup>44</sup> All other reports reside in the patent literature, preventing a fundamental understanding of this PA12 anionic dispersion polymerization process.<sup>32,45</sup>

In this work, an in-depth study of two commercially-available PA12 PBF powders, Duraform® PA and Orgasol® IS, demonstrated the presence of primary amine and carboxylic acid chain ends in Duraform and the lack of these respective functional groups in commercial Orgasol PA12 powder. A review of relevant academic and patent literature informs the synthesis and characterization of melt-stable PA12 microparticles in a manner similar to the Orgasol product, which directly precipitate from solution during the polymerization process, eliminating the need for post-processing steps traditionally required to transform bulk PA12 into powdered PA12. Finally, preliminary PBF of single-layer structures provides evidence of the importance of particle size and morphology.

## **10.3 Materials & Methods**

### **10.3.1 Materials**

12-Aminododecanolactam (laurolactam, 98 %), N,N'-Ethylenebis(stearamide) (EBS, beads, <840 µm). decane (anhydrous, ≥ 99 %), sodium hydride (NaH, 60 % dispersion in mineral oil), octadecyl isocyanate (98 %), cyclohexyl isocyanate (98 %), nylon 12 (pellets, 5 mm), trifluoroacetic anhydride (TFAA, ReagentPlus®, ≥99%), and silica gel (for column chromatography, 60) were purchased from Sigma Aldrich and used

as received unless otherwise noted. Chloroform, methanol, and isopropyl alcohol (IPA) were purchased from Fisher Scientific (all HPLC grade) and used as received. Chloroform-d (CDCl<sub>3</sub>, 99.8 %) was purchased from Cambridge Isotope Laboratories, Inc. and used as received. 3DS Duraform® Polyamide (PA) powder and Arkema Orgasol® Invent Smooth (IS) PBF powders were purchased from 3D Systems or Advanced Laser Materials (PA250), respectively, and used as received. Heating tape 5/8' x 7' (#80061-092), 12" needles (#89234-230, deflected needle 16G 12IN), grade 454 filter paper, and various sizes of glass syringes with metal "Luer lok" tip (#80089-568) were purchased from VWR and used as received. Lauro lactam, silica and EBS were dried at 60 °C for 18 h *in vacuo* before use.

### **10.3.2 Trifluoroacetylation of PA12 samples (TFA-PA12)**

PA12 (~0.18 g, either Duraform® PA, Orgasol® IS, or Sigma Aldrich) powder or pellets and magnetic stir bar were added to a 1-necked, 50 mL round-bottomed flask. A dry, house nitrogen inlet and needle outlet was attached to the flask after covering with a septum and subsequently purged for 10 min. Then, chloroform (~5 mL) and ~ 0.3 mL TFAA were added via syringe into the purged flask. The reactants were allowed to stir at 22 °C under ambient pressure until complete dissolution occurred (typically < 18 h for both powdered and bulk pellets). Upon septum removal, a distillation tube was attached to the 1-necked, 50 mL flask. A 2-necked, 50 mL round-bottomed flask equipped with 24/40 inlet adapter was attached to the receiving end of the distillation tube. After immersing the 1-necked flask in an oil bath at 40 °C and the 2-necked flask into a dry ice / IPA bath (-78 °C), the chloroform, excess TFAA, and resulting trifluoroacetic acid were slowly distilled off the 1-necked flask under reduced pressure, resulting in solidification of the

trifluoroacetylated PA12 (TFA-PA12) product. After removal of the distillation apparatus and subsequent nitrogen purge (~5 min) to prevent hydrolysis back to the amide, the product was stored in a vacuum desiccator and analyzed within 24 h.

### 10.3.3 Rheology with dodecanediamine

1.91 g PA12 powder (either Duraform® PA or Orgasol® IS) and 0.0195 g 1,12-dodecanediamine were added to a 6-dram vial and subsequently vortexed to ensure proper mixing, resulting in a homogeneous mixture of PA12 powder with 1 wt % dodecanediamine. These samples were stored in a vacuum desiccator before analysis, which occurred in an identical manner to the melt stability studies detailed in the analytical methods.

### 10.3.4 Synthesis of PA12 microparticles

Dry laurolactam (45.00 g, 0.2281 mol, 1 mol eq.), EBS (0.7208 g, 12.15 mmol, 5.32 mmol eq.), and if used, silica (0.0360 g) were added to a three-necked, 500 mL, round-bottomed flask equipped with copper-wire-tied septum for nitrogen inlet, mechanical stirring apparatus, and distillation tube. The distillation tube was attached to a separate, two-necked, 250 mL round-bottomed flask, as depicted in **Figure 10.7A**. The mechanical stirring apparatus consisted of an overhead mechanical stirrer attached to 10 mm diameter glass stir rod, PTFE stir blade, and 24/40 glass stir rod adapter. The two-necked, 250 mL flask also contained an inlet adapter attached to a bubbler. After purging the assembled reactor with dry nitrogen for 20 min, the 250 mL flask was placed in a dry ice / IPA bath (-78 °C). After cannulating the desired amount of dry decane (~200 mL) into the 500 mL flask, a slow nitrogen purge continued (~1-2 bubbles/s), and a 150 °C silicone oil bath was raised to fully immerse the 500 mL round bottom flask, while the mechanical stirrer

provided slight agitation to facilitate dissolution (~30 rpm). Note that only silicone oil can be employed in this oil bath, due to the low smoke point of mineral oil (~ 100 °C).

After complete dissolution, as depicted in **Figure 10.7B**, the bubbler hose was removed from the 250 mL flask and a vacuum hose from a Schlenk line was subsequently attached. Then, the pressure was carefully reduced to prevent bumping, allowing ~50 mL solvent to distill into the receiving flask, removing residual water from the reaction. After restoring ambient pressure with dry nitrogen from the Schlenk line, the vacuum hose was replaced with the bubbler hose, restoring the slow nitrogen purge. Note that this distillation step must occur at 150 °C; if done at the 120 °C working temperature, the monomer may precipitate out of solution during the reduced pressure step. After distillation, the oil bath temperature was subsequently lowered to the 120 °C working temperature. Upon reaching 120 °C, the sodium hydride dispersion in mineral oil was weighed out (0.0721 g dispersion, 0.0432 g alone, 1.80 mmol, 7.90 mmol eq.) After raising the nitrogen purge rate to a rapid ~20-30 bubbles/second, the distillation tube was temporarily removed from the 500 mL flask, the NaH quickly added, the distillation tube restored, and the purge lowered back to the regular, slow rate, in an attempt to prevent moisture from entering the reaction. The mechanical stirring was then increased to the desired rpm, employing a Monarch Instrument Pocket Laser Tach 200 (PLT200) to measure stir shaft rpm. After H<sub>2</sub> bubbling concluded (~ 20 min), the reaction remained optically clear but slightly more yellow, as depicted in **Figure 10.7C**. While waiting for H<sub>2</sub> production to cease, stearyl isocyanate (1.68 mL, 1.42 g, 4.81 mmol, 21.1 mmol eq.) was collected with a 5 mL glass syringe and equipped 12-in needle. After insertion of the syringe into the syringe pump, set to dispense the entire contents over the course of 2.5 h, the needle tip was carefully inserted into the

septum so as not to prematurely dispense the stearyl isocyanate. After H<sub>2</sub> bubbling concluded, the syringe pump was switched on, resulting in a gradual clouding of the reaction upon stearyl isocyanate addition, caused by PA12 particles slowly crashing out of solution. **Figure 10.7D** and **Figure 10.7E** depict the reaction partway and all the way through the 3 h stearyl isocyanate addition process, respectively. After 3 h from the initial time point of isocyanate addition, the oil bath was lowered, mechanical stirring halted, and the reaction was allowed to cool to room temperature.

After removal of the distillation and mechanical stirring apparatuses, the reaction was filtered through a Buchner funnel with filter paper and rinsed with methanol, and the resulting powder cake was retained. The powder cake was placed in a 1000 mL beaker containing a magnetic stir bar, which was subsequently filled with methanol. The powder/methanol solution was stirred for 18 h, which was subsequently filtered a second time through a Buchner funnel with filter paper and rinsed with methanol. Finally, the resulting powder was dried for 18 h at 80 °C under reduced pressure and stored in a vacuum desiccator before analysis.

### **10.3.5 Analytical Methods**

All PA12 samples were dried for 18 h at 80 °C under reduced pressure before analysis. All <sup>1</sup>H NMR spectroscopy was performed on an Agilent U4-DD2 500 MHz NMR spectrometer equipped with a 96 sample robot, at 22 °C. A TA Instruments DHR-2 rheometer enabled melt stability studies with 25 mm aluminum, disposable parallel plate geometry and was operated at 1.25 % strain and 1 Hz under constant N<sub>2</sub> purge. After equilibrating the rheometer chamber at the desired temperature and zeroing the gap, the upper geometry was raised to enable sample preparation. PA12 powder was added to the

bottom parallel plate and allowed to melt with the oven doors closed (~1 min). Additional PA12 powder was added once or twice more after melting, with additional melt steps in between powder addition to prevent crystallization. The upper parallel plate was then set to pre-shear at a constant 0.2 rad/s while lowering to the geometry gap, enabling proper spreading of the polymer melt and exclusion of excess polymer. Finally, use of a razor blade ensured uniform sample edges before beginning temperature equilibration and starting measurements. Particle size analysis occurred with a Horiba LA-950 laser particle size analyzer with water as a dispersant and maximum settings for sonication and stirring. DSC was performed on a TA Instruments Q2000 DSC outfitted with refrigerated cooling system (RCS), and operated at constant heating/cooling rates of 10 °C/min and constant nitrogen purge for all samples. Sample preparation for scanning electron microscopy (SEM) include a sputter coating step. A Leica ACE 600 sputter coater provided 10 nm coatings of either iridium or a platinum/palladium mixture that prevented sample charging during SEM imaging. SEM occurred with a SEM with LEO (Zeiss) 1550 equipped with field-emission electron source, in-lens secondary electron (SE) detector, and Robinson-type back-scatter electron detector. All images were obtained with the in-lens SE detector at 5 keV.

#### **10.3.6 Powder Bed Fusion**

A DTM Sinterstation® 2500+ was used to create single layer structures for comparative fusion evaluation. Only single layer specimens were evaluated due to the large minimum material requirement for fabricating multi-layer structures in the Sinterstation®. Operational parameters of 32 W and 5 m/s laser setting at 120 °C chamber temperature were used for the fusion of a rectangle 3.5 in. x 4 in. The Sinterstation® operates in an

inert, nitrogen atmosphere. The powder was spread at the standard operating parameter of 7 in/s translational roller speed.

#### **10.4 Results & Discussion**

Multiple recent literature reports discuss two common, commercially-available PA12 powders for use in PBF applications.<sup>1,5,30</sup> **Figure 10.1A/E** depict SEM images of 3D Systems Duraform® PA and Arkema Orgasol® Invent Smooth (IS), respectively. The Orgasol product possesses a spherical particle shape, a highly desirable attribute for PBF powders, while the Duraform product retains an oblong, ellipsoid shape, referred to as ‘potato-shaped’ in other reports.<sup>1,5</sup> Both this Duraform product and one from EOS (PA 2200) are based on Evonik Vestosint® powder, and gain their spheroid morphology from a precipitation process.<sup>30</sup> Due to established similarities in particle morphology and thermal properties to Duraform PA,<sup>30</sup> the EOS PA2200 product will not be discussed further. **Figure 10.1B/F** displays particle size distributions for Duraform and Orgasol respectively, depicting a bimodal size distribution for the Duraform product with maxima at 10  $\mu\text{m}$  and 51  $\mu\text{m}$ , again consistent with literature reports,<sup>5,46</sup> which provides advantages in the fusion process whereby smaller particles fill voids between larger particles.



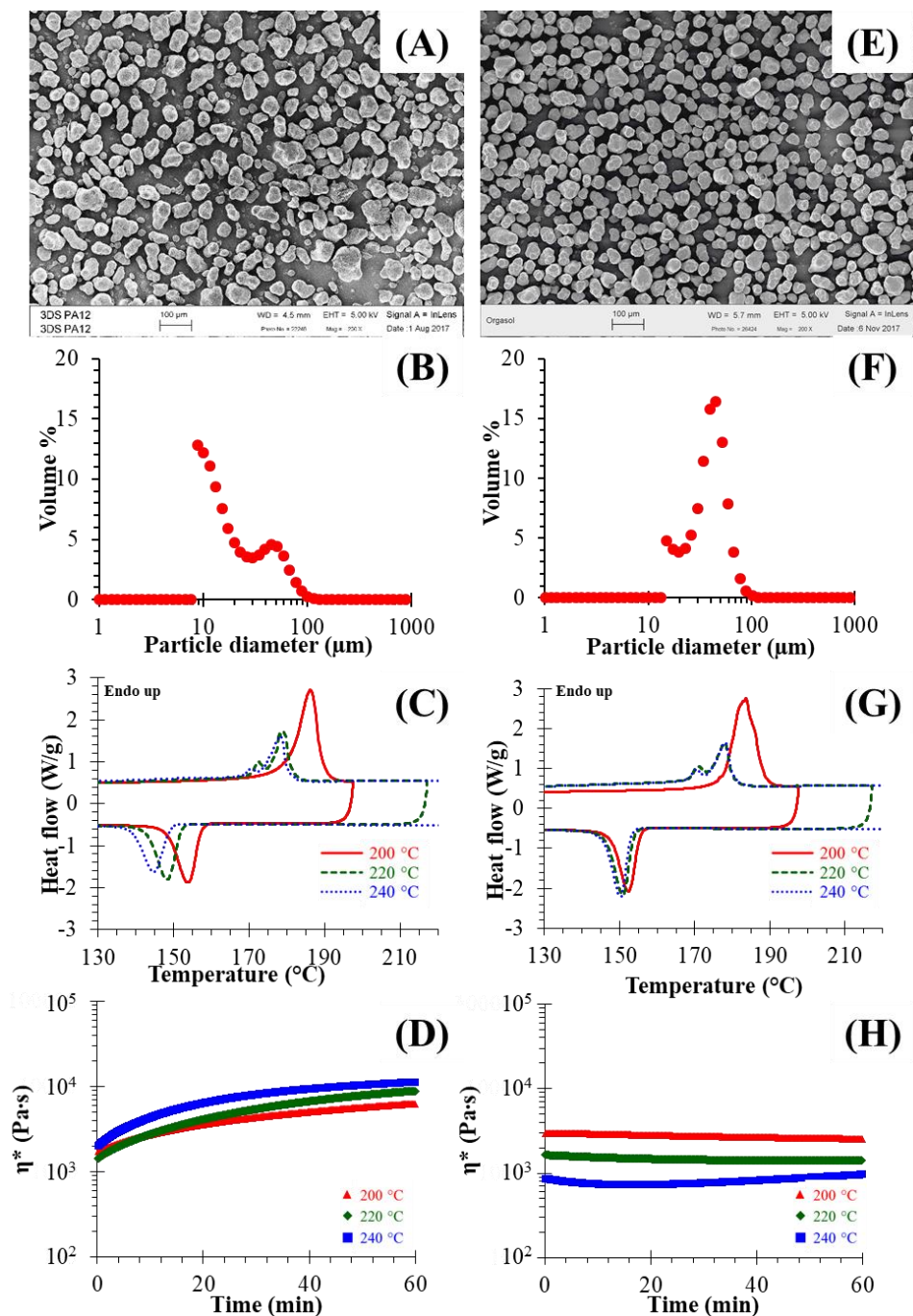
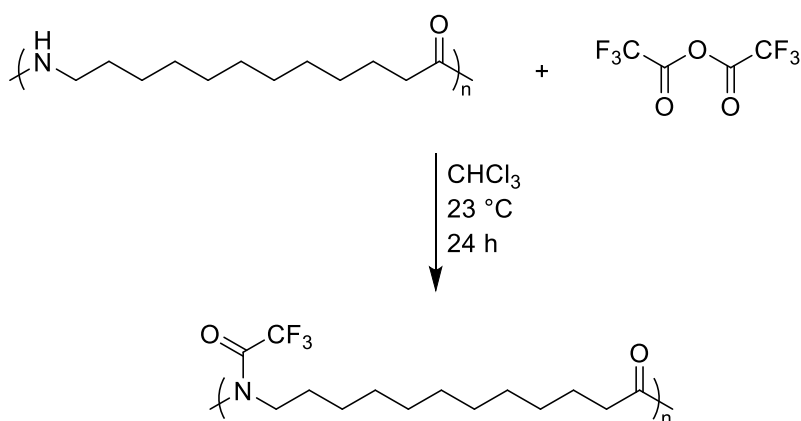


**Figure 10.1.** (A/E) Scanning electron microscope (SEM) micrographs, (B/F) particle size analysis, (C/G) differential scanning calorimetry heat/cool cycles with different maximum heating temperatures, and (D/H) melt rheology stability studies at various temperatures for (A-D) 3DS Duraform® PA and (E-H) Arkema Orgasol® IS commercial products.

In contrast, Orgasol particle size distribution remain much more uniform, with a mean diameter of 38  $\mu\text{m}$ , as depicted in **Table 10.1** and consistent with previously reported particle size analysis.<sup>5</sup> DSC under constant 10  $^{\circ}\text{C}/\text{min}$  heating/cooling with different

maximum heating temperatures, depicted in **Figure 10.1C/G**, indicates a change in crystallization temperature ( $T_c$ ) with increasing maximum temperature for Duraform, but not for Orgasol, suggesting changes polymer backbone chemical structure that influence crystallizability for the Duraform powder. Finally, melt stability studies shown in **Figure 10.1D/H** demonstrate remarkably consistent complex viscosity ( $\eta^*$ ) vs. time behavior, up to 60 min, for the Orgasol product, while Duraform undergoes an order-of-magnitude increase in melt viscosity during the same time period.<sup>5</sup> Though many literature reports corroborate these observations and hypothesize a difference in endgroup chemical structure between the two products, a definitive explanation for these thermal property differences has yet to be provided.



**Scheme 10.1.** Reaction of polyamide 12 (PA12) and trifluoroacetic anhydride in chloroform at 23 °C, yielding chloroform-soluble, trifluoroacetylated PA12.

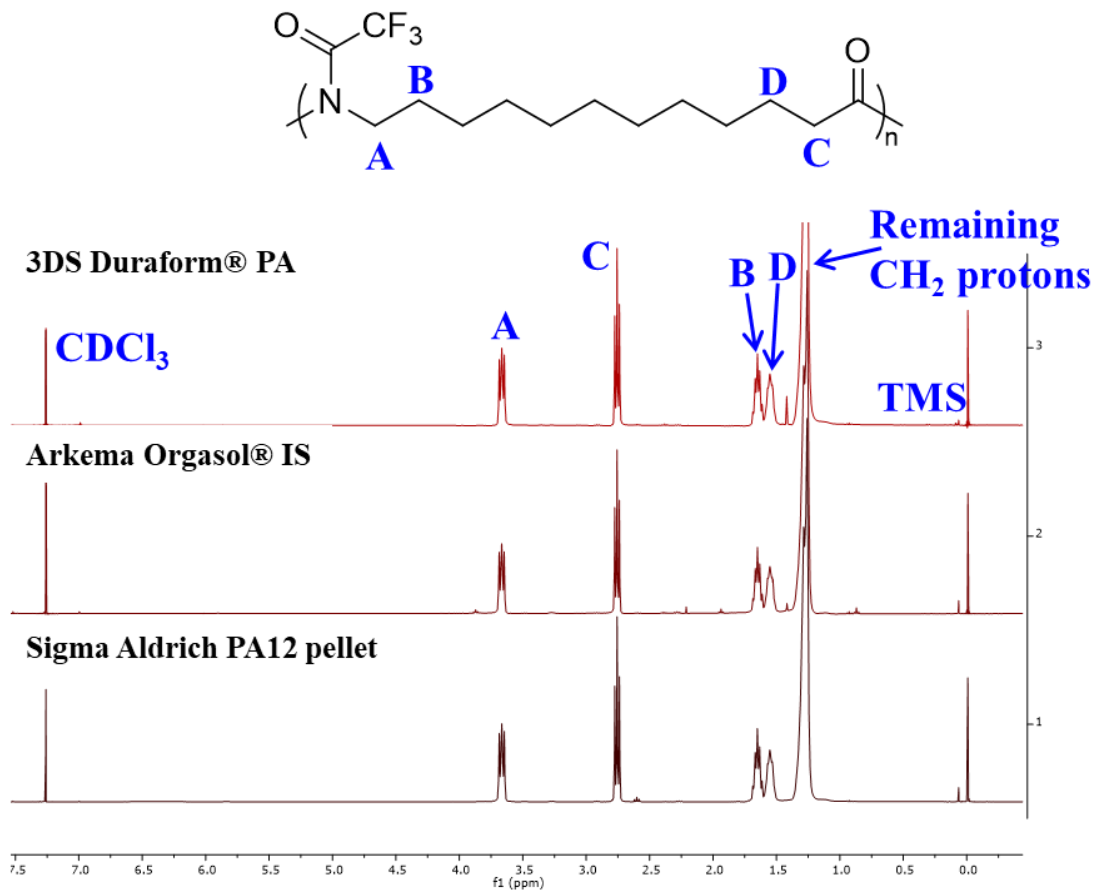
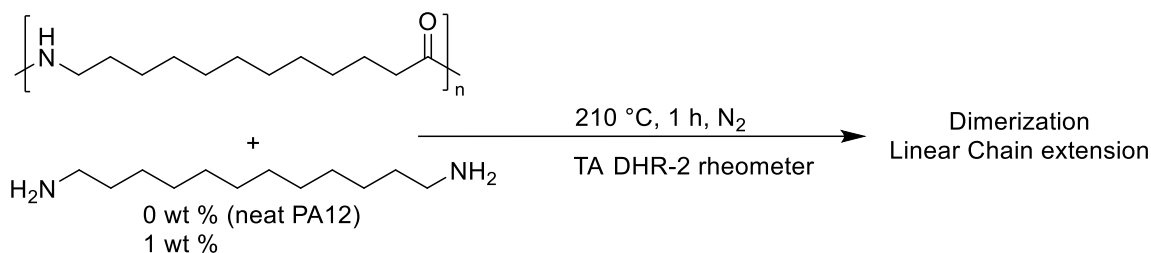


**Figure 10.2.** Proton nuclear magnetic resonance ( $^1\text{H}$  NMR) spectra of trifluoroacetylated Sigma Aldrich PA12 pellet, Arkema Orgasol® IS powder, and 3DS Duraform® PA powder in  $\text{CDCl}_3$

PA12 is known for its solvent resistance compared to other engineering thermoplastics, which precludes chemical analysis in common organic solvents, instead requiring more exotic solvents that include including hexafluoroisopropanol,<sup>47</sup> *m*-cresol,<sup>43</sup> and formic acid.<sup>44</sup> Fortunately, the literature provides a derivatization process that renders polyamides soluble in common organic solvents such as chloroform, as depicted in **Scheme 10.1**.<sup>48</sup> Products remain trifluoroacetylated as long as no moisture is present, which hydrolyzes the product back to the insoluble amide.<sup>48</sup> This derivatization process enabled proton nuclear magnetic resonance ( $^1\text{H}$  NMR) spectroscopy in deuterated chloroform ( $\text{CDCl}_3$ ), depicted in **Figure 10.2**, of the Duraform and Orgasol products, as well as a PA12

sample obtained from Sigma Aldrich, for comparative purposes. The Sigma Aldrich PA12, the Duraform, and Orgasol products possess very similar spectra, with distinct resonances for the four methylenes close to the trifluoroacetylated amide bond and one overlapping resonance for the remaining backbone methylenes.

To indirectly probe PA12 endgroup chemical structure, the Duraform and Orgasol powders were mixed with 1 wt % 1,12-dodecanediamine powder, thoroughly homogenized, and studied alongside the neat powders in a melt stability study depicted in **Scheme 10.2**. Here, if a PA12 chain possess a carboxylic acid endgroup, condensation could occur with dodecanediamine, leading to potential dimerization or linear chain extension. The Duraform product, hypothesized to have free carboxylic acid and amine chain ends,<sup>30</sup> likely acquires this endgroup functionality during the typical industrial-scale PA12 hydrolytic polymerization,<sup>26,29</sup> leading to the melt instability observed in this report and elsewhere.<sup>30</sup> Therefore, in the reaction depicted in **Scheme 10.2**, the hypothetical Duraform PA12 chain could undergo dimerization with dodecanediamine, or post-condensation with itself. Conversely, the amine functional group remains blocked with Orgasol (discussed further below), which likely also possesses a carboxylic acid on the other chain end. Therefore, a melt reaction of Orgasol in the presence of a diamine could only lead to dimerization.



**Scheme 10.2.** Reaction of homogenized PA12 and dodecanediamine powders on a parallel plate rheometer, in a probe of potential dimerization or chain extension

**Figure 10.3** depicts the results from this melt stability study, with complex viscosity ( $\eta^*$ ) for Orgasol remaining constant during the observed 60 min window. Intriguingly, Orgasol in the presence of 1 wt % dodecanediamine also possesses a slightly reduced, constant  $\eta^*$  and does not display any evidence of dimerization. Instead, dodecanediamine likely serves as plasticizer in this case.

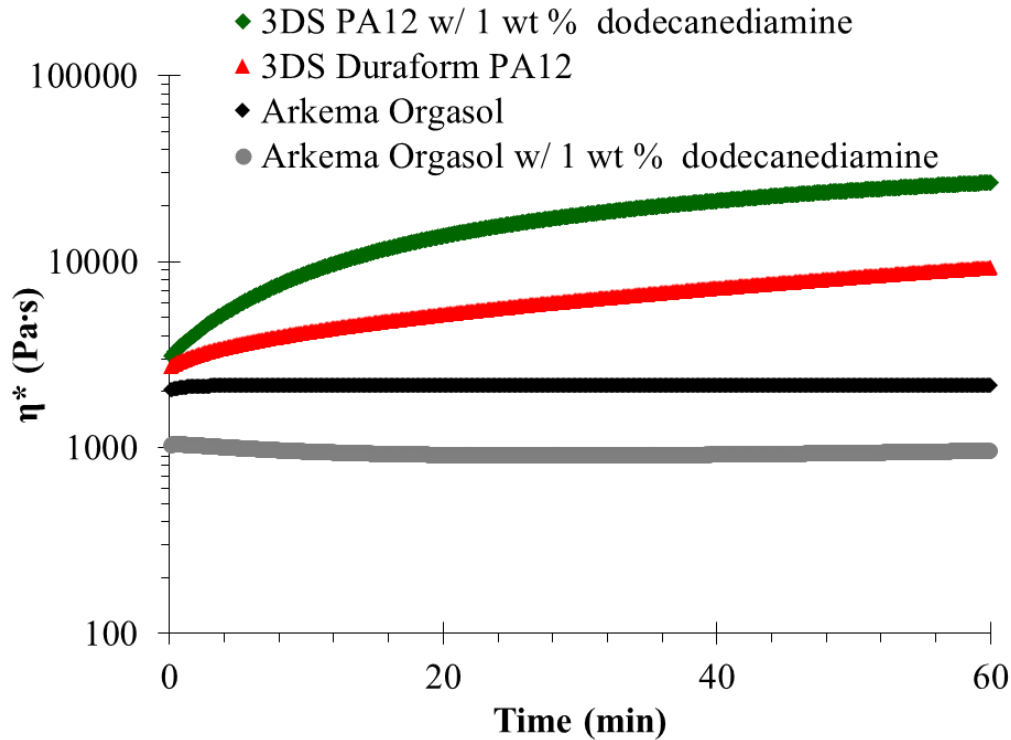


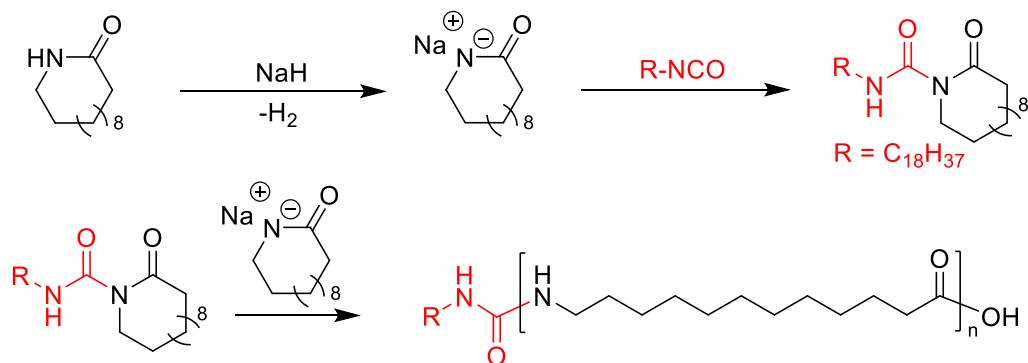
**Figure 10.3.** Melt rheology stability study of homogenized PA12 and dodecanediamine powders at 210 °C, 1.25 % strain, and 1 Hz.

Conversely, neat Duraform powder demonstrates striking melt instability, as previously discussed. Duraform in the presence of 1 wt % dodecanediamine possesses an even more marked melt instability, with almost an order-of-magnitude increase in  $\eta^*$  during the 60 min stability test. Though this experiment does not provide chemical information about the chain end chemical structure, it provides indirect evidence that supports the hypothesis of

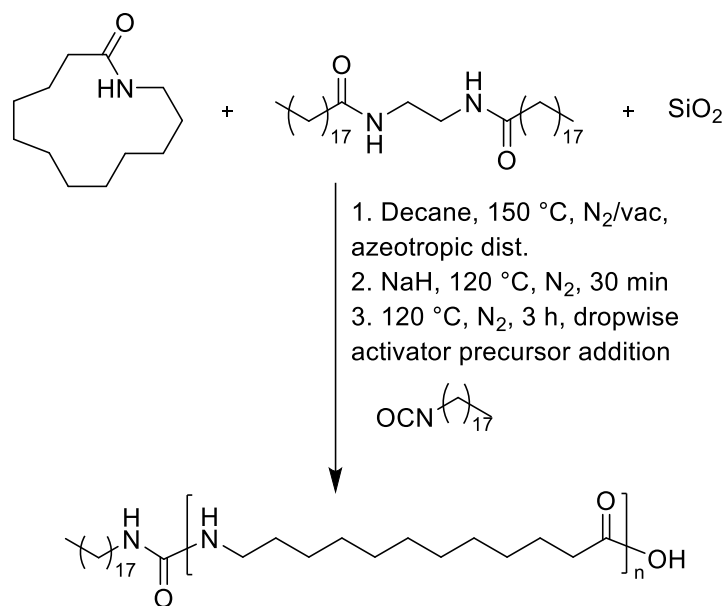
free amine / carboxylic acid and blocked amine endgroups for Duraform and Orgasol, respectively.

As detailed in the patent literature,<sup>32</sup> an anionic polymerization of lauro lactam in the presence of a steric stabilizer, catalyst, activator, and hydrocarbon solvent that solubilizes the lactam monomer but not the PA12, leads to production of melt-stable PA12 powder, directly from the polymerization process with only a post-processing washing step. Although this process remains publicly disclosed in the patent literature, in-depth process knowledge likely only exists with the patent holders. Therefore, an academic literature review and patent duplication process was undertaken to understand the polymerization mechanism and methods for tuning particle size and molecular weight. The literature provides a definitive lactam anionic polymerization mechanism, which proceeds via ring-opening of the lauro lactam monomer in the presence of an anion.<sup>29,49,50</sup> The literature states that upon anion introduction, e.g. sodium hydride (NaH) addition in this case, the rate constants of direct initiation and polymerization via the activated chain end mechanism are extremely low (e.g.  $\sim 10^{-7}$ ).<sup>50</sup> Instead, hydrogen transfer (disproportionation) occurs from the activated chain end to a monomer ( $k_H = 10^2 - 10^5$ ),<sup>50</sup> which polymerizes (initiates) only in the presence of an activator, a species that contains a sufficiently electrophilic carbonyl. Polymerization proceeds via the activated monomer mechanism ( $k_{p(AM)} = 68$ ).<sup>50</sup> As shown in **Scheme 10.3**, a lauro lactam monomer forms the sodium lactamate anion in the presence of NaH. Upon introduction of a monoisocyanate, which functions as an activator precursor, the lactamate anion reacts to form an N-carbamoyllactam, whereby the endocyclic carbonyl remains sufficiently electrophilic for attack from an anion. Activators or activator precursors need only possess a sufficiently

electrophilic carbonyl. While isocyanates are employed in this study, alternatives n-acyllactams, esters, and carbon dioxide.<sup>50</sup>



**Scheme 10.3.** Sodium lauroyl lactamate formation, activator formation with stearyl isocyanate activator precursor, and resulting anionic polymerization, yielding melt-stable, linear PA12 with endcapped terminal primary amine.



**Scheme 10.4.** Anionic dispersion polymerization of lauroyl lactam in the presence of ethylene bis(stearamide) steric stabilizer and silica, yielding melt-stable, linear PA12.

This anionic polymerization proceeds as a dispersion polymerization as depicted in **Scheme 10.4**, which remains distinct from the emulsion and suspension polymerization.<sup>34,51</sup> Initially homogeneous, dispersion polymerizations begin with the initiator and monomer soluble in the continuous phase and proceed in the presence of a

stabilizer and in the absence of a surfactant. Ethylene bis(stearamide) (EBS) stabilizer serves primarily to stabilize the growing PA12 chains in our case, complexing with the newly formed amides and presenting long, aliphatic hydrocarbon chains outward into the continuous phase. Here, decane serves as a good solvent for the lauro lactam, NaH, and stearyl isocyanate activator precursor, a selective solvent for EBS, a non-solvent for PA12, and a dispersant for silica. Polymerization occurs at 120 °C, which remains above the PA12 glass transition temperature ( $T_g$ , 48 °C) and below the crystalline melting point ( $T_m$ , 178 °C).<sup>6</sup> Therefore, upon activator formation, which represents the rate limiting step, the distinct stages of polymerization, phase separation from the continuous medium, primary particle coalescence into larger, fused agglomerate structures, and crystallization all occur rapidly, as detailed in previous literature that discusses anionic dispersion polymerization of PA6.<sup>36,37,39</sup> Though these reports discuss polymerization in the absence of steric stabilizer, they present great discussion of these discrete but potentially overlapping stages in polyamide microparticle production and will not be discussed further here.<sup>36,37,39</sup>

**Table 10.1** depicts all samples synthesized in this study, which investigates the effect of catalyst, activator precursor, and steric stabilizer concentrations, as well as stirring rate, on the resulting PA12 particle size and melt viscosity, the latter of which represents an indirect measure of molecular weight. First, this PA12 dispersion polymerization demonstrated excellent reproducibility as determined via three replicates with identical polymerization conditions (samples **#3-5**), resulting in similar isolated yields ( $95 \pm 2$  %), mean particle diameters ( $68 \pm 12$   $\mu\text{m}$ ), and  $\eta^*$  ( $341 \pm 35$  Pa·s), as depicted in **Figure 10.4A**. Adding stearyl isocyanate all at once (**#6**), instead of slow addition, resulted in reduced particle size (e.g. 32  $\mu\text{m}$  vs. 68  $\mu\text{m}$  mean diameter) and isolated yield (e.g. 73 % vs. ~ 95



%). Polymerization with 0.5x [NaH] as compared to samples #3-5 (**#8**) gave a reduction in isolated yield, e.g. 69 % vs. ~95 %, potentially due to the lack of available active polymerization centers, while polymerization with 3x [NaH] (**#7**) gave excellent isolated yield (94 %) but reduced particle size (e.g. 32  $\mu\text{m}$  vs. 68  $\mu\text{m}$  mean diameter). Polymerization with 0.5x [stearyl isocyanate] (**#10**) reduced isolated yield (e.g. 77 %), likely due to incomplete monomer consumption, while polymerization with 2x [stearyl isocyanate] (**#9**) gave excellent isolated yield (91 %). Activator formation likely remains highly dependent on activator precursor chemical structure, as polymerization with cyclohexyl isocyanate (**#16**) gave very low isolated yield (19 %) and  $\eta^*$  (9 Pa·s). Increased stirring rate (**#14**) (e.g. 300 rpm vs. 100 rpm) gave reduced mean particle diameter (e.g. 33 vs. 68  $\mu\text{m}$ ) but did not appreciably affect isolated yield or viscosity, likely hindering primary particle coalescence, providing smaller agglomerated structures (**Figure 10.4H**) than with 100 rpm stirring (**#3-5**, **Figure 10.4E**). Finally, polymerization in the absence of silica (**#15**) produced only a slight reduction in mean particle diameter (e.g. 57 vs. 68  $\mu\text{m}$ ), while isolated yield (97 %) and  $\eta^*$  (214 Pa·s) remained largely unaffected.

By and large, [EBS] demonstrated the largest effect on isolated yield, particle diameter, and  $\eta^*$ . As [EBS] increased from 0x to 2x (e.g. samples **#11** < **#12** < **#3-5** < **#13**), isolated yield remained relatively constant until 2x EBS, which gave only 20 % yield. Polymerization in the absence of EBS demonstrated an extreme lack of particle size control, yielding particle size that ranged from micron-sized particles (**Figure 10.4C**) all the way up to large chunks (**Figure 10.4B**) that precipitated directly out of solution.

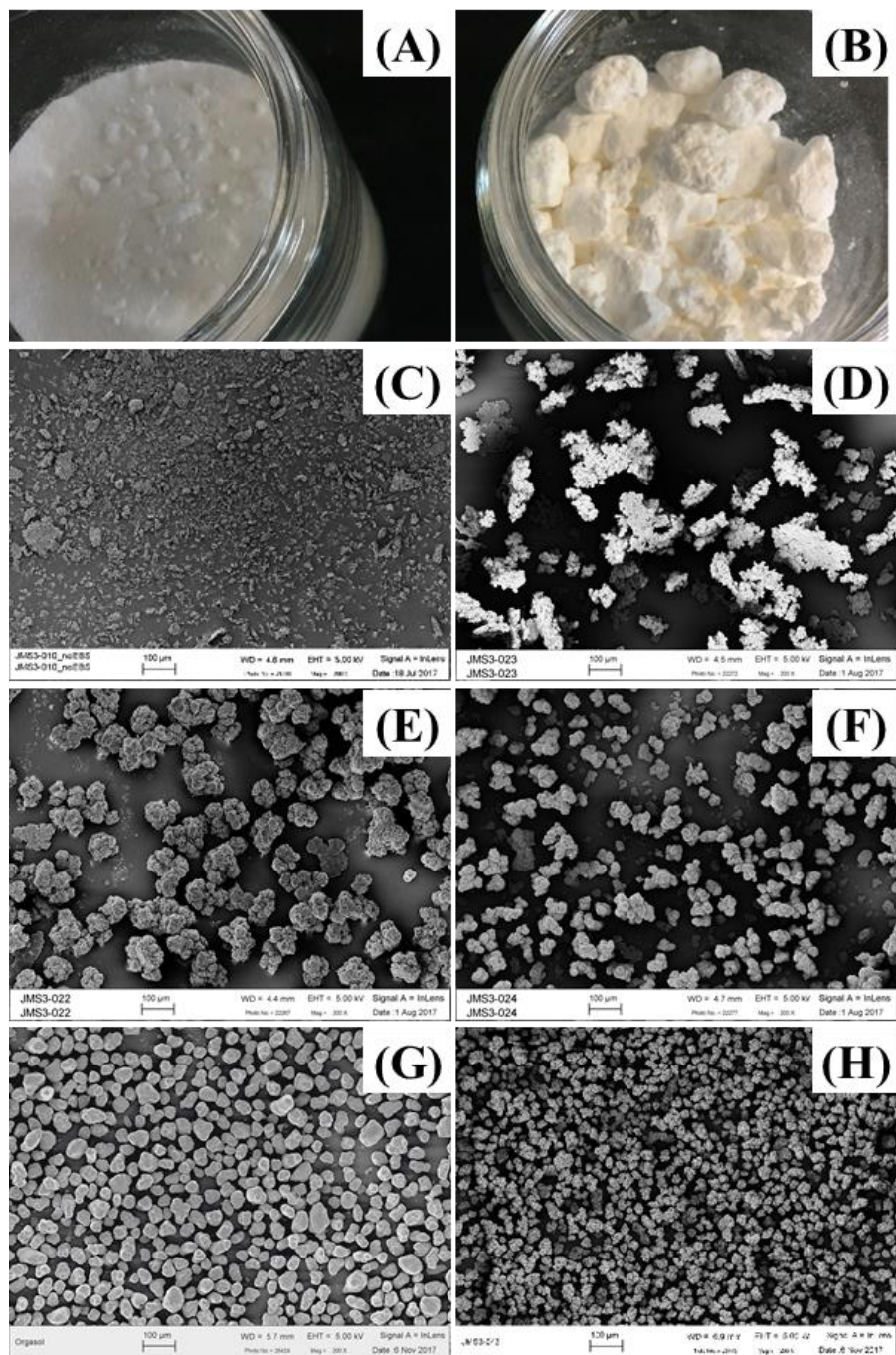


**Figure 10.4.** Images of products (A) PA12 microparticles v3 (sample #5) and (B) no EBS (#11). SEM images of (C) no EBS (#11), (D) 0.5x EBS (12), (E) PA12 microparticles v3 (#5, e.g. 1x EBS), (F) 2x EBS (13), (G) Arkema Orgasol® IS (#2), and (H) 300 rpm stir (#14).

Polymerization with 0.5x EBS (#12) gave much larger aggregated structures (**Figure 10.4D**), while polymerization with 2x EBS (#13) (**Figure 10.4F**) yielded reduced aggregate size as compared to 1x EBS (#3-5) (**Figure 10.4E**). As depicted in **Figure 10.5**, [EBS] also exhibited strong control of  $\eta^*$ , with a  $\eta^*$  range of more than four orders-of-magnitude, and systematically decreased with increasing [EBS]. Finally, Orgasol possesses a smoother outer particle surface (**Figure 10.4G**) as compared to all other samples, possibly due to a post-processing annealing step that reduces the presence of spherulitic lamellae on the outer agglomerate surface, which likely lends improvements in powder flow during the printing process.<sup>5</sup> Attempts to re-create this post-processing annealing step remained outside the scope of this work.

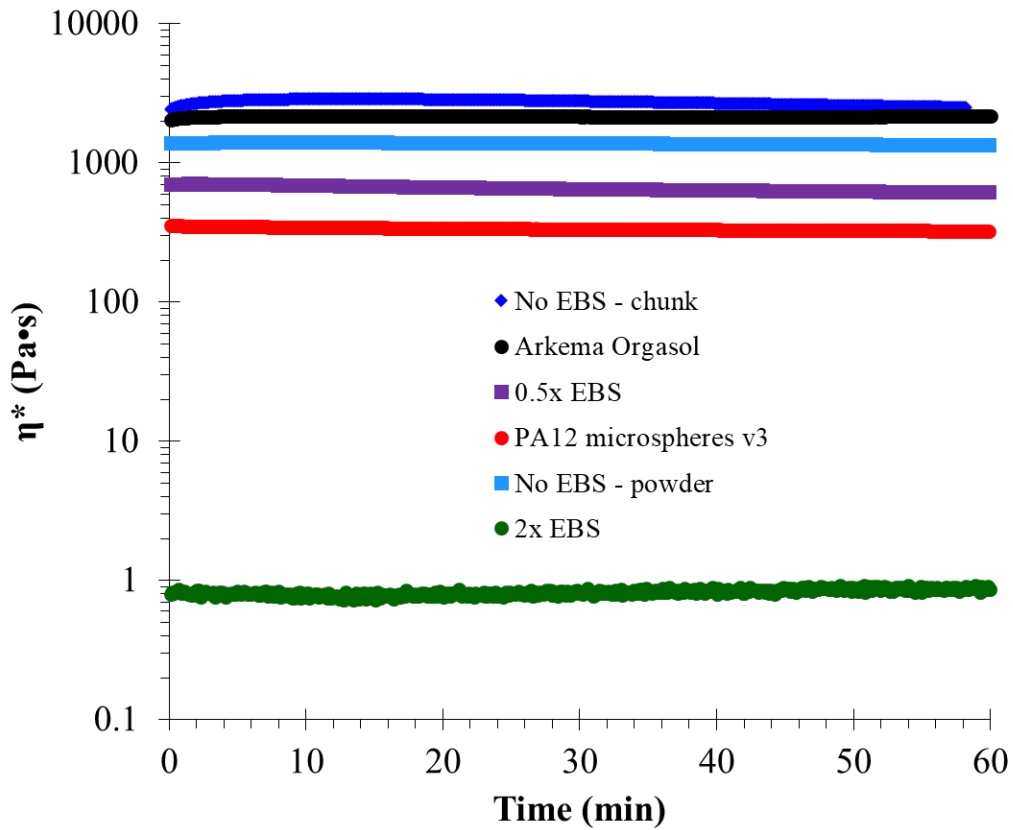


**Figure 10.5.** Melt stability study of Arkema Orgasol® IS and polymerization products synthesized with varying amounts of ethylene bis(stearamide) (EBS). Data gathered at 210 °C, 1.25 % strain, and 1 Hz.

**Table 10.1.** Summary of sample composition, polymerization conditions, isolated yields, particle size from laser diffraction, and complex viscosity at 210 °C from melt rheology stability studies.

Sample #	Sample ID	Sample Composition / Polymerization Conditions							Isolated Yield <sup>c</sup>	Particle Size (laser scattering)					Complex viscosity, 210 °C <sup>d</sup>
		Lactam	NaH	EBS.	Stearyl NCO	Stearyl NCO addition	<sup>a</sup> SiO <sub>2</sub>	<sup>b</sup> Mech. Stir		Median Diameter	Mean Diameter	St. Dev.	d <sub>10</sub>	d <sub>90</sub>	
		mol eq.	mmol eq.	mmol eq.	mmol eq.	-	wt %	rpm		%	µm	µm	µm	µm	
1	3DS Duraform® PA	-	-	-	-	-	-	-	-	13 ± 1	21 ± 1	16 ± 1	8 ± 1	46 ± 2	Not melt stable
2	Arkema Orgasol® IS	-	-	-	-	-	-	-	-	38 ± 1	38 ± 2	13 ± 1	21 ± 4	55 ± 1	1989
3	PA12 microparticles v1	1.0	7.9	5.3	21.1	dropwise	0.080	100	93	64	66	17	53	77	309
4	PA12 microparticles v2	1.0	7.9	5.3	21.1	dropwise	0.080	100	94	51	57	29	25	95	379
5	PA12 microparticles v3	1.0	7.9	5.3	21.1	dropwise	0.080	100	97	79	81	26	50	113	336
6	Stearyl NCO all at once	1.0	7.9	5.3	21.1	all at once	0.080	100	73	26	32	19	15	55	447
7	3x NaH	1.0	23.7	5.3	21.1	dropwise	0.080	100	94	29	32	14	17	49	212
8	1/2 NaH	1.0	4.0	5.3	21.1	dropwise	0.080	100	69	69	72	26	42	104	88
9	2x stearyl NCO	1.0	7.9	5.3	42.2	dropwise	0.080	100	91	55	58	25	28	91	203
10	0.5x stearyl NCO	1.0	7.9	5.3	10.5	dropwise	0.080	100	77	66	78	50	31	144	212
11	No EBS	1.0	7.9	0.0	21.1	dropwise	0.080	100	88	-	-	-	-	-	2741
12	0.5x EBS	1.0	7.9	2.7	21.1	dropwise	0.080	100	98	41	48	27	23	81	658
13	2x EBS	1.0	7.9	10.7	21.1	dropwise	0.080	100	20	28	35	20	17	63	0.83
14	300 rpm stir	1.0	7.9	5.3	21.1	dropwise	0.000	300	92	31	33	10	21	46	281
15	No silica	1.0	7.9	5.3	21.1	dropwise	0.000	100	97	51	57	28	28	94	214
16	Cyclohexyl isocyanate	1.0	7.9	5.3	21.1	dropwise	0.080	100	19	39	42	19	19	67	9

<sup>a</sup> wt % based on lactam weight. <sup>b</sup> Mechanical stirring rpm estimated from infrared sensor due to lack of rpm numerical output on mechanical stirrer. <sup>c</sup> Calculated as ratio of isolated polymer weight, when dried to the sum of lactam + silica + stearyl isocyanate weight. <sup>d</sup> Samples dried at 80 °C under vacuum for 18 h before analysis; values based on averaging all data gathered for 60 min stability study; typical standard deviation is ± 5 %; data gathered at 210 °C at 1 Hz for 60 min.

Preliminary, single-layer laser fusion experiments proceeded with Orgasol (#2), standard PA12 microspheres (#5), and 0.5x EBS (#12), which involved fusion of single layer structures from powdered precursors. As depicted in **Figure 10.6A**, the PBF process involves a layer-by-layer iterative process whereby fresh powder is deposited by a roller onto the build piston, and a scanning infrared laser provides the remaining thermal energy required for the polymer to surpass  $T_m$  and coalesce. The fabrication piston then moves down by a single layer thickness while the powder delivery piston raises, and fresh powder is deposited for the next layer. **Figure 10.6B** depicts the actual PBF machine employed in this study, which contains two powder feed pistons, while the single-layer fusion process is depicted in **Figure 10.6C**. For the purposes of this study and due to limited quantities of synthesized powder, only single-layered structures were fabricated. **Figure 10.6D-F** portray a photograph of the single-layer fused Orgasol structure, as well as a low- and high-magnification SEM image of the structure, respectively. **Figure 10.6G-I** and **J-L** depict the single-layer structures of samples #5 and #12, respectively. The Orgasol structure possess a high degree of uniformity, with evidence of an unvarying, fully-fused mat present below the partially fused and adhered particles atop this mat. Qualitatively, the structure for #5 (PA12 microparticles v3) possessed a slightly higher degree of porosity, with pores present in the high-magnification SEM image (**Figure 10.6I**), and a seeming reduction of adhered, partially-fused PA12 particles. Finally, the structure for #12 (2x EBS) possessed an even higher degree of porosity upon qualitative investigation of the two SEM images. This change in fabricated object porosity was likely influenced primarily by particle sphericity as opposed to mean particle diameter, as #12 possesses a smaller mean diameter than #5. This particle sphericity is most accurately reflected, qualitatively, in the SEM

micrograph (**Figure 10.4D**). This decreased sphericity likely impedes powder flow during the powder recoating process that occurs between layer fusion, which is consistent with our observations of this fusion process.

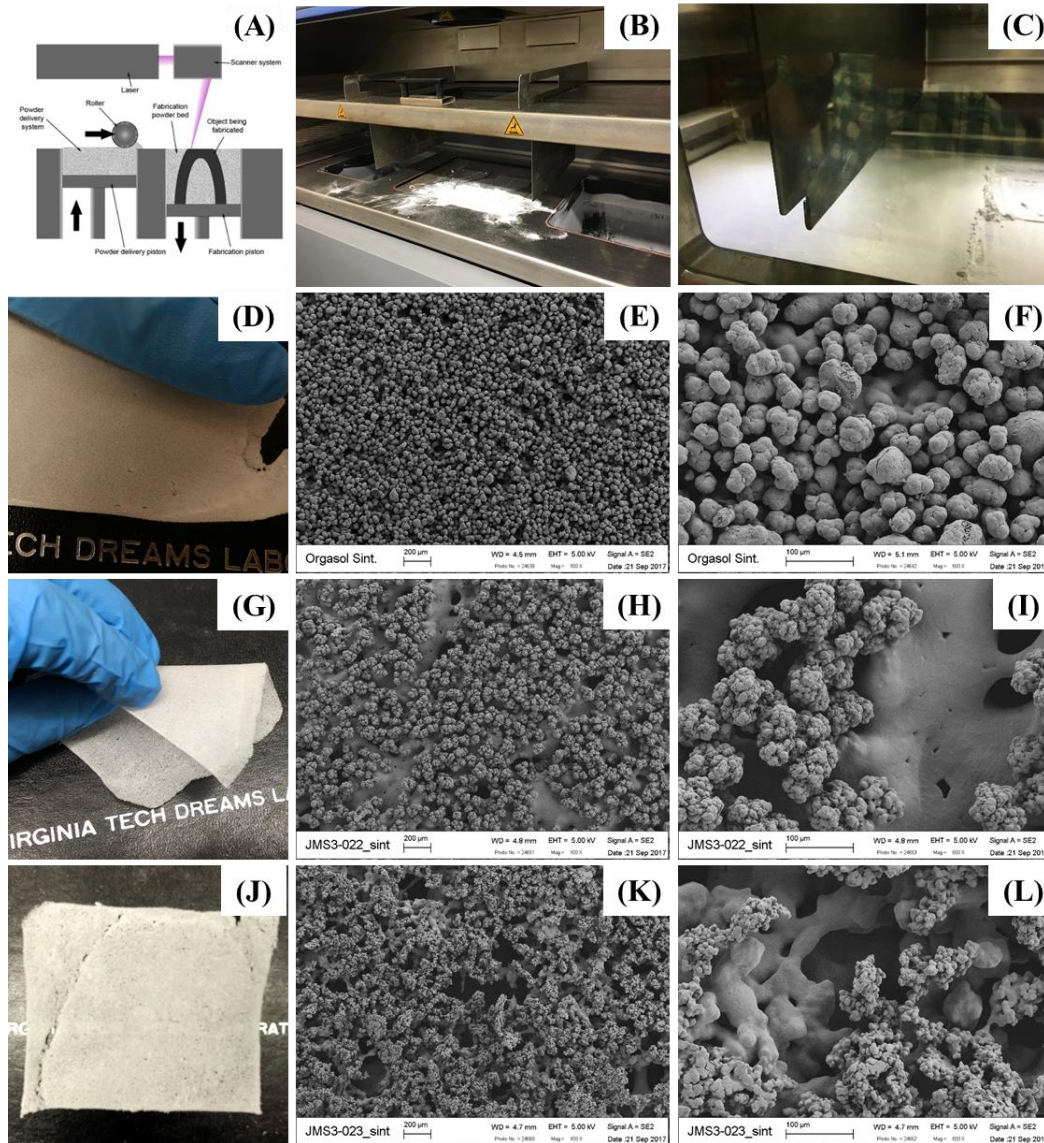


**Figure 10.6.** (A) schematic of powder bed fusion process. (B) photo of the DTM Sinterstation 2500 Plus with central build volume and left/right feed pistons. (C) fusion in progress. (D/G/J) Images of single-layer fused structures and (E/H/K) low- and (F/I/L) high-magnification SEM of (D-F) Arkema Orgasol® IS (#2), (G-I) PA12 microparticles v3 (#5), and (J-L) 0.5x EBS (#12).

## 10.5 Conclusions

This work verified the backbone chemical structure for various PA12 products employed for PBF printing, via amide trifluoroacetylation and subsequent  $^1\text{H}$  NMR spectroscopy in  $\text{CDCl}_3$ . Furthermore, a melt rheology stability study in the presence of a small molecule diamine demonstrated significant  $\eta^*$  increases for neat Duraform and Duraform with 1 wt % diamine, while neat Orgasol and Orgasol with 1 wt % diamine demonstrated consistent  $\eta^*$  during the probed 60 min window. Additionally, an examination of recent patent literature and relevant academic literature yielded a thorough understanding of the Orgasol anionic dispersion polymerization process, knowledge that previously existed only in a proprietary manner. This work established steric stabilizer (e.g. EBS) concentration as the most significant factor affecting mean particle diameter and  $\eta^*$ , an indirect measure of molecular weight. Future work will include scale-up of select compositions for multi-layer printing and tuning of activator precursor chemical structure to afford new polymer topologies, which may include branched structures and/or block copolymers.

## 10.6 Acknowledgements

The authors graciously acknowledge funding from the Department of Energy's (DOE) Kansas City National Security Campus, which is operated and managed by Honeywell Federal Manufacturing & Technologies, LLC, under Contract DE-NA-0002839.

## 10.7 References

- (1) Ligon, S. C.; Liska, R.; Stampfl, J.; Gurr, M.; Mülhaupt, R. Polymers for 3d Printing and Customized Additive Manufacturing. *Chemical Reviews* **2017**, *117*, 10212-10290.
- (2) Zarringhalam, H.; Majewski, C.; Hopkinson, N. Degree of Particle Melt in Nylon-12 Selective Laser-Sintered Parts. *Rapid Prototyping Journal* **2009**, *15*, 126-132.
- (3) Goodridge, R. D.; Tuck, C. J.; Hague, R. J. M. Laser Sintering of Polyamides and Other Polymers. *Progress in Materials Science* **2012**, *57*, 229-267.



- (4) Vasquez, M.; Haworth, B.; Hopkinson, N. Methods for Quantifying the Stable Sintering Region in Laser Sintered Polyamide-12. *Polymer Engineering & Science* **2013**, *53*, 1230-1240.
- (5) Verbelen, L.; Dadbakhsh, S.; Van den Eynde, M.; Kruth, J.-P.; Goderis, B.; Van Puyvelde, P. Characterization of Polyamide Powders for Determination of Laser Sintering Processability. *European Polymer Journal* **2016**, *75*, 163-174.
- (6) Salmoria, G. V.; Leite, J. L.; Paggi, R. A.; Lago, A.; Pires, A. T. N. Selective Laser Sintering of Pa12/Hdpe Blends: Effect of Components on Elastic/Plastic Behavior. *Polymer Testing* **2008**, *27*, 654-659.
- (7) Mazzoli, A.; Moriconi, G.; Pauri, M. G. Characterization of an Aluminum-Filled Polyamide Powder for Applications in Selective Laser Sintering. *Materials & Design* **2007**, *28*, 993-1000.
- (8) Goodridge, R. D.; Shofner, M. L.; Hague, R. J. M.; McClelland, M.; Schlea, M. R.; Johnson, R. B.; Tuck, C. J. Processing of a Polyamide-12/Carbon Nanofibre Composite by Laser Sintering. *Polymer Testing* **2011**, *30*, 94-100.
- (9) Dadbakhsh, S.; Verbelen, L.; Vandeputte, T.; Strobbe, D.; Van Puyvelde, P.; Kruth, J. P. Effect of Powder Size and Shape on the SIs Processability and Mechanical Properties of a Tpu Elastomer. *Physics Procedia* **2016**, *83*, 971-980.
- (10) Yuan, S.; Shen, F.; Bai, J.; Chua, C. K.; Wei, J.; Zhou, K. 3d Soft Auxetic Lattice Structures Fabricated by Selective Laser Sintering: Tpu Powder Evaluation and Process Optimization. *Materials & Design* **2017**, *120*, 317-327.
- (11) Shi, Y. S.; Li, Z. C.; Sun, H. X.; Huang, S. H.; Zeng, F. D. Development of a Polymer Alloy of Polystyrene (Ps) and Polyamide (Pa) for Building Functional Part Based on Selective Laser Sintering (Sls). *Proc. Inst. Mech. Eng. Pt. L-J. Mater.-Design Appl.* **2004**, *218*, 299-306.
- (12) Dotchev, K. D.; Dimov, S. S.; Pham, D. T.; Ivanov, A. I. Accuracy Issues in Rapid Manufacturing Castform™ Patterns. *Proceedings of the Institution of Mechanical Engineers, Part B: Journal of Engineering Manufacture* **2007**, *221*, 53-67.
- (13) Shi, Y.; Wang, Y.; Chen, J.; Huang, S. Experimental Investigation into the Selective Laser Sintering of High-Impact Polystyrene. *Journal of Applied Polymer Science* **2008**, *108*, 535-540.
- (14) Schmidt, M.; Pohle, D.; Rechtenwald, T. Selective Laser Sintering of Peek. *CIRP Annals* **2007**, *56*, 205-208.
- (15) Berretta, S.; Evans, K. E.; Ghita, O. Processability of Peek, a New Polymer for High Temperature Laser Sintering (Ht-Ls). *European Polymer Journal* **2015**, *68*, 243-266.
- (16) Williams, J. M.; Adewunmi, A.; Schek, R. M.; Flanagan, C. L.; Krebsbach, P. H.; Feinberg, S. E.; Hollister, S. J.; Das, S. Bone Tissue Engineering Using Polycaprolactone Scaffolds Fabricated Via Selective Laser Sintering. *Biomaterials* **2005**, *26*, 4817-4827.
- (17) Kruth, J. P.; Levy, G.; Klocke, F.; Childs, T. H. C. Consolidation Phenomena in Laser and Powder-Bed Based Layered Manufacturing. *CIRP Annals* **2007**, *56*, 730-759.
- (18) Shi, Y.; Chen, J.; Wang, Y.; Li, Z.; Huang, S. Study of the Selective Laser Sintering of Polycarbonate and Postprocess for Parts Reinforcement. *Proceedings*

- of the Institution of Mechanical Engineers, Part L: Journal of Materials: Design and Applications* **2007**, 221, 37-42.
- (19) Ho, H. C. H.; Cheung, W. L.; Gibson, I. Morphology and Properties of Selective Laser Sintered Bisphenol a Polycarbonate. *Industrial & Engineering Chemistry Research* **2003**, 42, 1850-1862.
  - (20) Drummer, D.; Wudy, K.; Drexler, M. Modelling of the Aging Behavior of Polyamide 12 Powder During Laser Melting Process. *AIP Conference Proceedings* **2015**, 1664, 160007.
  - (21) Barry, H.; Neil, H.; David, H.; Xiaotao, Z. Shear Viscosity Measurements on Polyamide-12 Polymers for Laser Sintering. *Rapid Prototyping Journal* **2013**, 19, 28-36.
  - (22) Martínez, A.; Ibáñez, A.; Sánchez, A.; León, M. A. Comparison of Aged Polyamide Powders for Selective Laser Sintering. *AIP Conference Proceedings* **2012**, 1431, 5-13.
  - (23) Dotchev, K.; Yusoff, W. Recycling of Polyamide 12 Based Powders in the Laser Sintering Process. *Rapid Prototyping Journal* **2009**, 15, 192-203.
  - (24) Pham, D. T.; Dotchev, K. D.; Yusoff, W. A. Y. Deterioration of Polyamide Powder Properties in the Laser Sintering Process. *Proceedings of the Institution of Mechanical Engineers, Part C: Journal of Mechanical Engineering Science* **2008**, 222, 2163-2176.
  - (25) Way, Y.; Pham, D.; Dotchev, K. In *Applied Mechanics and Materials*; Trans Tech Publ: 2014; Vol. 548, p 294-296.
  - (26) Griehl, W.; Ruestem, D. Nylon-12-Preparation, Properties, and Applications. *Industrial & Engineering Chemistry* **1970**, 62, 16-22.
  - (27) Schmid, M.; Amado, A.; Wegener, K. Polymer Powders for Selective Laser Sintering (Sls). *AIP Conference Proceedings* **2015**, 1664, 160009.
  - (28) Ziegelmeier, S.; Christou, P.; Wöllecke, F.; Tuck, C.; Goodridge, R.; Hague, R.; Krampe, E.; Wintermantel, E. An Experimental Study into the Effects of Bulk and Flow Behaviour of Laser Sintering Polymer Powders on Resulting Part Properties. *J. Mater. Process. Technol.* **2015**, 215, 239-250.
  - (29) Šebenda, J. A. N. Lactam Polymerization. *Journal of Macromolecular Science: Part A - Chemistry* **1972**, 6, 1145-1199.
  - (30) Schmid, M.; Kleijnen, R.; Vetterli, M.; Wegener, K. Influence of the Origin of Polyamide 12 Powder on the Laser Sintering Process and Laser Sintered Parts. *Applied Sciences* **2017**, 7, 462.
  - (31) Verbelen, L., KU Leuven, 2016.
  - (32) Loyen, K.; Senff, H.; Pauly, F.-X., Process for the Manufacture of Polyamide-12 Powder with a High Melting Point.
  - (33) Lok, K. P.; Ober, C. K. Particle Size Control in Dispersion Polymerization of Polystyrene. *Canadian Journal of Chemistry* **1985**, 63, 209-216.
  - (34) Ober, C. K.; Hair, M. L. The Effect of Temperature and Initiator Levels on the Dispersion Polymerization of Polystyrene. *Journal of Polymer Science Part A: Polymer Chemistry* **1987**, 25, 1395-1407.
  - (35) Awan, M. A.; Dimonie, V. L.; El-Aasser, M. S. Anionic Dispersion Polymerization of Styrene. I. Investigation of Parameters for Preparation of Uniform Micron-Size Polystyrene Particles with Narrow Molecular Weight

- Distribution. *Journal of Polymer Science Part A: Polymer Chemistry* **1996**, *34*, 2633-2649.
- (36) Dan, F.; Vasiliu-Oprea, C. Anionic Polymerization of Caprolactam in Organic Media. Morphological Aspects. *Colloid Polym Sci* **1998**, *276*, 483-495.
- (37) Suteu, D.; Bilba, D.; Dan, F. Synthesis and Characterization of Polyamide Powders for Sorption of Reactive Dyes from Aqueous Solutions. *Journal of Applied Polymer Science* **2007**, *105*, 1833-1843.
- (38) Zhao, X.; Xia, H.; Fu, X.; Duan, J.; Yang, G. Preparation of Polyamide-6 Submicrometer-Sized Spheres by in Situ Polymerization. *Macromolecular Rapid Communications* **2015**, *36*, 1994-1999.
- (39) Vasiliu-Oprea, C.; Dan, F. On the Relation between Synthesis Parameters and Morphology of Anionic Polycaprolactam Obtained in Organic Media. I. Influence of the Na[O(CH<sub>2</sub>)<sub>2</sub>OCH<sub>2</sub>]<sub>2</sub>AlH<sub>2</sub>/Isophorone Diisocyanate Catalytic System. *Journal of Applied Polymer Science* **1996**, *62*, 1517-1527.
- (40) Dencheva, N.; Denchev, Z.; Lancers-Méndez, S.; Ezquerro Sanz, T. One-Step in Situ Synthesis of Polyamide Microcapsules with Inorganic Payload and Their Transformation into Responsive Thermoplastic Composite Materials. *Macromolecular Materials and Engineering* **2016**, *301*, 119-124.
- (41) Qu, L.; Veca, L. M.; Lin, Y.; Kitaygorodskiy, A.; Chen, B.; McCall, A. M.; Connell, J. W.; Sun, Y.-P. Soluble Nylon-Functionalized Carbon Nanotubes from Anionic Ring-Opening Polymerization from Nanotube Surface. *Macromolecules* **2005**, *38*, 10328-10331.
- (42) Novitsky, T. F.; Mathias, L. J. One-Pot Synthesis of Polyamide 12,T-Polyamide-6 Block Copolymers. *Journal of Polymer Science Part A: Polymer Chemistry* **2011**, *49*, 2271-2280.
- (43) Rached, R.; Hoppe, S.; Jonquieres, A.; Lochon, P.; Pla, F. A New Macroinitiator for the Synthesis of Triblock Copolymers Pa12-B-Pdms-B-Pa12. *Journal of Applied Polymer Science* **2006**, *102*, 2818-2831.
- (44) Wang, G.; Wang, P.; Zhen, Z.; Zhang, W.; Ji, J. Preparation of Pa12 Microspheres with Tunable Morphology and Size for Use in SIs Processing. *Materials & Design* **2015**, *87*, 656-662.
- (45) Senff, H., Core-Shell Polyamide Powder.
- (46) Dupin, S.; Lame, O.; Barrès, C.; Charneau, J.-Y. Microstructural Origin of Physical and Mechanical Properties of Polyamide 12 Processed by Laser Sintering. *European Polymer Journal* **2012**, *48*, 1611-1621.
- (47) Laun, S.; Pasch, H.; Longiéras, N.; Degoulet, C. Molar Mass Analysis of Polyamides-11 and -12 by Size Exclusion Chromatography in Hfip. *Polymer* **2008**, *49*, 4502-4509.
- (48) Jacobi, E.; Schuttenberg, H.; Schulz, R. C. A New Method for Gel Permeation Chromatography of Polyamides. *Die Makromolekulare Chemie, Rapid Communications* **1980**, *1*, 397-402.
- (49) Hashimoto, K. Ring-Opening Polymerization of Lactams. Living Anionic Polymerization and Its Applications. *Progress in Polymer Science* **2000**, *25*, 1411-1462.
- (50) Carlotti, S.; Peruch, F. Cyclic Monomers: Epoxides, Lactide, Lactones, Lactams, Cyclic Silicon-Containing Monomers, Cyclic Carbonates, and Others. In *Anionic*

- Polymerization: Principles, Practice, Strength, Consequences and Applications*;  
Hadjichristidis, N., Hirao, A., Eds.; Springer Japan: Tokyo, 2015, p 191-305.
- (51) Qun, W.; Shoukuan, F.; Tongyin, Y. Emulsion Polymerization. *Progress in Polymer Science* **1994**, *19*, 703-753.

## 10.8 Supporting Information

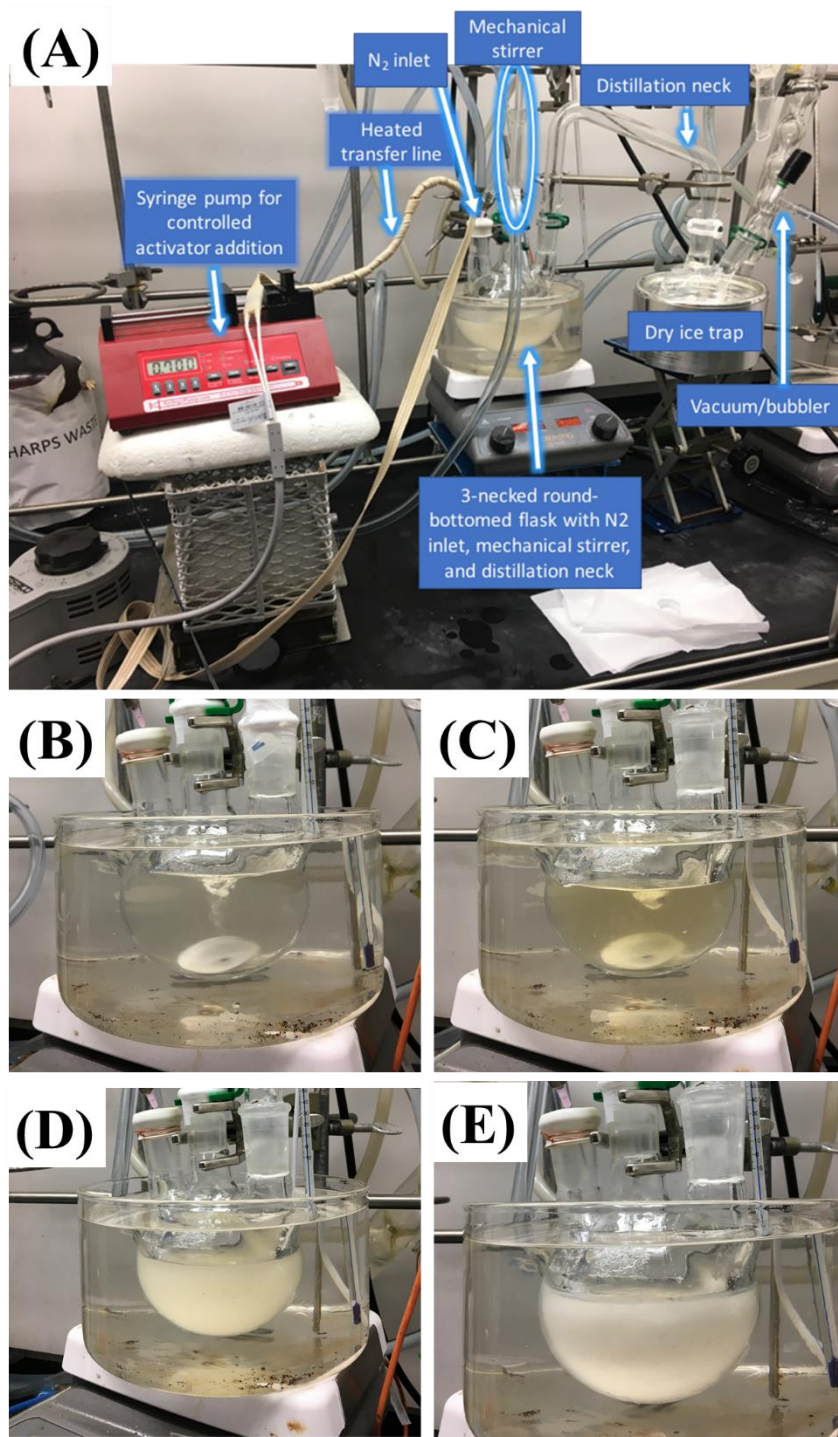


**Figure 10.7.** (A) Picture of anionic dispersion polymerization reactor. (B) Picture showing full laurilactam and EBS dissolution at 120 °C. (C) Reaction at 120 °C after NaH addition, displaying a slightly more yellow color. (D) Partway and (E) all the way through activator addition, at various stages of the dispersion polymerization.

## Chapter 11: Overall Conclusions

Synthesis, characterization, and additive manufacturing of novel functional polymers enabled the creation of PDMS-, PA12-, and PPG-containing oligomers and polymers for additive manufacturing in elastomeric, electronic, biological, and rapid prototyping applications. The synthesis, photocuring and AM of dithiol- and diacrylamide-functional PDMS oligomers enabled relatively low viscosity before photocuring but properties of higher molecular weight precursors after photocuring. A monomeric competition study confirmed preference for thiol-ene chain extension vs. acrylamide crosslinking at the functional group level, in the absence of diffusion. Photorheology and soxhlet extraction measured crosslinked network plateau moduli and gel fractions in excess of 90 % for multiple compositions, while photocalorimetry measurements enabled maximization of the photopolymerization exotherm. Tensile testing demonstrated a 2x increase in strain at break as compared to non-chain-extended, photocured oligomers, while maintaining an uncured photopolymer viscosity below that of the non-chain-extended oligomers. This photopolymer system enables rapid elastomer production *via* VP-AM while employing low viscosity precursors.

The characterization, photocuring, and VP-AM of DiPhS- or DiEtS-containing siloxane terpolymers was demonstrated, revealing high gel fractions and a rubbery plateau extending to greater than 200 °C for the photocured DiEtS-containing system. VP-AM of both DiPhS- or DiEtS-containing systems demonstrated well-defined geometries, including the printing of high aspect ratio structures. These 3D printed objects demonstrated utility for applications that require ultra-low temperature elastomeric performance. Finally, melt polymerization of PDMS diamines in the presence of a disiloxane diamine chain extender and urea yielded isocyanate-free PDMS polyureas in the

absence of solvent or catalyst. After compression molding of polymers isolated directly from the melt, these mechanically ductile and optically clear films revealed multiple relaxations *via* DMA, suggesting microphase separation. Tensile testing revealed strain at break between 495 to 1180 %. This facile, isocyanate-free approach provides a commercially-viable alternative to typical polyurea synthesis involving isocyanates.

Successive endcapping of a PPG diamine oligomer with a diisocyanate and subsequently hydroxyethyl acrylate yielded photocurable, urethane/urea-containing oligomers for VP-AM applications. SFC-ELSD measured oligomer molecular weight distributions with repeating unit resolution and demonstrated a decrease in oligomer  $M_n$  with increasing stoichiometric excess of HMDI and HEA. Dynamic mechanical analysis of photocured networks revealed an increased modulus at room temperature with increasing stoichiometric excess of HMDI and HEA. Photocuring in the presence of reactive diluents provided a reduction in crosslink density, resulting in a reduction in room temperature modulus with increasing diluent concentration, as determined by DMA. Finally, VP-AM with these PPG-based oligomers demonstrated well-defined geometries that included high aspect ratio pillars and a 3D scaffold structure.

Melt polymerization of adipic acid with a stoichiometric excess of tri(ethylene glycol) afforded low  $T_g$  aliphatic polyesters that were isolated directly from the melt. Subsequent derivatization with 2-isocyanatoethyl methacrylate afforded photocurable polyesters for VP-AM without producing acidic byproducts capable of inducing chain scission via ester hydrolysis. Photocuring, characterization, and VP-AM demonstrated highly efficient photocuring and significantly improved cell attachment as compared to

controls. Based on initial 3D printing, modulus measurements, and cell viability data, these results show potential for the 3D production of vascularized tissue scaffolds.

The anionic dispersion polymerization of laurolactam in the presence of NaH and EBS yielded melt-stable PA12 microspheres that precipitated directly during the polymerization, eliminating the need for expensive and time-consuming grinding or precipitation steps that typically occur during post-processing. The concentration of EBS and stirring rates demonstrated the greatest effect on PA12 microparticle size and complex viscosity, an indirect measure of molecular weight. Finally, preliminary sintering of single-layered PA12 structures provided insight into the particle size distribution required for the sintering of defect-free structures. This polymerization process demonstrates potential for the production of melt-stable, PA12-containing microparticles for use in PBF AM.

In summary, a systematic and fundamental approach to macromolecular design enabled the synthesis and characterization of novel polymeric systems for a wide variety of emerging applications.

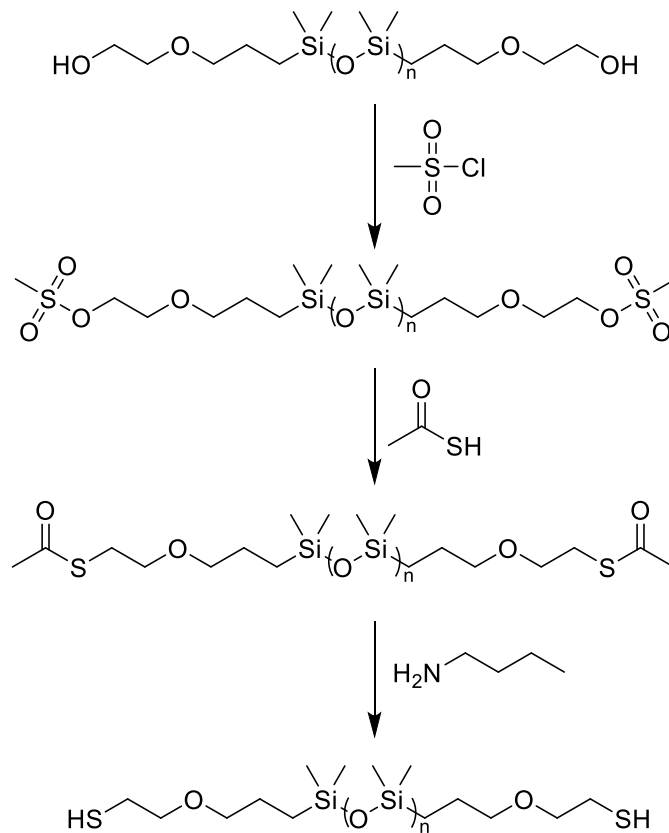


## Chapter 12: Future Work

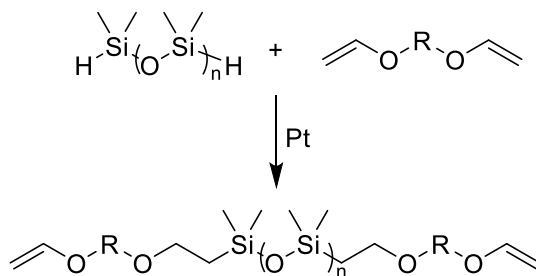
### 12.1 Thiol-ene photopolymers for simultaneous or sequential chain extension and crosslinking in air

The simultaneous chain extension and crosslinking of thiol- and acrylamide-terminated PDMS oligomers was previously demonstrated.<sup>1</sup> It is well known that the high solubility of oxygen in PDMS and resulting binding of oxygen to propagating acrylamide radicals causes increased termination events during acrylamide homopolymerization,<sup>2,3</sup> preventing the achievement of high gel fractions. Additionally, previous work demonstrates that increased ester hydrolysis rates occur with networks synthesized through thiol-acrylate or thiol-Michael reactions when the networks contain an ester in close proximity to a thioether functionality (e.g. 1 or 2 carbons away).<sup>4</sup> Therefore, a new photopolymer system is proposed that is both tolerant of the presence of oxygen and does not contain or produce sulfide linkages in close proximity to ester linkages. This system contains leverages the well-known poly(dimethyl siloxane) polymer backbone with established literature that details rapid, sequential thiol-ene free-radical and vinyl ether cationic hybrid photopolymerization in the presence of a photoinitiator that produces radical cations.<sup>5</sup> First, a dithiol is synthesized according to previous literature, as shown in **Scheme 12.1**.<sup>6</sup> Second, a vinyl ether functional PDMS oligomer is synthesized according to previous literature, as shown in **Scheme 12.2**.<sup>7</sup> Hoyle and coworkers achieved sequential free radical and cationic photopolymerization with a single photoinitiator that undergoes a radical-cation intermediate (e.g. triarylsulfonium hexafluoroantimonate) by leveraging the fact that cationic photopolymerization experiences an inhibition period in the presence of moisture.<sup>5</sup> Alternatively, the radical and cationic processes can separated into two distinct processes if three criteria are met. First, a cationic photoinitiator must be employed that does not undergo a radical cation intermediate.<sup>8</sup> Second, the two photoinitiators must absorb

at significantly different wavelengths such that one can form an excited state without the other one doing so. Third, the UV source must be capable of providing irradiation of one wavelength at a time.



**Scheme 12.1.** Synthesis of a carbonyl-free PDMS dithiol.

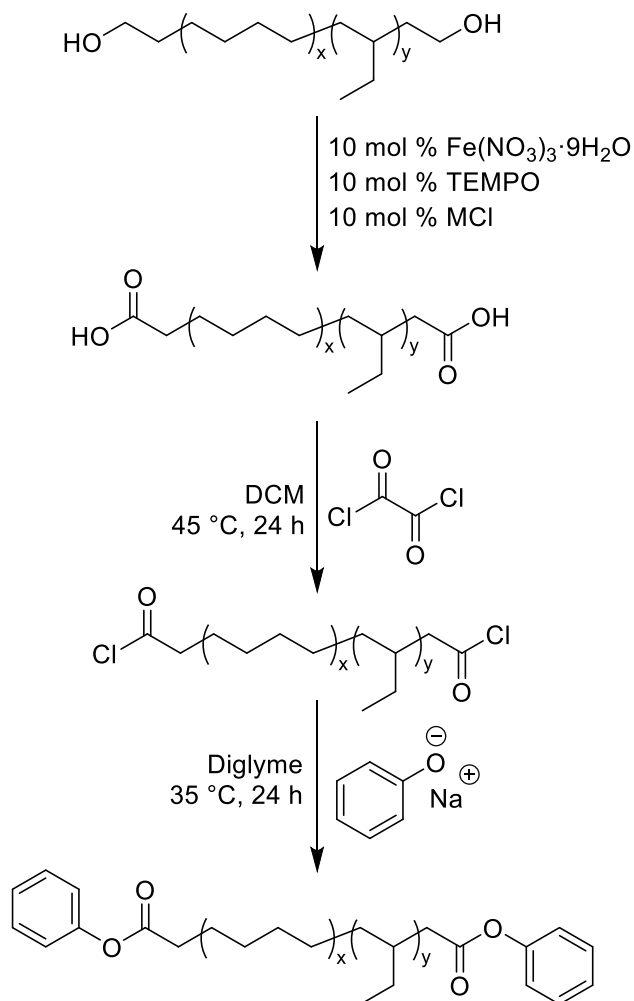


**Scheme 12.2.** Synthesis of a vinyl ether functional PDMS oligomer via hydrosilylation reaction.

## 12.2 PA12-HPBD-PA12 triblock copolymers via anionic dispersion polymerization

The anionic dispersion polymerization described in Chapter 10 can be adapted for use with a macromolecular activator precursor. Formation of triblock copolymers through anionic polymerization with a macromolecular activator precursor are well-known in the literature,<sup>9-12</sup> but all of these polymerizations occur in bulk. To the best of our knowledge we have not seen reports of the formation of triblock copolymers with an anionic dispersion polymerization, which would form thermoplastic elastomer powder directly from the polymerization, rather than requiring a post-processing grinding step. A post-processing grinding step would be energetically expensive in the case of a thermoplastic elastomer, so this process would directly provide thermoplastic elastomer powder for powder bed fusion additive manufacturing applications. Though Chapter 10 only demonstrated isocyanates as activator precursors, examination of previous literature reveals that esters are well-known to form activators in the presence of lactamate anion, as long as a sufficiently good leaving group is employed (e.g. phenyl ester).<sup>9,10,13</sup> Furthermore, initial experiments synthesized a macromolecular PDMS diisocyanate through simple endcapping of a PDMS diamine with a diisocyanate. Unfortunately, the anion produced by sodium hydride is strong enough to induce PDMS chain scission.<sup>14</sup> These authors described a bulk polymerization with a new initiating system based on  $\text{NaAlH}_2(\text{OCH}_2\text{CH}_2\text{OMe})_2$  that remains active toward caprolactam while remaining inert to the PDMS backbone.<sup>14</sup> Furthermore, as the aforementioned PDMS diisocyanate creates challenges as its two urea functional groups may themselves serve as a catalyst for ring-opening polymerization.<sup>15</sup> As shown in **Scheme 12.3** and based on relevant literature, a hydrogenated polybutadiene (HPBD) diphenyl ester is proposed that can act as an activator precursor for the anionic dispersion polymerization

of lauro lactam, ideally yielding PA12-HPBD-PA12 triblock copolymer microparticles directly from the polymerization. Based in the literature, this synthesis is based on a commercially-available HPBD diol that is oxidized to a diacid,<sup>16</sup> followed derivatization of carboxylic acids to acid chlorides to increase reactivity,<sup>17</sup> and finally reaction with sodium phenoxide to yield the HPBD diphenyl ester.<sup>18</sup>



**Scheme 12.3.** Synthesis of a hydrogenated polybutadiene diphenyl ester

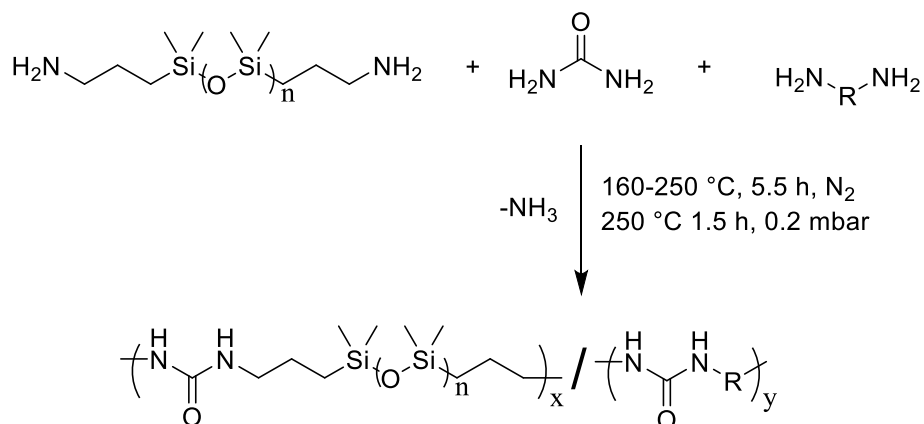
### **12.3 Investigation into the role of silica in the anionic dispersion polymerization of laurolactam**

The role of silica in the anionic dispersion polymerization described in Chapter 10 is described as a nucleating agent that controls particle size, in the patent literature.<sup>19,20</sup> In this literature, silica is described as a filler that is added at concentrations of 0.035 to 0.09 wt % and possesses a particle size between 0.01 and 10  $\mu\text{m}$ , whereby an increase in silica concentration decreases particle size. In Chapter 10, the role of the silica was investigated only through polymerizations with or without silica. Further investigation into the role of silica is desired. For example, all polymerizations with silica in Chapter 10 employed hydrophilic, non-fumed silica. It is hypothesized that the growing polyamide chains hydrogen bond with the silica surface, which likely contains Si-OH functional groups. Future work will include in-depth characterization of this hydrophilic silica, including surface chemistry identification, particle size measurements, and scanning electron microscopy. Future work may also include polymerizations with hydrophobic silica and/or silica with varying particle size, in order to determine the effect of the silica particle size and surface chemistry on PA12 viscosity and particle size.

### **12.4 Isocyanate-free, segmented PDMS polyureas**

The isocyanate-free PDMS polyureas reported in Chapter 6 and shown in **Scheme 12.4** can be modified to include virtually any diamine as the chain extender, instead of the disiloxane diamine (BATS) as the chain extender, as long as the melt polymerization remains homogeneous. Preliminary melt polymerizations with low hard segment content targets (e.g. 4 wt % HS) with 1,6-hexanediamine or 4,4'-diaminodicyclohexylmethane produced a phase separated melt at the 160 °C stage, and are not recommended. However,

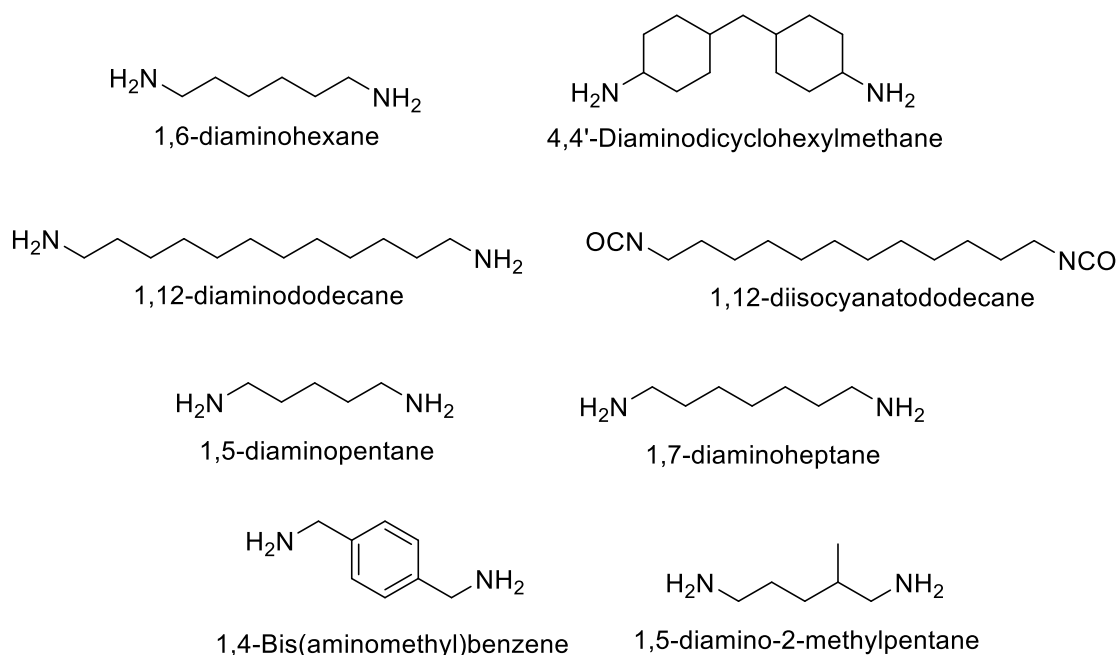
a preliminary melt polymerization with target 4 wt % HS with 1,12-diaminododecane yielded a homogeneous melt. We hypothesize that phase separation of the polymer melt occurs more readily in situations with higher density of urea functional groups. The melt homogeneity observed for BATS in Chapter 6, or here with 1,12-diaminododecane, may be facilitated. The higher molecular weight and/or greater flexibility of 1,12-diaminododecane or the BATS employed in Chapter 6 may decrease the density or packing efficiency of the urea functional groups, thus increasing the likelihood of melt homogeneity. Following this logic, the use of diamines with an odd number of methylenes in between the amine functional groups, for example 1,5-diaminopentane (e.g. cadaverine) or 1,7-diaminoheptane, may result in a homogeneous melt. Finally, the use of 1,4-bis(aminomethyl)benzene may prevent loss of the diamine chain extender at high temperatures and during the final vacuum step, due to its high melting and boiling points ( $T_m = 63\text{ }^\circ\text{C}$ ,  $T_b = 230\text{ }^\circ\text{C}$  at 10 mm Hg). Chemical structures of the various diamines discussed here are shown in **Scheme 12.5**.



**Scheme 12.4.** Synthesis of segmented PDMS polyureas in the absence of isocyanates, solvent, or catalyst.

Examination of polymer morphology as a function of composition also remains a key attribute of this research. Our hypothesis is that the microphase-separated morphology

that exists for PDMS polyureas made with this isocyanate-free method is the same as for PDMS polyureas made with isocyanates, for samples with equivalent hard segment content and soft segment molecular weight. One key experiment that may help investigate this hypothesis is the synthesis of a PDMS polyurea via two different synthetic methods, but identical chemical structure. First, the melt polymerization of PDMS diamines, 1,12-diaminododecane, and urea will yield a PDMS polyurea that can potentially contain multiple hard segments in succession. Second, the solution polymerization of PDMS diamines and 1,12-diisocyanatododecane will yield alternating PDMS (soft) and dodecanebisurea (hard) segments, except for the case of side products, e.g. a decarboxylated diisocyanate that forms a diamine, which will promptly react with an isocyanate functional group. Addition of a small amount of 1,12-diaminododecane to this second polymerization will rectify the chemical structure differences between the polyureas produce via solution vs. melt polymerization. This morphological investigation as a function of synthetic method may yield interesting results, particularly if appreciable side product formation occurs during melt polymerization (e.g. formation of 1,1-dialkylureas or urea biurets),<sup>21,22</sup> and if these side products influence polymer morphology or hard segment packing.



**Scheme 12.5.** Various diamine chain extenders and 1,12-diisocyanatododecane.

## 12.5 Organocatalyzed- or organometallic-catalyzed, isocyanate-free, segmented PDMS polyureas

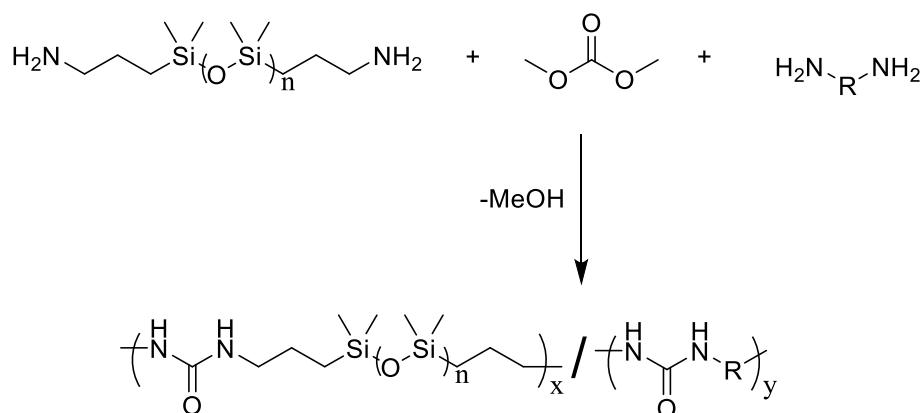
One unanswered question in the scientific literature is whether or not the isocyanate-free polyurea synthesis described in **Section 12.4** and shown in **Scheme 12.4**, and reported elsewhere,<sup>23</sup> can be catalyzed either with organometallic catalysts or organic catalysts. The mechanism for the reaction of urea with amines is reported elsewhere, and proceeds via in-situ generation of isocyanic acid in the case of urea, or an alkyl isocyanate in the case of 1-alkylurea.<sup>21</sup> The mechanism of organometallic or organic catalysis of the reaction of isocyanates with a nucleophile (e.g. R-OH) is well understood.<sup>24-26</sup> In the case of dibutyltin dilaurate, coordination of the isocyanate occurs upon alcoholysis of the initial tin molecule.<sup>25</sup> In the case of organocatalysis, a base (e.g. 1,4-diazabicyclo[2.2.2]octane or DABCO) deprotonates the intermediate formed by attack of the isocyanate carbon by a nucleophile.<sup>25</sup> Due to the fact that the isocyanate-free polyurea synthesis proceeds through



an isocyanate intermediate, organic or organometallic catalysis may provide improvements in reaction rate. Catalysis may also promote miscibility of the initially heterogeneous melt due to formation of PDMS urea oligomers. Though this catalysis effort is initially focused on PDMS polyureas, it may be applicable to any reaction of a nucleophile with urea.

## 12.6 Catalyzed synthesis of isocyanate-free polyureas with dimethylcarbonate or biscarbamates

Catalysts for the isocyanate-free synthesis of polyureas are discussed elsewhere.<sup>27,28</sup> Catalyst options include 1,5,7-triazabicyclo[4.4.0]dec-5-ene (TBD), potassium tert-butoxide (KO-t-Bu), potassium methoxide (KOMe), and potassium bis(trimethylsilyl)amide (KHMDs).<sup>27</sup>

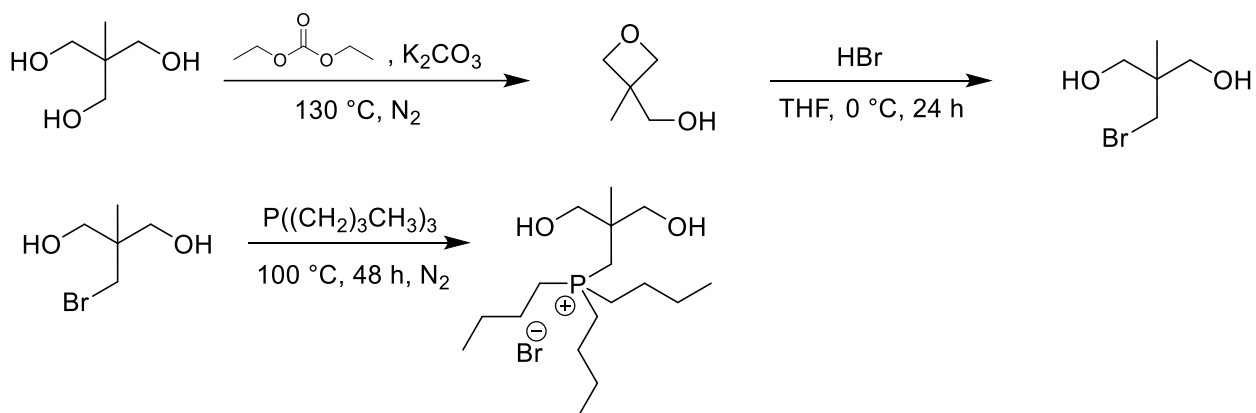


**Scheme 12.6.** Synthesis of segmented PDMS polyureas from dimethyl carbonate in the absence of isocyanates, solvent, or catalyst.

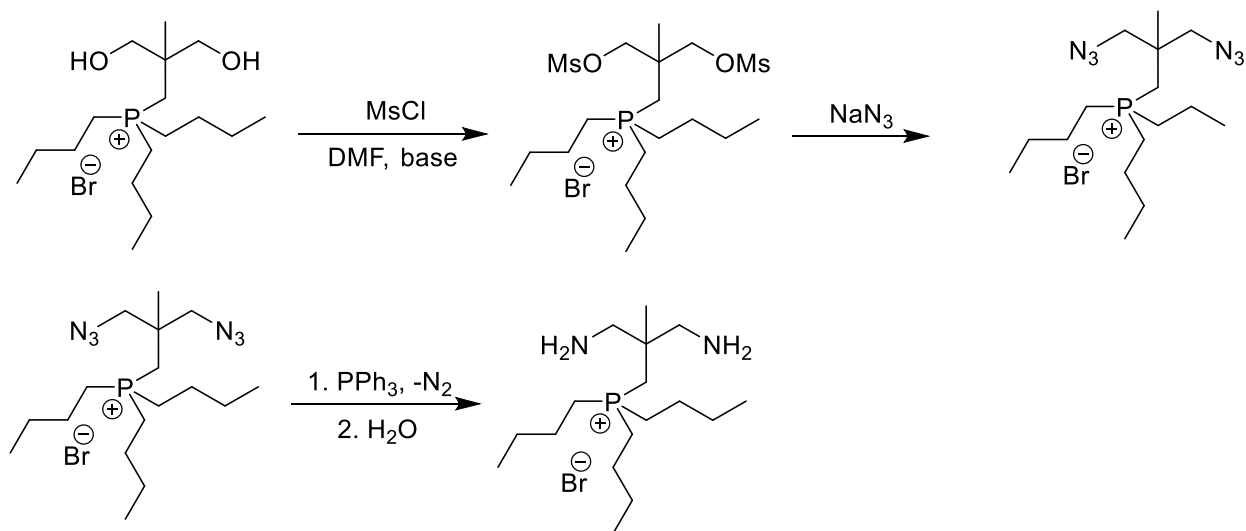
Another review discusses isocyanate-free routes towards polyurethanes.<sup>28</sup> Based on this literature and our previous work,<sup>23</sup> the isocyanate-free synthesis of polyureas from a carbonate, instead of urea, may also be possible, as shown in **Scheme 12.6**. As drawn, methanol is condensed during polymerization, but a carbonate with a better leaving group may also be used if needed, such as diphenyl carbonate. This may facilitate the rate and/or extent of reaction.

## 12.7 Synthesis of phosphonium-containing polyureas

Zhang and Long *et al.* recently reported the synthesis and characterization of phosphonium-containing, water-dispersible cationic polyurethanes.<sup>29</sup> This work also featured the synthesis of a novel phosphonium diol, shown in **Scheme 12.7**.



**Scheme 12.7.** Synthesis of phosphonium-containing diol from 1,1,1-tris(hydroxymethyl)ethane.



**Scheme 12.8.** Synthesis of phosphonium diamine

We propose the derivatization of this phosphonium diol to a diamine *via* the route presented in **Scheme 12.8**. Here, the diol functionality is mesylated in order to create a better leaving

group. Next, sodium azide displaces the mesyl leaving group, yielding a diazide. This diazide is then reduced to a diamine. Care must be taken during the synthesis and subsequent handling of the phosphonium diazide so as to avoid shock sensitivity. Use of plastic utensils for weighing of compounds and working with small quantities will help mitigate the shock sensitivity. Additionally, the carbon to nitrogen ratio should be calculated for any theoretical compound in order to determine if the azide is stable enough to work with. This ratio is shown in **Equation 1**.<sup>30</sup>

$$\frac{N_{carbon} + N_{oxygen}}{N_{nitrogen}} \geq 3 \quad (1)$$

Previous literature recommends isolating and storing up to 20 grams of compounds that possess a C/N ratio of  $\geq 3$ , while recommending synthesis and storage 5 grams or less (and in solution of no more than 1 M concentration) of compounds that possess a C/N ratio of between 1 and 3.<sup>30</sup> The authors recommend that organic azides with C/N ratio  $< 1$  should never be isolated.

## 12.8 References

- (1) Serrine, J. M.; Meenakshisundaram, V.; Moon, N. G.; Scott, P. J.; Mondschein, R. J.; Weiseman, T. F.; Williams, C. B.; Long, T. E. Functional Siloxanes with Photo-Activated, Simultaneous Chain Extension and Crosslinking for Lithography-Based 3d Printing. *Polymer* **2018**.
- (2) Melody, D. P. Advances in Room Temperature Curing Adhesives and Sealants—a Review. *British Polymer Journal* **1989**, *21*, 175-179.
- (3) de Buyl, F. Silicone Sealants and Structural Adhesives. *International Journal of Adhesion and Adhesives* **2001**, *21*, 411-422.
- (4) Rydholm, A. E.; Anseth, K. S.; Bowman, C. N. Effects of Neighboring Sulfides and Ph on Ester Hydrolysis in Thiol-Acrylate Photopolymers. *Acta biomaterialia* **2007**, *3*, 449-455.
- (5) Wei, H.; Li, Q.; Ojelade, M.; Madbouly, S.; Otaigbe, J. U.; Hoyle, C. E. Thiol–Ene Free-Radical and Vinyl Ether Cationic Hybrid Photopolymerization. *Macromolecules* **2007**, *40*, 8788-8793.
- (6) van den Berg, O.; Nguyen, L.-T. T.; Teixeira, R. F. A.; Goethals, F.; Özdilek, C.; Berghmans, S.; Du Prez, F. E. Low Modulus Dry Silicone-Gel Materials by Photoinduced Thiol–Ene Chemistry. *Macromolecules* **2014**, *47*, 1292-1300.

- (7) Cazaux, F.; Coqueret, X. Polydimethylsiloxanes with Vinyl Ether End-Groups—I. Synthesis and Properties as Polymerizable Wetting Agents. *European Polymer Journal* **1995**, *31*, 521-525.
- (8) Xiao, P.; Zhang, J.; Dumur, F.; Tehfe, M. A.; Morlet-Savary, F.; Graff, B.; Gigmes, D.; Fouassier, J. P.; Lalevee, J. Visible Light Sensitive Photoinitiating Systems: Recent Progress in Cationic and Radical Photopolymerization Reactions under Soft Conditions. *Progress in Polymer Science* **2015**, *41*, 32-66.
- (9) Pae, Y. Structure and Properties of Polyimide-G-Nylon 6 and Nylon 6-B-Polyimide-B-Nylon 6 Copolymers. *Journal of Applied Polymer Science* **2006**, *99*, 300-308.
- (10) Pae, Y. Preparation of Polyimide/Nylon 6 Graft Copolymers from Polyimides Containing Ester Moieties: Synthesis and Characterization. *Journal of Applied Polymer Science* **2006**, *99*, 309-318.
- (11) Pae, Y.; Harris, F. W. Synthesis and Properties of Novel Polyimide/Nylon-6 Triblock Copolymers. *Journal of Polymer Science Part A: Polymer Chemistry* **2000**, *38*, 4247-4257.
- (12) Rached, R.; Hoppe, S.; Jonquieres, A.; Lochon, P.; Pla, F. A New Macroinitiator for the Synthesis of Triblock Copolymers Pa12-B-Pdms-B-Pa12. *Journal of Applied Polymer Science* **2006**, *102*, 2818-2831.
- (13) Hadjichristidis, N.; Hiraio, A. *Anionic Polymerization: Principles, Practice, Strength, Consequences and Applications*; Springer, 2015.
- (14) Mougin, N.; Rempp, P.; Gnanou, Y. Synthesis and Characterization of Polysiloxane-Polyamide Block and Graft Copolymers. *Journal of Polymer Science Part A: Polymer Chemistry* **1993**, *31*, 1253-1260.
- (15) Lin, B.; Waymouth, R. M. Urea Anions: Simple, Fast, and Selective Catalysts for Ring-Opening Polymerizations. *Journal of the American Chemical Society* **2017**, *139*, 1645-1652.
- (16) Jiang, X.; Zhang, J.; Ma, S. Iron Catalysis for Room-Temperature Aerobic Oxidation of Alcohols to Carboxylic Acids. *Journal of the American Chemical Society* **2016**, *138*, 8344-8347.
- (17) Hegde, M.; Meenakshisundaram, V.; Chartrain, N.; Sekhar, S.; Tafti, D.; Williams, C. B.; Long, T. E. 3d Printing All-Aromatic Polyimides Using Mask-Projection Stereolithography: Processing the Nonprocessable. *Adv Mater* **2017**, *29*.
- (18) Lee, Y. H.; Allison, B. D.; Grutzner, J. B. Carbon-13 Nmr Relaxation Studies of Cycloalkylidene Bisphenols, Methyl Ethers, and Simple Benzoate Esters in Solution: Different Average Correlation Times for Dipole-Dipole and Chemical Shift Anisotropy Relaxation. *The Journal of Physical Chemistry* **1994**, *98*, 1783-1790.
- (19) Loyen, K.; Senff, H.; Pauly, F.-X., Process for the Manufacture of Polyamide-12 Powder with a High Melting Point.
- (20) Senff, H., Core-Shell Polyamide Powder.
- (21) Montarnal, D.; Cordier, P.; Soulié-Ziakovic, C.; Tournilhac, F.; Leibler, L. Synthesis of Self-Healing Supramolecular Rubbers from Fatty Acid Derivatives, Diethylene Triamine, and Urea. *Journal of Polymer Science Part A: Polymer Chemistry* **2008**, *46*, 7925-7936.

- (22) Erickson, J. G. Reactions of Long-Chain Amines. II. Reactions with Urea. *Journal of the American Chemical Society* **1954**, *76*, 3977-3978.
- (23) Dennis, J. M.; Steinberg, L. I.; Pekkanen, A. M.; Maiz, J.; Hegde, M.; Muller, A. J.; Long, T. E. Synthesis and Characterization of Isocyanate-Free Polyureas. *Green Chemistry* **2018**, *20*, 243-249.
- (24) Luo, S.-G.; Tan, H.-M.; Zhang, J.-G.; Wu, Y.-J.; Pei, F.-K.; Meng, X.-H. Catalytic Mechanisms of Triphenyl Bismuth, Dibutyltin Dilaurate, and Their Combination in Polyurethane-Forming Reaction. *Journal of Applied Polymer Science* **1997**, *65*, 1217-1225.
- (25) Sardon, H.; Pascual, A.; Mecerreyes, D.; Taton, D.; Cramail, H.; Hedrick, J. L. Synthesis of Polyurethanes Using Organocatalysis: A Perspective. *Macromolecules* **2015**, *48*, 3153-3165.
- (26) Niyogi, S.; Sarkar, S.; Adhikari, B. Catalytic Activity of Dbtdl in Polyurethane Formation. **2002**.
- (27) Ma, S.; Liu, C.; Sablong, R. J.; Noordover, B. A. J.; Hensen, E. J. M.; van Benthem, R. A. T. M.; Koning, C. E. Catalysts for Isocyanate-Free Polyurea Synthesis: Mechanism and Application. *ACS Catalysis* **2016**, *6*, 6883-6891.
- (28) Maisonneuve, L.; Lamarzelle, O.; Rix, E.; Grau, E.; Cramail, H. Isocyanate-Free Routes to Polyurethanes and Poly(Hydroxy Urethane)S. *Chemical Reviews* **2015**, *115*, 12407-12439.
- (29) Zhang, M.; Hemp, S. T.; Zhang, M.; Allen, M. H.; Carmean, R. N.; Moore, R. B.; Long, T. E. Water-Dispersible Cationic Polyurethanes Containing Pendant Trialkylphosphoniums. *Polymer Chemistry* **2014**, *5*, 3795-3803.
- (30) Bräse, S.; Gil, C.; Knepper, K.; Zimmermann, V. Organic Azides: An Exploding Diversity of a Unique Class of Compounds. *Angewandte Chemie International Edition* **2005**, *44*, 5188-5240.